Advanced Structured Materials

Volume 4

Series Editors

Andreas Öchsner
Lucas F. M. da Silva
Holm Altenbach

For further volumes:
http://www.springer.com/series/8611

Andreas Öchsner · Ali Shokuhfar
Editors

New Frontiers of Nanoparticles and Nanocomposite Materials

Novel Principles and Techniques

Springer

Editors
Andreas Öchsner
Faculty of Biosciences and Medical Engineering (FBME)
Universiti Teknologi Malaysia
Johor Bahru
Malaysia

Ali Shokuhfar
Faculty of Mechanical Engineering
Khajeh Nasir Toosi University of Technology
Tehran
Iran

ISSN 1869-8433 ISSN 1869-8441 (electronic)
ISBN 978-3-642-14696-1 ISBN 978-3-642-14697-8 (eBook)
DOI 10.1007/978-3-642-14697-8
Springer Heidelberg New York Dordrecht London

Library of Congress Control Number: 2013930453

Printed on acid-free paper

Springer is part of Springer Science+Business Media (www.springer.com)

Preface

In the heart of so-called nanotechnology, one can engineer the finest building blocks of atoms and molecules to achieve outstanding properties and qualities of materials and create nanostructured materials or nanomaterials. Nanomaterials include atomic clusters, layered films, filamentary structures, and bulk nanomaterials. More precisely nanomaterials are materials with at least one dimension in the range of 1–100 nm. They consist of atoms or clusters of single or mixed elements, all packed together to form a nanoparticle or at a larger scale, a bulk nanomaterial and in a special case a nanocomposite.

The development of nanomaterials opens the possibility for new materials with outstanding properties compared to classical engineering materials. These materials can find applications in different fields such as medical treatment or structural mechanics. This monograph focuses on two major groups of nanomaterials, i.e., nanoparticles and nanocomposites. Nanoparticles, for example in the form of hollow particles, allow for new possibilities in drug delivery. Different aspects of nanoparticles ranging from manufacturing to modeling and simulation are covered. Nanocomposite materials are formed by mixing two or more dissimilar materials at the nanoscale in order to control and develop new and improved structures and properties. The properties of nanocomposites depend not only on the individual components used but also on the morphology and the interfacial characteristics. Nanocomposite coatings and materials are one of the most exciting and fastest growing areas of research and novel properties being continuously developed which were previously unknown in the constituent materials. Thus, the second part of this monograph gives an overview on the latest developments in the area of composites based on nanomaterials.

Andreas Öchsner
Ali Shokuhfar

Contents

Part I
Nanoparticles

Recent Progress in Fabrication of Hollow Nanostructures

Ryusuke Nakamura and Hideo Nakajima

Abstract Hollow nanostructures are of great interest in many current and emerging areas of technology. In the last few years, a variety of ideas to fabricate hollow nanostructures (e.g., hollow nanospheres, nanoboxes, nanocages, and nanotubes) have been proposed. This review work covers several typical methods to fabricate hollow nanoparticles and nanotubes. The methods introduced in this article are categorized into two parts: one is based on the chemical synthesis routes including conventional templating-etching and galvanic replacement and the other is based on the Kirkendall effect, which is a diffusional phenomena at the solid–solid interface. Furthermore, structural stability of hollow nanoparticles and nanotubes during annealing at high temperatures is discussed.

1 Introduction

In recent years, considerable effort has been put into the design and fabrication of nanostructured materials with functional properties (e.g., nanoparticles, nanorods, etc.) [1]. Above all, it is important to obtain nanostructures with a specific size and morphology, taking into consideration their specific applications. Therefore, the control of the shape of nanoparticles and nanowires is one of the most important topics in the current research on nanomaterials. In particular, there is an increasing

R. Nakamura (✉) and H. Nakajima
The Institute of Scientific and Industrial Research, Osaka University,
Mihogaoka 8-1, Ibaraki, Osaka 567-0047, Japan
e-mail: rnakamur@sanken.osaka-u.ac.jp

H. Nakajima
e-mail: nakajima@sanken.osaka-u.ac.jp

Adv Struct Mater (2013) 4: 3–30
DOI: 10.1007/8611_2010_42

Published Online: 17 November 2010

interest in methods to fabricate hollow nanostructures because their unique shape makes them applicable as delivery vehicles, fillers as well as for catalysis, and is expected to bring about changes in chemical, physical, and catalytic properties. The recent progress in synthesis and applications of hollow nanoparticles and nantoubes has been already reviewed by Xia et al.[2], Fan et al. [3], Lou et al. [4], and An and Hyeon [5].

In general, the most popular concept of methods to fabricate hollow nanostructures can be recognized as the combination of templating, coating and chemical etching. By coating the surface of the template nanoparticles or nanowires and removing the template by chemical etching, a wide variety of materials with hollow structures have been successfully synthesized. Meanwhile, the other types of methods based on self-organization have become available; the specific phenomena such as the Kirkendall effect [6] and Ostwald ripening [7] have been applied to the fabrication of hollow nanostructures. Since Yin et al. [8] published the results of the synthesis of hollow nanoparticles using the Kirkendall effect, which is a diffusional phenomenon at the interface between different solids, in 2004, the number of reports are increasing up to now.

In this review, we will overview the recent progress on the fabrication of hollow nanostructures: first the reports based on chemical synthesis routes and next on the Kirkendall effect. In the last section, our latest studies on the structural stability of hollow nanoparticles and nanotubes at high temperatures will be introduced in detail.

2 Fabrication Routes to Hollow Nanostructures

2.1 Techniques Based on Chemical Routes

The combination of templating and etching is a conventional route to fabricating hollow nanostructures. In general, it involves the four steps illustrated in Fig. 1 [4] (1) preparation of hard templates (usually polymer or silica); (2) functionalization/

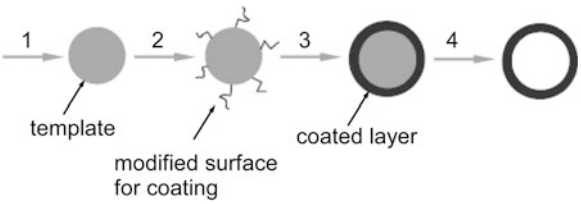

Fig. 1 Schematic illustration of a conventional hard templating process for hollow sphere synthesis. (*1*) preparation of hard templates such as polymer and silica, (*2*) modification of template surface, (*3*) coating the templates with designed materials, and (*4*) removal of templates and formation of hollow structures (reproduced with permission from [4])

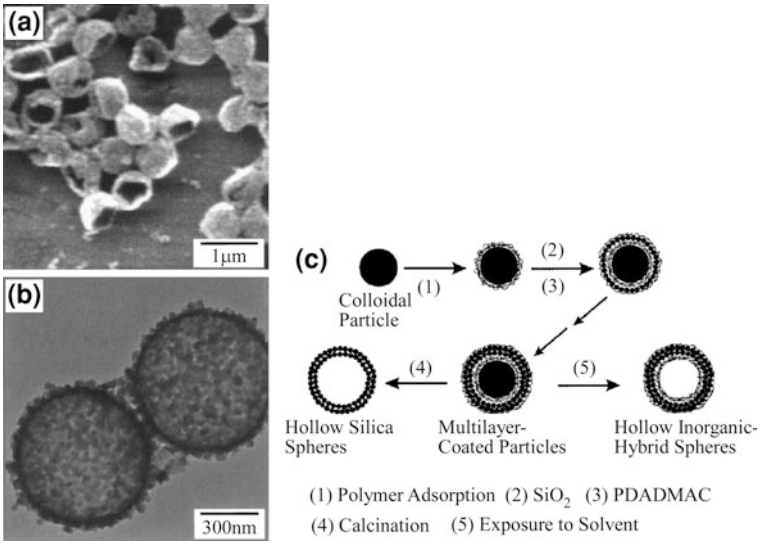

Fig. 2 **a** SEM and **b** TEM micrographs of hollow silica spheres produced by calcination of PS(Polystyrene) latices coated with one SiO_2-PDADMAC(poly-di-allyl-dimethyl-ammonium-chloride) multilayer. Both broken and intact hollow spheres were observed in these samples. The uniformity of the wall thickness can be seen in **b**. **c** Illustration of procedures for preparing inorganic and hybrid hollow spheres (reproduced with permission from [9])

modification of templated surface to achieve favorable surface properties; (3) coating the templates with designed materials or their precursors by various approaches; and (4) selective removal of the templates to obtain hollow nanostructures. Figures 2 and 3 show examples of hollow SiO_2 [9] and Pd [10] on the basis of the templating and etching methods, respectively. For example, the synthesis process of hollow Pd is as follows: (1) The uniform silica spheres were synthesized, (2) the surfaces of the silica spheres were functionalized with mercaptopropylsilyl (MPS) groups by refluxing the silica spheres and mercaptopropyltrimethoxysilane ($HS(CH_2)_3$-$Si(OCH_3)_3$) in toluene, (3) the palladium precursor, palladium acetylacetonate ($Pd(acac)_2$), was adsorbed onto the surfaces of these MPS-functionalized silica spheres and were then heated at 250°C for 3 h to obtain Pd metal-coated spheres, and finally (4) the silica template was removed by treating the Pd-coated silica spheres with 10 M HF. The technique has also been extensively applied to obtain hollow nanoparticles of a wide range of inorganic materials, including TiO_2 [11, 12], SnO_2 [13], Au [14], Fe_3O_4 [15]. Another examples are reviewed by Lou et al. [4], who categorized the conventional hard templating methods into six groups according to coating process. Furthermore, Lou et al. [4] summarized soft-template methods using liquid and gaseous templates against hard templates using solid materials.

The disadvantage of the template-mediated methods were pointed out by An and Heyon [5]; (1) the hollow nanostructures obtained via a template-mediated

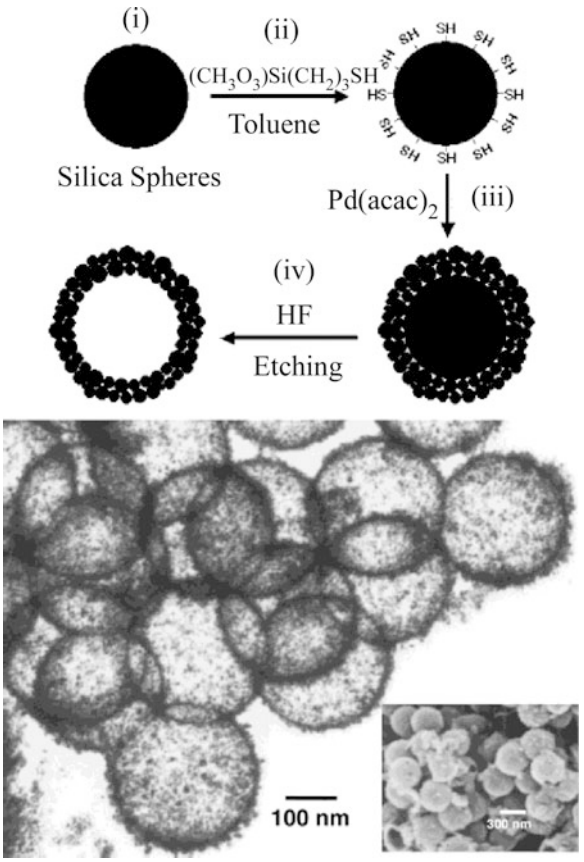

Fig. 3 Transmission electron micrograph and scanning electron micrograph (*inset*) of hollow palladium spheres and illustration of synthesis process: (*i*) preparation of uniform silica spheres, (*ii*) the functionalization of the surfaces of the silica spheres with mercaptopropylsilyl (MPS) and mercaptopropyl-trimethoxysilane ($HS(CH_2)_3$-$Si(OCH_3)_3$) in toluene, (*iii*) adsorption of the palladium precursor, palladium acetylacetonate ($Pd(acac)_2$) onto the surfaces of these MPS-functionalized silica spheresand and heating at 250°C for 3 h to obtain Pd metal-coated spheres, and finally (*iv*) removal of the silica template by treating the Pd-coated silica spheres with 10 M HF (reproduced with permission from [10])

route using silica or polymer particles as the templates are often larger than 200 nm because it is hard to make smaller template particles and (2) the post-treatment necessary to remove the templates adds complexity to the whole synthetic process and increases the chance of the structural deformation as well as the introduction of impurities.

This idea is also useful for fabricating nanotube structures. For example, GaN nanotubes were fabricated through the preparation of ZnO/GaN core/shell structures and the subsequent removal of ZnO nanowires, as shown in Fig. 4 [16]. The arrays of ZnO nanowires were grown on (110) sapphire wafers using a vapor deposition process and then GaN chemical vapor was deposited epitaxially on the ZnO nanowire arrays placed inside a reaction tube. The core part of ZnO can be removed from ZnO/GaN wires by chemical etching with ammonia at high temperature or thermal reduction at high temperatures (for example, 873 K in H_2). The synthesis of Zn_3P_2, Cd_3P_2 [17] and Al_2O_3 [18] nanotubes based on templating and etching method were also reported.

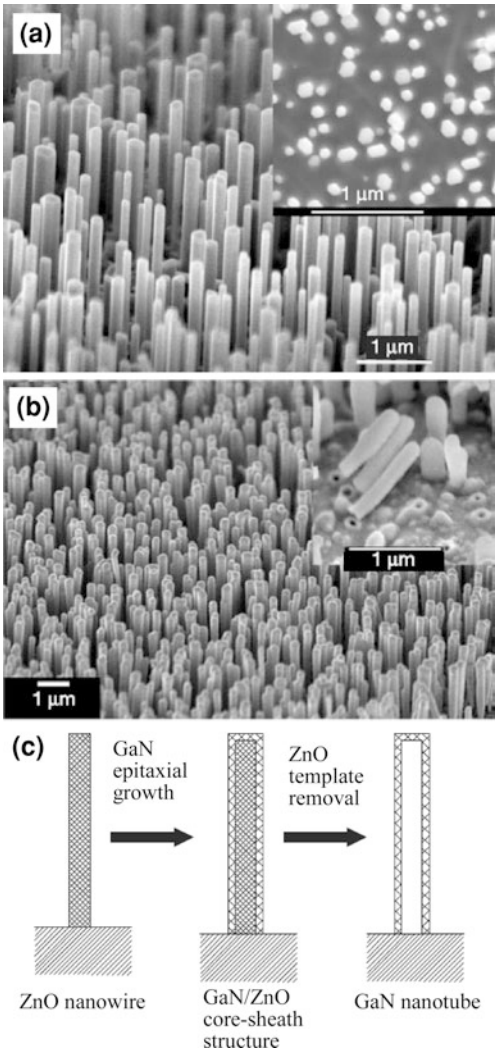

Fig. 4 Arrays of ZnO nanowires and GaN nanotubes. Shown are SEM images of the ZnO nanowire template arrays (**a**), and the resulting GaN nanotube array (**b**). *Inset* in **a** shows cross-sections of the ZnO nanowires. *Inset* in **b** shows the fractured interface between the GaN nanotubes and the substrate. **c** Schematic illustration of the 'epitaxial casting' process for making single-crystal GaN nanotubes (reproduced with permission from [16])

Schmidt and Eberl [19, 20] showed that layered Si-Ge rolled up to form nanoscrolls by strain release of the lattice-mismatched film-substrate interface. Figure 5 shows illustrations of the mechanisms and the obtained nanotubes according to the mechanisms: (a) General method to create a nanotube (method I). An etchant-sensitive material is deposited on a substrate surface. On top of this substrate, a thin film (or a series of thin films) is deposited. After selective etching of the substrate, the thin top layer is wrapped up and folded back onto the sample surface, where it can bond to itself. At the position where the layer bends, a nanotube has formed. (b) Specialized way to create a nanotube (method II). The layer sequence consists of an etchant-sensitive material, followed by a bilayer of

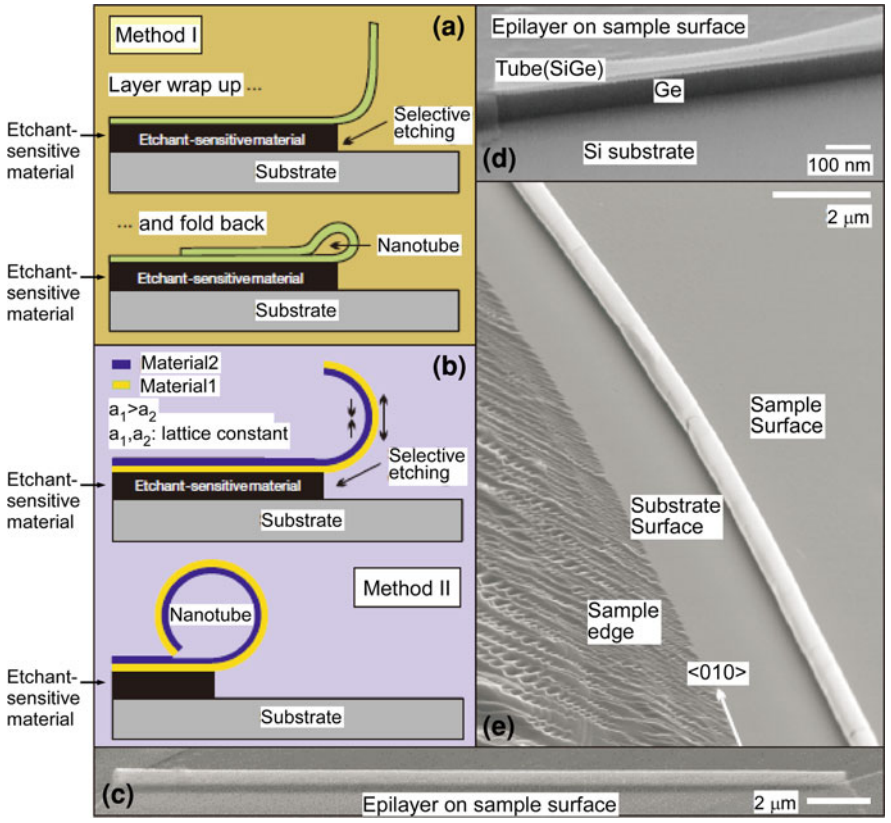

Fig. 5 Formation of solid-state nanotubes. **a** General method to create a nanotube (method I). **b** Specialized way to create a nanotube (method II). **c**, **d** Folded nanotubes fabricated according to method I. 'Epi' layer indicates epitaxial layer. **e** SiGe-based nanotube formed along the edge of a sample (by method II) (reproduced with permission from [19])

two different materials (materials 1 and 2). Material 1 has a larger lattice constant than material 2, so $a_1 > a_2$. Once the bilayer is released by selective etching, each material tends to acquire its inherent lattice constant. The bilayer bends upwards, finally forming a nanotube after one complete revolution. Longer etching times result in multiple revolutions. (c, d) Folded nanotubes fabricated according to method I. 'Epi' layer indicates epitaxial layer. (e) SiGe-based nanotube formed along the edge of a sample (by method II). Although this technique is based on the combination of templating and etching, the process of rolling up is different from the typical templating methods introduced above.

The galvanic replacement reaction has been applied for the synthesis of hollow nanostructures of novel metals such as Au, Pt and Pd. In the synthetic process for hollow Au nanoboxes or frames, for example, $HAuCl_4$ is added to the suspension of Ag nanocubes with the amount of $HAuCl_4$ and reaction temperature

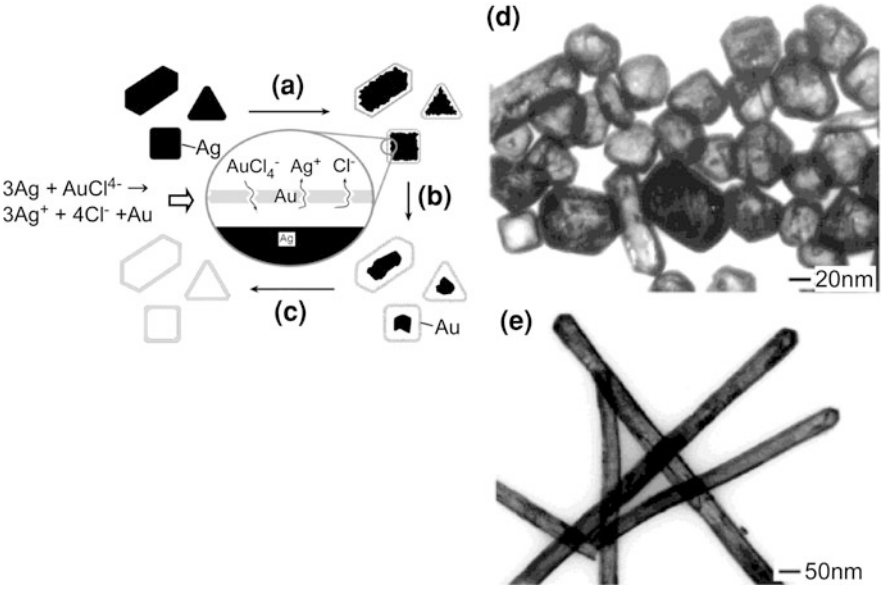

Fig. 6 Schematic illustration of the experimental procedure that generates nanoscale shells of gold from silver templates with various morphologies. The reaction is illustrated in the schematic as follows: **a** Addition of $HAuCl_4$ to a dispersion of silver nanoparticles and initiation of the replacement reaction; **b** The continued replacement reaction of $HAuCl_4$ with the silver nanoparticles; **c** Depletion of silver and annealing of the resultant shells to generate smooth hollow structures. **d**, **e** TEM image of gold nanoshells and nanotubes formed by reacting these silver nanoparticles with an aqueous $HAuCl_4$ solution (reproduced with permission from [21])

being controlled. The silver template-mediated galvanic replacement reaction is described as follows:

$$3Ag(s) + AuCl_4^-(aq) \rightarrow Au(s) + 3Ag^+(aq) + 4Cl^-(aq)$$

In the reaction, Ag nanoparticles act as a template. SEM images of the formation of Au nanoboxes and nanocages using the above reaction are shown in Fig. 6 [21]. According to the amount of $HAuCl_4$, the nanostructures develop; Au/Ag nanoboxes interior nanoholes → Au nanoboxes with uniform wall thickness → Au nanoframes with porous walls. Similarly, Pt/Ag and Pd/Ag hollow nanostructures have been prepared via the galvanic replacement because both $PtCl_4^-$ and $PdCl_4^{2-}$ ions have higher standard reduction potential than AgCl/Ag pair [22]. It has been pointed out that despite the simplicity of the chemistry, the formation mechanism of hollow structures via the galvanic replacement can be complicated, depending on the reaction system [23].

Finally, an example of template-free methods is introduced. Recently, one-step self-templated methods based on Ostwald ripening have been applied to synthesize hollow structures. Ostwald ripening, first described by Ostwald in 1896 [7], is a spontaneous process which refers to the growth of large precipitates at the expense

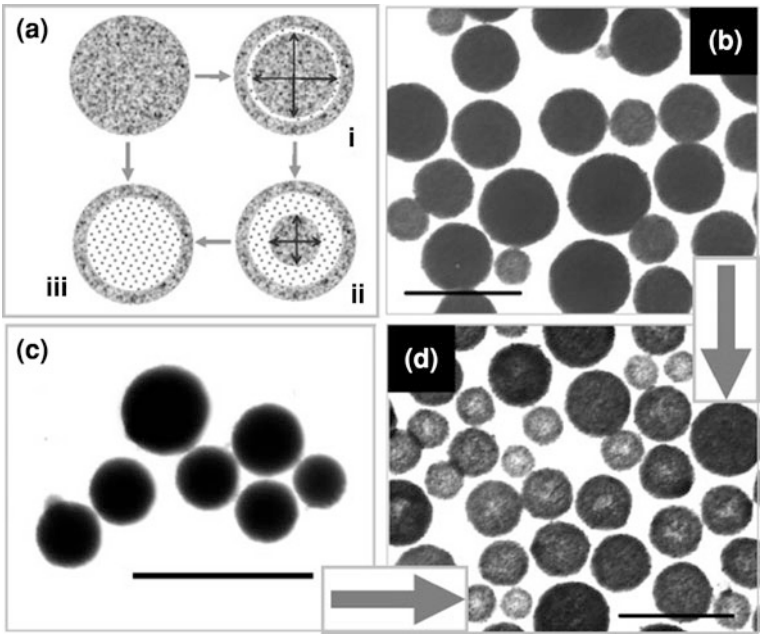

Fig. 7 **a** Schematic illustration (cross-sectional views) of the proposed inside-out ripening mechanism: inside-out evacuation can initiate from just below the surface to form particle (*i*) then evolve to core/shell particle (*ii*), and possibly to hollow particle *iii*, or start around the central region of the solid spheres and evolve to particle (*iii*) directly. **b** Typical TEM image of SnO_2 nanospheres obtained with 6 h reaction at 150°C (r = 37.5%, c = 14.0 mM, 0.1 M urea). **c** Typical TEM image of amorphous SnO_2 nanospheres obtained by aging the reaction mixture (r = 37.5%, c = 14.0 mM, 0.1 M urea) for several days at room temperature. D) Typical TEM image of SnO_2 hollow nanospheres synthesized at 150°C for 24 h with the reaction mixture (r = 37.5%, c = 14.0 mM, 0.1 M urea) aged for several days (corresponding to **c**) or without aging (18 h further reaction based on **b**). All three *scale bars* 500 nm (reproduced with permission from [24])

of smaller precipitates caused by energetic factors. Lou et al. [24] reported a simple one-pot template-free synthesis of polycrystalline SnO_2 hollow nanostructures, as shown in Fig. 7. At the initial stage of reaction, amorphous solid nanospheres are formed by hydrolyzation of stannate. With time, the surface layer of the nanospheres crystallizes first due to contact with surrounding solution. As a result, the materials inside the solids spheres have a strong tendency to dissolve, which provides the driving force for the spontaneous inside-out Ostwald ripening. Although fundamental evidence in support of this mechanism is not enough, it has been shown to be applicable in many systems, including TiO_2 [25], Cu_2O [26], ZnS and Co_3O_4 [27], etc. These hollow materials were synthesized through chemical reaction processes. Therefore, they have been introduced in this section although Ostwald ripening itself is not defined as a chemical reaction.

2.2 Kirkendall-Effect-Related Methods

2.2.1 Hollow Nanoparticles

Kirkendall effect as a classical phenomenon in metallurgy was established [6]. It basically refers to a nonreciprocal mutual diffusion process through an interface of two metals so that vacancy diffusion occurs to compensate for the unequality of the mass flow and that the initial interface moves. Smigelskas and Kirkendall observed a movement of the initial interface in a Cu/brass diffusion couple, as a result of a faster diffusion of zinc into the copper than that of copper into the brass (the intrinsic diffusion coefficient of Zn is 2.5 times as large as that of Cu at 785°C.) The Kirkendall experiment demonstrated two important facts: (1) atomic diffusion occurs via vacancies and (2) each metal diffuses at a different mobility. In some cases, condensation of excess vacancies can give rise to void formation, called 'Kirkendall voids', near original interface and within the faster diffusion side.

Formation of the Kirkendall voids is basically unfavorable from the viewpoint of technological application. Engineers try to avoid this effect in the case that interdiffusion occurs at the bonded-interface because the Kirkendall voids deteriorate the bonding strength of the bond-pad interface or may cause wire bond failure in integrated circuits. On the other hand, chemists applied the destructive effect constructively for synthesizing hollow nanostructures in a way that the Kirkendall voids coalesce into a single hollow core. Yin et al. [8] demonstrated that initially solid Co nanoparticles transformed into hollow nanoparticles through the reaction with sulfur, oxygen and selenium. An example of hollow cobalt sulfides is shown in Fig. 8. The sulfidation of cobalt nanoparticles resulted in the formation of hollow cobalt sulfide of either Co_3S_4 or Co_8S_9, depending on the molar ration of sulfur and cobalt. During the reaction, the surfaces of cobalt nanoparticles are covered with the sulfide layers and the diffusion of cobalt and sulfur atoms in opposite direction occurs through the sulfide layers. As the reaction proceeds, voids are formed in the cobalt side of the interface because the outward diffusion of cobalt ions is much faster than the inward diffusion of sulfur.

Their work has inspired a number of studies that attempt to apply the nanoscale Kirkendall effect to create hollow nanostructures [28–56]. Nanoscale hollow structures by a route related to the Kirkednall effect are listed in Table 1, where some reports published after 2007 were added to the original list given by Fan et al. [3]. Particularly, hollow oxide formation via oxidation of metal nanoparticles was investigated relatively for many metals such as Al, Cu [31], Fe [41–44], Ni [46] and Zn [52–54]. Nakamura et al. [31] demonstrated that a reaction of Pb nanoparticles with oxygen resulted in the formation of solid PbO because the diffusivity of oxygen is known to be larger than that of Pb in PbO, suggesting that the faster outward diffusion of metal ions than inward diffusion of oxygen ions is essential for the formation of hollow oxides through oxidation reaction.

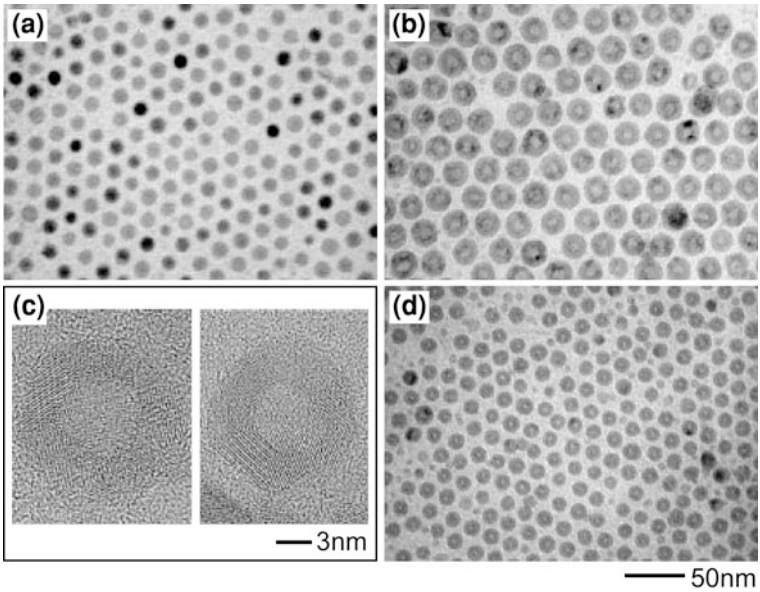

Fig. 8 **a** TEM image of cobalt nanocrystals synthesized by the injection of 0.54 g of $Co_2(CO)_8$ in 3 ml of o-dichlorobenzene into 0.1 ml of oleic acid and 0.1 g of trioctylphosphine oxide in 15 ml of *o*-dichlorobenzene at 182°C. **b** TEM image of the cobalt sulfide phase synthesized by the injection of sulfur in *o*-dichlorobenzene (5 ml) into cobalt nanocrystal solution with a Co/S molar ratio of 9:12. Co_3S_4 particles were synthesized from the cobalt sample shown in **a**. **c** HRTEM images of Co_3S_4 (*left*) and Co_9S_8 (*right*). **d** TEM image of the cobalt sulfide phase synthesized as in **b** (reproduced with permission from [8])

During the oxidation or sulfidation of metal nanoparticles, voids are formed at the interface. Tokozakura et al. [57] showed that voids formed at the interface retard the outward diffusion of remaining metals.

Formation of hollow oxide nanoparticles was found at low temperatures for Fe, Al and Zn. Nakamura et al. observed that in the case of smaller Zn (below 20 nm in diameter) and Al (below 8 nm in diameter) nanoparticles, the rapid outward migration of metal ions at the initial oxidation stages makes hollow oxide particles and that larger hollow oxide particles could not be formed by thermal oxidation at around 400 K. The fast outward diffusion of metal cations through the oxide layer is not thermally activated but driven by an electrical field built between the metal and an initial thin oxide layer according to the Cabrera–Mott theory. On the other hand, Cu nanoparticles were observed to turn into hollow Cu_2O regardless of initial diameter probably because the self-diffusion coefficient of Cu ions in Cu_2O at around 400 K is high enough to explain the growth of the Cu_2O layer via the thermal-activated diffusion process after the initial oxide formation.

Although hollow oxides with an almost uniform shell thickness were formed in the case of Co, Fe, Cu, and Al, a peculiar behavior of void formation during the oxidation of Ni nanoparticles can be seen [46]. In Fig. 9, the morphology change

Table 1 Hollow nanoparticles and nanotubes fabricated through the Kirkendall effect

Materials	Morphology	Ref.	Publication year
Ag_2Se	Nanotubes	[28]	2006
AlN	Hollow particles	[29]	2006
	Hollow particles	[30]	2007
Amorphous Al_2O_3	Hollow particles	[31]	2007
CdS	Polycrystal nanoshell	[32]	2005
Co_3S_4, CoO, CoSe	Hollow particles	[8]	2004
Co_3S_4	Porous nanowires	[33]	2006
	Nanotubes	[34]	2007
Co_3S_4, $CoSe_2$, CoTe	Hollow nanochains	[35]	2006
$CoSn_3$	Hollow nanorods	[36]	2008
Cu_2O	Hollow nanoparticles	[31]	2007
CuO	Hollow nanoparticles	[37]	2008
Cu_2O, CuO	Nanotubes	[38]	2009
CuS	Nanotubes	[39]	2007
Cu_7S_4	Nanocages	[40]	2005
Fe_xO_y	Hollow nanoparticles	[41]	2005
Fe_3O_4	Hollow nanoparticles	[42]	2007
γFe_2O_3	Hollow nanoparticles	[43]	2007
Fe_3O_4, γFe_2O_3	Hollow and porous nanoparticles and nanotubes	[44]	2009
MoS_2	Cubic microcages	[45]	2006
NiO	Hollow nanoparticles	[46]	2008
	Bamboo-like nanowires	[38]	2009
Ni_2P, Co_2P	Hollow nanoparticles	[47]	2007
SnO_2	Hollow nanoparticles	[48]	2008
PbS	Hollow nanoparticles	[49]	2005
$ZnAl_2O_4$	Nanotubes	[50, 51]	2006,2007
ZnO	Microcages	[52]	2004
	Dandelion	[53]	2004
	Hollow nanoparticles	[54]	2007
	Nanotubes	[55]	2008
$ZnSiO_4$	Nanotubes	[56]	2007

of Ni nanoparticles (1) after oxidation at 573 K for 7.2 ks and (2) at 673 K for 1.8 ks are shown. A single large void is formed at one off-center site of the interface between Ni and NiO (Fig. 9a) and hollow oxide nanoparticles with the nano-pores at localized position are formed (Fig. 9b). Although the formation mechanism of the nano-pore in NiO particles is similar with other hollow oxides such as Co-, Zn-, and Cu-oxides, hollow NiO has a peculiar morphology unlike them. The formation mechanism of a single localized void at the Ni/NiO interface during oxidation and an off-centered nano-pore in hollow NiO particles is discussed in terms of the atomic movement during oxidation. The growth behavior of the voids during the oxidation of Ni nanoparticles observed in Fig. 9a indicates that vacancies migrate toward a site of the interface and then become a large void at the site.

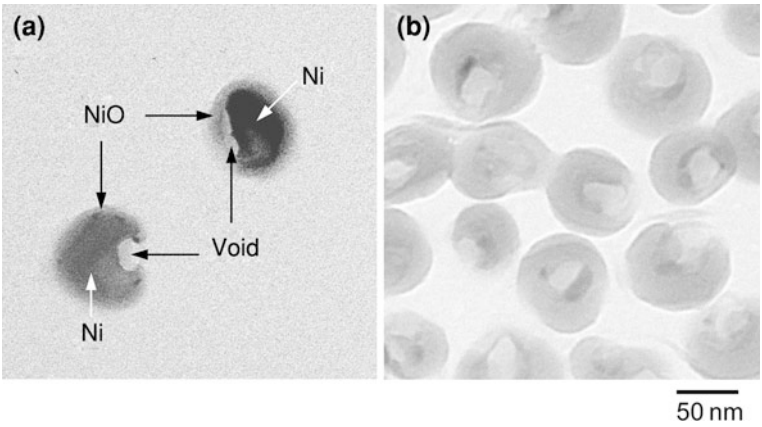

Fig. 9 TEM images of Ni nanoparticles after oxidation at **a** 300°C for 7.2 ks and **b** 400°C for 1.8 ks (reproduced with permission from [46])

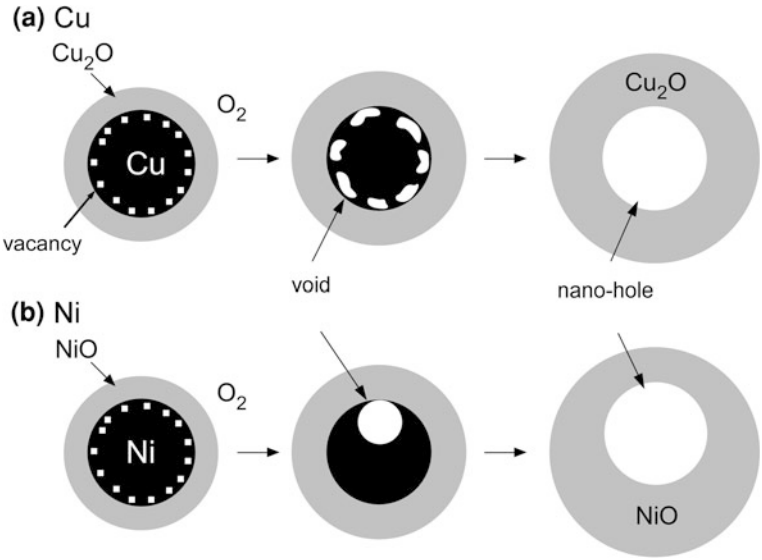

Fig. 10 Comparison of void formation behavior for oxidation of Cu nanoparticles with Ni nanoparticles (reproduced with permission from [46])

The formation of vacancies, voids and a nano-hole through the oxidation of Cu and Ni nanoparticles is illustrated in Fig. 10a, b, respectively. Vacancies are generated along the metal-side interface as a result of the outward diffusion of metal ions at the initial stage of oxidation. As oxidation proceeds, voids are formed uniformly along the Cu/Cu_2O interface by the clustering of neighboring vacancies (Fig. 10a), while they become large voids at one site on the Ni/NiO interface

(Fig. 10b) because of the long-range diffusion of vacancies. As a result, a nanohole is formed at the center part of Cu_2O particles, but it is off-centered in NiO particles. Vacancies generated in the oxidation process of Ni nanoparticles migrate to and aggregate at a site of the Ni/NiO interface since the mobility of vacancies inside Ni is large as the oxidation proceeds. This behavior can be interpreted as the self-assembly of vacancies and this allows an energetically more stable state to be achieved.

In general, the mechanism of metal sulfidation is known to be similar to that of metal oxidation. There are lots of reports on the formation of hollow sulfide nanoparticles such as Cu–S [39, 40], MoS_2 [45], and PbS [49].

2.2.2 Nanotubes

The Kirkendall effect has been extended to the fabrication of tubular structures. Fan et al. [50] demonstrated that $ZnAl_2O_4$ spinel nanotubes could be obtained using the Kirkendall effect. Figure 11 shows TEM images for the nanotubes together with the schematic illustrations of the formation process. As shown in the illustration, the starting material is a ZnO nanowire (10–30 nm thick, up to 20 μm long) coated by Al_2O_3 (10 nm thick). By annealing the core/shell nanowires, in air at 700°C for 3 h, a cylindrical interior nanopore is introduced during the solid-state diffusion between ZnO and Al_2O_3· ZnO/Al_2O_3 reaction is considered as a one-way transfer of ZnO into Al_2O_3 in a pseudo binary system. They pointed out that the conformity and uniformity of Al_2O_3 layers via atomic-layer-deposition are essential to the formation of smooth nanotubes. They reported that completely hollow $ZnAl_2O$ nanotubes could be obtained, whereas in the case of MgO/Al_2O_3, only porous $MgAl_2O_4$ nanowires were obtained without formation of complete nanotubes. They concluded that the difference in final morphology is attributed to that in crystal structure and diffusion of metal ions. Additionally, Fan et al. [51] showed the surface diffusion on the morphology evolution; the initial stage is the generation of small Kirkendall voids intersecting the compound interface via a bulk diffusion process, whereas the second stage is dominated by the surface diffusion of the core materials along the pore surface.

Another example of the formation of nanotubes through the Kirkendall effect is Ag_2Se [28]. TEM images of obtained Ag_2Se nanotubes are shown in Fig. 12, together with the schematic illustrations of the formation process. CSe_2 was first adsorbed onto the surfaces of the Ag nanowire templates, and subsequent photolysis causes the dissociation of C=Se bonds, giving rise to a high surface concentration of Se atoms. Ag_2Se layers are formed on the surface of Ag nanowires at 160°C and then growth of Ag_2Se layers is dominated by the outward diffusion of Ag^+ ions through the layer. The authors mentioned that the voids were observed to grow horizontally along the wire axis rather than isotropically because the adhesion of CSe_2 is preferred on the ends of the Ag nanowire rather than on its side faces. Hence, the high concentration of Se atoms at the nanowire ends promotes the diffusion of Ag^+ along the longitudinal axis, leading to the observed

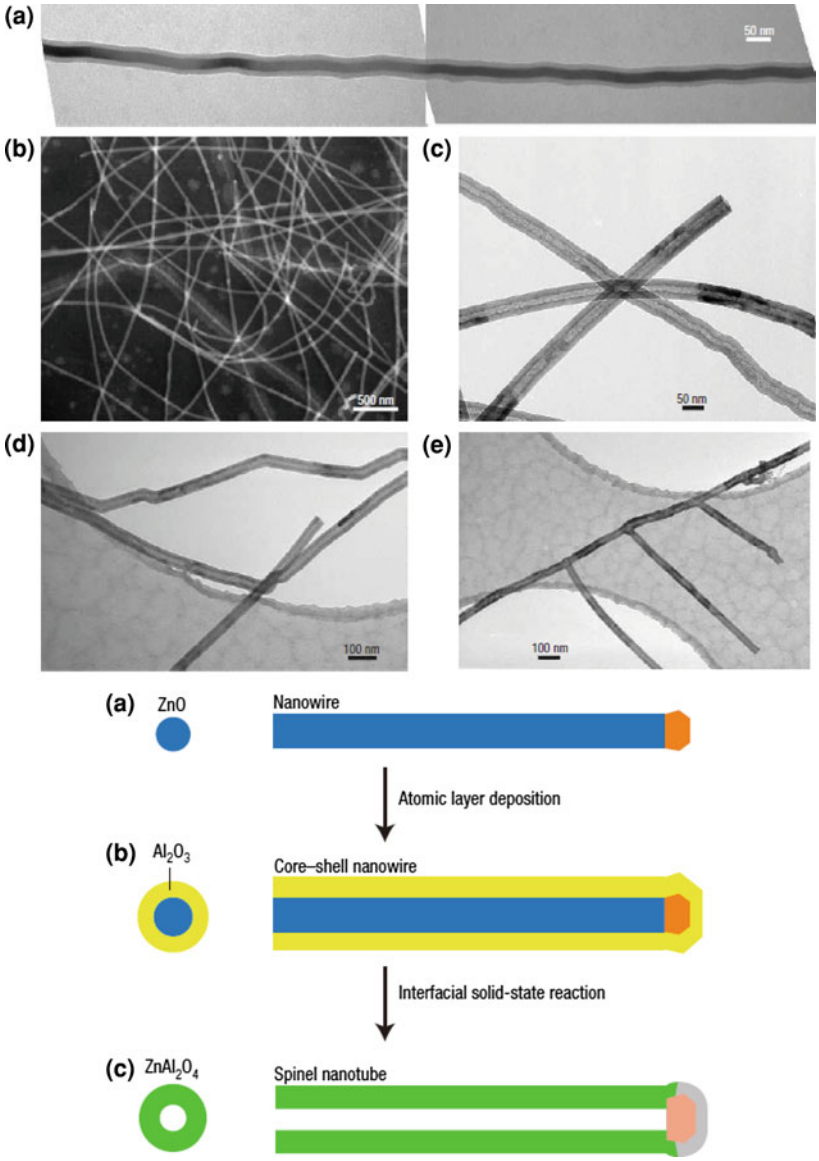

Fig. 11 Transformation of core–shell nanowires to nanotubes by means of the Kirkendall effect (*upper*). **a** TEM image of an example ZnO-Al_2O_3 core–shell nanowire. **b–e** Scanning electron microscopy (**b**) and TEM (**c–e**) images of $ZnAl_2O_4$ spinel nanotubes. Schematic diagram of the formation process of $ZnAl_2O_4$ spinel nanotubes (*lower*). **a** Single-crystal ZnO nanowires are grown by the vapor–liquid–solid mechanism using Au nanoparticles as a catalyst. **b** The nanowires are coated with a uniform layer of Al_2O_3 by ALD, forming core–shell ZnO–Al_2O_3 nanowires. **c** Annealing the core–shell nanowires leads to the formation of $ZnAl_2O_4$ nanotubes by a spinel-forming interfacial solid-state reaction involving the Kirkendall effect (reproduced with permission from [50])

anisotropic growth of vacancies along ⟨110⟩. This represents a different strategy of applying the Kirkendall effect to nanotube formation from the one presented in Fig. 11.

As mentioned in 2.2.1, the oxidation of metal nanoparticles is an effective route to fabricating hollow oxides because several metal nanoparticles such as Co, Cu, Fe, Zn, and Al turn into hollow oxide nanoparticles. It is expected, therefore, that the oxidation of such metal nanowires causes the formation of oxide nanotubes. Our latest results on the formation of oxide nanotubes through the oxidation of Fe, Cu and Ni nanowires [38] are introduced below.

Figure 13 shows the morphology changes of Fe, Cu and Ni nanowires before and after oxidation at 200–400°C. Voids were clearly observed along the interface

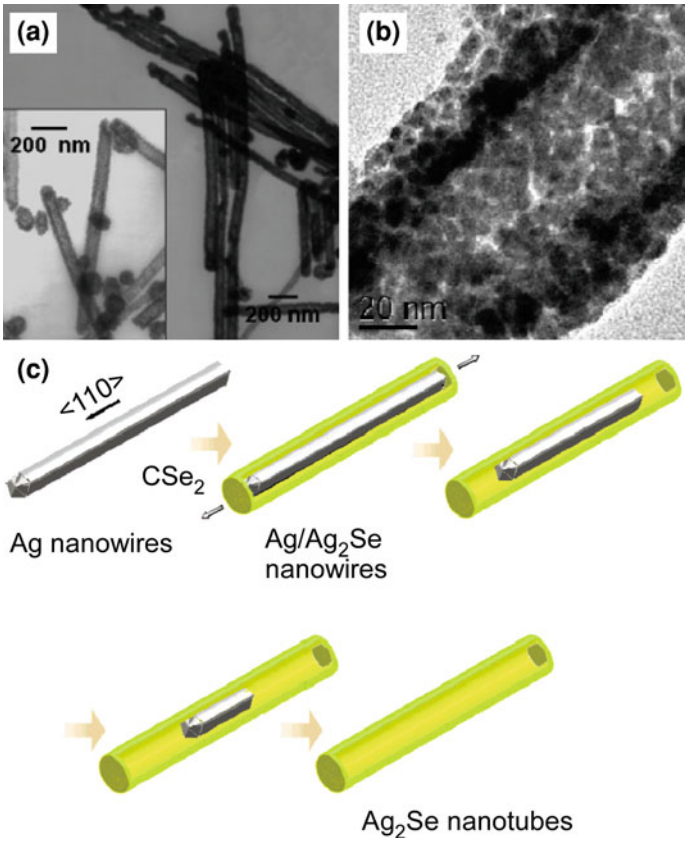

Fig. 12 Ag_2Se nanotubes formed based on the Kirkendall effect. **a** TEM image of the tubes. **b** Higher-magnification view of the tube showing that the tube wall is composed of multiple grains. **c** Schematic images of the diffusion process. Due to the higher concentration of CSe_2 adsorbed at the end (111) faces than on the side (100) faces of the Ag nanowires, the void grows along the longitudinal ⟨110⟩ direction from the ends. (Reproduced with permission from Ref. [28])

between the Fe nanowire and the outer oxide layer at 250°C for 3.6 ks. Finally, a Fe nanowire turned into a Fe_3O_4 (magnetite) nanotube with a cylindrical nanopore at 300°C for 3.6 ks. Similarly, interior voids with different sizes are fragmentarily generated inside the Cu nanowires after oxidation at 150°C for 1.2 ks. The oxidized Cu nanowires become nanotubes with a uniform inner and outer diameter at 150°C for 5.4 ks, as is the case with the oxidation of Fe nanowires. The crystal structure of the nanotubes obtained via the oxidation of the Cu nanowires at 150°C for 5.4 ks was identified to be Cu_2O. Cu_2O transformed into CuO at 300°C while maintaining the nanotube structure. In Fig. 13, representative electron micrographs of Ni nanowire after oxidation at 400 and 500°C are shown together. After oxidation at 400°C for 1.8 ks, large voids are formed at certain places at the interface between an inner remaining Ni wire and the outer oxide layer, as indicated by arrows. The formation behavior of voids at the interface between Ni and NiO is different from that between Fe and Fe_3O_4, where voids are uniformly formed along the interface. Ni nanowires became irregularly-shaped bamboo-like NiO with separate interior nanovoids of irregular diameters at 500°C for 3.6 ks.

The formation mechanism of Fe_3O_4 and Cu_2O nanotubes is illustrated in Fig. 14a; (1) an oxide layer is formed due to the oxidation reaction dominated by the outward diffusion of metal ions through the oxide layer, (2) voids are generated along the interface due to the inward diffusion of vacancies, which results from the Kirkendall effect, as the oxide layer grows, and (3) an oxide nanotube with a cylindrical pore is formed after all the metal atoms are consumed by reacting with oxygen. Fe_3O_4 and Cu_2O nanotubes obtained by oxidizing Fe and Cu nanowires have almost uniform inner and outer diameters, whereas NiO has separate interior voids and is irregular in shape. It can be expected that vacancies, which flow into the Ni side as a counter to the outward diffusion of Ni, migrate over a long-range distance, resulting in the growth of voids at certain places. A schematic illustration describing the void formation behavior during the oxidation of a Ni nanowire is shown in Fig. 14b. Vacancies, which are formed due to the outward diffusion of Ni at the interface between Ni and NiO, migrate toward a void (i). The growth of a localized void causes inhomogeneous oxide growth; the growth of the NiO layer is suppressed at the region with a void compared with the region without void in Ni (ii). As a result, a bamboo-like structure with separate interior voids and an irregular shape is formed (iii). As discussed in 2.2.1, both the localization of an interior void during the oxidation of Ni nanoparticles and nanowires seem to originate in the high mobility of vacancies in Ni during its oxidation.

3 Structural Stability of Hollow Nanostructures at High Temperatures

Thermal instability of hollow nanospheres was theoretically predicted by some groups [58–61]. Gusak et al. [59] proposed that vacancies flow outward from the

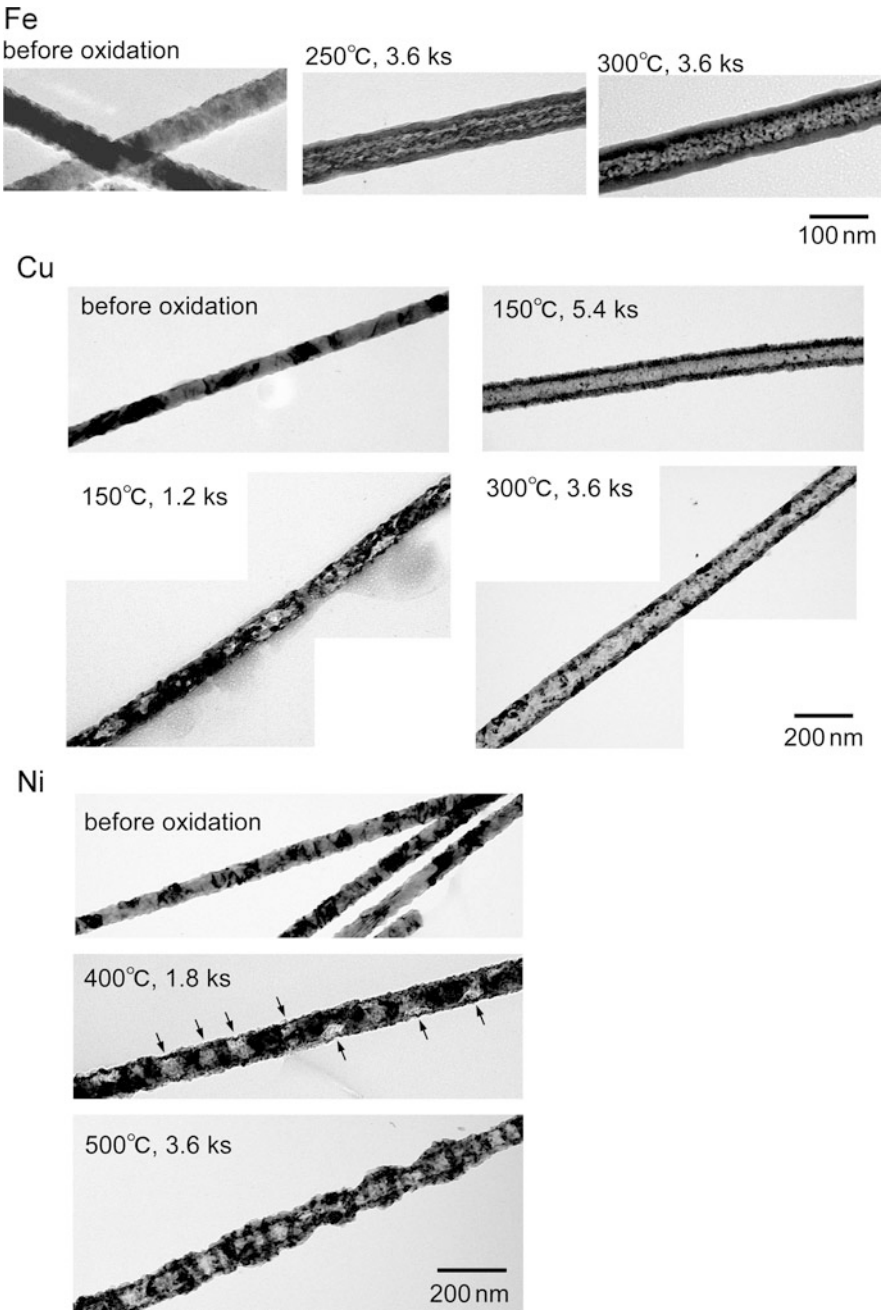

Fig. 13 TEM images of morphology change of Fe, Cu and Ni nanowires during oxidation (reproduced with permission from Ref. [38])

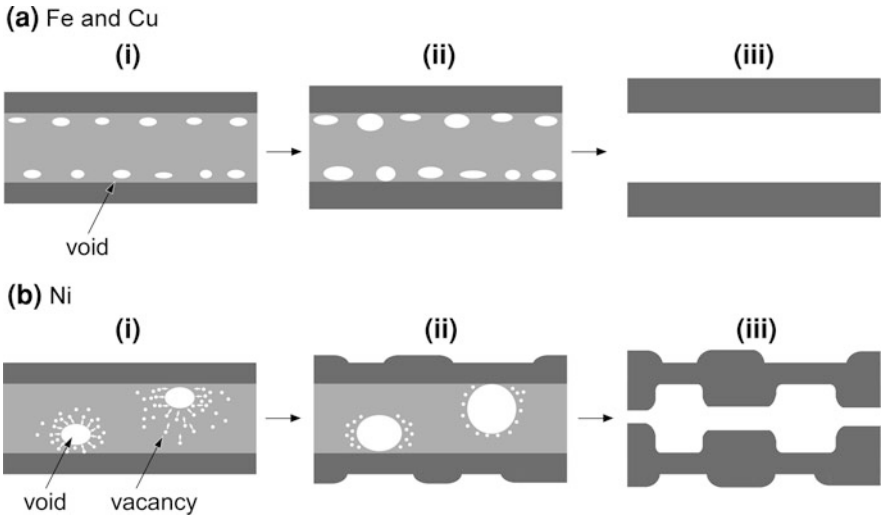

Fig. 14 Schematic illustration of morphological changes during oxidation of **a** Fe and Cu and **b** Ni: (*i*) formation of an oxide layer due to outward diffusion of metal ions through the initial oxide layer; (*ii*) formation of voids at the interface between the inner metal and outer oxide layer and (*iii*) formation of an oxide nanotube and bamboo-like structures with an interior nanopore (reproduced with permission from [38])

inner surface and absorbed at the outer surface since the vacancy concentration at the inner surface is higher than at the outer surface. As a result, the spheres shrink and finally end up eliminating the empty space to minimize the interface energy. According to their analysis, the rate of shrinking is controlled by the slow species in the case of a compound with a large difference between diffusivities of two components. On the other hand, experimental study on the stability of hollow nanostructures is limited to our reports [37, 38]. Shrinkage behavior of hollow oxide nanoparticles and nanotubes is reviewed in detail.

3.1 Shrinkage of Hollow Oxides

Figures 15a, b show changes in morphology of hollow Cu_2O and NiO nanoparticles during isochronal annealing under 4×10^{-5} Pa in a transmission electron microscope and their corresponding selected area electron diffraction (SAED) patterns [37]. The common characteristics are as follows: (i) hollow Cu_2O and NiO starts to shrink after annealing at a temperature where the reduction reactions from oxides to metals start, (ii) metal nanoparticles are formed at the inner surface of oxide shells, (iii) hollow oxides turn into metal nanoparticles without interior pores, and (iv) the changes in morphology and crystal structure through the

oxidation of metal nanoparticles and the reduction of hollow oxides can reversibly take place.

According to the kinetic models of reduction of oxides [62], oxygen ions are removed from the lattice of the surface leaving behind an anion vacancy and then

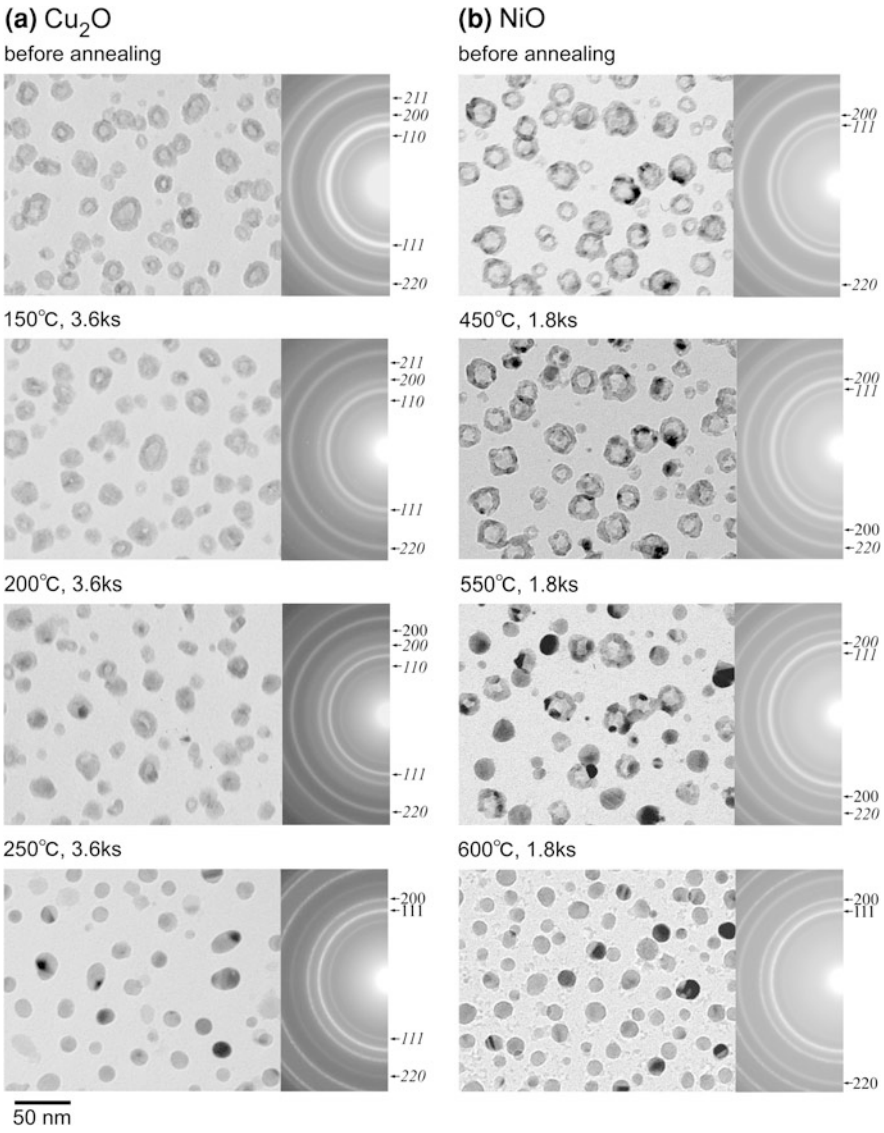

Fig. 15 Morphology changes of hollow Cu_2O and NiO nanoparticles before annealing and during isochronal annealing in TEM from 150 to 300°C. Initial diameters of hollow Cu_2O and NiO nanoparticles are 10–20 nm (reproduced with permission from [37])

reduced zone are formed on the surface at the initial stage of reduction. In general, a dominant process of reduction reaction is considered to be the outward diffusion of oxygen ions via the anion vacancies generated at the surface [62, 63]. Such mass transport results in the inward movement of the metal/reduced oxide interface. This is true of the reduction of hollow oxides; oxygen ions are removed from the outer surface to vacuum. As mentioned earlier, however, the formation of metal nanoparticles along the inner surface of hollow oxides during the reduction of Cu_2O to Cu and NiO to Ni, respectively, demonstrates that the reduced Cu and Ni atoms are generated at the inner surface of hollow Cu_2O and NiO. The formation of metal nanoparticles at the inner surface indicates that oxygen ions diffuse from the inner surface to the outer surface and that the reduced zone (i.e. Cu and Ni layers) is formed at the inner surface. After the formation of metal layers, metal atoms aggregate and make a particle in order to fill in the nano-hole. This behavior can be interpreted as the self-assembly of metal atoms which causes the extra energy of the inner surface of a hollow sphere to lower. The morphology change of hollow oxide nanoparticles annealed in reduction atmosphere is described in Fig. 16.

In the case of the annealing of hollow nanoparticles of CuO and NiO in air, shrinkage and collapse of hollow structures take place. Figures 17a, b show TEM images hollow CuO and NiO nanoparticles after annealing in air, respectively. The shrinkage of hollow CuO and NiO starts to occur at 400 and 650°C, respectively, and finally interior nanopores annihilate. CuO nanotubes and NiO bamboo-like (Fig. 13) structures also show a tendency to shrink and collapse through annealing at high temperatures, as shown in Fig. 18. It should be noted that the temperatures at which CuO nanotubes and NiO bamboo-like structures shrank are almost consistent with those for hollow nanoparticles of CuO and NiO.

According to the theoretical consideration on the shrinking of hollow binary alloy nanoparticles [59], the rate of shrinking is controlled by the slower diffusing species of the alloy. In fact, it was revealed that shrinking of both CuO and NiO by high-temperature oxidation starts at a temperature where the diffusion coefficient of the slower diffusion species reaches about 10^{-22} m^2s^{-1} [37].

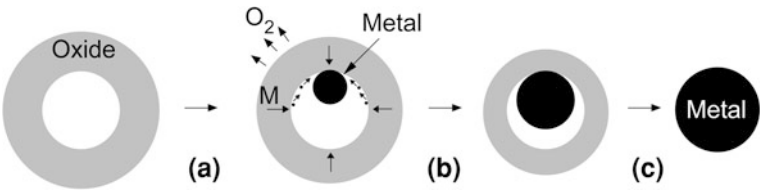

Fig. 16 Schematic illustration for morphology change of hollow oxide nanoparticles during annealing under reduction atmosphere: **a** desorption of oxygen from surface and the surface diffusion of reduced metal atoms at the inner surface, **b** growth of metal nanoparticles at the inner surface, and **c** formation of solid metal nanoparticles as a result of reduction of hollow oxides

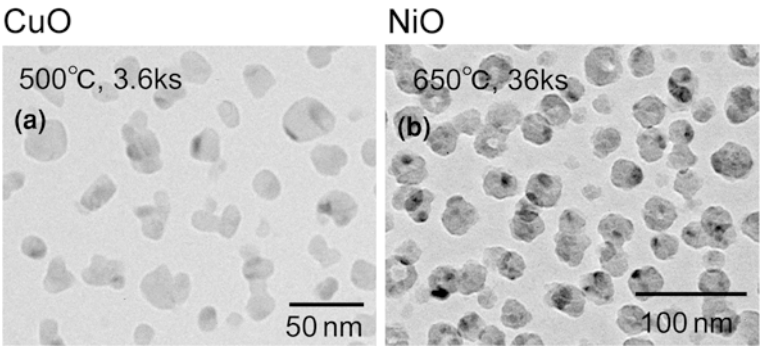

Fig. 17 CuO and NiO nanoparticles without interior nanopores after the annealing of hollow CuO and NiO at 500°C for 3.6 ks and 650°C for 36 ks, respectively (reproduced with permission from [37])

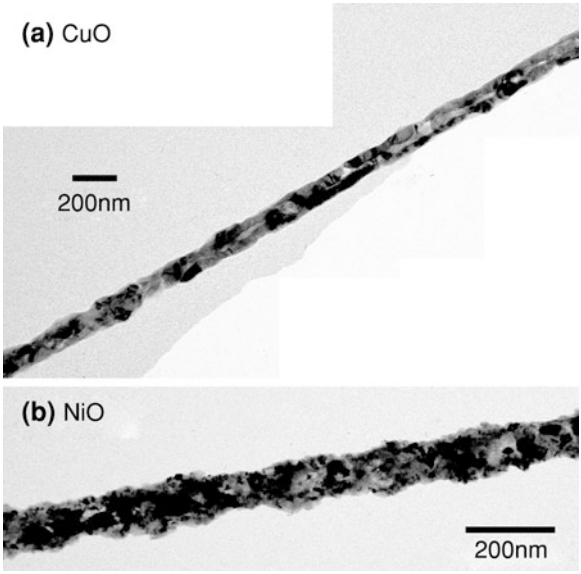

Fig. 18 TEM images of **a** CuO and **b** NiO nanotubes after annealing in air at 500°C for 3.6 ks and at 650°C for 3.6 ks, respectively (reproduced with permission from [38])

3.2 Transition in Porous Structures of Iron Oxides

Although hollow nanoparticles and nanotubes of Fe_3O_4 shrink and collapse by annealing at higher temperatures in air as is the case with Cu- and Ni-oxides, peculiar changes in morphology occur in the process from hollow structures to collapsed structures. In this section, the unique behavior is reviewed.

A typical example of the changes in the morphology after the oxidation of iron nanoparticles with the mean diameter of about 15 nm from 200 to 600°C is shown in Fig. 19. The morphology change from Fe nanoparticles to hollow Fe_3O_4 can be

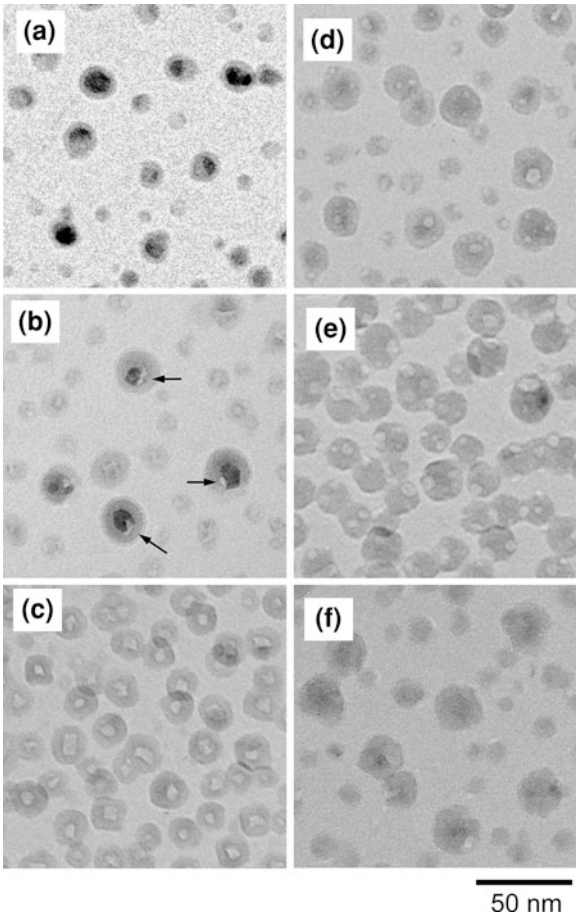

Fig. 19 A typical example of the morphology change of Fe nanoparticles (**a**) before and after oxidation at **b** 200°C for 18.0 ks, **c** 400°C for 90.0 ks, **d** 500°C for 3.6 ks, **e** 600°C for 3.6 ks and **f** 600°C for 14.4 ks (reproduced with permission from [44])

seen in Fig. 19a–c. After annealing at 500°C for 3.6 ks (Fig. 19d), two specific changes can be seen: (i) the nano-pores of the hollow particles become smaller and the location of nano-pores deviates from the center position, (ii) the additional smaller voids are generated in the particles; hollow nanoparticles with a single interior nano-pore turn into porous nanoparticles with a few voids by annealing the samples in air above 500°C. Furthermore, it was found that the interior closed pores became open surface pores at 600°C for 3.6 ks (Fig. 19e). Finally, porous iron oxide nanoparticles were observed to have turned into non-porous nanoparticles after the longer annealing time of 14.4 ks at 600°C, as shown in Fig. 19f.

Figure 20 shows representative electron micrographs of Fe_3O_4 nanotubes after annealing in air at 400 $\sim$ 600°C. As is the case with the oxidation of Fe nanoparticles, a further change in morphology can be seen after annealing at temperatures of 400°C and above; a number of voids with several nanometer sizes are formed along the inner side of the nanotube. These voids grow larger with increasing temperature. In addition, the duplex porous structures with a cylindrical

pore and a number of spherical pores transformed into porous structures without an inner cylindrical pore at 600°C for 3.6 ks, which was considered as a final form as a result of shrinkage. Above 673 K, both hollow nanoparticles and nanotubes of Fe_3O_4 transformed into γ-Fe_2O_3 [44].

The formation mechanism of hollow Fe_3O_4 nanoparticles and nanotubes via the oxidation of iron nanoparticles and nanowires below 400°C can be explained by a mechanism analogous to the Kirkendall effect in the Fe/oxide interface, where the outward diffusion of Fe is much faster than the inward diffusion of oxygen.

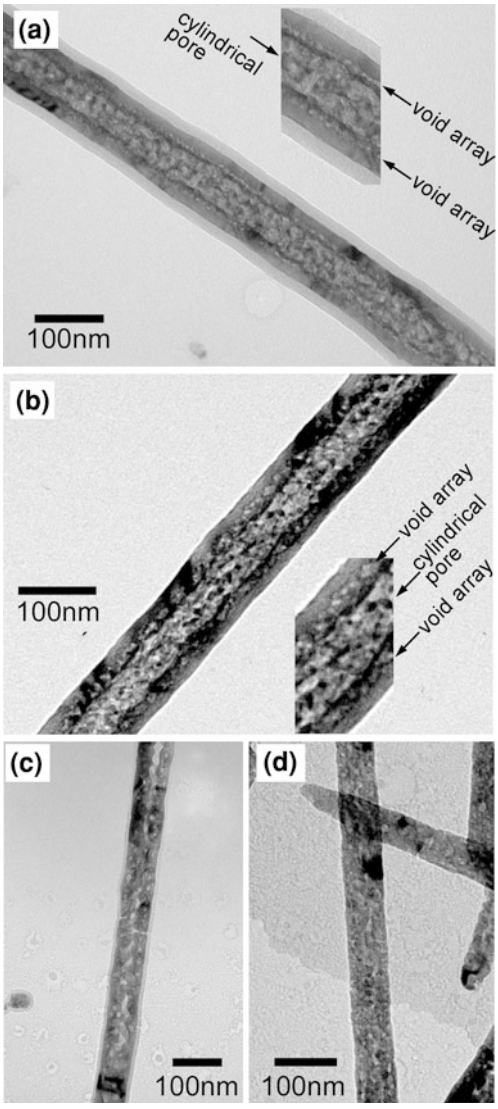

Fig. 20 A typical example of change in morphology of Fe_3O_4 nanotubes due to annealing in air: **a** 400°C, **b** 500°C and **c** 600°C for 3.6 ks. **d** The line profile of the corresponding diffraction patterns (reproduced with permission from [44])

The formation of an interior nano-pore inside an oxide particle and nanowire is due to the clustering of vacancies as a counter flow to the outward diffusion of iron ions.

It is noteworthy, however, that a peculiar change in morphology can be seen after annealing Fe_3O_4 hollow nanoparticles and nanotubes above 400°C in air; hollow structures with a single spherical and cylindrical nano-pore transform into porous structures with additional nano-voids. The morphology change from a hollow Fe_3O_4 nanoparticle and nanotube to porous structures is illustrated in Fig. 21; (i) vacancies diffuse outward from an interior pore as the pore shrinks, (ii) additionally spherical voids are introduced due to vacancy clustering, (iii) the shrinkage of the inner pore proceeds and the additional spherical voids grow larger, and (iv) γ-Fe_2O_3 nanoparticles and nanowires without nanopores were formed. This process is related to the phase transformation from Fe_3O_4 to γ-Fe_2O_3.

It is known that hollow nanostructures tend to shrink and collapse at high temperatures [37, 38]. As can be seen in Figs. 19 and 20, the interior pores of the hollow nanoparticles and nanotubes show a tendency to shrink and collapse. Therefore, the formation of additional nanovoids is associated with the annihilation of the interior nanopores in hollow nanoparticles and nanotubes. According to Gusak et al. [59], the shrinkage of hollow nanoparticles can be described as the outward diffusion of vacancies from the inner pores (vacancy source) to the surface (vacancy sink) of hollow nanoparticles. It is possible, therefore, to speculate that the vacancies, which generate from an inner pore, diffuse outward and then contribute to the formation of additional nanovoids. Furthermore, the phase transformation from Fe_3O_4 to γ-Fe_2O_3 occurs in the shrinkage process. Thus, the formation of additional nano-voids during the annealing of hollow Fe_3O_4 in air at

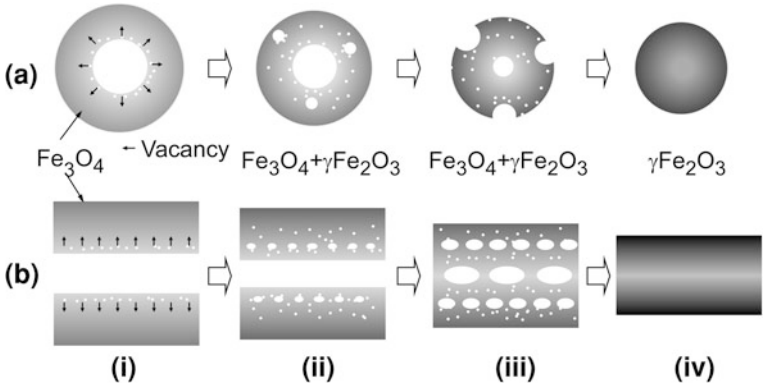

Fig. 21 Schematic illustrations of transition in the morphology of a Fe_3O_4: **a** hollow nanoparticle and **b** nanotube: (*i*) dissociation of vacancies at the inner surface of a hollow nanoparticle and nanotubes of Fe_3O_4; (*ii*) formation of additional spherical voids associated with shrinkage of an internal pore and phase transformation from Fe_3O_4 to γ-Fe_2O_3; (*iii*) growth of voids and shrinkage of an interior pore; and (*iv*) the formation of non-porous γ-Fe_2O_3.Vacancies are generated from inner surface and diffuse outward. The outward vacancy diffusion accompanies the phase transformation from Fe_3O_4 to γ-Fe_2O_3. The vacancies combine to form voids during the diffusion process (reproduced with permission from [44])

high temperatures is closely related to the phase transformation from Fe_3O_4 and γ-Fe_2O_3. The possible formation mechanism of additional nanovoids is the recombination of the out-going vacancies in the vicinity of the interface between Fe_3O_4 and γ-Fe_2O_3, which may result in the relaxation of interface strain. The details are given in Ref. [44].

Formation of hollow nanostructures by the Kirkendall effect is induced by the inward diffusion of excess vacancies during solid-state reactions. On the other hand, shrinkage behavior of hollow nanostructures is closely related to outward diffusion of vacancies from interior nanopores. Therefore, not only the inward but also the outward migration of vacancies may give rise to changes in morphology in the case of porous structures at elevated temperatures.

4 Summary

In the past few years, there have been considerable advancements concerning the synthesis of hollow nanoparticles and nanotubes. The synthesis routes based on chemical reactions such as chemical etching and galvanic replacement are broadly used for a wide variety of materials. More information on the chemical synthesis routes can be obtained in references [4] and [5]. In addition, different ideas have been applied to the fabrication of hollow nanomaterials. For example, the Kirkendall-effect-related processes have been recognized as one of the useful methods for the fabrication of oxides, sulfides and phosphides. Since the Kirkendall effect is related to the mass transport at the interface between different solids, there is much possibility to control hollow nanostructures of a variety of alloys and intermetallic compounds. The result by Fan et al., who successfully fabricated $ZnAl_2O_4$ spinel nanotubes from ZnO/Al_2O_3 core/shell nanowires, strongly suggests the formation of A–B alloys or compounds if A/B core/shell type nanostructures are easily obtained.

Our recent studies on the shrinkage behavior of hollow nanoparticles and nanotubes are also introduced. Hollow nanoparticles and nanotubes of metal oxides tend to shrink and collapse at higher temperatures both in reduction and oxidation atmosphere because hollow nanostructures with an inner surface are energetically unstable. The shrinking of hollow oxides occurs at temperatures where the reduction reactions from oxides to metals start in annealing them in reduction atmosphere. Hollow oxides turn into solid metal nanoparticles as a result of the shrinking associated with reduction. On the other hand, shrinking of hollow oxides occurs at temperatures where the diffusion coefficients of slower diffusing ions in the oxides are of the order of 10^{-22} m^2 s^{-1}. These results suggest that it is possible to control the size of interior nanopores and particles using annealing in high temperatures. In the case of hollow iron oxide, however, a peculiar morphology change is induced in the process of shrinkage; hollow oxides with an interior spherical and cylindrical nanopore transform into porous structures with additional multiple nanovoids. Transition in porous structure seems to be related to

the outward diffusion of vacancies from interior pore and the phase transition from magnetite to maghemite. It was found by our experiments that the outward diffusion of vacancies that takes place during shrinkage contribute to the formation of a unique nanoporous structure. It should be pointed out that annealing of hollow nanostructures at high temperatures may induce further change in morphology in some cases. Further research works should be carried out to investigate the performance of different nanostructures at high temperature.

References

1. Xia, Y., Halas, N.J.: Shape-controlled synthesis and surface plasmonic properties of metallic nanostructures. MRS Bull **30**, 338–343 (2005)
2. Xia, Y., Yang, P., Sun, Y., et al.: One-dimensional nanostructures: synthesis, characterization, and applications. Adv. Mater. **15**, 353–389 (2003)
3. Fan, H.J., Göele, U., Zacharias, M.: Formation of nanotubes and hollow nanoparticles based on Kirkendall and diffusion processes: a review. Small **3**, 1660–1671 (2007)
4. Lou, X.W., Archer, L.A., Yang, Z.: Hollow micro-/nanostructures: synthesis and applications. Adv. Mater. **20**, 3987–4019 (2008)
5. An, K., Hyeon, T.: Synthesis and biomedical applications of hollow nanostructures. Nano. Today **4**, 359–373 (2009)
6. Smigelskas, A.D., Kirkendall, E.O.: Zinc diffusion in alpha brass. Trans. AIME **171**, 130–142 (1947)
7. Ostwald, W.: On the assumed isomerism of red and yellow mercury oxide and the surface-tension of solid bodies. Z. Phys. Chem. **34**, 495 (1900)
8. Yin, Y., Rioux, R.M., Erdonmez, C.K., et al.: Formation of hollow nanocrystals through the nanoscale Kirkendall effect. Science **304**, 711–714 (2004)
9. Caruso, F., Caruso, R.A., Mohwald, H.: Nanoengineering of inorganic and hybrid hollow spheres by colloidal templating. Science **282**, 1111–1114 (1998)
10. Kim, S.-W., Kim, M., Lee, W.Y., et al.: Fabrication of hollow palladium spheres and their successful application to the recyclable heterogeneous catalyst for Suzuki coupling reactions. J. Am. Chem. Soc. **124**, 7642–7643 (2002)
11. Caruso, F., Shi, X., Caruso, R.A., et al.: Hollow titania spheres from layered precursor deposition on sacrificial colloidal core particles. Adv. Mater. **13**, 740–744 (2001)
12. Chen, G.-C., Kuo, C.-Y., Lu, S.-Y.: A general process for preparation of core-shell particles of complete and smooth shells. J. Am. Ceram. Soc. **88**, 277–283 (2005)
13. Martinez, C.J., Hockey, B., Montgomery, C.B., et al.: Porous tin oxide nano-structured microspheres for sensor applications. Langmuir **21**, 7937–7944 (2005)
14. Liang, Z., Susha, A., Caruso, F.: Gold nanoparticles-based core/shell and hollow spheres and ordered assemblies thereof. Chem. Mater. **15**, 3176–3183 (2003)
15. Caruso, F., Spasova, M., Susha, A., et al.: Magnetic nanocomposite particles and hollow spheres constructed by a sequential layering approach. Chem. Mater. **13**, 109–116 (2000)
16. Goldberger, J., He, R., Zhang, Y., et al.: Single-crystal gallium nitride nano-tubes. Nature **422**, 599–602 (2003)
17. Shen, G., Bando, Y., Ye, C., et al.: Single-crystal nanotubes of II_3–V_2 semi-conductors. Angew. Chem. Int. Ed. **45**, 7568–7572 (2006)
18. Ras, R.H.A., Kemell, M., Wit, J., et al.: Hollow inorganic nanospheres and nanotubes with tunable wall thicknesses by atomic layer deposition on self-assembled polymeric templates. Adv. Mater. **19**:102–106 (2007)
19. Schmidt, O.G., Eberl, K.: Nanotechnology: thin solid films roll up into nanotubes. Nature **410**, 168 (2001)

20. Schmidt, O.G., Schmarje, N., Deneke, C., et al.: Three-dimensional nano-objects evolving from a two-dimensional layer technology. Adv. Mater. **13**, 756–759 (2001)
21. Sun, Y., Mayers, B.T., Xia, Y.: Template-engaged replacement reaction: a one-step approach to the large-scale synthesis of metal nanostructures with hollow interiors. Nano. Lett. **2**, 481–485 (2002)
22. Chen, J., Wiley, B., McLellan, J., et al.: Optical properties of Pd/Ag and Pt/Ag nanoboxes synthesized via galvanic replacement reactions. Nano. Lett. **5**, 2058–2062 (2005)
23. Sun, Y., Xia, Y.: Mechanistic study on the replacement reaction between silver nanostructures and chloroauric acid in aqueous medium. J. Am. Chem. Soc. **126**, 3892–3901 (2004)
24. Lou, X.W., Wang, Y., Yuan, C., et al.: Template-free synthesis of SnO_2 hollow nanostructures with high lithium storage capacity. Adv. Mater. **18**, 2325–2329 (2006)
25. Yang, H.G., Zeng, H.C.: Creation of intestine-like interior space for metal-oxide nanostructures with a quasi-reverse emulsion. Angew. Chem. Int. Ed. **43**, 5206–5209 (2004)
26. Teo, J.J., Chang, Y., Zeng, H.C.: Fabrications of hollow nanocubes of Cu_2O and Cu via reductive self-assembly of CuO nanocrystals. Langmuir **22**, 7369–7377 (2006)
27. Liu, B., Zeng, H.C.: Symmetric and asymmetric Ostwald ripening in the fabrication of homogeneous core-shell semiconductors. Small **1**, 566–571 (2005)
28. Bernard Ng, C.H., Tan, H., Fan, W.Y.: Formation of Ag_2Se nanotubes and dendrite-like structures from UV irradiation of a CSe_2/Ag colloidal solution. Langmuir **22**, 9712–9717 (2006)
29. Ma, Y., Huo, K., Wu, Q., et al.: Self-templated synthesis of polycrystalline hollow aluminium nitride nanospheres. J. Mater. Chem. **16**, 2834–2838 (2006)
30. Zheng, J., Song, X., Zhang, Y., et al.: Nanosized aluminum nitride hollow spheres formed through a self-templating solid-gas interface reaction. J. Solid State Chem. **180**, 276–283 (2007)
31. Nakamura, R., Tokozakura, D., Nakajima, H., et al.: Hollow oxide formation by oxidation of Al and Cu nanoparticles. J. Appl. Phys. **101**, 074303 (2007)
32. Li, Q., Penner, R.M.: Photoconductive cadmium sulfide hemicylindrical shell nanowire ensembles. Nano. Lett. **5**,1720–1725 (2005)
33. Li, Y., Tan, B., Wu, Y.: Freestanding mesoporous quasi-single-crystalline Co_3O_4 nanowire arrays. J. Am. Chem. Soc. **128**, 14258–14259 (2006)
34. Chen, X., Zhang, Z., Qiu, Z., et al.: Hydrothermal fabrication and characterization of polycrystalline linneite (Co_3S_4) nanotubes based on the Kirkendall effect. J. Colloid Interface Sci. **308**, 271–275 (2007)
35. Gao, J., Zhang, B., Zhang, X., et al.: Magnetic-dipolar-interaction-induced self-assembly affords wires of hollow nanocrystals of cobalt selenide. Angew. Chem. Int. Ed. **45**, 1220–1223 (2006)
36. Chou, N.H., Schaak, R.E.: A library of single-crystal metal-tin nanorods: using diffusion as a tool for controlling the morphology of intermetallic nanocrystals. Chem. Mater. **20**, 2081–2085 (2008)
37. Nakamura, R., Tokozakura, D., Lee, J.G., et al.: Shrinking of hollow Cu_2O and NiO nanoparticles at high temperatures. Acta Mater. **56**, 5276–5284 (2008)
38. Nakamura, R., Matsubayashi, G., Tsuchiya, H., et al.: Formation of oxide nanotubes via oxidation of Fe, Cu and Ni nanowires and their structural stability: difference in formation and shrinkage behavior of interior pores. Acta Mater. **57**, 5046–5052 (2009)
39. Wang, Q., Li, J.-X., Li, G.-D., et al.: Formation of CuS nanotube arrays from CuCl nanorods through a gas-solid reaction route. J. Cryst. Growth **299**, 386–392 (2007)
40. Cao, H., Qian, X., Wang, C., et al.: High symmetric 18-facet polyhedron nanocrystals of Cu_7S_4 with a hollow nanocage. J Am Chem Soc **127**, 16024–16025 (2005)
41. Wang, C.M., Baer, D.R., Thomas, L.E., et al.: Void formation during early stages of passivation: Initial oxidation of iron nanoparticles at room temperature. J. Appl. Phys. **98**, 094307–094308 (2005)
42. Cabot, A., Puntes, V.F., Shevchenko, E., et al.: Vacancy coalescence during oxidation of iron nanoparticles. J. Am. Chem. Soc. **129**, 10358–10360 (2007)

43. Peng, S., Sun, S.: Synthesis and characterization of monodisperse hollow Fe_3O_4 nanoparticles. Angew. Chem. Int. Ed. **46**, 4155–4158 (2007)
44. Nakamura, R., Matsubayashi, G., Tsuchiya, H., et al.: Transition in nanoporous structure of iron oxides during the oxidation of iron nanoparticles and nanowires. Acta Mater. **57**, 4261–4266 (2009)
45. Ye, L., Wu, C., Guo, W., et al.: MoS_2 hierarchical hollow cubic cages assembled by bilayers: one-step synthesis and their electrochemical hydrogen storage properties. Chem. Commun. 4738–4740 (2006)
46. Nakamura, R., Lee, J.G., Mori, H., et al.: Oxidation behaviour of Ni nanoparticles and formation process of hollow NiO. Philos. Mag. **88**, 257–264 (2008)
47. Chiang, R.-K., Chiang, R.-T.: Formation of hollow Ni_2P nanoparticles based on the nanoscale Kirkendall effect. Inorg. Chem. **46**, 369–371 (2006)
48. Gaiduk, P.I., Hansen, J.L., Larsen, A.N.: Synthesis and analysis of hollow SnO_2 nanoislands. Appl. Phys. Lett. **92**, 193112 (2008)
49. Wang, Y., Cai, L., Xia, Y.: Monodisperse spherical colloids of Pb and their use as chemical templates to produce hollow particles. Adv. Mater. **17**, 473–477 (2005)
50. Fan, H.J., Knez, M., Scholz, R., et al.: Monocrystalline spinel nanotube fabrication based on the Kirkendall effect. Nat. Mater. **5**, 627–631 (2006)
51. Fan, H.J., Knez, M., Scholz, R., et al.: Influence of surface diffusion on the formation of hollow nanostructures induced by the Kirkendall effect: the basic concept. Nano. Lett. **7**, 993–997 (2007)
52. Fan, H.J., Scholz, R., Kolb, F.M., et al.: Growth mechanism and characterization of zinc oxide microcages. Solid State Commun. **130**, 517–521 (2004)
53. Liu, B., Zeng, H.C.: Fabrication of ZnO dandelions via a modified Kirkendall process. J. Am. Chem. Soc. **126**, 16744–16746 (2004)
54. Nakamura, R., Lee, J.G., Tokozakura, D., et al.: Formation of hollow ZnO through low-temperature oxidation of Zn nanoparticles. Mater. Lett. **61**, 1060–1063 (2007)
55. Lu, H.B., Li, H., Liao, L., et al.: Low-temperature synthesis and photocatalytic properties of ZnO nanotubes by thermal oxidation of Zn nanowires. Nanotechnology **19**, 045605 (2008)
56. Zhou, J., Liu, J., Wang, X., et al.: Vertically aligned Zn_2SiO_4 nanotube/ZnO nanowire heterojunction arrays. Small **3**, 622–626 (2007)
57. Tokozakura, D., Nakamura, R., Nakajima, H., et al.: Transmission electron microscopy observation of oxide layer growth on Cu nanoparticles and formation process of hollow oxide particles. J. Mater. Res. **22**, 2930–2935 (2007)
58. Tu, K.N., Gösele, U.: Hollow nanostructures based on the Kirkendall effect: design and stability considerations. Appl. Phys. Lett. **86**, 093111 (2005)
59. Gusak, A.M., Zaporozhets, T.V., Tu, K.N., et al.: Kinetic analysis of the instability of hollow nanoparticles. Philos. Mag. **85**, 4445–4464 (2005)
60. Evteev, A.V., Levchenko, E.V., Belova, I.V., et al.: Shrinking kinetics by vacancy diffusion of a pure element hollow nanosphere. Philos. Mag. **87**, 3787–3796 (2007)
61. Fischer, F.D., Svoboda, J.: High temperature instability of hollow nanoparticles. J. Nanoparticle Res. **10**, :255–261 (2008)
62. Kung, H.H.: Transition Metal Oxides: Surface Chemistry and Catalysis. Elsevier, New York (1989)
63. Scholz, J.J., Langell, M.A.: Kinetic analysis of surface reduction in transition metal oxide single crystals. Surf. Sci. **164**, 543–557 (1985)

Computer Simulation of Diffusion and Reaction in Metallic Nanoparticles

A. V. Evteev, E. V. Levchenko, I. V. Belova and G. E. Murch

Abstract In this chapter, we review the understanding that has been gained by the simulation methods of kinetic Monte Carlo and molecular dynamics of solid state diffusion in nanoparticles. We discuss the simulation of the formation and subsequent shrinkage by diffusion of hollow nanoparticles, the formation by diffusion of segregated bi-metallic nanoparticles and the diffusion with reaction to form intermetallic nanoparticles.

1 Introduction

Diffusion in nanoparticles has a number of special features that distinguish it from bulk diffusion. One is the very close proximity of the surface where defects can form and be annihilated. Another is the dominant role of the surface energy itself in the diffusion events and the stability of the structures formed. The potential for employing diffusion to 'self-assemble' nanoparticles having special spatial distributions of the components has been well recognized in recent years but the

A. V. Evteev (✉) · E. V. Levchenko · I. V. Belova · G. E. Murch
University Centre for Mass and Thermal Transport in Engineering Materials,
Priority Research Centre for Geotechnical and Materials Modelling,
School of Engineering, The University of Newcastle,
Callaghan, NSW 2308, Australia
e-mail: Alexander.Evteev@newcastle.edu.au

E. V. Levchenko
e-mail: Elena.Levchenko@newcastle.edu.au

I. V. Belova
e-mail: Irina.Belova@newcastle.edu.au

G. E. Murch
e-mail: Graeme.Murch@newcastle.edu.au

Adv Struct Mater (2013) 4: 31–59
DOI: 10.1007/8611_2011_60

Published Online: 22 January 2012

gaining of an understanding of the underlying processes is still in its relatively early stages. Much of the understanding has come from computer simulations, either using the methods of molecular dynamics or kinetic Monte Carlo. In the present chapter, we review some of the progress that has been made using computer simulation and related theory in understanding the formation and shrinkage of hollow nanospheres and the formation by diffusion alloying of bi-metallic and intermetallic nanoparticles. In both cases of hollow nanoparticles and bimetallic or intermetallic nanoparticles, the search for compositions, sizes, shapes and technological ways for fabricating them to exhibit desirable structures and properties is an exceedingly complex problem requiring a deep physical understanding of the diffusion processes and local stability that occur at the nanoscale.

2 Hollow Nanospheres

The synthesis of hollow nanospheres with tailored void sizes is of great interest because of the wide range of possible industrial applications of such nanoparticles. Applications include vehicles for precise medication delivery, nano-chemical reactors for the precise control of catalytic reactions in the petrochemical industry, containers of environmentally sensitive species, components of ultra-lightweight structural materials and many others. Yin et al. [1] were the first to demonstrate that the Kirkendall effect (with attendant Kirkendall porosity) [2], a phenomenon well-known in interdiffusion processes in metallic alloys, can be utilized at the nano-level for the formation of uniform hollow nanospheres of CdS, CdSe, CoO, CoSe, Co_3S_4, Co_9S_8. The general strategy is to start with the faster diffusing component as the core and surround it with a shell of the slower diffusing component. Upon interdiffusion, the net flux of vacancies into the material leads eventually to a pore in the absence of conventional vacancy sinks. Yin and colleagues' finding has encouraged many subsequent studies which have included, for example, the formation of hollow nanospheres of Fe_3O_4/Fe_2O_3 [3], Y_2O_3 [4], Cu_2O [5], ZnO [6], NiO [7] and Li_2NH [8] as well as nanotubes of Ag_2Se [9], $CoSe_2$ [10], CdS [11], $ZnAl_2O_4$ [12]. In principle, the structure and properties of hollow nanoparticles can be fine-tuned by varying the starting composition, size and shape, but this will only be possible once a thorough understanding of the phenomenon has been gained.

It is interesting to note that the formation of hollow micro-sized crystals by the Kirkendall effect was first demonstrated some thirty five years ago: Aldinger [13] obtained shells of a Be–Ni alloy after annealing Be microparticles of 33 μm diameter that had been coated with Ni. Similar findings were also reported in the Soviet Union literature at about the same time [14]. Alternative methods of synthesis of hollow nanoparticles, mainly using various template strategies, have been identified including a method to form hollow nanoparticles of noble metals [15]. In general, such methods do not make direct use of atomic diffusion.

Hollow nanoparticles can be expected to be unstable with respect to shrinkage via diffusion to a solid nanoparticle in order to reduce the total surface area.

This has recently been demonstrated experimentally [5]. The possibility of shrinkage and the resulting loss of longevity in-service of hollow nanoparticles mean that the shrinkage process needs to be thoroughly understood too.

2.1 Formation of Hollow Nanospheres

In general terms, the formation of hollow nanoparticles is simply a natural result of the phenomenon of Kirkendall porosity coming by way of the Kirkendall Effect. During interdiffusion of a bulk diffusion couple, say of two pure metals, the fluxes of the two opposing atomic components will in general not be equal. As a result, there will be a net flux of vacancies from the slow diffuser side to the fast diffuser side. This is known as the Kirkendall Effect and was the outcome of the famous experiment performed in the late 1940s that proved conclusively that vacancies were the principal vehicles for atomic diffusion in metals [2].

In an 'ideal' interdiffusion situation, vacancies are maintained at equilibrium everywhere in the diffusion zone. For this to happen, vacancies are created and annihilated as locally required (1) by the process of dislocation climb (in alloy systems) and/or (2) at grain boundaries and/or (3) at free surfaces. This requires of course that such vacancy sources and sinks are sufficiently numerous and efficient for the purpose. However, on the faster diffuser side, the usual sinks for vacancies mentioned above may be unable to cope with the influx of vacancies, especially when the diffusion rates of the two atomic species are very different. On the faster diffuser side, vacancies above saturation concentrations then start to aggregate into pores. In effect, the vacancies are forming their own sinks. Pores formed in this way are collectively referred to as Kirkendall porosity. Over time, these pores can eventually join together to form large voids. In the joining technology that depends on diffusion-bonding, the phenomenon of Kirkendall porosity has generally been viewed as a considerable nuisance because of the significant loss of mechanical strength that can ensue.

At the nano-scale, the small distances involved in the interdiffusion process and the absence of many conventional vacancy sinks such as dislocations has meant that Kirkendall porosity can become especially prominent and in fact turns out to be a valuable method for fabricating hollow nanoparticles. The recent demonstration by Yin and co-workers [1] of the formation of a very large void in the centre of a nanosphere, thus creating a hollow nanosphere, attracted widespread interest because of the significant potential for new technological applications as mentioned above.

Several papers appeared in 2005 that provided the formal beginning of a theory of formation of a hollow nanosphere. We will briefly describe them here. Tu and Gösele [16] considered the role of the Gibbs–Thomson potential on the rate of change of radius r of the nanosphere to obtain:

$$\frac{dr}{dt} \approx \frac{D_A}{kT}\left(-\frac{\Delta\mu}{r_{II} - r_I}\right) \tag{1}$$

where

$$\Delta\mu = \Delta G_f + 2\Omega\left(\frac{\gamma_{II}}{r_{II}} + \frac{\gamma_I}{r_I}\right)$$

and ΔG_f is the free energy of formation of the product phase, γ_I, γ_{II} are the interfacial energies at inner and outer surfaces I and II. Ω is the atomic volume, D_A is the diffusivity of the faster moving component and k and T are the Boltzmann constant and absolute temperature respectively. Since the interfacial energies are not generally known, the growth rate cannot be determined from Eq. 1. Within limits, the driving force will probably not change much in the nano-range. In principle, for very high values of γ and small values of r, the Gibbs–Thomson potential may be positive, potentially preventing out-diffusion of the high mobility component and therefore preventing the formation of a hollow nanosphere.

Starting with the Onsager formalism of irreversible thermodynamics, Belova and Murch [17] sketched an alloy interdiffusion theory for the general case of interdiffusion of two completely miscible metals A and B to form an isomorphous alloy but where there are no implied sources and sinks of vacancies (in contrast with the conventional treatment of bulk interdiffusion of two miscible metals where the vacancies are assumed to be always at equilibrium [18]). This model would correspond to the formation of a shell of an alloy AB starting from a core of metal A (of high mobility) surrounded by a shell of metal B (of low mobility). Expressions were developed for the fluxes of the components in the Manning random alloy diffusion kinetics approximation [19]. Kinetic Monte Carlo simulations of interdiffusion for such a model in a constant gradient of vacancies (and therefore a moving boundary) verified the expressions. The simulations showed that in principle, at very late times, after the formation of a homogeneous alloy shell, any continued flux of vacancies should then produce some segregation of the atomic components. This phenomenon is sometimes referred to as the Inverse Kirkendall Effect and is known to occur in the net flux of vacancies occurring during radiation damage annealing of alloys.

Prasad and Paul [20] addressed the rate of appearance of a phase β from an inner phase α (A-rich) and an outer phase γ (B-rich) for the geometry of a nanorod. At the interface I (between α and β) and identified by the radius r_I, A will be dissociated from the α phase to produce the β phase. Dissociated A will also diffuse through the β phase to react with the γ phase to produce more β phase at the II interface (identified by r_{II}). The β phase thus grows from both interfaces I and II. Using Wagner's suggestion of an integrated diffusion coefficient of a 'line compound' Prasad and Paul showed that for a pure element core and shell an integrated diffusion coefficient of the β phase can be written as:

$$\tilde{D}^{\beta}_{\text{int}} = \frac{(r_{II} - r_I)N_B^{\beta}\left(1 - N_B^{\beta}\right)\Delta A_r^{I/II}}{4\pi t(r_0 - r_I)} = N_B^{\beta}\left(1 - N_B^{\beta}\right)k_g \qquad (2)$$

where $\Delta A_r^{I/II}$ is the area between interfaces *I* and *II*, N_B^{β} is the average composition of the β phase and k_g is a growth constant. The growth rate of the product phase and the consumption rate of shell and core should follow parabolic kinetics and could then be determined in principle. When vacancies are at equilibrium during interdiffusion, vacancies should be created in the region between r_K (the Kirkendall radius) and r_{II} and annihilated in the region r_I to r_K. Since few vacancy sinks are available at the nanolevel, porosity should in fact occur. Prasad and Paul showed that for a pure element core, porosity should occur only at interface *I* and a good nanotube will thus form from a nanorod.

A molecular dynamics (MD) simulation of the formation by diffusion of a hollow nanosphere has not been performed. It is likely to be computationally extremely time consuming because of the two requirements of a fairly large difference in mobility of the two atomic species in order to obtain observable porosity and a relatively long annealing time.

Kinetic Monte Carlo (KMC) calculations represent a computationally much more attractive alternative to molecular dynamics to demonstrate the formation of a hollow nanosphere. However it should be recognized that KMC calculations in general require at the outset the specification of a basic diffusion mechanism, e.g. the vacancy mechanism. This might not appear to be a problem since vacancies certainly provide the principal means for diffusion in bulk metals. However, it has been found in MD simulations of the shrinkage of very small hollow Pd nanospheres (see further below) that vacancies do not necessarily provide the only vehicles for atomic mobility: atoms have been found to move by means of moving Shockley partial dislocations that form at the surface of the nanosphere.

KMC calculations provide a useful means for visualizing the evolution of kinetics processes. Furthermore, the inter-site transition rates can be readily scaled to real time. KMC simulations of the formation (and shrinkage) of a hollow nanosphere have been performed very recently by the authors [21]. An Ising alloy model on f.c.c. lattice was employed where the nearest neighbour interactions between the atoms (A–A, B–B and A–B) were all set equal thus resulting in a random distribution of the atomic species.

However, the model is not identical to Manning's well known random alloy model [19] because there is both a small indirect attraction between neighbouring vacancies and a definable equilibrium vacancy concentration. In the study, the values of the interactions $\phi_{\mathrm{AA}} = \phi_{\mathrm{BB}} = \phi_{\mathrm{AB}} = -1.5\ kT$ were adjusted so that the vacancy composition was close to a typical bulk value at diffusion temperatures $c_{\mathrm{V}}^{\mathrm{eq}} \sim 1.24 \times 10^{-4}$. In the simulation, the fast diffuser A (the core) was set to have an atom-vacancy attempt frequency $v_{0\mathrm{A}}$ three orders of magnitude larger than the slow diffuser B (the shell), $v_{0\mathrm{B}}$. The well-known Metropolis transition probability was used in the calculations [22]. Although this transition probability is not particularly realistic for a diffusion process, the number of Monte Carlo jump attempts scale transparently to real time. Furthermore, in the particular case of a very small vacancy composition any Monte Carlo transition probability in principle should generate much the same evolution of configurations.

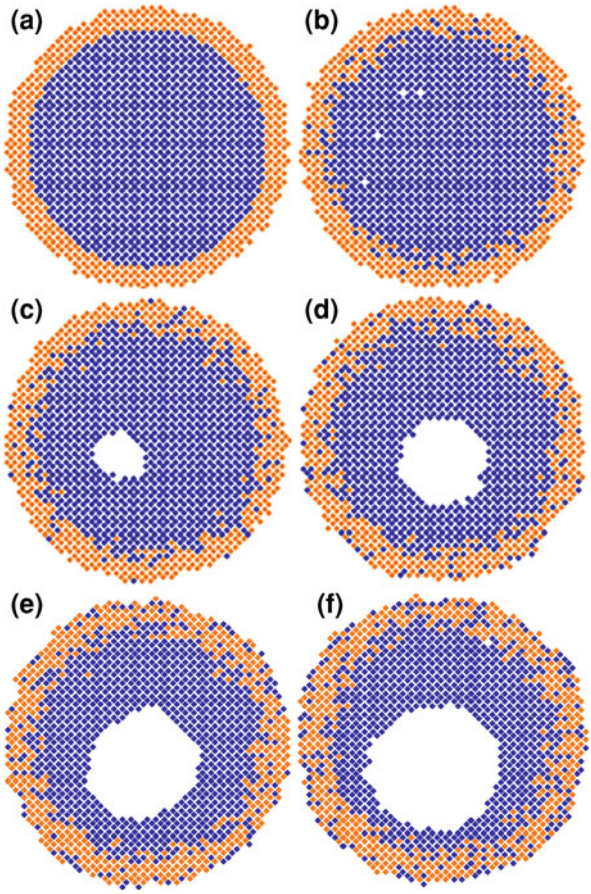

Fig. 1 Selected snapshots of the interdiffusion process in the initially A-core−B-shell random alloy nanoparticle model. Snapshots are taken at the beginning of the simulation (**a**) and after $v_{0A}t \approx 345955$ (**b**), $v_{0A}t \approx 449741$ (**c**), $v_{0A}t \approx 657314$ (**d**), $v_{0A}t \approx 864886$ (**e**), $v_{0A}t \approx 1349220$ (**f**) (v_{0A} is the effective attempt frequency of A atoms for exchange with a vacancy). Only the same central cross-sections are shown [21]

In Fig. 1, a sequence of snapshots at various times for a system $A_{0.6}B_{0.4}$ of 76,429 atoms shows the formation process of a hollow nanosphere of an alloy starting from two pure metals. The interdiffusion process has not gone to completion in this figure. There are no internal interfaces in this model: the core (A), the shell (B) and the formed alloy are all isomorphous. The structure contained no vacancies at the commencement of the simulation. During interdiffusion, vacancies form at the surface of this bimetallic nanosphere and diffuse into the interior via a small number of percolating paths of A through the shell of slow moving atoms (B). Once the vacancies reach the core they quickly mix with A atoms and lose connections to the percolating paths to the surface. Since there are no existing vacancy sinks, very considerable vacancy supersaturation now builds up in the core. This is clearly shown in Fig. 2 which shows the vacancy concentration in the core and the diffusion zone as a function of time. (In this figure $\varepsilon = r_i/r_e$, where r_i is the radius of the void and r_e is an external radius of the hollow nanosphere.) As time progresses, the vacancy composition in both the core and diffusion zone is seen to increase by

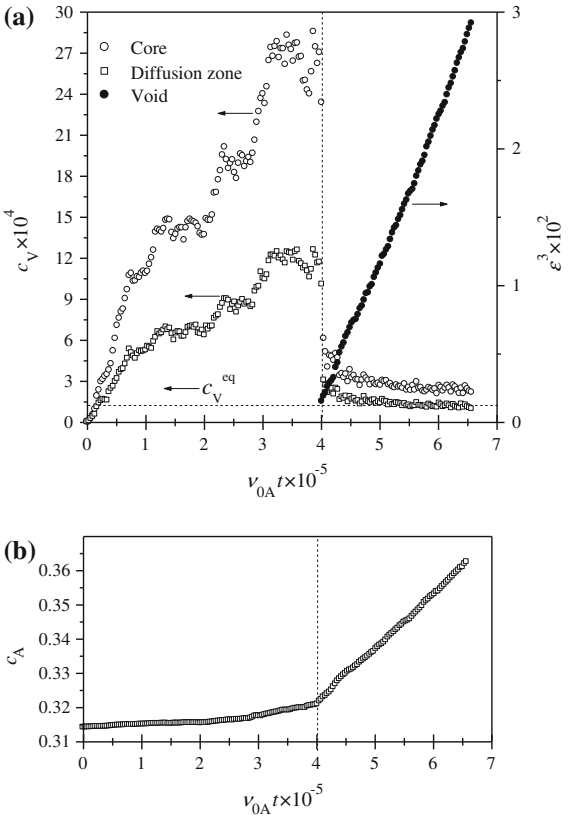

Fig. 2 Time-dependencies of: **a** the average vacancy compositions inside the core and diffusion zone of the nanoparticle model as well as the ratio ε^3 of the number of virtual lattice sites within the void to the total number of lattice sites inside the whole of the nanoparticle, and **b** the average composition of A atoms inside the 'diffusion zone' (ν_{0A} is the effective attempt frequency of A atoms for exchange with a vacancy). The horizontal dashed line shows the equilibrium vacancy composition c_V^{eq} for this model. The vertical dashed line indicates the time at which the void appears to form [21]

about a factor of thirty (in this case) over the equilibrium vacancy composition value. The increase is greatest in the core region. The vacancies are in effect kinetically trapped in the core of the nanoparticle: they cannot return to the surface because there are insufficient paths to provide the long range diffusion back there.

Supersaturation of the vacancies inside the core results in a steep vacancy composition gradient in the diffusion zone and in fact, the vacancies actually diffuse uphill i.e. against their concentration gradient as they enter from the surface. The increase of the vacancy composition gradient is seen to restrict the out-flux of A atoms into the shell and hence tends to suppress the entire inter-diffusion process. After a gestation time, the vacancies nucleate quickly into a large void forming roughly in the centre of the nanoparticle. The vacancy concentration everywhere in the core and diffusion zone thus suddenly collapses, essentially down to the equilibrium vacancy composition level. It is also seen in the same figure that at the same time, the average concentration of A in the diffusion zone increases significantly as the vacancy in-flux now suddenly increases the rate of mixing of A and B.

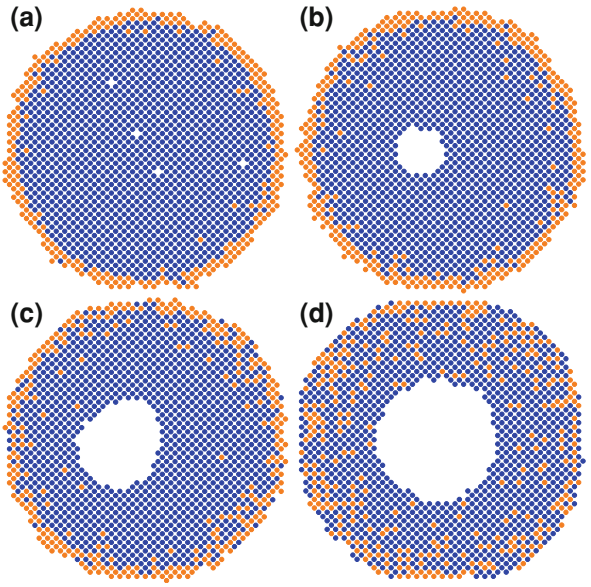

Fig. 3 Selected snapshots, **a**–**d**, taken during the evolution of the interdiffusion process in the initially A-core–B-shell nanoparticle model with an A_3B ordering tendency. The simulation was done at a temperature which is just below the order–disorder temperature. The pair-interaction energies are $\phi_{AA} = \phi_{BB} = -1.5\ kT$ and $\phi_{AB} = -2.8\ kT$. The equilibrium vacancy composition for the faster component in the core is $\sim 1.24 \times 10^{-4}$. The ratio of the atom-vacancy attempt frequencies is ν_{0A}/ν_{0B}=3. Only the same central cross-sections are shown

Furthermore, we have observed that for the initially A-core–B-shell binary random alloy system at a temperature which provides an equilibrium vacancy composition $\sim 10^{-4}$ in pure A and B as well as in the binary A_xB_{1-x} random alloy, void nucleation can be observed if the atomic jump frequency ratio is of the order of 10^3 and the atomic fraction of the fast diffuser A is within the range $0.6 \leq x \leq 0.8$. In contrast to the binary random alloy system with its solely entropy-driven interdiffusion, we have observed that the formation of a hollow nanosphere by interdiffusion in an initially A-core–B-shell binary alloy system with an A_3B ordering tendency requires a much smaller value of the atomic jump frequency ratio at the same value of the equilibrium vacancy composition for pure A and B (the equilibrium vacancy composition for the A–B alloy is even lower). The atomic jump frequency ratio is of the order of 10 above the order–disorder temperature and can be as small as 2 below the order–disorder temperature. In all our simulations with the nearest neighbour interactions between atoms that provide the equilibrium vacancy composition $\sim 10^{-4}$ or lower, we have observed only single void formation followed by its growth (see, as examples, Figs. 1 and 3). However, it is noted that an increase of the equilibrium vacancy composition in the model (especially for the faster component in the core) up to 10^{-3}–10^{-2} results in the formation of multiple pores and then their later agglomeration into a single void (see, as an example, Fig. 4). This has occurred because the vacancy composition in the core under supersaturation during initial stage of interdiffusion is high enough to supply the vacancy clustering and, as a result, the void nucleation problem is avoided. Then, the vacancy clusters simply grow owing to the vacancy flux during a further stage of interdiffusion imitating the formation of multiple pores. The observation is also in accordance with recent KMC simulation results of Gusak and Zaporozhets [23].

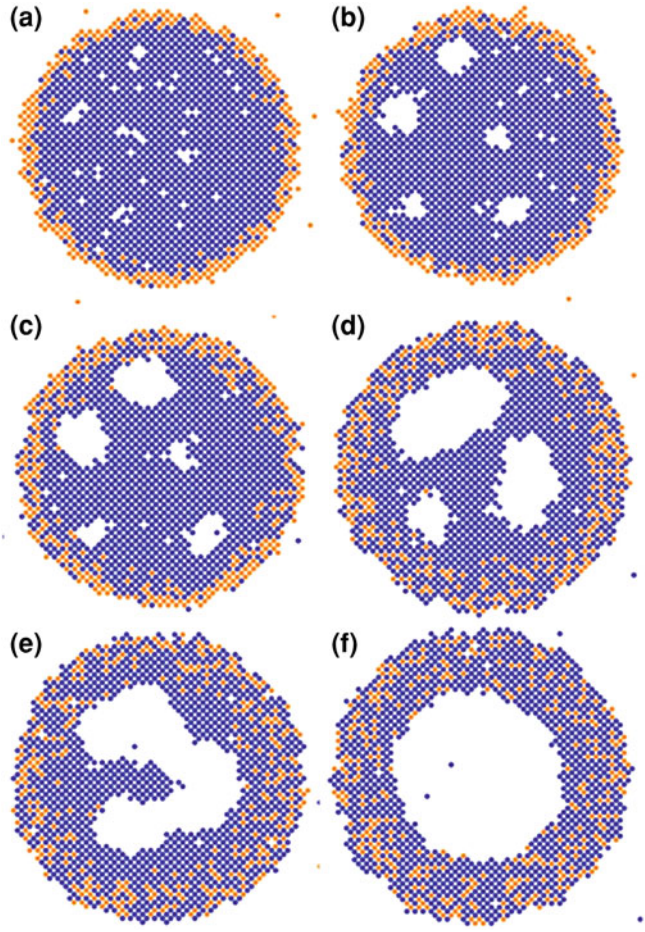

Fig. 4 Selected snapshots, **a**–**f**, taken during the evolution of the interdiffusion process in the initially A-core–B-shell nanoparticle model with an A_3B ordering tendency. The simulation was performed at a temperature which is well above the order–disorder temperature. The pair-interaction energies are $\phi_{AA} = \phi_{BB} = -0.86\ kT$ and $\phi_{AB} = -1.23\ kT$. The equilibrium vacancy composition for the faster component in the core is $\sim 6 \times 10^{-3}$. The ratio of atom-vacancy attempt frequencies is $\nu_{0A}/\nu_{0B} = 10$. Only the same central cross-sections are shown

2.2 Shrinkage of Hollow Nanoparticles

It was noted in [16] that hollow nanospheres should be unstable in principle and, with time, will have a tendency to shrink into a solid nanosphere. This is because the resulting reduction in surface area should be more advantageous from an energy reduction point of view: $\gamma\left(r_i^2 + r_e^2\right) > \gamma\ r_f^2$ (γ is the surface energy, r_i and r_e are the inner and external radii of a hollow nanosphere, r_f is the radius of a

collapsed compact nanosphere). Shrinkage of hollow nanoparticles has recently been observed in the case of Cu_2O [5]. A considerable body of theoretical work and computer simulations have been published that explore the shrinkage phenomenon. In accordance with [16] the mechanism of shrinking can be considered as a result of the vacancy flux going from the inner surface to the outer surface. The driving force for such a flux is the difference between the vacancy concentrations c_V on the inner and external surfaces.

This physical picture of the shrinking of hollow nano-objects seems reasonable if we make the assumption that the equilibrium vacancy concentration c_V^{eq} in the bulk of the system does not differ strongly from the equilibrium vacancy concentration near a planar surface ($c_V^{eq} \approx c_V^0$) or if $c_V^{eq} < c_V^0$, and either the external radius is much larger than the inner radius (so we can consider such a hollow nano-objects as an infinite bulk system with a spherical void inside) or conversely, when the nanoshell is so thin, that the equilibrium vacancy composition c_V^{eq} in the bulk is unreachable.

Starting with a one-component hollow nanosphere, Gusak and colleagues [24] used Gibbs–Thomson type expressions to describe the vacancy concentrations at the inner and outer curved surfaces. For a hollow nanosphere with an internal radius r_i and external radius r_e, the variation of vacancy composition near the surfaces with the number of vacancies in the void N_V^{void} is given by the Gibbs–Thomson equation:

$$c_V^{\pm} = c_V^{eq} \exp\left(\pm \frac{\partial \Delta G_S / \partial N_V^{void}}{kT}\right), \tag{3}$$

$\Delta G_S = \gamma S$ is the free energy of the spherical surface with a principal radius of curvature r ($r = r_i$ or $r = r_e$) and S is the surface area. In the above formula, the curvature is taken as positive for the inner surface and negative for the external surface. Since for a spherical geometry, we have that:

$$\frac{\partial \Delta G_S}{\partial N_V^{void}} = \frac{\partial \Delta G_S}{\partial r} \frac{\partial r}{\partial N_V^{void}} = \frac{2\gamma\Omega}{r}, \tag{4}$$

Equation 3 reduces to:

$$c_V^{\pm} = c_V^{eq} \exp\left(\frac{\beta}{\pm r}\right), \tag{5}$$

where $\beta = 2\gamma\,\Omega/kT$ for a hollow nanosphere and Ω is the atomic volume. Assuming steady state for the vacancy concentration and a linear approximation of the Gibbs–Thomson equation, Gusak et al. [24] found a numerical solution for the collapse time of a hollow nanosphere by diffusion. Using the same model, Evteev et al. later derived exact solutions for the collapse time for both one component hollow nanospheres [25] and nanotubes [26]. KMC calculations have verified their expressions [27].

MD simulation has been used to study defect formation and distribution in a hollow Pd nanosphere (76,657 atoms) as well as its stability/shrinkage behaviour [28].

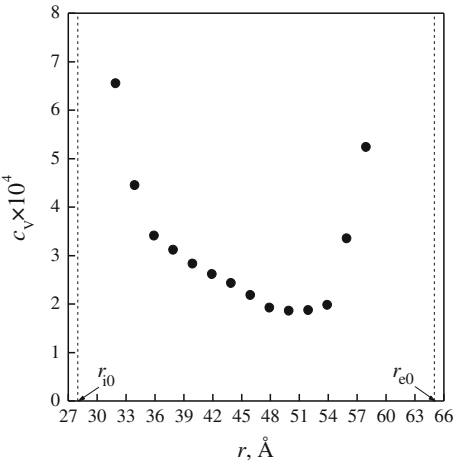

Fig. 5 MD simulation of the distribution of vacancies within a Pd hollow nanosphere at 1450 K [28]

Interestingly, it was shown that at 1500 K, which is probably the melting point of the simulated system, the hollow Pd nanosphere does not actually shrink until it is completely melted. The melting starts from the outside surface.

At 50 degrees below the melting point the results of MD simulation very clearly demonstrate that the vacancy composition profile across the nanoshell then develops a minimum [28], see Fig. 5. These results are consistent with the concept that the free energy of vacancy formation with respect to a planar surface in a crystal depends on the distance from the surface because of surface and subsurface relaxation, with the result that $\Delta g_f^0 + 2\gamma\Omega/r_e < \Delta g_f^{eq}$ (Δg_f^0 and Δg_f^{eq} are vacancy formation free energies near the reference planar surface and in the bulk of the crystal system, respectively). Furthermore, surface and subsurface relaxation processes can influence (in varying degrees) the relative changes of Δg_f^0 and vacancy formation free energies near the inner (Δg_f^i) and external (Δg_f^e) surfaces of the hollow nanoparticle, because of the difference in sign and value of the curvature of the surfaces. Indeed, because of surface and subsurface relaxation processes, it can be supposed that the largest relative decrease being to Δg_f^e (a negative curvature surface has the highest surface free energy) followed by Δg_f^0 and Δg_f^i. Thus, unlike a simple treatment (c.f. Eq. 5), we can expect $c_V^i > c_V^{eq} < c_V^e$. In other words, a vacancy composition profile across a hollow nanoshell can then have a minimum and a hollow nanosphere should actually be in a state corresponding to a local minimum of the free energy. Accordingly, the growing of the vacancy composition in the shell should result in the increasing of the free energy of such a system, namely to an increase of the free energy part responsible for the volume of the nanoshell. Thus, a free energy barrier should obstruct the transition of the hollow nanosphere (by the vacancy mechanism) to a state corresponding to the global minimum of the free energy (shrinkage to a solid nanosphere).

The MD results were obtained just below the melting temperature, where one should expect the most extensive surface and subsurface relaxation. Unfortunately,

at present it is impossible to determine on a MD simulation time-scale the vacancy composition profile inside a nanoshell at more moderate temperatures. Furthermore, the vacancy formation free energy near a surface in an alloy should be a function of atomic composition because of surface and subsurface segregation phenomena. Moreover, for different kinds of hollow nanospheres (pure element, alloy, compound) with various types of atomic bonds (metallic, covalent, ionic) the vacancy composition profile across the nanoshell might well have quite different shapes.

The MD simulations also showed that besides vacancies, which formed on both surfaces of the hollow nanosphere, other defects such as Shockley partial dislocations, twins and stacking faults nucleated on the external surface as a result of its significant reconstruction. The density of the defects on the external surface increased with reduction of nanoshell size. It was shown that for very small hollow nanospheres a Shockley partial dislocation can transport material from the external surface to the inner one and lead to its shrinking. It is certainly conceivable that such mechanisms can account principally for the shrinkage of small hollow nanospheres without the participation of point defects such as vacancies.

The case of the shrinkage of a binary alloy nanoshell has also been investigated and is rather more complicated. The vacancy flux from inner to external surface, caused by the Gibbs–Thomson effect, leads to inward atomic fluxes of the atomic components of the binary alloy [23, 24, 29, 30]. If diffusion of one species, for example A, proceeds faster, then A will segregate near the inner surface (another example of the Inverse Kirkendall Effect). The resulting composition gradient of A will reduce the vacancy flux and hence will generate a tendency to suppress the shrinking process [23, 24, 29, 30]. In a phenomenological analysis, Gusak and colleagues [24] showed that the shrinkage rate of a hollow nanosphere of an intermetallic compound will be controlled by the diffusion of the slower species. In addition, it was implied [24] that the steady-state approximation for both vacancies and atoms appears to be a valid one for a hollow nanosphere of an intermetallic compound.

Evteev and colleagues [29] considered diffusion via vacancies in a hollow binary AB alloy nanosphere under the Gibbs–Thomson effect. They made use of the Onsager flux equations for the situation where there are no sources and sinks for vacancies. They found that the controlling parameter D of vacancy motion within a binary alloy nanoshell (or shrinking rate) can be written in the form:

$$D = \frac{\Omega kT}{c_{\mathrm{V}}} \frac{L_{\mathrm{AA}}L_{\mathrm{BB}} - L_{\mathrm{AB}}^2}{(c_{\mathrm{A}}L_{\mathrm{BB}} - c_{\mathrm{B}}L_{\mathrm{AB}})\dfrac{J_{\mathrm{A}}}{J_{\mathrm{A}} + J_{\mathrm{B}}} + (c_{\mathrm{B}}L_{\mathrm{AA}} - c_{\mathrm{A}}L_{\mathrm{AB}})\dfrac{J_{\mathrm{B}}}{J_{\mathrm{A}} + J_{\mathrm{B}}}} \phi_{\mathrm{V}}, \qquad (6)$$

where L_{AA}, L_{BB} and L_{AB} are the phenomenological coefficients, c_{A}, c_{B} and c_{V} are the compositions of species A, B and vacancies respectively, J_{A} and J_{B} are the atomic fluxes and

$$\phi_{\mathrm{V}} = 1 + \frac{c_{\mathrm{V}}}{kT} \frac{(\partial \Delta g_{\mathrm{f}}/\partial r) + (\partial \Delta g_{\mathrm{f}}/\partial c_{\mathrm{A}})(\partial c_{\mathrm{A}}/\partial r)}{(\partial c_{\mathrm{V}}/\partial r)} \qquad (7)$$

can be regarded as the vacancy thermodynamic factor. This factor should arise if the vacancy formation free energy, Δg_f, depends either on the distance from a surface due to subsurface relaxation or on atomic composition due to surface and subsurface segregation phenomena or both. Accordingly, the vacancy thermodynamic factor may well be important for the analysis of diffusion by vacancies inside a nano-object because in such a system the fractions of subsurface and bulk atoms are of comparable magnitude. If it is assumed however that the vacancy thermodynamic factor is close to unity $\phi_V \approx 1$, then a steady-state approximation for vacancies should be quite reasonable. A range for the collapse time of a hollow binary alloy nanosphere can then be estimated by making use of the Moleko et al. [31] diffusion kinetics theory:

$$\left(c_V^{eq} D_V\right)^{-1} < \frac{12\gamma\Omega t_c}{kTr_f^3\tau_c} < \left(c_V^{eq} D^{(SS)}\right)^{-1} \tag{8}$$

where D_V is the diffusion coefficient of the vacancies and $D^{(SS)}$ is a controlling parameter for shrinkage at steady state:

$$D^{(SS)} = \frac{\Omega kT}{c_V} \frac{L_{AA}L_{BB} - L_{AB}^2}{\left(c_A L_{BB} - c_B L_{AB}\right)\dfrac{c_A}{c_A + c_B} + \left(c_B L_{AA} - c_A L_{AB}\right)\dfrac{c_B}{c_A + c_B}}, \tag{9}$$

and

$$\tau_c \approx \ln\left[\frac{(1-\varepsilon_0)(1+\varepsilon_0)^3}{\left(1-\varepsilon_0^3\right)\frac{4}{3}}\right] - 2\varepsilon_0\frac{1-\varepsilon_0}{1-\varepsilon_0^3}, \quad \varepsilon_0 = \frac{r_{i0}}{r_{e0}} \tag{10}$$

Here r_{i0} and r_{e0} are the inner and the external radii of the hollow nanosphere at the initial point of time $t = 0$.

KMC calculations of the shrinking process have been performed [23, 29, 30] on an initially homogeneous equi-atomic hollow nanosphere of a random binary alloy using a model identical with that described above for the formation of a hollow nanosphere. It was found that the faster moving species (A) segregates near the inner surface (Inverse Kirkendall Effect). The appearance of a composition gradient of the component A reduces the vacancy flux and hence generates a tendency to suppress the shrinking process as had been noted earlier [24]. At the same time, the increase of the collapse time of the KMC model of the hollow random binary alloy nanosphere with increasing ratio of the jump frequencies is much smaller than could be expected at the steady-state approximation for atomic components. It was found that the collapse time of the KMC model of the hollow random binary alloy nanosphere is much less than the time required for obtaining steady-state conditions for the atomic components. KMC calculations of the shrinking process of a hollow nanosphere of an intermetallic compound have not yet been performed.

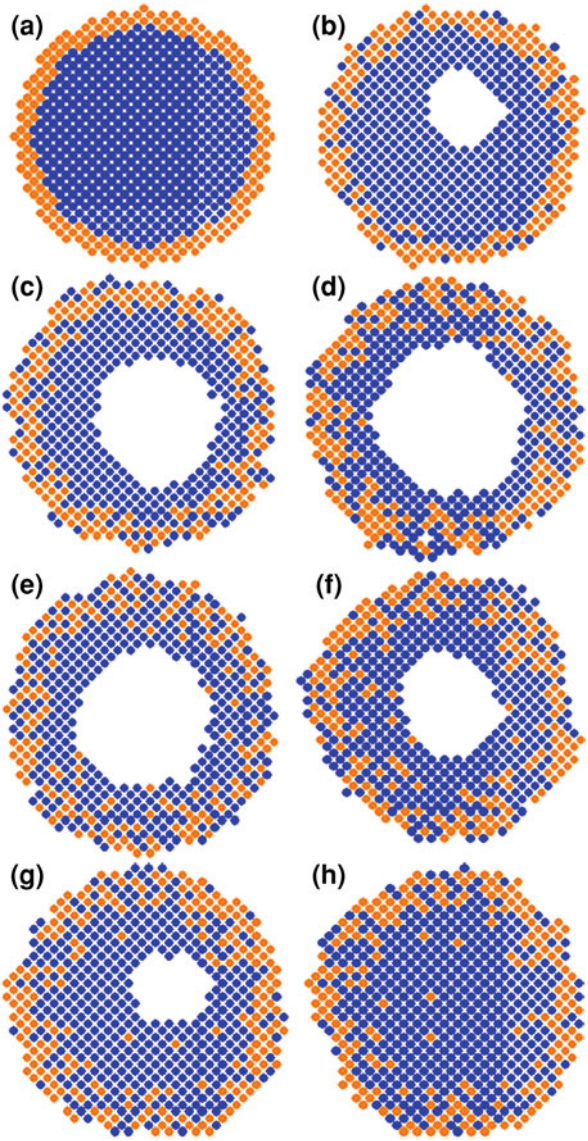

Fig. 6 Selected snapshots of the 'whole of life' interdiffusion process in the initially A-core−B-shell nanoparticle model. Snapshots are taken at the initial time of the simulation (**a**), after about 2.5% of the final time (**b**), after about 5% of the final time (**c**), after about 30% of the final time (maximum volume of the pore was observed at this time) (**d**), after about 55% of the final time (**e**), after about 90% of the final time (**f**), after about 99.9% of the final time (**g**), at the finial time (**h**)

'Whole-of-life' KMC simulations for the formation of a hollow binary alloy nanosphere and subsequent shrinking have been carried out in [23, 32]. In Fig. 6, a sequence of snapshots at various times for a system $A_{0.62}B_{0.48}$ of 16, 757 atoms demonstrate the formation and shrinking processes of a hollow nanosphere of a random binary alloy starting from two pure metals [32]. In the study, the pair-interaction energies $\phi_{AA} = \phi_{BB} = \phi_{AB} = -1.5\ kT$ were chosen to provide an equilibrium vacancy composition $c_V^{eq} \sim 1.24 \times 10^{-4}$ in the model, while the

ratio of atom-vacancy attempt frequencies was chosen as $\nu_{0A}/\nu_{0B} = 10^3$. Thus, apart from the size of the model, all other parameters were similar to ones from our previous KMC studies [21, 29, 30] of the formation and shrinking of hollow random binary alloy nanospheres. This simulation starts from the initial bi-metallic A-core–B-shell configuration of (Fig. 6a), proceeds to the formation stage of the hollow nanosphere (Fig. 6b–d) as described above and then proceeds to the final subsequent shrinkage stage to a solid alloy nanosphere (Fig. 6e–h). At least two important observations can be made from this preliminary 'whole-of-life' KMC simulation. First, it can be seen in (Fig. 6d) that the shrinkage stage started before complete intermixing had been reached. Second, the shrinkage time is only about three times longer than the formation time (see Fig. 7). This result additionally demonstrates that at least for hollow random binary alloy nanospheres, the shrinkage here is clearly not a steady-state process and it is not controlled by the slower diffusing species (we recall that in this KMC model the fast diffuser A was set to have a atom-vacancy exchange rate three orders of magnitude larger than the slow diffuser B). Qualitatively similar results at a much high temperature (which provide the equilibrium vacancy composition $c_V^{eq} \sim 5 \times 10^{-3}$) were obtained in [23] for a binary alloy system $A_{0.075}B_{0.925}$ of 82,421 atoms with some tendency to ordering and with the ratio of atom-vacancy attempt frequencies ν_{0A}/ν_{0B}=10.

3 Bi-metallic Nanoparticles

In general, at the nanoscale, bimetallic particles can form various kinds of structure, ranging from the high entropy situation such as a solid solution 'random alloy' to the low entropy structure such as a layered compound or core–shell structure. Segregation of a component such as a noble metal can be superimposed on this. In principle, the structure and properties of bimetallic nanoparticles can be tuned by varying the composition, size and shape and making use of the different surface energies. All of these make use of diffusion.

It is well-known that Ag and Pd are metals with important existing and potential applications as catalysts in heterogeneous catalysis. With their very high surface areas, Ag and Pd nanoparticles are especially efficient catalysts, but there are still substantial negative economic aspects because of the very high cost of such metals. Since catalytic reactions occur at the surface of the nanoparticles, a large fraction of metal in the core of the nanoparticle is of course wasted. Bimetallic nanoparticles are currently attracting a great deal of interest due to their unique physical and chemical properties [33]. An interesting bimetallic nanoparticle alloys involves Ag and Pd with a lower cost and higher surface energy metal such as Ni [34–40]. It would of course be economically attractive for the precious and catalytically active Ag and Pd atoms to be allowed to segregate (by diffusion) to the surface.

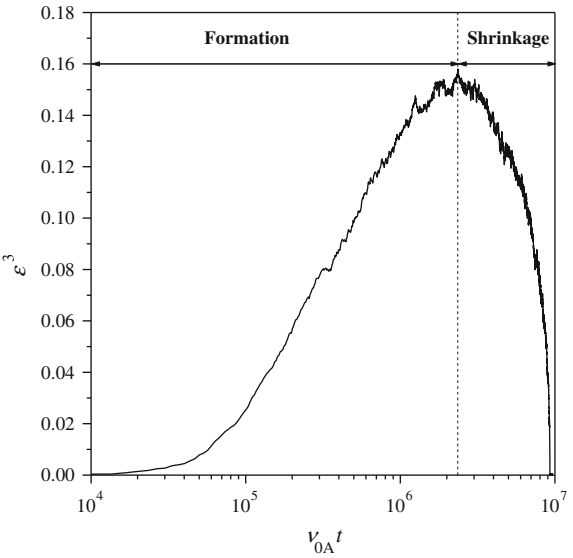

Fig. 7 Time-dependence of the void volume relative to the total volume of the sphere (ν_{0A} is the effective attempt frequency of A atoms for exchange with a vacancy; $\varepsilon = r_i/r_e$, where r_i is the radius of the void and r_e is an external radius of the hollow nanosphere)

3.1 Interdiffusion in Bimetallic Nanoparticles

Here, we discuss two rather extreme cases of interdiffusion in bi-metallic nanoparticles, both of which lead to segregation. In the first case (Ag–Ni), the two metals are almost immiscible in the bulk. In the second case (Pd–Ni) the two metals show complete miscibility in the bulk. It should also be noted that Ni has a much higher surface energy than Ag and Pd.

3.1.1 Interdiffusion in a Ag–Ni Bi-metallic Nanoparticle

Interdiffusion was simulated by the MD method starting with a diffusion couple consisting of a core of Ag (959 atoms) covered by a shell of Ni (2,504 atoms) [41]. Representative snapshots from the MD simulation during isothermal annealing at $T = 950$ K are shown in Fig. 8. It can be seen that Ag atoms diffuse quite rapidly through the Ni-shell and begin to accumulate on the surface of the nanosphere. The first Ag atoms that arrive at the surface of the nanosphere reside preferentially at edges, vertices and at sites at high energy faces. The later Ag atoms that come to the surface of the nanoparticle meet the previous Ag atoms on the surface and form small clusters there. However, this interdiffusion rate soon becomes very slow and almost stops when the average number of nearest Ag neighbours of the Ag atoms on the surface reaches two.

Thus, the Ag atoms coming from the core to the surface by diffusion through the Ni-shell form quite a dispersed single surface layer. On the other hand, a well-defined Ag core remains to occupy the centre of the nanosphere. In Fig. 9 the

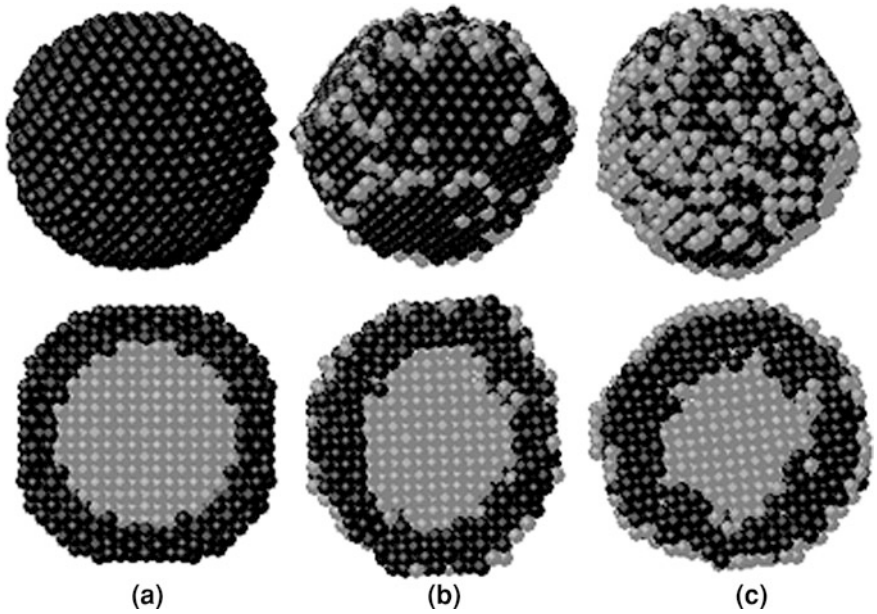

Fig. 8 Selected snapshots (after static relaxation) of the interdiffusion of a Ag-core−Ni-shell nanoparticle during annealing at $T = 950$ K. Snapshots are taken at the beginning of the simulation **a** and after ~ 0.03 μs **b** and ~ 0.3 μs **c**. The surface and a central cross-section of the nanoparticle are shown in the top and bottom rows, respectively. Ag and Ni atoms are represented in *gray* and *black*, respectively

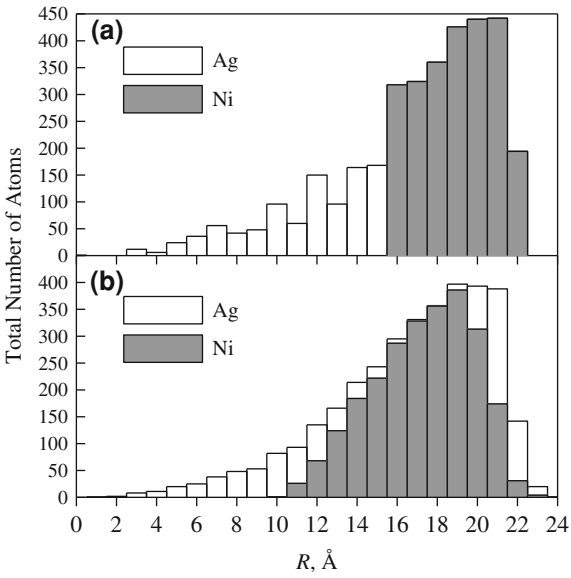

Fig. 9 Atomic radial distribution in the Ag–Ni nanosphere model at the initial time (**a**) and after the annealing at $T = 950$ K during ~ 0.3 μs (**b**)

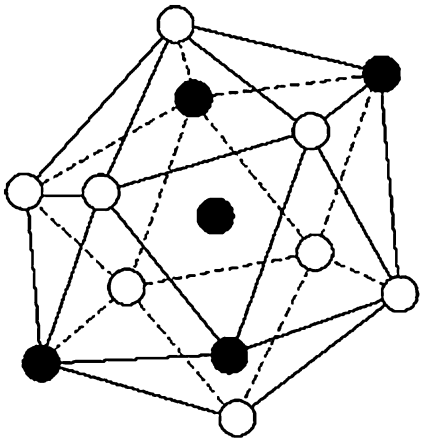

Fig. 10 The most preferred icosahedral environment of Ni atoms in the Pd–Ni nanoparticle model: four Ni and eight Pd nearest neighbours (Ni is *black*, Pd is *white*)

atomic radial distributions of the Ag and Ni atoms illustrates the separation of the initial Ag-core–Ni-shell structure into a Ag-core–Ni-intermediate shell–Ag-dispersed surface sub-monolayer. It can be seen in Fig. 9b that only few Ag atoms exist in the intermediate shell of the nanosphere.

These results agree well with an earlier MD simulation of the growth of Ag–Ni nanospheres by deposition of Ni atoms onto a Ag core [42], where the final number of atoms in the system was $\sim$400, which is one order of magnitude less. Thus, it is evident that the phenomenon of segregation of Ag to form a Ag–Ni–Ag surface–sandwich structure in Ag-core–Ni-shell nanoparticles is quite general and apparently does not have a strong dependence on size.

3.1.2 Interdiffusion in a Pd–Ni Bi-metallic Nanoparticle

In the Pd–Ni system, in complete contrast with the Ag–Ni system, there is complete miscibility in the bulk. MD simulations of interdiffusion in the bi-metallic nanoparticle were performed starting from a core of Ni (1088 atoms) surrounded by a shell of Pd (2132 atoms) [41, 43, 44]. During the first $\sim$0.03 μs of MD annealing at 1000 K, the distorted crystal order of the nanoparticle starts to be broken at the interface between the core and shell rather quickly. Then the structure of the whole nanoparticle evolves by interdiffusion to a disordered Pd-rich solid solution. Monitoring of the structure of the nanoparticle by Voronoi polyhedron analysis shows a significant increase of icosahedral short-range ordering during the next stage of annealing up to $\sim$0.5 μs. The centres of the icosahedral cages are almost always the smaller Ni atoms, surrounded by four Ni and eight Pd atoms (see Fig. 10). The most favourable sites for Ni icosahedra are in the subsurface shell. Indeed, after $\sim$0.5 μs of the annealing, among the 790 Ni

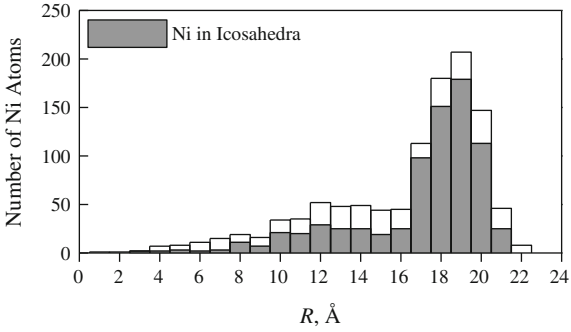

Fig. 11 Radial distribution of Ni atoms having an icosahedron as a coordination polyhedron in the Pd–Ni nanoparticle model after annealing at $T = 1000$ K for ~ 0.5 μs

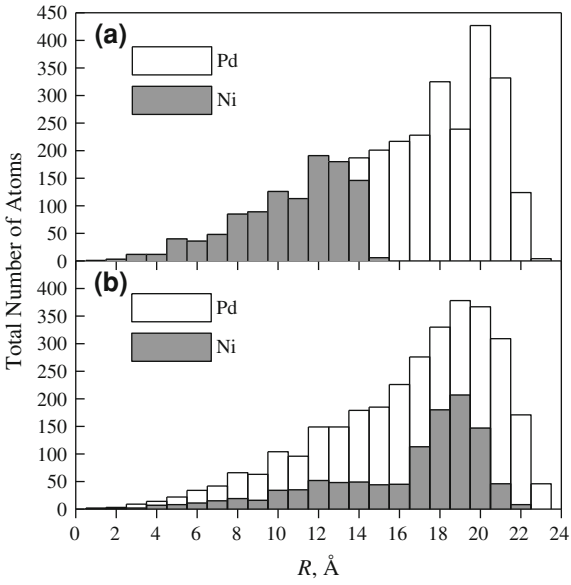

Fig. 12 Atomic radial distribution in the Pd–Ni nanoparticle model **a** at the initial time and **b** after the annealing at $T = 1000$ K for ~ 0.5 μs

atoms that have gone from the initial core to the shell, the icosahedra fraction is $\sim 78\%$ whilst $\sim 52\%$ of the 298 Ni atoms remain in the core (see Figs. 11, 12).

It was established that Ni atoms coming by way of interdiffusion to the shell begin to accumulate in a layer just below the surface, and then locate themselves in the centres of interpenetrating icosahedra in order to generate a subsurface layer (shell) as a Kagomé net (see Fig. 13a), which is almost completely covered by Pd atoms on both sides. Planar layers of Kagomé nets are the basic structure of the well-known bulk Frank-Kasper phases of certain intermetallic alloys [45, 46]. This subsurface Kagomé net shell of Ni atoms efficiently allows the minimization of the nanoparticle surface energy by increase of the average number of nearest neighbours of Pd surface atoms in comparison with the close-packed f.c.c. (111) surface. Indeed, the

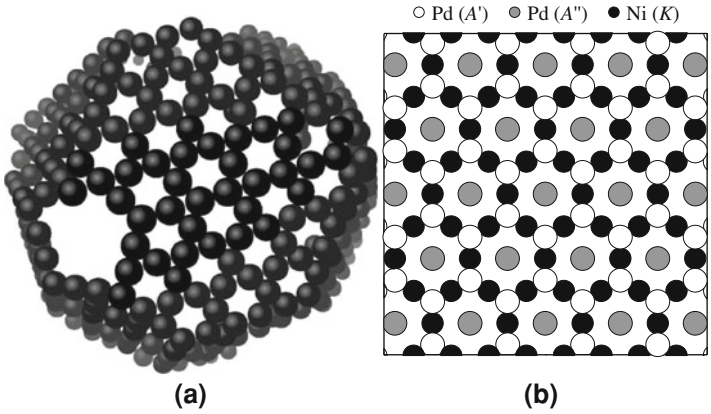

Fig. 13 **a** Snapshot of the Ni subsurface shell having a structure of the Kagomé net with 'sequence faults' after ~0.3 μs of annealing at $T = 1000$ K. The great majority of Ni atoms of the subsurface shell are located in the centres of interpenetrating icosahedra and have four Ni and eight Pd nearest neighbours. For clarity, only a half of the shell and only Ni atoms at centres of icosahedra are shown on the perspective projection with size and grey-scale graduation. **b** Illustration of atomic positions of Pd and Ni atoms on a perfect fragment of surface structure $A'A''KA''A'$. Layers A' and A'' of *Pd* can be obtained by splitting of a layer *A*—close packed f.c.c. (111) layer; layer K of Ni is a Kagomé net layer

Kagomé net layer (*K*) of Ni is covered from each side by two Pd layers (A' and A''), which can be obtained by splitting of a layer *A*—close packed f.c.c. (111) layer (see Fig. 13b). The formation of such a five-layer $A'A''KA''A'$ surface structure results in a third of the surface Pd atoms having increased their number of nearest neighbours from 9 (the close packed f.c.c. (111) surface) to 13. The number of Pd atoms in each couple layers A' and A'' coincides with the number of Ni atoms in the Kagomé net layer, therefore, the total atomic fraction involved in the build up of the five-layer $A'A''KA''A'$ Pd_2Ni ordering surface–sandwich structure in the nanoparticle with consideration of some imperfection of icosahedral order in Kagomé net layer estimated at ~70%. Thus, only ~30% atoms are located in the core of nanoparticle and form there a non-crystalline Pd-rich solid solution with quite strongly developed icosahedral short-range order. This final arrangement of the nanoparticle is the result of competition between the shell (~70% atoms) and the core (~30% atoms) contributions to the excess energy.

Thus, the MD experiments demonstrate that under certain conditions diffusion-driven segregation phenomena at the nanoscale can be observed in systems with completely different phase diagrams in the bulk. For the Ag–Ni system, where the miscibility is very low, it is seen that Ag partially segregates to the surface, ostensibly to lower the surface energy associated with Ni. For the Ni–Pd system, where miscibility in the bulk is complete, at the nano-scale, a new type of chemical ordering occurs.

4 Reaction Synthesis of Intermetallic Nanoparticles

Reaction synthesis (sometimes called combustion synthesis) has received considerable interest as an economic route for the production of certain intermetallic compounds especially nickel aluminide (NiAl) for next generation high-temperature structural and oxidation-resistant materials [47–52]. The reaction synthesis technique utilizes exothermic reaction processing, which reduces the time and energy associated with conventional synthesis methods, e.g. intensive sintering processing [51]. The advantages of reaction synthesis also include the potential for rapid near-net shape processing and phase pure products. Furthermore, reaction-synthesized products have been reported to possess superior mechanical and physical properties [53].

Reaction synthesis is a process wherein once the reactants are ignited they spontaneously transform to products in an exothermic reaction in a very short processing (reaction) time [50]. Experimentally, the self-sustaining reaction can be started either by igniting the sample at one end (combustion wave propagation mode) or by heating the whole volume of the sample to the ignition temperature T_{ig} (simultaneous combustion mode). An important parameter in an experimental reaction synthesis process is the adiabatic temperature T_{ad}. This temperature represents the upper limit of the temperatures achieved by self-heating during a particular exothermic reaction whose rate can be high enough to assume adiabatic conditions [50]. Therefore, it is assumed that all of the heat of formation raises the temperature of the reacting system to the adiabatic temperature with zero heat losses. The ignition and adiabatic temperatures and the reaction time are fundamental processing parameters which help to clarify and classify reactions mechanisms; they can show the expected physical state of the reactants and product during a particular reaction [48–52].

In practice, the synthesis of bulk nickel aluminides is usually achieved by using conventional coarse-grained powders where the grain sizes are of the order of micrometers [48–52]. However, distinct advantages have been reported by using nanometer size particles to synthesize NiAl [54]. It has been shown [54] that due to the physical and chemical characteristics of nanoparticles (especially their high stored energy and therefore high chemical activity) the reaction mode and mechanism are distinctly different from those where conventional coarse-grained powders are used. In particular, it was demonstrated [54] that using nanoparticles can dramatically decrease the ignition temperature of the reaction process. Furthermore, due to the significant brittleness of intermetallic NiAl, a refinement of the grain size to the nanometer level could be a promising way to overcome a limitation of applying the material industrially, since enhancement of hardness and strength can be expected with nano-structures according to the Hall–Petch relation [55]. Moreover, mixtures of nano-sized reactant nanoparticles of Ni and Al that undergo an exothermic reaction can be considered as promising nano-energetic materials for a wide range of advanced applications such as localized heat sources

for chemical and bio neutralization and disease treatment, environmentally clean primers and detonators, welding, ultrafast fuses, and smart thermal barriers [56].

4.1 Formation of NiAl Nanoparticles

Recently, MD efforts have started to focus on reaction diffusion of Ni–Al nanoparticles [57–60]. Delogu [57, 58] performed MD simulations with a tight-binding potential based on the second-moment approximation to the electronic density of states to investigate demixing phenomena in NiAl nanoparticles after melting and the mechanical response of Al-core/Ni-shell nanoparticles on melting of the Al-core. Henz and coworkers [59, 60] performed MD simulations with an embedded-atom method potential [61] to investigate the kinetic sintering of separate [59, 60] and coated [60] liquid Al and solid Ni nanoparticles with an atomic ratio of Al and Ni equal to unity. It was assumed [59, 60] that the reactions begin with the reactants at 600 K where Al is liquid while Ni is solid. These authors showed that under adiabatic conditions for the separate nanoparticle case, a liquid Al nanoparticle first coats the solid Ni nanoparticle and alloying is only completed after the Ni nanoparticle has melted. The sintering processes of the Al-coated Ni nanoparticle and Ni-coated Al nanoparticle are simply the alloying of Ni and Al atoms during the melting of the Ni core or shell [60]. In all cases investigated, the final states were completely alloyed liquid Ni–Al nanoparticles. The effect of nanoparticle size on sintering time, adiabatic temperature and liquid solution formation were also analyzed.

Levchenko and coworkers [62] made MD simulations with an embedded-atom method potential [63] to study the alloying reaction in a Al-coated Ni nanoparticle with equi-atomic fractions and a diameter of $\sim$4.5 nm. This system can be considered as a useful model for a highly compacted mixture of Ni and Al nanoparticles or a powder blend which can be approximated by an ensemble of identical Ni spherical nanoparticles surrounded by a continuous Al matrix [49]. They found that the alloying reaction in the nanoparticle is accompanied by solid state amorphization of the Al-shell and Ni-core in the vicinity of the interface region. The large driving force for alloying of Ni and Al promotes the solid state amorphization of the nanoparticle because it makes intermixing of the components more probable compared with the crystalline state. A fraction of Al atoms remain segregated to the surface of the nanoparticle since Al has a lower surface energy than Ni. This is followed by the crystallization of the Ni–Al amorphous alloy into the B2-NiAl ordered crystal structure. This sequence of events is shown in Fig. 14. The heat of the transformation of the initial Al-coated Ni nanoparticle into the B2-NiAl ordered nanoparticle can be estimated as ~ -0.46 eV/at. The B2-NiAl ordered nanoparticle melts at a temperature of $\sim$1500 K. The adiabatic temperature for the alloying reaction in the initial Al-coated Ni nanoparticle can be estimated to be below the melting temperature of the B2-NiAl ordered nanoparticle. It is shown that very rapid intermixing and Ni–Al amorphous alloy formation

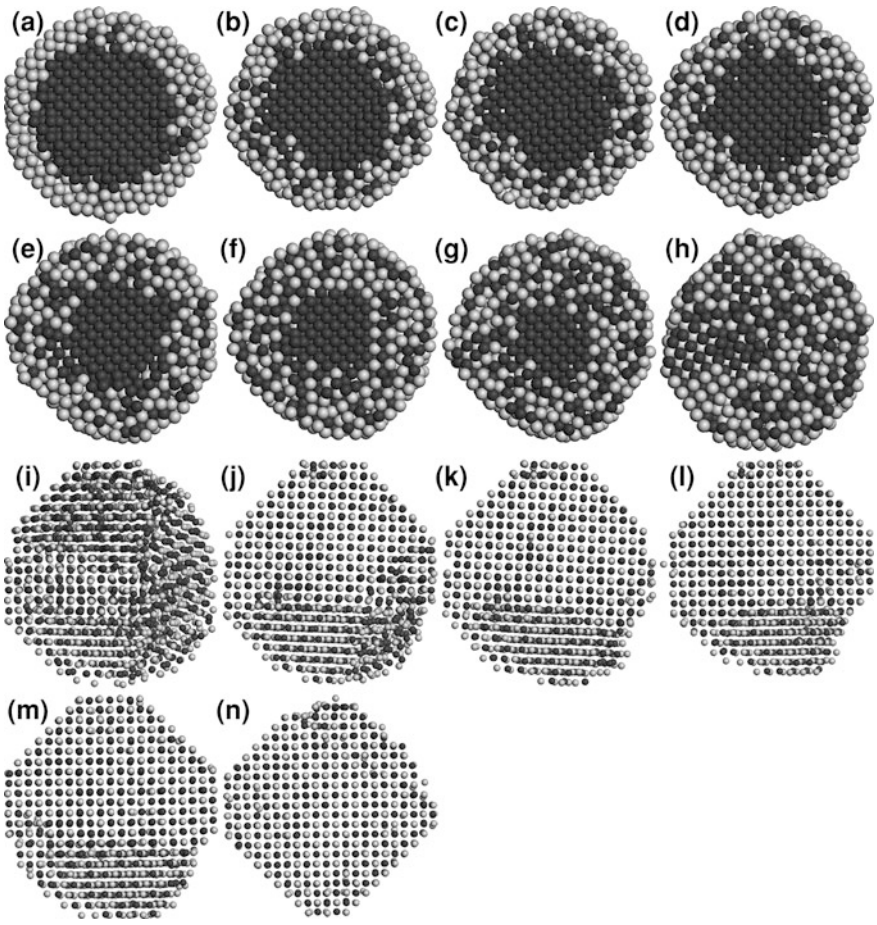

Fig. 14 Central cross-sections of the nanoparticle model after static relaxation at different temperatures in the alloying reaction during isochronal heating with rate $\sim$13.3 K/ns of the initial Al-coated Ni nanoparticle with equi-atomic fractions and diameter of $\sim$4.5 nm: **a** 100 K, **b** 200 K, **c** 300 K, **d** 400 K, **e** 500 K, **f** 600 K, **g** 700 K, **h** 800 K, **i** 900 K, **j** 1000 K, **k** 1100 K, **l** 1200 K, **m** 1300 K and **n** 1400 K. Ni and Al atoms are shown as *dark* and *light grey* spheres, respectively. For better elucidation of B2-NiAl crystalline ordering size of the snapshots of the nanoparticle model is increased and sizes of Ni and Al atoms are decreased (**i**–**n**)

with a reaction self-heating rate $\sim$1 K/ps may occur when the reaction is ignited. It was proposed that this takes a place before any ordering of the Ni–Al interfacial layer. In this case, the ignition temperature can be as low as $\sim$100 K. The alloying reaction will be limited by the degree of pre-heating within the system, which if insufficient, will reduce the interdiffusion rate and hence promote interfacial ordering. The formation of a thin ordered Ni–Al layer at the interface will produce a strong interfacial diffusion barrier, slowing the alloying reaction within the nanoparticle.

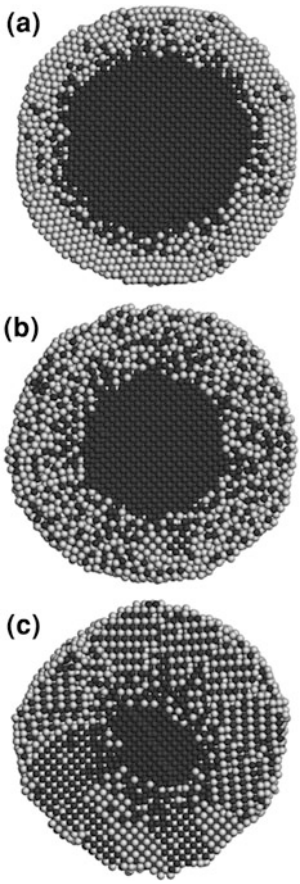

Fig. 15 Central cross-sections of the nanoparticle model after static relaxation at different temperatures in the alloying reaction during isochronal heating with rate $\sim$66.7 K/ns of the initial Al-coated Ni nanoparticle with equi-atomic fractions and diameter of $\sim$9.5 nm: **a** 700 K, **b** 900 K, **c** 1100 K. Ni and Al atoms are shown as dark and light grey spheres, respectively

Furthermore, preliminary MD simulations of the alloying reaction in a Al-coated Ni nanoparticle with equi-atomic fractions and a diameter of $\sim$9.5 nm (which is more than two times longer compared with the earlier study [62]) demonstrate the possibility of the formation of a hollow B2-NiAl nanoparticle. In this case, the following stages of the transformation can be observed (see Fig. 15): intermixing between the f.c.c. Al-shell and f.c.c. Ni-core (Fig. 15a); amorphization of the shell and then intermixing between the amorphous Al-rich shell and f.c.c. Ni-core (Fig. 15b); crystallization (in the shell) of the Al-rich amorphous alloy into an Al-rich B2-NiAl and then intermixing between Al-rich B2-NiAl shell and f.c.c. Ni-core (Fig. 15c). Taking into account that B2-NiAl is a triple-defect compound [64, 65], it was verified that deviation from the exact stoichiometric composition toward the Al-rich composition in the B2-NiAl shell of the nanoparticle is predominantly accommodated by vacancies on the Ni sublattice. Therefore, under certain conditions, interdiffusion between an Al-rich B2-NiAl shell and a f.c.c. Ni-core in such a nanoparticle may result in a flux of the vacancies from the shell into the core and then eventually to form a hollow B2-NiAl nanoparticle.

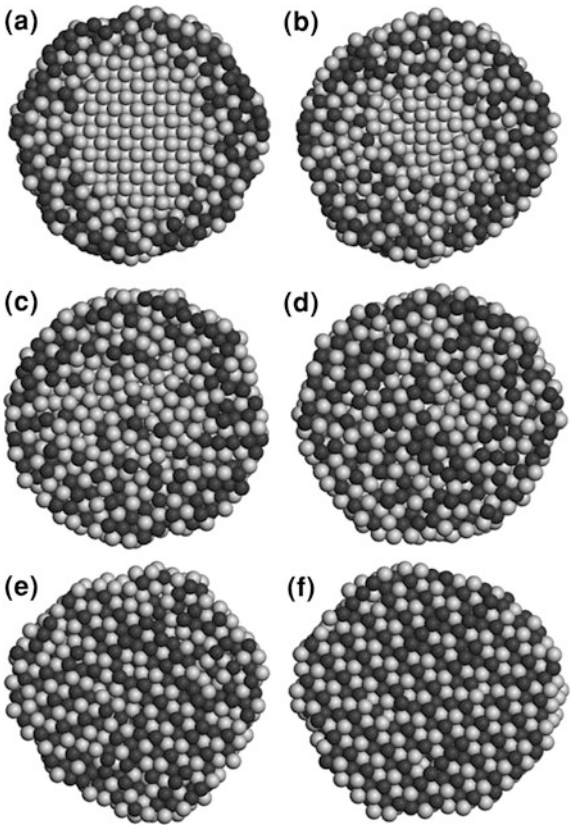

Fig. 16 Central cross-sections of the nanoparticle model after static relaxation at different temperatures in the alloying reaction during isochronal heating with rate ~ 13.3 K/ns of the initial Ni-coated Al nanoparticle with equi-atomic fractions and diameter of ~ 4.5 nm: **a** 500 K, **b** 600 K, **c** 700 K, **d** 800 K, **e** 900 K and **f** 1400 K. Ni and Al atoms are shown as dark and light grey spheres, respectively

In a related MD study with the same embedded-atom method potential [63] Evteev and coworkers [66] investigated the alloying reaction in a nickel coated aluminum nanoparticle with equi-atomic fractions and a diameter of ~ 4.5 nm (see Fig. 16). It was found that the large driving force for the alloying of Ni and Al provokes solid state amorphization of the nanoparticle with the formation of a $Ni_{50}Al_{50}$ amorphous alloy. Amorphization makes intermixing of the components much easier compared with the crystalline state. The average rate of penetration of Ni atoms can be estimated to be about two times higher than Al atoms, whilst the total rate of inter-penetration can be estimated to be of the order of 10^{-2} m/s. The heat of the intermixing can be estimated at ~ -0.34 eV/at. Next, the crystallization of the $Ni_{50}Al_{50}$ amorphous alloy into B2-NiAl ordered crystal structure is observed. The heat of the crystallization can be estimated as ~ -0.08 eV/at. Then, the B2-NiAl ordered nanoparticle melts at a temperature of ~ 1500 K. The adiabatic temperature for the reaction of the initial Ni-coated Al nanoparticle was estimated to be below the melting temperature of the nanoparticle with the B2-NiAl ordered structure.

5 Outlook

This chapter highlighted progress that has been made in atomistic computer simulation of diffusion and reaction in metallic nanoparticles over recent years. We would like to conclude the chapter by discussing some important challenges and promising directions of future research.

In recent years, continuous progress in the field of development of reliable semi-empirical interatomic potentials [67] has already opened possibilities for molecular dynamics simulation of reactive diffusion in nanoparticle with solid-state phase transformations. An example of such a reaction is described in this chapter for Ni–Al nanoparticles. Furthermore, the simulation demonstrates that the time of the reaction can be short enough to precisely describe the whole process on the time scale of molecular dynamics calculations. Thus, molecular dynamics simulation in conjunction with reliable semi-empirical interatomic potentials is likely to become the major modeling technique to describe interdiffusion in nanoparticles. For this reason, the development of new interatomic potentials is critical for expanding molecular dynamics simulations to other classes of nanoparticles. In particular, the first qualitative understanding of hollow nanoparticle formation by interdiffusion gained by applying on-lattice kinetic Monte-Carlo modeling could be extended in the future using molecular dynamics simulation of oxidation of metal nanoparticles in direct parallel with experimental fabrication of hollow nanoparticles. Such molecular dynamics simulations would need to be carried out with a semi-empirical interatomic potential which includes variable charge transfer between anions and cations [68].

In the field of stability of hollow, segregated and core–shell nanoparticles, molecular dynamics and off-lattice Monte-Carlo calculations should be employed to study the surface and interface properties and their interactions with point defects. The influence of the surface/interface properties on the stability of the nanoparticles appears to be very important because in such systems the fraction of atoms at the surface/interface and in the bulk are of comparable magnitudes. In the future, the behaviour of the surface/interface stress and energy with radius, sign of curvature and temperature of the nanoparticles should be explored.

Acknowledgments We acknowledge support from the Australian Research Council under the Discovery Grants Scheme. One of us (E.V.L.) wishes to thank the University of Newcastle for the award of a University Fellowship.

References

1. Yin, Y.D., Rioux, R.M., Erdonmez, C.K., Hughes, S., Somorjai, G.A., Alivisatos, A.P.: Formation of hollow nanocrystals through the nanoscale Kirkendall effect. Science **304**, 711–714 (2004)
2. Smigelskas, A.D., Kirkendall, E.O.: Zinc diffusion in alpha brass. Trans. AIME **171**, 130–142 (1947)

3. Wang, C.M., Baer, D.R., Thomas, L.E., Amonette, J.E., Antony, J., Qiang, Y., Duscher, G.: Void formation during early stages of passivation: initial oxidation of iron nanoparticles at room temperature. J. Appl. Phys. **98**, 94308-1−94308-7 (2005)
4. Han, C., Wu, X., Lin, Y., Gu, G., Fu, X., Hi, Z.: Preparation and characterization of Y2O3 hollow spheres. J. Mater. Sci. **41**, 3679–3682 (2006)
5. Nakamura, R., Tokozakura, D., Nakajima, H.: Hollow oxide formation by oxidation of Al and Cu nanoparticles. J. Appl. Phys. **101**, 074303-1–074303-7 (2007)
6. Nakamura, R., Lee, J.G., Tokozakura, D., Mori, H., Nakajima, H.: Formation of hollow ZnO through low-temperature oxidation of Zn nanoparticles. Mater. Lett. **61**, 1060–1063 (2007)
7. Nakamura, R., Lee, J.G., Tokozakura, D., Mori, H., Nakajima, H.: Oxidation behaviour of Ni nanoparticles and formation process of hollow NiO. Phil. Mag. **88**, 257–264 (2008)
8. Xie, L., Zhang, J., Liu, Y., Li, Y., Li, X.: Synthesis of Li2NH hollow nanospheres with superior hydrogen storage kinetics by plasma metal reaction. Chem. Mater. **20**, 282–286 (2008)
9. Ng, C.H., Tan, H., Fan, W.Y.: Formation of Ag2Se nanotubes and dendrite-like structures from UV irradiation of a CSe2/Ag colloidal solution. Langmuir **22**, 9712–9717 (2006)
10. Gao, J., Zhang, B., Zhang, X., Xu, B.: Magnetic-dipolar-interaction-induced self-assembly affords wires of hollow nanocrystals of cobalt selenide. Angew. Chem. Int. Ed. **45**, 1220–1223 (2006)
11. Li, Q., Penner, R.M.: Photoconductive cadmium sulfide hemicylindrical shell nanowire ensembles. Nano Lett. **5**, 1720–1725 (2005)
12. Fan, H.J., Knez, M., Scholz, R., Nielsch, K., Pippel, E., Hesse, D., Zacharias, M., Gösele, U.: Monocrystalline spinel nanotube fabrication based on the Kirkendall effect. Nat. Mater. **5**, 627–631 (2006)
13. Aldinger, F.: Controlled porosity by an extreme Kirkendall effect. Acta Met. **22**, 923–928 (1974)
14. Geguzin, Y.E.: Why and how vacancies disappear. Science, Moscow (1976)
15. Sun, Y., Mayers, B., Xia, Y.: Metal nanostructures with hollow interiors. Adv. Mater. **15**, 641–646 (2003)
16. Tu, K.N., Gösele, U.: Hollow nanostructures based on the Kirkendall effect: design and stability considerations. Appl. Phys. Lett. **86**, 093111-1−093111-3 (2005)
17. Belova, I.V., Murch, G.E.: Analysis of the formation of hollow nanocrystals: theory and Monte Carlo simulation. J. Phase. Equil. Diffus. **26**, 430–434 (2005)
18. Philibert, J., Atom movements: diffusion and mass transport in solids. editions de physique, les ulis (1991)
19. Manning, J.R.: Diffusion kinetics for atoms in crystals. Van Nostrand Reinhold, Princeton (1968)
20. Prasad, S., Paul, A.: Theoretical consideration on the formation of nanotube following the Kirkendall effect. Appl. Phys. Lett. **90**, 233114-1−233114-3 (2007)
21. Evteev, A.V., Levchenko, E.V., Belova, I.V., Murch, G.E.: Formation of a hollow binary alloy nanosphere: a kinetic Monte Carlo study. J. Nano Res. **7**, 11–17 (2009)
22. Metropolis, N., Rosenbluth, A.W., Rosenbluth, M.N., Teller, A.H., Teller, E.: Equation of state calculations by fast computing machines. J. Chem. Phys. **21**, 1087–1092 (1953)
23. Gusak, A.M., Zaporozhets, T.V.: Hollow nanoshell formation and collapse in binary solid solutions with large range of solubility. J. Phys. Condens. Mat. **21**, 415303-1–415303-11 (2009)
24. Gusak, A.M., Zaporozhets, T.V., Tu, K.N., Gösele, U.: Kinetic analysis of the instability of hollow nanoparticles. Phil. Mag. **85**, 4445–4464 (2005)
25. Evteev, A.V., Levchenko, E.V., Belova, I.V., Murch, G.E.: Shrinking kinetics by vacancy diffusion of a pure element hollow nanosphere. Phil. Mag. **87**, 3787–3796 (2007)
26. Evteev, A.V., Levchenko, E.V., Belova, I.V., Murch, G.E.: Stability and shrinkage by diffusion of hollow nanotubes. Def. Diff. Forum **266**, 39–47 (2007)
27. Evteev, A.V., Levchenko, E.V., Belova, I.V., Murch, G.E.: Theoretical analysis and atomistic modelling of diffusion and stability of pure element hollow nanospheres and nanotubes. Def. Diff. Forum **277**, 21–26 (2008)

28. Evteev, A.V., Levchenko, E.V., Belova, I.V., Murch, G.E.: Stability of hollow nanospheres: a molecular dynamics study. Sol. St. Phen. **129**, 125–130 (2007)
29. Evteev, A.V., Levchenko, E.V., Belova, I.V., Murch, G.E.: Shrinking kinetics by vacancy diffusion of hollow binary alloy nanospheres driven by the Gibbs-Thomson effect. Phil. Mag. **88**, 1524–1541 (2008)
30. Evteev, A.V., Levchenko, E.V., Belova, I.V., Murch, G.E.: Composition effect on shrinkage of hollow binary alloy nanospheres. Def. Diff. Forum **289–292**, 665–672 (2009)
31. Moleko, L.K., Allnatt, A.R., Allnatt, E.L.: A self-consistent theory of matter transport in a random lattice gas and some simulation results. Phil. Mag. A **59**, 141–160 (1989)
32. Murch, G.E., Evteev, A.V., Levchenko, E.V., Belova, I.V., Murch, G.E.: Recent progress in the simulation of diffusion associated with hollow and bi-metallic nanoparticles. Diffus. Fundam. **11**, 42.1–42.22 (2009)
33. Toshima, N., Kanemaru, M., Shiraishi, Y., Koga, Y.: Spontaneous formation of core/shell bimetallic nanoparticles: A calorimetric study. J. Phys. Chem. B **109**, 16326–16331 (2005)
34. Takenaka, S., Shigeta, Y., Tanabem, E., Otsuka, K.: Methane decomposition into hydrogen and carbon nanofibers over supported Pd−Ni catalysts: Characterization of the catalysts during the reaction. J. Phys. Chem. **108**, 7656–7664 (2004)
35. Sao-Joao, S., Giorgio, S., Penisson, J.M., Chapon, C., et al.: Structure and deformations of Pd−Ni core-shell nanoparticles. J. Phys. Chem. **109**, 342–347 (2005)
36. Hungría, A.B., Calvino, J.J., Anderson, J.A., Martínez-Arias, A.: Model bimetallic Pd–Ni automotive exhaust catalysts: Influence of thermal aging and hydrocarbon self-poisoning. Appl. Catal. **62**, 359–368 (2006)
37. Miegge, P., Rousset, J.L., Tardy, B., Massardier, J., et al.: Pd1Ni99 and Pd5Ni95-Pd surface segregation and reactivity for the hydrogenation of 1,3-butadiene. J. Catal. **149**, 404–413 (1994)
38. Hermann, P., Guigner, J.M., Tardy, B., Jugnet, Y., et al.: The Pd/Ni(110) bimetallic system: surface characterisation by LEED, AES, XPS, and LEIS techniques; new insight on catalytic properties. J. Catal. **163**, 169–175 (1996)
39. Michel, A.C., Lianos, L., Rousset, J.L., Delichère, P., et al.: Surface characterization and reactivity of Pd8Ni92 (111) and (110) alloys. Surf. Sci. **416**, 288–294 (1998)
40. Porte, L., Phaner-Goutorbe, M., Guigner, J.M., Bertolini, J.C.: Structuring and catalytic activity of palladium thin layers deposited on the Ni(110) surface. Surf. Sci. **424**, 262–270 (1999)
41. Levchenko, E.V., Evteev, A.V., Belova, I.V., Murch, G.E.: Surface-sandwich segregation phenomena in bimetallic Ag−Ni and Pd−Ni nanoparticles: a molecular dynamics study. Def. Diff. Forum **289–292**, 657–664 (2009)
42. Baletto, F., Mottet, C., Ferrando, R.: Growth of three-shell onionlike bimetallic nanoparticles. Phys. Rev. Lett. **90**, 135504-1–135504-4 (2003)
43. Evteev, A.V., Levchenko, E.V., Belova, I.V., Murch, G.E.: Modelling of the formation of Pd−Ni alloy nanoparticles by interdiffusion. Def. Diff. Forum **277**, 207–212 (2008)
44. Evteev, A.V., Levchenko, E.V., Belova, I.V., Murch, G.E.: Interdiffusion and surface–sandwich ordering in initial Ni-core−Pd-shell nanoparticle. Phys. Chem. Chem. Phys. **11**, 3233–3240 (2009)
45. Frank, F.C., Kasper, J.S.: Complex alloy structures regarded as sphere packings.1. Definitions and basic principles. Acta. Cryst. **11**, 184–190 (1959)
46. Frank, F.C., Kasper, J.S.: Complex alloy structures regarded as sphere packing.2. Analysis and classification of representative structures. Acta. Cryst. **12**, 483–499 (1958)
47. Westbrook, J.H., Fleischer, R.L. (eds.): Intermetallic Compounds: Structural Applications Vol. 4. Wiley, New York (2000)
48. Dunand, D.C.: Reactive synthesis of aluminide intermetallics. Mater. Manuf. Proc. **10**, 373–403 (1995)
49. Farber, L., Klinger, L., Gotman, I.: Modeling of reactive synthesis in consolidated blends of fine Ni and Al powders. Mater. Sci. Eng. A **254**, 155–165 (1998)

50. Morsi, K.: Review: reaction synthesis processing of Ni−Al intermetallic materials. Mater. Sci. Eng. A **299**, 1–15 (2001)
51. Li, H.P.: Influence of ignition parameters on micropyretic synthesis of Ni−Al compound. Mater. Sci. Eng. A **404**, 146–152 (2005)
52. Kim, H.Y., Chung, D.S., Hong, S.H.: Intermixing criteria for reaction synthesis of Ni/Al multilayered microfolls. Scripta. Mater. **54**, 1715–1719 (2006)
53. Li, H.P., Bhaduri, S.B., Sekhar, J.A.: Metal-ceramic composites based on the Ti–B–Cu porosity system. Metall Mater. Trans. A **24**, 251–261 (1992)
54. Dong, S., Hou, P., Cheng, H., Yang, H., Zou, G.: Fabrication of intermetallic Ni−Al by self-propagating high-temperature synthesis reaction using aluminium nanopowder under high pressure. J. Phys. Condens. Mat. **14**, 11023–11030 (2002)
55. Fukumuto, M., Yamasaki, M., Nie, M., Yasui, T.: X. Synthesis and characterization of nano-structured Ni−Al intermetallic compound coating. Q. J. Jpn. Weld. Soc. **24**, 87–92 (2006)
56. Zhao, S.J., Germann, T.C., Strachan, A. Atomistic simulations of shock-induced alloying reactions in Ni/Al nanolaminates. J. Chem. Phys. **125**, 164707-1–1647-8 (2006)
57. Delogu, F.: Demixing phenomena in Ni−Al nanometre-sized particles. Nanotechnology **18**, 065708-1–065708-7 (2007)
58. Delogu, F.: Numerical simulation of the thermal response of Al core/Ni shell nanometer-sized particles. Nanotechnology **18**, 505702-1–505702-7 (2007)
59. Henz, B.J., Hawa, T., Zachariah, M.: Molecular dynamics simulation of the kinetic sintering of Ni and Al nanoparticles. Mol. Simul. **35**, 804–811 (2009)
60. Henz, B.J., Hawa, T., Zachariah, M. Molecular dynamics simulation of the energetic reaction between Ni and Al nanoparticles. J. Appl. Phys. **105**, 124310-1–124310-10 (2009)
61. Angelo, J.E., Moody, N.R., Baskes, M.I.: Trapping of hydrogen to lattice-defects in nickel. Model. Simul. Mater. Sci. Eng. **3**, 298–307 (1995)
62. Levchenko, E.V., Evteev, A.V., Riley, D.P., Belova, I.V., Murch, G.E.: Molecular dynamics simulation of the alloying reaction in Al-coated Ni nanoparticle. Comput. Mater. Sci. **47**, 712–720 (2010)
63. Mishin, Y., Mehl, M.J., Papaconstantopoulos, D.A.: Embedded-atom potential for B2-NiAl. Phys. Rev. B **65**, 224114-1–224114-14 (2002)
64. Bradley, A.J., Taylor, A.: An X-ray analysis of the nickel–aluminium system. Proc. R. Soc. Lond. A **159**, 56–72 (1937)
65. Taylor, A., Doyle, N.J.: Further studies on nickel−aluminum system. J. Appl. Crystallogr. **5**, 201–215 (1972)
66. Evteev, A.V., Levchenko, E.V., Riley, D.P., Belova, I.V., Murch, G.E.: Reaction of a Ni-coated Al nanoparticle to form B2-Ni−Al: A molecular dynamics study. Phil. Mag. Lett. **89**, 815–830 (2009)
67. Mishin, Y.: Interatomic potentials for metals. In: Yip, S. (ed.) Handbook of materials modeling. Springer, Dordrecht (2005)
68. Streitz, F.H., Mintmire, J.W.: Electrostatic potentials for metal-oxide surfaces and interfaces. Phys. Rev. B **50**, 11996–12003 (1994)

Controlled Synthesis of Gold Nanorods via Seeded Growth Approach

Teoh Poay Ling, Khairunisak Abdul Razak, Azlan Abdul Aziz and Rahmah Noordin

Abstract This work describes the synthesis of gold nanorods (AuNRs) produced using the seeded growth method. The properties of AuNRs with varying synthesis parameters such as amount of cetyltrimethylammonium bromide (CTAB), concentration of ascorbic acid, volume of seed solution and amount of HNO_3 were studied. Sufficient CTAB amount is important in order to obtain AuNRs. Below 0.2 M CTAB, aspect ratio of AuNRs (length divide by width) was low because the AuNRs formed were short and thick. Insufficient CTAB amount could not form micelles that blocked the seed in a certain direction for growth of AuNRs. The aspect ratio of AuNRs increased up to 0.2 M CTAB, beyond which the spherical shaped Au nanoparticles were formed. The addition of ascorbic acid up to 0.08 M increased the aspect ratio of AuNRs. However, further increase in ascorbic acid concentration caused the aspect ratio to decrease due to fast reduction of Au ions.

T. P. Ling · K. A. Razak (✉)
School of Materials and Mineral Resources Engineering, Engineering Campus, Universiti Sains Malaysia, 14300 Nibong Tebal, Penang, Malaysia
e-mail: khairunisak@eng.usm.my

T. P. Ling
e-mail: pink_teoh86@hotmail.com

K. A. Razak · A. A. Aziz · R. Noordin
NanoBiotechnology Research and Innovation (NanoBRI), Institute for Research in Molecular Medicine (INFORMM), Universiti Sains Malaysia, 11800 USM, Penang, Malaysia
e-mail: lan@usm.my

A. A. Aziz
School of Physics, Universiti Sains Malaysia, 11800 USM, Penang, Malaysia

R. Noordin
e-mail: rahmah@usm.my

Adv Struct Mater (2013) 4: 61–72
DOI: 10.1007/8611_2011_63

Published Online: 2 February 2012

The aspect ratio of AuNRs rose with increasing the volume of seed solution of up to 50 μl, beyond which the aspect ratio decreased. The addition of HNO_3 was beneficial to increase the aspect ratio of AuNRs up to 300 μl due to slower Au ions reduction. However, further addition of HNO_3 formed shorter and unstable AuNRs colloids.

1 Introduction

Gold nanoparticles (AuNPs) are noble metal nanoparticles that have strong surface plasmon resonance absorption and scattering, do not react with oxygen at atmospheric and chemical environment, facile synthesis and are non-toxic [1, 2]. Among the AuNPs, gold nanorods (AuNRs) are of interest owing to their unique properties such as strong light absorption and scattering at their longitudinal plasmon resonance, easy resonance tunability, chemically inert and biologically compatible. AuNRs have two plasmon resonances as oscillation of the conduction electrons corresponding to the transverse surface plasmon band (TSP) ~520 nm and longitudinal surface plasmon band (LSP) at 700–1300 nm. TSP normally represents diameter, while LSP represents length of AuNRs. By varying the aspect ratio of AuNRs, the plasmon resonance can be tuned close to the near-infrared region (NIR), where absorbance by cells and tissue is minimal [3]. This unique property makes AuNRs extremely attractive in various applications such as contrast agents for optical imaging techniques, photothermal therapy, and biosensing [4, 5].

AuNRs have been synthesized using various methods including templating method, photochemical (UV-irradiation) and electrochemical synthesis. However, most methods have several drawbacks such as low processing yield, long reaction time, and tedious synthesis steps. Therefore, the seed mediated growth method has been used to overcome these problems. The seed mediated growth method is capable to produce high yield AuNRs with simple setup at shorter reaction time [6, 7]. Moreover, the seed mediated growth method also can produce monodispersed nanoparticles with predetermined size [8]. The seed-mediated growth method can eliminate nucleation and promote growth of AuNRs.

Jana et al. [9] used a stepwise citrate seed-mediated method whereby low yield of AuNRs was formed. Subsequently, Sau and Murphy [8] modified their approach with replacement of the citrate with cetyltrimethylammonium bromide (CTAB) molecules in the seed formation step. The yield of AuNRs was improved but short AuNRs were produced with a certain amount of bone-shaped Au. Nikoobakht and El-Sayed [10] have successfully used CTAB capped seed mediated growth method to synthesis high yield AuNRs. However, it is difficult to control the orientation of AuNRs in their method. Meanwhile, Wu et al. [11] and Bai et al. [12] used a three steps CTAB capped seed-mediated growth method in the presence of nitric acid (HNO_3). Their method managed to improve the aspect ratio and growth direction of AuNRs. Moreover, three-step growth is time consuming and requires more

chemicals to synthesise AuNRs. In order to improve the aspect ratio and orientation of AuNRs in this work, the procedure by Nikoobakht and El-Sayed [10] was modified using nitric acid.

In this work AuNRs were produced using a one-step CTAB capped seed-mediated method in the presence of HNO_3. Four synthesis parameters were systematically studied; CTAB concentration, ascorbic acid concentration, volume of seed solution and volume of nitric acid.

2 Experimental Details

The seed solution was prepared by mixing a solution of 5 ml various concentrations of CTAB (0.10, 0.15, 0.20, and 0.30 M) with 5.0 ml of 0.0005 M $HAuCl_4$. The prepared solution was stirred for 15 min. After that, 0.60 ml of ice-cold 0.01 M $NaBH_4$ was added into the prepared solution that formed a brownish solution. The solution was continuously stirred for 2 min and kept at 25°C.

The growth solution was prepared by combining 150 μl of 0.0040 M $AgNO_3$ solution into 5 ml of various concentrations of CTAB solution (0.10, 0.15, 0.20, and 0.30 M). Then, 5.0 ml of 0.0010 M $HAuCl_4$ was added into the prepared solution. After that, 70 μl ascorbic acid with varying concentrations (0.07, 0.08, 0.09, and 0.10 M) and 100–400 μl HNO_3 were added into the prepared solution. The ascorbic acid was used as a mild reducing agent that changed the growth solution from dark yellow to colorless. After 2 h, (10, 30, 50, or 70) μl of the seed solution was added into the growth solution. For varying CTAB concentration study, the ascorbic acid concentration and seed solution were fixed to 0.08 M and 50 μl, respectively. For the study on ascorbic acid concentration, the CTAB concentration was fixed to 0.20 M and 50 μl seed solution was used. The effect of seed solution volume was performed by fixing the CTAB concentration to 0.20 M and ascorbic acid concentration to 0.08 M. The effect of the HNO_3 volume was carried out by fixing the CTAB concentration to 0.20 M, ascorbic acid concentration to 0.08 M, and 50 μl seed solution.

The samples were centrifuged at 14000 rpm for 45 min and re-dispersed in 3 ml deionised water. The transverse surface plasmon (TSP) and longitudinal surface plasmon (LSP) of the solution were characterized using UV–visible NIR spectrophotometer (UV-3600, Shimadzu). Size and shape of the AuNRs were observed using transmission electron microscopy (TEM) (Philips CM12, Version 3.2). The dimension and size distribution of AuNRs was carried out by using the Image J software.

3 Results and Discussion

The size and shape of AuNRs produced were highly dependent on the initial precursors such as concentration of CTAB, concentration of ascorbic acid, volume of seed solution and volume of nitric acid. The transverse surface plasmon (TSP)

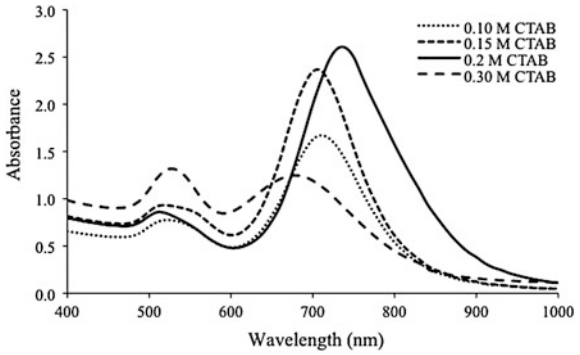

Fig. 1 UV-Vis NIR spectra of the AuNRs solution with varying CTAB concentration

and longitudinal surface plasmon (LSP) of AuNRs synthesized with varying CTAB concentrations of 0.10, 0.15, 0.20 and 0.30 M are shown in Fig. 1. The absorbance values in the spectra represent the yield of AuNRs. The increase of CTAB concentration from 0.1 to 0.2 M caused increasing yield of AuNRs, which could be seen from decreasing of TSP absorbance intensity and the increasing of LSP absorbance intensity. TSP of AuNRs slightly decreased from 524 to 513 nm up to 0.2 M, while LSP absorbance increased from 710 to 757 nm. However, further increased of CTAB concentration to 0.3 M, the TSP position increased, and the LSP position of AuNRs dropped significantly (Table 1).

The results from UV–Vis spectra were further proven by TEM analysis as shown in Fig. 2 and summarized in Table 1. With increasing CTAB concentration, AuNRs grew longer and became thinner (Fig. 2a–c). Further increased of CTAB concentration until 0.3 M, the diameter of AuNRs became thicker and slower growth in length (Fig. 2d). Figure 2c shows a TEM image of the sample by adding 0.2 M CTAB. The increase of CTAB concentration increased the CTAB adsorption on the particles surface mainly on {110} facet. The adsorptions of CTAB molecules (monomers) on the AuNRs surface disturbed the equilibrium of the monomers and decomposed the unbound monomers. The diffusivity rate of the monomer was directly proportional to CTAB concentration. As a result, the monomers diffused and more efficiently adsorbed on {110} facet of growing AuNRs [13]. Therefore, the high yields of AuNRs were produced with increasing CTAB concentration of up to 0.2 M. However, when high concentration of CTAB was used (0.3 M), viscosity and viscoelasticity of the solution increased. Hence, CTAB blocked diffusion of Au ions and formed Au nanoparticles. As a result, the yield of AuNRs decreased.

The aspect ratio of AuNRs can also be tuned by varying the ascorbic acid concentration; 0.07, 0.08, 0.09 and 0.10 M. The ascorbic acid plays the role of a weak reducing agent in the seed-mediated growth method. The reduction process of gold (Au) ions by ascorbic acid is shown in Eqs. 1–3. Equation 1 represents confined Au ions in the metallomicelles. In the growth solution, the ascorbic acid reduced Au ions (Au^{3+}) to intermediate Au (Au^{1+}) in the presence of CTAB. Whilst Eq. 2 occurred after the addition of seed solution into the growth solution.

Table 1 Physical properties of AuNRs with varying CTAB concentration; transverse surface plasmon (TSP), longitudinal surface plasmon (LSP) position, length, diameter and aspect ratio

CTAB concentration (M)	TSP (nm)	LSP (nm)	Length, L (nm)	Diameter, D (nm)	Aspect ratio (L/D)
0.10	524	710	26	9	2.8
0.15	515	715	27	8	3.3
0.20	513	757	29	8	3.6
0.30	528	697	30	13	2.3

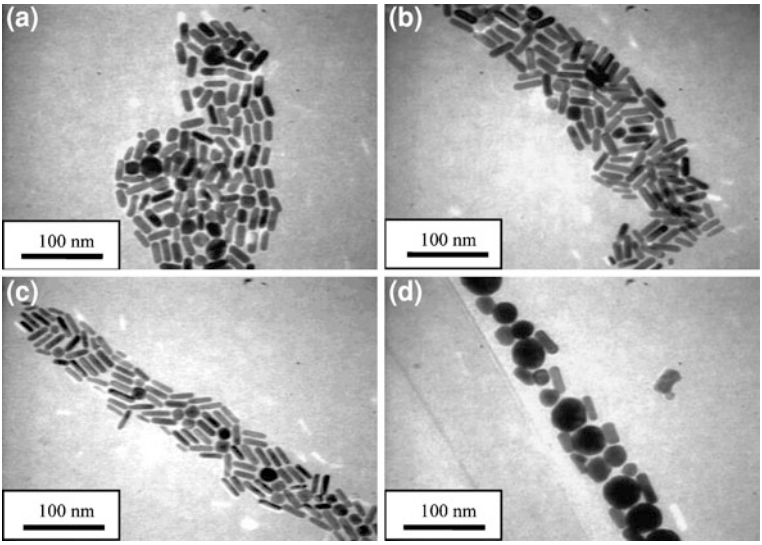

Fig. 2 TEM images of AuNRs synthesized using different CTAB concentrations; **a** 0.10 M, **b** 0.15 M, **c** 0.20 M, and **d** 0.30 M

The unconsumed ascorbic acid reduced intermediate Au (Au^{1+}) to Au atoms (Au^0). Meanwhile, Eq. 3 represents the overall reaction.

First reduction: $Au^{3+} \rightarrow Au^{1+}$

$$CTA - AuBr_4 + C_6H_8O_6 \rightarrow AuBr_2 + C_6H_6O_6 + 2H^+ + 2Br^- \quad (1)$$

Second reduction: $Au^{1+} \rightarrow Au^0$

$$2CTA - AuBr_2 + C_6H_8O_6 \rightarrow 2Au + C_6H_6O_6 + 2CTA^+ + 2H^+ + 4Br^- \quad (2)$$

Overall reaction:

$$2CTA - AuBr_4 + 3C_6H_8O_6 \rightarrow 2Au + 3C_6H_6O_6 + 2CTA^+ + 6H^+ + 8Br^- \quad (3)$$

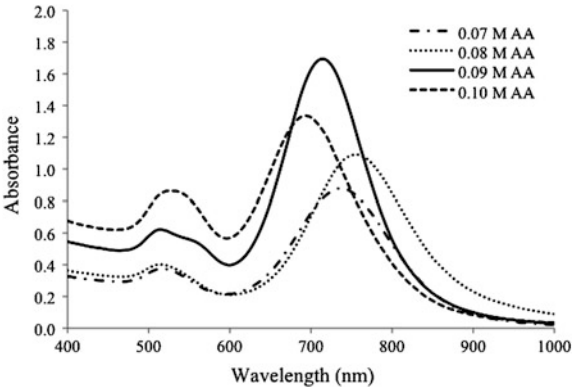

Fig. 3 UV-Vis-NIR spectra of the AuNRs solution with varying ascorbic acid concentration

Figure 3 shows the UV–Vis spectra of AuNRs with varying ascorbic acid concentration; 0.07, 0.08, 0.09 and 0.10 M. AuNRs have spherocylinder for all ascorbic acid concentration as shown in Fig. 4. The edge of the AuNRs has a flat end with tapered side. Increasing the ascorbic acid concentration from 0.07 to 0.08 M, the aspect ratio increased from 2.6 to 3.6 (Fig. 4a–b). This was due to the decrease in diameter and increase in length of AuNRs as summarised in Table 2. At the same time, the LSP shifted to longer region. The reduction rate of Au ions was dependent on the ascorbic acid concentration. Low concentration of ascorbic acid caused slower reduction kinetic, hence allows slow diffusion of Au ions on the Au seeds particles surface. As a result, longer AuNRs were produced. The ascorbic acid reduced Au^{3+} to Au^{1+} in the growth solution, and unconsumed ascorbic acid reduced Au^{1+} to Au^{0} with the presence of seed solution [14]. However, excess ascorbic acid caused forced reduction, resulted in the decrease of AuNRs aspect ratio from 3.6 to 2.5 (Fig. 4c–d).

In the seed-mediated growth method, the seed particles acted as active sites for crystals to grow. Then, gold atoms (Au^{0}) suspended in the solution and grew on the surface of seed particles. Therefore, varying the volume of seed solution was important in determining the size and shape of AuNRs. Figure 5 shows the UV–Vis spectra of the AuNRs obtained by varying the volume of seed solution; 10, 30, 50, and 70 μl. LSP position was directly proportional to the aspect ratio of AuNRs because the aspect ratio of AuNRs was linearly dependent on the oscillation of free electron along the long axis. The increase in aspect ratio caused the LSP position shifted to a higher wavelength region [15]. The obtained results demonstrated that when the volume of the seed solution was increased from 10 to 50 μl, the LSP position shifted from 643 to 760 nm as their aspect ratios increased from 2.6 to 3.6 (Table 3). When the volume of seed solution increased, the ratio of Au ions to seed particles in the growth solution decreased. Therefore, lesser Au ions were available in the growth solution and the seed particles were in more stable condition. Also, it may control the sudden formation of much Au nuclei, thus inhibiting the uncontrollable growth of AuNRs. Then, the seed particles induced of nucleation of Au crystals. As a result, more AuNRs were grown following the CTAB direction [8, 16].

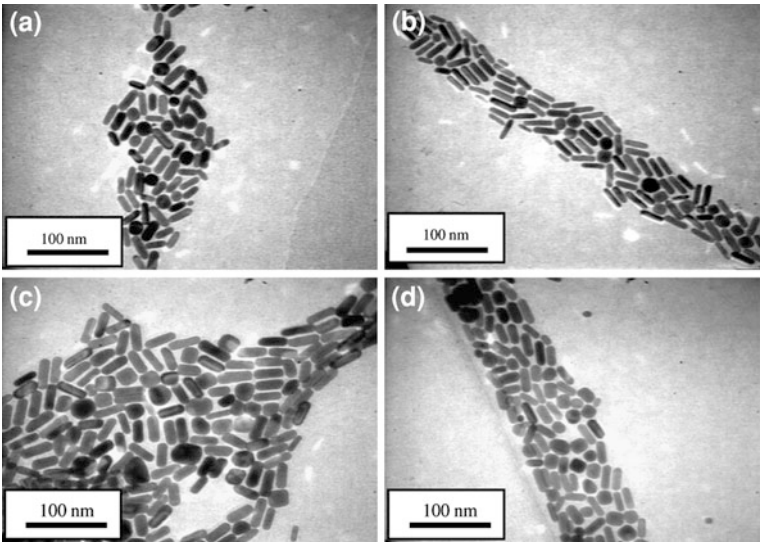

Fig. 4 TEM images of the gold nanorods with varying ascorbic acid concentrations; **a** 0.07 M, **b** 0.08 M, **c** 0.09 M, and **d** 0.10 M

Table 2 Physical properties of AuNRs with varying ascorbic acid concentration; transverse surface plasmon (TSP), longitudinal surface plasmon (LSP) position, length, diameter and aspect ratio

Ascorbic acid concentration (M)	TSP (nm)	LSP (nm)	Length, L (nm)	Diameter, D (nm)	Aspect ratio (L/D)
0.07	515	734	26	10	2.6
0.08	516	756	29	8	3.6
0.09	514	713	32	12	2.7
0.10	528	695	25	10	2.5

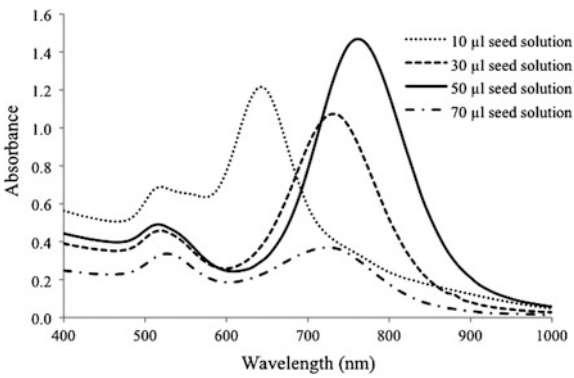

Fig. 5 UV-Vis NIR spectra of the NRs solution with adding 10 until 70 µl of seed solution

Table 3 Physical properties of AuNRs with varying volume of seed solution; transverse surface plasmon (TSP), longitudinal surface plasmon (LSP) position, length, diameter and aspect ratio

Volume of seed solution (μl)	TSP (nm)	LSP (nm)	Length, L (nm)	Diameter, D (nm)	Aspect ratio (L/D)
10	518	643	41	16	2.6
30	518	731	30	9	3.3
50	514	760	29	8	3.6
70	527	724	21	7	3.0

TEM images (Fig. 6a–d) analysis clearly show the change of length and diameter of AuNRs with varying the volume of seed solution. When 50 μl of seed solution was added, a large quantity of AuNRs was formed. The diameter of the AuNRs decreased with increasing the volume of seed solution. The length of AuNRs synthesized using 10 μl seed solution was the longest, but the diameter of AuNRs was thicker compared to other volumes of seed solution. In addition, the length of the AuNRs produced using 30 and 50 μl seed solution did not change much (Table 3). However, when the volume of seed solution was increased to 70 μl, the length and aspect ratio of AuNRs clearly decreased. When more seeds were added into the growth solution, lesser gold ions per nuclei were available for growth to take place. Thus, the length and aspect ratio of AuNRs became smaller. Besides, when a high volume of seed solution was added into the growth solution, CTAB formed smaller micelles to cover seeds. Then, the growth of AuNRs was terminated by the accumulation of multilayers of CTAB on the surface growing particles that blocked the access of Au ions to the growing AuNRs [17]. As a result, the growth process of AuNRs became slower.

In seed-mediated synthesis, HNO_3 acted as an additive to improve the yield of high aspect ratio AuNRs. Nitric acid (HNO_3) is a highly reactive oxidizing agent. The influence of pH on the redox potential of Au is important because Au^{3+} ions are involved in the reduction process. The driving force for the reaction is the difference between the redox potentials (ΔE) of the two half cell reactions (reduction of Au ion and oxidation of reducing agent). The oxidation–reduction reaction slowed upon decreasing the value of ΔE. During growth process, the Au ions reduced from $AuCl_4^-$ to $AuCl_2^-$ by ascorbate (with donor an electron).

In this seed-mediated synthesis of AuNRs, the kinetics of reaction is directly proportionally to the pH of react solution. When the pH of solution is low (volume of HNO_3 increasing), the value of the ΔE decreased. This is because the reduction ability of ascorbic acid becomes slower. This condition leads to decreasing the redox potential of Au ions as well. Since the growth was slow, the CTAB can effectively grow in the AuNRs growing direction. Therefore, the Au ions from the growth solution diffused on the seed surface after capping by CTAB. Besides, decreasing the ΔE (at low ionic strength or low pH), it increased the solution stability. This is because the electrostatic interaction reduced between NO_3 ions and CTAB bilayer on AuNRs. So, agglomeration decreased. At the same time, nitrate ions absorbed on {110} facet of AuNRs and stabilized the NRs structure

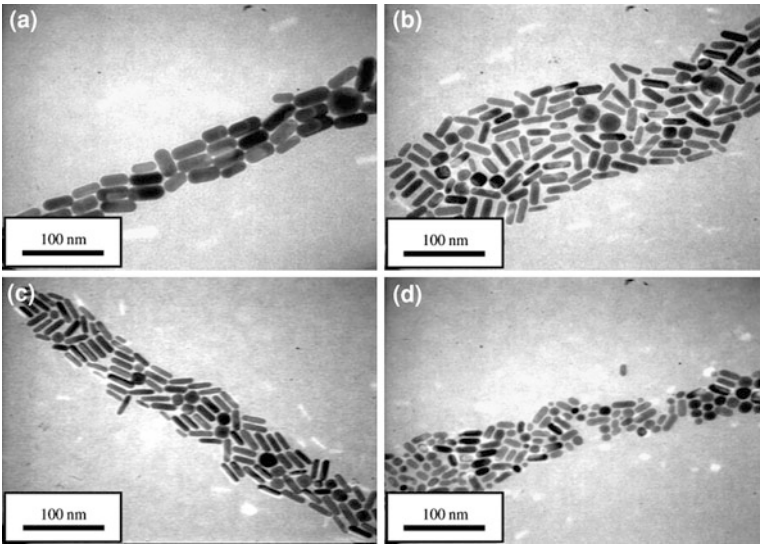

Fig. 6 TEM images of AuNRs with varying volume of seed solution; **a** 10 μl, **b** 30 μl, **c** 50 μl, and **d** 70 μl

Fig. 7 UV-Vis NIR spectra of the solution with varying volume of HNO_3

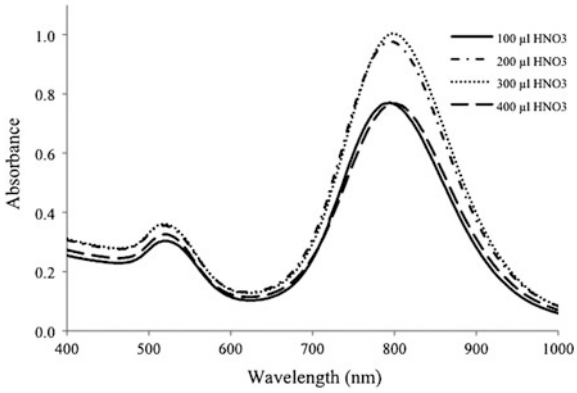

and assisted the growth of AuNRs along the [100] direction. As a result, high aspect ratio of AuNRs was produced after the addition of HNO_3.

Figure 7 and Table 4 show that the longitudinal plasmon wavelength and the aspect ratio AuNRs increase up to 4.9 as the pH of the solution decreases (volume of HNO_3 increase up to 300 μl). However, further addition beyond 300 μl HNO_3 (at high ionic strength), the longitudinal plasmon wavelength decreased. From Fig. 8a–c and Table 4, whereby the length of AuNRs grew gradually longer with the increase of HNO_3 up to 300 μl HNO_3. Excess HNO_3 (more than 300 μl) formed the shorter AuNRs (Fig. 8d). Low pH of the growth solution caused

Table 4 Physical properties of AuNRs with varying volume of nitric acid; transverse surface plasmon (TSP), longitudinal surface plasmon (LSP) position, length, diameter and aspect ratio

Volume of HNO_3 (μl)	TSP (nm)	LSP (nm)	Length, L (nm)	Diameter, D (nm)	Aspect ratio (L/D)
100	518	793	31	8	3.9
200	518	794	33	8	4.1
300	520	799	39	8	4.9
400	514	796	35	8	4.4

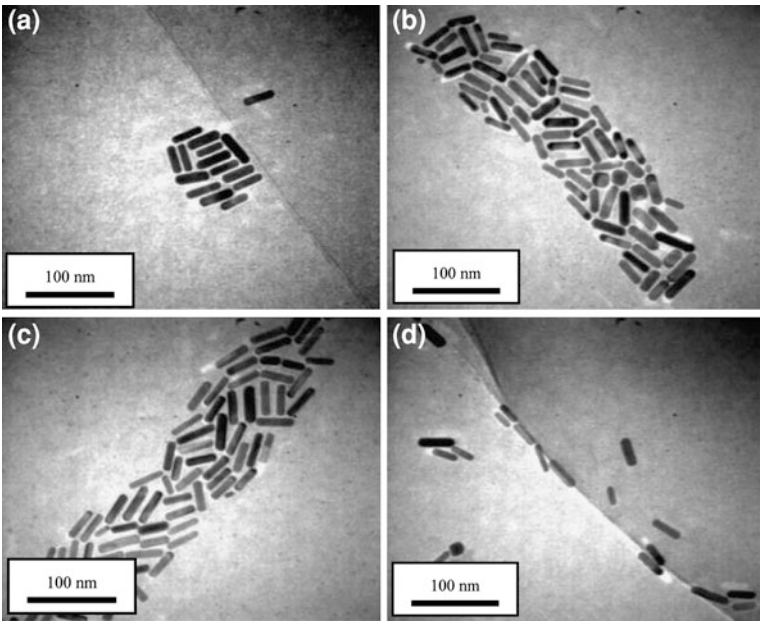

Fig. 8 TEM images of AuNRs synthesized using different volume of HNO_3; **a** 100 μl, **b** 200 μl, **c** 300 μl, **d** 400 μl

weaker electrostatic repulsion among nanoparticles. Therefore, the surface charge of dispersed nanoparticles was different and lead to an instability of the solution. As a result, shorter AuNRs were formed. Similar result was observed by Lee et al. [18].

4 Conclusion

A modified CTAB-capped seed-mediated growth method was successfully used to produce high aspect ratio of AuNRs. The length and diameter of AuNRs were highly dependent on initial precursors; CTAB concentration, ascorbic acid

concentration, volume of seed solution and volume of nitric acid. Optimum synthesis parameters to produce AuNRs were 0.2 M CTAB, 0.08 M ascorbic acid, 50 μl seed solution and 300 μl HNO_3.

Acknowledgments The authors appreciate the technical support from School of Materials and Mineral Resources Engineering and INFORMM, Universiti Sains Malaysia. This research was supported by Research University grant (8630019 and 814113).

References

1. Jain, P.K., Huang, X.H., El-Sayed, I.H., El-Sayed, M.A.: Noble metals on the nanoscale: optical and photothermal properties and some applications in imaging, sensing, biology, and medicine. Acc. Chem. Res. **41**, 1578–1586 (2008)
2. Singh, A.K., Senapati, D., Wang, S.G., Griffin, J., Neely, A., Candice, P., Naylor, K.M., Varisli, B., Kalluri, J.R., Ray, P.C.: Gold nanorod based selective identification of Escherichia coli bacteria using two-photon Rayleigh scattering spectroscopy. ACS Nano **3**, 1906–1912 (2009)
3. Weissleder, R.: A clearer vision for in vivo imaging. Nat. Biotechnol. **19**, 316–317 (2001)
4. Huang, X.H., El-Sayed, I.H., Qian, W., El-Sayed, M.A.: Cancer cell imaging and photothermal therapy in the near-infrared region by using gold nanorods. J. Am. Chem. Soc. **128**, 2115–2120 (2006)
5. Durr, N.J., Larson, T., Smith, D.K., Korgel, B.A., Sokolov, K., Ben-Yakar, A.: Two-photon luminescence imaging of cancer cells using molecularly targeted gold nanorods. Nano Letters **7**, 941–945 (2007)
6. Park, W.M., Huh, Y.S., Hong, W.H.: Aspect-ratio-controlled synthesis of high-aspect-ratio gold nanorods in high-yield. Curr. Appl. Phys. **9**, 140–143 (2009)
7. Wu, H.L., Chen, C.H., Huang, M.H.: Seed-mediated synthesis of branched gold nanocrystals derived from the side growth of pentagonal bipyramids and the formation of gold nanostars. Chem. Mater. **21**, 110–114 (2009)
8. Sau, T.K., Murphy, C.J.: Seeded high yield synthesis of short Au nanorods in aqueous solution. Langmuir **20**, 6414–6420 (2004)
9. Jana, N.R., Gearheart, L., Murphy, C.J.: Wet chemical synthesis of high aspect ratio cylindrical gold nanorods. J. Phys. Chem. B **105**, 4065–4067 (2001)
10. Nikoobakht, B., El-Sayed, M.A.: Preparation and growth mechanism of gold nanorods (NRs) using seed-mediated growth method. Chem. Mater. **15**, 1957–1962 (2003)
11. Wu, H.Y., Chu, H.C., Kuo, T.J., Kuo, C.L., Huang, M.H.: Seed-mediated synthesis of high aspect ratio gold nanorods with nitric acid. Chem. Mater. **17**, 6447–6451 (2005)
12. Bai, X.T., Gao, Y., Liu, H.G., Zheng, L.Q.: Synthesis of amphiphilic ionic liquids terminated gold nanorods and their superior catalytic activity for the reduction of nitro compounds. J. Phys. Chem. C **113**, 17730–17736 (2009)
13. Gao, J.X., Bender, C.M., Murphy, C.J.: Dependence of the gold nanorod aspect ratio on the nature of the directing surfactant in aqueous solution. Langmuir **19**, 9065–9070 (2003)
14. Chen, S.H., Wang, Z.L., Ballato, J., Foulger, S.H., Carroll, D.L.: Monopod, bipod, tripod, and tetrapod gold nanocrystals. J. Am. Chem. Soc. **125**, 16186–16187 (2003)
15. Murphy, C.J., Sau, T.K., Gole, A.M., Orendorff, C.J., Gao, J.X., Gou, L.F., Hunyadi, S.E., Tan, L.: Anisotropic metal nanoparticles: synthesis, assembly, and optical applications. J. Phys. Chem. B **109**, 13857–13870 (2005)
16. Hu, S.H., Chen, Y.C., Hwang, C.C., Peng, C.H., Gong, D.C.: Development of a wet chemical method for the synthesis of arrayed ZnO nanorods. J. Alloy Compd **500**, 17–21 (2010)

17. Aslan, K., Leonenko, Z., Lakowicz, J.R., Geddes, C.D.: Fast and slow deposition of silver nanorods on planar surfaces: application to metal-enhanced fluorescence. J. Phys. Chem. B **109**, 3157–3162 (2005)
18. Lee, G.J., Shin, S.I., Kim, Y.C., Oh, S.G.: Preparation of silver nanorods through the control of temperature and pH of reaction medium. Mater. Chem. Phys. **84**, 197–204 (2004)

Calculation of Surface Enhanced Raman Scattering in Metal Nanoparticles

Carlos Caro, Ana Paula Zaderenko and Patrick Jacques Merkling

Abstract Theoretical studies on the interactions of rhodamine 6G (R6G) with silver nanoparticles have been carried out. R6G exhibits Surface Enhanced Raman Scattering (SERS) effect on most sensors and has been extensively studied experimentally, so it is a suitable benchmark. By means of density functional quantum chemical calculations by the B3LYP method at the DGDZVP or LANL2DZ level, the chemical enhancement was studied. Shape and enhancement of Raman spectra dependent on nanoparticle system size was investigated systematically in two-dimensional metal clusters and it was found that for 4, 6, and 8 silver atoms no substantial changes in the chemically enhanced magnification occurs. To complement this study, infrared spectra were also calculated. The spectra compare generally well with experimental results. Finally, the influence of the metal was tested within the copper group: in order of increasing chemical enhancement, the metals rank gold, copper, and silver, but the increase is very moderate.

C. Caro · A. P. Zaderenko · P. J. Merkling (✉)
Department of Physical, Chemical and Natural Systems,
Universidad Pablo de Olavide, Carretera de Utrera Km 1,
41013 Sevilla, Spain
e-mail: pjmerx@upo.es

C. Caro
e-mail: teneo18@hotmail.com

A. P. Zaderenko
e-mail: apzadpar@upo.es

Adv Struct Mater (2013) 4: 73–83
DOI: 10.1007/8611_2012_65

Published Online: 25 February 2012

1 Introduction

Raman scattering is a very inefficient spectroscopic process and, in spite of the valuable structural information obtained by Raman spectroscopy, its use for detection purposes is limited by its low sensitivity. Nonetheless, when a molecule is located in the vicinity of a metal nanoparticle the Raman cross section can be amplified dramatically, and the intensity of the Raman signals is amplified by factors as high as 10^{14}–10^{15} [1–3]. This enhancement effect is known as *Surface Enhanced Raman Scattering* (SERS).

The SERS effect is generally recognized to be due to the contribution of two mechanisms, the Electromagnetic Mechanism (EM) and the Chemical Mechanism (CM) [4]. The EM is a consequence of the local enhancement of electric fields in the surroundings of the metal nanoparticles, due to the surface plasmon excitation. This enhancement leads to more intense electronic transitions in molecules placed in the vicinity of the nanoparticle, and enhanced Raman scattering [5]. The CM results from changes in the polarizability of the molecule, owing to charge transfer interaction between electronic states of the molecule and the metal nanoparticle surface, which leads to increased Raman signals [6]. Therefore, the CM depends on properties of the molecule whereas the EM only depends on optical properties of the metal nanoparticle.

The largest Raman scattering enhancements have been found in increasing order for copper, gold, and silver nanostructures, respectively. Indeed, the SERS effect on silver achieves detection limits as low as a single molecule [1, 7, 8]. According to the latest findings, Raman spectroscopy can be considered as one of the most powerful techniques now available for sensing applications [9–18].

Rhodamine 6G (R6G) is a quite rigid molecule composed basically of a xanthene ring, an ethoxycarbonylphenyl group, and two ethylamino groups. R6G exhibits SERS effect on most sensors and has been extensively studied experimentally, so it represents a suitable benchmark. Specifically, it has been shown to exhibit SERS effect on the type of nanoparticles prepared in this work [18]. Additionally, it has been proven that both the electromagnetic and chemical mechanism contribute to the enhancement [19]. Some studies have focused on the vibrational analysis of the R6G cation [20–22].

The SERS effect on silver nanoparticles has been studied computationally by several authors in order to characterize the HOMO and LUMO states [23], the effect of geometry on SERS of minimal silver clusters [24], or the spectroscopic states involved in the transition in resonance Raman [25].

The aim of this work is to characterize the effect of silver, gold and copper clusters on the Raman spectrum of rhodamine 6G (R6G), and to ascertain the dependence of silver cluster size on the chemical enhancement mechanism.

2 Materials and Methods

2.1 Materials

All the chemicals are of reagent grade and have been used without further purification: tetraethylrhodamine hydrochloride (Rhodamine 6G) from Sigma Aldrich, silver nitrate and hydroxylamine hydrochloride from Panreac. Water was purified using a Milli-Q (18.2 MΩ) reagent grade water system from Millipore.

2.2 Synthesis of Silver Nanoparticles

Aqueous colloidal suspensions of SNPs were obtained by reduction of silver nitrate with hydroxylamine in aqueous media, following the method described by Leopold et al. [26]. Immediately before immobilization of SNPs on glass substrates, silver nanoparticles are aggregated by treating the suspension with KNO_3 to a final concentration of 10^{-2} mol/L.

2.3 Immobilization of Silver Nanoparticles on Glass Substrates

Standard microscopy glass slides were immersed in a freshly prepared aqua regia solution for 10 min, thoroughly rinsed with water and dried at room temperature. The so prepared substrates were used to deposit the aqueous colloidal suspension of SNPs and/or R6G as follows: 100 μL of the aqueous colloidal suspension of SNPs or R6G (10^{-3} M aqueous solution) are dropped on the glass slide and allowed to dry at room temperature. The obtained substrates will be called further on SNP-substrate and R6G-substrate, respectively. Mixed substrates were also prepared by sequential depositions, by dropping 100 μL of R6G (10^{-3} M aqueous solution) over a SNP-substrate. The Raman spectra were recorded upon these substrates.

2.4 Raman Spectroscopy

Raman spectra were measured on a Bruker Senterra Confocal Raman Microscope equipped with a 785 nm Ne laser and a DU420A-OE-152 detector. We make use of the 50× objective for all the measurements, the slit aperture is fixed to 50 μm and the integration time is 100 s with a laser power of 10 mW. All the spectra are recorded with a 3–5 cm^{-1} resolution.

2.5 Fourier Transform Infrared Spectroscopy

Infrared spectra were recorded on a Bruker IFS 66/s spectrometer equipped with a DTGS detector. We averaged 150 scans with a scan frequency of 2.5 Hz and 1 cm^{-1} resolution.

2.6 Computational Methods

The Density functional theory (DFT) calculations have been performed with the Gaussian 2009 program [27], using B3LYP exchange and correlation functionals as a well established and robust method along with either the DGDZVP or the LANL2DZ basis sets. Structure optimizations of the R6G molecule, of the metal/R6G complex have been carried out in vacuum with a very tight convergence criterion. All the presented spectra lack imaginary frequencies, indicating that the minimization yielded indeed true (at least local) minima. The spectra were broadened by a 5 cm^{-1} convolution to facilitate comparison with experimental spectra. No shifting or scaling of wavenumbers was performed in any of the represented spectra. Raman spectra were obtained according to the methodology known from the literature [23, 28]. Spectra were calculated at room temperature and for a 785 nm wavelength. The basis set DGDZVP has been applied to the silver-R6G adsorbates. For calculations that aimed at comparing the three noble metals Cu/Ag/Au, the basis set LANL2DZ has been used due to the lack of parametrization of gold in DGDZVP. DGDZVP, as a full electron basis set, provides roughly 50% more basis functions than LANL2DZ (that, on the other hand, incorporates a relativistic effective core potential) and the spectra obtained were found to compare more favourably in preliminary calculations. This has also been reported for related systems [29, 30]. However, the convergence of calculations was also found to be less robust with the bigger basis set. For this reason, the preliminary search for stable silver clusters was conducted at the LANL2DZ level. The scaling of wavenumbers required for reproduction of the IR and Raman spectra is 0.975 both with DGDZVP and LANL2DZ. This scaling must be applied for the fine tuning of the spectra due to limitations of the basis set and anharmonicities.

3 Results and Discussion

Pure solid rhodamine 6G crystals, R6G on SNP-substrates, and the computed R6G adsorbed on a nanoparticle (made up of 6 silver atoms) have very similar spectra, as can be seen in Fig. 1. The intensities of the spectra have been scaled so as to be comparable. R6G on SNP-substrates provides a low-noise Raman spectrum due to SERS effect, whereas at the same R6G concentration conditions, no measurable signal was obtained on glass substrate. Experimentally, the similarity of the spectra (a and b in Fig. 1) is

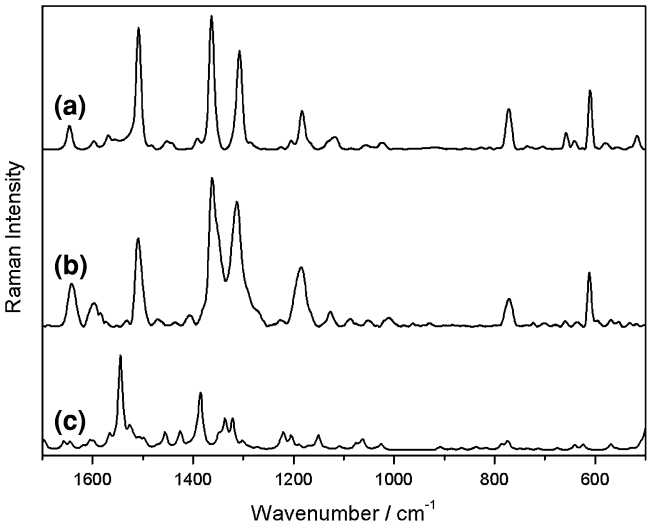

Fig. 1 Raman spectra of experimental R6G (**a**), experimental R6G evaporated upon silver nanoparticles (**b**), computed R6G adsorbed on Ag_6 (**c**)

useful for the identification of the adsorbed compound. The computational spectrum shows similarities to both experimental condensed phase spectra.

Small two-dimensional silver clusters of 2, 4, 6, and 8 atoms were constructed. The most stable clusters found were two-dimensional up to order 6, in accordance with results reported by most other authors [31, 32]. This situation is unmodified when R6G is added. Given that R6G is a singly charged cation and deposited silver was assumed to be neutral, our aggregates bear a charge of +1 lel. Surprisingly, R6G interacts with silver nanoparticles through the amino group, and not as may perhaps have been expected, through the stacking of aromatic rings (no minimum found) or the interaction with the carbonyl of the ester group. The final structure of the most stable optimization of the six silver atoms cluster is shown in Fig. 2 and will be referred to as R6G-Ag_6 further on.

The Infrared (IR) spectra of R6G (experimental and computed) and the computed spectrum R6G-Ag_6 are compared in Table 1. The two computed spectra are very similar and reproduce the splitting observed in the experimental spectrum at 1502/1529 cm^{-1}, provided the wavenumbers of the computed spectra are scaled by a factor 0.975 as mentioned previously.

The effect of "switching on" the intermolecular interactions of R6G to the silver nanoparticle obtained by comparing the theoretical R6G and R6G-Ag_6 spectra has consequences mainly in the increase in intensities of a few bands, as a result of the chemical enhancement being strongly localized. A thorough analysis of the Raman spectra in Fig. 3, their comparison with the experimental spectra in Fig. 1 lead to the following observations: one of the most intense experimental lines is found at 1509 cm^{-1}. It corresponds to a C–C stretching vibration of the

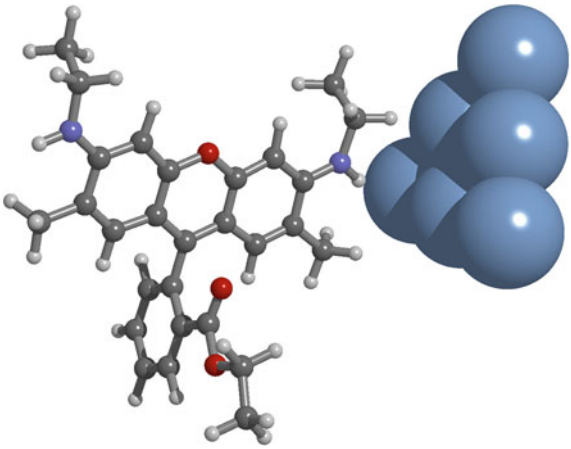

Fig. 2 R6G adsorbed on Ag_6 model silver nanoparticle surface

Table 1 Main absorption bands of infrared spectra of experimental rhodamine crystals, computed R6G and R6G-Ag_6

Experimental R6G, ν/cm^{-1}	R6G, ν/cm^{-1}	Int	R6G-Ag_6, ν/cm^{-1}	Int
1649	1654	350	1654	330
1608	1617	1170	1616	1420
1570	1558	470	1558	570
1529	1530	560	1527	820
1502	1503	690	1503	770
1321	1316	1300	1316	1420
1307	1303	670	1316	1410
1273	1275	720	1269	580
1188	1225	320	1195	80

Wavenumbers of computed spectra were scaled by a factor 0.975. Intensities are arbitrary, but comparable between both computed spectra

fused rings that is also IR active (Table 1). In the computed spectra, vibrations are found at slightly higher wavenumbers due to the aforementioned scaling factor. In this case, it corresponds to vibrations in the computed spectra at 1544 cm^{-1}. In the R6G-Ag_6 cluster, this line roughly doubles its intensity with respect to the free R6G molecule, that is separated in position by only 4 cm^{-1} from the IR active vibration (this vibration, after scaling, is found at 1503 cm^{-1} in Table 1).

The other salient features of the experimental spectra of Fig. 1 are the intense lines at 1363 and 1308 cm^{-1}. In both calculated spectra, these lines are present, although at the 5 cm^{-1} resolution they are split at the lower of these wavenumbers. In the calculated spectra of Fig. 3, these lines are also enhanced. A closer attention to the details of the vibrations helps us rationalize this observation. The involvement of nitrogen, through which the R6G molecule interacts with silver, plays a role in the increase of absorption intensities.

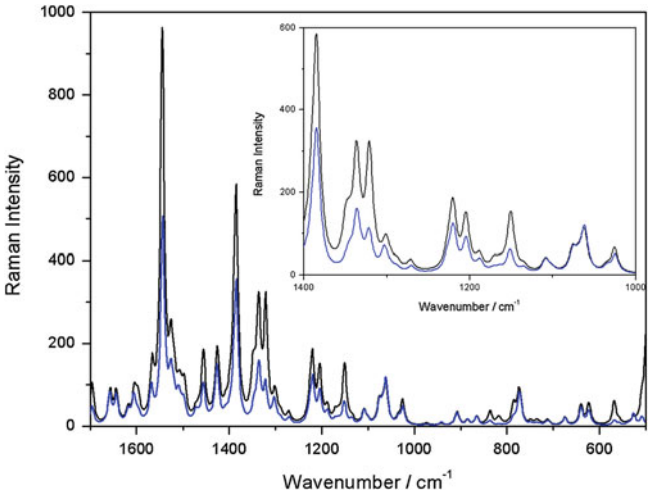

Fig. 3 Computed Raman spectra for R6G (*blue line*) and R6G-Ag_6 (*black line*). The *inset* shows a magnification of the 1400–1000 cm^{-1} region

On the other side, the vibration at around 1195 cm^{-1} (scaled frequency) is only moderately increased. According to Watanabe et al. [20], the contribution of this group to the Raman intensity in the free R6G is 10%. The same happens at 770 cm^{-1}, a vibration that is not noticeably enhanced (it is mainly concerned with in plane vibration of the phenyl C–H and out of plane of the xanthenes C–H). From the vibrations at 610/620 cm^{-1}, the lower is being enhanced, and the other not. This is consistent with the contribution of the N-ethyl group to the vibration at the lower of these wavenumbers. In the experimental spectra of Fig. 1, only the absorption line due to the lower vibration has an appreciable intensity in the R6G on NP.

This idea can be extended more systematically to study the influence of growing system sizes. In Fig. 4, spectra at increasing number of silver atoms have been studied. It is striking to notice how fast the spectra apparently converge, denoting that the chemical enhancement due to charge transfer is strongly localized. The chemical enhancement is virtually the same at four, six and eight silver atoms.

The study was extended to the other noble metals of the copper group, namely copper and gold. Their spectra, computed using the LANL2DZ basis set, are shown in Fig. 5 for the R6G-M_6 cluster (M being either Cu, Ag, or Au). This cluster size was chosen because at that size, the chemical enhancement effect was big in silver. The most stable metal clusters of six atoms formed by gold and copper have a geometry similar to the one shown in Fig. 2, while at bigger cluster sizes than 6, copper forms three-dimensional clusters [31]. The chemical enhancement was found to be very similar in all cases, as shown in Fig. 5. It is highest in silver, followed by copper and then gold.

The R6G-Ag_6 spectra shown in Fig. 5 and, for example, in Fig. 4 differ only in the basis set employed. As a result, the optimized geometry is almost unaffected (not shown), although distances within the silver cluster contract by around 3% and

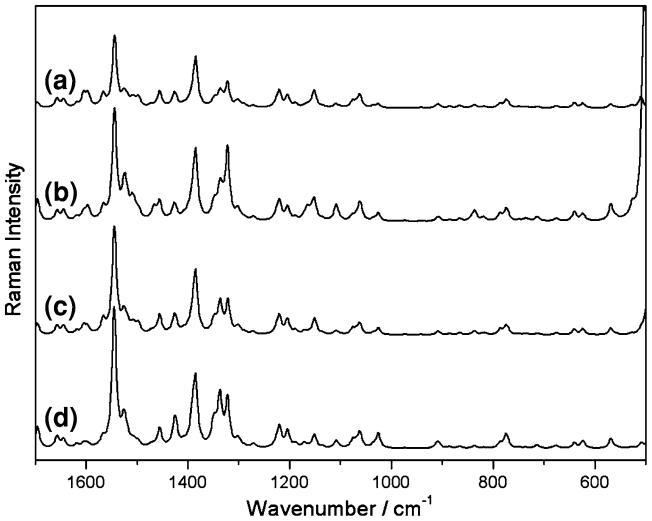

Fig. 4 Computed Raman spectra at different cluster sizes: R6G-Ag_8 (**a**), R6G-Ag_6 (**b**), R6G-Ag_4 (**c**) and R6G-Ag_2 (**d**)

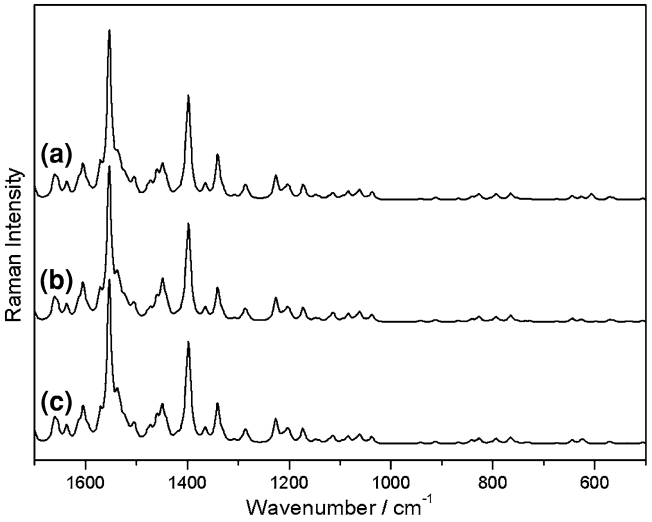

Fig. 5 Computed Raman spectra for R6G adsorbed on six silver (**a**), six copper (**b**) and six gold atoms (**c**)

distances from the N to the closest metal atoms by around 1%. The LANL2DZ basis reproduces the splitting in the 1360/1310 cm^{-1} region of the Raman spectrum, although it underestimates the 1310 cm^{-1} while overestimating vibrations at around 1410 cm^{-1} (after wavenumber scaling), distorting the general appearance of the

spectrum. Taking this into account helps to validate the spectra of the other noble metals: due to the similarity between them, we may conclude that the 1410 cm^{-1} line is overestimated in all of them.

4 Conclusions

Raman and IR spectra of R6G, both isolated and adsorbed on a silver nanoparticle were computed with the B3LYP method using the DGDZVP basis set. The reproduction of the spectra compare generally well with the experimental ones, undertaken with our nanoparticles at our lab.

According to the calculations, R6G links to the nanoparticle through the amino group. The R6G adsorbed on up to eight silver atoms produces chemical enhancement due to charge transfer of several lines of a factor two in Raman while the enhancement in IR is limited to 30%. It must be noted however that these conclusions are limited to single metal layers.

Finally, copper and gold were also investigated. The chemical enhancement was found to be very similar in all of them. The metals, in order of increasing chemical enhancement, are gold, copper, and silver, unlike the SERS effect, which is known to be copper, gold, and silver.

Acknowledgments The authors would like to acknowledge financial support from the Junta de Andalucía (P07-FQM-02595), the Regional Ministry of Health (PI-0070/2008 to A.P.Z), and the PAIDI Program from the Regional Government (RFM; FQM319). C. Caro is grateful to the Junta de Andalucía P07-FQM-02595 for his pre-doctoral fellowship. C. Caro is indebted to the late Jose Antonio Mejías for introducing him in nanotechnology.

References

1. Kneipp, K., Wang, Y., Kneipp, H., et al.: Single molecule detection using surface-enhanced Raman scattering (SERS). Phys. Rev. Lett. **78**, 1667–1670 (1997)
2. Xu, H., Bjerneld, E.J., Käll, M., et al.: Spectroscopy of single hemoglobin molecules by surface enhanced Raman scattering. Phys. Rev. Lett. **83**, 4357–4360 (1999)
3. Futamata, M., Maruyama, Y., Ishikawa, M.: Microscopic morphology and SERS activity of Ag colloidal particles. Vib. Spectrosc. **30**, 17–23 (2002)
4. Lombardi, J.R., Birke, R.L.: A unified approach to surface-enhanced Raman spectroscpy. J. Phys. Chem. C **112**, 5605–5617 (2008)
5. Schatz, G.C., Young, M.A., Van Duyne, R.P.: Localized surface plasmon resonance spectroscopy and sensing. In: Kneipp, K., Moskovits, M., Kneipp, H. (eds.) Surface-Enhanced Raman Scattering Physics and Applications. Topics in Applied Physics. Springer, Berlin (2006)
6. Otto, A., Futamata, M.: Electronic mechanisms of SERS. In: Kneipp, K., Moskovits, M., Kneipp, H. (eds.) Surface-Enhanced Raman Scattering Physics and Applications. Topics in Applied Physics. Springer, Berlin (2006)
7. Nie, S., Emory, S.R.: Probing single molecules and single nanoparticles by surface-enhanced Raman scattering. Science **275**, 1102–1106 (1997)

8. Le Ru, E.C., Meyer, M., Etchegoin, P.G.: Proof of single-molecule sensitivity in surface enhanced Raman scattering (SERS) by means of a two-analyte technique. J. Phys. Chem. B. **110**, 1944–1948 (2006)
9. Ji, X., Xu, S., Wang, L., et al.: Immunoassay using the probe-labeled Au/Ag core-shell nanoparticles based on surface-enhanced Raman scattering. Coll. Surf. A: Physicochem. Eng. Aspects **257**, 171–175 (2005)
10. Fabris, L., Dante, M., Nguyen, T., et al.: SERS aptatags: new responsive metallic nanostructures for heterogeneous protein detection by surface enhanced Raman spectroscopy. Adv. Funct. Mater. **18**, 2518–2525 (2008)
11. Guerrini, L., Garcia-Ramos, J.V., Domingo, C., et al.: Nanosensors based on viologen functionalized silver nanoparticles: few molecules surface. enhanced Raman spectroscopy detection of polycyclic aromatic hydrocarbons in interparticle hot spots. Anal. Chem. **81**, 1418–1425 (2009)
12. Abalde-Cela, S., Ho, S., Rodríguez-González, B., et al.: Loading of exponentially grown LBL films with Ag nanoparticles and their application for generalized SERS detection. Angew. Chem. Int. Ed. **48**, 5326–5329 (2009)
13. Kneipp, K., Kneipp, H., Bohr, H.G.: Single molecule sers spectroscopy in surface enhanced Raman scattering. In: Kneipp, K., Moskovits, M., Kneipp, H. (eds.) Surface-Enhanced Raman Scattering Physics and Applications. Topics in Applied Physics. Springer, Berlin (2006)
14. Sánchez-Iglesias, A., Aldeanueva-Potel, P., Ni, W., et al.: Chemical seeded growth of Ag nanoparticle arrays and their application as reproducible SERS substrates. Nano Today **5**, 21–27 (2010)
15. Alvarez-Puebla, R.A., Liz-Marzán, L.M.: SERS-based diagnosis and biodetection. Small **6**, 604–610 (2010)
16. Das, A., Zhao, J., Schatz, G.C., et al.: Screening of type I and II drug binding to human cytochrome P450-3A4 in nanodiscs by localized surface plasmon resonance spectroscopy. Anal. Chem. **81**, 3754–3759 (2009)
17. Castillo, P.M., Herrera, J.L., Fernandez-Montesinos, R., et al.: Tiopronin monolayer-protected silver nanoparticles modulate IL-6 secretion mediated by toll-like receptor ligands. Nanomed. **3**, 627–635 (2008)
18. Caro, C., Lopez-Cartes, C., Zaderenko, A.P., et al.: Thiol-immobilized silver nanoparticle aggregate films for surface enhanced Raman scattering. J. Raman Spectrosc. **39**, 1162–1169 (2008)
19. Futamata, M., Maruyama, Y.: Electromagnetic and chemical interaction between Ag nanoparticles and adsorbed rhodamine molecules in surface-enhanced Raman scattering. Anal. Bioanal. Chem. **388**, 89 (2007)
20. Watanabe, H., Hayazawa, N., Inouye, Y., et al.: DFT vibrational calculations of Rhodamine 6G adsorbed on silver: analysis of tip-enhanced Raman spectroscopy. J. Phys. Chem. B **109**, 5012–5020 (2005)
21. Saini, G.S.S., Sharma, A., Kaur, S., et al.: Rhodamine 6G interaction with solvents studied by vibrational spectroscopy and density functional theory. J. Molec. Struct. **931**, 10–19 (2009)
22. Jensen, L., Schatz, G.C.: Resonance Raman scattering of rhodamine 6g as calculated using time-dependent density functional theory. J. Phys. Chem. A **110**, 5973–5977 (2006)
23. Morton, S.M., Jensen, L.: Understanding the molecule-surface chemical coupling in SERS. J. Am. Chem. Soc. **131**, 4090–4098 (2009)
24. Pagliai, M., Muniz-Miranda, M., Cardini, G., et al.: Solvation dynamics and adsorption on ag hydrosols of oxazole: a Raman and computational study. J. Phys. Chem. A **113**, 15198–15205 (2009)
25. Avila, F., Soto, J., Arenas, J.F., et al.: Outstanding role of silver nanoparticles in the surface-enhanced resonance Raman scattering of p-benzosemiquinone. J. Phys. Chem. C **113**, 105–108 (2009)
26. Leopold, N., Lendl, B.: A new method for fast preparation of highly SERS active silver colloids at room temperature by reduction of silver nitrate with hydroxylamine hydrochloride. J. Phys. Chem. B **107**, 5723–5727 (2003)
27. Frisch M.J., Trucks G.W., Schlegel H.B. et al.: Gaussian 09, Revision A.02. Gaussian, Inc., Wallingford (2009)

28. Michalska, D., Wysokinski, R.: The prediction of Raman spectra of platinum(II) anticancer drugs by density functional theory. Chem. Phys. Lett. **403**, 211–217 (2005)
29. Kaczor, A., Malek, K., Baranska, M.: Pyridine on colloidal silver. Polarization of surface studied by surface-enhanced Raman scattering and density functional theory methods. J. Phys. Chem. C **114**, 3909–3917 (2010)
30. Yurieva, A.G., Poleshchuk, O.K., Filimov, V.D.: Comparative analysis of a full-electron basis set and pseudopotential for the iodine atom in DFT quantum-chemical calculations of iodine-containing compounds. J. Struct. Chem. **49**, 548–552 (2008)
31. Baletto, F., Ferrando, F.: Structural properties of nanoclusters: energetic, thermodynamic, and kinetic effects. Rev. Mod. Phys. **77**, 371–423 (2005)
32. Chiu, Y.P., Wei, C.M., Chang, C.S.: Density functional study of surface-supported planar magic Ag nanoclusters. Phys. Rev. B **78**, 115402–115409 (2008)

Inorganic–Organic Hybrid Nanoparticles for Medical Applications

Cristina I. Olariu, Humphrey H. P. Yiu and Laurent Bouffier

Abstract Recent advancement in the synthesis of inorganic nanoparticles provides scientists a wide range of nanomaterials for their research. Biomedical applications of inorganic nanoparticles have received much attention because of their potential to carry out specific tasks inside our body. To make these small particles compatible and functional inside a human body, designed organic groups are usually attached onto the surface of these particles. In this chapter, we focus on three most commonly used functional inorganic nanoparticles (gold, iron oxides, and quantum dots) for biomedical applications. Gold nanoparticles can be used as a contrast agent for CT scans. Iron oxides nanoparticles have already been used in clinical trials as a contrast agent for MRI scans. Quantum dots can provide strong luminescence for labeling cells and other biological species. Synthesis, functionalization and applications of these inorganic nanoparticles will be discussed.

1 Introduction

Particles with a diameter less than 100 nm are classified as nanoparticles. On the other hand, the identity of particles with diameter between 100 nm and 1 μm is somehow debatable. In biological terms, the major difference between these two

C. I. Olariu · L. Bouffier
Department of Chemistry, University of Liverpool, Liverpool, L69 7ZD, UK
e-mail: cristina.olariu@liv.ac.uk

L. Bouffier
e-mail: Laurent.Bouffier@enscbp.fr

H. H. P. Yiu (✉)
Chemical Engineering, School of Engineering and Physical Sciences,
Heriot-Watt University, Edinburgh, EH14 4AS, UK
e-mail: h.h.yiu@hw.ac.uk

Adv Struct Mater (2013) 4: 85–133
DOI: 10.1007/8611_2010_30

Published Online: 7 July 2010

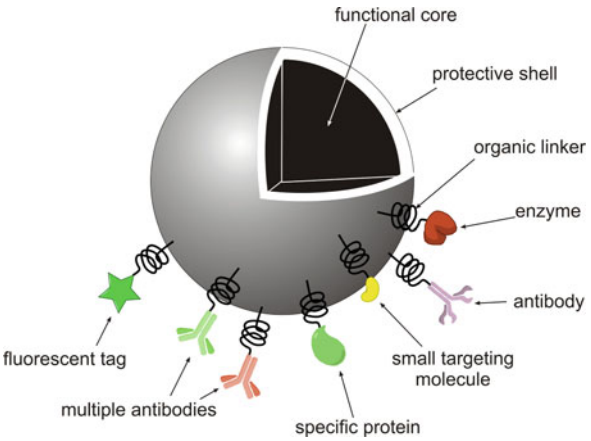

Fig. 1 A typical design of an inorganic nanoparticles functionalized with biomolecules for biomedical applications

types of particles is on their ability to penetrate the cell membranes. Particles of size smaller than 150 nm are thought to be internalized into cells via endocytosis processes. Therefore, nanoparticles should have no size problem while internalization of larger "sub-micron" particles may not be so straightforward.

Due to their small size, which is hundred or thousand times smaller than red blood cells, nanoparticles can travel through our circulation system and access many organs. Such property in penetration across our body makes them possible to carry out some specific tasks. This can well be developed into advanced therapy for the next generation, in particular to those diseases with ineffective treatment at the moment.

Recently, nanoparticles have been on the spotlight of scientific community. With the advancement in nanotechnology, nanoparticles of many materials, in particular inorganic nanoparticles, have been successfully prepared with various methodologies. This made inorganic nanoparticles widely available for scientists to choose for their research interests.

However, for medical applications, use of inorganic nanoparticles still has many obstacles. One major issue is their biocompatibility and toxicity. This is especially important when the final products are to be used in vivo. Therefore, not many inorganic nanomaterials are suitable for medical use. In order to improve their biocompatibility, inorganic nanoparticles are usually coated with protective coating. The coating material needs to be non-toxic in nature. Natural polymer (carbohydrate, peptides), synthetic polymer [polyethylene glycol (PEG), polyvinyl alcohol (PVA), and polyglycolic acid (PGA)], gold and silica are commonly used for coating nanoparticles because these materials are found to be non-toxic and relatively inert inside human body. Such protective coating is only unnecessary if the core material is non-toxic, such as gold nanoparticles. Also, biospecific entities are normally tagged onto the surface of these coated nanoparticles in order to provide specific targeting towards certain tissues, or certain cell types, or even particular compartments inside a cell. Figure 1 illustrates a typical design of a functionalized inorganic nanoparticle for biomedical applications.

Nonetheless, inorganic nanoparticles exhibit some physical properties that their organic counterparts lack. In this chapter, we focus on three types of inorganic

nanoparticles: gold, iron oxides and quantum dots. This includes their preparation procedures, physical and chemical properties, coating and functionalization methodologies, and their applications in advanced medicine.

2 Gold (Au)

2.1 Introduction

Gold is the most fascinating metal and has attracted constant attention from mankind since its very first discovery. Nowadays, gold is still playing a central role in art, jewellery and particularly in the finance world as a strong value indicator [1, 2]. It is also interesting to stress that the price of gold has never been as high as today and gradually increased new records were set up during the autumn 2009 with an all-time high above $1,217 an ounce on the 2nd of December 2009 (gold is traditionally weighed in Troy ounces, i.e. 31.1035 g).

Chemically, gold is extraordinary stable. It does neither tarnish nor oxidize on exposure to the atmosphere and retains its shiny bright aspect over very long time. But the strong stability of gold does result in a proportional lack of reactivity as a bulk metal. And this is essentially why gold had not attracted the attention of chemist until recently simply because it belongs to the family of noble metals which implies that it is very inert under normal pressure and temperature conditions.

This state of fact has changed in the 1980s with the discovery of Haruta that small aggregates of gold atoms can generate a fantastic catalytically activity [3–6]. Indeed this major breakthrough has opened a new era for modern gold chemistry at the nanoscale. Since that reports, gold is a hot topic of research in almost all fields from chemistry, biology, physics and engineering. This new nanochemistry of gold has found highly useful applications in synthetic chemistry thanks to the catalytic activity [7–10] but also in biology and medicine because these tiny clusters of gold could be employing as smart addressable scaffolds to promote multiple applications like for examples: drug delivery, specific targeting, local in vitro or in vivo imaging [11, 12]. It is noteworthy that all these applications in biology or medicine have raised issues about gold nanoparticles toxicity but non-relevant harmful effect to human cells has been noticed by Wyatt and co-workers with 4, 12 and 18 nm in diameter particles [13].

2.2 Synthesis of Gold Nanoparticles

The preparation of monodisperse nanoparticles with controlled size and shape is a key challenge in the area of biotechnology. Realistic applications in that field of research require a fairly good colloidal stability over hours or days and indeed the

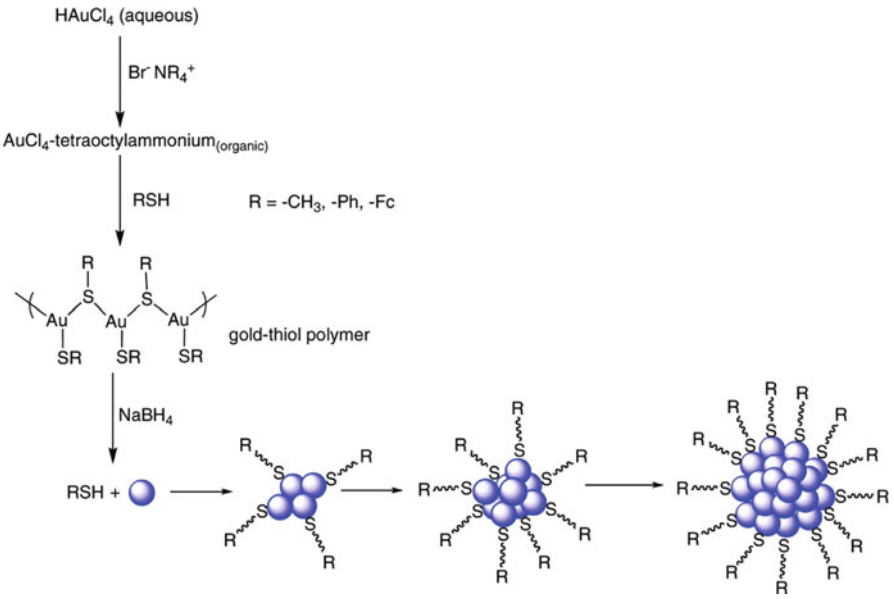

Fig. 2 Scheme for Au nanoparticle synthesis by the Brust–Schiffrin two-phase approach. Reprinted with permission from Ref. [16]. Copyright 2009 American Chemical Society

smaller nanoparticles have a strong tendency to aggregate and settle down in order to minimize the free energy of the system. The most common strategy developed to overcome that thermodynamic constraint consists in coating the surface of the corresponding particles to increase inter-particles repulsion and stabilize the dispersion within an adequate solvent.

2.2.1 Thiolate-Capped Gold Nanoparticles

The most effective way to make noble metal nanoparticles is the so-called bottom-up approach based on the chemical reduction of metal ions under conditions that allow the control of both nucleation and growing thanks to protective capping ligands. The resulting nanoparticles size distribution is directly determined and controlled by the molar *ratio* between the metal ions and the coating agent.

A real breakthrough synthesis has been reported in 1994 by Brust et al. at the University of Liverpool [14]. This work which has more than 2200 citations on SciFinder (December 2009) 15 years after its initial publication is summarized in Fig. 2. $HAuCl_4$ salt initially dissolved in an aqueous phase is transfer into an organic solvent by using tetraoctylammonium bromide as a phase transfer agent while the addition of a thiol R−SH (with R = Me, Ph, Fc) and the subsequent reduction with an excess of sodium borohydride leads to the perfectly controlled growth of thiolate-protected gold nanoparticles. The so-called Brust–Schiffrin

method has been thoroughly studied by several groups and in particular the versatility of this approach has been highlighted by Murray and colleagues [15].

The main advantage of this methodology arises from the precise control of the average size of the Au nanoparticles by the reduction condition as well as the stoichiometry of the available gold salt with respect to the concentration of capping thiol molecules.

2.2.2 Dendrimer-Protected Gold Nanoparticles

Several years after the design of thiolate-protected particles, dendrimer molecules have also been reported to thermodynamically stabilize Au nanoparticles [17]. In 2005, Crooks and co-authors rationalized the improved stabilization of the nanoparticles within the dendrimer matrix and therefore opened the door to substantial new applications. Their work reported in details the preparation of alloy as well as core/shell particles by applying three different strategies (co-complexation method, sequential method and partial displacement method according to their own terminology). This innovative approach is now a relevant alternative to prepare Au nanoparticles thanks to several inerrant advantages. First, the dendrimer architecture strongly protects the resulting nanoparticles from aggregation (site isolation). Secondly, the functionality of the dendrimers on the periphery of the structure can be adjusted in order to tune the solubility or colloidal stability of the nanoparticles in an organic or aqueous medium depending on the targeted application.

On the other hand, extremely small gold clusters (Au_8 nanodots) have been stabilized in hydroxyl-terminated dendrimers earlier in 2003 [18] and the resulting material exhibited highly tunable fluorescent properties that correlate with the size of the Au nanoparticles. This unprecedented radiative emission at short wavelengths (blue emission at 450 nm with excitation at 384 nm) was not observed with thiolate-protected nanoparticles which do emit at near-infrared wavelengths.

2.2.3 Immobilization Through Monolayer Films

Immobilization of these capped-nanoparticles has been intensively investigated thanks to a major significance at the fundamental level as well as potential applications in synthetic chemistry (supported heterogeneous catalysis) or nanotechnology (optical or electrochemical biosensors). In that context, the first report of citrate and alkanethiol-stabilized gold colloid monolayers electrophoretically deposited onto carbon-coated copper grids was published in 1993 by Mulvaney [19]. This approach could be applied to the specific modification of electrodes for generating electrochemical sensors and Murray extensively reviewed the state-of-the-art in a recent issue of *Chemical Reviews* [20].

More complexity and potential sensitivity has been reached with the formation of multilayers of thiolate-protected nanoparticles instead of a monolayer. Several strategies could be identified such as non-specific electrostatic interactions,

coupling *via* dithiol linker or controlled covalent grafting using either amide or ester chemical bonding. Multilayer films of organic compounds deposited on solid surfaces have been studied for many years. An alternative approach to classical Langmuir–Blodgett technique or chemisorption consists in the fabrication of multilayers by consecutive adsorption of polyanions and polycations [21]. The ligand shell of the capped-Au nanoparticles which could be either cationic or anionic acts as a polyelectrolyte and drives the layer by layer deposition. This latter approach allows precise fabrication of multilayer architectures by precisely controlling the number of layers and the subsequent properties of the polyelectrolyte film.

Stellacci and co-workers at the Massachusetts Institute of Technology described an original control of the Au-nanoparticle shell by preparing mixed self-assembled monolayers from a binary mixture of 1-nonanethiol and 4-methylbenzenethiol [22]. The strong disparities between both molecules generate a phase separation at the surface of the nanoparticles which appeared under the form of striped surface ordering in highly contrasted STM imaging. This interesting work was shown in August 2009 during the 42nd IUPAC congress in Glasgow (Adaptive Nanomaterials symposium).

2.2.4 Post-modification of Gold Nanoparticles

The capping ligand plays a central role in the control of the average size and the colloidal stability of the Au nanoparticles but could also increase the functionality level after a post-modification step. This has been done either by exchanging the coated molecules of the shell with another capping ligand (so-called ligand exchange) or by direct reaction on the initial ligand when bearing a reactive functional group (post-functionalisation) [23, 24].

The most popular example is the exchange of the weakly attached citrate ligand against a thiolate. One can assume that this fairly simple exchange reaction procedure drives a complete ligands exchange as the thiolate exhibits a stronger binding to gold atoms than citrate ligands. This strategy was successfully used by Mirkin and co-workers in 1996 to functionalize 13 nm in diameter Au nanoparticles with a single-stranded synthetic DNA. The self-assembly of a 12-mer oligonucleotide with its complementary strand *via* specific hybridization through Watson–Crick base-pairing interactions controls the resulting assembly (Fig. 3) [25]. More recently, the same group also highlighted how this initial work on DNA and the fundamental understanding of the aggregation *versus* colloidal stability process had successful applications in the area of bioanalysis with the objective of improving both sensitivity and speed (Fig. 4) [26].

The exchange of thiolate ligands on Au-nanoparticles is also possible but matrix dissolution rather than full exchange tends to take place. One should keep in mind than the whole exchange mechanism is still subject to discussion. First of all, the capping of thiol on gold substrate is still being investigated and the direct evidence that hydrogen release occurs during the binding was only reported

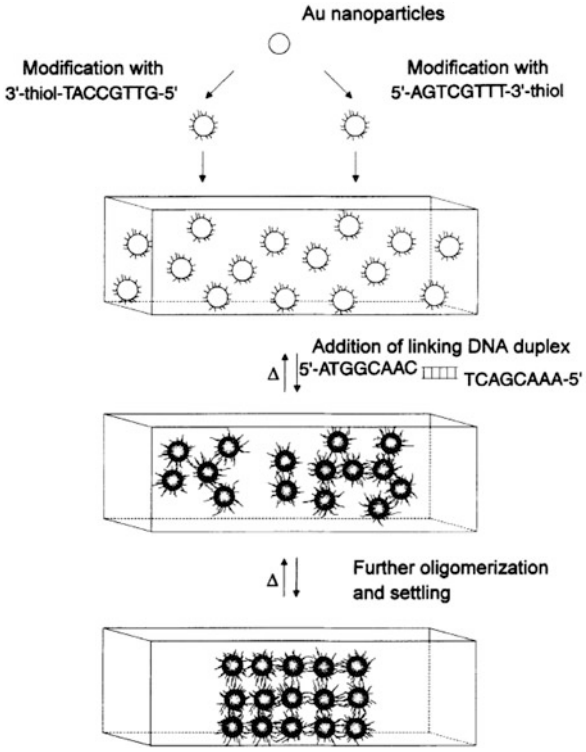

Fig. 3 Scheme illustrating the DNA-based colloidal nanoparticle assembly strategy (the hybridized 12-base pair portion of the linking duplex is represented by ladder). Reprinted with permission from Ref. [25]. Copyright 1996 Nature Publishing Group

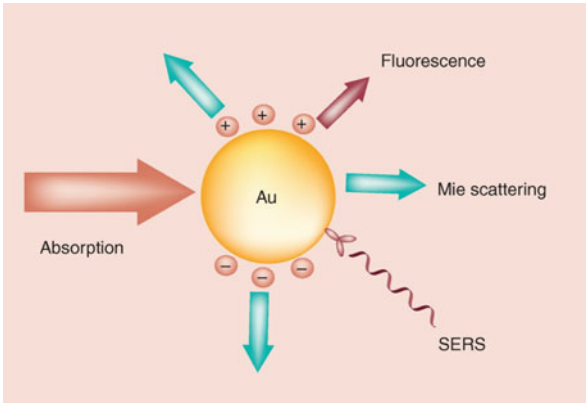

Fig. 4 Optical processes resulting from the interaction of the light with a gold nanoparticle. Reprinted with permission from Ref. [30]. Copyright 2007 Future Medicine Limited

recently [27]. Murray and Mulvaney discussed the mechanism and kinetics of the exchange in a perspective article published in *Langmuir* [16]. The exchange of a molecule of thiol ligand by another could be described as a serial process and the number of exchanged ligands on an individual nanoparticle was found to vary statistically following a Poisson distribution.

Moreover, the kinetics of the ligand exchange has been investigated in details by the same group and others [28, 29]. While Murray and co-workers reported a second-order kinetics during the early stages of the exchange with average constant rates between 1.6×10^{-3} and 1.01×10^{-2} M^{-1} s^{-1} depending on the nature of the incoming ligand; Lennox et al. fitted long time reaction data to Langmuir diffusion kinetics. It is noteworthy that these apparently contradictory results are in fact compatible as in the latter case; the system reached the thermodynamic equilibrium. The reaction was then described by a single rate constant of 1.37×10^{-2} $s^{-1/2}$ which was independent in incoming ligand concentration (i.e. zero-order kinetics).

2.3 Gold Nanoparticles for Bioimaging

2.3.1 Interaction with Light and Surface Plasmon Resonance

Au nanoparticles are offering a significant contribution in the field of labeling and biomedical visualization. Essentially, the particles are used as passive markers which concentration could be either naturally or artificially enriched within the region of interest. In that case, the inerrant physical properties of Au-nanoparticles are used to carry out and/or enhance the imaging by using a large variety of techniques.

Gold particles strongly absorb and scatter visible light and therefore most of the detection methods are based on the interaction between gold particles and light [30]. When Au particles are illuminated, the light energy excites the free electrons of the metal which generates an electromagnetic surface oscillation (surface plasmon) [31]. At the resonance frequency, the excited electron plasmon relaxes thermally by transferring the energy to the crystal lattice of the gold atoms which leads to heating of the particles.

20 nm in diameter gold nanoparticles modified with nuclear localization peptides were imaged by several techniques and their subcellular distribution in cells evaluated by enhanced differential interference contrast microscopy and transmission electron microscopy [32]. Pasqualini and colleagues reported an approach for fabrication of spontaneous, biologically active molecular networks consisting of bacteriophage directly assembled with larger Au nanoparticles (44 ± 9 nm). The spontaneous organization of these targeted networks has been manipulated further by post-functionalization with an imidazole moiety, which induces changes in near-infrared optical properties. The resulting networks were successfully used as labels for enhanced fluorescence and dark-field microscopy, surface-enhanced Raman scattering detection, and near-infrared photon-to-heat conversion [33].

2.3.2 Photothermal Imaging and Luminescence

As previously mentioned, absorbed light eventually leads to heating of the particles which tend to transfer this energy to the surrounding environment. The spatially localized heating can be directly exploit for imaging as reported in 2002

by Lounis and co-workers from the University of Bordeaux [34]. They demonstrated that photothermal method that combines high-frequency modulation and polarization interference contrast allows far-field optical detection of gold colloids down to diameters of 2.5 nm.

This method has been also used to give a dynamic picture of the movement of receptors selectively labeled with 5 nm Au nanoparticles [35]. Small gold particles (size < 2 nm) with high surface to volume *ratio* do emit fluorescence upon photoexcitation and thus can be potentially visualized with fluorescence microscopy. Murray and co-workers reported visible-near-IR luminescence in the range from 700 to 1300 nm depending on the nature of the protecting monolayer and claimed that the emission results from localized electronic surface states [36].

One can note that these aforementioned methods involving photoexcitation (interference contrast microscopy, dark field microscopy, photothermal imaging, or fluorescence microscopy) are now sensitive enough to detect and image mater at the single particle level. As an example, 20–30 nm in diameter Au nanoparticles that scattered light individually can be visualized with high-resolution dark field microscopy [37].

2.3.3 Contrast Agent in X-ray Imaging

The intrinsic physical properties of gold and notably the high atomic weight provide high contrast in transmission electron microscopy (TEM), on the other hand gold nanoparticles scatter X-rays very efficiently and thus provides opportunities in X-ray imaging.

Current computed tomography contrast agents such as iodine-based compounds have several limitations, including short imaging times due to rapid renal clearance, renal toxicity, and vascular permeation. In that context, new contrast agents based on 30 nm gold nanoparticles that overcome these limitations were described in 2007 by Jon and co-workers [38]. Measurement of the X-ray absorption coefficient in vitro revealed that the attenuation of PEG-coated Au nanoparticles is 5.7 times higher than that of the current iodine-based contrast agent. Furthermore, colloidal gold nanoparticles are likely to cause less cytotoxic damage than the last generation iodine-based agents.

2.4 Local Heat Induced by Gold Nanoparticles

Parak and co-workers published a state-of-the-art review entitled “Biological applications of gold nanoparticles” in the special issue of *Chemical Society Review* dedicated to gold (guest editors: Hutchings, Brust and Schmidbaur) [2, 12]. The authors focused on gold nanoparticles as a heat source in a whole section of this extensive review.

As mentioned previously, the heat from the gold particles which results from the localized electronic excitation (Plasmon) is dissipated into the surrounding media. And this can not only be useful for imaging techniques, but also for anti-cancer therapy (hyperthermia).

2.4.1 Hyperthermia

Cells are extremely sensitive to changes in temperature because this affects metabolism kinetics as well as adhesion properties. Even temperature rises of only a few degrees can be lethal to cells.

The general idea here is to deliver colloidal nanoparticles to the cancerous tissue. This can be achieving for instance by functionalizing the particle surface with targeted molecules (such as specific ligands or monoclonal antibody) that are specifically recognized by receptors over-expressed at the surface of cancer cells and could therefore locally concentrate/accumulate close to tumor cells. One possible strategy here is to take advantage of the specific binding between the ubiquitous triad sequence Arg-Gly-Asp (RGD) and $\alpha_v\beta_3$ integrin receptor [39, 40].

If the particles can be heated up by an external stimulus; then the cells in the vicinity of the particles can be selectively killed thanks to a local raised in temperature. Wei and co-workers demonstrated that gold nanorods coated with a cationic surfactant (cetyltrimethylammonium bromide) can be internalized within hours into KB cells by a non-specific pathway [41]. The nanorods render the tumor cells highly susceptible to photothermal damage when irradiated, generating extensive blending of the cell membrane at laser intensity as low as 30 J/cm^2.

Xia and co-workers prepared 45 nm in edge length gold nanocages which can achieve strong absorption in the near-infrared (NIR) region for photothermal cancer treatment [42]. Numerical calculations show that the nanocages have a large absorption cross section, facilitating conversion of NIR irradiation into heat. The gold nanocages were successfully conjugated with monoclonal antibodies (anti-HER2) to target epidermal growth factor receptors (EGFR) that are over-expressed on the surface of breast cancer cells (SK-BR-3).

2.4.2 Heat-Induced Molecular Motion and Delivery

Photo-induced heating of Au particles can also be used for the cleavage of weak chemical and for the opening of synthetic vehicles or macromolecular “cargo” designed to specific targeting.

Puntes and co-workers shown that the local heat delivered by Au nanoparticles (10 nm in diameter) capped with hexa-peptide (Cys-Leu-Pro-Phe-Phe-Asp) can be used as a molecular surgery to safely remove toxic aggregates [43]. This strategy was applied to protein aggregates [amyloid beta (Aβ) protein] involved in Alzheimer’s disease. The authors reported the possibility to redissolve the protein deposits and to interfere with their growth, using the local heat generated with a

low gigahertz range electromagnetic field and subsequently dissipated by gold nanoparticles selectively attached to the aggregates. A letter to *Nature* published in 2002 by Jacobson and co-workers demonstrated remote electronic control over the hybridization of DNA molecules, by inductive coupling of a radio-frequency magnetic field to a 1.4 nm gold nanocrystal covalently linked to a 15-mer oligonucleotide [44]. Inductive coupling to the gold-based assembly increases the local temperature of the bound DNA, triggering efficient thermal denaturation. This is a clear example of specific control of hybridization and biological function at the nanoscale; and moreover, the switch is fully reversible thanks to the extremely fast heat dissipation ($\sim$50 ps timescale).

More recently but based on the same principle, Feldmann and colleagues reported that double-stranded DNA assembly that melts (i.e. denatures) within microseconds could induces the irreversible desaggregation of gold nanoparticle on a millisecond timescale [45]. This concept was exploited to distinguish a single point-mutated DNA from a perfectly matching sequence even in a 1 to 1 mixture of both targets.

The work of Caruso and co-workers published in 2005 did report the preparation and characterization of light-responsive delivery microcapsules composed of multiple polyelectrolyte layers and Au nanoparticles assembly [46]. Further encapsulated material was released from the nanostructured capsule on demand upon irradiation with 10 ns laser pulses in the near-infrared region (1064 nm). Finally, the release of encapsulated material from polyelectrolyte-multilayer capsules has been demonstrated inside living cells [47]. Metal nanoparticles were incorporated inside the walls of the capsules, and served as energy absorbing centers for illumination by laser light. Even if this was done with larger than 20 nm Ag nanoparticles, this strategy could clearly be extended to Au-based nanomaterials.

2.5 Gold Nanoparticles-Assisted Drug Delivery

Inorganic/organic hybrid nanomaterials exhibit a wide range of attributes that make them highly promising candidates for successful drug delivery. The inorganic moiety which is generally the centre core of these materials provides unique and tunable properties to the resulting assembly. Moreover, the surface of the inorganic-based structures also generates scaffolds for the controlled presentation or encapsulation within an addressable vehicle of drugs, imaging or contrast agents.

Gold nanoparticles are not only capable of delivering small drugs but also much larger biomolecules like synthetic peptides, natural or modified proteins, and nucleic acids (i.e. DNA for gene delivery or RNA in case of RNA interference strategy).

2.5.1 Small Drugs Delivery

In the context of photodynamic therapy of cancer, Au nanoparticles could be employed in localized delivery of diatomic therapeutic agents like nitrogen

monoxide (NO) or singlet oxygen ($^1O_2$) that are cytotoxic because they generate oxidative stress and/or triggered oxidative chain reactions. Moreover, nitric oxide plays a key regulating role in several cellular processes like angiogenesis or immune system response. The therapeutic opportunities and the potential application in cancer biology have been reviewed in 2007 by Mocellin and colleagues [48].

Russell et al. stabilized Au nanoparticles (2–4 nm in diameter) with zinc porphyrine-like phthalocyanine photosensitizer elongated with a –SH terminated spacer [49]. Energy-dispersive X-ray analysis confirmed the presence of the drug and the resulting nanocomposite was shown to generate singlet oxygen with enhanced quantum yields from 45 to 65% as compared to the free phthalocyanine. The group of Schoenfisch reported that NO can be reversibly immobilized at the surface of gold nanoparticles by covalent linking with a polyamine-based anchoring group *via* formation of *N*-diazeniumdiolate [50]. They demonstrated efficient and controlled acido-labile release of nitric oxide at pH $\sim$ 3 which highlight the feasibility of realistic applications thanks to slightly acidic media localized in lysosomes or endosomes.

Another advantage of engineering delivery systems is to improve the intrinsic properties of the "free" drug (solubility and in vivo stability or even biodistribution). The control of the drug loading combines to efficient vectorization and release of the active form of a prodrug could result in decreasing the side-effect.

Zubarev and co-workers described in 2007 the first example of gold nanoparticles covalently functionalized with paclitaxel which is one of the most effective chemotherapeutic drug against a large range of cancers [51]. The immobilization method involves the attachment of a short flexible polyethylene glycol linker on the paclitaxel pharmacophore followed by conjugation to 2 nm in diameter gold nanocrystals under mild esterification conditions. Thermogravimetric analysis (TGA) evidenced a high content of organic shell (67 weight percents) which corresponds to a well-defined number of molecules of paclitaxel (73 $\pm$ 4 per nanoparticle).

Another step toward a greater control of the release of the drug has been achieved with glutathione (GSH)-mediated process. GSH is the most abundant thiol in the cytoplasm and the major reducing agent in biochemical processes, providing a potential in situ releasing source in living cells [52]. This methodology relies on the significant difference in intracellular GSH concentration (1–10 mM) *versus* extracellular levels (2 μM in blood plasma). Methods are based on disulfide linkages between the drugs and the carriers that can be displaced in presence of the competitive GSH thiol (see Ref. [53] for review). But an uncontrolled parameter in the release process as well as bioavailability relies on thiol–disulfide exchange which can occur with cysteine residues exposed at the surface of blood proteins. In that context, Rotello and co-workers published a proof of principle when reporting in 2006 the cellular delivery and subsequent GSH-mediated release of a thiolated dye (BODIPY) mimicking hydrophobic drugs [54]. Au nanoparticles with a core dimension of about 2 nm were functionalised with short PEG cationic ligand and fluorophore *via* SAM methodology. The authors explained that the cationic nature of the shell facilitates the crossing of cell membrane barrier

whereas the steric shielding of the gold–thiol interface enhances the resistance to exchange with competitive proteins.

2.5.2 Gold Nanoparticles for Biomolecules Delivery

For gene therapy and therefore DNA delivery, two different strategies can be distinguished; involving either non-covalent or covalent (but usually cleavable) binding between the nanoparticle and the DNA material.

Viral vectors are generally used in gene therapy because they provide highly efficient biocompatible carrier. In that case, the corrective genes have been packaged into modified retroviruses, which can incorporate themselves into a host cell's DNA. Yet, viruses have already raised many health and safety issues concerning non-predictable toxicity and/or unexpected immune responses. The biomedical correspondent of *Nature* reported a tragic case in 2002 when a French gene therapy patient had unfortunately developed a form of cancer while being treated for severe combined immune deficiency [55].

Therefore, non-viral gene delivery using inorganic-based nanocarriers presents a promising and relevant alternative to the aforementioned side-effect. Yet, a remaining problem that should be addressed concerns limitations in both transfection efficiency and associated pharmacokinetics.

In 2003, Klibanov and Thomas did report an enhance transfection while using polycation-mediated DNA delivery with gold nanoparticles [56, 57]. For this approach, 2 kDa branched polyethylenimine (PEI) chains have been covalently attached to gold nanoparticles (between 2.3 and 4.1 nm in size), and the authors evaluated the potency of the resulting conjugates as vectors for the delivery of plasmid DNA into kidney cells. The transfection efficiency was found to vary as a function of the PEI to gold molar *ratio* with the best candidate being about 12 times more potent than the unmodified polycation. Moreover, the intracellular trafficking of the DNA complexes of these vectors, monitored by transmission electron microscopy (TEM) was detected in the nucleus within 1 h timescale after transfection.

Rotello and co-workers investigated a mixed monolayer protected gold clusters functionalized with quaternary ammonium chains for transfection in mammalian cell cultures [58]. The success of these method assemblies depended on several variables, including the *ratio* of DNA to nanoparticle during the incubation period, the number of charged substituents in the monolayer core (several candidates with cationic coverage percentage found between 58 and 100%), and the hydrophobic packing surrounding these amines. The most efficient nanoparticle studied was eight fold more effective than 60 kDa PEI used as a positive control transfection agent. Later in 2006, the same group reported another positively charged gold nanocarrier bearing a photoactive ester linkage, which allows temporal and spatial release of DNA by light. These cationic photocleavable nanoparticles are initially associated with DNA through electrostatic interaction [59]. Irradiation at $\lambda = 350$ nm cleaves the *o*-nitrobenzyl linkage, releasing the DNA from the nanoparticle, and resulting in a high level of recovery of in vitro DNA transcription. Furthermore, effective DNA

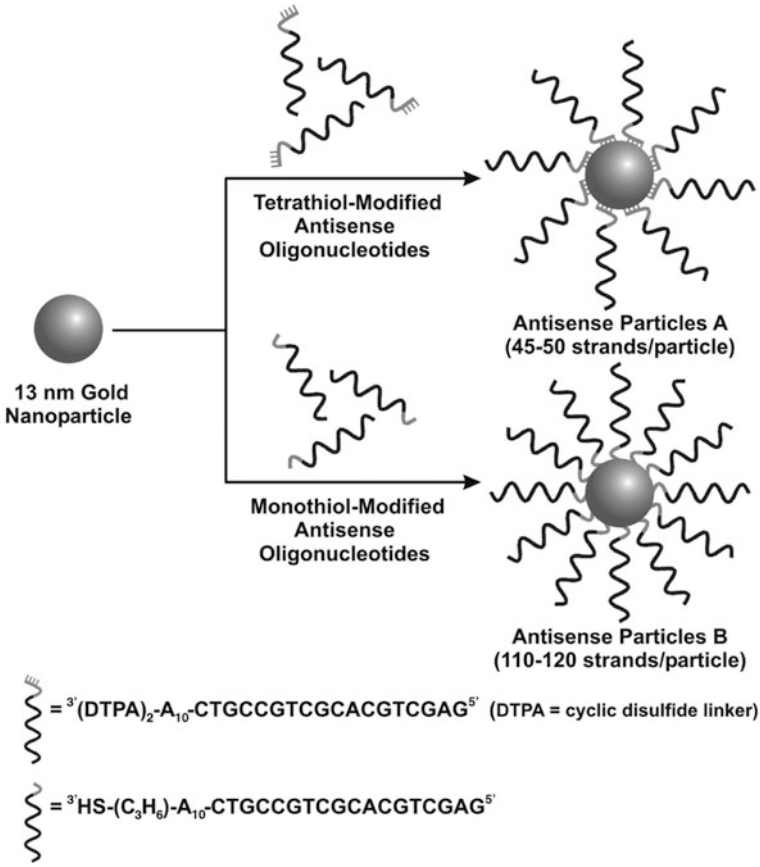

Fig. 5 Preparation of antisense citrate-stabilized gold nanoparticles with tether or single alkylthiol anchoring groups respectively. Reprinted with permission from Ref. [60]. Copyright 2006 Science Magazine

delivery and release in living cells with significant nuclear localization of the DNA were obtained with this system, thus providing the first proof of concept for the development of light-regulated drug-delivery systems.

Mirkin and co-workers described in 2006 the use of Au nanoparticle/oligonucleotide assemblies as intracellular gene regulation agents for the control of protein expression in cells (Fig. 5) [60]. These highly tunable gene transporters (with precise control of the DNA loading) are less susceptible to degradation by nuclease activity and exhibit as high as 99% cellular uptake. This was a significant breakthrough to introduce oligonucleotides at a higher effective concentration than conventional transfection agents. The following year, the same group demonstrated the whole mechanism of cellular uptake of these DNA/nanoparticles conjugates by endocytosis process which is initiated by adsorption of serum proteins onto the surface of the particles [61].

To conclude this section and to demonstrate that gold nanoparticles can also carry larger biomolecules (i.e. proteins), a recent study by Pokharkar et al. has reported functionalized gold nanoparticles as carriers of insulin [62]. Their strategy relies on the loading of gold nanoparticles with chitosan, a widely available biocompatible polymer. As expected, chitosan improved the surface properties for binding of biomolecules and zeta potential measurements have shown an increase from +4.23 to +62.7 mV depending on the chitosan loading (study between 0.01 and 1%). Finally, the pharmacodynamic activity was also improved after oral and nasal administration of insulin loaded samples.

2.5.3 In Vivo Limitations and Targeting

Efficient in vivo applications where the inorganic/organic delivery system is directed to his target following administration into circulatory system is the next step to achieve. For that, two approaches for targeting have been developed: passive and active targeting [63–65].

To summarize, passive targeting tries to take advantage of differential properties of specific unhealthy tissues or hyper-vascularized cells while active targeting relies on presenting ligands on the nanocarrier surface for at least selective but possibly specific recognition by cell surface receptors. The ligands could be short peptidic sequences for vectorization, proteins or specific substrates. Potentially, the combination of both types of targeting will further improve the properties of an optimized carrier for in vivo delivery. Nanocarriers efficiency is limited by non-specific uptake and potential degradation in macrophages (immune response). Therefore, proper targeting is essential for maximizing drug efficacy but others physical parameters of the inorganic moiety need to be considered such as average size, monodispersity, morphology and shape anisotropy. In recent works, Chan and colleagues investigated both size and shape dependence of Au nanoparticles on mammalian cell uptake. They showed that kinetics and saturation concentrations are highly dependent upon the physical dimensions of the nanoparticles by measuring uptake half-life of 14, 50, and 74 nm nanoparticles (2 h 06 min, 1 h 54 min and 2 h 15 min respectively at a rate of 622, 1,294, and 417 nanoparticles per hour respectively) [66]. They have also elucidated the mechanism by which transferrin-coated gold nanoparticles of different sizes and shapes entered mammalian cells *via* clathrin-mediated endocytosis pathway. The nanoparticles exocytosis process was also found to correlate linearly with size which was a different conclusion from their previous work on cell uptake [67]. Furthermore, they developed a model to predict the relationship of size *versus* exocytosis for different cell lines which has major implications in determining nanotoxicity.

2.6 Gold Nanoparticles-Based Biosensors

The function of a biosensor is to detect target molecules (or analytes) and to generate a recordable signal which will possibly allow a fully-quantitative

measurement [68]. Two main aspects are governing the efficiency of such sensors: the molecular recognition step which plays a major role in the selectivity/specificity and the transduction process responsible for the sensitivity. Researches in nanotechnology are growing exponentially since the past 10 years and the integration of biosensoring systems is still a key stake. At the nanoscale level, gold nanoparticle-based biosensors could therefore have a significant impact in modern diagnostics due to their small adaptative size and high degree of functionality.

2.6.1 Nanoscale Surface Plasmon

The intrinsic Plasmon resonance frequency in gold nanoparticles (diameter up to 40 nm) offers a typical "signature" with wavelengths centered around 520 nm and that can be directly exploited for sensing applications. Indeed, the interaction and/or binding of molecules to the particle surface can be responsible for shift in the Plasmon resonance frequency. Raschke and co-workers reported a method for biomolecular recognition using light scattering of a single gold nanocrystal functionalized with biotin [69]. Addition of streptavidin and subsequent specific binding events modify the dielectric properties at the interface between the nanoparticle and the surrounding environment, resulting in a spectral shift of the particle Plasmon resonance.

By analogy to the well-known H and J aggregation in organic chromophores, El-Sayed et al. observed that nanorods exhibiting shape anisotropy can be assembled in two distinct orientational modes (i.e., end-to-end *versus* side-by-side) [70]. A red-shift of the longitudinal Plasmon band for the end-to-end linkage of nanorods resulting from the Plasmon coupling between neighboring nanoparticles was already reported. But here, the authors did observe a blue-shift of the longitudinal Plasmon band of side-by-side linkage with a concomitant red-shift of the transverse Plasmon band.

The pioneering work by Mirkin and co-workers used Plasmon coupling shift to design colorimetric assay method which is nowadays probably the most cited example of a gold-based sensor [25, 71]. In the original assay developed for DNA sensoring, Au nanoparticles and oligonucleotides that are complementary to the specific target sequence are conjugated. The colloidal solution initially appears red because the nanoparticles are well-dispersed without the specific target sequence in solution. Then, the presence of the DNA complementary strands drives the molecular recognition process (hybridization) which results in the formation of small aggregates of Au nanoparticles. The subsequent violet/blue coloration originates from a change in the Plasmon resonance. Several DNA assays are based on this concept and the perfecting of this method has allowed quantitative detection of DNA sequences of concentrations as low as 5 fM [72].

The same concept was eventually extended to non-DNA analytes. Brust and colleagues reported the use of specifically designed, peptide-stabilized gold nanoparticles as artificial substrates for kinases [73, 74]. A very simple colorimetric protocol for the evaluation of kinase activity and inhibition was then

developed by using aptamers-based strategy (i.e. nucleic acid or peptide sequences that change their conformation upon specific binding). The inter-particle distance which is the key parameter is modulated and thus the color of the gold colloids changes from red to violet/blue. Lu and Liu demonstrated in a work published in *Chemical Communication* the possibility of designing nanoparticle-based colorimetric sensors using Cu^{2+}-dependent DNAzyme catalyzed ligation reactions [75]. Compared to DNA or RNA cleaving enzymes, ligation enzymes are intrinsically more sensitive due to the lack of non-specific background.

Interestingly, Li and co-workers investigated the effect of the aptamer folding on the colloidal stability of two different aptamers-tethered Au nanoparticles (adenosine and K^+-dependent aptamers). After the folding process, the particles were in fact found to be more stable toward salt induced aggregation than those tethered to unfolded aptamers. The local conformation adopted on the surface appears to be a key factor that determines the relative stability of the nanoparticles. Finally, on the basis of this unique phenomenon, colorimetric biosensors have been developed for the detection of adenosine, K^+, adenosine deaminase, and its inhibitors [76].

2.6.2 Surface-Enhanced Raman Scattering (SERS)

Most of molecules can be detected by Raman scattering and unequivocally identified by their characteristic spectra. Theory of Raman scattering are well-known and basically, the inelastic scattering process could statistically happen either at lower (Stokes) or higher (anti-Stokes) energy than those of the incident light. However, typical Raman signals are very weak and as a consequence, high surface concentration of the analyte is compulsory in order to provide a recordable signal. SERS provides an efficient circumventing of this limitation by taking advantage of the enhance response when the molecules are close enough to a gold surface with very high curvature, such as nanoscale Au particles [77, 78]. As a result, a much higher scatter probability is achieved and the Raman-scattered light intensity that is detected increases dramatically by several orders of magnitude. The use of SERS allows a major breakthrough in sensitivity and spectroscopic detection of single molecules and single nanoparticles have since been achieved. For single rhodamine 6G molecules adsorbed on the selected nanoparticles, the intrinsic Raman enhancement factors were on the order of 10^{14} to 10^{15} much larger than the ensemble-averaged values derived from conventional measurements. This enormous enhancement leads to vibrational Raman signals that are even more intense and more stable than single-molecule fluorescence [79, 80].

Mirkin et al. performed the multiplexed detection of oligonucleotide targets with labeled Au nanoparticle probes. The gold particles facilitate the formation of a silver coating that acts as a surface enhanced Raman scattering promoter for the dye-labeled particles that have been immobilized onto an underlying chip in microarray format. The strategy provides equally-high sensitivity and selectivity and adds multiplexing capability because a very large number of probes can be addressed based on the concept of using a Raman spectroscopic fingerprint [81]. The current unoptimized detection limit of this method is 20 fM.

Kneipp and colleagues improved further more this concept by the mean of surface-enhanced hyper-Raman scattering (SEHRS) which exploits the incoherent inelastic scattering of two photons on the vibrational quantum states [82]. The authors reported effective two-photon cross-sections for SEHRS on the order of 10^{-46} to 10^{-45} cm^4/s which made the method an extremely promising spectroscopic tool for ultrasensitive bioanalytical applications.

2.6.3 Fluorescence Quenching

Most of fluorophores are quenched when they are close enough to gold surfaces. This phenomenon was evidenced with lissamine dye molecules chemically attached to different size gold nanoparticles [83]. A pronounced fluorescence quenching was observed already for nanoparticles as small as 1 nm radius. The quenching is caused by an increased nonradiative rate as well as a drastic decrease in the dye's radiative rate. Assuming resonant energy transfer to be responsible for the nonradiative decay channel, the experimental finding was compared with theoretical results derived from the Gersten–Nitzan model. This effect can be used for several sensor strategies and the most common example relies on competitive displacement assay which have been formalized by Mc Ghee and von Hippel [84]. For that, gold particles are conjugated with ligands that specifically bind to the targeted analyte. The binding sites of the ligands should be fully blocked by saturating them with analyte-like molecules modified with fluorophores. As the fluorophores are in close proximity to the Au particles they do not emit light (quenching). Then, if these particles are now immersed in a solution containing the specific analyte molecules, they will progressively displace the fluorophore-labeled competitor and therefore enhance the light emission. For thermodynamic reason, the corresponding luminescence correlates to the concentration of analyte molecules in solution and a calibration curve allows a quantitative sensoring.

Kim and co-workers reported in 2005 an inhibition assay method based on the modulation in FRET efficiency between quantum dots (QDs) and gold nanoparticles conjugated with biomolecules [85]. In their strategy, QDs are conjugated with streptavidin (rod shape with a length of 10–15 nm and a diameter of 5 nm) while Au particles are coupled with biotin (spherical shape with 2–3 nm in diameter). By employing the most popular molecular recognition process as a model system, this sensing system allows determining the avidin concentration in sample solution by direct monitoring of the changes in the photoluminescence quenching. Parak and colleagues measured the fluorescence quantum yield of Cy5 dyes attached to gold nanoparticles *via* modulated single-stranded DNA spacers [86]. The distance between the core particle and Cy5 was tuned from 2 to 16 nm. The change in both radiative and nonradiative molecular decay rates with distance was determined using time-resolved photoluminescence spectroscopy. Remarkably, the distance dependent quantum efficiency was almost exclusively governed by the radiative rate.

Brust and co-workers developed "The Peptide Route to Multifunctional Gold Nanoparticles" which used cysteine-containing peptides as capping agents [87]. Based on the fluorescence quenching principle, they designed highly stable peptide-capped gold nanoparticles functionalized with two different biomolecular recognition motifs and measured their binding to DNA and protein microarrays.

2.6.4 Electrochemical Sensors

Joseph Wang authored a review in *Electroanalysis* in 2007 about nanoparticle-based electrochemical bioassays of proteins in order to emphasize the input of electrochemistry in recent sensoring progresses [88]. This work pointed out a variety of new nanoparticle/biomolecule assemblies for advanced electrical detection of proteins. Thanks to electrochemical transduction, ultrasensitive monitoring of biomolecular interactions particularly in the field of DNA can be achieved without any time-consuming PCR-like amplification step.

A pioneering contribution from Mirkin et al. reported a DNA array detection method in which the binding of oligonucleotides functionalized with gold nanoparticles leads to conductivity changes associated with target-probe binding events [89]. Silver deposition improved measurable conductivity changes and an unusual salt concentration-dependent hybridization behavior associated with these nanocomposite probes was exploited to achieve high selectivity. 50 fM in DNA detection was achieved with this method, with a point mutation selectivity factor of 1×10^5 to 1. The very next year, Willner and co-workers described the reconstitution of potent apo-proteins on a functionalized 1.4-nm Au nanocrystal integrated into a conductive film [90]. This construction (Fig. 6) yields to a bioelectrocatalytic system with a turnover rate of $\sim$5000 per second, which is seven times faster to the corresponding rate at which the natural co-substrate accepts electrons. The gold nanoparticle acts as an electron relay or "electrical nanoplug" for the alignment of the enzyme on the conductive support and for the electrical wiring of its redox-active center.

In parallel, Caruso reported another electrochemical sensors based on 4-(dimethylamino)pyridine-stabilized gold nanoparticle hybrid films prepared by infiltration into polyelectrolyte multilayers preassembled on indium tin oxide (ITO) electrodes [91]. Quartz crystal microgravimetry (QCM) and UV–Vis spectroscopy showed that composite films achieved high density. Electrochemical experiments revealed that the presence of gold nanoparticles in the multilayers significantly improves the electron-transfer characteristics of the films, which showed high electrocatalytic activity to the oxidation of nitric oxide (NO). The sensitivity of the composite films for measuring NO could be eventually further tailored by controlling the gold nanoparticle loading within the film.

More recently, Holzinger and co-authors at the University of Grenoble developed a concept of three-dimensional biostructures immobilized on electrode surface *via* affinity reactions [92]. The 3D architectures based on single-walled carbon nanotubes (SWCNTs) frameworks interconnected with gold nanoparticles

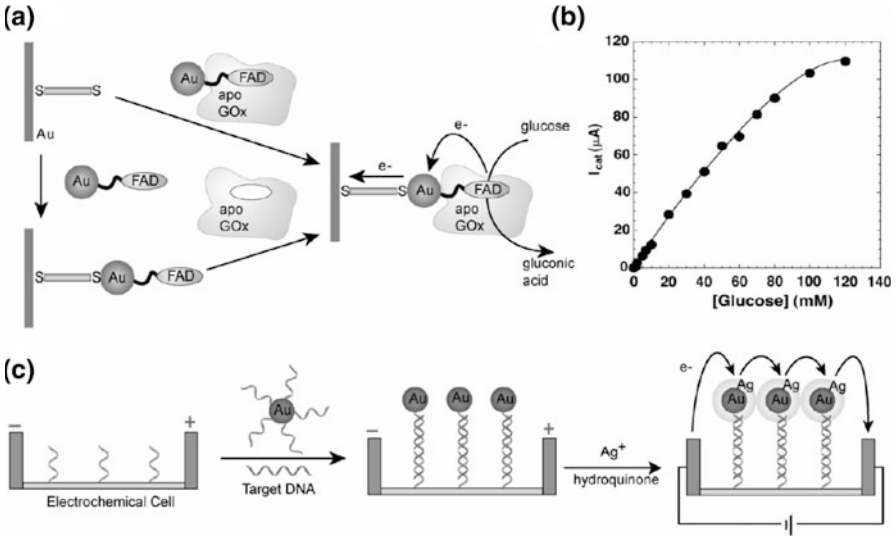

Fig. 6 **a** Fabrication of a GOx electrode by the reconstitution of apo-enzyme on a FAD-functionalized gold nanoparticle and **b** plot of the current developed by the reconstituted GOx electrode in the presence of different concentrations of glucose. **c** Electrical detection of DNA based on the ''sandwich'' hybridization with DNA-functionalized AuNPs followed by silver deposition. Reprinted with permission from Ref. [11]. Copyright 2008 Wiley-VCH

relays were applied to glucose sensoring *via* glucose oxidase (GOx) anchoring. This electrocatalytical model process was used as a proof of principle and the authors highlighted a combined synergetic effect of SWCNTs and gold nanoparticles that provides a higher amount of immobilized enzyme as well as improved electrochemical performances.

3 Iron Oxides (FeO_x)

3.1 Introduction

Magnetic nanoparticles have long been of technological and scientific interest as they behave like small magnets having either ferromagnetic or superparamagnetic character which makes them attractive for a broad range of applications like electronic devices, information storage, catalysis, magnetic inks, etc. [93, 94]. Furthermore, magnetic nanoparticles have also attracted much attention in biomedicine in applications such as magnetic drug delivery, biosensing, magnetic hyperthermia, regenerative medicine and magnetic resonance imaging (MRI) as contrast enhancers [95–97]. Each of these applications requires that the magnetic nanoparticles have specific properties. For example, the most important properties

required for biomedical use are: biocompatibility, superparamagnetic character at room temperature (no magnetic remanence), stable at physiological pH and salinity, long blood half-life and efficient internalisation [98, 99]. Colloidal properties of the magnetic fluid are also essential and depend firstly on the particles dimensions and secondly on surface chemistry and charge.

3.2 Synthesis Methods for Magnetic Nanoparticles

Considering the wide range of possible applications for this type of nanoparticles, it is no surprise that there are numerous chemical methods for synthesis: coprecipitation [100, 101], microemulsion [102], high temperature decomposition of precursors [103], polyol methods [104], sonolysis [105].

3.2.1 Coprecipitation Methods

The precipitation from iron salts is probably the most extensively utilized route of preparation. Typically, iron oxides are prepared by addition of a basic solution to a mixture of ferric and ferrous salts. Generally the reaction for the formation of Fe_3O_4 can be written as:

$$Fe^{2+} + 2Fe^{3+} + 8OH^- \rightarrow Fe_3O_4 + 4H_2O$$

This reaction is taking place at a pH ranging between 8 and 14 and in an oxygen free environment [106], otherwise the formed magnetite is not very stable and it undergoes oxidation into Fe_2O_3:

$$4Fe_3O_4 + O_2 \rightarrow 6Fe_2O_3$$

The process of coprecipitation is characterized by a nucleation phase followed by a growth phase which is responsible for the particle's shape, size and dispersity. To produce monodisperse nanoparticles, the two phases must be separated as shown in the LaMer diagram in Fig. 7 [107].

Other parameters which can influence the size, shape, magnetic properties are pH, temperature, oxygen presence, nature of salts (chlorides, sulfates, nitrates) or Fe^{2+}/Fe^{3+}*ratio* [109].

Massart was the first who synthesized superparamagnetic iron oxide nanoparticles using alkaline precipitation of ferric and ferrous chloride [110]. The original method was varied by many groups to achieve smaller size particles (from 8 to 3 nm) or to allow coating with different groups like hydroxyacids (citric, gluconic acids), dimercaptosuccinic acid, silica [111–113]. Several researchers have studied the influence of mixing rate upon particle size and showed that increasing this parameter the size and polydispersity decreases [110]. Other investigations show that rising the temperature of the reaction reduces the nanoparticles formation

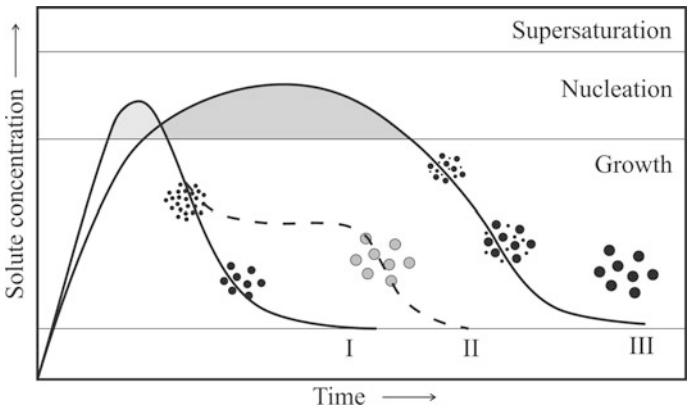

Fig. 7 Schematic representation of proposed mechanisms of formation of uniform particles: *curve I*. Single nucleation and uniform growth: *curve II*. Nucleation, growth and aggregation of small particles: *curve III*. Multiple nucleation events. Adapted with permission from Ref. [108]

[109]. This method offers the advantage that it is easy to follow and produces large quantities of nanoparticles.

3.2.2 Microemulsion Method

The water-in-oil (W/O) microemulsions (inverse micelles) are systems of fine nanodroplets of aqueous phase trapped by surfactant molecules dispersed in an oil phase. This method can also be used for the preparation of iron oxide nanoparticles as illustrated in Fig. 8. Compared with coprecipitation this method has certain advantages due to the presence of surfactant stabilized cavities which act as a constraining environment for the particles growth and agglomeration [114, 115].

W/O microemulsion method offers the opportunity to modulate the size of the nanoparticles by varying the size of the nanodroplets, which is the major advantage. Lee et al. have prepared nanoparticles with an adjustable diameter between 2 and 10 nm by varying the solvent, surfactant or concentration of iron salt [117]. Also this method was used by Carpenter to synthesize thin layer gold-coated iron oxide particles. Gold protects the core from oxidation, providing biocompatibility and functionality at the same time [118].

Vidal-Vidal et al. reported a one-pot microemulsion preparation for coated and uncoated monodisperse magnetic nanoparticles [119]. Numerous types of surfactants can be employed in the preparation procedure like ionic or non-ionic surfactants. The main disadvantage of using the ionic ones is that the produced nanoparticles are less crystalline [120] than the ones formed in the presence of non-ionic surfactants [121]. However, this technique has major drawbacks as it is very difficult to be scaled up and the surfactant molecules adhered to the nanoparticles are hard to be removed. The surfactant traces on the surface are an impediment to be used in biological applications.

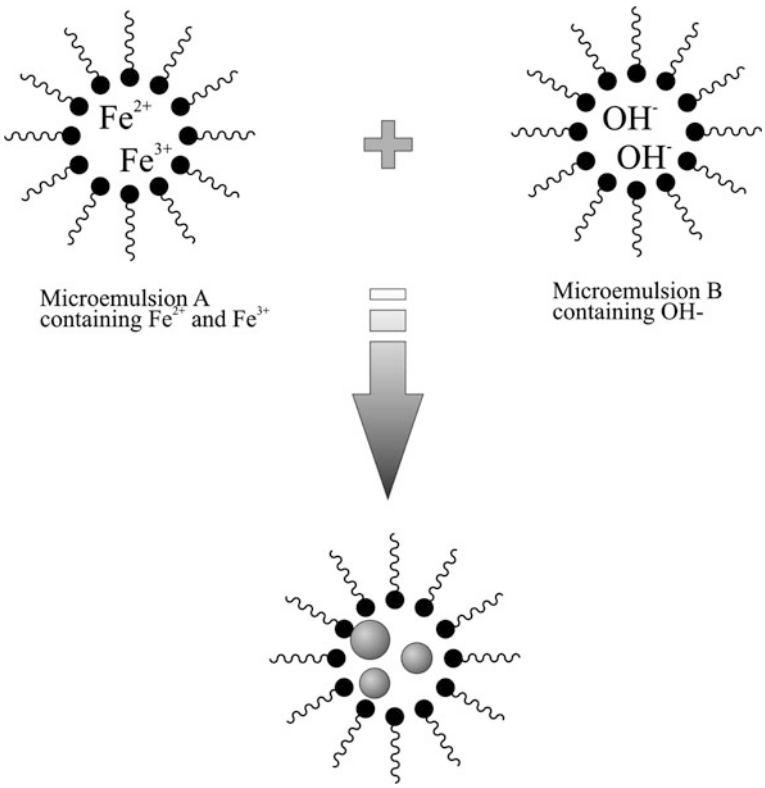

Fig. 8 Schematic representation of formation of magnetite nanoparticles using W/O microemulsion. Adapted with permission from Ref. [116]

3.2.3 High Thermal Decomposition

This method is based on the decomposition of different types of iron precursors like iron oleate, iron acetylacetonate [$Fe(acac)_3$] or iron pentacarbonyl [$Fe(CO)_5$], at a high temperature in the presence of organic solvents and stabilizing molecules like oleic acid, oleylamine or steric acids. The presence of surfactants clearly improves size control, narrow size distribution and crystallinity of the individual iron oxide nanoparticles. For example, highly monodispersed maghemite nanoparticles were produced by Hyeon et al. at 100°C by thermally decomposing $Fe(CO)_5$ in the presence of oleic acid, followed by a second step consisting in aging the iron oleic acid complexes at 300°C. With this procedure particles with controllable sizes between 4 and 16 nm were prepared [122]. More recently Sun et al. have reported the preparation of monodisperse iron oxide nanoparticles with sizes from 4 to 20 nm using the high temperature decomposition reaction of $Fe(acac)_3$ in phenyl ether in presence of stabilizing oleic acid and oleylamine

[103]. To obtain nanoparticles with diameters up to 20 nm a seed-mediated growth method was necessary. The parameters which can be varied during the process to produce different size particles are reaction time, nature of solvents, stabilizing agents, addition of seeds, precursors. However, this method produces hydrophobic magnetic nanoparticles and following reactions to transform them into hydrophilic ones are required. For instance, after the thermal decomposition of $Fe(acac)_3$ in high boiling point solvent the oleic acid nanoparticles have been coated with dimercaptosuccinic acid using a ligand exchange reaction to disperse the nanoparticles in water without aggregation [123]. Another example of successful phase transfer from hydrophobic to hydrophilic character was reported using the Pluronic block copolymer on oleic acid capped magnetite particles [96]. Also Li and co-workers recently reported that thermal decomposition of ferric triacetylacetonate in 2-pyrrolidone in presence of mPEG-COOH could produce crystalline PEGylated nanoparticles [124].

3.2.4 Synthesis Using Liquid Polyols

The polyol process is a chemical method of nanoparticle synthesis which uses the liquid polyol to reduce the metal precursors to particles with improved properties, crystallinity, monodispersity, higher magnetization [125, 126]. The polyols (for example, polyethylene glycol) act as solvents which are able to dissolve the inorganic compounds and at the same time are stabilizing the in situ formed nanoparticles. Cai and Wan [104] have reported a facile route of preparing directly non-aggregated superparamagnetic magnetite nanoparticles *via* polyol reaction. They investigated the influence of four types of polyol (mono-, di-, tri-, and tetraethylene glycol) in the direct reaction with $Fe(acac)_3$ and the results showed that only triethylene glycol produces non-aggregated nanoparticles due to suitable number of coordinating groups of the polymer with the particles surface. In comparison with the precipitation method, this route has the advantage to produce much narrower particle sizes and the surface will be coated with the hydrophilic polyol ligands.

3.3 Surface Modification of Iron Oxide Nanoparticles

Although there has been important progress regarding synthesis methods for magnetic nanoparticles, maintaining their stability for a long period of time without aggregation or precipitation is still an issue [127]. The agglomeration of nanoparticles may cause problems when they are to be used for in vivo applications because of the possibility of causing capillary blockage. As a result, it is very important to coat the surface of the magnetic nanoparticles with inorganic or organic layers and to form stable colloids. Also the protective coating may not only be used against degradation but also for further functionalization with drugs,

targeting molecules, or other functional groups. The coating is also a key factor for the biocompatibility properties of the nanoparticles. The colloidal stability can be achieved either by electrostatic or by steric repulsion as exemplified in Fig. 9.

The key parameter to generate good magnetic colloids is to control the strength of these two forces. The steric repulsion can be controlled by using polymers and it depends mostly on the molecular weight and density of the polymer [129]. The electrostatic repulsion can be generated with charged molecules bound to the surface of nanoparticles [130, 131]. The surface of iron oxide is rather inactive compared to other kind of nanoparticles (quantum dots, gold) and there is only limited number of functional groups that are able to anchor on it. It is known that carboxylates and phosphates are functional groups that bind to the surface of magnetite [132]. Citric acid is a one type of stabilizing agent which is commonly used to make magnetite surface negatively charged and hydrophilic at the same time. It has been used by many groups during the coprecipitation process to control the growth phase and magnetic properties of nanoparticles and because of these characteristics, citric acid stabilized iron oxide nanoparticles (VSOP C184) are now under clinical trials [133, 134]. Cheon and co-workers were able to prepare water-dispersible iron oxide nanoparticles using 2,3-dimercaptosuccinic acid, which has a bidentate carboxyl group [123]. Alkanephosphonic acids are also suitable ligands for magnetite stabilization and coating. Yee et al. reported that phosphonate ions are able to anchor on iron oxide surface through bidentate or monodentate bonding [135].

Silica is the most used inorganic coating for iron oxide nanoparticles. Generally, the silica shell prevents the aggregation phenomenon of magnetite nanoparticles and improves their chemical stability [136]. Although the toxicity of silica shells is still uncertain, there have been promising reports on the use of silica encapsulated nanoparticles for in vitro and in vivo use [137]. Ying and co-workers reported on silica-protected iron oxide nanoparticles synthesized using an inverse microemulsion method. The thickness of the silica layer can be varied from 2 to 100 nm depending on the synthesis method and the concentration of precursors used [138].

Functional organosilane compounds also form strong interactions with the metal oxide and for this reason can be successfully used as stabilization materials and at the same time to give functionality to the magnetic nanoparticles [139, 140].

Gold is another inorganic type of coating material which can be used in case of iron oxide nanoparticles because it offers functionality for the surface of magnetic particles and also improves their stability in aqueous dispersions. Superparamagnetic nanoparticles with a gold nanoshell have been reported only recently by Kim et al. [141].

Polymers have as well been used for magnetic nanoparticles surface modification on their own or in conjunction with other elements. The polymer encapsulation can be achieved during the particles formation or post-synthesis. Various natural and synthetic polymers have been used as a coating for iron oxide nanoparticles but the most common ones are dextran, carboxymethyl dextran, polyethylene glycol (PEG), polyvinyl alcohol (PVA), starch and chitosan.

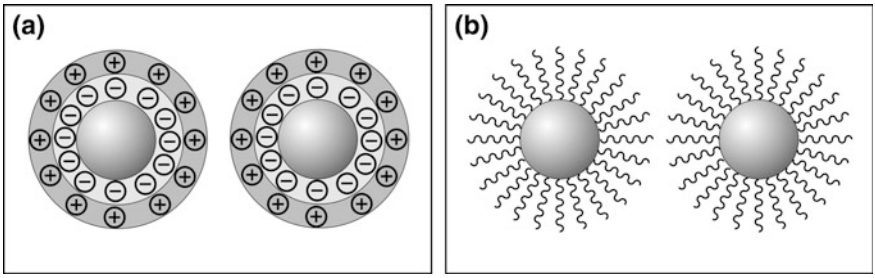

Fig. 9 Stabilisation techniques for magnetic nanoparticles: **a** electrostatic stabilisation; **b** steric stabilisation. Adapted with permission from Ref. [128]

Dextran is a natural polysaccharide and has been used for coating iron oxide particles due to its biocompatibility properties. For example, Feridex, Resovist and Combidex are all MRI contrast agents based on dextran-coated iron oxide nanoparticles. These particles show a long blood resistance time which allows their uptake by the macrophages in kidney, brain, osteoarticular tissues. A detailed structural and magnetic study on iron oxide formed in presence of dextran (MW = 40,000) has been elaborated by Pardoe et al. Their results show that dextran has an important role in particle size [142]. Dextran-coated magnetic nanoparticles based on physical absorption are unstable as dextran tends to dissociate from the magnetic cores [116]. The usual method to avoid desorption is to use a cross-linking agent such as epichlorhydrin which makes tighter association with the superparamagnetic iron oxide nanoparticles (commonly termed as SPIONs) [143]. Covalently bound dextran-SPIONs can be prepared using functional aminopropyl silane to modify the surface of the particles and then covalently conjugate them with partially oxidized dextran [144].

Polyvinyl alcohol (PVA)-coated magnetic nanoparticles are also of great interest as PVA prevents nanoparticles from aggregation. Recently Lin et al. have synthesized PVA encapsulated iron oxide particles according to the Massart method of coprecipitation [145]. The results showed that the polymer restricts the growth in size of the particle and that it binds irreversibly to the surface.

Polyethylene glycol (PEG) is a representative synthetic, hydrophilic, biocompatible polymer. The surface coverage with PEG minimizes the protein absorption onto magnetic nanoparticles surface increasing the blood time circulation. The unique property of PEG of non-specific absorption events is still in debate but is believed to be related with the large hydration volume, osmotic repulsion by the PEG chains and its unique interaction with water [146]. PEG-coated magnetic nanoparticles are prepared using different surface anchoring materials like phospholipids, copolymers, and silica because PEG itself is very inert. LaConte et al. reported the preparation of water-dispersible PEG-phospholipids block-copolymers magnetic nanoparticles which are based on the hydrophobic interaction between the hydrophobic tail group of surfactants and phospholipids parts [147]. Functional silane coupling agents such as 3-aminopropyltriethoxysilane are

commonly employed to immobilize PEG onto the SPIONs surface. Because PEG molecules have only a hydroxyl at the end, the polymer was further modified to generate amine or carboxyl groups [139].

Chitosan with its biodegradable, bioadhesive and biocompatible properties has been used in the pharmaceutical industry for a long time and nowadays have started to attract attention as a coating material for iron oxide nanoparticles. Chitosan-coated SPIONs prepared by a sonochemical method have been reported to have superior properties as contrast agents for MRI [148]. Other examples of polymers which have been employed in the stabilization of magnetic nanoparticles include poly(caprolactone), poly(lactic)acid, poly(acrylic acid), arabinogalactan or polyethyleneimine [149–151].

3.4 Biomedical Applications of Magnetic Nanoparticles

3.4.1 Magnetic Nanoparticles as Contrast Agents in MRI

At present MRI (magnetic resonance imaging) is one of the most powerful imaging techniques in medicine but often the difference in the relaxation times between abnormal and normal tissue times is very small and the image might provide a false diagnostic. To allow a better interpretation of the MRI image, contrast agents like iron oxide nanoparticles or gadolinium chelates have been introduced. Since their first use as MRI contrasting agents 20 years ago, nanoscale iron oxides have received enormous attention due to their ability to shorten T_2 relaxation time in liver, spleen, bone marrow because of their selective uptake by the cells of the reticuloendothelial system (RES). The mechanism for contrast in MRI is quite complicated and it mostly results from the dipolar interactions between the water proton spins and the magnetic moment of the iron oxide nanoparticles (Fig. 10) [152].

Several different formulations are currently used clinically for MRI and are based on superparamagnetic cores and a polymeric coating (dextran). Table 1 summarizes these types of contrast agents.

These types of contrast agents can be applied only for imaging the mentioned organs based on the biological distribution of nanoparticles. Recently iron oxide nanoparticles have attracted interest for targeted molecular imaging because of their large surface area to which targeting probes can be coupled. These include aptamers, oligonucleotides, peptides, antibodies, small molecules (folic acid) or other imaging molecules for improving the detectability of nanoparticles. At the beginning, monoclonal antibodies (mAbs) were the first to be used for targeting the magnetic nanoparticles. For example, Suzuki et al. have prepared an MRI contrast agent based on the covalent bonding between polyethylene glycol-coated iron oxide and a surface antibody specific for human glioma [153]. Recently, research is focused on using only fragments of the antibody which are still functional to direct the magnetic nanoparticles to the area of interest [154].

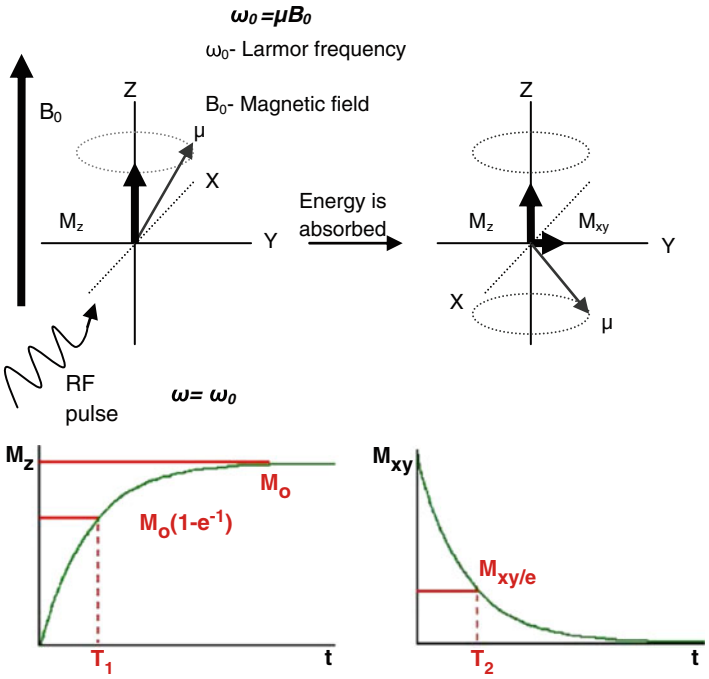

Fig. 10 Longitudinal and transverse magnetization mechanism (above); T_1 and T_2 relaxation time curves (below). Adapted with permission from Ref. [152]

Sun et al. have developed an imaging/drug delivery dual system that include PEG-coated SPIONs with chlorotoxin (peptide which binds to brain cancer cells) and methotrexate (a chemotherapeutic drug). This system has demonstrated promising results for in vivo applications [155]. There is no doubt that the current advances in the area of multifunctional magnetic nanoparticles will improve the sensitivity and quality of MRI.

3.4.2 Magnetic Hyperthermia

Hyperthermia, which is based on the fact that cancerous cells are more sensitive to temperature than normal cells, is a very promising treatment for cancer. The major technical difficulty with the application of hyperthermia is to heat only abnormal cells without affecting the normal surrounding tissue. Magnetic nanoparticles are good candidates for an effective treatment since they can be directed to and concentrated at the tumor site (due to the leaky hypervasculature) and can generate heat reaching 42–45°C under an applied alternating magnetic field [156]. The key qualities of SPIONs as mediators of hyperthermia are: (1) higher specific absorption rate and (2) the high cellular selectivity via surface functionalisation.

Table 1 Iron oxide-based MRI contrast agents

Name	Formulation	Particle size (NM)	Target organs
Feridex®/Endorem® (Ferumoxide)	SPION/dextran	160	Liver Spleen
Resovist® (Ferucarbotran)	SPION/carboxydextran	60	Liver Spleen
Combidex®/Sinerem® (Ferumoxtran)	SPION/dextran	20–40	Lymph nodes
Lumirem®/Gastromark® (Ferumoxsil)	SPION/silane	300	Bowel marker

Recent reports have highlighted that 10–30 nm magnetic nanoparticles have been effectively heated on human breast cancer models, but the control of the distribution of nanoparticles is still an issue [157]. A clear progress in hyperthermia research is the start of human clinical trials of magnetic hyperthermia treatment for brain and prostate cancer conducted by Jordan and co-workers at the Charité Hospital in Berlin. Preliminary results are encouraging because of the direct injection in multiple sites in the tumor rather than the use of targeted magnetic nanoparticles [158].

3.4.3 Magnetic Drug Targeting (MDT)

Conventional chemotherapy and radiotherapy are the current options for treating the majority of cancers but side effects are a common consequence of the systemic delivery of drugs. The principle of magnetic drug delivery is based on the use of an external magnetic field targeting and accumulating the magnetic carriers loaded with drugs at a specific location in the body (solid tumour). Afterwards the drug is released from the magnetic complexes *via* enzymatic cleavage, change in pH or temperature [116]. For instance, Alexiou et al. have reported the use of magnetic ferrofluids loaded with mitoxantrone for treatment of squamous cells carcinoma in rabbits [159]. Recently, a new MDT technique has begun to be the focus of the research community. This new technique is based on two steps: first, intravenous injection of the magnetic drug carriers and second, localization of the magnetic nanoparticles at the target site using an implanted magnetizable stent [160]. Although the MDT results are promising on animal models, the human trials still remain as a challenge.

3.4.4 Stem Cell Tracking

In recent years, magnetic nanoparticles have also been emerging as an attractive system for labeling and tracking stem cells in vivo. Magnetic nanoparticles offer the possibility to non-invasively monitor the stem cells migration and

differentiation after transplantation using MRI. There are an increasing number of stem cell tracking studies using magnetic nanoparticles with MRI, particularly in the area of brain and spinal cord regenerative medicine [161]. Sometimes the MRI results can be confirmed by using fluorescence imaging of the animal which means that bifunctional magnetic nanoparticles are needed to label the stem cells. The study reported by Frank et al. shows how is possible to follow the migration of neuronal restricted precursors labeled with superparamagnetic iron oxide contrast agents such as Feridex© using ex vivo MRI and histological methods [162]. Although many research studies demonstrate the advantages of using such systems, there are still many challenges that need more focus such as the lack of a rapid cell delivery system that does not use a toxic transfecting agent or suitable coating materials for the magnetic nanoparticles to enable the survival of these in the cellular environment.

3.4.5 In Vitro Separation and Purification of Targets

Another important type of application of the magnetic nanoparticles is the functionalization for in vitro separation of cells and proteins. In this procedure the iron oxide nanoparticles are added to the solution or suspension which contains the cells/proteins of interest. The cell or the protein reacts with the specifically tagged magnetic nanoparticles and then is separated from the mixture using a magnetic separator. This approach offers clear advantage over classical chromatography methods: simplicity, time efficiency and possibility to be carried out in a small scale. Commercially available products can be found for a variety of applications such as DNA, RNA or protein separation and purification [163, 164]. Interesting results have been reported in this area by Xu et al. who used dopamine functionalized magnetic nanoparticles to separate histidine-tagged proteins from a cell lysate with high efficiency. Another good example is the immobilization of vancomycin to the magnetic cores using the amino group of the antibiotic. This system was able to capture vancomycin-resistant enterococci or Gram-positive bacteria even at low concentration [165].

4 Quantum Dots (QDs)

Quantum dots (QDs) are inorganic colloidal semiconductors with a nanocrystal structure. These inorganic nanoparticles are luminescent at a particular range of wavelength. The first report for preparing these semiconducting nanocrystals was published in 1993 [166]. In 1994, Alivasatos reported a material with CdSe particles dispersed in a conducting polymer and a fluorescent blue color was observed [167]. This paper has been widely regarded as the major breakthrough in the research of quantum dots and rapid development has been observed in the next 15 years.

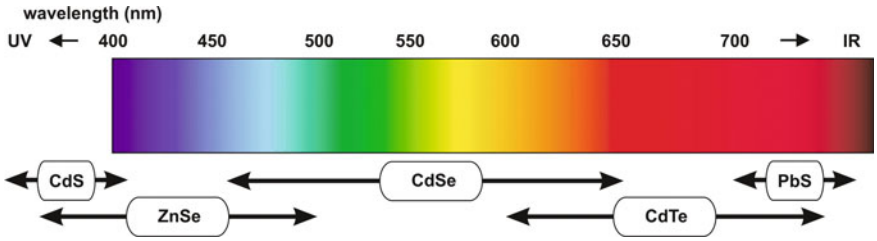

Fig. 11 Emission spectra of common quantum dots

Generally, when the crystal size of a semiconductor material decreases to a level of several hundreds to several thousands of atoms, the quantum-confinement effect becomes observable. Such an effect is defined by an increase in band gap together with the quantization of energy levels to discrete values. This effect is usually observed with semiconductor particles of size around a few nanometers and the extent of this effect is directly related to the size of the particle. The wavelength of their emission radiation increases as their particle size increases. For example, CdSe nanoparticles of 2.6 nm in diameter emit greenish-blue color (510 nm) while a red color (610 nm) is emitted from larger particles of 4.8 nm [168]. However, the equation governs this luminescent property is rather complicated and varies from one semiconducting material to another. It is rather impossible to predict the emission wavelength of a new quantum dots material.

There are many nanosized semiconducting materials show such quantum-confinement effects. Commonly used materials include ZnS, ZnSe, CdS, CdSe (types II–VI), GaN, GaP, InN, InP (types III–V) and PbS (types IV–VI). These materials all have their characteristic emission spectrum (see Fig. 11). Among all these semiconducting materials, CdSe covers the widest range of color or wavelength in the visible spectrum. For biomedical labeling, visual effect is important and, therefore, CdSe quantum dots are the most popular choice for biologists.

Although use of organic fluorescent molecules (e.g. fluorescein) for labeling biological species has been well documented, scientists continue to find new materials to replace these organic molecules. This is because organic fluorescent molecules usually have problems of bleaching, i.e. losing fluorescent intensity over long exposure to light, which may temporarily alter their structure. In contrast to fluorescent molecules, the emission wavelength of quantum dots is not only determined by their chemical formulation, but also their particle size. Also, bleaching is much less likely to quantum dots, due to their inorganic nature. Quantum dots present scientists a new opportunity to be used as an alternative for fluorescent labeling in biology.

However, the problem of using quantum dots for labeling biological samples is not associated with their optical property. Many semiconducting materials are highly toxic with notorious elements such as Cd, Se and Te [169]. Hence, the primary task for scientists to develop quantum dots for in vivo use is to protect them from exposure directly to our body system and a very robust coating is undoubtedly essential.

4.1 Preparation of QDs

Quantum dots are now commercially available but they are not difficult to synthesize in a standard laboratory with equipments for synthetic chemistry. Similar to nanoparticles of inorganic oxides, quantum dots are usually prepared with decomposition of organometallic precursors at high temperature (usually about 250–300°C) in the presence of ligands. The combination of trioctylphosphine and trioctylphosphine oxide (TOP/TOPO) as a high temperature solvent and ligand has been widely used in the preparation of CdSe quantum dots. In the original paper, trioctylphosphineselenide $(C_8H_{17})_3PSe$ and dimethylcadmium $Cd(CH_3)_2$ were used as precursors [166]. Since then, there are many modifications of this method were reported including the use of a single precursor diselenocarbamates and CdSe quantum dots of high crystallinity was prepared with this precursor [170]. Other ligands used for preparing quantum dots include hexadecylamine $C_{16}H_{33}NH_2$, replacing the highly toxic phosphine [171].

One of the tricky parts of the synthesis of quantum dots is the transfer of nanoparticles from the oil phase to an aqueous medium. Since the quantum dots were prepared in these "oily" ligands and they are stabilizing the quantum dots by assembling a hydrophobic shell, as-prepared quantum dots are only oil-soluble. This is particular troublesome to many biomedical applications, especially in vivo, as the reagents for such applications have to be water soluble or dispersible in aqueous phase. One relatively simple way on tackling this problem is to coat these ligand-stabilized quantum dots with amphiphilic polymers with both hydrophobic and hydrophilic segments. In such these multilayered quantum dots will have a hydrophilic surface (usually PEG or –COOH) and be readily transferable to an aqueous phase [172].

4.2 Coating the QDs

As mentioned previously, most of the materials for quantum dots are highly toxic. In order to use in biomedicines, particularly for in vivo applications, these quantum dots have to be sealed with an inert and robust coating. Because of their similarity in crystal structure, ZnO and ZnS are popular choices for coating CdSe quantum dots. In the first report on these core–shell quantum dots, a ZnS shell was coated over CdSe quantum dots [173]. It was found that such a ZnS shell not only protected the core materials from chemical reactions but also stabilized it against photobleaching.

At the beginning, precursors for preparing the ZnS shell are dimethylzinc and hexamethyldisilanthiane. However, these compounds are difficult to handle and scaling up becomes problematic. Zinc carboxylates and elemental sulfur then become the preferred precursors. Also, monomolecular precursor (both Zn and S in one compound) such as zinc xanthates and zinc dithiocarbamates are also used for coating CdSe quantum dots [174].

There are a number of methods for coating quantum dots but the two-step method (synthesis of CdSe core, purification, and coating with ZnS) is usually the preferred procedure. In general, up to five monolayers of the ZnS are coated onto the cores in order to preserve the optical property of the core material. To avoid nucleation between cores, the temperature of coating needs to be lower than that during the synthesis of cores. Slow addition, possibly aided by an automatic syringe, is required to ensure homogeneous coating. Controlling the thickness of coating is simply carried out by stoichiometric calculation of the core and shell materials. Detailed experimental procedures are widely available in the literature [175].

4.3 Surface Modification of QDs

As discussed previously, CdSe coated with ZnS or ZnO are the most commonly used quantum dots for biomedical applications due to their optical property. Therefore, we focus on the surface functionalization based on the ZnS shell. There are many different routes for functionalization but we can group them into several mechanisms according to the chemical interaction between the quantum dots and the designed functional molecules.

4.3.1 Thiols

Thiol groups are not only suitable for functionalizing gold surface, several other transition metals such as Cd, Pt, Pd and Hg also interact strongly with thiol groups. Besides, thiol also forms –S–S– interaction with the sulfur atoms on the ZnS coating. With a ZnS shell, quantum dots can be functionalized in a similar way as gold nanoparticles.

One of the early examples of using thiol as a functionalization agent for quantum dots was demonstrated by Chan et al. [176]. In this report, the thiol-carboxylic acid analogue has been used to functionalize CdSe/ZnS quantum dots (Fig. 12a). With the thiol groups strongly bound to the ZnS shell, the carboxylic acid groups become available for further functionalization, through ester or amide linkage. The carboxylic acid groups also make the quantum dots water soluble, which is essential for most of the biomedical applications. Coupling of carboxylic acids on nanoparticle surface with the amine groups on a protein molecules using coupling agents such as EDC, 1-ethyl-3-(3-dimethylamino-propyl)carbodiimide is commonly used in binding proteins onto nanoparticles. This protocol is easily applicable to –COOH functionalized quantum dots. In fact, this method is used to manufacture streptavidin-tagged quantum dots. This material has about 20 streptavidin molecules per particle and retains its high quantum yield. With streptavidin on the surface, these quantum dots bind biotinylated species, including antibodies and proteins, and the product can be used in targeted imaging [177]. Using the same principle, alkylthiol terminated DNA has also been tagged onto CdSe/ZnS quantum dots [178].

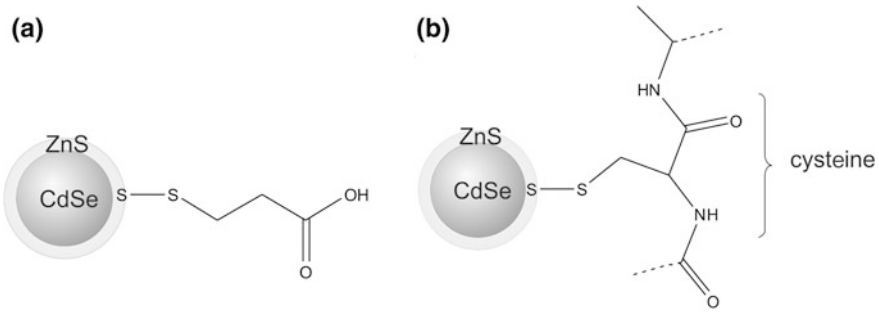

Fig. 12 Schematic showing the –S–S– interaction between a thiol group and the ZnS surface. **a** A carboxylic acid group is hence attached onto the quantum dot, and **b** a peptide with a cysteine unit in the amino acid sequence can bind to a ZnS-coated quantum dot with the same interaction

Similar to gold, ZnS-coated quantum dots has strong affinity to cysteine due to its –SH group. Therefore, these quantum dots can be functionalized by binding peptides with cysteine in the amino acid sequence. Logically, the more cystine units are in the sequence, the stronger its interaction to the ZnS coating (Fig. 12b). For example, Pinaud et al. used Biotin-G**C**E**C**GG**C**E**C**G-Cha-C_2H_4-Cha-Cmd (**C** = cysteine, Cha = 3-cyclohexylalamine, Cmd = carboxamide) and other similar sequences to functionalize quantum dots for efficiently binding to streptavidin and are specifically targeted to GPI-anchored avidin-CD14 chimeric proteins expressed on the membranes of live HeLa cells [179].

4.3.2 Phosphine and Phosphine Oxide

The success of preparation of CdSe quantum dots was due to the discovery of strong interactions of Cd–O=P and Se–P. These specific interactions can also be used in surface functionalization. However, it would still be better to use a ZnS-coated CdSe in order to minimize any concern about toxicity of CdSe. Fortunately, the equivalent Zn–O=P and S–P interactions are just as strong and exploitable for surface functionalization (see Fig. 13). Oligomeric phosphines with carboxylic acids on branches have been used to functionalize CdSe/ZnS quantum dots and the material was used for binding streptavidin and these quantum dots were shown to be able to conjugate with biotinlyated quantum dots [180]. However, the main concern regarding use of phosphine or phosphine oxide to functionalize quantum dots is that these are toxic chemical and leaching can cause serious health issues. Unlike thiol, there is no natural analogue to substitutes for either phosphine or phosphine oxide.

4.3.3 Histidine

Histidine is an amino acid with an imidazole group. When two histidines adjacent to each other in a peptide sequence, a strongly chelating site to transition metals

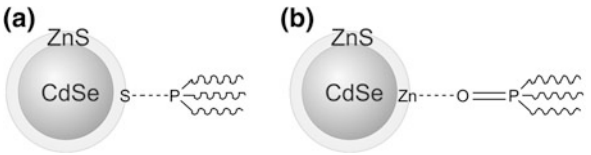

Fig. 13 Interaction between ZnS-coated quantum dots and **a** phosphine, or **b** phosphine oxide ligands

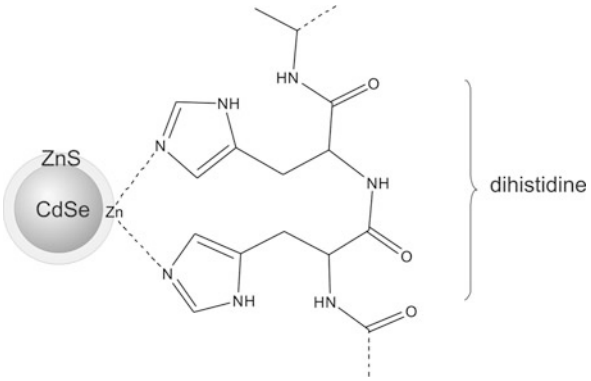

Fig. 14 Binding of dihistidine to Zn on ZnS-coated quantum dots

is created. Such chemistry has been exploited in biochemistry. For example, supported Ni^{2+}–NTA groups (a Ni organometallic complex) have been wildly used to chelate dihistidine unit of peptides as such interaction is measured to be a lot stronger than that of antibody binding [181]. Dihistidine has been found to chelate several transition metals strongly, including Ni, Zn, Fe, Cu, Co, and Mn. As a result, peptides with dihistidine group can be used to functionalize the CdSe/ZnS quantum dots by binding directly onto the ZnS shell (see Fig. 14).

Despite their harmless nature, use of dihistine to functionalize is still relatively rare. This is because not many natural peptides have a dihistidine unit in their sequence and many of these dihistidine ligands are synthetic or genetically engineered. As a result, the cost of using dihistidine ligands is high. Another difficulty of using dihistidine ligands for functionalizing quantum dots is the drawback of their own harmless nature. Because these ligands are mainly peptides, it is difficult to bind functional units other than amino acids or peptides onto the ligands. For example, binding a carbohydrate molecule onto a dihistidine ligand may not be straightforward.

4.3.4 Aliphatic Chains

Use of aliphatic chains to functionalize quantum dots is different from using other ligands because there is no direct interaction with these ligands to the quantum dot surface. Instead, they interact with the phosphine/phosphine oxide shell with strong hydrophobic interaction. And because of such hydrophobic interaction, unlike other mechanism, this functionalization retained the phosphine/phosphine oxide shell. In other words, this is an indirect method to functionalize quantum dots. The advantage about this strategy is that a hydrophobic shell is self-assembled round

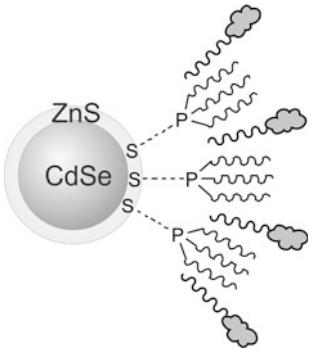

Fig. 15 Self-assembly of functional molecules with a hydrophobic, aliphatic tail onto the phosphine shell of quantum dots

the quantum dot and this can serve as an extra protecting layer against any hydrophilic reactants (see Fig. 15).

Several examples have been reported using this functionalization mechanism. For example, modified acrylic acid polymer has been coated onto quantum dot surface by hydrophobic interaction with the TOP/TOPO shell [182]. These polymer-coated particles have been used in imaging in vivo [183]. Other examples using this mechanism include quantum dots coated with amphiphilic triblock copolymer [184] and amphiphilic saccharides [185].

4.4 Medical Applications of Surface Functionalized QDs

4.4.1 Bioassays Using QDs

Bioassays using labeled quantum dots can detect specific DNA, proteins and other biomolecules. For example, DNA-labeled quantum dots have been used as probes for human chromosomes, single-nucleotide and multi-allele DNA detections [186]. Usually, this is carried out using a specific single-stranded DNA labeled quantum dots for binding their complement DNA molecules. Because of their high quantum yield, these DNA-labeled quantum dots show a high sensitivity compared with fluorescent molecules.

In addition to DNA, antibody-tagged quantum dots have been used to detect specific proteins. The principle is similar to those detecting DNA. A multi-colored system using antibody-tagged quantum dots have shown to be able to analyze biomolecules including toxins [187]. Because these bioassays are all ex vivo analysis, there is no problem associated with the toxicity of quantum dots.

4.4.2 Cell Labeling Using QDs

Recently, rapid development has been seen on using quantum dots to label cells, thanks to the improvement in controlling their cytotoxicity and internalizing into cells. Use of quantum dots for cell labeling has experienced significant

advancement in the past few years. One of the major areas of development was on a multicolor labeling system for cells [188]. The advantages of using quantum dots over traditional fluorophores have been discussed earlier.

Quantum dots can be used to label both live and fixed cells. Labeling fixed cells are relatively straightforward because these cells are dead and can withstand rather harsh conditions. To label live cells, a certain amount of functionalized quantum dots are needed to be internalized into the cells unless the specific receptors are on the cell membrane. There are several strategies for the internalization of quantum dots into cells for internal labeling.

1. *Endocytosis*. Functionalized quantum dots are being taken up by the cells non-specifically through endocytosis and the quantum dots are normally localized in the cytoplasm initially.
2. *Transfection*. Similar to endocytosis, functionalized quantum dots are being non-specifically internalized but with the assistance of a transfecting reagent, e.g. DOTAP or lipofectamine. These reagents are normally used for gene delivery but can be used for transporting other negatively charged species. A much higher uptake efficiency is usually observed using commercial transfecting reagent than uptake through normal endocytosis.
3. *Microinjection*. Functionalized quantum dots are being injected into the cells using micro-needles. This method only allows a small number of cells to be labeled.
4. *Electroporation*. In this method, functionalized quantum dots are delivered into the cells using charge. By applying an external electrical field, the electrical conductivity of the cell membrane is increased, hence its permeability. Quantum dots can therefore be internalized easily. This method has also been used in gene delivery.

After internalization, these functionalized quantum dots need to find their way to the target compartments of the cell. Usually specific peptides or antibody will be tagged onto these quantum dots for this purpose. There are many examples of using targeting peptides and antibody for labeling particles. For example, Wu et al. tagged monoclonal anti-Her2 antibody onto CdSe/ZnS core–shell QDs (both green QD-535 and red QD-630) and successfully labeled the Her2 receptors on the surface of breast cancer SK-BR-3 cells [189]. In contrast, unlabelled quantum dots were scattered around the cells.

4.4.3 In Vivo Imaging Using QDs

For in vivo tissue imaging, quantum dots emitting near-infrared (NIR) radiations (e.g. 840 nm) have been used to map lymph nodes for cancer surgery in an animal model [190]. Use of NIR quantum dots can avoid the problem of auto-fluorescence from tissues. Compared with the use of NIR dyes, emissions from quantum dots can be detected from deeper locations. For example, lymph nodes in 1 cm deep in tissue have been imaged with the associated lymphatic vessels clearly seen.

Moreover, the fluorescence of quantum dots in tissues can still be detectable in vivo after 4 months. This provides an advantageous possibility for using quantum dots for a long-term experiments or monitoring. Such observation can also be used in tumor imaging as tumors normally have a poor lymphatic drainage system and quantum dots tend to accumulate inside.

Tumor imaging can also be achieved by active targeting using quantum dots tagged with specific antibodies. For example, prostate-specific membrane antigen (PSMA) has been tagged onto quantum dots as a marker for diagnosis of prostate cancer in a mouse model [191].

The major drawback in using quantum dots for in vivo diagnosis is, without a doubt, their toxicity. As discussed earlier, scientists have been making progress in this area by coating the CdSe core with less toxic ZnS shell [192]. However, this is still not enough to prevent the release of highly toxic Cd^{2+} ions into the body. In particular, these quantum dots are highly toxic to cells under UV radiation for an extended period of time because Cd^{2+} ions were thought to be released during photolysis under UV. Unfortunately, many of the in vivo imaging experiments using quantum dots require UV or visible radiation of high energy for excitation. Therefore, there is an urgent need for a robust coating for quantum dots. Many studies showed polymer-coated quantum dots are non-toxic in vitro. Nonetheless, these are only short-term studies on cultured cell lines. The long-term cytotoxicity effect of these polymer-coated quantum dots is still to be tested in vivo. Under an extended time period, the polymer coating is likely to disintegrate due to enzymatic digestion and the cores of quantum dots become exposed to the body fluid. It is still unknown if such an effect can be eliminated completely. As a result, use of quantum dots in vivo still needs detailed studies on their long-term effects in animal bodies.

5 Bimodal Core–Shell Nanoparticles

There are a lot of concerns about the accuracy of diagnosis using one single imaging technique. Hence, a combination of more than one imaging techniques was developed in order to enhance the resolution of scans. For example, the combined CT–MRI scans have been regarded as a diagnostic technique with much improved results. Whilst physicists and engineers are trying to develop the latest machines for combined imaging and mathematicians are working out the digital merging of these images, chemists are given the task to assemble a single contrast reagent for this combined technique. Unfortunately, there is no such a universal compound as a contrast agent for multiple imaging. As a result, scientists have been working hard in developing bimodal contrast agents. A core/shell nanostructure of two compounds would be the ideal materials for this task.

For example, gold-coated iron oxide nanoparticles can be used as a contrast agent for a combined CT–MRI scan [193]. With the gold coating, simple modification using a thiolated compound, such as thiolated PEG, can be carried out for

biocompatibility and biospecificity. However, a homogeneous gold coating on iron oxide particles is still difficult to achieve. Silver is another possible coating material and has some similar chemical property as gold. Silver-coated iron oxide nanoparticles has also been developed recently [194] but their biomedical applications are still to be explored. Platinum, despite its high cost, is another possible coating material for such use.

On the other hand, bimodal core–shell nanoparticles with quantum dots are rear. This is mainly because the fluorescence property of quantum dots is sensitive to coatings. Therefore, it is likely that the semiconducting materials are to be the coating rather than the core. In spite of this limitation, gold–CdS nanocomposite material has been reported [195]. This material was constructed using silica-coated CdS quantum dots coupling with Au nanoparticles. Again, their applications are not yet studied. Recently, a layer-by-layer (LbL) method was published for preparing iron oxide nanoparticles coated with Au nanoparticles or CdTe quantum dots [196]. A silica layer is also used as an intermediate for coupling these materials together. Nonetheless, in-depth investigation on their medical applications are still needed, particularly their cytotoxicity.

6 Future Developments

Development of inorganic nanoparticles with delicate structures has experienced significant advancement in the past decade. Nowadays, nanoparticles of a wide range of sizes can be prepared and sometimes at a large scale. Preparation of bimodal and multimodal nanoparticles is still a challenge but, for medical applications, the major concerns are on their localization and their specification. Although we have seen many reports on nanoparticles targeting certain cell types with antibodies or specific ligands, many of these research works are still carried out in vitro or ex vivo. In vivo studies are still limited and less successful. This is due to the complexity of the cell systems. A precise, robust, reliable targeting system is still to be developed.

In addition, multifunctional nanoparticles are also very much in the agenda. A small body capable of multi-tasking, including imaging, diagnosis, and therapy, will be the holy grail for the medical community. So far, magnetic nanoparticles with drug storage and delivery capability have been reported and the delivery of anticancer agents has also been tested [197]. Another area to be developed is a multiple targeting system for the precise delivery of drugs. A designed nanoporous iron oxide–silica composite material tagged with antibody has been developed for drug storage and delivery [198]. Such a complex material opens up a research direction for magnetic-antibody dual targeting drug delivery. The iron oxide particles in the composite can also act as a contrast agent for MRI scans. Multiple targeting systems for localization of particles with a high accuracy may well be available soon. Clinical trials of these complex nanomaterials are yet to be carried out but an entirely new therapeutic system based on nanoparticles may be commonly used in medicine in a few decades time.

References

1. Hutchings, G.: A golden future. Nat. Chem. **1**, 584 (2009)
2. Hutchings, G.J., Brust, M., Schmidbaur, H.: Gold—an introductory perspective. Chem. Soc. Rev. **37**, 1759–1765 (2008)
3. Haruta, M.: When gold is not noble: catalysis by nanoparticles. Chem. Rec. (N.Y.) **3**, 75–87 (2003)
4. Sinha, A.K., Seelan, S., Tsubota, S., Haruta, M.: A three-dimensional mesoporous titanosilicate support for gold nanoparticles: vapor–phase epoxidation of propene with high conversion. Angew. Chem. Int. Ed. **43**, 1546–1548 (2004)
5. Daté, M., Okumura, M., Tsubota, S., Haruta, M.: Vital role of moisture in the catalytic activity of supported gold nanoparticles. Angew. Chem. Int. Ed. **43**, 2129–2132 (2004)
6. Haruta, M.: Catalysis: gold rush. Nature **437**, 1098–1099 (2005)
7. Hashmi, A.S.K., Rudolph, M.: Gold catalysis in total synthesis. Chem. Soc. Rev. **37**, 1766–1775 (2008)
8. Marion, N., Nolan, S.P.: N-Heterocyclic carbenes in gold catalysis. Chem. Soc. Rev. **37**, 1776–1782 (2008)
9. Della Pina, C., Falletta, E., Prati, L., Rossi, M.: Selective oxidation using gold. Chem. Soc. Rev. **37**, 2077–2095 (2008)
10. Corma, A., Garcia, H.: Supported gold nanoparticles as catalysts for organic reactions. Chem. Soc. Rev. **37**, 2096–2126 (2008)
11. De, M., Ghosh, P.S., Rotello, V.M.: Applications of nanoparticles in biology. Adv. Mater. **20**, 4225–4241 (2008)
12. Sperling, R.A., Rivera Gil, P., Zhang, F., Zanella, M., Parak, W.J.: Biological applications of gold nanoparticles. Chem. Soc. Rev. **37**, 1896–1908 (2008)
13. Connor, E.E., Mwamuka, J., Gole, A., Murphy, C.J., Wyatt, M.D.: Gold nanoparticles are taken up by human cells but do not cause acute cytotoxicity. Small **1**, 325–327 (2005)
14. Brust, M., Walker, M., Bethell, D., Schiffrin, D.J., Whyman, R.J.: Synthesis of thiol-derivatised gold nanoparticles in a two-phase liquid–liquid system. J. Chem. Soc. Chem. Commun. 801–802 (1994)
15. Hostetler, M.J., Wingate, J.E., Zhong, C.-J., Harris, J.E., Vachet, R.W., Clark, M.R., Londono, J.D., Green, S.J., Stokes, J.J., Wignall, G.D., Glish, G.L., Porter, M.D., Evans, N.D., Murray, R.W.: Alkanethiolate gold cluster molecules with core diameters from 1.5 to 5.2 nm: core and monolayer properties as a function of core size. Langmuir **14**, 17–30 (1998)
16. Sardar, R., Funston, A.M., Mulvenay, P., Murray, R.W.: Gold nanopartciles: past, present, and future. Langmuir **25**, 13840–13851 (2009)
17. Scott, R.W.J., Wilson, O.M., Crooks, R.M.: Synthesis, characterization, and applications of dendrimer-encapsulated nanoparticles. J. Phys. Chem. B **109**, 692–704 (2005)
18. Zheng, J., Petty, J.T., Dickson, R.M.: High quantum yield blue emission from water-soluble Au8 nanodots. J. Am. Chem. Soc. **125**, 7780–7781 (2003)
19. Giersig, M., Mulvaney, P.: Preparation of ordered colloid monolayers by electrophoretic deposition. Langmuir **9**, 3408–3413 (1993)
20. Murray, R.W.: Nanoelectrochemistry: metal nanoparticles, nanoelectrodes, and nanopores. Chem. Rev. **108**, 2688–2720 (2008)
21. Decher, G.: Fuzzy nanoassemblies: toward layered polymeric multicomposites. Science **277**, 1232–1237 (1997)
22. DeVries, G.A., Brunnbauer, M., Hu, Y., Jackson, A.M., Long, B., Neltner, B.T., Uzun, O., Wunsch, B.H., Stellacci, F.: Divalent metal nanoparticles. Science **315**, 358–361 (2007)
23. Templeton, A.C., Wuelfing, W.P., Murray, R.W.: Monolayer-protected cluster molecules. Acc. Chem. Res. **33**, 27–36 (2000)
24. Daniel, M.C., Astruc, D.: Gold nanoparticles: Assembly, supramolecular chemistry, quantum-size-related properties, and applications toward biology, catalysis, and nanotechnology. Chem. Rev. **104**, 293–346 (2004)

25. Mirkin, C.A., Letsinger, R.L., Mucic, R.C., Storhoff, J.J.: A DNA-based method for rationally assembling nanoparticles into macroscopic materials. Nature **382**, 607–609 (1996)
26. Rosi, N.L., Mirkin, C.A.: Nanostructures in biodiagnostics. Chem. Rev. **105**, 1547–1562 (2005)
27. Kankate, L., Turchanin, A., Gölzhäuser, A.: On the release of hydrogen from the S–H groups in the formation of self-assembled monolayers of thiols. Langmuir **25**, 10435–10438 (2009)
28. Guo, R., Song, Y., Wang, G., Murray, R.W.: Does core size matter in the kinetics of ligand exchanges of monolayer-protected Au clusters? J. Am. Chem. Soc. **127**, 2752–2757 (2005)
29. Kassam, A., Bremner, G., Clark, B., Ulibarri, G., Lennox, R.B.: Place exchange reactions of alkyl thiols on gold nanoparticles. J. Am. Chem. Soc. **128**, 3476–3477 (2006)
30. Huang, X.H., Jain, P.K., El-Sayed, I.H., El-Sayed, M.A.: Gold nanoparticles: Interesting optical properties and recent applications in cancer diagnostics and therapy. Nanomedicine **2**, 681–693 (2007)
31. Sonnichsen, C., Franzl, T., Wilk, T., von Plessen, G., Feldmann, J.: Plasmon resonances in large noble–metal clusters. New J. Phys. **4**, 93.1–93.8 (2002)
32. Tkachenko, A.G., Xie, H., Liu, Y., Coleman, D., Ryan, J., Glomm, W.R., Shipton, M.K., Franzen, S., Feldheim, D.L.: Cellular trajectories of peptide-modified gold particle complexes: comparison of nuclear localization signals and peptide transduction domains. Bioconjug. Chem. **15**, 482–490 (2004)
33. Souza, G.R., Christianson, D.R., Staquicini, F.I., Ozawa, M.G., Snyder, E.Y., Sidman, R.L., Miller, J.H., Arap, W., Pasqualini, R.: Networks of gold nanoparticles and bacteriophage as biological sensors and cell-targeting agents. Proc. Natl. Acad. Sci. U.S.A. **103**, 1215–1220 (2006)
34. Boyer, D., Tamarat, P., Maali, A., Lounis, B., Orrit, M.: Photothermal imaging of nanometer-sized metal particles among scatterers. Science **297**, 1160–1163 (2002)
35. Lasne, D., Blab, G.A., Berciaud, S., Heine, M., Groc, L., Choquet, D., Cognet, L., Lounis, B.: Single nanoparticle photothermal tracking (SNaPT) of 5-nm gold beads in live cells. Biophys. J. **91**, 4598–4604 (2006)
36. Wang, G.L., Huang, T., Murray, R.W., Menard, L., Nuzzo, R.G.: Near-IR luminescence of monolayer-protected metal clusters. J. Am. Chem. Soc. **127**, 812–813 (2005)
37. Cang, H., Wong, C.M., Xu, C.S., Rizvi, A.H., Yang, H.: Confocal three dimensional tracking of a single nanoparticle with concurrent spectroscopic readouts. Appl. Phys. Lett. **88**, 223901 (2006)
38. Kim, D., Park, S., Lee, J.H., Jeong, Y.Y., Jon, S.: Antibiofouling polymer-coated gold nanoparticles as a contrast agent for in vivo X-ray computed tomography imaging. J. Am. Chem. Soc. **129**, 7661–7665 (2007)
39. Garanger, E., Boturyn, D., Jin, Z., Dumy, P., Favrot, M.-C., Coll, J.-L.: New multifunctional molecular conjugate vector for targeting, imaging, and therapy of tumors. Mol. Ther. **12**, 1168–1175 (2005)
40. Foillard, S., Jin, Z.-h., Garanger, E., Boturyn, D., Favrot, M.-C., Coll, J.-L., Dumy, P.: Synthesis and biological characterisation of targeted pro-apoptotic peptide. ChemBioChem **9**, 2326–2332 (2008)
41. Huff, T.B., Tong, L., Zhao, Y., Hansen, M.N., Cheng, J.X., Wei, A.: Hyperthermic effects of gold nanoreods on tumor cells. Nanomedicine **2**, 125–132 (2007)
42. Chen, J., Wang, D., Xi, J., Au, L., Siekkinen, A., Warsen, A., Li, Z.Y., Zhang, H., Xia, Y., Li, X.: Immuno gold nanocages with tailored optical properties for targeted photothermal destruction of cancer cells. Nano Lett. **7**, 1318–1322 (2007)
43. Kogan, M.J., Bastus, N.G., Amigo, R., Grillo-Bosch, D., Arraya, E., Turiel, A., Labarta, A., Giralt, E., Puntes, V.F.: Nanoparticle-mediated local and remote manipulation of protein aggregation. Nano Lett. **6**, 110–115 (2006)
44. Hamad-Schifferli, K., Schwartz, J.J., Santos, A.T., Zhang, S., Jacobson, J.M.: Remote electronic control of DNA hybridization through inductive coupling to an attached metal nanocrystal antenna. Nature **415**, 152–155 (2002)

45. Stehr, J., Hrelescu, C., Sperling, R.A., Raschke, G., Wunderlich, M., Nichtl, A., Heindl, D., Kürzinger, K., Parak, W.J., Klar, T.A., Feldmann, J.: Gold nanostoves for microsecond DNA melting analysis. Nano Lett. **8**, 619–623 (2008)
46. Angelatos, A.S., Radt, B., Caruso, F.: Light-responsive polyelectrolyte/gold nanoparticle microcapsules. J. Phys. Chem. B **109**, 3071–3076 (2005)
47. Skirtach, A.G., Javier, A.M., Kreft, O., Köhler, K., Alberola, A.P., Möhwald, H., Parak, W.J., Sukhorukov, G.B.: Laser-induced release of encapsulated materials inside living cells. Angew. Chem. Int. Ed. **45**, 4612–4617 (2006)
48. Mocellin, S., Bronte, V., Nitti, D.: Nitric oxide, a double edged sword in cancer biology: searching for therapeutic opportunities. Med. Res. Rev. **27**, 317–352 (2007)
49. Hone, D.C., Walker, P.I., Evans-Gowing, R., FitzGerald, S., Beeby, A., Chambrier, I., Cook, M.J., Russell, D.A.: Generation of cytotoxic singlet oxygen via phthalocyanine stabilized gold nanoparticles: a potential delivery vehicle for photodynamic therapy. Langmuir **18**, 2985–2987 (2002)
50. Polizzi, M.A., Stasko, N.A., Schoenfisch, M.H.: Water-soluble nitric oxide-releasing gold nanoparticles. Langmuir **23**, 4938–4943 (2007)
51. Gibson, J.D., Khanal, B.P., Zubarev, E.R.: Paclitaxel-functionalized gold nanoparticles. J. Am. Chem. Soc. **129**, 11653–11661 (2007)
52. Meister, A., Anderson, M.E.: Glutathione. Annu. Rev. Biochem. **52**, 711–760 (1983)
53. Saito, G., Swanson, J.A., Lee, K.D.: Drug delivery strategy utilizing conjugation via reversible disulfide linkages: role and site of cellular reducing activities. Adv. Drug Deliv. Rev. **55**, 199–215 (2003)
54. Hong, R., Han, G., Fernandez, J.M., Kim, B.J., Forbes, N.S., Rotello, V.M.: Glutathione-mediated delivery and release using monolayer protected nanoparticle carriers. J. Am. Chem. Soc. **128**, 1078–1079 (2006)
55. Check, E.: Gene therapy: a tragic setback. Nature **420**, 116–118 (2002)
56. Thomas, M., Klibanov, A.M.: Conjugation to gold nanoparticles enhances polyethylenimine's transfer of plasmid DNA into mammalian cells. Proc. Natl. Acad. Sci. U.S.A. **100**, 9138–9143 (2003)
57. Thomas, M., Klibanov, A.M.: Non-viral gene therapy: polycation-mediated DNA delivery. Appl. Microbiol. Biotechnol. **62**, 27–34 (2003)
58. Sandhu, K.K., McIntosh, C.M., Simard, J.M., Smith, S.W., Rotello, V.M.: Gold nanoparticle-mediated transfection of mammalian cells. Bioconjug. Chem **13**, 3–6 (2002)
59. Han, G., You, C.C., Kim, B.J., Turingan, R.S., Forbes, N.S., Martin, C.T., Rotello, V.M.: Light-regulated release of DNA and its delivery to nuclei by means of photolabile gold nanoparticles. Angew. Chem. Int. Ed. **45**, 3165–3169 (2006)
60. Rosi, N.L., Giljohann, D.A., Thaxton, C.S., Lytton-Jean, A.K.R., Han, M.S., Mirkin, C.A.: Oligonucleotide-modified gold nanoparticles for intracellular gene regulation, Science **312**, 1027–1030 (2006)
61. Giljohann, D.A., Seferos, D.S., Patel, P.C., Millstone, J.E., Rosi, N.L., Mirkin, C.A.: Oligonucleotide loading determines cellular uptake of DNA-modified gold nanoparticles. Nano Lett. **7**, 3818–3821 (2007)
62. Bhumkar, D.R., Joshi, H.M., Sastry, M., Pokharkar, V.B.: Chitosan reduced gold nanoparticles as novel carriers for transmucosal delivery of insulin. Pharm. Res. **24**, 1415–1426 (2007)
63. Brannon-Peppas, L., Blanchette, J.O.: Nanoparticle and targeted systems for cancer therapy. Adv. Drug Deliv. Rev. **56**, 1649–1659 (2004)
64. Brigger, I., Dubernet, C., Couvreur, P.: Nanoparticles in cancer therapy and diagnosis. Adv. Drug Deliv. Rev. **54**, 631–651 (2002)
65. Ghosh, P., Han, G., De, M., Kim, C.K., Rotello, V.M.: Gold nanoparticles in delivery applications. Adv. Drug Deliv. Rev. **60**, 1307–1315 (2008)
66. Chithrani, B.D., Ghazani, A.A., Chan, W.C.W.: Determining the size and shape dependence of gold nanoparticle uptake into mammalian cells. Nano Lett. **6**, 662–668 (2006)

67. Chithrani, B.D., Chan, W.C.W.: Elucidating the mechanism of cellular uptake and removal of protein-coated gold nanoparticles of different sizes and shapes. Nano Lett. **7**, 1542–1550 (2007)
68. Mohanty, S.P., Kougianos, E.: Biosensors: a tutorial review. IEEE Potentials **25**, 35–40 (2006)
69. Raschke, G., Kowarik, S., Franzl, T., Sonnichsen, C., Klar, T.A., Feldmann, J., Nichtl, A., Kurzinger, K.: Biomolecular recognition based on single gold nanoparticle light scattering. Nano Lett. **3**, 935–938 (2003)
70. Jain, P.K., Eustis, S., El-Sayed, M.A.: Plasmon coupling in nanorod assemblies: optical absorption, discrete dipole approximation simulation, and exciton–coupling model. J. Phys. Chem. B **110**, 18243–18253 (2006)
71. Elghanian, R., Storhoff, J.J., Mucic, R.C., Letsinger, R.L., Mirkin, C.A.: Selective colorimetric detection of polynucleotides based on the distance-dependent optical properties of gold nanoparticles. Science **277**, 1078–1081 (1997)
72. Nam, J.M., Stoeva, S.I., Mirkin, C.A.: Bio-bar-code-based DNA detection with PCR-like sensitivity. J. Am. Chem. Soc. **126**, 5932–5933 (2004)
73. Wang, Z., Lévy, R., Fernig, D.G., Brust, M.: Kinase-catalyzed modification of gold nanoparticles: a new approach to colorimetric kinase activity screening. J. Am. Chem. Soc. **128**, 2214–2215 (2006)
74. Wang, Z., Lee, J., Cossins, A.R., Brust, M.: Microarray-based detection of protein binding and functionality by gold nanoparticle probes. Anal. Chem. **77**, 5770–5774 (2005)
75. Liu, J., Lu, Y.: Colorimetric Cu^{2+} detection with a ligation DNAzyme and nanoparticles. Chem. Commun. 4872–4874 (2007)
76. Zhao, W., Chiuman, W., Lam, J.C.F., McManus, S.A., Chen, W., Cui, Y., Pelton, R., Brook, M.A., Li, Y.: DNA aptamer folding on gold nanoparticles: from colloid chemistry to biosensors. J. Am. Chem. Soc. **130**, 3610–3618 (2008)
77. Campion, A., Kambhampati, P.: Surface-enhanced Raman scattering. Chem. Soc. Rev. **27**, 241–250 (1998)
78. Kneipp, K., Kneipp, H., Kneipp, J.: Surface-enhanced Raman scattering in local optical fields of silver and gold nanoaggregates—from single-molecule Raman spectroscopy to ultrasensitive probing in live cells. Acc. Chem. Res. **39**, 443–450 (2006)
79. Nie, S., Emory, S.R.: Probing single molecules and single nanoparticles by surface-enhanced Raman scattering. Science **275**, 1102–1106 (1997)
80. Krug, J.T., Wang, G.D., Emory, S.R., Nie, S.: Efficient Raman enhancement and intermittent light emission observed in single gold nanocrystals. J. Am. Chem. Soc. **121**, 9208–9214 (1999)
81. Cao, Y.C., Jin, R., Mirkin, C.A.: Nanoparticles with Raman spectroscopic fingerprints for DNA and RNA detection. Science **297**, 1536–1540 (2002)
82. Kneipp, J., Kneipp, H., Kneipp, K.: Two-photon vibrational spectroscopy for biosciences based on surface-enhanced hyper-Raman scattering. Proc. Natl. Acad. Sci. U.S.A. **103**, 17149–17153 (2006)
83. Dulkeith, E., Morteani, A.C., Niedereichholz, T., Klar, T.A., Feldmann, J., Levi, S.A., van Veggel, F.C.J.M., Reinhoudt, D.N., Möller, M., Gittins, D.I.: Fluorescence quenching of dye molecules near gold nanoparticles: radiative and nonradiative effects. Phys. Rev. Lett. **89**, 203002-1–203002-4 (2002)
84. McGhee, J.D., von Hippel, P.H.: Theoretical aspects of DNA-protein interactions: co-operative and non-co-operative binding of large ligands to a one-dimensional homogeneous lattice. J. Mol. Biol. **86**, 469–489 [*Erratum* (1976) J. Mol. Biol. **103**, 679] (1974)
85. Oh, E., Hong, M.-H., Lee, D., Nam, S.-H., Yoon, H.C., Kim, H.-S.: Inhibition assay of biomolecules based on fluorescence resonance energy transfer (FRET) between quantum dots and gold nanoparticles. J. Am. Chem. Soc. **127**, 3270–3271 (2005)
86. Dulkeith, E., Ringler, M., Klar, T.A., Feldmann, J., Javier, A.M., Parak, W.J.: Gold nanoparticles quench fluorescence by phase induced radiative rate suppression. Nano Lett. **5**, 585–589 (2005)

87. Wang, Z., Lévy, R., Fernig, D.G., Brust, M.: The Peptide route to multifunctional gold nanoparticles. Bioconjug. Chem **16**, 497–500 (2005)
88. Wang, J.: Nanoparticle-based electrochemical bioassays of proteins. Electroanalysis **19**, 769–776 (2007)
89. Park, S.-J., Taton, T.A., Mirkin, C.A.: Array-based electrical detection of DNA with nanoparticle probes. Science **282**, 1503–1506 (2002)
90. Xiao, Y., Patolsky, F., Katz, E., Hainfeld, J.F., Willner, I.: "Plugging into enzymes": nanowiring of redox enzymes by a gold nanoparticle. Science **299**, 1877–1881 (2003)
91. Yu, A., Liang, Z., Cho, J., Caruso, F.: Nanostructured electrochemical sensor based on dense gold nanoparticle films. Nano Lett. **3**, 1203–1207 (2003)
92. Holzinger, M., Bouffier, L., Villalonga, R., Cosnier, S.: Adamantane/β-cyclodextrin affinity biosensors based on single-walled carbon nanotubes. Biosens. Bioelectron. **24**, 1128–1134 (2009)
93. Sun, S., Murray, C.B., Weller, D., Folks, L., Moser, A.: Monodisperse FePt nanoparticles and ferromagnetic FePt nanocrystal superlattices. Science **287**, 1989–1992 (2000)
94. Yi, D.K., Lee, S.S., Ying, J.Y.: Synthesis and applications of magnetic nanocomposite catalysts. Chem. Mater. **18**, 2459–2461 (2006)
95. Miller, M.M., Prinz, G.A. Cheng, S.F., Bounnak, S.: Detection of a micron-sized magnetic sphere using a ring-shaped anisotropic magnetoresistance-based sensor: a model for a magnetoresistance-based biosensor. Appl. Phys. Lett. **81**, 2211–2213 (2002)
96. Jain, T.K., Morales, M.A., Sahoo, S.K., Leslie-Pelecky, D.L., Labhasetwar, V.: Iron oxide nanoparticles for sustained delivery of anticancer agents. Mol. Pharm. **2**, 194–205 (2005)
97. Chourpa, I., Douziech, E.L., Ngaboni-Okassa, L., Fouquenet, J.F., Cohen, J.S., Souce, M., Marchais, H., Dubois, P.: Molecular composition of iron oxide nanoparticles, precursors for magnetic drug targeting, as characterized by confocal Raman microspectroscopy. Analyst **130**, 1395–1403 (2005)
98. Weissleder, R., Bogdanov, A., Neuwelt, E.A., Papisov, M.: Long-circulating iron oxides for MR imaging. Adv. Drug Deliv. Rev. **16**, 321–334 (1995)
99. Stella, B., Arpicco, S., Peracchia, M.T., Desmaele, D., Hoebeke, J., Renoir, M., D'Angelo, J., Cattel, L., Couvreur, P.: Design of folic acid conjugated nanoparticles for drug targeting. J. Pharm. Sci. **89**, 1452–1464 (2000)
100. Sun, Y.K., Ma, M., Zhang, Y., Gu, N.: Synthesis of nanometer-size maghemite particles from magnetite. Colloids Surf. A **245**, 15–19 (2004)
101. Lee, S.J., Jeong, J.R., Shin, S.C., Kim, J.C., Kim, J.D.: Synthesis and characterization of superparamagnetic maghemite nanoparticles prepared by coprecipitation technique. J. Magn. Magn. Mat. **282**, 147–150 (2004)
102. Park, J., Lee, E., Hwang, N.M., Kang, M., Kim, S.K., Hwang, S., Park, J.-G., Noh, H.-J., Kim, J.-Y., Park, J.-H., Hyeon, T.: One-nanometer scale size-controlled synthesis of monodisperse magetic iron oxide nanoparticles. Angew. Chem. Int. Ed. **44**, 2872–2877 (2005)
103. Sun, S., Zeng, H., Robinson, D.B., Raoux, S., Rice, P.M., Wang, S.X., Li, G.: Monodisperse MFe_2O_4 (M = Fe, Co, Mn) nanoparticles. J. Am. Chem. Soc. **126**, 173–279 (2004)
104. Cai, W., Wan, J.: Facile synthesis of superparamagnetic magnetite nanoparticles in liquid polyols. J. Coll. Inter. Sci. **305**, 366–370 (2007)
105. Charles, S.W., Popplewell, J.: Properties and applications of magnetic liquids. Endeavour **6**, 153–61 (1982)
106. Jolivet, J.P., Chaneac, C., Tronc, E.: Iron oxide chemistry. From molecular clusters to extended solid networks. Chem. Commun. **5**, 481–487 (2004)
107. LaMer, V.K., Dinegar, R.H.: Theory, production and mechanism of formation of monodispersed hydrosols. J. Am. Chem. Soc. **72**, 4847–4854 (1950)
108. Tartaj, P., Morales, M.P., Veintemillas-Verdaguer, S., Gonzales-Carreno, T., Serna, C.J.: The preparation of magnetic nanoparticles for applications in biomedicine. J. Phys. D **36**, R182–R197 (3003)

109. Babes, L., Denizot, B., Tanguy, G., Le Jeune, J.J., Jallet, P.: Synthesis of iron oxide nanoparticles used as mri contrast agents: a parametric study. J. Colloid Interface Sci. **212**, 474–482 (1999)
110. Massart, R., Cabuil, V.: Monodisperse magentic nanoparticles: preparation and dispersion in water and oils. J. Chim. Phys. **84**, 2975–2981 (1987)
111. Bee, A., Massart, R., Neveu, S.: Synthesis of very fine maghemite particles. J. Magn. Magn. Mater. **149**, 6–9 (1995)
112. Fauconnier, N., Pons, J.N., Roger, J., Bee, A.: Thiolation of maghemite nanoparticles by dimercaptosuccinic acid. J. Colloid Interface Sci. **194**, 427–433 (1997)
113. Liu, X., Xing, J., Guan, Y., Shan, G., Liu, H.: Synthesis of amino-silane modified superparamagnetic silica supports and their use for protein immobilization. Colloids Surf. A **238**, 127–131 (2004)
114. Heath, J.R.: The chemistry of size and order on a nanometer scale. Science **270**, 1315–1316 (1995)
115. Neru, M., Tapas, K.D., Amarnath, M.: Size modulation of polymeric nanoparticles under controlled dynamics of microemulsion droplets. J. Colloid Interface Sci. **109**, 387–391 (1997)
116. Lin, M.M., Kim, D.K., Haj, A.J., Dobson, J.: Development of superparamagnetic iron oxide nanoparticles for translation to clinical applications. IEEE Nanobiosci. **7**, 298–305 (2008)
117. Lee, Y., Lee, J., Bae, C.J., Park, J.-G., Noh, H.-J., Park, J.-H., Hyeon, T.: Large-scale synthesis of uniform and crystalline magnetite nanoparticles using reverse micelles as nanoreactors under reflux conditions. Adv. Funct. Mater. **15**, 503–509 (2005)
118. Carpenter, E.E.: Iron nanoparticles as potential magnetic carriers. J. Magn. Magn. Mater. **225**, 17–20 (2001)
119. Vidal-Vidal, J., Rivas, J., Lopez-Quintela, M.A.: Synthesis of monodisperse maghemite nanoparticles by the microemulsion method. Colloid Surf. A **288**, 44–51 (2006)
120. Kandori, K., Fukuoka, M., Ishikawa, T.: Effects of citrate ions on the formation of ferric oxide hydroxide particles. J. Mater. Sci. **26**, 3313–3319 (1991)
121. Dimitrova, G.T., Tadros, T.F., Luckham, P.F., Kipps, M.R.: Investigations into the phase behavior of nonionic ethoxylated surfactants using 2H NMR spectroscopy. Langmuir **12**, 315–318 (1996)
122. Hyeon, T., Lee, S.S.: Synthesis of highly crystalline and monodisperse maghemite nanocrystallites without a size-selection process. J. Am. Chem. Soc. **123**, 12798–12801 (2001)
123. Jun, Y.W., Huh, Y.M., Choi, J.: Nanoscale size effect of magnetic nanocrystals and their utilization for cancer diagnosis via magnetic resonance imaging. J. Am. Chem. Soc. **127**, 5732–5733 (2005)
124. Li, Z., Chen, H., Bao, H., Gao, M.: One-pot reaction to synthesize water-soluble magnetite nanocrystals. Chem. Mater. **16**, 1391–1393 (2004)
125. Viau, G., Fievet-Vincent, F., Fievet, F.: Monodisperse iron-based particles: precipitation in liquid polyols. J. Mater. Chem. **6**, 1047–1053 (1996)
126. Toneguzzo, P., Viau, G., Acher, O., Fievet-Vincent, F., Fievet, F.: Monodisperse ferromagnetic particles for microwave applications. Adv. Mater. **10**, 1032–1035 (1998)
127. Lu, A.H., Salabas, E.L., Schuth, F.: Magnetic nanoparticles: synthesis, protection, functionalization and application. Angew. Chem. Int. Ed. **46**, 1222–1244 (2007)
128. Xu, C., Sun, S.: Monodisperse magnetic nanoparticles for biomedical applications. Polym. Int. **56**, 821–826 (2007)
129. Fritz, G., Schaedler, V., Willenbacher, N., Wagner, N.J.: Electrosteric stabilization of colloidal dispersions. Langmuir **18**, 6381–6390 (2002)
130. Holthoff, H., Egelhaaf, S.U., Borkovec, M., Schurtenberger, P., Sticher, H.: Coagulation rate measurements of colloidal particles by simultaneous static and dynamic light scattering. Langmuir **12**, 5541–5549 (1996)
131. Lattuada, M., Sandkuhler, P., Wu, H., Sefcik, J., Morbidelli, M.: Aggregation kinetics of polymer colloids in reaction limited regime: experiments and simulations. Adv. Colloid Interface Sci. **103**, 33–56 (2003)

132. Sahoo, Y., Pizem, H., Fried, T., Golodnitsky, D., Burstein, L., Sukenik, C.N., Markovich, G.: Alkyl phosphonate/phosphate coating on magnetite nanoparticles: a comparison with fatty acids. Langmuir **17**, 7907–7911 (2001)
133. Sahoo, Y., Goodarzi, A., Swihart, M.T., Ohulchanskyy, T.Y., Kaur, N., Furlani, E.P., Prasad, P.N.: Aqueous ferrofluid of magnetite nanoparticles: fluorescence labeling and magnetophoretic control. J. Phys. Chem. B **109**, 3879–3885 (2005)
134. Taupitz, M., Wagner, S., Schnorr, J., Kravec, I., Pilgrimm, H., Bergmann-Fritsch, H., Hamm, B.: Phase I clinical evaluation of citrate-coated monocrystalline very small superparamagnetic iron oxide particles as a new contrast medium for magnetic resonance imaging.Invest. Radiol. **39**, 394–405 (2004)
135. Yee, C., Kataby, G., Ulman, A., Prozorov, T., White, H., King, A., Rafailovich, M., Sokolov, J., Gedanken, A.: Self-assembled monolayers of alkanesulfonic and -phosphonic acids on amorphous iron oxide nanoparticles. Langmuir **15**, 7111–7115 (1999)
136. Ma, D., Guan, J., Normandin, F., Denommee, S., Enright, G., Veres, T., Simard, B.: Multifunctional nano-architecture for biomedical applications. Chem. Mater. **18**, 1920–1927 (2006)
137. Bulte, J.W.M., Modo, M.M.J.: Nanoparticles in Biomedical Imaging-Emerging Technologies and Applications. Springer, New York (2008)
138. Lu, Y., Yin, Y., Mayers, B.T.: Modifying the surface properties of superparamagnetic iron oxide nanoparticles through a sol-gel approach. Nano Lett. **2**, 183–186 (2001)
139. Kohler, N., Fryxell, G.E., Zhang, M.: A bifunctional poly(ethylene glycol) silane immobilized on metallic oxide-based nanoparticles for conjugation with cell targeting agents. J. Am. Chem. Soc. **126**, 7206–7211 (2004)
140. Hirsch, R., Katz, E., Willner, I.: Magneto-switchable. J. Am. Chem. Soc. **122**, 12053–12054 (2000)
141. Kim, J., Park, S. et al.: Designed fabrication of multifunctional magnetic gold nanoshells and their application to magnetic resonance imaging and photothermal therapy. Angew. Chem. Int. Ed. **45**, 7754–7758 (2006)
142. Pardoe, H., Chua-anusorn, W., St. Pierre, T.G., Dobson, J.: Structural and magnetic properties of nanoscale iron oxide particles synthesized in the presence of dextran or polyvinyl alcohol. J. Magn. Magn. Mater. **225**, 41–46 (2001)
143. Fournier, C., Leonard, M., Le Coq, L.I., Dellacherie, E.: Coating polystyrene particles by adsorption of hydrophobically modified dextran. Langmuir **11**, 2344–2347 (1995)
144. Mornet, S., Portier, J., Duguet, E.: A method for synthesis and functionalization of ultrasmall superparamagnetic covalent carriers based on maghemite and dextran. J. Magn. Magn. Mater. **293**, 127–134 (2005)
145. Lin, H., Watanabe, M., Kimura, M., Hanabusa, K., Shirai, H.: Preparation of magnetic poly(vinyl alcohol) (PVA) materials by in situ synthesis of magnetite in a PVA matrix. J. Appl. Polym. Sci. **87**, 1239–1247 (2003)
146. Majewski, P., Thierry, B.: Functionalized magnetite nanoparticles—synthesis, properties and bio-applications. Crit. Rev. Solid State Mater. Sci. **32**, 203–215 (2007)
147. LaConte, L.E., Nitin, N., Zurkiya, O., Caruntu, D., O'Connor, C.J., Hu, X., Bao, G.: Coating thickness of magnetic iron oxide nanoparticles affects R2 relaxivity. Magn. Reson. Imaging **27**, 1634–1641 (2007)
148. Albornoz, C., Jacobo, S.E.: Preparation of a biocompatible magnetic film from an aqueous ferrofluids. J. Magn. Magn. Mater. **305**, 12–15 (2006)
149. Kim, D.K., Mikhaylova, M., Wang, F.H., Kehr, J., Bjelke, B., Zhang, Y., Tsakalakos, T., Muhammed, M.: Starch-coated superparamagnetic nanoparticles as MRI contrast agents. Chem. Mater. **15**, 4343–4351 (2003)
150. Gomez-Lopera, S.A., Arias, J.L., Gallardo, V., Delgado, A.V.: Colloidal stability of magnetite/poly(lactic acid) core/shell nanoparticles. Langmuir **22**, 2816–2821 (2006)
151. Flesch, C., Bourgeat-Lami, E., Mornet, S., Duquet, E., Delaite, C., Dumas, P.: Synthesis of colloidal superparamagnetic nanocomposites by grafting poly(epsilon-caprolactone) from the surface of organosilane-modified maghemite nanoparticles. J. Polym. Sci. A **43**, 3221–3231 (2005)

152. Hyon, B.N., In, C.S., Taeghwan, H.: Inorganic nanoparticles for MRI contrast agents. Adv. Mater. **21**, 2133–2148 (2009)
153. Suzuki, M., Honda, H., Kobayashi, T., Wakabayashi, T., Yoshida, J., Takahashi, M.: Development of a target directed magnetic resonance contrast agent using monoclonal antibody-conjugated magnetic nanoparticles. Brain Tumor Pathol. **13**, 127–132 (1996)
154. Yang, L., Mao, H., Wang, Y.A., Cao, Z., Peng, X., Wang, X., Duan, H., Ni, C., Yuan, Q., Adams, G., Smith, M.Q., Wood, W.C., Gao, X., Nie, S.: Single chain epidermal growth factor receptor antibody conjugatednanoparticles for in vivo tumor targeting and imaging. Small **2,** 235–243 (2009)
155. Sun, C., Fang, C., Stephen, Z., Veiseh, O., Hansen, S., Lee, D., Ellenbogen, R.G., Olson, J., Zhang, M.: Tumor-targeted drug delivery and MRI contrast enhancement by chlorotoxin-conjugated iron oxide nanoparticles. Nanomedicine **3**, 495–505 (2008)
156. Fortin, J.P., Gaxeau, G., Wilhelm, C.: Intracellular heating of living cells through Neel relaxation of magnetic nanoparticles. Eur. Biophys. J. **37**, 223–228 (2008)
157. Salloum, M., Ma, R.H., Weeks, D., Zhu, L.: Controlling nanoparticle delivery in magnetic nanoparticle hyperthermia for cancer treatment: experimental study in agarose gel. Int. J. Hyperthermia **24**, 337–345 (2008)
158. Berry, C.C.: Progress in functionalisation of magnetic nanoparticles for applications in biomedicine. J. Phys. D **42**, 224003 (2009)
159. Lubbe, A.S., Alexiou, C., Bergemann, C.: Clinical applications of magnetic drug targeting. J. Surg. Res. **95**, 200–206 (2000)
160. Rosengart, A.J., Kaminski, M.D., Chen, H., Caviness, P.L., Ebner, A.D., Ritter, J.A.: Magnetizable implants and functionalised magnetic carriers: a novel approach for noninvasive yet targeted drug delivery. J. Magn. Magn. Mater. **293**, 633–638 (2005)
161. Muzzarelli, R.A.A., Muzzarelli, C.: Chitosan chemistry: relevance to the biomedical sciences. Adv. Ploym. Sci. **186**, 151–209 (2005)
162. Frank, J.A., Miller, B.R., Arbab, A.S., Zywicke, H.A., Jordan, E.K., Lewis, B.K., Bryant, L.H., Bulte, J.W.M.: Clinically applicable labeling of mammalian and stem cells by combining superparamagnetic iron oxides and trasfection agents. Radiology **228**, 480–487 (2003)
163. Franzreb, M., Hobley, T.J., Siemann-Herzberg, M., Thomas, O.R.T.: Protein purification using magnetic adsorbent particles. Appl. Microbiol. Biotechnol. **70**, 505–516 (2006)
164. Berensmeier, S.: Magnetic particles for the separation and purification of nucleic acids. Appl. Microbiol. Biotechnol. **73**, 495–504 (2006)
165. Gu, H., Ho, P.L., Tsang, K.W.T., Wang, L., Xu, B.: Using biofunctional magnetic nanoparticles to capture vancomycin-resistant enterococci and other gram-positive bacteria at ultralow concentration. J. Am. Chem. Soc. **125**, 15702–15703 (2003)
166. Murray, C.B., Norris, D.J., Bawendi, M.G.: Synthesis and characterization of nearly monodisperse CdE (E = S, Se. Te) semiconductor nanocrystallites. J. Am. Chem. Soc. **115**, 8706–8715 (1993)
167. Colvin, V.L., Schlamp, M.C., Alivisatos, A.P.: Light-emitting-diodes made from cadmium selenide nanocrystals and a semiconducting polymer. Nature **370**, 354–357 (1994)
168. Medintz, I.L., Clapp, A.R., Mattoussi, H., Goldman, E.R., Fisher, B., Mauro, J.M.: Self-assembled nanoscale biosensors based on quantum dot FRET donors. Nat. Mater. **2**, 630–638 (2003)
169. Kirchner, C., Liedl, T., Kudera, S., Pellegrino, T., Javier, A.M., Gaub, H.E., Stolzle, S., Fertig, N., Parak, W.J.: Cytotoxicity of colloidal CdSe and CdSe/ZnS nanoparticles. Nano Lett. **5**, 331–338 (2005)
170. Ludolph, B., Malik, M.A., O'Brien, P., Revaprasadu, N.: Novel single molecule precursor routes for the direct synthesis of highly monodispersed quantum dots of cadmium or zinc sulfide or selenide. Chem. Commun. **17**, 1849–1850 (1998)
171. Hines, M.A., Guyot-Sionnest, P.: Bright UV-blue luminescent colloidal ZnSe nanocrystals. J. Phys. Chem. B **102**, 3655–3657 (1998)
172. Susumu, K., Uyeda, H.T., Medintz, I.L., Pons, T., Delehanty, J.B., Mattoussi, H.: Enhancing the stability and biological functionalities of quantum dots via compact multifunctional ligands. J. Am. Chem. Soc. **129**, 13987–13996 (2007)

173. Dabbousi, B.O., Rodriguez Viejo, J., Mikulec, F.V., Heine, J.R., Mattoussi, H., Ober, R., Jensen, K.F., Bawendi, M.G.: (CdSe)ZnS core-shell quantum dots: synthesis and optical and structural characterization of a size series of highly luminescent materials. J. Phys. Chem. B **101**, 9463–9475 (1997)
174. Pradhan, N., Katz, B., Efrima, S.: Synthesis of high-quality metal sulfide nanoparticles from alkyl xanthate single precursors in alkylamine solvents. J. Phys. Chem. B **107**, 13843–13854 (2003)
175. Reiss, P., Protière, M., Li, L.: Core/shell semiconductor nanocrystals. Small **5**, 154–168 (2009)
176. Chan, W.C.W., Nie, S.M.: Quantum dot bioconjugates for ultrasensitive nonisotopic detection. Science **281**, 2016–2018 (1998)
177. Medintz, I.L., Uyeda, H.T., Goldman, E.R., Mattoussi, H.: Quantum dot bioconjugates for imaging, labelling and sensing. Nat. Mater **4**, 435–446 (2005)
178. Mitchell, G.P., Mirkin, C.A., Letsinger, R.L.: Programmed assembly of DNA functionalized quantum dots. J. Am. Chem. Soc. **121**, 8122–8123 (1999)
179. Pinaud, F., King, D., Moore, H.P., Weiss, S.: Bioactivation and cell targeting of semiconductor CdSe/ZnS nanocrystals with phytochelatin-related peptides. J. Am. Chem. Soc. **126**, 6115–6123 (2004)
180. Kim, S., Bawendi, M.G.: Oligomeric ligands for luminescent and stable nanocrystal quantum dots. J. Am. Chem. Soc. **125**, 14652–14653 (2003)
181. Hainfeld, J.F., Liu, W., Halsey, C.M.R., Freimuth, P., Powell, R.D.: Ni- NTA gold clusters target His-tagged proteins. J. Stuct. Biol. **127**, 185–198 (1999)
182. Dubertret, B., Skourides, P., Norris, D.J., Noireaux, V., Brivanlou, A.H., Libchaber, A.: In vivo imaging of quantum dots encapsulated in phospholipids micelles. Science **298**, 1759–1762 (2002)
183. Ballou, B., Lagerholm, B.C., Ernst, L.A., Bruchez, M.P., Waggoner, A.S.: Noninvasive imaging of quantum dots in mice. Bioconj. Chem. **15**, 79–86 (2004)
184. Gao, X., Cui, Y., Levenson, R.M., Chung, L.W.K., Nie, S.: In vivo cancer targeting and imaging with semiconductor quantum dots. Nat. Biotechnol. **22**, 969–976 (2004)
185. Osaki, F., Kanamori, T., Sando, S., Sera, T., Aoyama, Y.: A quantum dot conjugated sugar ball and its cellular uptake on the size effects of endocytosis in the subviral region. J. Am. Chem. Soc. **126**, 6520–6521 (2004)
186. Kricka, L.J.: Source. Ann. Clin. Biochem. **39**, 114–129 (2002)
187. Goldman, E.R., Clapp, A.R., Anderson, G.P., Uyeda, H.T., Mauro, J.M., Medintz, I.L., Mattoussi, H.: Multiplexed toxin analysis using four colors of quantum dot fluororeagents. Anal. Chem.**76**, 684–688 (2004)
188. Jaiswal, J.K., Mattoussi, H., Mauro, J.M., Simon, S.M.: Long-term multiple color imaging of live cells using quantum dot bioconjugates. Nat. Biotechnol. **21**, 47–51 (2003)
189. Wu, X.Y., Liu, H.J., Liu, J.Q., Haley, K.N., Treadway, J.A., Larson, J.P., Ge, N.F., Peale, F., Bruchez, M.P.: Immunofluorescent labeling of cancer marker Her2 and other cellular targets with semiconductor quantum dots. Nat. Biotechnol. **21**, 41–46 (2003)
190. Kim, S., Lim, Y.T., Soltesz, E.G., De Grand, A.M., Lee, J., Nakayama, A., Parker, J.A., Mihaljevic, T., Laurence, R.G., Dor, D.M., Cohn, L.H., Bawendi, M.G., Frangioni, J.V.: Near-infrared fluorescent type II quantum dots for sentinel lymph node mapping. Nat. Biotechnol. **22**, 93–97 (2004)
191. Shi, C.M., Zhu, Y., Xie, Z.H., Qian, W.P., Hsieh, C.L., Nie, S.M., Su, Y.P., Zhau, H.E., Chung, L.W.K.: Visualizing human prostate cancer cells in mouse skeleton using bioconjugated near-infrared fluorescent quantum dots. Urology **74**, 446–451 (2009)
192. Derfus, A.M., Chan, W.C.W., Bhatia, S.N.: Probing the cytotoxicity of semiconductor quantum dots. Nano Lett. **4**, 11–18 (2004)
193. Mikhaylova, M., Kim, D.K., Bobrysheva, N., Osmolowsky, M., Semenov, V., Tsakalakos, T., Muhammed, M.: Superparamagnetism of magnetite nanoparticles: dependence on surface modification. Langmuir **20**, 2472–2477 (2004)
194. Garza-Navarro, M., Torres-Castro, A., Gonzalez, V., Ortiz, U., De la Rosa, E.: Magnetite and magnetite/silver core/shell nanoparticles with diluted magnet-like behavior. J. Solid State Chem. **183**, 99–104 (2010)

195. Pal, B., Torimoto, T., Iwasaki, K., Shibayama, T., Takahashi, H., Ohtani, B.: Synthesis of metal-cadmium sulfide nanocomposites using jingle-bell-shaped core-shell photocatalyst particles. J. Appl. Electrochem. **35**, 751–756 (2005)
196. Salgueirino-Maceira, V., Correa-Duarte, M.A., Lopez-Quintela, M.A., Rivas, J.: Advanced hybrid nanoparticles. J. Nanosci. Nanotechnol. **9**, 3684–3688 (2009)
197. Kohler, N., Sun, C., Wang, J., Zhang, M.Q.: Methotrexate-modified superparamagnetic nanoparticles and their intracellular uptake into human cancer cells. Langmuir **21**, 8858–8864 (2005)
198. Yiu, H.H.P., Niu, H.J., Biermans, E., van Tendeloo, G., Rosseinsky, M.J.: Designed multifunctional nanocomposites for biomedical applications. Adv. Funct. Mater. **20**, 1599–1609 (2010)

Transport Processes of Nanoparticles in Gases and Liquids

V. Ya. Rudyak and A. A. Belkin

Abstract This review is devoted to the transport processes in nanofluids. The mechanisms of transport processes in nanofluids are discussed. The kinetic theory of transport processes in gas nano-suspensions is described. The base of this theory is the special potential of interaction of nanoparticle with carrier medium molecule. The results of the kinetic theory are compared with the experimental data. Transport processes of nanoparticles in dense gases and liquids are simulated by the molecular dynamics method. It is shown that in general case the transport processes of nanoparticles in fluids are not described by the classical relations for Brownian particles. In particular the transport coefficients depend on density of nanoparticles.

1 Introduction

Nanofluids are two-phase systems consisting of a carrier medium (gas or liquid) and nanoparticles. Nanoparticles are the particles whose typical size is from 1 to 100 nm, they can generally be solid, liquid, or gaseous. Typical carriers are water and organic liquids (ethylene–glycol, oil and other lubricants, bio-fluids), polymer solutions, etc. Typical solid nanoparticles are usually particles of chemically resistant metals or metal oxides. The smallest nanoparticle is likely to be a fullerene with a diameter of about 1 nm; viruses, whose typical sizes are several tens of nanometers, are in the

V. Ya. Rudyak (✉) · A. A. Belkin
Department of Theoretical Mechanics, Novosibirsk State University of Architecture and Civil Engineering, Novosibirsk, Russia
e-mail: valery.rudyak@mail.ru

A. A. Belkin
e-mail: a_belkin@ngs.ru

Adv Struct Mater (2013) 4: 135–168
DOI: 10.1007/8611_2010_31

Published Online: 23 July 2010

middle of the range. Nanofluids based on nanotubes are also of great interest. A special feature of the latter is that their diameter varies from one to several nanometers while their length can reach tens, hundreds, and even thousands of microns, so that their length can be quite macroscopic. Such fluids are different from conventional nanofluids and are, at least structurally, similar to polymer fluids.

Three criteria should be used to classify nanofluids (see [44]). First, according to the state of aggregation, nanofluids can be divided into gas nanosuspensions (gas + solid nanoparticles), nanosols (gas + liquid nanoparticles), nanosuspensions (liquid + solid nanoparticles), nanoemulsions (liquid + liquid nanoparticles), and liquids with nanobubbles. Second, these media should be differentiated according to the volume fraction of nanoparticles ϕ. Here it is possible to distinguish rarefied nanofluids in which $\phi \leq 10^{-3}$, moderately rarefied nanofluids with $10^{-3} \leq \phi \leq 10^{-1}$, and dense ones, $10^{-1} < \phi \leq 4 \times 10^{-1}$. In the case of even higher nanoparticle volume fraction, we deal with nanopowders. Finally, nanofluids should also be classified according to the ratios of the internal structural elements: sizes of nanoparticles and carrier molecules, mean free paths of nanoparticles and carrier molecules, etc. This is especially important for gas nanosuspensions, in which the carrier fluid density can vary widely. As a result, the mean free path of a carrier gas l can be larger or smaller than the nanoparticle radius R.

The term "nanofluids" is fairly new although colloid chemistry has been studying colloid solutions for several recent decades and nanofluids are, of course, colloid solution. Colloid chemistry, however, has focused primarily on various surface phenomena. Moreover, nanofluids per se, i.e. fluids with nanoparticles as the dispersed phase, have not been studied. Research on the physics of nanofluids and especially their transport properties has started recently and has been motivated by their various applications. The small size of nanoparticles is responsible for their special properties, which differ greatly from those of macroparticles. Nanofluids are also characterized by special transport properties; unlike coarse dispersed particles, they do not undergo sedimentation or cause erosion in channels in which they move. For these and some other reasons, nanoparticles have been successfully used:

- in various chemical processes, including catalysis;
- for cooling various devices;
- in designing new systems for transportation and heat generation;
- in biomechanical and microelectromechanical systems and nanotechnologies for various applications;
- for developing new drugs and cosmetics;
- for delivery of drugs, nanosensors, and nanoactivators;
- in designing systems for identifying contamination of various natures, including biological and viral ones;
- in designing systems for air and water cleaning;
- in developing new lubricants;
- in designing new lacquers and paints.

This list can be continued, but in all cases the transport processes in nanofluids and the nature of their flows play a key role. In addition to their practical value, the

transport properties of nanofluids are of great theoretical interest as even a qualitative understanding of these processes is not available, let alone a consistent physical theory.

The purpose of the present paper is to review the results accumulated in this area over recent decades. We will consider nanoparticle diffusion in gases and liquids and the effective viscosity and thermal conductivity of nanofluids, with particular emphasis placed on the mechanisms of transport processes in nanofluids.

2 Interaction Potential between a Nanoparticle and a Molecule

For a long time it has been assumed that nanoparticle transport processes can be described in the same way as similar process for Brownian particles or even molecules. This point of view is maintained even today. Until recently, many researchers believed that the Einstein–Stokes diffusion model with the drag force acting on a particle treated as a hydrodynamic force is suitable for describing diffusion up to molecular diffusion. Of course, the kinetic theory of gases disproves this view. Nor is it consistent with experimental data on diffusion of molecules [6, 7, 14, 22] and fullerenes [4, 25, 66] in organic solvents.

The diffusion of aerosol particles in rarefied gases is usually described by the Einstein formula with the Millikan correction, or the so-called Cunningham–Millikan–Davies (CMD) correlation. In fact, some methods of measuring the size of aerosol nanoparticles and their diffusion coefficient have this CMD correlation built in the hardware (see, for example [28]). However, this correlation was obtained by processing experimental data on the diffusion of Brownian particles with a characteristic size of 240 nm or larger.

In order to understand what relations should be used to describe transport processes in nanofluids, one should of course understand the mechanisms which determine these processes. These mechanisms, in turn, are related to nanoparticle–molecule and nanoparticle–nanoparticle interactions. When the nanoparticle volume fraction is low, which is typical of nanofluids, nanoparticle–molecule interaction plays a dominant role. This interaction has not been studied experimentally for several reasons. First, it depends on too many factors (nanoparticle size, material, shape, temperature). Secondly, nanoparticles are fairly large objects consisting of many atoms or molecules that are mobile themselves. Suffice to say that many of these can diffuse along the surface. Furthermore, this interaction is collective. A carrier-fluid molecule colliding with a nanoparticle interacts simultaneously with most of (or even all) the atoms (molecules) constituting the nanoparticle.

The simplest model describing this interaction is the hard-sphere potential

$$\Phi(r) = \begin{cases} \infty, & \text{if } r \le (D+d)/2 \\ 0, & \text{if } r > (D+d)/2 \end{cases}, \tag{1}$$

where r is the distance between the centers of the particle and the molecule and d and D are the diameters of the carrier-fluid molecule and nanoparticle, respectively. This potential is widely used to calculate transport coefficients in both rarefied gases and liquids, but it has the drawback that it does not include the temperature dependence of the transport coefficients.

In the literature, this dependence is considered by using the WCA potential [69]

$$\Phi(r) = \begin{cases} 4\varepsilon_{ij}\left[\left(\sigma_{ij}/r\right)^{12} - \left(\sigma_{ij}/r\right)^{6}\right] + \varepsilon_{ij}, & \text{if } r \le 2^{1/6}\sigma_{ij} \\ 0, & \text{if } r > 2^{1/6}\sigma_{ij} \end{cases}, \tag{2}$$

where ε_{ij}, σ_{ij} are parameters of the intermolecular Lennard-Jones potential. The WCA potential does not take into account the potential energy well and in fact specifies only repulsive forces. In addition, potential (2) assumes that a nanoparticle is simply a large molecule whose interaction with a carrier-gas molecule is described by the Lennard-Jones potential. Because, as noted above, a nanoparticle consists of a large number of molecules, the potential (1) is more realistic than potential (2).

In a paper [54] (see also Ref. [47]), a special potential was developed. A solid dispersed particle was modeled as a set of solid-state atoms (molecules) enclosed in a sphere of diameter D. The interaction potential between a carrier-gas molecule and a nanoparticle atom i is described by the pair potential $\Phi(|\mathbf{q} - \mathbf{r}_i|)$, where $\mathbf{q}$, $\mathbf{r}_i$ are the radius vectors of the molecule and atom i of the nanoparticle, respectively. Assuming the interaction potential to be additive, we can express it as

$$\Phi(r) = \sum_{i=1}^{N} \Phi(|\mathbf{q} - \mathbf{r}_i|), \tag{3}$$

where N is the number of atoms (molecules) of the particle. It is impossible to perform the summation of series (3) analytically, but it can be integrated. Physically, this means that the solid is approximated by a continuum model, which is quite realistic. Using the Lennard-Jones potential 6–12 as the interaction potential between an incident molecule and the particle atoms, we arrive at the following formula for the particle–molecule potential

$$\Phi(r) = \Phi_9(r) - \Phi_3(r),$$
$$\Phi_i(r) = C_i\left\{\left[(r-R)^{-i} - (r+R)^{-i}\right] - a_i\left[(r-R)^{-(i-1)} - (r+R)^{-(i-1)}\right]\right\}, \quad i = 9, 3, \tag{4}$$

where $C_9 = 4\pi\varepsilon_{ij}\sigma_{ij}^{12}/(45V)$, $C_3 = 2\pi\varepsilon_{ij}\sigma_{ij}^{6}/(3V)$, $a_9 = 9/8r$, $a_3 = 3/2r$, $V = v/(\rho_p N_A)$ is the effective volume per molecule of the dispersed particle; R is the nanoparticle radius, v is the molecular weight of the nanoparticle molecules, ρ_p is the nanoparticle material density, and N_A is the Avogadro number.

Potential (4) differs significantly from both the hard-sphere potential (1) and the WCA potential (2) in that it has a potential energy well. It also differs radically from the Lennard-Jones potential: its radius of influence far exceeds σ_{ij} and the

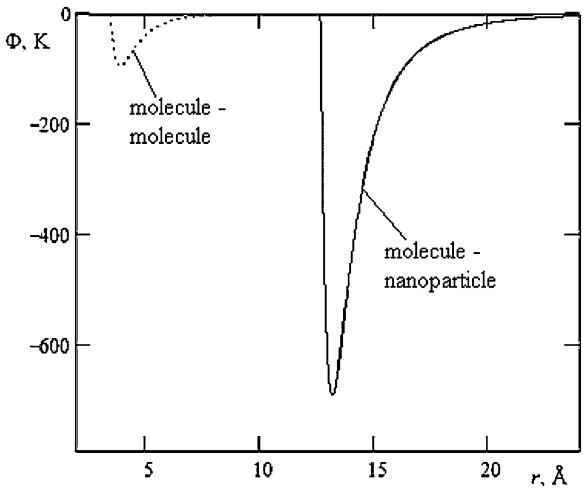

Fig. 1 Comparison of the Lennard-Jones interaction potentials for Li and Ar molecules (*dotted curve*) and potential (4) for an Ar molecule and a Li nanoparticle of 2 nm diameter (*solid curve*)

depth of the potential energy well greatly exceeds ε_{ij}. As an example, Fig. 1 shows the Lennard-Jones potential for Li and Ar molecules and potential (4) for an Ar molecule and a 2-nm diameter Li nanoparticle. As the nanoparticle size increases, the interaction radius and the depth of the potential well also increase.

The type of nanoparticle–molecule interaction potential determines the relaxation characteristics of the nanoparticle in a molecular medium. If the carrier gas is rarefied, the main relaxation mechanism is the kinetic mechanism due to individual collisions of the nanoparticle with gas molecules. However, the time of interaction between the molecules and the nanoparticle may then be comparable to or even larger than the mean free path time of the particle with respect to the molecules. As a result, even in a rarefied gas, multiple collisions can contribute to relaxation processes (see Refs. [18, 19, 46]).

If the carrier medium is a liquid or a dense gas, the existence of a deep and extended area of influence of attractive forces and a cage effect around a nanoparticle results in the formation of a "cloud" of carrier fluid molecules around the nanoparticle, with the velocities of the molecules being correlated with the nanoparticle velocity. Thus, an additional relaxation mechanism appears due to the interaction between the nanoparticle and this cloud. It should be noted that this mechanism should also be observed in hard-sphere systems, due to the cage effect.

3 Kinetic Theory of Rarefied Gas Nano-suspensions

The difficulty of developing a consistent theory of transport processes in nanofluids is related to several factors. First, the thermodynamics and rheology of nanofluids have not been adequately studied experimentally. There is no

information on the forces acting on nanoparticles in gases and liquids. This hampers the development of nanofluid thermodynamics. On the other hand, the characteristic nanoparticle size is of the order of the hydrodynamic infinitesimal scale for the carrier fluid [46]. For this reason, nanoparticles are material points in the metric of a continuous carrier medium and, hence, the interaction between these particles and the carrier medium cannot be described using hydrodynamic methods, as is done for typical dispersed fluids.

An alternative to the ordinary phenomenological description of the transport processes is a description based on nonequilibrium statistical mechanics and kinetic theory. Through the use of potential (4) one can hope to bring all the implications of this theory up to a number, calculating, in particular, the transport coefficients. However, the practical implementation of this approach involves a number of systematic difficulties. It has been shown [18, 19, 43, 45, 46] that rigorous kinetic equations for the single-particle distribution function can be derived only for the so-called rarefied finely dispersed gas suspensions. When the carrier medium is a liquid or a dense gas, one should use general methods of nonequilibrium statistical mechanics. However, in all cases, the calculation of the transport properties involves solving the multi-particle scattering problem, which is only possible using molecular dynamics methods (see, for example, [42]). All these approaches are used below. In this section, we consider nanoparticle suspensions in rarefied gases. Here and below, by a rarefied gas is meant a gas in which only binary collisions between its molecules take place. The dynamics of this gas is described by the Boltzmann equation or a more general Klimontovich equation (see [27]). However, the pressures (densities) of such gases can vary over a wide range, from normal pressure to free molecular flow in which molecular collisions are absent.

3.1 Diffusion of Nanoparticles in Rarefied Gases

There is no consensus in the literature on how to describe nanoparticle diffusion. On the one hand, some authors argue that it can be described in the same way as Brownian particle diffusion, i.e., using the Einstein diffusion coefficient [11]

$$D_E = kT/\gamma_S, \quad \gamma_S = 6\pi\eta R, \tag{5}$$

where R is the particle radius, η is the viscosity of the carrier medium, and T is the temperature of the carrier medium. The drag coefficient involved in formula (5) γ_S is the drag coefficient that corresponds to the Stokes drag force acting on a spherical particle in an incompressible fluid. Diffusion of dispersed particles in a rarefied gas is described using the CMD correlation mentioned above [17]

$$\begin{aligned} &D_{CMD} = kT/\gamma_{CMD} \\ &\gamma_{CMD} = 6\pi\eta R[1 + 1,257\ \mathrm{Kn}_R + 0,4\ \mathrm{Kn}_R \exp(-1,1/\mathrm{Kn}_R)]^{-1} = \gamma_S/C, \end{aligned} \tag{6}$$

where $\mathrm{Kn}_R = l_g/R$ is the Knudsen number for the carrier gas molecules based on the particle radius. As mentioned earlier, correlation (6) is widely used in various applications.

On the other hand, there have been attempts to describe nanoparticle diffusion by means of the kinetic theory of gases, treating nanoparticles as molecules. The first formula for the diffusion coefficient of aerosol particles was obtained by Epstein [14], see also a review by Mädler and Friedlender [35] for the case of large Knudsen numbers. Later, an approximate solution for the drag force acting on a small particle in a gas was obtained by Phillips [41]. Using the Einstein equation (5), one can obtain the corresponding diffusion coefficient. However, all these formulae are semi-empirical because they contain accommodation coefficients. The latter are not the universal constants; they depend on the nanoparticle material, the type of carrier gas, temperature, and even the shape of the particles and their surface layer condition, the energy of the incident particles, etc. Sufficiently full information on the values of these coefficients is not available.

As mentioned above, the dynamics of rarefied gas nanosuspensions can be described using the Boltzmann kinetic equations. Solving these equations by conventional methods, we arrive at the following diffusion coefficient of nanoparticles in a rarefied gas [52, 53]

$$D_{12} = \frac{3\sqrt{2kT(m+M)}}{16n\sqrt{\pi mM}R^2\Omega_{12}^{(1,1)*}(T^*, \sigma_{12}/R)}, \tag{7}$$

where $T^* = T/\varepsilon_{12}$, m, M are the molecular weights of the carrier gas and nanoparticle, respectively, and $\Omega_{12}^{(1,1)*}$ are the so-called reduced Ω-integrals (see Ref. [5]). A major characteristic of the nanoparticle diffusion coefficient is its dependence on the nanoparticle radius. For Brownian particles, this dependence is defined by the Einstein formula (5) $D_E \sim R^{-1}$. In the free molecular limit where $R \ll l_g$, D_E is proportional to R^{-2} [14]. In formula (7), this dependence is much more complex because the value of the Ω-integral also depends on the radius of the dispersed particle, and this dependence can be written as follows [53]

$$D_{12} \sim \frac{1}{R^2}\left(1 + \frac{a_1}{\sqrt{R}} + \frac{a_2}{R}\right).$$

Figure 2 shows curves of the diffusion coefficient versus radius for Zn nanoparticles in neon at a temperature $T = 300$ K and atmospheric pressure. The CMD correlation is in good agreement with our data in most of the range considered. However, in the range of small particle sizes, there is a great discrepancy between the CMD correlation and kinetic theory.

To evaluate the adequacy of kinetic theory and the CMD correlation for small particle radii, we performed measurement of particle sizes and diffusion coefficients [63]. Particle sizes were measured using a differential electrical mobility analyzer (DMA) and transmission electron microscopy (TEM) to ensure objective experimental data. Next, based on the experimentally measured

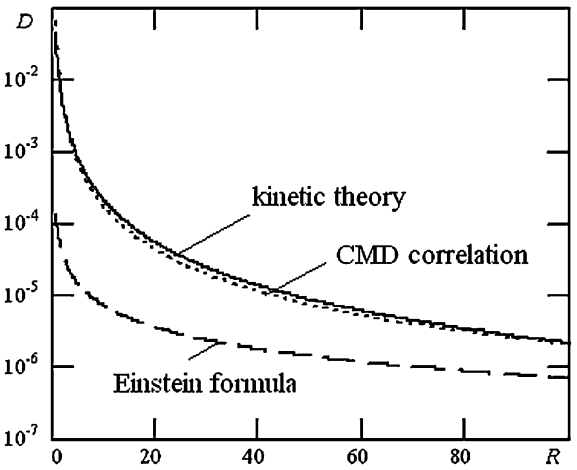

Fig. 2 Diffusion coefficient D (cm^2/s) versus radius (nm) for Zn nanoparticles in Ne. The *solid curve* is the diffusion coefficient obtained with kinetic theory (7), the *dashed curve* corresponds to the Einstein formula (5), and the *dotted curve* to the experimental CMD correlation (6)

electromobility and sizes of the particles, the corresponding diffusion coefficients were determined. The diffusion coefficients D_K were obtained from particle sizes measured using DMA and diffusion coefficients D_e were determined from sizes measured by TEM. The experimental data obtained in this manner were compared with theoretical results. In the experiment, diffusion of copper oxide nanoparticles, Cu_2O, was studied. Pure nitrogen was used as the carrier gas. As it turned out, in the range of small particle diameters, the particle size distributions obtained by the two methods differ by 20 – 30%. Consequently, the measured nanoparticle diffusion coefficient D_K differs greatly from the true value D_e. The obtained Cu_2O particle diffusion coefficients are shown in Fig. 3. The dashed curve corresponds to D_K, and squares to D_e. In the range of small particle diameters, the values of

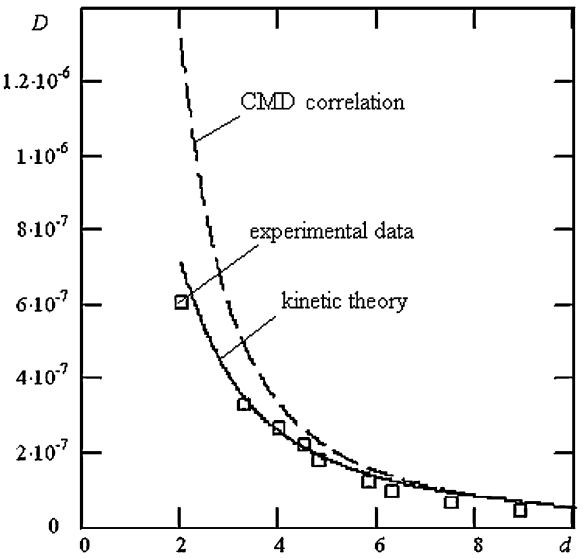

Fig. 3 Comparison between the kinetic theory results and experimental data on the dependence of the diffusion coefficient D (cm^2/s) on the nanoparticle diameter (nm). The *dashed curve* corresponds to D_K, the *solid curve* to diffusion coefficient obtained using kinetic theory and *squares* to D_e

these coefficients differ greatly. The dependence of the diffusion coefficient on the nanoparticle diameter obtained using kinetic theory is shown by a solid curve in Fig. 3. The theoretical curve agrees well with the TEM-based experimental data up to a particle size of 1 nm. As the particle diameter decreases, the CMD correlation differs more and more from both the calculation using kinetic theory and the experimental data. For small particle diameters, the CMD correlation (6) yields inflated values of the diffusion coefficient. For example, according to Eq. 6, particles with a characteristic size of about 2 nm have a diffusion coefficient which is more than twice the TEM experimental value and the kinetic theory result.

3.2 Temperature Dependence of Nanoparticle Diffusivity

The diffusion coefficients, or diffusivities, of both nanoparticles and molecules depend strongly on temperature. It has been shown [56] that the CMD correlation (6) incorrectly describes the dependences of the diffusivity of dispersed particles on temperature. Furthermore, this is true not only for nanoparticles but also for macroscopic particles. This result could have been expected because the constants in the CMD correlation were determined by Millikan (and later, by other authors) in a very narrow temperature range (19–24°C). Particle diffusivity relations obtained using the CMD correlation agree with kinetic theory with an accuracy of 15% or better only in a temperature range from 100 to 300 K. A number of experiments have been performed to study these relations [61, 62]. The experiments were performed for WO_x nanoparticles (mostly WO_3 particles with a small fraction of WO_2), NaCl, and Pt. The particle diameter was varied from 3 to 100 nm, and temperature from 295 to 650 K. These measurements were performed using diffusion batteries. A comparison between the experimental data and CMD correlation (6) is presented in Figs. 4 and 5. Figure 4 gives experimental diffusivities for 3.5 nm diameter nanoparticles of WO_3 and data obtained using the

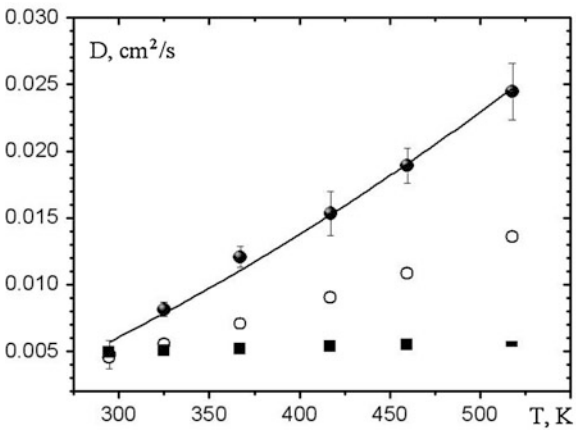

Fig. 4 Measured temperature dependence of the WO_3 particle diffusivity in air (*filled circles*) in comparison with the data obtained using the CMD correlation (*open circles*) and the correlation of [2] (*filled squares*)

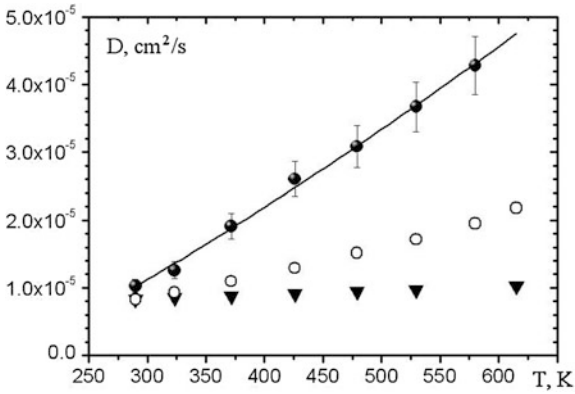

Fig. 5 Measured temperature dependence of the NaCl particle diffusivity in air (*filled circles*) in comparison with the data obtained using the CMD correlation (*open circles*) and the correlation of [2] (*filled squares*)

CMD correlation (6) and the correlation given in Baron and Willeke [2]. Figure 5 compares the experimental temperature dependence of the diffusivity of NaCl particles in air and the same correlations. The nanoparticle diameter is 84 nm. Both correlations prove inapplicable at temperatures over 350 K.

The fact that the CMD correlation (6) has been widely and successfully used can be explained by two factors. First, it has the Einstein formula (5) as the basis, and second, it agrees well with the free molecular asymptotic value of the drag force applicable at $Kn \gg 1$. However, its parameters were determined within a narrow temperature range, and thus, it is valid only in a very narrow domain.

On the other hand, the CMD correlation is designed quite sensibly and, as shown above, fits several limiting asymptotic values. For this reason, it could be used to develop a more general correlation, applicable within a wide temperature range. In order to make correlation (6) applicable within a wide temperature range, it has been modified as follows [62]

$$D_k = kT/\gamma_k, \quad \gamma_k = 6\pi\eta R[1 + A^*Kn + Q^*Kn\exp(-b/Kn)]^{-1}$$

so that its parameters become functions of temperature

$$A^* = A(T/295)^j, \quad Q^* = Q(T/295)^j,$$

where the j parameter is given by the following correlation

$$j = 1.03 + 0.57[1 + 10^{(2.703d_p - 10.45)}]^{-1}.$$

Here d_p is the nanoparticle diameter in nanometers.

3.3 Thermodiffusion

Thermodiffusion is one of the most interesting and subtle transport processes. Usually, the thermodiffusion coefficient is much smaller than the concentration

diffusion coefficient. However, thermodiffusion has practical applications. It is used to separate components of gas mixtures, especially isotopes, and is a valuable tool for studying intermolecular forces. Thermodiffusion may prove to be an additional factor of mixing processes in microchannels.

Thermodiffusion of nanoparticles is often confused with thermophoresis, a process typical of larger aerosol particles (e.g., see a review by Mädler and Friedlander [35]). Strictly speaking, thermophoresis is the motion due to a nonuniformly of heated particle surface. However, the nanoparticle size is of the order of the hydrodynamic infinitesimal scale of the carrier gas (if the gas is not too rarefied); i.e., it can be considered a material point in the metric of the carrier gas, and, hence, it makes no sense to speak of nonuniform heating. For the same reason, this nonuniformity cannot arise for physically reasonable temperature gradients. Thus, nanoparticle motion in a nonuniform temperature field is nothing thermophoresis but thermodiffusion.

A rigorous expression for the thermodiffusion coefficient can be derived from kinetic theory based on the Boltzmann equations for gas mixtures. In particular, for a binary mixture, the thermodiffusion coefficient D_T is linked to the diffusion coefficient D by the thermodiffusion relation k_T: $D_T = k_T D$ [16], where k_T is determined by the mole fractions x_i of components 1 and 2 and by the so-called thermodiffusion factor α_T: $k_T = \alpha_T x_1 x_2$, which is given by

$$\alpha_T = \left(6C_{12}^* - 5\right)\frac{S_1 x_1 - S_2 x_2}{Q_1 x_1^2 + Q_2 x_2^2 + Q_{12} x_1 x_2}, \tag{8}$$

$$S_1 = \frac{m_1 + m_2\lambda_{12}}{2m_2 \quad \lambda_1} - \frac{15 \;\; m_2 - m_1}{4A_{12}^* \quad 2m_1} - 1 \quad S_2 = \frac{m_1 + m_2\lambda_{12}}{2m_1 \quad \lambda_2} - \frac{15 \;\; m_1 - m_2}{4A_{12}^* \quad 2m_2} - 1,$$

$$Q_1 = \frac{\lambda_{12}}{\lambda_1}\left[3\frac{m_2}{m_1} + \left(\frac{5}{2} - \frac{6}{5}B_{12}^*\right)\frac{m_1}{m_2} + \frac{8}{5}A_{12}^*\right],$$

$$Q_2 = \frac{\lambda_{12}}{\lambda_2}\left[3\frac{m_1}{m_2} + \left(\frac{5}{2} - \frac{6}{5}B_{12}^*\right)\frac{m_2}{m_1} + \frac{8}{5}A_{12}^*\right],$$

$$Q_{12} = \frac{16}{5}\frac{(m_1 + m_2)^2}{4m_1 m_2}A_{12}^*\frac{\lambda_{12}^2}{\lambda_1\lambda_2} + \left(11 - \frac{12}{5}B_{12}^*\right) + \frac{15 \;\; (m_1 - m_2)^2}{8A_{12}^* \quad m_1 m_2}\left(5 - \frac{12}{5}B_{12}^*\right),$$

$$A_{ij}^* = \frac{\Omega_{ij}^{(2,2)*}}{\Omega_{ij}^{(1,1)*}}, \quad B_{ij}^* = \frac{5\Omega_{ij}^{(1,2)*} - 4\Omega_{ij}^{(1,3)*}}{\Omega_{ij}^{(1,1)*}}, \quad C_{ij}^* = \frac{\Omega_{ij}^{(1,2)*}}{\Omega_{ij}^{(1,1)*}},$$

$$\lambda_{ij} = \frac{25}{32}\frac{\sqrt{2\pi m_{ij}kT} \;\; 3k}{\pi\sigma_{ij}^2\Omega_{ij}^{(2,2)*} \; 4m_{ij}}, \quad D_{ij} = \frac{3}{16}\frac{1}{n}\frac{1}{\sigma_{ij}^2\Omega_{ij}^{(1,1)*}}\sqrt{\frac{2kT}{\pi m_{ij}}},$$

where m_i is the mass of the i-th molecule, $m_{ij} = m_i m_j/(m_i + m_j)$ is the reduced mass, and $\Omega_{ij}^{(k,l)*}$ are the Ω-integrals.

The sign of the thermodiffusion factor α_T and the direction of thermodiffusion are determined mainly by the factors S and Q in Eq. 8, which, in turn, depend on the

mass ratio of the molecules and their effective scattering cross sections $\left(\sigma_{ij}^2 \Omega_{ij}^{(1,s)*}\right)$. The following typical cases can be distinguished. For not too low temperatures, the factor $\left(6C_{12}^* - 5\right)$ in formula (8) is positive, and the nature of thermodiffusion is determined by the mass ratio and size ratio of the molecules. If the molecular masses are different, e.g., $m_1 > m_2$, then $\alpha_T > 0$, and heavier molecules tend to migrate to cooler areas. If the molecular masses are similar, larger molecules tend to migrate to cooler areas. If the heavier-gas molecules are larger than the lighter-gas molecules, the thermodiffusion factor increases only slightly or even decreases. Moreover, in such cases, the thermodiffusion factor can become negative.

Typically, textbooks and reference books on kinetic theory (e.g., [16]) state that the thermodiffusion factor depends weakly on the mixture composition. Generally, this is not so. Indeed, in the case of a mixture of heavy isotopes, the thermodiffusion factor is almost independent on the concentration of the components. For instance, for a $U^{238}F_6$–$U^{235}F_6$ mixture, the thermodiffusion factor changes by 0.4% as the mole fraction of $U^{238}F_6$ varies from 0.01 to 0.99. The same is observed for the dependence of the thermodiffusion factor on the mole fraction of Xe^{132} in a Xe^{132}–Xe^{129} mixture. This is also true for the thermodiffusion factor of a H_2–He mixture.

On the other hand, the thermodiffusion ratio for rarefied gas mixtures with significantly different masses of molecules is very sensitive to the mole fractions of components. As an example, Fig. 6 shows the thermodiffusion factor of a Xe–Ne mixture as a function of the mole fraction of Xe [56]. As one can see, the thermodiffusion factor varies by more than a factor of two. A similar situation is observed for a Ar–He mixture. Here the thermodiffusion factor of the mixture is positive and increases by almost a factor of three with increasing mole fraction of the lighter gas.

Although the dependence of the thermodiffusion factor on the mixture composition seems too complex and non-universal, the reciprocal of the thermodiffusion factor α_T^{-1} for so-called "normal" systems was found to be linear [31]. Its linearity has been confirmed by experiments, as reported by several authors.

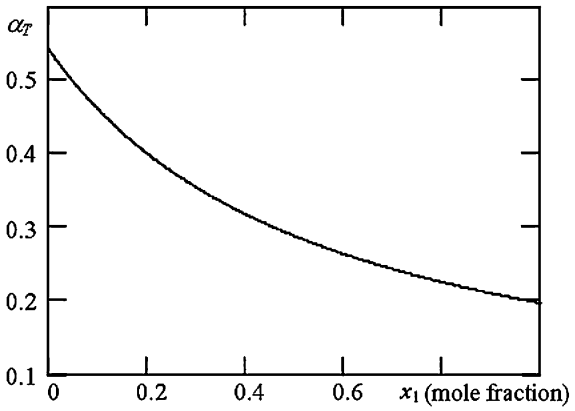

Fig. 6 Thermodiffusion factor α_T of a rarefied Xe–Ne gas mixture versus the mole fraction x_1 of Xe. $T = 300$ K

Exceptions are the so-called anomalous systems in which the sign of α_T varies as a function of the mole fraction of one of the components. This phenomenon is called the temperature inversion of the thermodiffusion factor. Detection of temperature inversion in computations depends strongly on the intermolecular potential used. Such a subtle dependence of the thermodiffusion factor on the parameters of the potential is a useful tool for determining whether these parameters are obtained correctly. For instance, the hard-sphere potential does not describe this temperature inversion.

This inversion has been confirmed by experiments. Studies of mixtures of inert gases and nitrogen [20] have shown that the observed dependences of α_T agree with those computed using the Lennard-Jones 6–12 potential or the exp-6 potential, both qualitatively and quantitatively.

A characteristic feature of nanoparticle thermodiffusion by which it differs from thermodiffusion of gas molecules is the dependence of the thermodiffusion coefficient and other parameters on the nanoparticle size. Naturally, the thermodiffusion coefficient decreases with increasing nanoparticle size. In addition, the thermodiffusion coefficient (just as the thermodiffusion ratio k_T) depends strongly on the nature of nanoparticles and carrier gas. As an example, Fig. 7 shows the thermodiffusion coefficients for Zn, Li, and U nanoparticles in Ne as functions of their radius for a fixed volume fraction of nanoparticles $\phi = 0.001$. Small particles have significantly different values of the thermodiffusion coefficient. At the same time, even for particle sizes larger than 3 nm, these values are almost identical.

Another important feature that distinguishes thermodiffusion of molecules from that of nanoparticles is the absence of inversion of the thermodiffusion factor. Finally, the thermodiffusion coefficient of nanoparticles and other parameters depend on the volume concentration of nanoparticles. Figure 8 shows typical curves of the thermodiffusion factor versus volume fraction of nanoparticles (or molecules of a heavier component) at a fixed temperature $T = 300$ K for U–Ne gas nanosuspensions ($R = 20$ nm and $R = 1$ nm), and Xe–Ne gas mixtures [56]. One can see that the thermodiffusion factors of different media differ by several

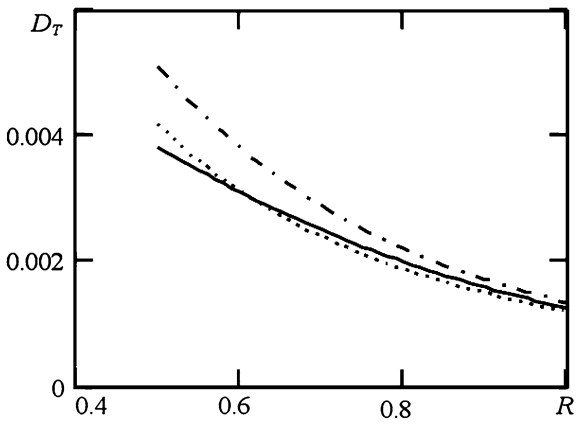

Fig. 7 Thermodiffusion coefficient D_T (cm^2/s) of various nanoparticles in Ne versus their radius R (nm). The *solid*, *dash*, and *dot*-and-*dash* curves correspond to U, Li, and Zn nanoparticles, respectively, $T = 300$ K

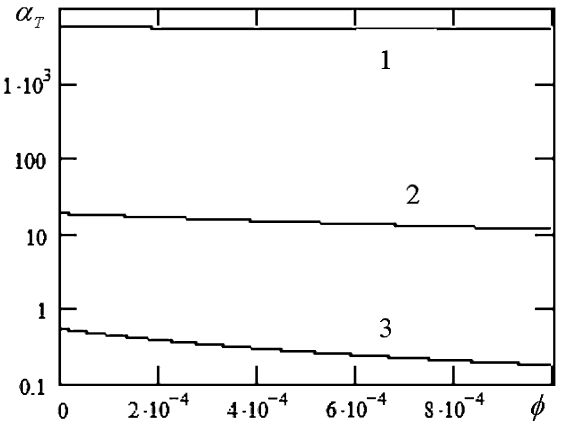

Fig. 8 Thermodiffusion factor α_T as a function of the volume fraction ϕ of nanoparticles for U–Ne gas nanosuspensions, $R = 20$ nm (*curve 1*) and $R = 1$ nm (*curve 2*) and Xe–Ne gas mixtures (*curve 3*)

orders of magnitude, increasing with increasing ratios of the masses and radii of the heavy and light components.

3.4 Effective Viscosity of Gas Nano-suspensions

The effective viscosity of rarefied nanosuspensions was first calculated by Einstein [12], who took into account the influence of the particles on the hydrodynamic field of the carrier-fluid velocity and, consequently, on the stress tensor and viscosity. It has been found that the effective viscosity of suspension

$$\eta = \eta_0[1 + (5/2)\phi] \tag{9}$$

is always greater than the carrier-fluid viscosity η_0. Here ϕ is the volume concentration of dispersed particles. Subsequent experiments have shown that the Einstein formula is valid only for $\phi \leq 10^{-3}$. Many attempts have been made to extend the Einstein theory to the case of higher volume concentrations. Traditionally, research can be divided according to three approaches. First, there are studies in which corrections to the velocity and pressure fields of the carrier fluid due to the interaction of dispersed particles have been determined [3]. The second approach is concerned with the use of methods of nonequilibrium statistical mechanics (see, for example, [68]). Finally, in the third approach, the velocity and pressure fields are simulated using some stochastic laws [15]. All these approaches yield relations of the form

$$\eta(\phi) = \eta_0\left(1 + 2.5\phi + k\phi^2\right), \tag{10}$$

where the coefficient k varies from 5.92 to 6.25 in different studies (see also the Sect. 5.1).

In practice, a typical carrier medium is a rarefied gas. What is the effective viscosity of rarefied gas suspensions and how it depends on the dispersed particle

concentration? At present, there are no answers to these questions. To calculate the effective viscosity of gas nanosuspension, we will use the same approach as for nanoparticle diffusion, i.e., the Boltzmann kinetic theory for the binary system with the interaction potential (4). At present, a reliable interaction potential (or interaction model) for dispersed particles is not available. Therefore, in the present paper, particle-to-particle interaction is modeled using the hard-sphere potential. In the first approximation of the Sonine polynomial expansion, the viscosity of a rarefied gas nanosuspension is described by the following formula [24]:

$$\eta = (1 + Z)/(X + Y) \tag{11}$$

where

$$X = \frac{x_1^2}{\eta_1} + 2\frac{x_1 x_2}{\eta_{12}} + \frac{x_2^2}{\eta_2}, \quad Y = 0.6A_{12}^*\left\{\mu\frac{x_1^2}{\eta_1} + 0.5x_1x_2\frac{(1+\mu)^2}{\mu}\frac{\eta_{12}}{\eta_1\eta_2} + \frac{1}{\mu}\frac{x_2^2}{\eta_2}\right\},$$

$$Z = 0.6A_{12}^*\left\{\mu x_1^2 + 2x_1x_2\left[\frac{(1+\mu)^2}{4\mu}\left(\frac{\eta_{12}}{\eta_1} + \frac{\eta_{12}}{\eta_2}\right) - 1\right] + \frac{1}{\mu}x_2^2\right\},$$

$$\eta_i = \frac{5}{16}\frac{(\pi m_i kT)^{1/2}}{\pi\sigma_{ii}^2\Omega_i^{(2,2)*}}, \quad \eta_{12} = \frac{5}{16}\frac{(\pi m_{12} kT)^{1/2}}{\pi\sigma_{12}^2\Omega_{12}^{(2,2)*}}.$$

Here x_1, x_2 are the mole fractions of components 1 and 2, $\mu = m_1/m_2$, m_1, m_2 are the masses of the carrier-gas molecule and nanoparticle, respectively (subscript 2 refers to nanoparticles, unless stated otherwise), $m_{12} = m_1m_2/(m_1 + m_2)$. $A_{12}^* = \Omega_{12}^{(2,2)*}/\Omega_{12}^{(1,1)*}$, $\sigma_{22} = 2R$, and R is the nanoparticle radius.

The Boltzmann kinetic theory is applicable to gas nanosuspensions only if the volume fraction of dispersed particles is small or, more precisely, if the corresponding Van der Waals parameter is small: $n_2R^3 \ll 1$. In the first approximation with respect to x_2, the viscosity equation (11) becomes

$$\eta = \eta_1\left\{1 + \frac{x_2}{(1 + 0.6A_{12}^*\mu)}\left[\frac{1.2\sqrt{2}\alpha\Omega_{11}^{(2,2)*}}{s\Omega_{12}^{(1,1)*}} + 2 - 1.2A_{12}^* - 2\frac{\sqrt{2}\Omega_{12}^{(2,2)*}}{4s^2\Omega_{11}^{(2,2)*}}\right]\right\}. \tag{12}$$

Here

$$s = \frac{\sigma_{11}}{\sigma_{22}} = \frac{\sigma_{11}}{2R} \ll 1, \quad \alpha = \frac{s^3}{\mu} = \frac{m_2\sigma_{11}^3}{m_1\sigma_{22}^3} = \frac{\pi}{6}\frac{\rho_p\sigma_{11}^3}{m_1},$$

where ρ_* is the density of the nanoparticle material, so that the parameter α has the physical meaning of the ratio of the density of the nanoparticle material to the density of the carrier-gas molecules. The parameter x_2 can be related to the nanoparticle volume concentration $\phi = x_2v_pp/kT$, where v_p is the volume of a nanoparticle and p is the gas nanosuspension pressure. Then, formula (12) takes a form similar to the Einstein formula (9), but there is an important difference. Function (12) depends strongly on the mass ratio, μ, and effective diameters, s, of

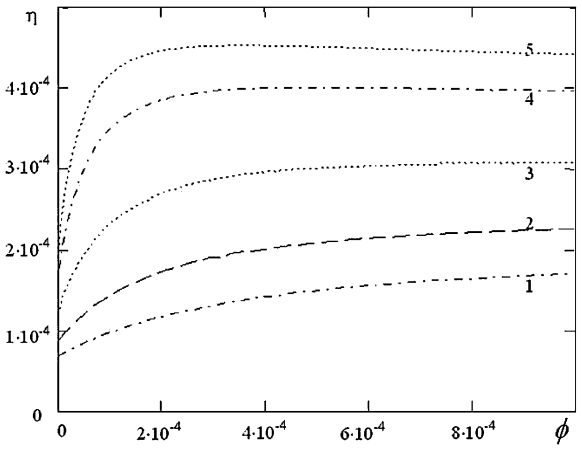

Fig. 9 Effective viscosity (poise) of a U–H_2 gas nanosuspension versus volume fraction of nanoparticles. Curve 1 corresponds to a temperature $T = 200$ K, curve 2 to $T = 300$ K, curve 3 to $T = 500$ K, curve 4 to $T = 800$ K, and curve 5 to $T = 1{,}000$ K

the molecules and nanoparticles, temperature, and the parameters of potential (4). In particular, for certain values of these parameters, the term in square brackets in (12) can change sign. This means that when we add small volume fractions of solid dispersed particles to a pure gas, the effective viscosity of the medium can both increase and decrease.

Systematic calculations [54, 55] have shown that it is indeed the case. A decrease in the effective viscosity with respect to the pure gas viscosity can be expected for relatively small values of the parameter α. As an example, Fig. 9 shows the dependence of the effective viscosity of a U–H_2 gas nanosuspension on the volume concentration of nanoparticles of radius $R = 0.5$ nm at various temperatures. Here curve 1 corresponds to a temperature $T = 200$ K, curve 2 to $T = 300$ K, 3 to $T = 500$ K, 4 to $T = 800$ K, and 5 to $T = 1{,}000$ K. This gas nanosuspension has the largest parameter α. Thus, at low U particle concentrations, the effective viscosity of this gas nanosuspension is higher than that of the carrier gas. As the temperature increases, this effect is increased too. At concentrations of about 2×10^{-4} and room temperature, the viscosity of the gas nanosuspension is higher than that of the carrier gas by about 90%. This effect depends strongly on temperature, and at $T = 1{,}000$ K the ratio $\eta/\eta_1 \sim 2.3$ for the same concentrations.

On the other hand, the effective viscosity depends strongly on the nanoparticle size. According to formula (12), adding fairly large particles to the suspension can lead to a drop in viscosity compared to the pure hydrogen viscosity. This is indeed observed for a U–H_2 gas nanosuspension, a relevant example is given in a paper [54]. For a gas nanosuspension of U particles of $R = 70$ nm at $T = 300$ K the effective viscosity turns out to be lower than the viscosity of hydrogen by about 1% for a U particle concentration of 2×10^{-4}.

Figure 10 presents calculations of the viscosity of a Zn–Ne gas nanosuspension. The viscosity of the gas nanosuspension is always lower than that of the carrier gas. At room temperature and nanoparticle volume fraction of 2×10^{-4}, the

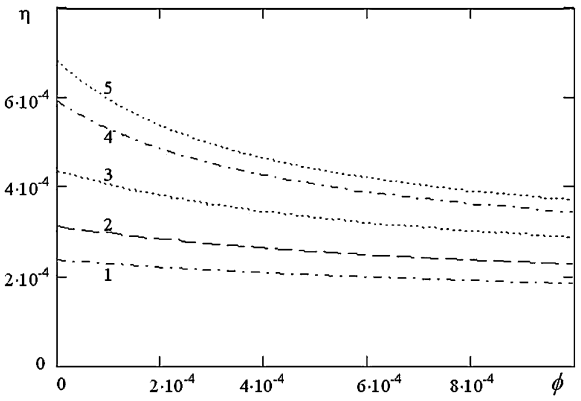

Fig. 10 Viscosity (poise) of Zn nanoparticles suspended in Ne versus their volume fraction. Curve 1 corresponds to a temperature $T = 200$ K, curve 2 to $T = 300$ K, curve 3 to $T = 500$ K, curve 2 to $T = 800$ K, and curve 5 to $T = 1{,}000$ K

effective viscosity of this gas nanosuspension is about 15% lower than that of pure neon, and this effect is enhanced with increasing temperature.

The main conclusion that can be drawn from these data is that the viscosity of gas nanosuspensions, unlike that of conventional suspensions, can be both higher and lower than the carrier-gas viscosity. The factors determining whether the viscosity of such gas nanosuspensions increases or decreases with respect to the carrier-gas density depends primarily on the nanoparticle radius and the density ratio of the nanoparticle material to the carrier gas. The effect of increase or decrease in the viscosity of gas nanosuspensions is considerably enhanced with decreasing nanoparticle radius. Increasing the gas nanosuspension temperature also enhances this effect.

4 Mechanisms of Nanoparticles Transport Processes in Gases and Liquids

4.1 Rarefied and Moderately Dense Gas Nanosuspensions

As was noted in the previous section, the dynamics of rarefied gas nanosuspensions can be described by the set of the Boltzmann equations. It can be shown [48] that this description is valid only if the following conditions hold

$$\varepsilon_g = n_g r_0^3 \ll 1, \quad \varepsilon_p = n_p R^3 \ll 1, \quad n_g R_0^3 = \varepsilon_g (R_0/r_0)^3 \ll 1, \tag{13}$$

where n_g and n_p are the number densities of molecules and nanoparticles in the gas nanosuspension, respectively, whereas r_0 and R are the characteristic radii of the molecules and nanoparticles, respectively. In this case, the only mechanism involved in nanoparticle transport is the kinetic one. Nanoparticle transport is related to binary collisions between carrier-gas molecules and nanoparticles and binary collisions between nanoparticles, with the contribution of the latter to the

transport coefficients being small. Indeed, in this case, the virial parameter of the nanoparticle pseudo-gas should be such that $\varepsilon_p \ll n_p/n_g$, which implies that real particle concentrations are low and their collisions are unlikely.

Equations (13) are true when the dispersed particle size is small, unless the carrier gas is highly rarefied. Thus, the Boltzmann equations are applicable to gas nanosuspensions only in the case of ultra-dispersed systems. As the nanoparticle size increases, or as the carrier gas becomes moderately rarefied, one should employ more general kinetic equations for single-particle distribution functions of gas molecules F_g and nanoparticles F_p [18, 19]

$$\partial F_g/\partial t + L_{1g}F_g = J_B^{gg} + J_B^{gp} + J_1^{gp}, \quad \partial F_p/\partial t + L_{1p}F_p = J_B^{pg} + J_1^{pg}. \tag{14}$$

Here L_{1g} and L_{1p} are the single-particle Liouville operators for molecules and nanoparticles, respectively; J_B^{gg}, J_B^{gp}, J_B^{pg} are the Boltzmann integrals for collisions between carrier-gas molecules and between carrier-gas molecules and nanoparticles, respectively. Compared to the Boltzmann equations for ultra-dispersed gas nanosuspensions, Eq. 14 contain integrals of triple collisions which include certain sequences of correlated binary collisions; examples are shown in Fig. 11. Here, the large circle shows a particle, and molecule trajectories are marked by arrows.

If the particle concentration is increasing but still low, interactions between nanoparticles also begin to affect transport processes. However, their direct interactions can still be neglected because the main contribution comes from their indirect interaction through the medium. This specific exchange interaction between two particles via exchange of a molecule is illustrated in Fig. 12.

Thus, in rarefied gas nanosuspensions [i.e., suspensions satisfying the first two conditions in (13)], all transport processes are of kinetic nature and are due to individual collisions of nanoparticles with carrier-gas molecules. To understand how these collisions are related to and determine transport processes, it is necessary to define these processes.

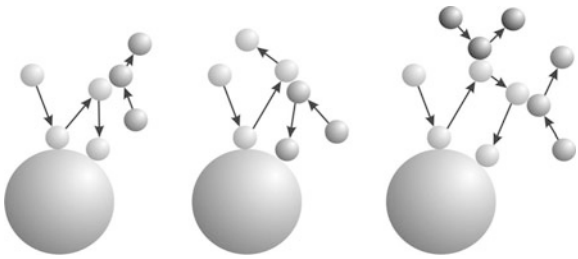

Fig. 11 Examples of triple collisions including sequences of correlated binary collisions between carrier-gas molecules and nanoparticles that determine the integrals J_1^{pg}, J_1^{gp}

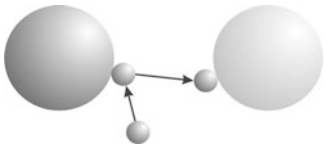

Fig. 12 Exchange interaction between two particles via exchange of a molecule

Transport processes are processes of smoothing certain macroscopic parameters of a system, such as density, momentum, or energy. Because any system consists of molecules, local microfluctuations in density, momentum, or energy do take place. Under equilibrium conditions, these fluctuations are inversely proportional to the square root of the number of particles in the system: $N^{-1/2}$. Therefore, in equilibrium macroscopic systems with $N \gg 1$, macroscopically observed fluctuations are absent. In nonequilibrium systems, fluctuations are observed on scales much larger than molecular dimensions. Hence, reaching equilibrium means eliminating large-scale fluctuations, and transport processes are processes that eliminate large-scale fluctuations. Mathematically, this statement is formulated as the so-called fluctuation–dissipation theorems, which establish relations between the transport coefficient μ_i and the corresponding correlation function χ_i

$$\mu_i = \int_0^\infty \chi_i(t)dt.$$

These relations can be derived from the first principles using methods of nonequilibrium statistical mechanics (e.g., see [47, 74] and are known as the Green–Kubo formulas. Diffusion, one of the key transport processes, is given by

$$D = \frac{1}{3}\int_0^\infty dt\chi'_{\mathrm{vv}}, \tag{15}$$

where $\chi'_{vv} = \langle \mathbf{v}(0) \cdot \mathbf{v}(t) \rangle$ is the velocity autocorrelation function and the angular brackets denote averaging over a statistical ensemble. When the diffusion of rarefied gas molecules is considered, this is the molecular velocity autocorrelation function

$$\chi'_{\mathrm{vv}}(t) = \frac{3kT}{m}\exp\left(-\frac{kT}{D}t\right) = \frac{3kT}{m}\exp\left(-\frac{t}{\tau_r}\right), \tag{16}$$

where D is the molecular diffusion coefficient and τ_r is the molecular-velocity relaxation time, which is of the same order of magnitude as the mean free path time of molecules. The existence of a single relaxation time[1] is due to the single relaxation mechanism involving individual molecular collisions.

Nanoparticle relaxation in a rarefied gas can also be described by an autocorrelation function of the form (16) but with the nanoparticle diffusion coefficient in accordance to (7).

[1] Strictly speaking, the relaxation processes for density, momentum, or kinetic energy in rarefied gas are characterized by different relaxation times, but still, all these times are of the order of the mean free path time of the molecules.

4.2 Brownian Particles

The dynamics of a Brownian particle in a liquid is described by the Langevin equation

$$M\dot{V} = -\gamma_s \mathbf{V} + \mathbf{f},$$

where M is the mass of the Brownian particle, $\mathbf{f}$ is the stochastic force acting on the particle due to its individual collisions with carrier molecules, $\mathbf{V}$ is the velocity of the center of mass of the Brownian particle, and γ_s is the Stokes drag coefficient (5). It is easy to show that the Brownian-particle velocity autocorrelation function equals

$$\chi'_{vv}(t, t+\tau) = \langle \mathbf{V}^2(t) \rangle e^{-\tau/\tau_B} = (3kT/M) e^{-\tau/\tau_B}, \tag{17}$$

where the particle velocity relaxation time is determined by the systematic Stokes drag force acting on the particle

$$\tau_B = M/\gamma_s = M/6\pi\eta R. \tag{18}$$

Substituting function (17) into Eq. 15 and integrating the result, we arrive at the Einstein formula for the Brownian particle diffusion coefficient

$$D = kT/(6\pi\eta R). \tag{19}$$

Historically, that was the first example of the fluctuation–dissipation theorem.

4.3 Liquids and Dense Gases

Even though formulae (16) and (17) look very similar, they describe different relaxation mechanisms. The former describes the kinetic mechanism due to individual molecular collisions. The latter describes relaxation due to collective effects. Because the mass of a Brownian particle is much greater than that of the molecule, $M \gg m$, individual collisions with molecules have little effect on the particle. On the other hand, during the time of collision between a molecule and a Brownian particle, i.e., $\tau_{0B} \sim 10^{-10}$s, many such collisions occur (10^8 – 10^{10}). Even at this short time, the effect of multiple impacts of a great number of molecules on one particle takes place. Thus, along with the kinetic mechanism of relaxation, there is a collective mechanism involving the correlated behavior of a large number of molecules. The correlated state of a large number of molecules means the occurrence of large-scale, macroscopic fluctuations in the system. Therefore, Brownian-particle velocity relaxation is due to interactions with the fluctuations occurring in the carrier medium and their subsequent evolution.

It has been mentioned above that only microfluctuations occur in rarefied gases. They arise and decay during molecular collisions. Having collided at a particular moment, molecules fly apart to never meet again. In liquid and dense gases,

the situation is different. Due to the high density of the medium, long-time correlations coexist with short-lived ones. As a result, the molecular velocity autocorrelation function has a power law asymptotic behavior $\chi'_{vv} \sim t^{-3/2}$ [1]. Fairly accurate molecular dynamic simulations for hard-sphere systems have shown that, starting at certain times $t > \tau$, this long-time tail is well described by the following function [58]

$$\chi_{vv}(0,t) = \frac{3kT}{m}\left[\exp(-t/\tau) + B(t-t_*)^{-\frac{3}{2}}\right] \tag{20}$$

whose parameters B and t_* depend on the density of the medium. The presence of the second term in (20) means, in particular, that the diffusion of liquid molecules does not follow the classical Einstein law $\langle R^2(t)\rangle = 6Dt$, where $\langle R^2(t)\rangle$ is the mean square distance traveled by the Brownian particle. For liquids, the following equation is valid: $\langle R^2(t \gg \tau)\rangle = 6Dt(1 - 4Bt^{-1/2})$, i.e., a superposition of ordinary classical diffusion and subdiffusion takes place [50, 58].

4.4 Nano-suspensions

Nanoparticles are intermediate in size between molecules and Brownian particles. The smallest nanoparticles are only two or three times larger than molecules; therefore, they certainly experience individual collisions with carrier-fluid molecules and a kinetic relaxation mechanism should be typical of these particles. On the other hand, large nanoparticles are closer in size to Brownian particles, and interactions with microfluctuations in the carrier medium should also be typical of them. Finally, as was shown in Sect. 2, the interaction potential between nanoparticles and carrier molecules is long-range and is characterized by a deep potential well (see Fig. 1). This means that, in a fairly dense carrier medium, a cloud of molecules appears around a nanoparticle, and velocities of these molecules correlate with the nanoparticle velocity. It is at this microfluctuation that the nanoparticle begins to relax. This effect should also take place in the case of hard-sphere liquids due to the so-called cage effect, where carrier molecules remain near a nanoparticle for a long time after collision. Thus, there are at least two different nanoparticle relaxation mechanisms, each of which is characterized by its own relaxation time: τ_1 and τ_2. Therefore, the nanoparticle velocity autocorrelation function can be represented as

$$\chi'_{vv}(0,t) = a_1 \exp(-t/\tau_1) + a_2 \exp(-t/\tau_2), \tag{21}$$

where the parameters a_1, a_2, τ_1, τ_2 depend on the size and mass ratios of the nanoparticle to the carrier molecule. This nanoparticle velocity autocorrelation function has been determined using molecular dynamics methods [64, 65]. The contribution of each exponent changes with changes in the above-mentioned size and mass ratios; as the nanoparticle size increases, the contribution of the first term

decreases and that of the second, increases. As the nanoparticle mass decreases, the relaxation time τ_1 tends to the nanoparticle mean free time with respect to the carrier-gas molecules. On the other hand, as the nanoparticle size and mass increase, the time τ_2 tends to the Brownian particle relaxation time (18). The coefficient a_2 decreases as well. It should be noted, however, that structure (21) is characteristic of the velocity autocorrelation function of even very small nanoparticles. The occurrence of microfluctuations around nanoparticles and interactions between microfluctuations and nanoparticles are characteristic features of nanoparticle dynamics.

The structure of density and momentum microfluctuations of carrier molecules has been systematically studied and simulated using the molecular dynamics method in our papers [50, 59].

Microfluctuations that arise around a nanoparticle are characterized primarily by local changes in carrier-molecule concentration. As an example, Fig. 13 shows the dimensionless (normalized by the mean concentration) concentration of carrier-fluid molecules $g_2(r'/r, \theta, t)$ (radial distribution function) around a nanoparticle for a fixed time $t = 2\tau$ at $M/m = 100$, $R/r = 3$. Here r' is the shortest distance between the surfaces of the particle and molecule, θ is the angle between the line connecting their centers and the initial velocity direction of the nanoparticle, and τ is the mean free time of the molecule. At the initial time when the nanoparticle loses equilibrium, the function $g_2(r'/r, \theta, t)$ is isotropic and then it becomes anisotropic, as shown in Fig. 13. The first maximum in the forefront (at $\theta \leq 40°$)

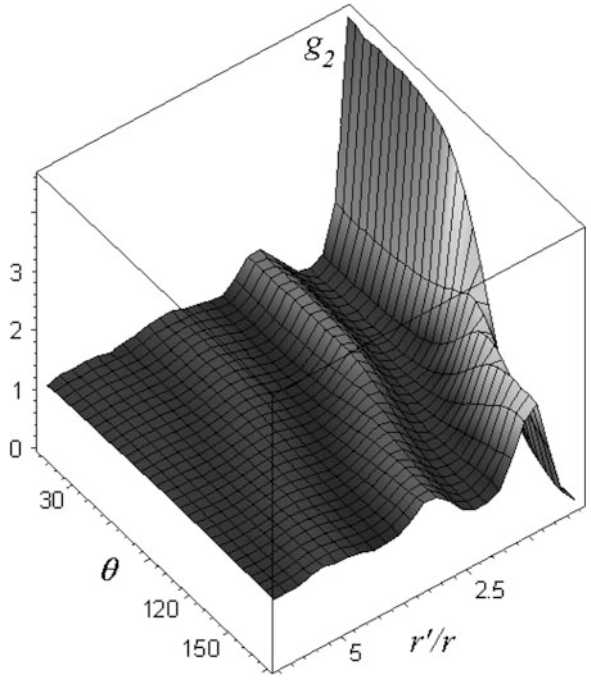

Fig. 13 Radial distribution function of carrier-fluid molecules around a nanoparticle

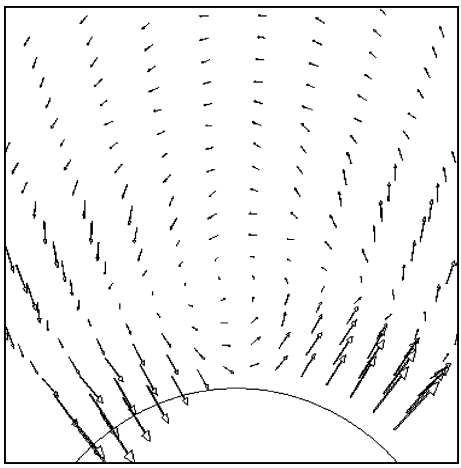

Fig. 14 Carrier-fluid velocity field around a moving nanoparticle

increases by 30 – 50%, compared to the equilibrium value, and it is 3 – 5 times greater than the mean concentration, which equals unity. Behind the particle, a highly rarefied region is formed. Therefore, nanoparticle velocity relaxation in a dense medium (liquid and dense gas) is accompanied by an increase in density in the region to which the particle moves.

In addition to density fluctuations, local fluctuations of the carrier-fluid momentum play an important role because the efficiency of nanoparticle velocity relaxation depends on momentum microfluctuations. Correlations for the mean carrier velocity and mean particle velocity in the forefront are the highest in the range of the maximal concentrations.

The velocity field of the carrier medium around a nanoparticle changes during nanoparticle relaxation. Figure 14 shows a fragment of the velocity field of the carrier medium for $t = 10\tau$ ($M/m = 25$, $R/r = 2$). Arrows show the directions and values of the carrier-fluid velocity. The nanoparticle velocity is directed to the right; the arch shows part of the nanoparticle boundary. Near the particle surface one can see a vortical structure. It has a toroidal shape and is located in the plane through the center of the particle and perpendicular to the velocity direction. For the given parameters of the system, the time of formation of this structure is about 10 molecular mean free times. The diameter of the vortex is comparable to the nanoparticle size. The mean velocity of the carrier-fluid molecules below the center of the vortex is directed along the particle motion direction. It is in this region that the carrier-fluid velocity is the highest.

The microfluctuation, i.e., the vortex "pushes" the particle and thus slows down the relaxation process. This is responsible for the appearance of the second relaxation time τ_2.

Due to the complex nature of the nanoparticle velocity relaxation, the force exerted on the nanoparticle by the carrier is unsteady [60]. As an example, Fig. 15 shows simulation results for the drag coefficient $\mu(t) = \tilde{\mu}(t)/6\pi\eta R$ (normalized by the Stokes drag coefficient) for a nanoparticle with a radius $R = 4r$ and mass ratios

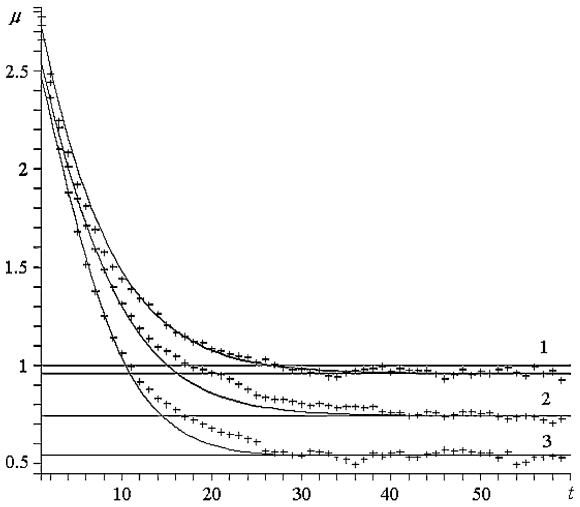

Fig. 15 Time dependence of the drag coefficient of the force acting upon the nanoparticle in liquid for a nanoparticle with a radius $R = 4r$ and mass ratios $M/m = 200$ (curve 1), 100 (curve 2), 50 (curve 3). *Crosses* show the simulation results; the time is in molecular mean free times

$M/m = 200$, 100, 50 in a liquid. The relaxation zone is fairly extended, about 30 molecular mean free times. At the beginning, the drag force acting on the particle is two or three times greater than the Stokes force. With time, the drag coefficient decreases and reaches a certain steady-state value μ_∞ which is smaller than the corresponding Stokes force. The value of μ_∞ increases with increasing nanoparticle mass, and for large particles, it reaches the Stokes coefficient. The relaxation of the drag force can be described by the correlation

$$\tilde{\mu}(t) = \frac{M[a_1 \exp(-t/\tau_1)/\tau_1 + a_2 \exp(-t/\tau_2)/\tau_2]}{a_1 \exp(-t/\tau_1) + a_2 \exp(-t/\tau_2)}, \tag{22}$$

whose parameters are determined by the parameters of function (21).

5 Transport Coefficients for Nanosuspensions

Recently, there has been a revolutionary advance in micro heat exchangers. They have proven to be much more energy efficient than macroscopic heat exchanges. The heat fluxes removed by micro heat exchangers exceed 1,000 W/cm^2. Two-phase flows in channels of small cross section are used in membrane fuel cells and evaporation–condensation systems of spacecraft thermal control. Tiny thermal pipes are used and developed for cooling the microelectronic equipment, micro and mini channels with single-phase and two-phase flows.

Along with the miniaturization of heat exchangers and other power devices, there has been rapid progress in studies of the use of nanofluids in them. There is a hope that such devices will be far superior in efficiency to devices based on conventional heat-transfer media. In addition, the use of nanofluids allows heat

removal at room temperature of the coolant, unlike with traditional low-temperature coolants. The thermal conductivity of currently existing nanofluids of various compositions with a small volume fraction of metal nanoparticles can exceed the thermal conductivity of pure fluids by tens of percent. Even greater success can be expected at use carbon nanotubes, which are known to have high strength and elasticity and whose thermal conductivity along the tube is several orders of magnitude higher than the thermal conductivity of pure fluids. At the same time, the practical application of nanofluids and control of their properties requires an understanding of the dependence of their transfer properties on the concentration and characteristics of nanoparticles. This section gives an overview of current research on the effective viscosity of nanofluids and their thermal conductivity.

5.1 Effective Viscosity of Nanofluids

The approaches to the description of the effective viscosity of coarse-dispersed fluids were discussed in Sect. 3.4. Correlation (10) adequately describes experimental data to concentrations of approximately $\phi \sim 0.3$. Recently, attempts have been made to obtain more general relations. For example, Verberg et al. [68] derived the formula

$$\eta(\phi) = \eta_\infty(\phi) + \eta_d(\phi, \omega = 0) = \eta_0 g_2 \left(\frac{1 + 1.44\phi^2 g_2^2}{1 - 0.1241\phi + 10.46\phi^2} \right), \qquad (23)$$

which is claimed by the authors to be valid to concentrations $\phi \sim 0.5$, including for nanofluids (g_2 is the pair radial distribution function). In studies of nanofluids, it is also common to use relations (9) and (10).

Although the viscosity of nanofluids is an extremely important factor in the transfer processes occurring in them, experimental data on the effective viscosity of nanosuspensions are few in number and contradictory. Thus, the viscosity of cyclohexane–SiO_2 nanofluids with a particle diameter of 28, 46, and 76 nm was measured in Van der Werff et al. [67]. The authors of Ref. [68] argue that results of these measurements are well described by the formula (23). At the same time, the experimental data of [30] obtained for an ethylene glycol–CuO suspension with an average particle diameter of 12 nm do not fit this theory.

Dependences of the effective viscosity coefficient on the volume fraction for two nanofluids: ethylene glycol–Al_2O_3 and water–Al_2O_3 with an average particle size of about 28 nm were obtained in Ref. [69]. The results cited above, however, are so different that it is not possible to establish any correlation among them.

The viscosity of water + Al_2O_3 nanoparticle nanofluids was studied by Pak and Cho [39], who showed that the viscosity of nanosuspensions was three times higher viscosity of water at low particle concentrations. Masoumi et al. [32], investigating the dependence of the viscosity coefficient of the same nanofluid on

the volume concentration of nanoparticles of diameter 13, 28, and 36 nm, found that the effect of the particles increased with decreasing particle size. Thus, for a volume fraction $\phi = 2\%$, an increase in viscosity is about 12% for $d = 36$ nm and about 100% for $d = 13$ nm.

Attempts to describe the experimental data with any theoretical formulas such as (10) have been unsuccessful. This is due to several factors. First, in experiments, it is not possible, in principle, to obtain a monodisperse nanofluid. There is always a certain particle size distribution which cannot be controlled in practice. Furthermore, the nanofluid rheology can change with increasing nanoparticle concentration. For example, in a study [30] of the viscosity of an ethylene glycol suspension with CuO particles with sizes of 10–30 nm, a sharp increase in the effective viscosity coefficient was observed beginning at a volume fraction of about 0.002, which is obviously not described by a formula of the type (10). It should be noted again, however, that in those experiments, the nanoparticle size varied over a wide range.

Finally, a recent study [8] of the effect of nanoparticle shape on effective viscosity gave a fairly reasonable result: Al_2O_3 nanorods increased the viscosity to a greater extent than spherical particles at the same volume fraction.

In the absence of reliable experimental data, molecular dynamics simulation methods have become an extremely important tool for studying viscosity. These methods make possible an ideal experiment with controllable nanoparticle size, concentration, etc. However, there are few studies in this direction. The reason for this is the extreme complexity of the corresponding calculations. Simulation of the viscosity of real nanofluids even with small particles requires tens and even hundreds of thousands of molecules. In addition, such calculations are very time consuming since we deal with a system with very different relaxation times. The kinetic theory of gas nanosuspensions, briefly considered in the second section of this paper, and available experimental data show that the transfer properties of nanofluids depend significantly not only on the volume concentration of particles but also on their size, mass, and possibly other parameters. This is also indirectly supported by the results of MD simulations of molecular mixtures with markedly different masses (see Ref. [36]). In our work (Rudyak, Belkin and Egorov 2008), we showed that, for a fixed volume concentration and size of nanoparticles, the viscosity of nanofluids is the higher the greater the nanoparticle mass. This is illustrated in Fig. 16, which gives the dependence of the normalized viscosity coefficient of a nanofluid on the volume concentration of nanoparticles of size $D/d = 3$ at various ratios of the nanoparticle mass M and to the molecule's mass m.

An important fact is that Einstein's theory does not describe the behavior of the effective viscosity of nanosuspensions even at low concentrations of nanoparticles. The dotted line in Fig. 16 corresponds to the formula (23). It is coincided with molecular dynamics data only for this single value of the mass ratio. The data presented in Fig. 17 provide an understanding of the nature of the dependence of the viscosity coefficient on the nanoparticle diameter. The figure gives the viscosity coefficients for various diameter ratios D/d. At low nanoparticle

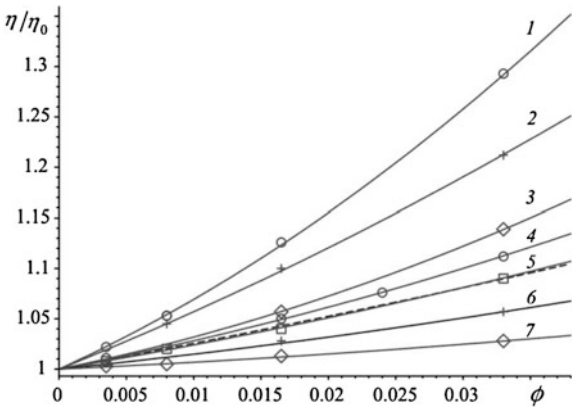

Fig. 16 Viscosity coefficient of suspensions versus nanoparticle volume fraction. Curves 1, 2, 3, 4, 5, 6, and 7 correspond to mass ratios $M/m = 500$, 300, 150, 100, 50, 10, and 0.5, respectively. *Labels* correspond to simulation data, the *dashed curve* is the approximation (23)

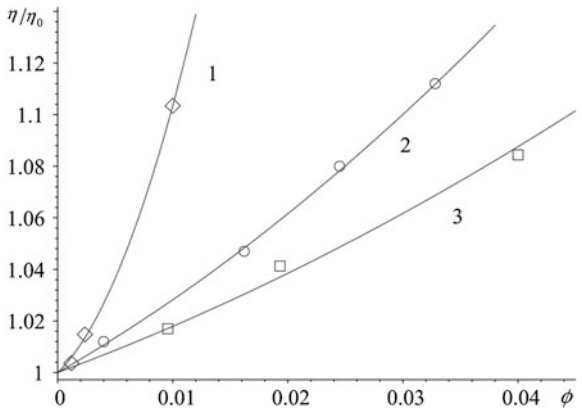

Fig. 17 Viscosity coefficient versus volume fraction of nanoparticles of various diameters. Curves 1, 2, 3 correspond to diameter ratios $D/d = 2$, 3, and 4, respectively. *Labels* correspond to simulation data

concentrations, the increase in the viscosity coefficient is almost independent of the particle size. However, as the volume concentration of nanoparticles is increased, the viscosity coefficient of nanosuspensions with smaller particles becomes much higher than that of nanosuspensions with large particles. Thus, for example, at a 2% volume concentration of particles, the viscosity coefficients of nanosuspensions with $D/d = 2$ and 4 differ by almost 40%.

The dependence of the viscosity coefficient on the volume fraction of nanoparticles is described by a quadratic function of the form

$$\eta = \eta_0\left[1 + k_1(R, M)\phi + k_2(R, M)\phi^2\right], \tag{24}$$

if only these volume fractions are not too great. The coefficients of this correlation are functions of both size and mass of nanoparticles. Thus, an important criterion determining the increase in the effective viscosity coefficient of nanosuspensions is the mass density of the nanoparticle material ρ_p. At least, for not too large particles, this dependence is linear. Therefore, the following correlation can be proposed by Rudyak et al. [57]

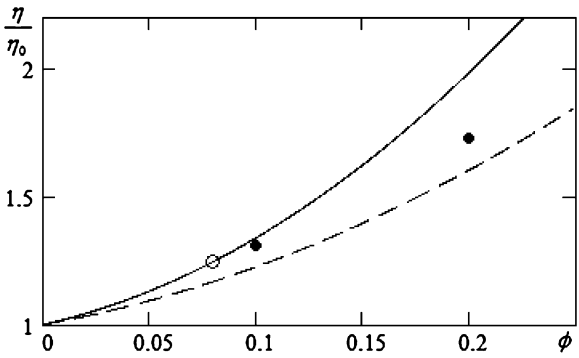

Fig. 18 Comparison of the experimental data of [67] (*filled circles*) and [40] (*open circles*) with correlation (25). The *solid* and *dashed curves* correspond to $\tilde{\rho} = 1.85$ and $\tilde{\rho} = 0.77$, respectively

$$\eta(\phi) = \eta_0[a(\phi) + b(\phi)\tilde{\rho}],$$
$$a(\phi) = 1 + 1.25\phi + 2.1\phi^2,\ b(\phi) = 0.32\phi + 7.2\phi^2, \tag{25}$$

where $\tilde{\rho} = \rho_p/\rho$.

In contrast to formula (24), correlation (25) depends on the volume fraction of nanoparticles and their material density. Therefore, it can be used to predict the viscosity of nanofluids with any size of nanoparticles. As an example, Fig. 18 gives a comparison of the experimental data obtained by Van der Werff et al. [67] (filled circles, $\tilde{\rho} = 1.85$) and Papir and Krieger [40] (open circle, $\tilde{\rho} = 0.77$) and the results obtained using formula (25). The agreement between the experimental and MD data is not poor, but the accuracy of correlation (25) can be improved by increasing the number of calculations. In addition, the accuracy of determination of the viscosity coefficient by correlation (25) depends on the accuracy of the density ratio $\tilde{\rho}$ (in particular, the accuracy of the molecule density determination).

5.2 *Effective Thermal Conductivity of Nanofluids*

Interest in the effective thermal conductivity of nanofluids arose about two decades years ago, stimulated by the need to considerably increase the thermal conductivity of fluids in the microchannels used to cool computer boards, various thermal microcells, and other microelectromechanical systems (MEMS). It was clear that the addition of relatively large (with characteristic sizes of the order of microns) metal particles would be impossible because of their sedimentation and extreme erosion susceptibility. On the other hand, miniaturization and use of nanofluids facilitates the problem of heat transfer and removal. In microsystems, the surface area to volume ratio is increased, nanoparticles do not produce obstructions to flow, and use of nanofluids allows heat to be removed at room temperature of the coolant.

The first experimental studies of heat transfer in nanofluids [9, 10, 33, 70] showed that the thermal conductivity of suspensions with nanoparticles of metals

and their oxides in water and ethylene glycol exceeded the thermal conductivity of pure fluids by tens of percent at a volume concentration of particles of the order of several percent. There have been attempts to compare experimental results with available theoretical models for coarse disperse fluids, first of all, with Maxwell theory [34], which predicts the following relation between the effective thermal conductivity of a suspension λ and the volume concentration of particles ϕ

$$\lambda = \lambda_0 \left[1 + \frac{3(1-\varpi)\phi}{1 + 2\varpi - \phi(1-\varpi)} \right], \tag{26}$$

where $\varpi = \lambda_0/\lambda_p\, \lambda_0$, λ_p are the thermal conductivities of the fluid and dispersed particles. Formula (26) was obtained for spherical particles using a hydrodynamic approximation. Later, it was extended to the case of nonspherical particles [21]. The formation of chains of particles is taken into account by Hashin and Shtrikman theory [23], which gives the following inequality for the effective thermal conductivity

$$\lambda_0 \left(1 + \frac{3(1-\varpi)\phi}{1 + 2\varpi - \phi(1-\varpi)} \right) \le \lambda \le \lambda_p \left[1 - \frac{3(1-\phi)(1-\varpi)}{3 - (1-\varpi)\phi} \right]. \tag{27}$$

Heat losses on the nanoparticle surface can also be taken into account [38]. The correlations obtained by the above-mentioned authors extend the range of applicability of the Maxwell formula. Do they describe nanofluids? The authors of a recently published review [26] believe that most of available experimental data fall in the range given by inequality (27). However, it should be borne in mind that the theory of Hashin and Shtrikman hardly applies directly to nanofluids. Of course, in usual nanofluids, there is always a certain particle size distribution, but particles of different sizes cannot be modeled by chains of small particles. Coagulation promotes the formation of coupled states that can be modeled by chains, but this is only one of realizable opportunities. In addition, chains of particles considerably increase the thermal conductivity if they are oriented in a particular manner. In nanofluids, however, their orientation is random, and this should lead to a certain decrease in the integral effect.

Available experimental data are contradictory. There are data that obviously do fit (27) (see, for example, [37, 72, 73]. Data on increased thermal conductivity of nanofluids with gold particles cannot be described by relations (26) and (27) because at very low concentrations of nanoparticles (about 0.1%), the increase in thermal conductivity reached 10% (see Ref. [26]).

Next, experimental data show (though not systematically) that the effective viscosity of a nanofluid depends greatly on the nanoparticle size and material (which is completely ignored in theories (26), (27)) and the temperature of the carrier fluid. There are data [29, 30, 33, 71] indicating that the smaller the nanoparticle diameter, the greater the increase in thermal conductivity. Dependences of thermal conductivity on the material and temperature of the carrier fluid are of course included in the indicated formulas, but they do not describe experimental findings.

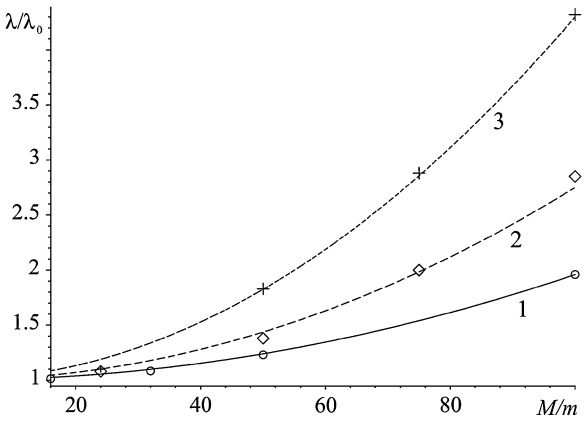

Fig. 19 Effective thermal conductivity versus mass ratio. *Curves 1*, *2*, *3* correspond to $\phi = 0.12, 0.24,$ and 0.48%, respectively

As in the case of the viscosity of nanofluids, obtaining objective information on their thermal conductivity requires systematic molecular dynamic simulations, along with further experimental studies. Here it is also necessary to investigate the effect of nanoparticle size and the ratio of the nanoparticle mass to the mass of a carrier-fluid molecule.

The first results obtained in our studies indicate that, for a fixed nanoparticle size, the thermal conductivity of a nanofluid, similarly to the viscosity coefficient, depends significantly on the ratio of the nanoparticle mass to the mass of a molecule of the carrier fluid. This dependence is nonlinear and is illustrated in Fig. 19, which gives calculation results for three volume concentrations of nanoparticles; curves $1 \div 3$ correspond to the same concentration and were obtained by square-law approximation of calculated data.

Here $nd^3 = 0.707$, $D/d = 3$. Each curve in Fig. 19 is constructed for a fixed radius, and these dependences can therefore be reduced to dependences on material density. In contrast to the viscosity coefficient, which increases linearly with increasing density, the thermal conductivity of nanofluids increases in proportion to the square of the density ratio: $(\lambda - \lambda_0)/\lambda_0 \sim (\rho_p/\rho)^2$. That high increase in the thermal conductivity of suspensions even at $\varphi \leq 1\%$ is due to the high density of the particle material. This, however, is in agreement with the results of experiments, in which the material density was also high [29].

6 Conclusions

Wide application of nanofluids in various applications requires the development of appropriate theory. The present review of research on the transfer processes highlights the possible paths for optimization of the efforts involved. Today it can be argued that the kinetic theory of rarefied gas nanosuspensions has been generally constructed. There is a need for systematic studies of the thermal conductivity of such media. Success in the construction of the kinetic theory is

related, in particular, to the use of the potential (4). Of course, a nanoparticle is a complex object and its interaction with a molecule can generally be inelastic. Here the situation is similar to molecular interaction, which is usually also inelastic. During molecular collision, internal degrees of freedom are excited and the energy of translation is redistributed over all possible channels. Nevertheless, by using the intermolecular potential, it is possible to calculate the transfer coefficients and describe the corresponding processes. In some cases, it is necessary to introduce some corrections to take into account the contribution of rotational degrees of freedom, etc. It is possible that something like that will be required for systems with the potential (4). Nevertheless, this potential can be treated as an effective four-parameter potential with constants C_i, a_i [see formula (4)], which should be determined from experimental data. This is what is done for molecular systems. In this case, at least, part of inelastic processes will be taken into account.

Diffusion of nanoparticles in dense gases and liquids is adequately modeled by molecular dynamics methods. There are several ways, using nonequilibrium statistical mechanics, to construct theory that leads to the autocorrelation velocity function (21) of nanoparticles. However, in the interpretation of experimental data, the Einstein–Stokes formula (5) or its analogs taking into account slip, nonsphericity, etc. should be used with care. Generally, this formula does not describe nanoparticle diffusion.

In the interpretation of experimentally measured effective viscosity of nanosuspensions, particular attention should be paid to determining the size and characteristics of nanoparticles. In practice, of course, it is not possible to produce a monodisperse nanofluid. This is not a big problem per se. However, the correct interpretation of data requires information on the nanoparticle size distribution. In addition, it should be born in mind that the use of various surfactants to prevent the coagulation of nanoparticles significantly changes their characteristics. This is especially important for small nanoparticles. In this case, the surfactant film thickness is comparable to the particle radius, and this film considerably changes the characteristics of the particle, for example, its density.

Acknowledgments This work was supported in part by the Russian Foundation for Basic Research (Grant No. 10-01-00074) and the Federal Special Program of Russian Federation "Scientific and scientific-pedagogical personnel of innovative Russia in 2009-2013" (Project No. P230).

References

1. Alder, B.J., Wainwright, T.E.: Decay of the velocity autocorrelation function. Phys. Rev. A. **1**, 18–21 (1970)
2. Baron, P.A., Willeke, K. (eds.): Aerosol Measurement: Principles, Techniques, and Applications. Wiley, New York (2001)
3. Batchelor, G.K.: The effect of Brownian motion on the bulk stress in a suspension of spherical particles. J. Fluid Mech. **83**, 97–117 (1977)

4. Bezmelnitsyn, V.N., Eletsky, A.V., Okun M.V.: Fullerenes in solutions. Phys. Usp. **41**, 1091–1114 (1998)
5. Chapman, S., Cowling, T.G.: The Mathematical Theory of Non-Uniform Gases. Cambridge University Press, Cambridge (1952)
6. Chen, S.H., Davis, H.T., Evans, D.F.: Tracer diffusion in polyatomic liquids. II. J. Chem. Phys. **75**, 1422–1426 (1981)
7. Chen, S.H., Davis, H.T., Evans, D.F.: Tracer diffusion in polyatomic liquids. III. J. Chem. Phys. **77**, 2540–2544 (1982)
8. Christianson, R., Townsend, J.: INPBE result and analyses. http://mit.edu/nse/nanofluids/benchmark/workshop/Christianson-Townsend%20presentation.pdf (2009)
9. Eastman, J.A., Choi, S.U.S., Li, S., Thompson, L.J., Lee, S.: Enhanced Thermal Conductivity Through the Development of Nanofluids. 3–11. Materials Research Society. Fall Meeting, Boston (1998)
10. Eastman, J.A., Choi, S.U.S., Li, S., Yu, W., Thompson, L.J.: Anomalously increased effective thermal conductivities of ethylene glycol-based nanofluids containing copper nanoparticles. Appl. Phys. Lett. **78**, 718–720 (2001)
11. Einstein, A.: Über die von der molekularkinetischen Theorie der Wärme geforderte Bewegung von in ruhenden Flüssigkeiten suspendierten Teilchen. Annalen der Physik. **17**, 549–560 (1905)
12. Einstein, A.: A new determination of molecular sizes. Ann. Phys. **19**, 289–306 (1906)
13. Epstein, H.S.: In the resistance experienced by spheres in their motion through gases. Phys. Rev. **23**, 710–733 (1924)
14. Evans, D.F., Tominaga, T., Davis, H.T.: Tracer diffusion in polyatomic liquids. J. Chem. Phys. **74**, 1298–1306 (1981)
15. Felderhof, B.U.: The effect of Brownian motion on the transport properties of a suspension of spherical particles. Physika A. **118**, 69–78 (1983)
16. Ferziger, J.H., Kaper, H.G.: Mathematical Theory of Transport Processes in Gases. North-Holland Publishing Company, Amsterdam (1972)
17. Friedlander, S.K.: Smoke, Dust, Haze. Fundamentals of Aerosol Dynamics. Oxford University Press, New York (2000)
18. Gladkov, M.Yu., Rudyak, V.Ya.: Kinetic equations for a finely dispersed rarefied gas suspension. Fluid Dyn. **29**, 285–290 (1994)
19. Gladkov, M.Yu., Rudyak, V.Ya.: Kinetic equations of a finely dispersed gas suspension. Sov. Phys. Tech. Phys. **39**, 441–443 (1994b)
20. Grew, K.E., Mundy, J.N.: Thermal diffusion in some mixtures of inert gases. Phys. Fluids. **4**, 1325–1332 (1961)
21. Hamilton, R.L., Crosser, O.K.: Thermal conductivity of heterogeneous two-component. I&EC Fund. **1**, 187–191 (1962)
22. Haselmeyer, R., Holz, M., Kappes, M.M., Michel, R.H.: Translational diffusion in C_{60} and C_{70} fullerene solutions. Ber. Bunsenger Phys. Chem. **98**, 878–881 (1994)
23. Hashin, Z., Shtrikman, S.J.: A variational approach to the theory of the effective magnetic permeability of multiphase materials. Appl. Phys. **33**, 3125–3130 (1962)
24. Hirschfelder, J.O., Curtiss, Ch.F., Bird, R.B.: Molecular Theory of Gases and Liquids. Wiley, New York (1954)
25. Kato, T., Kikuchi, K., Achiba, Y.J.: Measurement of the self-diffusion coefficient of C_{60} in benzene-D_6 using ^{13}C pulsed-gradient spin echo. Phys. Chem. **97**, 10251–10253 (1993)
26. Keblinski, P., Prasher, R., Eapen, J.: Thermal conductance of nanofluids: is the controversy over? J. Nanopart. Res. **10**, 1089–1097 (2008).
27. Klimontovich, Yu.L.: Kinetic Theory of Nonideal Gases and Nonideal Plasmas. Pergamon Press, New York (1982)
28. Knutson, E.O.: History of diffusion batteries in aerosol measurements. Aerosol Sci. Technol. **31**, 83–128 (1999)
29. Kumar, D.H., Patel, H.E., Kumar, V.R., Sundararajan, T., Pradeep, T., Das, S.K.: Model for heat conduction in nanofluids. Phys. Rev. Lett. **93**, 144301-1–144301-4 (2004)

30. Kwak, K., Kim, C.: Viscosity and thermal conductivity of copper oxide nanofluids dispersed in ethylene glycol. Korea-Aust. Rheol. J. **17**, 35–40 (2005)
31. Mason, E.A., Munn, R.J., Smith, F.J.: Thermal diffusion in gases. In Bates, D.R. (ed.) Advances in Atomic and Molecular Physics. Academic Press, New York. 484 (1966)
32. Masoumi, N., Sohrabi, N., Behzadmehr, A.: A new model for calculating the effective viscosity of nanofluids. J. Phys. D. Appl. Phys. **42**, 055501-1–055501-6 (2009)
33. Masuda, H., Ebata, A., Teramae, K., Hishinuma, N.: Alteration of thermal conductivity and viscosity of liquid by dispersing ultra-fine particles (dispersions of-Al_2O_3, SiO_2, and TiO_2 ultra-fine particles). Netsu Bussei. **4**, 227–239 (1993)
34. Maxwell, J.C.: A Treatise on Electricity and Magnetism, vol. 1, 2nd edn. Clarendon Press, Oxford, pp 435 (1881)
35. Mädler, L., Friedlender, S.K.: Transport of nanoparticles in gases: overview and recent advances. Aerosol Qual. Res. **7**, 304–342 (2007)
36. McPhie, M.G., Daivis, P.J., Snook, I.K.: Viscosity of a binary mixture: approach to the hydrodynamic limit. Phys. Rev. E. **74**, 021301-1–021301-13 (2006)
37. Murshed, S. M. S., Leong, K. C., Yang, C.: Enhanced thermal conductivity of TiO_2-water based nanofluids. Int. J. Therm. Sci. **44**, 367–373 (2005)
38. Nan, C.-W., Birringer, R., Clarke, D.R., Gleiter, H.: Effective thermal conductivity of particulate composites with interfacial thermal resistance. J. Appl. Phys. **81**, 6692–6701 (1997)
39. Pak, B.C., Cho, Y.I.: Hydrodynamics and heat transfer study of dispersed fluids with submicron metallic oxide particles. Exp. Heat Transf. **11**, 151–170 (1998)
40. Papir, Y.S., Krieger, I.M.: Rheological studies of dispersions of uniform colloidal spheres. J. Colloid Interface Sci. **34**, 126–130 (1970)
41. Phillips, W.F.: Drug on a small sphere moving through a gas. Phys. Fluids. **18**, 1089–1093 (1975)
42. Rapaport, D.C.: The Art of Molecular Dynamics Simulation. Cambridge University Press, Cambridge (2005)
43. Rudyak, V.Ya.: Nonlocality solution of the Boltzmann equation. Sov. Phys. Tech. Phys. **40**, 29–40 (1995)
44. Rudyak, V.Ya.: Classification principles of dispersed media. J. Aerosol Sci. **27**, S271–S272 (1996)
45. Rudyak, V.Ya.: The kinetic equations of rarefied gas suspensions. In: Rarefied Gas Dynamics XXI. Proceedings of 21st International Symposium on RGD, vol. 1, pp 271–278. Gépadués-Éditions, Toulouse (1999)
46. Rudyak, V.Ya.: Statistical Aerohydromechanics of Homogeneous and Heterogeneous Media, vol. 1. Kinetic Theory. Civil Engineering. University Press, Novosibirsk (in Russian) (2004)
47. Rudyak, V.Ya.: Statistical Aerohydromechanics of Homogeneous and Heterogeneous Media, vol. 2. Hydromechanics. Civil Engineering University Press, Novosibirsk (in Russian) (2005)
48. Rudyak, V.Ya.: Kinetic theory of nanoparticles transport and relaxation processes in gases and liquids. In: Proceedings of 25th International Symposium on Rarefied Gas Dynamics, pp 39–46. Publ. House of SB RAS, Novosibirsk (2007)
49. Rudyak, V.Ya., Belkin, A.A.: Nanoparticle velocity relaxation in condensed carrying medium. Tech. Phys. Lett. **29**, 560–562 (2003).
50. Rudyak, V.Ya., Belkin, A.A.: Noclassical properties of molecular diffusion in liquids and dense gases. Defect Dif. Forum. **273–276**, 560–565 (2008)
51. Rudyak, V.Ya., Krasnolutskii, S.L.: The interaction potential of carrier gas molecules with dispersed particles. In: Rarefied Gas Dynamics XXI. Proceedings of 21st Interantional Symposium on RGD, vol. 1, pp 263–270. Gépadués-Éditions, Toulouse (1999)
52. Rudyak, V.Ya., Krasnolutskii, S.L.: Kinetic description of nanoparticles diffusion in rarefied gases. Russ. Phys. Dokl. (USA). **46**, 1336–1339 (2001)
53. Rudyak, V.Ya., Krasnolutskii, S.L.: Diffusion of nanoparticles in a rarefied gas. Tech. Phys. **47**, 807–813 (2002).

54. Rudyak, V.Ya., Krasnolutskii, S.L.: About viscosity of rarefied gas suspensions with nanoparticles. Dokl. Phys. **48**, 583–586 (2003)
55. Rudyak, V.Ya., Krasnolutskii, S.L.: Effective viscosity coefficient for rarefied nano gas suspensions. Atmos. Ocean Opt. **17**, 468–475 (2004)
56. Rudyak, V.Ya., Krasnolutskii, S.L.: Nanoparticles thermodiffusion in gases. In: Proceedings of Novosibirsk Civil Engineering University, vol. 12, pp 54–66 (in Russian) (2009)
57. Rudyak, V.Ya., Belkin, A.A., Egorov, V.V.: On the effective viscosity of nanosuspensions. Tech. Phys. **54**, 1102–1109 (2009)
58. Rudyak, V.Ya., Belkin, A.A., Ivanov, D.A., Egorov, V.V.: On the nonclassical diffusion of molecules of liquid and dense gases. Dokl. Phys. **52**, 115–118 (2007)
59. Rudyak, V.Ya., Belkin, A.A., Krasnolutskii, S.L.: Statistic theory of nanoparticle transport processes in gases and liquids. Thermophys Aeromech. **10**, 489–507 (2005)
60. Rudyak, V.Ya., Belkin, A.A., Tomilina, E.A.: Force acting on nanoparticle in fluid. Tech. Phys. Lett. **34**, 76–78 (2008)
61. Rudyak, V.Ya., Dubtsov, S.N., Baklanov, A.M.: Temperature dependence of the diffusion coefficient of nanoparticles. Tech. Phys. Lett. **34**, 519–521 (2008)
62. Rudyak, V.Ya., Dubtsov, S.N., Baklanov, A.M.: Measurements of the temperature dependent diffusion coefficient of nanoparticles in the range of 295–600 K at atmospheric pressure. J. Aerosol Sci. **40**, 833–843 (2009)
63. Rudyak, V.Ya., Krasnolutskii, S.L., Nasibulin, A. G., Kauppinen, E. I.: About measurement methods of nanoparticles sizes and diffusion coefficient. Dokl. Phys. **47**, 758–761 (2002)
64. Rudyak, V.Ya., Kharlamov, G.V., Belkin, A.A.: The velocity autocorrelation function of nanoparticles in hard-sphere molecular system. Tech. Phys. Lett. **26**, 553–556 (2000)
65. Rudyak, V.Ya., Kharlamov, G.V., Belkin, A.A.: Diffusion of nanoparticles and macromolecules in dense gases and liquids. High Temp. **39**, 264–271 (2001)
66. Tominaga, T., Tenma, S., Watanabe, H (1996) Diffusion of cyclohexane and cyclopentane derivatives in some polar and non-polar solvents. J. Chem. Soc. Faraday Trans. **92**, 1863–1867
67. Van der Werff, J.C., De Kruif, C.B., Blom, C., Mellema, J.: Linear viscoelastic behaviour of dense hard-sphere dispersions. Phys. Rev. A. **39**, 795–807 (1989)
68. Verberg, R., De Schepper, I.M., Cohen, E.G.D.: Viscosity of colloidal suspensions. Phys. Rev. E. **55**, 3143–3158 (1997)
69. Weeks, J.D., Chandler, D., Anderson, H.C.: Role of repulsive forces in determining the equilibrium structure of simple liquids. J. Chem. Phys. **54**, 5237–5247 (1971)
70. Wang, X., Xu, X., Choi, S.U.S.: Thermal conductivity of nanoparticle-fluid mixture. J. Thermophys. Heat Transf. **13**, 474–480 (1999)
71. Xuan, Y., Li, Q., Hu, W.: Aggregation structure and thermal conductivity of nanofluids. AIChE J. **49**, 1038–1043 (2003)
72. Zhang, X., Gu, H., Fujii, M.: Experimental study on the effective thermal conductivity and thermal diffusivity of nanofluids. Int. J. Thermophys. **27**, 569–580 (2006)
73. Zhu, H., Zhang, C., Liu, S., Tang, Y., Yin, Y.: Effects of nanoparticle clustering and alignment on thermal conductivities of Fe_3O_4 aqueous nanofluids. Appl. Phys. Lett. **89**, 0231231–0231233 (2006)
74. Zubarev, D.N.: Nonequilibrium Statistical Thermodynamics. Consultants Bureau, New York (1974)

Part II
Nanocomposites

Nanocomposite Materials from Theory to Application

H. R. Rezaie, A. Shokuhfar and F. Arianpour

Abstract The idea of the limiting size scale of a miniaturized technology is fundamentally interesting, appealing for several reasons. As sizes are limited to the atomic scale, the relevant physical laws change from the classical to the quantum-mechanical laws of nanophysics. A clear distinction between nanostructures and microstructures is given here arbitrarily using length measurements. Nanostructures are defined according to their geometrical dimensions. This definition addresses technical dimensions, induced by external shaping processes; with the key feature of shaping process, the orientation and the positioning are known in accordance to an external reference system, such as the geometry of a substrate. A narrow definition of nanostructures is that they include structures with at least two dimensions below 100 nm. An extended definition also suggests structures with one dimension below 100 nm and a second dimension below 1 μm. Following this definition, ultrathin layers with lateral submicrometer structure sizes are also considered as nanostructures

H. R. Rezaie (✉) · F. Arianpour
School of Metallurgy and Materials Engineering,
Iran University of Science and Technology, Tehran, Iran
e-mail: hrezaie@iust.ac.ir

F. Arianpour
e-mail: arianpour@iust.ac.ir

A. Shokuhfar
Mechanical Engineering Faculty, K. N. Toosi University of Technology,
Tehran, Iran
e-mail: shokuhfar@kntu.ac.ir

Adv Struct Mater (2013) 4: 171–232
DOI: 10.1007/8611_2012_66

Published Online: 20 November 2012

1 Introduction and Definitions

The idea of the limiting size scale of a miniaturized technology is fundamentally interesting appealing for several reasons. As sizes are limited to the atomic scale, the relevant physical laws change from the classical to the quantum-mechanical laws of nano physics [1].

A clear distinction between nanostructures and microstructures is given here arbitrarily using length measurements. Nanostructures are defined according to their geometrical dimensions. This definition addresses technical dimensions, induced by external shaping processes; with the key feature of shaping process, the orientation and the positioning is known in accordance an external reference system, such as the geometry of a substrate. This is of less importance, whether this process uses geometrical tools, media or other instruments [2].

A narrow definition of nanostructures is that they include structures with at least two dimensions below 100 nm. An extended definition also suggests structures with one dimension below 100 nm and a second dimension below 1 μm. Following this definition, ultra thin layers with lateral sub-micrometer structure sizes are also considered as nanostructures [2].

Interactions between atoms, groups of atoms, ions and molecules can vary widely with respect to their intrinsic character and their strength. In order to differentiate these interactions, they were divided into classes known as bond types. These classes are well suited for a description of bonds. In contrast to classical synthetic chemistry where strong bonds are important, often the medium and weak bonds are of particular importance in nanotechnology [2].

There are two ways of approaching the properties of nanoscale objects: the bottom-up approach and the top-down approach. According to the bottom-up approach, it consists of assembling of atoms and molecules into objects whose properties vary discretely with the number of constituent entities, and then increases the size of the object until this discretisation gives way in the limit to continuous variation. The relevant parameter becomes the size rather than the exact number of atoms contained in the object [3].

In the latter case, it considers the evolution of the properties of a sample as its size is whittled down from macroscopic toward nanometric lengths. We will examine this approach here, whilst mentioning zones of overlap and exclusion between the two approaches [3].

Considering a homogeneous solid material of compact shape and macroscopic dimensions, most of its properties will be related to its chemical composition and crystal structure. This is the case that is studied in the physics and chemistry of solids. For an object in this size, the surface atoms comprise a negligible proportion of the total number of atoms and will therefore play a negligible role in the bulk properties of the materials. Note that, however, the surface atoms will nevertheless play a predominant role in properties involving exchanges at the interface between the object and the surrounding medium [3].

The specific surface energy γ (J/m^2) could be presented as the energy produced by cleaving a crystal which causes division of the surface area thereby created. More generally, the specific surface energy can be defined as follows. In order to increase the surface area of an object by the amount "dA", e.g. through changing the shape of the object, the amount of work required to do this will be measured by: $\mathrm{d}W = \gamma \mathrm{d}A$. Here γ is the specific surface energy. In this case, the area of the object is increased by displacing atoms from the bulk to the surface. However, one could also increase the area by stretching it, i.e., keeping constant the number of surface atoms [3].

The physical properties of conventional materials may change with the size of the grains as their constituent units even becoming totally different from what is observed in the bulk solid system. Now, in case of grain size dependence, this dependence can be categorized into two related effects:

- Size effect or confinement effects:

The nanograin behaves like a kind of box, within which a specific property may or may not exist. Below a certain critical size, characteristics of the property directly and strictly depend on the grain size. This is called the size or confinement effect. The way these characteristics vary as a function of size, is often non-monotonic.

- A surface or interface effect:

Through nanograin, the contribution of layers close to the surface occupies a more considerable and substantial role in the overall behavior of the material as the grain size decreases. The surface energy gradually becomes the dominating contributor to the total energy of the material. Such a property will evolve monotonically with size and can be treated within the framework of thermodynamics [3].

There are many examples of phase transitions occurring while the characteristic dimensions of a material go beyond a certain critical value. More interestingly, such transitions are not restricted to any particular type of material.

The grain size dependence of a phase transition in a ceramic can be normally illustrated by the monoclinic–tetragonal transition occurring in zirconia. This property has been known and exploited for a long period of time. At standard atmospheric pressure and room temperature, zirconia crystallizes in a monoclinic (low temperature) structure, whereas at high temperature, above 1100–1150 °C, its crystal structure tends to be tetragonal. If ZrO_2 crystallizes in the form of 'crystals' with order of 10 nm, it is a tetragonal form that is stable at room temperature. The transition temperature, somewhere between 1100 and 1150 °C for micrometric crystals becomes lower as the dimensions of the nanocrystals decrease [3].

Another situation where the grain size dependence has been established is in the case of the Verwey transition, first observed in 1939 by the discontinuous change in conductivity it causes. This transition occurs in magnetite Fe_3O_4, with the so-called spinel crystal structure. Experiments have also demonstrated a remarkable difference between the temperature predicted for large grains and that

observed for nanometric grains (a difference of more than 70 K). It would thus reveal that the Verwey transition proves another example of grain-size-dependent phase transitions [3].

An example of a grain-size-dependent phase transition in metals is evident in case of Nickel. In the bulk solid, the structure of the element is face centered cubic (FCC). However, recent experiments have brought about to prove a grain size dependent phase transition of small Ni nanoparticles, chemically synthesized in solution. Indeed for diameters less than 4 nm, the structure still remains crystalline, but it becomes hexagonal close packed (HCP) rather than FCC. In the bulk materials, an HCP structure is metastable, although it can be obtained in thin films in certain conditions. It should also be noted that the melting temperature of various metals are known to be dependent on the grain size [3].

2 Nanomaterials

2.1 Introduction

During the last decades, not only nanotechnology has evolved from an imaginary concept into a promising and fast-growing field of science, but has found its way into our everyday life [4]. You have undoubtedly heard of sunscreens or refrigerators featuring some tiny particles which though can't be seen, but are supposed to improve your state of health or the quality of the product. That is true; at the heart of nanotechnology, lie so vast and versatile, nanomaterials. These are no new class of materials, but the same ones used for so many years by humans, manipulated at the finest levels by means of nanotechnology. Today, we can engineer the finest building blocks of materials, i.e., to move single atoms and molecules and place them in the desired locations, to achieve an improved quality in one or more characteristic properties of that material and create the so called "Nanostructured materials" [5]. Nanostructured materials include atomic clusters, layered (lamellar) films, filamentary structures, and bulk nanostructured materials.

More precisely, nanostructured materials are materials with at least one dimension in range of 1–100 nm. They consist of atoms of elements or clusters of mixed elements, all packed together to form a nanoparticle or at a larger scale, a bulk nanostructured material with nanosized crystallites [4].

The type of atoms and their arrangement, i.e., composition and structure, are the key elements which determine the properties of a material. However, when the dimensions become smaller than a certain size, then the size effects also influence the material properties. As discussed above, here, the size of nanoparticle or the crystallite size is equal or smaller than a characteristic length concerning a certain property. The other reason for extraordinary properties of nanostructured materials is the high surface to volume ratio (A/V); that is, the presence of a large fraction of atoms at surfaces or interfaces. This factor indicates that the inter-atomic forces

and chemical bonds play an important role in the behavior of material. In polycrystalline nanostructures, for example, more than half of the atoms could be located in grain boundaries [5].

2.2 Metals

There are many routes and techniques introduced, developed and applied for fabricating and synthesizing nanostructured metals, elemental or alloying systems. Metals, as their solid physics interestingly proves, due to their special bodings, exhibit specific attributes such as high thermal and electrical conductivity. So most of the daily affairs are directly connected with application of metallic and alloying materials, hence myriads of attempts have been always dedicated to improve and develop the properties of them. For this goal, nanostructured metals and alloys and, metal matrix nanocomposites, nanofilms, nanolayers, nanorods and nanotubes of metals have been synthesized. Here, two methods for fabrication and synthesizing nanostructured and nanoparticle metallic materials are introduced [5].

2.2.1 Photo Lithography

Typical photolithographic process consists of producing a mask carrying the requisite pattern information and subsequently transferring that pattern, using some optical technique into a photoactive polymer or photo resist (or simply resist). There are two basic photolithographic approaches: (i) shadow printing, which can be rather divided into contact printing (or contact-mode printing), and proximity printing, and (ii) projection printing. The terms "printing" and "photolithography" are used interchangeably in the literature. Figure 1 outlines the basic steps of the photolithographic process, in which the resist material is applied as a thin coating over some base and subsequently exposed in an image-wise fashion through a mask, such that light strikes selected areas of the resist material. The exposed resist is then subjected to a development step. Depending on the chemical nature of the resist material, the exposed areas may be rendered more soluble in some developing solvent than the unexposed areas, thereby producing a positive tone image of the mask. Conversely, the exposed areas may be rendered less soluble, producing a negative tone image of the mask. The effect of this process is to produce a three-dimensional relief image in the resist material that is a replication of the opaque and transparent areas of the mask. The areas of resist that remain following the imaging and developing processes are used to mask the underlying substrate for subsequent etching or other image transfer steps. The resist material resists the etchant and prevents it from attacking the underlying substrate in those areas where it remains in place after development. Following the etching process, the resist is removed by stripping to produce a positive or negative tone relief image in the underlying substrate. Diffraction sets the limit of the

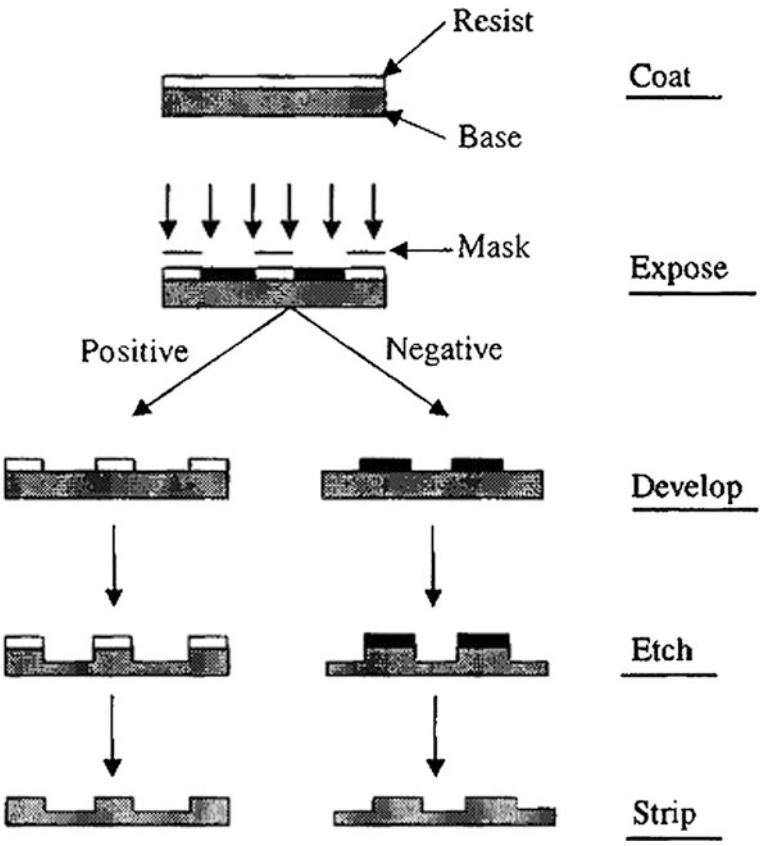

Fig. 1 Schematic representation of the photolithographic process sequences, in which images in the mask are transferred to the underlying substrate surface [6]

maximum resolution or the minimum size of the individual elements by photolithography, which can be obtained [6].

2.2.2 Synthesis of Metallic Nanoparticles

Reduction of metal complexes in dilute solutions is the general method in the synthesis of metal colloidal dispersions, and a variety of methods have been developed to initiate and control the reduction reactions. The formation of monosized metallic nanoparticles is achieved in most cases by a combination of a low concentration of solute and polymeric monolayer adhered onto the growth surfaces. Both a low concentration and a polymeric monolayer would hinder the diffusion of growth species from the surrounding solution to the growth surfaces, so that the diffusion process is likely to be the rate limiting step of subsequent growth of initial nuclei, resulting in the formation of uniformly sized nanoparticles. In the synthesis

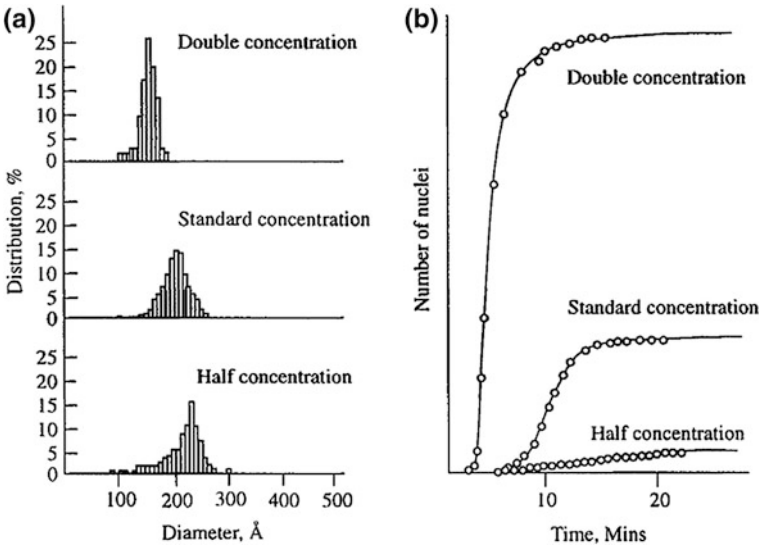

Fig. 2 **a** Particle size distribution curves of gold sol prepared at different concentrations. **b** Nucleation rate curves for gold sols prepared at different concentrations [6]

of metallic nanoparticles, or more specifically speaking, metallic colloidal dispersion, various types of precursors, reduction Reagents, other chemicals, and methods were used to promote or control the reduction reactions, the initial nucleation and the subsequent growth of initial nuclei. The precursors include: elemental metals, inorganic salts and metal complexes, such as, Ni, Co, $HAuCl_4$, H, PtCl, RhCl and $PdCI_2$. Reduction reagents includes: sodium citrate, hydrogen peroxide, hydroxylamine hydrochloride, citric acid, carbon monoxide, phosphorus, hydrogen, formaldehyde, aqueous methanol, sodium carbonate and sodium hydroxide. Examples of polymeric stabilizers include polyvinyl alcohol (PVA) and sodium polyacrylate. Colloidal gold has been studied extensively for a long time. In 1857 Faraday published a comprehensive study on the preparation and properties of colloidal gold. A variety of methods have been developed for the synthesis of gold nanoparticles, and among them, sodium citrate reduction of chlorauric acid at 100 °C was developed more than 50 years ago and remains the most commonly used method. The classical (or standard) experimental conditions are as follows. Chlorauric acid dissolves into water to make 20 ml very dilute solution of $\sim 2.5 \times 10^4$ M. Then 1 ml 0.5 % sodium citrate is added into the boiling solution. The mixture is kept at 100 °C till color changes, while maintaining the overall volume of the solution by adding water. Such prepared colloidal sol has excellent stability and uniform particle size of 20 nm in diameter. It has been demonstrated that a large number of initial nuclei formed in the nucleation stage would result in a larger number of nanoparticles with smaller size and narrower size distribution. Figure 2 compares the size and size distribution of gold nanoparticles and the nucleation rates when the colloidal gold was prepared at different concentrations [6].

2.3 Ceramics

Currently considerable interest in nanocrystalline oxide materials exists owing to their unusual properties. Decreasing particle size results in some remarkable phenomenon. It has been found as particle becomes smaller it leads to:

- Higher catalytic activity (Pt/Al_2O_3).
- Higher mechanical reinforcement (carbon black in rubber).
- Higher electrical conductivity of ceramics (CeO_2).
- Lower the electrical conductivity of metals (not in general but: Cu, Ni, Fe, Co, and Cu alloys).
- Higher photocatalytic activity (TiO_2).
- Higher luminescence of semiconductors.
- Higher blue-shift of optical spectra of quantum dots.
- Higher hardness and strength of metals and alloys.
- Superparamagnetic behavior of magnetic oxides.

Unusual optical and electrical properties in nanostructured materials take place due to a phenomenon known as quantum confinement. The large surface area to volume ratio of nanomaterials leads to their use as catalysts. Excellent sintering characteristics of these fine powders are also useful in ceramics and composites. Dispersion of minute amounts of ceramic particles in various fluids causes the production of corrosion resistant coatings and thin films [7].

The impetus and the ultimate goal in processing of ceramic and oxide materials is to control physical and chemical variability by the assemblage of uniquely homogeneous structures, nanosized second phases, controlled surface compositional gradients, and unique combinations of dissimilar materials to achieve desired properties. Significant improvements in environmental stability and performance should be obtained from such nanoscale or molecular design of materials.

Oxide materials are usually prepared by solid-state reactions, i.e., either by the high temperature method or by precipitation from solution and subsequent decomposition. A variety of metal oxides, with simple or complex compositions are prepared by the conventional ceramic methods. This involves the mixing of constituent metal oxides, carbonates and etc., and their repeated heating and grinding. These methods are used in both laboratory and industrial scale. However, there is an increasing demand for alternate routes of the synthesis of oxide materials that give superior properties when compared with those available from conventional methods. It should not be construed that conventional methods are substandard in any way; they are still used in the industrial production of several oxide materials [7].

Nonuniform powder compositions make reproducible component fabrication difficult because of chemical inhomogeneity and voids in microstructure. Greater purity and homogeneity from novel methods can lead to improved physical properties. Soft chemical routes are now increasingly becoming important to prepare a variety of oxides including nanocrystalline oxide materials. These approaches make it possible the use of simple chemical reactions like co-precipitation, sol–gel, ion

exchange, hydrolysis, acid leaching, and so on, at considerably low temperatures compared to the conventional ceramic methods. Use of precursors, intercalation reactions, electrochemical methods, hydrothermal process, and self-propagating high temperature synthesis (SHS) are some of the other contemporary methods. Although SHS has been successfully used to make non-oxide materials, its application for synthesis of oxide materials was delayed due to economic reasons. Furthermore, it is being a solid-state method, phase purity and particle size control is not possible. Combustion process is different from pyrolysis since once ignited it does not require external heating. In the synthesis of nanomaterials by soft routes there are two approaches: (i) breaking-down and (ii) building-up processes. Solution combustion synthesis of nanocrystalline oxide materials while appearing to be a breaking-down process is in fact an integrated approach, as the desired oxide products nucleate and grow from the combustion residue [7].

2.4 Semiconductors

Semiconductors as most important materials for MEMs and NEMs are being used vastly in electronic devices, as these devices are becoming smaller. The crucial role of nanotechnology in fabricating nanosemiconductors becomes clear. Here, there are some approaches to manufacture nanosemicondutors, but the most applicable one is nanolithography which is developing fast nowadays.

Some examples of this methodology are described below. Very narrow structures have been fabricated through a combination of electron beam lithography with reactive ion etching and ion beam etching or lift-off techniques, yielding, for example, GaAs lines of 10 nm. Silicon structures with high aspect ratios (up to 7) were fabricated by masking Si surfaces with gold nanoparticles and subsequent reactive ion etching in SiC, and plasma. Using 15 nm diameter particles, Si column with a height of up to 100 nm could be achieved. Particles as small as 2 nm were still efficient etching masks [2].

Si needles with extremely high aspect ratios and very small tip diameters were fabricated by a combination of the so-called vapor liquid solid (VU) techniques with ion beam etching. Initially, silicon needles several micrometers in length but only a few micrometers in diameter were created by catalytic deposition on Si from a $SiCl/H_2$ gas mixture. In a second step, these needles were sharpened using Ar or N ions at 30 keV, resulting in tip radii as low as 2 nm. Comparable values were realized by deposition of gold particles on single silicon crystals prior to silicon wafer growth.

Silicon has been subjected to a variety of scanning probe nanolithography experiments. The preferred approach was the oxidation of Si–H surfaces or the direct oxidation of Si into the oxide for local structure fabrication. Another approach applies the direct extraction or deposition of silicon atoms. The width of STM-based, anodically oxidizedlines in silicon increases with voltage, tip current or exposure time. Similar to metals, nanostructured semiconductor materials are of

great interest for the fabrication of single electron tunneling devices. Thus free-standing nanobars of highly-doped silicon with a length of 800 nm and a cross-section of 24 × 80 nm have been fabricated. These dimensions are of great interest to single electron memory devices at room temperature [2].

2.5 Carbon

Carbon is a unique material, and can be a good metallic conductor in the form of graphite, a wide band gap semiconductor in the form of diamond, or a polymer when reacted with hydrogen. Carbon provides examples of materials showing the entire range of intrinsic nanometer scaled structures from fullerenes, which are zero-dimensional nanoparticles, to carbon nanotubes, one-dimensional nanowires to graphite, a two-dimensional layered anisotropic material, to fullerene solids, three-dimensional bulk materials with the fullerene molecules as the fundamental building block of the crystalline phase. In this section, we will briefly discuss the synthesis and some properties of fullerenes, fullerene crystals and carbon nanotubes. For more general research information about carbon science or detailed information on carbon fullerenes and carbon nanotubes, the readers are referred to excellent review articles and books, such as that by Dresselhaus and references therein [8].

Nano-objects of carbon are of particular interest in nanotechnology. They include Buckminster-fullerenes and carbon nanotubes. While the regular, spherical Buckminster fullerenes (e.g., CbOe) exhibit properties of individual single molecules with dimensions in the lower nanometer range, the carbon nanotubes represent a class of nanoobjects that combine properties of molecules with those of solid substrates, and cover a range of dimensions from several micrometers (length) down to a few nanometers (diameter). Therefore, carbon nanotubes exhibit properties of both the mesoscopic world, such as controlled single electron transport, with access to manipulations typical for micro objects. The fabrication of larger quantities of carbon nanotubes has been demonstrated [2, 9].

Carbon nanotubes are often complex structures. Multi-walled tubes reach diameters above 100 nm with hierarchies of several orders of helical structures. Beside continuous walls, spiral cross-sections are also observed. Such tubes with a certain rigidity and length are interesting objects for nanomechanics. One application is their use as ultra thin tips for scanning force microscopy that can be enhanced by subsequent chemical modification for chemical affinity scanning force microscopy. Fullerenes are not only interesting as individual nanoobjects, but also as material for structures in the medium nanometer range. Regular structures in this dimension can be realized by a self-organization process during the thermal activation of fullerene crystals. Single crystals of CG0 exhibit a photon-induced surface reconstruction that leads to periodic structures with dimensions of 30–40 nm [2, 10].

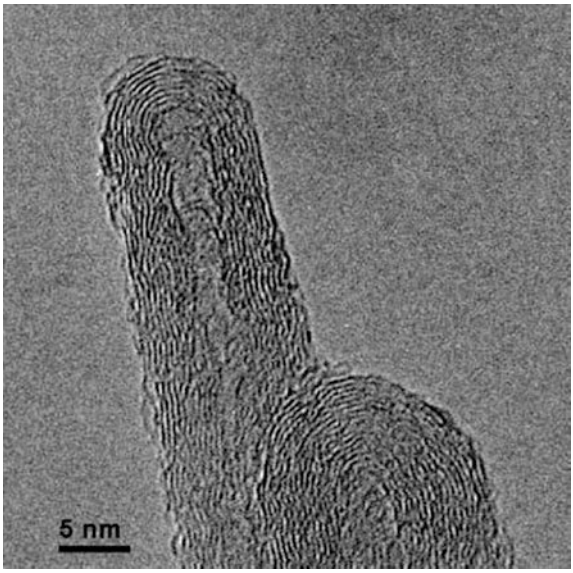

Fig. 3 Carbon nanotubes [11]

Carbon nanotubes, long thin cylinders of carbon, were discovered in 1991. These are large macromolecules that are unique for their size, shape, and remarkable physical properties. They can be thought of as a sheet of graphene (a hexagonal lattice of carbon) rolled into a cylinder. These intriguing structures have sparked much excitement in recent years and a large amount of research has been dedicated to their properties. Currently, the physical properties are still being discovered and disputed. Carbon nanotubes, (Figs. 3, 4) exist as a macromolecule of carbon, analogous to a sheet of graphite (the pure, brittle form of carbon in your pencil lead) rolled into a cylinder. Graphite looks like a sheet of chicken wire, a tessellation of hexagonal rings of carbon. Sheets of graphite in your pencil lay stacked on top on one another, but they slide past each other and can be separated easily, which is how the graphite is used for writing [11].

However, when coiled, the carbon arrangement becomes special and bonding becomes very strong. In fact, nanotubes have been known to be up to 100 times as strong as steel. These nanotubes have a hemispherical "cap" at each end of the cylinder. They are light, flexible, thermally stable, and are chemically inert. They have the ability to be either metallic or semi-conducting depending on the "twist" of the tube. Carbon nanotubes can be found in both single-walled (SWCNT) and multiwalled forms (MWCNT). Determining the elastic properties of SWNTs has been one of the most hotly disputed areas of nanotube study in recent years. On the whole, SWNTs are stronger than metallic glasses and have a much larger elastic limit than steels, and are resistant to damage from physical forces. Pressing on the tip of the nanotube will cause it to bend without damage to the tip or the whole CNT. When the force is removed, the tip of the nanotube will recover to its original state. Quantizing these effects, however, is rather difficult

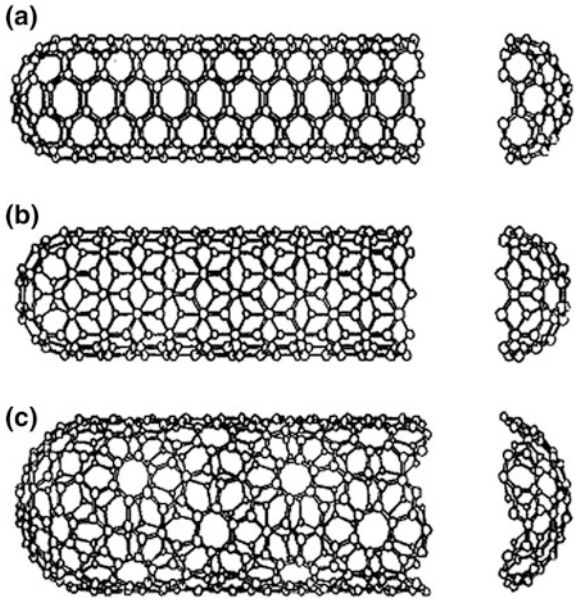

Fig. 4 Schematic models for single-wall carbon nanotubes **a** an armchair nanotube; **b** a zigzag nanotube; and **c** a chiral nanotube [8]

and an exact numerical value cannot be agreed upon. The value of Young's modulus (elastic modulus) for SWNTs lies close to 1 TPa. The maximum tensile strength is close to 30 GPa [11].

2.6 Coatings and Thin Films

Coatings and thin films are applied to structural bulk materials in order to improve the desired properties of the surface, such as wear resistance, friction, corrosion resistance and keeping the bulk properties of the material unchanged. A typical example is nitriding and carbonitriding of steel parts for engines and other surface applications at relatively low temperatures of about 500 °C in order to increase the hardness of the surface and reduce the wear rate [11].

Modern nanostructured coatings and thin films for structural and functional applications, which were developed during the past decades, are used mainly for wear protection of machining tools and for the reduction of friction in sliding parts and matting surfaces. One distinguishes between nanolayered coatings, where a few nanometers thin layers of two different materials are deposited subsequently, and nanocomposites, which are, in the optimum case, isotropic. The superhard nanocomposites, such as nc-$(Ti1 - xAl_x)N$/a-Si_3N_4 (nc- and a- stand for nano-crystalline and X-ray amorphous, respectively), show superior cutting performance as compared with conventional, state-of-the art hard coatings $(Ti1 - xAl_x)N$ that presently dominate the applications for dry machining. The costs of their

large-scale industrial production are comparable with those of the conventional coatings. Also, the heterostructures and multilayer coatings are successfully applied on industrial scale. Low-friction nanostructured coatings consisting of a hard transition-metal carbide or nitride in combination with a solid lubricant, such as diamond-like carbon (DLC), $MoSi_2$, WS_2 and others that combines with a high hardness and low friction. They are applied in a variety of bearings and sliding parts operating without liquid lubricants, which is an important advantage particularly in a hostile environment, and when the movable parts have to stop and go very frequently, e.g. in the textile industry. The recent development of nanocomposites consisting of a hard transition-metal nitride or carbide in combination with soft and ductile metal is likely to find numerous applications in a variety of machine parts. The hardness of these coatings varies between about 13 and 30 GPa depending on the composition. When deposited under energetic ion bombardment and temperatures below about 350 °C, an enhancement of the hardness up to about 50 GPa was found, in a similar way as for hard transition-metal nitrides (e.g. 100 GPa for TiAlVN and 80 GPa for TiN). However, this hardness enhancement is of a little use because, upon annealing to $\geq$500 °C, these coatings soften. Unfortunately, these nanocomposites were often confused with the thermally highly stable superhard nanocomposites prepared according to the generic design principle [11].

2.7 Mesoporous Materials

According to the classification made by IUPAC, porous solids can be grouped into three categories, depending on their pore diameter: microporous ($d < 2$ nm), mesoporous ($2 \text{ nm} < d < 50$ nm), and macroporous ($d > 50$ nm) materials. Almost all of zeolites and their derivatives are microporous, whereas surfactant template mesoporous materials and most xerogels and aerogels are mesoporous materials. In this section, we will briefly introduce these mesoporous materials and their respective synthesis techniques. This field has been extensively covered with excellent review articles [12, 13].

Though periodic mesoporous silica had been discovered in 1990, or even much earlier, this type of materials did not attract much attention until 1992, upon the publication of two groundbreaking papers by a group of Mobil's scientists describing the so-called M41S family of mesoporous silicas. Since then, research in this topic has grown so dramatically that it has developed into a separate field. Well over 3000 papers dealing with such materials have been published and a number of international meetings were also devoted to mesoporous materials [14].

Currently, periodic mesoporous silicas may bereadily prepared under an extremely wide range of conditions. Figure 5 shows schematically, the structural parameters that have been explored in the design and synthesis of periodic mesoporous materials. In addition to cationic alkyltrimethylammonium surfactants, a large variety of amphiphile molecules including cationic, anionic, neutral,

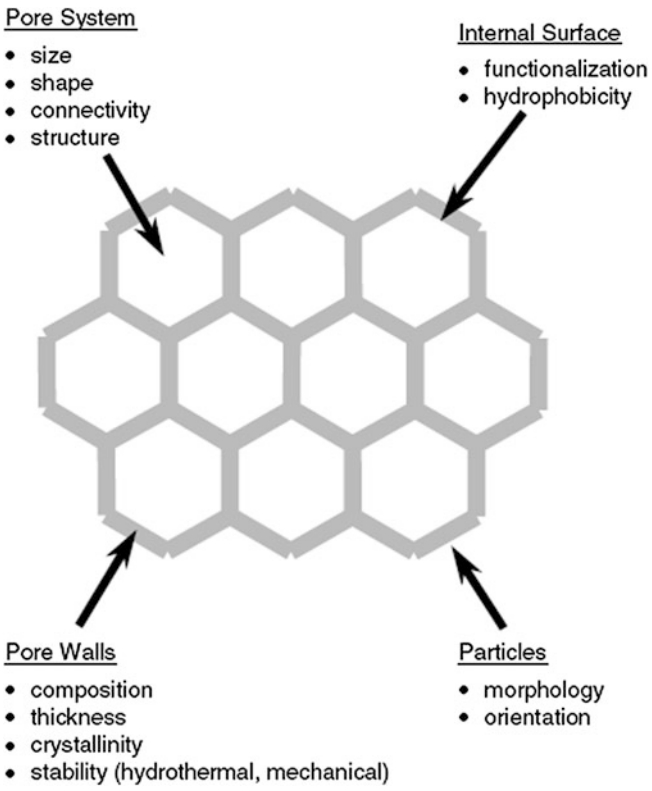

Fig. 5 Structural parameters for the design of mesostructured materials [14]

zwitterionic, bolaamphiphile, gemini anddivalent surfactants as well as many commercially available oligomers and triblockcopolymers and appropriate mixtures were found to be suitable for the preparation of periodic mesoporous silicas. The pH and temperature conditions ranged from extremely acidic to highly basic and from sub ambient to ca. 170 °C, respectively [14].

Furthermore, silica mesophases were in turn used as templates for the synthesis of a variety of other materials such as nanoporous carbons and polymers, as well as metallic and semiconductor nanowires. This extensive effort in the area of synthesis was paralleled by the development of innovative applications not only inconventional fields such as adsorption, separation and catalysis, but also in the area of advanced materials based on their often unique electronic, magnetic and optical properties, or as hosts for quantum dots and sensing species [14].

Since the discovery of the M41S family of silica mesophases, the supramolecular templating technique became a powerful method for the synthesis of mesostructured materials with narrow pore size distributions. Figure 5 lists the main experimental parameters that have been explored in the design and synthesis of such materials [14].

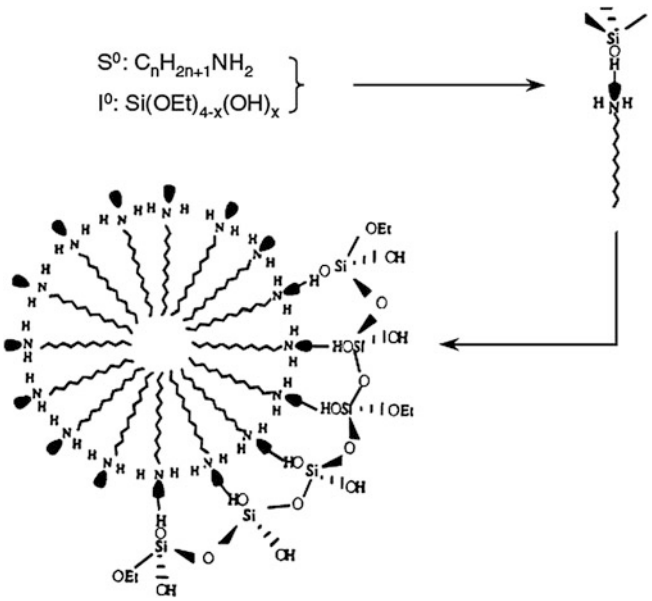

Fig. 6 Neutral templating mechanism [14]

On average, every 2 years since 1992, a new and exciting development in this field occurs. As far as the synthesis of mesostructured materials is concerned, the most important milestones are (i) generalization of synthesis strategies, (ii) framework and surface modified silicas, (iii) non-silica mesostructured materials, (iv) mesoporous organosilicates, and (v) assembly of zeolite seeds into mesoporous structures [14].

Parallel to this remarkable progress in synthesis, a wide variety of potential applications were also investigated. Surface and framework modified mesoporous silicates were tested in a wide range of catalytic processes. The recent discovery that zeolite seeds can be assembled in the presence of amphiphilic molecules into hydrothermally stable mesoporous structures will undoubtedly provide a new impetus to research in acid, redox and photo-catalytic applications using such materials. Moreover, mesoporous silicates were used as molds or nanoreactores for the synthesis of other advanced materials such as metallic or semiconducting nanowires and nanoparticles, as well as nanoporous carbons, metals and polymers [14].

Many mesostructured non-silica oxides and transition metal chalcogenides showed promising applications based on their unique electronic, magnetic or optical properties. The area of synthesis having reached a high level of maturity, it is anticipated that in the future, more attention will be focused on developing innovative applications using mesostructured materials. Figure 6 illustrates neutral templating mechanism [14].

2.8 Nano Crystalline Alloys and Magnetic Materials

A wide variety of nanocrystalline metallic alloys have been developed in recent years, manufactured by rapid solidification from the liquid, condensation from the vapor, electrodeposition and heat treatment of an amorphous precursor. These nanocrystalline alloys have produced considerable scientific interest in understanding the relationships between processing methods and circumstances, structure and properties, and considerable technological interest in use of the resulting products with a wide variety of novel mechanical, magnetic and other properties [15].

High resolution electron microscopy (HREM) has been applied to the understand structure of amorphous alloys, which are strongly dependent on their quenching history in forming the amorphous structure. Atomic medium range order (MRO) in which atomic correlation extends more than several atomic distances often exists in amorphous alloys formed by rapid-quenching and sputter-deposition. The structures of these medium range order regions can be estimated by high-resolution electron microscopy and image simulation when the medium range order sizes are as large as 1–2 nm on the basis of local lattice-fringe spacing and cross-angles of fringes. In amorphous Fe84B16 body centered cubic medium range ordered structures were identified, while in amorphous Pd77:5Cu6Si16:5 and Pd82Si18 face centered cubic medium range ordered structures were identified in the as-formed states by high-resolution electron microscopy. The high-resolution electron microscopy identification of the structure, however, becomes uncertain when the atomic arrangements of medium range order become complex. In such cases, a nanoelectron probe with a probe size of 0.5–2 nm in a field-emission transmission electron microscope (FE-TEM) helps to produce electron diffraction structure analysis of the medium range order [15].

High-strength Al- and Mg-based bulk alloys consisting of novel nanoscale non-equilibrium phases have been produced by rapid solidification and powder metallurgy techniques in Al-Ln-LTM, Al-ETM-LTM and Al-(V,Cr,Mn)-LTM (Ln¼lanthanide metal, LTM¼VII and VIII group transition metals, ETM¼IV to VI group transition metals) alloys with high Al contents of 92–95 % as well as in Mg-Zn-Y alloys with high Mg contents of 96–97 %. Excellent mechanical properties have been obtained by controlling the composition, clustered atomic configuration and stability of the super cooled liquid. The non-equilibrium structures are composed of amorphous, icosahedral quasicrystalline or long periodic hexagonal phases [15].

2.9 Quantum Dots

Nanotechnology is providing an ever increasing number of devices and structures having one, or more than one, dimension less than or equal to about 100 angstroms. The question naturally arises as to the effect of dimensional confinement on the

properties on the phonons in such nanostructures as well as the properties of the phonon interactions in nanostructures. Phonon interactions are altered unavoidably by the effects of dimensional confinement of the phonon modes in nanostructures. These effects exhibit some similarities to those for an electron confined in a quantum dot [16].

Nanoscale materials frequently show behavior which is intermediate between that of a macroscopic solid and that of an atomic or molecular system. Consider, for instance, the case of an inorganic crystal composed of few atoms. Its properties will be different from those of a single atom, but we cannot imagine that they will be the same as those of a bulk solid. The number of atoms on the surface of crystal, for instance, is a significant fraction of the total number of atoms (as discussed above), and therefore will have a large influence on the overall properties of the crystal. We can easily imagine that this crystal might have a higher chemical reactivity than the corresponding bulk solid and that it will probably melt at lower temperatures. A fundamental aspect of quantum mechanics is the particle-wave duality, introduced by De Broglie, according to which any particle can be associated with a matter wave whose wavelength is inversely proportional to the particle's linear momentum. Whenever the size of a physical system becomes comparable to the wavelength of the particles that interact with such a system, the behavior of the particles is best described by the rules of quantum mechanics. The solutions of the Schrodinger equation in such case are standing waves confined in the potential well, and the energies associated with two distinct wave functions are, in general, different and discontinuous. This means that the particle energies cannot take on any arbitrary value, and the system exhibits a discrete energy level spectrum. Transitions between any two levels are seen as discrete peaks in the optical spectra, for instance. The system is then also referred to as "quantum confined". If all the dimensions of a semiconductor crystal shrink down to a few nanometers, the resulting system is called a "quantum dot" [17].

Quantum dots are the ultimate example of a solid in which all dimensions shrink down to a few nanometers. Moreover, semiconductor quantum dots are probably the most studied nanoscale systems. When charge carriers and excitations are confined in all three dimensions, the system is called a "quantum dot". The division is somewhat arbitrary, since, for instance, clusters made of very few atoms are not necessarily considered as quantum dots. Although clusters are smaller than the De Broglie wavelength, their properties depend critically on their exact number of atoms. Large clusters have a well-defined lattice and their properties no longer depend critically on their exact number of atoms. The ultimate technique for the fabrication of quantum dots should be able to produce significant amounts of sample, with such a high control of quantum dot size, shape and monodispersity that single-particle properties are not averaged by sample inhomogeneity. So far, ensembles of quantum dots produced by the best available techniques still show behavior deriving from a distribution of sizes, but this field is evolving very rapidly. Various techniques lead to different typologies of quantum dots. The confinement can be obtained in several different ways, and in addition the quantum dot itself can have a peculiar arrangement with respect to its

surrounding: it can be embedded into a matrix or grown onto a substrate, or it can be a "free" nanoparticle. Each of these cases is strictly related to the preparative approach chosen [17].

2.10 Nanostructured Biological Materials

Several billion years of evolution have led to the generation of an astonishing variety of biological organisms. These organisms vary in many ways, but their fundamental building blocks remain the chemical structures of nucleic acids, proteins, and lipids that make life possible. The hierarchical assembly of these fundamental building blocks into working biochemical machinery is the foundation of cellular function. Many of these assembly processes, however, occur at a size regime in which visualization and characterization are difficult. Detailed structural characterization is an essential goal, not only for understanding these processes, but also for harnessing this technology for later technological application [18].

Each of the biological materials mentioned (nucleic acids, proteins, and lipids) is nanostructured in different ways. Nucleic acids, through base stacking and specific hydrogen bond base pairing, are the informational media for the genetic code. Furthermore, nucleic acids can fold into complex structures that are chemically active. The structure of biological materials is a result of both their chemical composition and their environment. Chemical composition, such as the polypeptide sequence of a protein or the sequence of bases in a nucleic acid strand, is a key determinant of structure. Environment affects the structure of these materials in much more subtle and deterministic ways than most man-made materials. The components found in an aqueous solution, as well as their concentrations, will determine the detailed structure of a bimolecular system. The behavior of these biomaterials varies and often goes beyond a simple assessment of their function. For example, although an enzyme's duty may be converting a substrate into a product, its behavior in a given system may involve not only that catalytic process, but also such processes as diffusive motions, regulatory controls, conformational changes, and environmental factors. These behaviors are important, for they dictate what is actually occurring with the enzyme in the broadest sense; they are not limited, for example, to a simple chemical transformation. As biological systems are utilized more and more for technological applications, their behavior in particular, nonphysiological environments becomes more critical.

Manipulation of these biomolecular assemblies and the nanomaterials they are used in involves engineering and control at the nanometer-scale. This often means ordering a material by crystallization or confining it to nanometer scale regions through the use of patterning or lithography. The ability to change a system at the nanometer scale to construct new, scientifically interesting systems or to suit new design requirements is one of the most exciting aspects of this field and is broadly termed nanostructured materials research [18].

3 Nanocomposites

3.1 Introduction

The field of nanocomposite materials has been under close attention, imagination, and close scrutiny of scientists and engineers in recent years. This scrutiny results from the simple premise that using building blocks with dimensions in the nanosize range makes it possible to design and create new materials with unprecedented flexibility and improvements in their physical properties.

Nanocomposites and nanograined materials have been studied extensively mainly for improved physical properties [19] Nanocomposites refer to materials consisting of at least two phases with one dispersed in another that is called matrix and forms a three-dimensional network, whereas nanograined materials are generally multi-grained single phase polycrystalline materials. A reduced particle size would definitely promote the densification of composites and polycrystalline materials, due to the large surface area and short diffusion distance [6].

The ability to tailor composites by using nanosize building blocks of heterogeneous chemical species has been demonstrated in several interdisciplinary fields. The most convincing examples of such designs are naturally occurring structures such as bone, which a hierarchical nanocomposite is built from ceramic tablets and organic binders. Because the constituents of a nanocomposite have different structures and compositions and hence properties, they serve various functions. Thus, the materials built from them can be multifunctional. Taking some clues from nature and based on the demands that emerging technologies put on building new materials that can satisfy several functions at the same time for many applications, which scientists have been devising synthetic strategies for producing nanocomposites. These strategies have clear advantages over those used to produce homogeneous large-grained materials. Behind the push for nanocomposites is the fact that they offer useful new properties compared to conventional materials [20].

Nanocomposites can be considered solid structures with nanometer-scale dimensional repeat distances between the different phases that constitute the structure. These materials typically consist of an inorganic (host) solid containing an organic component or vice versa. Or they can consist of two or more inorganic/organic phases in some combinatorial form with the constraint that at least one of the phases or features is in the nanosize [20].

Many efforts are under way to develop high-performance ceramics that have promising properties for engineering applications such as highly efficient gas turbines, aerospace materials, automobiles, etc. Even the best processed ceramic materials used in applications pose many unsolved problems; among them, relatively low fracture toughness and strength, degradation of mechanical properties at high temperatures, and poor resistance to creep, fatigue, and thermal shock. Attempts to solve these problems have involved incorporating second phases such as particulates, platelets, whiskers, and fibers in the micron-size range at the matrix

grain boundaries. However, results have been generally disappointing when micron-size fillers are used to achieve these goals. Recently the concept of nanocomposites has been considered, which is based on passive control of the microstructures by incorporating nanometer-size second-phase dispersions into ceramic matrices [20]. Dispersing metallic second-phase particles into ceramics improves their mechanical properties (e.g., fracture toughness). A wide variety of properties, including magnetic, electric, and optical properties, can also be, tailored in the composites due to the size effect of nanosized metal dispersions. Conventional powder metallurgical methods and solution chemical processes like sol–gel and co-precipitation methods have been used to prepare composite powders for ceramic/metal nanocomposites such as Al_2O_3/W, Mo, Ni, Cu, Co, Fe, ZrO_2/Ni, Mo, MgO/Fe, Co, Ni; and so on [20].

Nanocomposite technology is also applicable to functional ceramics such as ferroelectric, piezoelectric, varistor, and ion-conducting materials. Incorporating a small amount of ceramic or metallic nanoparticles into $BaTiO_3$, ZnO, or cubic ZrO_2 can significantly improve their mechanical strength, hardness, and toughness, which are very important in creating highly reliable electric devices operating in severe environmental conditions [20].

Advanced bulk ceramic materials that can withstand high temperatures (>1500 °C) without degradation or oxidation are needed for applications such as structural parts of motor engines, gas turbines, catalytic heat exchangers, and combustion systems. Such hard, high-temperature stable, oxidation-resistant ceramic composites and coatings are also in demand for aircraft and spacecraft applications [20].

Considerable attention has been devoted to "functionally graded nanocomposite materials", for which gradually varying the dispersion (nanoparticles) to matrix ratio in chosen directions continuously changes the material. An example of such a material is SiC dispersions in a C (pyrolytic graphite) matrix, which has served well as thermal barriers on the space shuttle due to its excellent resistance to oxidation and thermal shock [20].

Thin-film nanocomposites are films consisting of more than one phase, in which the dimensions of at least one of the phases are in the nanometer range. These nanocomposite films can be categorized as multilayer films, in which the phases are separated along the thickness of the film, or granular films, in which the different phases are distributed within each plane of the film. Multilayered thin-film nanocomposites consist of alternating layers of different phases and have a characteristic thickness on the order of nanometers. These films are usually used for their enhanced hardness, elastic moduli, and wear properties [20].

Improved wear resistance, good high-temperature stability, and improved friction properties are important characteristics of good coatings for use in applications such as cutting tools. Most widely used coatings are made from TiN, TiC, TiAlN, CrN, diamond-like carbon (DLC), WC/C, MoS_2, Al_2O_3, etc. For improved coatings in which lower friction, increased life time, increased toughness, higher thermal stability, and in some cases, environmental (biomedical, for

example) compatibility are needed, new types of materials are being considered, including nanocomposite materials.

The mechanical behavior of carbon nanotubes is exciting, since nanotubes are seen as the ultimate carbon fiber ever made. The most important application of nanotubes, based on their mechanical properties, will be as reinforcements in composite materials. The nanotube reinforcements promise to increase the fracture toughness of the composites by absorbing energy through their highly flexible elastic behavior during deformation, which will be especially important for nanotube-based ceramic matrix composites. Possible applications are in light-weight armor or conductive durable ceramic coatings [20].

Polymer composites are important commercial materials with applications that include filled elastomers for damping, electrical insulators, thermal conductors, and high-performance composites for use in aircraft. Materials with synergistic properties are chosen to create composites with tailored properties; for example, high-modulus but brittle carbon fibers are added to low-modulus polymers to create a stiff, lightweight composite with some degree of toughness. Recently, a large window of opportunity has opened to overcome the limitations of traditional micrometer-scale polymer composites–nanoscale filled polymer composites in which the filler is <100 nm in at least one dimension. Although some nanofilled composites (carbon black and fumed silica filled polymers) have been used for more than a century, research and development of nanofilled polymers has greatly increased in recent years, for several reasons. The small size of nanofillers can also lead to unique properties of the particles themselves [20].

For example, single-walled nanotubes are essentially molecules, free from defects, and have a modulus as high as 1 TPa and strengths that may be as high as 500 GPa. In addition to the effect of size on particle properties, the small size of the fillers leads to an exceptionally large interfacial area in the composites. The interface controls the degree of interaction between the filler and the polymer and thus controls the properties. Therefore, the greatest challenge in developing polymer nanocomposites may be learning to control the interface. Thus, it seems relevant to define the interfacial region and discuss its properties [20].

Nanocomposites and nanograined materials are not necessarily limited to the bulk materials made by sintering nanosized powders. Deposition of a solid inside a porous substrate, by vapor chemical reactions, is one established technique, referred to as chemical vapor infiltration, for the synthesis of composite [21]. Nanocomposites of polymers and metals or polymers and semiconductors are reviewed by Caseri [22]. Extensive research on various carbon nanotube composites were reviewed by others. A variety of nanostructured materials that have been discussed in previous chapters including this one can be perfectly grouped as nanocomposites or nanograined materials. For example, class I organic–inorganic hybrids can be considered as an organic–inorganic nanocomposite, anodic alumina membrane filled with metal nanowires is metal-ceramic composite.

3.2 Ceramic Nanocomposites

In the past few years, considerable attention has been paid to the development of nanocrystalline ceramics with improved mechanical strength and stiffness, and enhanced wear resistance. Decreasing the grain size of ceramics to the submicrometer/nanometer scale leads to a marked increase in hardness and fracture strength. However, nanocrystalline ceramics generally display worse fracture toughness than their microcrystalline counterparts. The toughness of nanoceramics can be enhanced by adding second phase reinforcements. Grain size refinement in ceramics and their composites can yield superplasticity at high strain rates. Superplasticity is a flow process in which crystalline materials exhibit very high tensile ductility or elongation prior to final failure at high temperatures. Superplastic deformation is of great technological interest because it leads to lower processing temperature and time, and enables near net shape forming of ceramic products. The ability to prevent premature failure of ceramics at high strain rates can have a large impact on the production processes. The development of advanced technologies in the aeronautics, space and energy sectors requires high performance materials with excellent mechanical properties, high thermal conductivity and good wear resistance. Metallic composites can meet these requirements but they suffer from corrosion and oxidation upon exposure to severe aggressive environments [23].

Ceramic-based materials such as zirconia (ZrO_2), alumina (Al_2O_3), silicon carbide (SiC), silicon nitride (Si_3N_4) and titanium carbide (TiC) have been used in industrial sectors at high temperatures due to their intrinsic thermal stability, good corrosion resistance, high temperature mechanical strength and low density. However, ceramics are known to exhibit low fracture toughness since plastic deformation in ceramics is very limited. Several approaches have been adopted to improve the fracture toughness of ceramics. Transformation toughening involves the occurrence of phase transformation in zirconia-based ceramics to arrest the propagation of cracks. Pure zirconia exhibits three different crystalline structures: monoclinic (room temperature to 1170 °C), tetragonal (1170–2370 °C) and cubic (>2370 °C). Several stabilizers or dopants are known to stabilize the tetragonal and cubic phases at room temperature in the metastable state. Partial stabilization enables retention of the metastable tetragonal phase of zirconia at ambient temperature by adding appropriate dopants such as MgO, CaO and Y_2O_3 [23].

Fracture toughness of ceramics can also be improved by the addition of ceramic reinforcements in the forms of particulates, whiskers, and fibers to form ceramic matrix composites (CMCs). The reinforcing effect of fibers is much higher that of particulates and whiskers. Continuous silicon carbide and carbon fibers have been widely used to reinforce ceramics. The toughening mechanisms of fiber-reinforced CMCs are mainly attributed to the crack deflection at the fiber-matrix interface, crack bridging and fiber pull-out. It has been demonstrated that weak fiber-matrix interfacial bonding facilitates the fiber pull-out toughening mechanism to operate.

This is due to strong interfacial bonding which allows the crack to propagate straight through the fibers, resulting in low fracture toughness [23].

3.3 Carbon Nanotube Reinforced Ceramic Nanocomposites

Carbon nanotubes (CNTs) with high aspect ratio, extraordinary mechanical strength and stiffness, excellent thermal and electrical conductivity (as briefly discussed above in previous sections) are attractive nanofillers which produce high-performance ceramic composites with multifunctional properties. The reinforcing effect of CNTs with high aspect ratio is considered to be analogous to that of continuous or short-fiber-reinforcement. The superior flexibility of CNTs is very effective in improving the fracture toughness of brittle ceramics. This is accomplished by means of crack deflection at the CNT-matrix interface, crack-bridging and CNT pull-out mechanisms. Recently, Huang et al. reported that SWNTs exhibit super plastic deformation with an apparent elongation of 280 % at high temperatures. This finding shows the potential application of CNTs as reinforcing fillers for CMCs with improved ductility. Thus, such ceramic-CNT nanocomposite could possess superplastic deformability. Peigney et al. investigated the extruding characteristics of metal oxide-CNT nanocomposites at high temperatures. They indicated that superplastic forming of nanocomposites will become easier through addition of CNTs. All these attractive and unique properties of CNTs enable materials scientists to create novel strong and tough ceramic and metallic nanocomposites. Moreover, the electrical and thermal conductivities of ceramics can be improved markedly by adding nanotubes. The electrical conductivity of alumina-CNT composites can reach up to twelve orders of magnitude higher than their monolithic counterpart. Recent study has shown that the thermal conductivity of alumina-CNT nanocomposites exhibits anisotropic behavior. The nanocomposites conduct heat in one direction, along the alignment of the nanotube axial direction, but reflect heat at right angles to the nanotubes. This anisotropic thermal behavior makes alumina-CNT nanocomposites potential materials for application as thermal barrier layers in microelectronic devices, microwave devices, solid fuel cells, chemical sensors, and so on [23].

3.4 Preparation of Carbon Nanotube Reinforced Ceramic Nanocomposites

Despite the fact that the CNTs exhibit remarkable mechanical properties, the reinforcing effect of CNTs in ceramics is far below our expectation. The problems arise from inhomogeneous dispersion of CNTs within the ceramic matrix, inadequate densification of the composites and poor wetting behavior between CNTs and the matrix. All these issues are closely related to the fabrication processes for

making ceramic-CNT nanocomposites. As recognized, CNTs are hard to disperse in ceramics. They tend to form clusters caused by van der Waals force interactions. Such clustering produces a negative effect on the physical and mechanical properties of the resulting composites. Individual nanotubes within clusters may slide against each other during mechanical deformation, thereby decreasing the load transfer efficiency. Furthermore, toughening of the ceramic matrix is difficult to achieve if the CNTs agglomerate into clusters. Carbon nanotube clusters minimize crack bridging and pull-out effects greatly. Therefore, homogeneous dispersion of CNTs in the ceramic matrix is a prerequisite of achieving the desired mechanical properties [23].

Spark plasma sintering (SPS) is recognized as an effective process for achieving higher densification of ceramics at a relatively lower temperature with short holding time. Accordingly, several researchers have used the SPS method to consolidate ceramic-CNT nanocomposites. For instance, Balazsi et al. compared the effects of HIP and SPS treatments on the microstructural and mechanical properties of Si_3N_4/MWNT nanocomposites. Large differences in the properties of composites prepared by these two sintering techniques have been found. Fully dense nanocomposites with improved mechanical properties can be achieved using the SPS method. In contrast, HIP-treated composites exhibit a partially dense structure with coarse grains [23].

One possible approach to improve the wettability between CNTs and inorganic ceramic host is to coat CNT surfaces with proper surfactants. However, surfactants may introduce undesirable impurities that can affect the sintering process and resulting ceramic-CNT composite properties. It has been reported that molecular level mixing, aqueous colloid and polymer-derived ceramics processes can yield homogeneous dispersion of CNTs and strong interfacial strength in the ceramic-CNT nanocomposites. For example, Fan et al. reported that the fracture toughness of the alumina/SWNT nanocomposites is twice that of monolithic alumina. They attributed this to the strong interfacial CNT-alumina bonding obtained by heterocoagulation [23].

3.5 Oxide-Based Ceramic Nanocomposites

For most Al_2O_3/CNT nanocomposites, CNTs were synthesized independently, and then introduced into micro- or nano alumina powders under sonication to form nanocomposites. This may lead to poor dispersion of nanotubes in the alumina matrix. A growing interest has been directed toward the synthesis of Al_2O_3/CNT nanocomposites by the in situ reaction method. This can be achieved by exposing transition metal/metal oxide catalysts to reactive gases at high temperatures. The advantage of this technique is that the CNTs formed in situ are directly incorporated into the alumina matrix during the synthetic process. For instance, Peigney et al. used a catalysis method for the in situ production of composite powders [23].

Silica-based ceramics are attractive materials for use in optical devices but their brittleness limits their applications. The incorporation of CNTs into silica can improve its mechanical performance markedly. Since CNTs have unique linear and nonlinear optical properties, silica-CNT nanocomposites show promise for photonic applications including optical switching, optical waveguides, and optical limiting devices and so on. The nanocomposites also exhibit excellent low dielectric constant and electromagnetic shielding characteristics. Silica-CNT nanocomposites can be produced by direct powder mixing, sol–gel and electrophoretic deposition (EPD) processes. Among them, sol–gel is often used to make silica-CNT nanocomposites with better dispersion of CNTs in silica [23].

Titania (TiO_2) is a semiconducting oxide with high photocatalytic ability. It finds application in many technological areas such as microelectronics, photocatalysis and sensors. Titania is also an important bioceramic coating material for metal implants due to its excellent biocompatibility. Incorporating CNTs into titania can lead to the development of novel composite materials with advanced functional properties for photocatalytic, microelectronic and biomedical applications. The techniques used for forming titania-CNT nanocomposites include heterocoagulation, sol–gel and hydrothermal treatment [23].

Zirconia-based ceramics are well recognized for their excellent mechanical, electrical, thermal and optical properties. They find a broad range of industrial applications including oxygen sensors, solid oxide fuel cells and ceramic membranes. The physical and mechanical properties of zirconia can be further enhanced by adding low loading level of CNTs. Zirconia-CNT nanocomposites can be fabricated by hot-pressing, heterocoagulation and hydrothermal crystallization [23].

3.6 Non Oxide-Based Ceramic Nanocomposites

Non-oxide ceramics such as silicon carbide, boron carbide and silicon nitride are attractive structural materials for high temperature applications because of their low density, super hardness, and excellent thermal and chemical stability. Despite these advantages they are susceptible to fast fracture during mechanical loading due to their inherently brittle nature. The incorporation of metal nanoparticles into such ceramics can mitigate the problems associated with brittleness. Carbon nanotubes with high aspect ratios are excellent reinforcing and toughening materials for improving the toughness of non-oxide ceramics. Silicon carbide exhibits different crystalline structures from hexagonal (α-SiC), cubic (β-SiC) to rhombohedral. The cubic β-SiC is particularly important due to its higher bending strength, hardness, stiffness and fracture toughness when compared with α-SiC. Because of the high melting point of silicon carbide, the M-method becomes the primary processing technique for making ceramic products. Further, silicon carbide exhibits poor sinterability due to its strong covalent bonding and high melting point. Thus, sintering aids must be added to obtain dense ceramic specimens. SiC-CNT

nanocomposites have been fabricated by spray pyrolysis, conventional powder mixing followed by hot pressing or by SPS, microwave synthesis and preceramic polymer precursor methods. Spark plasma sintering with very short processing time is an alternative consolidation route for SiC-CNT nanocomposites. However, SPS of SiC-based materials must be carried out at 1800 °C due to the strong covalent bonding of ceramics. Hirota et al. studied the effect of SPS temperature on the microstructure of monolithic SiC and its composites reinforced with carbon nanofibers. Monolithic SiC and its composites were prepared by direct mixing of powder constituents in methyl alcohol followed by ball milling and SPS [23].

It is recognized that silicon nitride is difficult to sinter and consolidate into a dense material using conventional sintering processes. The incorporation of CNTs into silicon nitride would further impair its sinterability. Balazsi et al. fabricated the Si_3N_4/1 % MWNT nanocomposite using hot isostatic pressing and SPS. For the hipping process, ball-milled composite powder mixtures were sintered at 1700 °C under a pressure of 20 MPa for 3 h, and under 2 MPa for 1 h, respectively. In the case of SPS, ball-milled composite powder mixtures were consolidated at 1500 °C under 100 MPa for 3 min, and at 1650 °C under 50 MPa for 3 min, respectively [23].

4 Properties

When interpreting the experimental results, obtained for bulk nanomaterials, it is important to be able to distinguish grain boundary (associated with interfaces) from volume (associated with small grain size) effects. This problem is far beyond being solved because till now, investigations of bulk nanomaterials are in the stage of collecting experimental results. For this reason, the level of understanding of the structure and properties of the bulk nanocrystalline materials is considerably lower in comparison with isolated nanoparticles. The properties of bulk nanomaterials are significantly related to the particle size and the state of the grain boundaries [24].

4.1 Magnetic Properties

Three main phenomena that characterize magnetism in matter are:

- The formation of the magnetic moment on the atomic scale,
- The occurrence of magnetic order, resulting from the strong interactions existing between atomic moments,
- The alignment of moments along some favored crystallographic axis, leading to the phenomenon of magnetic anisotropy.

Iron, cobalt and nickel belong to the first series of magnetic elements, the 3rd series, whilst the second series comprises the 14 rare earth elements. A moving

electric charge is the source of a magnetic field and a magnetic moment can be associated with it. On the atomic scale, magnetism results from electron motion [3].

The main interactions between electrons in matter are due to electrostatic repulsion. In quantum mechanics, the Hamiltonian describing them contains the so-called exchange term, resulting from the in distinguish ability of electrons. As Heisenberg showed, magnetism then arises naturally as soon as the Pauli Exclusion Principle is taken into account. This states that two electrons cannot occupy the same quantum state defined by the space and spin variables, and thus requires the wave function for the electron ensemble to be antisymmetric in those variables. This in turn means that the interaction energy between electrons depends on their spin states. As mentioned above, it is the exchange interactions that cause the atomic magnetic moment. Then, insofar as the electrons in different atomic sites affect one another by exchange interactions, a magnetic coupling exists between the atomic moments of different atoms, and this is the source of magnetic order in a material [3].

Ferromagnetic particles become unstable when the particle size reduces below a certain size, since the surface energy provides a sufficient energy for domains to spontaneously switch polarization directions. As a result, ferromagnetics become paramagnetics. However, nanometer sized Ferro-magnetic turned to paramagnetic behaves differently from the conventional paramagnetic and is referred to as superparamagnetics. Nanometer sized ferromagnetic particles of up to $N = 10^5$ atoms ferro- magnetically coupled by exchange forces, form a single domain [25], with a large single magnetic moment p with up to l05 Bohr magnetons, μB. Beam and Livingston demonstrated that these clusters or particles at elevated temperatures can be analogously described as paramagnetic atoms or molecules, however with much larger magnetic moments [6]. The magnetization behavior of single domain particles in thermodynamic equilibrium at all fields is identical with that of atomic paramagnetism, except that an extremely large moment is involved, and thus large susceptibilities are involved. An operational definition of super paramagnetism would include at least two requirements. First, the magnetization curve must show no hysteresis, since that is not a thermal equilibrium property. Second, the magnetization curve for an isotropic sample must be temperature dependent to the extent that curves taken at different temperatures must approximately superimpose when plotted against H/T after correction for the temperature dependence of the spontaneous magnetization. Superparamagnetism was first predicted to exist in small ferromagnetic particles below a critical size by Frankel and Dorfman [26]. This critical size was estimated to be 15 nm in radius for a spherical sample of the common ferromagnetic materials [27]. The first example of superparamagnetic property was reported in the literature as early as 1954 on nickel particles dispersed in silica matrix [28]. Figure 7 shows the typical magnetization. Below some real experiments are described in measuring the magnetization potential of materials [29].

In nanoparticles of transition metal oxides, measurements reveal a reduction in the average magnetization. This happens for maghemite nanoparticles (γ-Fe_2O_3), a collinear ferrimagnetic material in the bulk. For an insulating system, such a

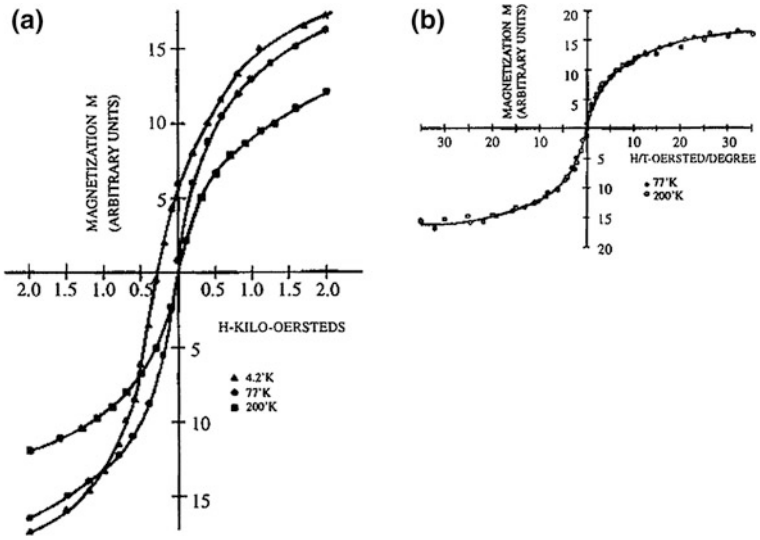

Fig. 7 Typical magnetization curves of 2.2 nm iron particles suspended in mercury at various temperatures and the approximate H/T superposition observed for their 77 and 200 K data [29]

reduction in magnetization cannot be attributed to a lower iron moment, since the latter does not depend on the size of the system. In fact, Mossbauer spectroscopy on the Fe57 nucleus reveals non-collinear arrangements of the moments. Such arrangements are characteristic of atoms located in a low-symmetry environment and subject to magnetic interactions of various signs. Numerical simulation confirms the highly non-collinear nature of the calculated arrangements whenever the reduced symmetry of the environment of surface atoms is taken into account [3]. Non-collinear arrangements of the same origin also occur in nanoparticles of systems that are antiferromagnetic in the bulk state, such as NiO. There is no reason why the moments should cancel one another exactly. The result is that antiferromagnetic nanoparticles carry a small magnetic moment.

4.2 Electrical Properties

The ability to transport charge (electric current), spin (magnetic current), and energy (heat, sound) through nanostructures is of great importance in both scientific studies and technological applications. The quantum nature of matter on the nanometer scale leads to new transport phenomena and necessitates the development of new theoretical descriptions. The electrons that flow through the nanostructure are supplied from macroscopic metal contacts. The energy and electron number of the large reservoirs are not affected by the presence of the nanostructure. It is thus natural to denote the metal contacts as electron reservoirs

[30]. To become more specific on nanomaterials electrical conductivity, there is some explanation as follow:

The effects of size on electrical conductivity of nanostructures and nanomaterials are complex, since they are based on distinct mechanisms. These mechanisms can be generally grouped into four categories: surface scattering including grain boundary scattering, quantized conduction including ballistic conduction, Coulomb charging and tunneling, and widening and discrete of band gap, and change of microstructures. In addition, increased perfection, such as reduced impurity, structural defects and dislocations, would affect the electrical conductivity of nanostructures and nanomaterials [6]. Below a critical size, properties become more likely to change in the bulk itself, thereby affecting the cluster as a whole. On the structural level, the icosahedral transition is well known. Size-dependent transitions also occur for the electronic structure. This can be exemplified by the metal–insulator transition in clusters of divalent metals, induced by the separation of the "s" and "p" energy bands at small sizes. When the number of atoms or constituents is decreased further, one ends up in a regime where properties are reconstructed at each new size. At this point, a discrete form of behavior is superposed on the laws of scaling. This is the size range characterized by finite size effects. These are partially due to the discrete nature of the atomic structure, which must now be taken into account explicitly and partly to the quantum nature of the electrons participating in the chemical binding. In covalent systems, binding is ensured by electron delocalization among several atoms. This delocalization may sometimes be more extensive, as in the π systems, even extending to the whole cluster, as in the case of delocalized electrons in metals. At small sizes, electronic and geometrical properties can become highly interdependent. Ionization or addition of an electron is likely to have repercussions for the structure. An external perturbation in the form of an electric or magnetic field, or some specific type of environment, e.g., solvent, matrix, can also strongly perturb or even determine the properties of such a system. Another feature here is that classical concepts as simple as volume or area can no longer be clearly defined, owing to the spatial extension of the electron wave function in quantum mechanics. This spatial extension also leads to the tunneling effect, which is significantly in near-field microscopy and manipulation techniques which have underscored the rise of nanoscience. In addition to all this, the energy levels, which are grouped into bands in periodic solids, become discrete in confined systems. Hence, small metallic clusters always exhibit a finite gap between the highest occupied molecular orbital (HOMO) and the lowest unoccupied molecular orbital (LUMO) [3].

Stability of clusters involving certain well defined numbers of electrons indicates a structuring of the electron shells and establishes an analogy with the properties of super atoms or the shell structure of atomic nuclei. In this context, electronic properties are determined by the quantum nature of a system of fermions confined within a spherical potential well. This novel electronic structure plays a key role in the stability, fragmentation, optical properties, or reactivity of metallic particles [3].

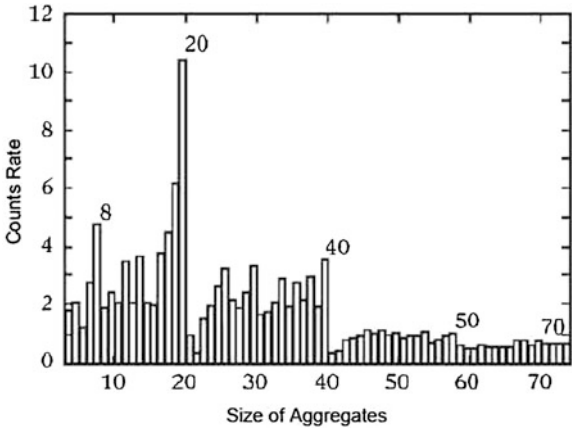

Fig. 8 Mass spectrum of sodium clusters in a molecular beam [3]

Theory and simulation are of the utmost importance, especially when it comes to electronic structure. Joint progress in computing, theory and calculation techniques mean that electronic structure can be determined ab initio (from the beginning), i.e., from first principles, for an ever wider range of increasingly complex systems, by directly solving the equations of quantum mechanics without introducing empirical parameters. This approach has been the source of many computational codes for electronic structure, developed by solid-state physicists and quantum chemists. Although not specifically designed to deal with nanoparticles, certain codes can now be used to tackle non-periodic systems containing more than a hundred atoms (at least for calculating the electronic structure in a given geometric configuration). Certain versions are also integrated into dynamical codes. The advantage with "ab initio" calculations is not only quantitative. When it used to analyze data concerning small or periodic systems, they often provide a way of building appropriate approximate models which make calculation and simulation possible in size ranges that cannot be tackled directly. In the field of electronic structure and molecular simulation, numerical experimentation has become an indispensable complement to laboratory experimentation using real systems [3].

As shown in Fig. 8, a reduction in characteristic dimension below a critical size, i.e. the electron de Broglie wavelength, would result in a change of electronic structure, leading to widening and discrete band gap. Effects of such a change of band gap on the optical properties has been extensively studied and discussed in the previous section. Such a change generally would also result in a reduced electrical conductivity. Some metal nanowires may undergo a transition to become semiconducting as their diameters are reduced below certain values, and semiconductor nanowires may become insulators. Such a change can be partially attributed to the quantum size effects, i.e. increased electronic energy levels when the dimensions of materials are below a certain size as discussed in the previous section. For example, single crystalline Bi nanowires undergo a metal-to-semiconductor transition at a diameter of $\sim$52 nm [31] and the electrical resistance of Bi nanowires of $\sim$40 nm

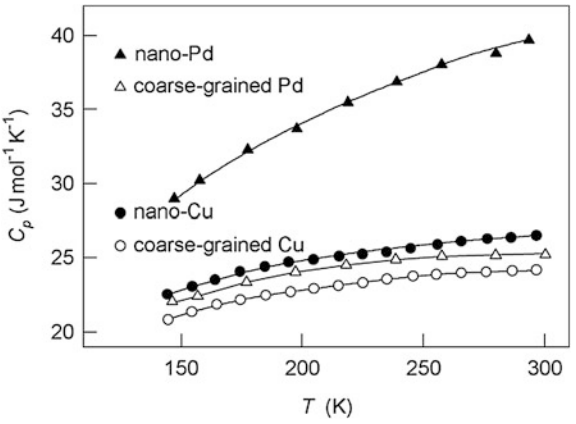

Fig. 9 Effect of the nanostructured state on the temperature dependence of heat capacity Cp(T) of copper and palladium [24]

was reported to decrease with decreasing temperature. GaN nanowires of 17.6 nm in diameter were found to be still semiconducting, however, Si nanowires of ~15 nm became insulating [32].

4.3 Thermal Properties

The theoretical analysis and calorimetric investigations show that in the temperature range 10 K $\leq T \leq \theta_D$ the heat capacity of nanopowders is from 1.2 to 2 times higher than that of the coarse-grained bulk materials. The increased heat capacity of the nanopowders is determined both by the size effect and by the very large surface area, which introduces an additional contribution to heat capacity. In contrast to the nanoparticles, investigations of the heat capacity of nanocrystalline bulk materials are limited to several studies [24].

The heat capacity C_p of nanocrystalline compacted specimens of nc-Pd ($D = 60$ nm) and nc-Cu ($D = 8$ nm), prepared by compacting nanoclusters, was measured in the temperature range from 150 to 300 K. The relative density of the nc-Pd specimens was equal to 80 % and that of the nc-Cu specimens was equal to 90 % of the density of pore-free polycrystalline coarse-grained palladium Pd and copper Cu. Measurements revealed that the Cp of nc-Pd and nc-Cu specimens are 29–53 % and 9–11 % higher than the heat capacity of conventional polycrystalline Pd and Cu, respectively (Fig. 9). When nc-Pd was heated at $T = 350$ K, an exothermic effect was observed but the grain size remained constant or increased up to 10 nm. The heat capacity of nc-Pd heated to 350 K, was found to exceed the heat capacity of coarse-grained palladium by 5 %. It is assumed that the observed elevated heat capacity is caused by the 'looser' structure of the interfaces. This explanation is not plausible because it has been established on the structure of the grain boundaries in the compacted nanomaterials containing free volumes with the

size of monovacancy or deviancy. It though the effect of this frees volumes is not large enough in order to explain excess of heat capacity. One of the explanations of excess could be about the impurities in palladium [24].

4.4 Optical Properties

Novel optical properties arise in nanoparticles, due to resonance in the absorption spectrum of the nanoparticles, the surface plasmon resonance. Its characteristics, such as spectral width and position, and sensitivity to light polarization, depend not only on the intrinsic properties of the nano-objects (composition, structure, size, shape), but also on their environment. In the case of noble metals, it occurs in the visible region of the spectrum, in the blue somewhere near 400 nm and in the green around 520 nm for small silver and gold spheres, respectively, and it produces yellow and red coloring, respectively, of the material in which they are included [3].

Apart from such decorative applications, this possibility of modifying the optical properties of nanomaterials and may be even controlling them in such a way as to achieve specific functions, by adjusting their characteristics or those of their surroundings, has generated a good deal of interest recently. The impact of these novel materials in the field of photonics has already made itself felt, and it is only in its early stages, extending to a wide range of different areas, e.g., linear and nonlinear optics, polarisers, solar cells, chemical and biosensors, nano-optical devices, optical switches, local electromagnetic field enhancement, and molecular labeling in biology. In addition, their optical response provides a way of studying the characteristics of nano-objects and hence constitutes a powerful tool for analyzing their fundamental properties [3].

In contrast to semiconducting nanoparticles or quantum dots, the optical properties arising with size reduction in metallic media are due to a classical enhancement effect on the electric field, often called dielectric confinement. The discretisation of electronic states (quantum confinement) which underlies the optical properties of quantum dots only leads to small corrections to the observed responses down to nanometric sizes. Actually, this difference results from the very high electron density in metals (5×1022 cm^{-3}) compared with typical values in semiconductors (1018 cm^{-3}). In metallic media of nanometric size, electronic properties stem from high energy quantized states, close to the Fermi level. The separations between these energy levels are very small compared with their widths and the thermal energy (at room temperature).

For the nanoparticle sizes considered here, greater than one nanometer, these states can therefore be modeled to a first approximation by a quasi-continuum of states similar to what is observed in the bulk metal [3].

4.5 Mechanical Properties

The growing interest in nanomaterials over the past decade or so can be put down to their unique structure, characterized by grains with nanometric dimensions and by a rather high density of crystal defects, which will undoubtedly lead to quite exceptional properties. In particular, extrapolating the constitutive laws of large-grained materials down to the nanoscale leads one to expect interesting mechanical behavior for nanomaterials. Materials can be produced with high levels of hardness, ductility, and sometimes superplasticity at relatively low temperatures. These characteristics lead to remarkable mechanical performance and machining possibilities, by virtue of which such nanomaterials have immediate scope for technological innovation.

The elastic limit of a material (the stress beyond which a permanent plastic strain is observed) is intimately related to its elastic constants. Indeed, a plastic strain only occurs in order to reduce the energy associated with the elastic strain of the material. The elastic constants reflect the nature and density of atomic bonds. In nanomaterials, the high densities of structural defects and grain boundaries have an effect on the elastic constants [3].

The first measurements of Young's modulus revealed a significant difference between nanostructured materials and the corresponding large-grained materials. In some cases the modulus was much higher, as for superlattices, and in others much lower, as for materials produced by sintering. However, it was subsequently demonstrated that these early results were due to experimental artifacts and often to the presence of defects, such as fractures and high porosity, introduced during fabrication and not properly taken into account when interpreting the observations. More recent results obtained on dense materials have finally shown that the Young's modulus gradually falls off only for grain sizes below 10 nm, i.e., when the fraction of atoms associated with grain boundary and triple junctions becomes very high [3].

The nanoindentation technique is a mechanical test derived from the standard hardness test. The idea is to sink a hard tip of known geometry into the material under investigation and monitor the depth of penetration as a function of the applied load. By carrying out a loading–unloading cycle, a characteristic force-penetration curve is obtained. By analyzing the unloading curve and modeling the material as an elastic and isotropic continuous medium, one can deduce the relevant parameter here, which is the true contact area between the indenter and the material under maximal load. One can then deduce not only the hardness, but also the Young's modulus of the material. The applied forces range from a few tenths to several hundred millinewtons, and the depths of penetration from a few nanometers to several microns [3].

Extrapolating this law to grains of around ten nanometers, very high values of the hardness are predicted, the only limit being the theoretical limiting stress of a perfect crystal, generally taken as $G/10$, where G is the transverse shear modulus. However, although the hardness does indeed increase at small grain sizes, the

observed effects are generally much smaller than would be predicted in this way, and at very small grain sizes, or for very small periods in the case of multilayer films, the opposite trend to the Hall–Petch relation is sometimes observed, i.e., a reduction in hardness with reduced grain size (or period). This 'negative' Hall–Petch effect has nevertheless been explained for nanocrystalline materials that have undergone thermal treatment, by invoking densification or phase transformation phenomena [3, 24].

4.6 Superplasticity

The fabrication of dense fine-grained materials is certainly the most delicate stage in the lead-up to a forming process based on superplasticity. In order to develop new alloys with grain sizes of a few tens of nanometers, metallurgists have turned to cold working processes by severe plastic deformation, torsion straining (TS), and forced shear obtained by extrusion through a channel bent through an angle of as much as 90° (equal channel angular extrusion ECAE). These processes have led to a certain degree of success, especially for light alloys, and are able to obtain submicron grain sizes. However, they cannot produce large solid items. Today, aluminum, zinc and titanium alloys (e.g., Al–Mg, Al–Zn and Ti–Al) are the main metal alloys used in superplastic forming processes [3].

Superplasticity provides a rapid way of obtaining items with complex geometry in a single forming operation and with relatively low flow stresses. It is thus easy to understand the growing interest shown by the world of industry for this property and the superplastic forming (SPF) and diffusion bonding (DB) processes it makes possible, which reduce the required quantities of matter and fabrication costs. However, industrial applications are still restricted mainly to the aeronautic industry and on the whole concern light aluminum and titanium alloys. Titanium alloys are the most widely used today because these were the superplastic alloys first developed industrially, with TA6 V being the main representative. Superplastic forming can be used to obtain in a single operation an element that would otherwise have required the assembly of several parts by riveting. Assembly times are thereby greatly reduced and, by avoiding extra thickness due to assembly, superplastic forming can also make lighter elements. Although superplasticity has been demonstrated in fine-grained ceramics, and in particular in stabilized tetragonal phase zirconia (Y-TZP), the fabrication of ceramic items using this property remains a laboratory curiosity that has barely entered the research and development stage. There are nevertheless several remarkable examples: the fabrication of missile nozzles and axially symmetric elements by the US group Lockheed, and the forming of parabolic sheaths to protect the leading edges of helicopter rotor blades at the National Industrial Research Institute of Nagoya (NIRIN, Japan) [3].

4.7 Thermodynamics of Nanocrystalline Materials

Materials termed nanocrystalline may display very different structures. A first type is entirely made of small crystals produced by techniques for atom condensation and eventual compaction. A second type consists of ensembles of particles deposited on top of a substrate to form a film or a coating. The material may be nanostructured due to the thickness of the film and/or because the film contains fine particles. A third type is represented by bulk solids processed by thermal and/or mechanical means so that crystal sizes are in the nanometer range. There is no unique thermodynamic description for all categories. It is usually stated that materials composed fully or partially of nanocrystals are not in stable equilibrium since they retain a large amount of excess free energy [15].

Nanocrystalline substances are prepared by means of various techniques such as vapor condensation, ball milling and electro deposition. The particles constituting these materials are usually of sizes as small as a few nanometers; therefore it is legitimate to question whether they possess special thermodynamic properties. However, it can be clearly stated that nanocrystals of the elements display bulk properties in many respects. It was shown in the early 1980s that clusters of some 100–150 atoms exhibit photoelectron spectra characteristic of the bulk metals so their internal energies should have corresponding values. However, materials prepared by means of the techniques mentioned above are unstable in the as-prepared state mostly because their interfaces are not equilibrated and need to relax to structural states of lower energy. As an example consider high purity elements processed by heavy deformation. Careful thermal analysis shows that recovery may occur even at room temperature, whereas recrystallization takes place at higher temperature. Therefore the material is unstable at room temperature with respect to defect recovery [15].

In order to evaluate the free energy trend, consider pure elements: nanocrystalline Cu obtained by deformation or deposition. The free energy will be easily taken, neglecting second order contributions due to specific heat differences. As for the enthalpy difference, high purity Cu, heavily deformed by rolling, gives a single DSC peak of 55 J/mol due to recrystallization at 500 K when heated at 30 K/min. If transition elements (e.g. Mn) are added in amounts of parts per million, the recrystallization peak is shifted to higher temperatures (above 673 K) and anew peak appears, due to recovery, at temperatures below 473 K. Extrapolating this behavior to pure Cu, it can be envisaged that recovery of defects should occur dynamically during both deformation and the storage of samples. Therefore, deformed Cu is unstable at room temperature with respect to defect concentration. Once recovery occurs, it will remain in a metastable state up to the temperature of start of recrystallization [15].

Nanocrystalline Cu, prepared as a powder by vapor deposition and compacted, behaves similarly. It releases 300 J/mol around 430 K when analyzed immediately after compaction and 53 J/mol around 450 K when analyzed 5 days after preparation. Such values of enthalpy release have been confirmed by a study on

nanocrystalline Cu prepared by electro deposition and cold rolled to variable amounts. On the other hand, nanocrystalline Cu films obtained by sputtering release 1200–1700 J/mol starting at 450 K and powders prepared by ball milling release 5 kJ/mol. The enthalpy release occurs over a broad temperature range. From these values it was deduced that the interfacial enthalpy may exceed 1 J/m^2. Comparison of all data shows that these materials are far from equilibrium soon after preparation, not only because they contain a large amount of interfaces but also because these interfaces are not equilibrated. Their thermodynamic state is defined and a series of metastable states may be attained after suitable annealing [15].

5 Synthesis

5.1 Gas Phase Synthesis

Isolated nanoparticles are usually produced by evaporation of metal, alloy or semiconductor at a controlled temperature in the atmosphere of a low-pressure inert gas with subsequent condensation of the vapor in the vicinity or on the cold surface. This is the simplest method of producing nanocrystalline powders. In contrast to vacuum evaporation, the atoms of the substance, evaporated in a rarefied inert atmosphere, lose their kinetic energy more rapidly as a result of collisions with gas atoms and form segregations. The nanocrystalline particles with a size of $\leq$20 nm, produced by evaporation and condensation, are spherical, and large particles may be faceted [24].

The systems using the principle of evaporation and condensation, differ in the method of input of evaporated material; the method of supplying energy for evaporation; the working medium; setup of the condensation process; the system for collecting the produced powder [24].

5.2 Plasma Chemical Technique

One of the most widely used chemical methods of producing highly dispersed powders of nitride, carbides, borides and oxides is plasma chemical synthesis. The main conditions of producing highly dispersed powders by this method is the occurrence of a reaction away from equilibrium and the higher rate of formation of nuclei of a new phase at a low growth rate of this phase. In the real conditions of plasma chemical synthesis, the formation of nanoparticles can be carried efficiently [24].

By increasing the cooling rate of the plasma flow in which condensation from the gas phase takes place; this decreases the size of particles and also suppresses the growth of particles by their coalescence during collisions. Plasma chemical synthesis is carried out with the use of low temperature (4000–8000 K) nitrogen,

ammonia, hydrocarbon plasma, argon plasma of arc, glow, high frequency or microwave discharges. Starting materials are represented by elements, halides and other compounds. The characteristics of the produced powders depend on the starting materials used, synthesis technology and the type of reactor. The particles of plasma chemical powders are single crystals and their size varies from 10 to 100–200 nm or larger [24].

5.3 Thermal Spraying

Thermal spraying is a coating process used to produce metallic, non-metallic and ceramic coatings in which a spray of molten or semi-molten solid particles generated from a thermal source are deposited onto substrate by mechanical bonding. The microstructure of the coating results from rapid solidification of the particulates. In principle, powders, rods, and wires which do not sublimate or decompose at temperatures close to their melting points can be used as spraying materials. Metals and alloys in the form of rods or wires are commonly used in arc spraying (AS) and flame spraying (FS). Powders of metals, alloys, ceramic oxides, cermets, and carbides are often used in thermal spraying to produce a homogeneous microstructure in the resulting coating. In most cases, the sprayed surface should be degreased, masked, and roughened prior to spraying to maximize the bonding strength between the coating and the sprayed material. Today, flame spraying (FS), atmospheric plasma spraying (APS), arc spraying (AS), detonation gun (D-gun) spraying, high-velocity oxy-fuel spraying (HVOF), vacuum plasma spraying (VPS), and controlled atmosphere plasma spraying (CAPS) are widely used to produce various coatings for various industrial applications. In general, the heat source for thermal spraying processes may be generated by an electrical or a chemical (combustion) source [33].

5.4 Precipitation from Colloidal Solution

Precipitation from colloid solutions is evidently the first method of producing nanoparticles. The conventional method of producing nanoparticles from colloid solutions is based on a chemical reaction between the components of the solution and interrupting the reaction at a specific moment in time. Subsequently, the dispersed system is transferred from the liquid colloidal state to the nanocrystalline solid state. Nanoparticles can also be produced by means of ultrasound treatment of colloid solutions, containing large particles. Precipitation from colloid solutions makes it possible to synthesize nanoparticles of a mixed composition, i.e. nanocrystalline heterostructures [24].

In the group of all the methods of producing isolated nanoparticles and other powders, the method of precipitation from colloid solutions is characterized

by high selectivity and makes it possible to produce stabilized nanoclusters with a narrow size distribution which is very important for the application of nanoparticles as catalysts or in nanoelectronic devices. The main problem of precipitation from colloid solutions is how to avoid coalescence of the produced nanoparticles [24].

5.5 Thermal Decomposition and Reduction

Thermal decomposition is usually carried out using complex element-organic and organometallic compounds, hydroxides, carbonyls, formiates, nitrates, oxalates, amides and imides of metals which at a specific temperature decompose with the formation of a synthesized substance and generation of the gas phase. A combination of thermal decomposition and condensation is the supersonic discharge of gases from a chamber, in which increased constant pressure and temperature is maintained, through a nozzle into vacuum. In this case, the thermal energy of gas molecules is transformed into the kinetic energy of the supersonic flow [24].

The highly dispersed powders of silicon carbide and nitride are produced by pyrolysis of polycarbosilanes, polycarbosiloxanes and polysilazanes. Initial heating is carried out by a means of low temperature plasma or laser radiation and the products of pyrolysis are subsequently annealed at a temperature of $\sim$1600 K to stabilize the structure and composition [24].

5.6 Milling and Mechanical Alloying

The basis of mechanical alloying is the mechanical treatment of solid mixtures leading to refining and plastic deformation of substances, acceleration of mass transfer and mixing of the components of the mixture on the atomic level, together with the activation of chemical reaction of the solid reagent A stress field forms in the near-contact regions of the solid substance as a result of the mechanical treatment. A relaxation of the stress field may take place by the generation of heat, formation of a new surface, formation of different defects in crystals, excitation of chemical reactions in the solid phase [15].

Non-equilibrium processing of materials has attracted the attention of a number of scientists and engineers due to the possibility of producing better and improved materials than is possible by conventional methods [34]. Rapid solidification processing (RSP) and mechanical alloying (MA) are two such processing methods with somewhat similar capabilities. RSP has started as an academic curiosity in 1960 and matured into an industrially accepted technology with its use for the production of amorphous ferromagnetic sheets for transformer core applications by Allied Signal. On the other hand, MA started as an industrial necessity in 1966 to produce oxide dispersion strengthened (ODS) nickel- and iron-based super alloys for applications

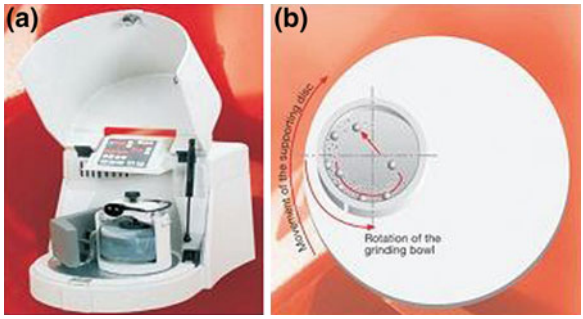

Fig. 10 **a** A High Energy Ball mill machine **b** A schematic representation of the movements of grinding medium in the container [4]

in the aerospace industry and it is only recently that the science of this "apparently" simple processing technology has begun to be investigated. While the scientific basis underlying RSP was investigated in detail from the beginning, applications for the products of RSP were slow to come about mostly because of the limitations on the size and shape of the RSP materials. Thus, invention of the melt spinning technique to produce long and continuous ribbons and of the planar flow casting method to produce wide ribbons accelerated the applications of RSP alloys. Even today use in transformer core laminations remains the major (and most voluminous) application of the RSP alloys. The developments in the science of RSP and the applications of RSP products can be found in several monographs and proceedings of the RQ conferences (see, e.g., [34]). In contrast, the technique of MA was used for industrial applications from the beginning and the basic understanding and mechanism of the process is beginning to be understood only now. There have been several reviews and conference proceedings on this technique too, but the present status of MA has been most recently reviewed by Suryanarayana [35]. The MA literature available up to 1994 has been collected together in an annotated bibliography [35].

Mechanical milling is the most productive method of producing large quantities of nanocrystalline powders of different materials: metals, alloys, intermetallics, ceramics, and composites. Mechanical milling and mechanical alloying may lead to the complete solubility in the solid state of elements characterized by very low mutual solubility in the equilibrium condition [15].

In recent years, nanostructures of brittle ceramics, polymer blends and metal-ceramic nanocomposites have been investigated, which demonstrates the high flexibility of this process.

Figure 10a shows a high energy ball mill machine and Fig. 10b a schematic representation of the movements of grinding medium in the container [4]. The process starts by mixing powders of different elements with the desired proportion and particle size of 1–200 μm. Then, the mixture along with the grinding medium is loaded into a sealed container which, depending upon the type of milling equipment employed, the container is moved or agitated. Collision of the charge and the balls, delivers a high energy to the powder, and the material undergoes a severe plastic deformation. The powder deforms plastically and the rest of energy

is converted into heat and stored in the metal, raising its internal energy. Plastic deformation at high strain rates within particles refines the grain size to nanoscale after prolonged milling. The grain refinement mechanism by the ball milling process has been proposed by Fecht [4], and includes three basic stages:

- Initially, the deformation is localized in shear bands consisting of an array of dislocations with high density.
- At a certain strain level, these dislocations annihilate and recombine to small angle grain boundaries separating the individual grains. The subgrains formed via this route are already in the nanometer size range (about 20–30 nm).
- The orientations of the single-crystalline grains with respect to their neighboring grains become completely random, and the high-angle grain boundaries replace low-angle grain boundaries.

Basically, there are two types of this process. The first one is mechanical milling in which a high energy ball mill is used to crush and refine powders.

The second type is reaction milling which involves in situ solid state chemical reactions between different powders during mixing and milling. Like any other method, mechanical alloying has its own advantages and drawbacks. Advantages include simplicity, relatively inexpensive equipment, versatility in production of a wide range of materials and possibility of producing large quantities, that can be scaled up to several tons. A serious problem, concerning mechanical alloying is the surface contamination from the milling media (balls and vial) and/or atmosphere. Though it is not possible to completely overcome this problem, evacuating the container or using inert gas atmospheres, may help. It should be noted that the degree of contamination depends on a number of factors like mechanical properties of the powder and its chemical affinity for milling media. Other drawbacks of mechanical alloying include rough structures of produced powder, non-homogeneity in particle size and inhomogeneous chemical composition. In order to improve the roughness of the final structure, Cryomilling, in which the milling operation is carried out at cryogenic (very low) temperatures and/or milling of materials is done in cryogenic media such as liquid nitrogen, can be employed to modify the deformation behavior of materials, i.e., increasing the brittleness. This could also help in reducing the degree of contamination. By adjusting the energy received by the powder through a number of variables like ball-powder ratio (BPR), and the milling time, homogeneity of particle size and chemical composition should be improved. As already indicated, this method can be used to produce amorphous or nanocrystalline structures, whether in pure elements or equilibrium and nonequilibrium alloys. Nanocrystalline structure of a large number of elements has been investigated, and crystallite size of the final nanostructure has been determined by standard X-ray analysis methods. The minimum grain size achieved is, however, dependent upon a number of variables as well as the properties of the element, alloy, or compound being milled. The minimum grain size obtainable by milling, $d_{\min}$, has been attributed to a balance between the defect/dislocation structure introduced by the plastic deformation of milling and its recovery by thermal processes. It has been found that the minimum grain size induced by milling scales inversely with the

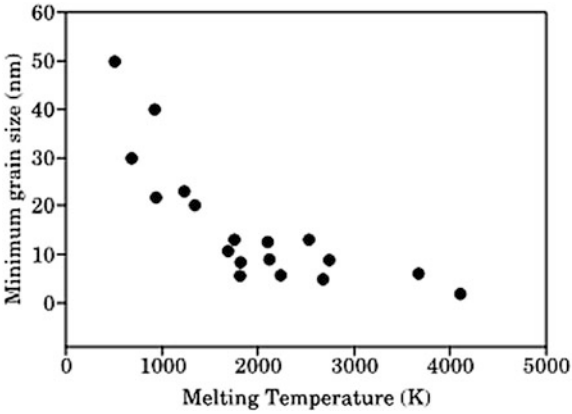

Fig. 11 Minimum grain size versus melting temperature [4]

melting temperature of a group of face-centered cubic (FCC) structure metals studied [36]. These data are plotted in Fig. 11 along with data for other metallic elements and carbon (graphite) [37]. For these data, only the lower-melting-point metals show a clear inverse dependence of minimum grain size on melting temperature. Recent progress in chemical engineering for elements with higher melting temperatures ($>T_m$ for Ni), exhibit essentially constant values with melting temperature for given crystal structure classes. For these elements it appears that d_{min} is in the order: FCC < BCC < HCP [4]. Equilibrium and nonequilibrium solid solutions with nanocrystalline structures are in Ti, Al, Cu and Fe [4].

Systems along with many others have been successfully produced via mechanical alloying and the solid solution formation mechanisms, structure–property relationship and many other facts have been investigated.

Figure 11 shows minimum grain size vs. melting temperature. The metal powders (Ti, Fe, V, Zr, W, Hf, Mo, etc.) transform to a nanocrystalline nitride by high-energy ball milling under nitrogen gas flow. Nanostructured materials in the solid-state interdiffusion reaction during reactive ball milling is triggered by fragmentation of the starting powder, thus creating new surfaces. These freshly created surfaces react with the flowing nitrogen gas to form a nitride surface layer over the unreacted core particle. With further milling, this reaction continues and a homogeneous nitride phase is formed and the unreacted core of metal disappears resulting in a nanostructured (often metastable) metal-nitride with a typical grain size of 5 nm. Mechanical alloying is a complex process and hence involves optimization of a number of variables to achieve the desired product phase and/or microstructure [4]. Some of the important parameters that have an effect on the final constitution of the powder are:

- Type of mill,
- Milling container,
- Milling speed,
- Milling time,

- Type, size, and size distribution of the grinding medium,
- Ball-to-powder weight ratio,
- Extent of filling the vial,
- Milling atmosphere,
- Process control agent, and
- Temperature of milling.

All these process variables are not completely independent. For example, the optimum milling time depends on the type of mill, size of the grinding medium, temperature of milling, ball-to-powder ratio, etc. [4].

Reviewing a number of investigations by our research teams, some examples of different applications, underlying mechanisms in formation of nanocrystalline structures and the effects of a number of process variables are studied [4].

5.7 Self-Propagation High-Temperature Synthesis

The self-propagating high-temperature synthesis (SHS) represents a rapid process of solid combustion of reagents (a metal and carbon for carbides or a metal in nitrogen for nitrides) at a temperature from 2500 to 3000 K. Usually carbides are synthesized in a vacuum or an inert atmosphere (argon). The mean size of grains in carbides produced by the SHS method is 10–20 mm, while the size of nitride grains usually is smaller and they are in the range of 5–10 mm. SHS synthesized carbides and nitrides of group IV and V transition metals have, as a rule, an inhomogeneous composition and require additional grinding and annealing for homogenization. To decrease the grain size in synthesized carbides or nitrides, the starting mixture is diluted with the final product (for example, up to 20 mass% TiC is added to the Ti + C mixture). For the same purpose, some carbon in the mixture is replaced by polymers (polystyrene, polyvinylchloride) during synthesis of carbides. As a result, carbides and nitrides with grains 1–5 mm in size on the mean can be synthesized [24].

5.8 Sol Gel Synthesis

The top-down approach corresponds essentially to the research of miniaturization process in electronics. Clearly, chemistry is not really involved in this approach. In contrast, the bottom up approach which aims to prepare materials with well defined optical, magnetic, mechanical, chemical, etc. corresponds perfectly to the chemists, know-how. In this approach, chemistry is needed on the one hand for the synthesis of the nano-objects, and on the other hand, for the assembling and organizing of these nano-objects into nanomaterials [38, 39].

A very active area of research especially in the ceramics field involves using the sol gel route to fabricate crystalline and amorphous products which may be dense or porous bulk solids, fibers, thin films, or powders. The term of sol gel includes products made from both inorganic colloidal particles suspended in aqueous solutions (particulate systems) and via alkoxides which can be partially hydrolyzed and then polymerized into a gel (polymeric systems) where a classical sol never existed [40, 41].

A colloid is a suspension in which the dispersed phase is so small (1–1000 nm) that gravitational forces are negligible and interactions are dominated by short range forces, such as van der Waals attraction and surface charge. The inertia of the dispersed phase is small enough that is exhibit Brownian motion, a random walk driven by momentum imparted by collision with molecules of the suspension medium. A sol is colloidal suspension of solid particles in liquid [42].

The resultant force on molecules varies with time because of the movement of the molecules; the molecules at the surface will be pointed downward into the bulk phase. The nearer the molecule is to the surface, the greater the magnitude of the force due to asymmetry. The region of asymmetry plays a very important role. Thus, when the surface area of a liquid is increased, some molecules must move from the interior of the continuous phase to the interface. The surface of a liquid can thus be regarded as the plane of potential energy. Colloids are an important class of materials, intermediate between bulk and molecularly dispersed systems. The colloid particles may be spherical, but in some cases one dimension can be much larger than the other two (as in a needle shape). The size of particles also determines whether they can be seen by the naked eye [43].

The development of sol–gel technology has at very early step put forward a request on development of precursor compounds-chemical substances that have high solubility in organic solvents, are easily transformed into chemically reactive forms of hydrated oxides on hydrolysis. They should display considerable stability in solution to guarantee the reproducibility of the materials preparation and, last but not the least, be easy to be purified to provide sufficient chemical quality of the final products. Metal alkoxides, are derivatives of alcohols, ROH, which are usually easily accessible and inexpensive organic compounds, and are extremely weak as acids, easily removable via hydrolysis and thermal treatment, leaving high purity hydrated oxides. This circumstance made metal alkoxides the most common candidates for the role of molecular precursors [44].

The works in this field during the last 20 years, including both the studies of the molecular and crystal structure and the reactivity of these compounds, have considerably changed their image in the eyes of both chemists and the materials scientists. It turned out that sometimes the compounds that are the most stable products in the reactions of synthesis of metal alkoxides and that were earlier considered to be M(OR)n are in fact oxo alkoxides [44].

In many cases, especially for the preparation of complex solutions, including derivatives of several metals, it turned out impossible to use only the derivatives of aliphatic alcohols, because of their poor solubility, stability or reactivity. This gave rise to development of two new types of alkoxide precursors—derivatives of

functional alcohols (alkoxyalcohols and aminoalkohols), on one hand, and heteroleptic alkoxides including other ligands (such as carboxylate and amino-alkoxide ones) in addition to common aliphatic alkoxide groups, on the other. The complexity of situation has been increased even more by the rise of a still quite small but quickly growing family of alkoholates highly soluble complexes of metal carboxylates or with functional alcohols. The latter do not contain formally the alkoxide ligands but are related to metal alkoxides in many of their properties and find the increasing application in sol–gel technology [44].

The sol–gel dip process is almost exclusively applied for the fabrication of transparent layers, primarily for the deposition of oxide films on float glass as a transparent substrate with a high degree of planarity and surface quality. Other substrates are possible, provided they can withstand the required curing temperature of about 500 °C. Film thicknesses up to 1 μm can be deposited, preferred are well defined thicknesses within the wavelength range of visible light. Several additive layers can be superimposed. The chemical reaction involved is based on metal compounds in alcoholic solutions which can be readily hydrolyzed. The oxides are formed through polycondensation at about 500 °C [45].

In the sol–gel technique, fibrous gels are drawn from the sols around room temperature, and then are converted to glass or ceramic fibers by heating at several hundred to one thousand degrees centigrade. Recently, various kinds of glassy fibers, such as silica, alumina-silica and zirconia-silica fibers, and ceramic fibers, such as SiC, zirconia, alumina and titania fibers, have been prepared by this type of sol gel technique, that is, the method based on the conversions sol to gel fiber and then to glass or ceramic fiber [45].

By a careful control of sol preparation and processing, monodispersed nanoparticles of various oxides, including complex oxides,organic- inorganic hybrids, and biomaterials, can be synthesized. The key issue is to promote temporal nucleation followed by diffusion-controlled subsequent growth. The particle size can be varied by changing the concentration and aging time. In a typical sol, nanoclusters formed by hydrolysis and condensation reactions commonly have a size ranging from 1 to 100 nm [6]. Sol–gel and other techniques can be used for preparation of different nanomaterials and nano composites.

5.8.1 Sol Gel Synthesis and Characterization of Al_2O_3–SiC Nanocomposite

α-alumina is the harder and more dense the other forms of alumina, which is commonly formed by heating of other forms of alumina to high temperature in the range of 1100–1200 °C or even higher. One of the main purposes of introducing the second phase particles into alumina was to enhance the inherent mechanical properties by deflecting the cracks on the grain boundaries into the matrix grains. In addition, the properties of the composites can be tailored by controlling parameters such as reinforcement particle distribution, size, volume fraction, orientation, and matrix microstructure. Silicon carbide (SiC) powder is an excellent reinforcement for ceramic composites because of its high hardness, high strength, chemical

inertness and oxidation resistance. Since the coefficient of thermal expansion of alumina is much higher than that of silicon carbide, the residual stress states in alumina–silicon carbide composites are such that the second phase particles are in approximately hydrostatic compression, and there are tensile hoop stresses in the surrounding matrix. The tensile stresses in the alumina matrix can promote crack propagating and so reduce its toughness. Simultaneously, the counter forces (compressive stresses of the second phase particles) can be passed to the grain boundaries and consequently resulting in toughening. The change of grain and grain boundary toughness can dramatically change the fracture behavior of the composites. There are several common synthesizing methods of ceramic nanopowders such as mechanical synthesis, vapor phase reaction, precipitation, combustion and sol–gel methods. But among them sol–gel method because of homogeneous mixing condition in liquid phase is the most promising one. Homogeneous mixing cause accelerating reaction rate and lower reaction temperature and consequently producing finer powders. Nanocomposites usually have been densified by using hot pressing. But hot pressing is costly, and also puts restrictions on the sample geometry. Pressureless sintering generally gives rise to lower density nanocomposites because the driving force for grain boundary movement is lower. As result work has been done by using sintering aids [46].

In this research the fabrication process for high dense pressureless sintered Al_2O_3-5 vol% SiC nanocomposites were investigated. The precursor solutions for Al_2O_3 nano powder were prepared by sol–gel method using $AlCl_3$ anhydrous, distilled water and NH_4OH. At first, the aluminum chloride was mixed with distilled water. The solution was stirred using a magnetic stirrer at 25 °C for 1 h to obtain a transparent solution. Then NH_4OH was gradually added to the solution. The amount of base in the mixture must be precisely controlled. The obtained gel was dried at 80 °C for 24 h. The dried gel was then ground and calcined in a furnace at 1000, 1100 and 1200 °C with the heating rate and soaking time of 10 °C/min and 2 h correspondingly [46].

The chemical reagents used for preparing saccharose-SiO_2 gel as β-SiC precursors were tetraethoxysilicate (TEOS, $(C_2H_5)_4SiO_4$) and saccharose ($C_{12}H_{22}O_{11}$) as silicon and carbon source respectively. Ethanol and distilled water were solvents and also oxalic acid and ammonia were catalysts. Firstly, tetraethylorthosilicate and ethanol were added into saccharose solution with the molar ratio of C:Si = 4:1. During the process of stirring for homogeneity, the pH value of the mixture was kept at 2–3 by using oxalic acid. After 4 h of stirring at room temperature ammonia was added and raised the pH up to 4.

The prepared dark brown gel was placed in drying oven at 100 °C for 24 h. The xerogel was ground and poured into a graphite crucible inside a sintering furnace and then fired at 1500 °C for 1 h in 0.1 MPa argon atmosphere for carbothermal reduction reactions with the heating rate of 10 °C/min. Because of the existence of some residual carbon in obtained powders and probability of no desirable effect on final product the prepared powders were fired at 700 °C in air atmosphere for 1 h to remove the extra carbon [46].

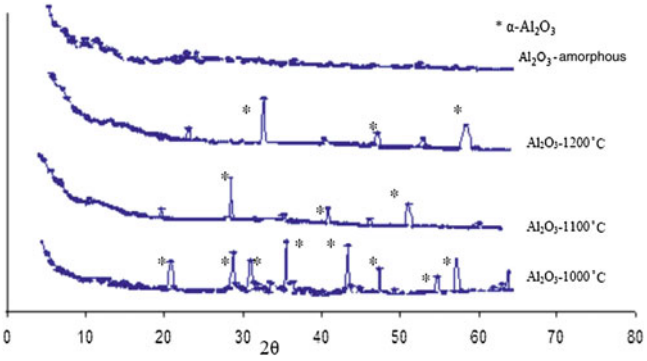

Fig. 12 The XRD pattern of alumina xerogel and powders heat treated at various temperatures for 2 h [46]

A powder mixture of nano α-Al_2O_3 and 4.1 wt% nano SiC was prepared by agate. Doped samples were also prepared by adding TiO_2 (0.5–2 %wt with respect to the Al_2O_3 content). The TiO_2 powder, which is a standard material in the field of photocatalytic reactions, contains anatase and rutile phases in a ratio of about 3:1. To help green pallets formation 2 wt% polyvinyl alcohol (PVA) was added. The mixed powders were uniaxially hand pressed at 137 MPa by using a small mold ($r = 1$ cm, $h = 1$ cm). The green pallets were placed in an Al_2O_3 protective powder bed in an alumina crucible and pressureless sintered in nitrogen atmosphere with a flow rate of 5 l/min at 1600 and 1630 °C. The heating rate of the furnace was 10 °C/min and cooling at the same rate. The densities of the sintered samples were determined by using a technique based on Archimedes principle with distilled water [46].

Aluminum chloride anhydrous was hydrolyzed in distilled water to produce the sol. The initial pH of the sol should be fixed at 3–3.5. The hydroxides groups that were produced in this step finally linked together to form the gel at pH = 9. The appearance of sol would be opaque or translucent when the ratio of NH_4OH/H_2O was lower than 0.2. Adding more base than this ratio would result in a decrease of the gelation time which may be attributed to the catalytic effect. Generally the gelation time decreases by increasing aluminum chloride powder due to increasing the rate of hydrolysis and condensation reactions. However, increasing the amount of aluminum content in the sol decreases transparency due to inadequate solubility of aluminum chloride in the sol. It seems that 2 is an optimum ratio of NH_4OH/H_2O. As can be seen in Fig. 12 the first peaks of α-Al_2O_3 phase are detected in the gel heat treated at 1000 °C. By raising the temperature to 1100 °C, the intensity of their corresponding peaks increases. Usually transformation of the metastable phases of alumina to the final stable α-alumina start at about 1100 °C but in this investigation α-Al_2O_3 was appeared at 1000 °C and completely crystallizes at 1200 °C [46].

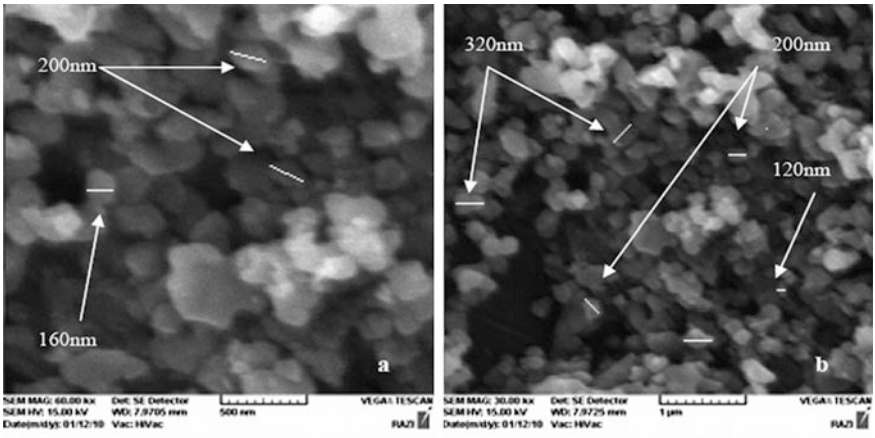

Fig. 13 SEM images of α-Al_2O_3 in two magnitudes **a** 6000, **b** 3000 [46]

As shown in Fig. 13 most of the particles heat treated at 1200 °C are in the range of 100–200 nm and spherical in shape. The crystallite size calculations were done by using Scherrer's equation resulted in 30–90 nm [46].

In the gel formation from TEOS, at first hydrolysis of Si-OC_2H_5 groups produced Si–OH groups. Then condensation between two Si–OH groups or between a Si–OH group and a Si-OC_2H_5 formed Si–O-Si chains. At the end the chains cross-link and/or entangle with each other in the whole liquid to form the gel. It is proved that hydrolysis and condensation rates of TEOS were greatly dependent upon the catalyst and the pH value. Typically when pH was below 7 hydrolysis rate increased with decreasing pH, but condensation rate decreased and reached its lowest point at pH = 2, the isoelectric point of silica. The dark brown dried gel should be reduced to form the SiC powder. The gas–solid reactions of SiC formation proceed in these two steps (Eqs. 1, 2):

$$SiO_{2(s)} + C_{(s)} \rightarrow SiO_{(g)} + CO_{(g)} \tag{1}$$

$$C_{(s)} + SiO_{(g)} \rightarrow SiC_{(s)} + CO_{(g)} \tag{2}$$

But there are some intermediate reactions between these two steps. The first step begins with the reduction of SiO_2 by carbon to form SiO gas according to reaction Eq. (1). Once carbon monoxide (CO) is formed, SiO can also be produced according to this reaction:

$$SiO_{2(s)} + CO_{(g)} \rightarrow SiO_{(g)} + CO_{2(g)} \tag{3}$$

Any CO_2 produced will be consumed shortly by the surrounding carbon particles to form CO gas (Eq. 4):

$$CO_{2(g)} + C_{(s)} \rightarrow 2CO_{(g)} \tag{4}$$

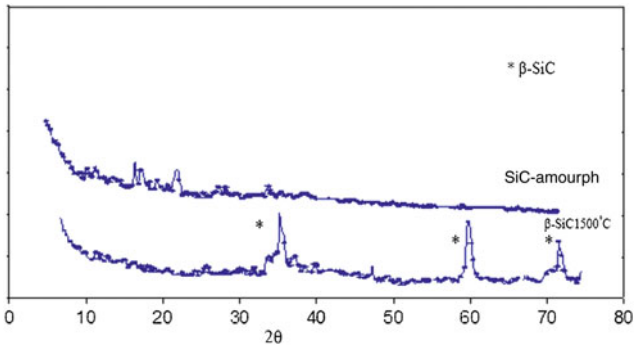

Fig. 14 The XRD patterns of SiO_2-saccharose xerogel and β-SiC powder heat treated at 1500 °C for 1 h [46]

The gaseous silicon monoxide (SiO) following reacts with C and CO according to reactions Eqs. (5) and (6):

$$SiO_{(g)} + C_{(s)} \rightarrow SiC_{(s)} + CO_{(g)} \quad (5)$$

$$SiO_{(g)} + CO_{(g)} \rightarrow SiO_{(g)} + CO_{2(g)} \quad (6)$$

The reaction Eq. (6) is followed by reaction Eq. (4) to synthesize CO, which in turn reacts with SiO according to reaction Eq. (3) and SiO according to reaction Eq. (6), and to continue the cycle. Silicon carbide can be formed by continuing the cycle. Silicon carbide can be formed by heterogeneous nucleation according to reaction Eq. (5) [46].

XRD analysis in Fig. 14 shows that β-SiC is formed, and no other crystalline phases such as silica, carbon or other impurities are detected. This SiC has a well crystalline structure. The widths and intensities of the diffraction peaks in the XRD patterns are related to the average crystallite size, and they are often used to estimate the particle size. According to Scherer's equation it was calculated that the crystallite size were mainly between 30–70 nm. There was an interesting effect of small TiO_2 additions on densification at 1600 °C and 1630 °C (Table 1) [46].

Sample 2 that doped with TiO_2 reached 93.9 and 94.2 % of full density at 1600 °C and 1630 °C respectively, while the undopped material (sample 1) reached almost the same result at the same temperature. By increasing the percentage of TiO_2 densities were raised but these intensifies are not as high as the desired result. Effect of TiO_2 additions on density was more pronounced at the higher sintering temperature 1630 °C. The smallest grain size is belonged to sample 4. Its grain boundaries and triple grain junctions were shown in Fig. 15. In this sample the highest density and hardness were achieved [46].

Comparing samples 4 and 5 resulted that there is an optimum amount of sintering aid and adding more TiO_2 at high temperature had a converse result. This is because more TiO_2 than optimum value with attendant of SiC at higher

Table 1 Experimental samples [46]

Samples name	TiO_2 (%wt)	Sintering temperature (°C)	Density (%)	Hardness (GPa)	Grain size (μm)
1	–	1600/1630	93.9–94.1	14.1–13.3	0.7
2	0.5	1600/1630	93.9–94.2	14.8	1.5
3	1	1600/1630	95.1–6	15.2	1.9
4	1.5	1600/1630	97–97.3	16.5	2
5	2	1600/1630	96.5–97	16.3	2.3

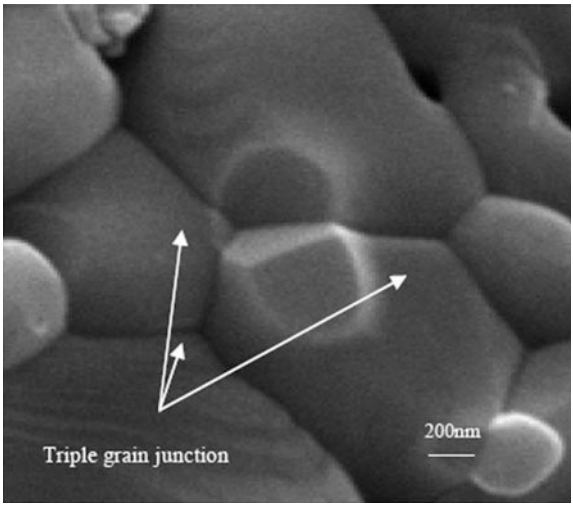

Fig. 15 Triple grain junctions in sample 4 [46]

temperature would prepare the situation for oxidation of more SiC and producing of more SiO_2 and this causes more grain growth and lower density.

Vickers hardness of the doped materials increased with density (Table 1). The material without the addition of TiO_2 had the lowest hardness of 14.1 GPa and 13.3 GPa respectively at 1600 and 1630 °C and the addition of 1.5 %wt TiO_2 resulted in a hardness of 16.5 GPa. The samples hardness that sintered at 1630 °C varied between 14.8 and 16.5 GPa (Table 1) [46].

It is well substantiated that a small addition (a few hundred ppm) of MgO is an effective densification aid during sintering of Al_2O_3 ceramics at temperatures in the range of 1600–1900 °C. In this work for the first time the effect of TiO_2 was investigated. Small additions of TiO_2 have controlled the Al_2O_3 grain size by repressing excessive grain growth according to Zener pinning. Zener pinning is the influence of a dispersion of fine particles on the movement of low and high angle grain boundaries through a polycrystalline material. Small particles act to prevent the motion of such boundaries by exerting a pinning pressure which counteracts the driving force pushing the boundaries. Zener pinning is very important in materials processing as it has a strong influence on recovery, recrystallization and grain growth. The small additions of TiO_2 in the samples in the present

investigation did not have any obvious effect on matrix grain size during sintering at a particular temperature (Table 1) and only a limited number of larger matrix grain section areas were present. This exhibits that local abnormal grain growth did occur under the applied sintering conditions and it didn't related to the existence of TiO_2. Also TiO_2 may promote a more homogeneous grain size distribution by solute pinning of grain boundaries. Other mechanisms that may operate in the presence of a glassy/liquid phase include modification of liquid–solid interfacial energies and glass viscosity. Also by adding these sintering aids to this nanocomposite the significant segregation of Si and Ti in the grain boundaries would be occurred. Whether this causes a glassy grain boundary layer and in continues the segregation simply forms a boundary with a high diffusivity grain boundary layer. The much increased segregation in this material is apparently related to some interaction between SiC and TiO_2. Such an interaction has previously been reported by Ding et al. They found a much greater rate of oxidation of SiC in the presence of MgO and Al_2O_3 than they did when just Al_2O_3 was present. They associated this with the lower eutectic temperature of SiO_2–Al_2O_3–MgO glass compared to SiO_2–Al_2O_3 glass. With the same words by adding TiO_2 the glassy phases of Al_2O_3–TiO_2–SiO_2 with the eutectic temperature of 1470 °C, would be formed. This phenomenon would be affected on process in two different ways. First is that by reaching this temperature with different percentage of components the sintering temperature would be decreased. And the second is the greater oxidation of SiC will release more SiO_2 which can contribute to the grain boundary glass or segregated layer, either of which may allow faster grain boundary diffusion [46].

5.8.2 Synthesis of Biodegradable Nanocomposite Scaffold for Bone Tissue Engineering

Over the past decade, tissue engineering has been widely inspected as a promising approach towards regeneration of bone tissue. Biomaterials are necessary in tissue engineering strategies for the manufacture of scaffolds where pertinent cells attach, grow, proliferate and differentiate. Thus, as the main target, bone tissue engineering has applied developed biodegradable materials as bone graft substitutes for filling large bone defects. In bone tissue engineering, scaffold serves as the matrices of tissue formation and plays a pivotal role. Thus, the choice of the most appreciated material to produce a scaffold is an indispensably important step in the construction of a tissue-engineered product, since its characteristics will identify the properties of the scaffold Polyhydroxyalkanoates (PHAs) are a class of biodegradable polyesters that have been used in combination or alone for biomedical applications such as sutures, repair devices, repair patches, slings, cardiovascular patches, orthopedic pins, adhesion barriers, stents, guided tissue repair/regeneration devices,

articular cartilage repair devices, nerve guides, tendon repair devices, bone marrow scaffolds, and wound dressings. Poly (3-hydroxybutyrate), as a member of the polyhydroxyalkanoates family, known as PHB, has attracted much attention for a variety of medical applications because of its biodegradation which exhibits a much longer degradation time than polymers of the poly (a-hydroxyacid) group (e.g. PLA or PLGA) and its excellent biocompatibility which has a good degree with various cell lines Several composites of PHB and bioactive inorganic phases, like hydroxyapatite, wollastonite and bioglass, have been produced to give strength and bioactivity to the composites. Inorganic phases can be augmented to the polymer matrix in their micro or nanosize. However, for PHB composites, mainly microparticles have been investigated. Recently, nanotechnology and its production have been utilized in a wide variety of medical engineering applications. Nanoscience is particularly useful in tissue engineering since the interactions between cells and biomaterials occur in nanoscale and the components of biological tissues are nanomaterials. Nanoscales of hydroxyapatite, tricalcium phosphate, bioactive glass, titanium oxide, carbon nanotubes and diamonds, for example, have been prepared and used as reinforcement materials in biopolymer matrix composites. The greater specific surface area of the nanoparticles should lead to higher interface effects and also cause improved bioactivity and mechanical properties when compared to micro size particles. In addition, their utilization in a polymeric matrix closely mimics the structure of a natural bone. PHB/bioglass nanocomposite scaffold was prepared using a combination of published salt-leaching techniques. Briefly, 2 g PHB and 0.2 g nano bioglass were dissolved in chloroform with 6 %w/v and refluxed at 60 °C for 6 h. Then, they were sonicated for 30 min using a sonicating probe, and subsequently, the solution was poured into a bed of sieved sodium chloride particles 250–300 nm and the sodium chloride: polymer weight ratio was 90:10. The scaffold was placed under vacuum in a desiccator for 24 h for the solvent to evaporate completely. Then it was rinsed with distilled water for leaching the salt. After the salt leaching process, the microporous polymer scaffold was obtained and then vacuum dried. The microstructure of nanocomposite scaffold containing 10 wt% nano bioglass particles is shown in Fig. 16a–c. The SEM images demonstrated uniform porosities of 250–300 nm pore size that is suitable for osteoblast migration [47].

Also there have been many other experiences by the author in the fields of nanomaterials and nano technology in order to develop new methods for synthesis of advanced nano materials, new characterization techniques, phase and microstructural evolution. Some of these works including synthesis and characterization of ceramic nano composites [48–50], nano ceramic synthesis [51–53], nano biomaterials [54–58], nano coatings [59], sol–gel synthesis [60], mechanochemical synthesis [61–65], nano structured metallic alloys [66–68], nano polymer-silicate composites [69].

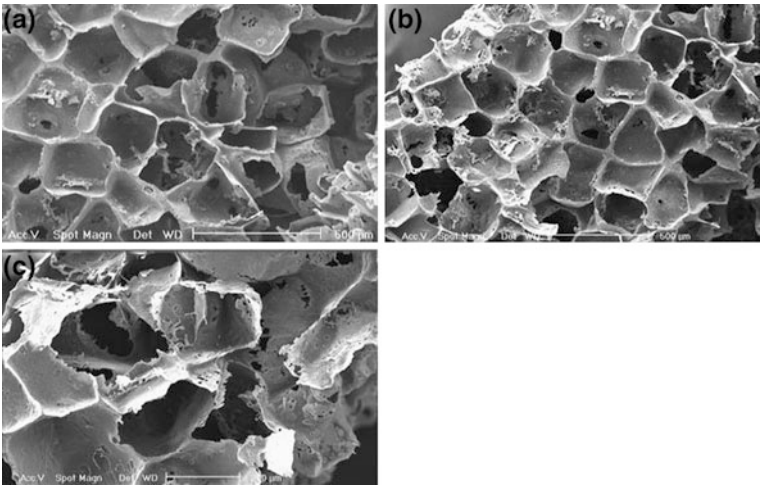

Fig. 16 **a** The SEM of nanocomposite scaffold's surface with 50× magnification. **b** The SEM of nanocomposite scaffold's cross section with 50× magnification. **c** The SEM of nanocomposite scaffold's cross section with 90× magnification [47]

6 Applications

6.1 Introduction

The early application of nanomaterials and nanocompositesare utilized in systems that nanopowders are used in their free form, without consolidation or blending. For a simple example, nanoscale titanium dioxide and zinc oxide powders are now commonly used by cosmetics manufacturers for facial base creams and sunscreen lotions for UV protection. Nanoscale iron oxide powder is now being used as a base material for rouge and lipstick. Paints with reflective properties are also being manufactured using nanoscale titanium dioxide particles. Nanostructured wear-resistant coatings for cutting tools and engineering components have used for several years. Nanostructured cemented carbide coatings are used on some Navy ships for their increased durability. Recently, more sophisticated applications of nanoscale materials have been realized. Nanostructured materials are in wide use in the area of information technology, integrated into complex products such as the hard disk drives that provide faster communication in today's world [11].

Many uses of nanoscale particles have already appeared in specialty markets, such as defense applications, and in markets for scientific and technical equipments. Producers of optical materials and electronics substrates such as silicon and gallium arsenide have embraced the use of nanosize particles for chemomechanical polishing of these substrates for chip manufacturing. Nanosize particles of silicon carbide, diamond, and boron carbide are used as lapping compounds to reduce the waviness of finished surfaces from corner to corner and produce surface

finishes to 1–2 nm smoothness. The ability to produce such high-quality components is significant for scientific applications and could become even more important as electronic devices and optical communications systems become a larger part of the nation's communications infrastructure [11].

6.2 Ceramic Nanocomposites for Load-Bearing Applications

Researchers have observed unusual behavior, in the form of high contact-damage resistance with no corresponding improvement in toughness, in Al_2O_3/nanotube composites. Researchers from the University of Connecticut and the National Institute for Materials Science in Tsukuba, Japan, used the spark-plasma sintering (SPS) method to produce the Al_2O_3/single-walled nanotube (SWNT) composites and observed their behavior under Vickers (sharp) and Hertzian (blunt) indentation tests. These composites are not tough in the classical sense, but are resistant to indentation (contact) damage. Such a combination is uncommon in ceramics. The researchers observed similar behavior in Al_2O_3/graphite composites. The reason for this is the unique way in which SWNTs go to the grain boundaries in alumina and provide shear weakness under indentation [11].

6.3 Nanotechnology in Automotive Applications

Diesel particulate-based filters for cars are being developed using a nanotechnology approach. Nano Pt-CeOx particles are improved to optimize the contact between the particle and diesel soot. Because of the lower particle size a relatively lower filter regeneration temperature is achieved (less than 450 °C). Nanocomposites are currently used in Toyota or GM cars instead of regular plastic. In addition to being stronger and longer-lasting than conventional plastics, nanocomposites also have a significant advantage: they are lighter. It is important for a car to be as light as possible. Lighter cars use less fuel, which means that they are less expensive for people to own [11].

6.4 Nanoclay-Polymer Composites for Structural Applications

Emerging nanotechnologies offer the potential for revolutionary new polymer materials with enhanced physical features: reduced thermal-expansion coefficients, increased stiffness and strength, barrier properties, and heat resistance, without loss of impact strength. Nanocomposites, which contain nanometer-scale particles that are homogeneously dispersed throughout traditional polymers, can provide stiffness and strength approaching that of metals, but with significant reductions in

weight. While the most cost-effective nanosized reinforcing particles are clays, they require surface modification with surfactants to achieve homogeneous dispersion at the nanoscale. Even at a cost of $3–7/lb, commercially available nanoclays are only truly compatible with polar polymers like nylon. The proper design of surfactant coatings used to make nanoclays remains a critical technical/economic obstacle to the commercial production of engineered plastics for high-volume applications like automobile body panels [11].

Researchers at Argonne National Laboratory have focused on the improvement of an integrated approach to achieve good exfoliation of nanosized clays in a broad range of polymers, including polyolefins. The Argonne approach begins with a patented clay purification process that selectively separates and recovers exfoliated nanoclays. The surface modification of the mineral surface begins during the early stages of the purification process and uses a range of unique surface chemistries with enhanced thermal stability and unusually high affinity for nonpolar polymers like polypropylene [11].

6.5 Metal Matrix Nanocomposites for Structural Applications

Metal matrix composites (MMCs) such as continuous carbon or boron fiber reinforced aluminum and magnesium, and silicon carbide reinforced aluminum, have been used for aerospace applications owing to their lightweight and tailorable properties. There is much interest in producing metal matrix nanocomposites that incorporate nanoparticles and nanotubes for structural applications, as these materials show even greater improvements in their physical, mechanical and tribological properties as compared to composites with micron-sized reinforcements. The incorporation of carbon nanotubes in particular, which have much higher strength, stiffness, and electrical conductivity compared with metals, can improve these properties of metal matrix composites. Currently metal matrix nanocomposites are being explored for structural applications in the defense, aerospace and automotive sectors [11].

Concurrent with the interest in producing novel nanocomposite materials is the need to develop low-cost means to produce these materials. Most of the previous work in synthesizing nanocomposites involved the use of powder metallurgy techniques, which are not only high cost, but also result in the presence of porosity and contamination. Solidification processing methods, such as stir mixing, squeeze casting, and pressure infiltration are advantageous over other processes in rapidly and inexpensively producing large and complex near-net-shape components; however, this area remains relatively unexplored in the synthesis of nanocomposites. Stir mixing techniques, widely utilized to mix micron-size particles in metallic melts, have recently been modified for dispersing small volume percentages of nanosized reinforcement particles in metallic matrices. Although there are some difficulties in mixing nanosize particles in metallic melts resulting from their tendency to agglomerate. A research team in Japan worked on

dispersing nanosize particles in aluminum alloys using a stir mixing technique and other researchers at the Polish Academy of Science has recently demonstrated the incorporation of greater than 80 Vol% nanoparticles in metals by high-pressure infiltration with pressures in the GPa range. Composites produced by this method possess the unique properties of nanosized metallic grains and are certainly useful in structural nanocomposites [11].

6.6 Application of Ferrofluids with Magnetic Nanoparticles

A ferrofluid is a simple liquid medium containing a colloidal suspension of ferromagnetic nanoparticles. Ferrofluids show remarkable properties in the presence of a magnetic field. Typical ferrofluids consist of 10 nm particles of magnetite suspended within an appropriate solvent. Most commercial ferrofluids utilize an oil-based liquid solvent. The nanoparticles in the ferrofluids are special permanent magnets; when placed in suspension, the net magnetization of the ferrofluid is zero until a magnetic field is applied. What distinguishes ferrofluids from other fluids are the body and surface forces and torques that arise in the ferrofluids when magnetic fields are applied to them, which in turn give rise to unusual fluid-mechanical response [11].

6.7 Nanocomposite Coatings

The industrialization of the "Ti–Al–Si–N" coatings with Si dissolved in the (Ti1–xAlx)N metastable solid solution was pioneered by Tanaka et al. (2001), whereas Jilek and Holubarwere developing industrial applications of the nc-(Ti1–x Alx)N/a-Si_3N_4 nanocomposites. Already the "Ti–Al–Si–N" metastable solution coatings showed an enhanced hardness, improved oxidation resistance and a better cutting performance as compared to the state-of-the art (Ti1–xAl_x)N ones (Tanaka et al. 2001). However, as pointed out by Tanaka later, the nc-(Ti1–xAl_x)N/a-Si_3N_4 nanocomposites exhibited an even better cutting performance (Tanaka et al., 2004). The "Ti–Si–N"solid-solution coatings with the FCC structure of TiN were recently studied in detail by Flink et al. (2005). These researchers have shown that, in this solid solution, the hardness increases almost linearly with silicon content and reaches about 45 GPa for Si content of 14 %. Upon annealing, the hardness remains nearly constant up to about 900 °C and decreases afterward reaching about 26 GPa after annealing at 1100 °C. Compared with the results, it is clear that the nanocomposites possess a higher thermal stability [11].

6.8 Electrodeposited Nanostructures

Electrodeposition is a one-step process for production of nanostructured materials. It is based on the old technology, but with refinements such as pulse plating much work has been done in recent years to develop nanocrystalline materials by electrodeposition. Electrodeposited nanocrystalline metals can exhibit both high strength and good ductility. Electrodeposited nanocrystalline materials can be in the form of thick coatings, and free-standing foils, plates, or tubes, so may be considered to be bulk structural materials. Palumbo et al. have reviewed the applications for electrodeposited nanostructures. These researchers listed a wide variety of applications, some already in commercial use, some potential. One example of a large-scale structural application of a bulk nanostructured material was the use of an electrodeposited nickel microalloy as an in situ repair technique for nuclear steam generator tubing [11].

6.9 Military Applications

Nanocrystalline materials can be tough, due to the possible combination of high strength and good ductility. Zhong et al. found that Ni–Fe armor plating can be twice as tough as the required specifications for military vehicles when made in nanocrystalline form [11].

Electromagnetic launchers, rail guns, utilize electrical-magnetic energy to propel penetrators/projectiles at velocities up to 2.5 km/s. This improvement in velocity over conventional explosives can deliver projectiles with an impact velocity of Mach 5 to targets at ranges of 250 miles. Since a rail gun operates on electrical energy, the rails need to be very good conductors of electricity. They also need to be strong, tough and rigid so that the rail gun does not sag while firing and buckle under its own weight. While a good electrical conductor like Cu might be the choice for the rails, Cu is too weak and does not have sufficient wear resistance or high temperature strength. Therefore, nanocomposites of tungsten, copper, and titanium diboride are being studied which may provide the combination of good electrical conductivity and strength required [11].

6.10 Nanoelectronic

These are mainly silicon based microelectronic devices which have invaded our life. Integrated circuits are now found everywhere not only in personal computers but also in a lot of equipment we use each minute as cars, telephones, etc. We always need more memory as well as faster and cheaper processors. If the reduction in size of electronic devices continues at its present exponential pace, the

size of entire devices will approach that of molecules within few decades. However, major limitations will occur well before this happens. For example, whereas in current devices electrons behave classically, at the scale of molecules, they behave as quantum mechanical objects. Also, due to the increasing cost of microelectronic factories, there is an important need for much less expensive manufacturing process. Thus, an important area of research in nanotechnology and nanoscience is molecular electronics, in which molecules with electronics functionality are designed, synthesized and then assembled into circuits through the processes of self-organization and self-alignment. This could lead to new electronics with a very high density of integration and with a lower cost than present technologies [70].

7 Environmental Implications

7.1 Introduction

Nanotechnology is concerned with the world of invisible miniscule particles that are dominated by force of physics and chemistry that cannot be applied at the macro or human scale level. These particles have come to be defined as nanomaterials, and these materials posses unusual properties not presenting traditional and/or ordinary materials.

It is important to note that the environmental health and hazard risks associated with both the nano particles and the application of nanotechnology in industry is at present not fully known. Some early studies indicate that nanoparticles can serves as environmental poisons that accumulate in organs. Although these risks may prove to be either minor, avoidable, or both, the engineer and scientist is duty bound to investigate if there are in fact any health, safety, and environmental impacts associated with nano technology [71].

Some examples of nanotechnology in commercial use under series investigation include as follow:

- Semiconductor chips and other microelectronic applications.
- High surface-to-volume catalysts which promote chemical reactions more efficiently and selectively.
- Ceramic, lighter weight alloys, metal oxides and other metallic compounds,
- Coatings, paints, plastic, fillers, and food packaging applications.
- Polymer-composite materials, including tires with improved mechanical properties.
- Transparent composite materials such as sunscreen containing nanosize titanium dioxide and zinc oxide particles.
- Use in fuel cells, battery electrodes, communications applications, photographic film developing and gas sensors.
- Nano barcodes.

- Tips for scanning probe microscopes.
- Purification of pharmaceuticals and enzymes.

7.2 Classifications and Sources of Pollutants

It is relatively reasonable to say that there will be two classifications of nano emissions: particulates and gases. Additional details cannot be provided at this time since many of new processes and their corresponding emissions have yet to be formulated. It seems reasonable to conclude that many of these emissions will be similar in classifications to what presently exists. The classification and sources of pollutants of necessity have to be emitted to traditional contaminants. Recently the nation's natural resources were exploited indiscriminately. Water ways served as industrial pollution sinks, skies dispersed smoke from factories and power plants, and the land provided to be a cheap and convenient place to dump industrial and urban wastes. However, society is now more aware of the environmental and the need to protect it. While economic growth and prosperity are still important goals, opinion polls exhibit overwhelming public support for pollution controls and a pronounced willingness to pay for them [71].

7.2.1 Air Pollutant

Major air pollutants termed criteria pollutants under the act, include: ozone, carbon, air born particulates, sulfur dioxide, lead and nitrogen oxide. Although the Environmental Protection Agency (EPA) has made considerable progress in controlling air pollution, all of the six criteria except lead and nitrogen oxide are currently a major concern in a number of areas in the countries.

Generally, the main air pollutant can be classified to ozone and carbon monoxide, air born particulates, air born toxics, sulfur dioxide, acid deposition, indoor air pollutant, radon, environmental tobacco smoke, asbestos, formaldehyde and other volatile organic compounds and pesticides [71].

7.2.2 Water Pollutants

The EPA in partnership with governments is responsible for developing and maintaining water quality. These efforts are organized around three themes. The first is maintaining the quality of drinking water this is addressed by monitoring and treating drinking water prior to consumption and by minimizing the contamination of the surface water protecting against contamination of ground water needed for human consumption. The second is preventing the degradation and destruction of critical aquatic habitats, including wet lands, near shore coastal waters, oceans and lakes. The third is reducing the pollution of free flowing surface waters and protecting their uses [71].

7.2.3 Land Pollutants

Historically land has been used as the dumping ground for wastes, including those removed from the air and water. Early environmental protection efforts focused on cleaning up air and water pollution. It was not until the 1970s that there was much public concern about pollution of the land. There are five different forms of land pollutant. These include:

1. Industrial hazardous wastes
2. Municipal wastes
3. Mining wastes
4. Radioactive wastes
5. Underground storage tanks.

7.3 Health and Safety Issues

As for the potential environmental, health and safety risks associated with nanotechnology, critics not that since the plethora of nanosized materials (such as metal and metal oxides, polymers, ceramics and carbon derivatives) are not biodegradable, rigorous ongoing investigation is required to determine what their behavior will be in various ecosystems, in term of absorption or desorption, biotic uptake, and accumulation in plants and animals, similarly, questions remain about the potential toxicity of nano scaled materials to human, in terms of all potential modes of exposure to such ultra fine particles. Short term and long term mode of exposure, such as skin absorption, ingestion, and inhalation among others, must be systematically studied to determine any potential for organ or tissue damage, inflammation, a triggering of autoimmune diseases, and other health related consequences.

Recently it is reported that exposure to fullerenes, or bucky balls, (C-60 molecules) can cause extensive brain damage and alter the behavior of genes in the liver cells of juvenile large mouth bass. Meanwhile in an unrelated 2003 study, researchers found that carbon nanotubes can damage the lungs if inhaled. The animal studies show that the nanotubes are so small that the cells that normally resist other air contaminant are not equipped to handle them.

These reports are among several studies that raise questions about the potential health and environmental effects of nanoscaled materials, and while the initial toxicological data are preliminary, they underscore the need to learn more about how bucky balls and other nanoscaled materials are absorbed, how they might damage living organism, and what level of exposure create unacceptable hazards [71].

References

1. Wolf, E.L.: Nanophysics and Nanotechnology, An Introduction to Modern Concepts in Nanoscience. Wiley, Weinheim (2004)
2. Kohler, M., Fritzsche, W.: Nanotechnology, An Introduction to Nanostructuring Techniques. Wiley, Weinheim (2004)
3. Brechignac, C., Houdy, P., Lahmani, M.: Nanomaterials and Nanochemistry. Springer, Germany (2007)
4. Shokuhfar, A., Mohebali, M.: Nanostructured Materials in Current Trends in Chemical Engineering. In: Delgado, J.M.P.Q (ed) Studium Press LLC, Houston, USA (2010)
5. Shokuhfar, A., Momeni, K.: An Introduction to Nanotechnology (In Persian). Nashr Gostar, Tehran (2005)
6. CaoSeattle, G.: Nanostructures and Nano Materials, Synthesis, Properties, and Applications. Imperial College Press, London (2004)
7. Patil, K.C., Hegde, M.S., Rattan, T., Aruna, S.T.: Chemistry of Nanocrystalline Oxide Materials Combustion Synthesis Properties and Applications. World Scientific Publishing, Singapore (2008)
8. Dresselhaus, M.S., Dresselhaus, G., Eklund, P.C.: Science of Fullerenes and Carbon Nanotubes. Academic Press, San Diego (1996)
9. Tang, Z., Sheng, P.: Nano Science and Technology: Novel Structures and Phenomena. Taylor & Francis, New York (2003)
10. Poole, C.P., Owense, F.J.: Introduction to Nanotechnology. Wiley, New York (2003)
11. Koch, C.C., Ovidko, I.A., Seal, S., Veprek, S.: Structural Nanocrystalline Materials Fundamentals and Applications. Cambridge University Press, New York (2007)
12. Soler-ILLia, G.J. de A.A., Sanchez, C., Lebeau, B., Patarin, J.: Chem. Rev. **102**, 4093 (2002)
13. Galarneau, A., Di Renzo, F., Fajula, F., Vedrine, J.: Zeolites and Mesoporous, Materials at the Dawn of the 21st Century. Elsevier, Amsterdam (2001)
14. Yang, P.: Chemistry of Nanostructured Material. World Scientific Publishing, Singapore (2003)
15. Cantor, B.: Novel Nanocrystalline Alloys and Magnetic Nanomaterials. IOP Publishing Ltd, Bristol (2005)
16. Stroscio, M.A., Dutta, M.: Phonons in Nanostructures. Cambridge University Press, Cambridge (2004)
17. Schmid, G.: Nanoparticles from Theory to Applications. Wiley-VCH Verlag GmbH & Co KGaA, Weinheim (2004)
18. Nalwa, H.S.: Nanostructured Materials and Nanotechnology. Academic Press, San Diego (2000)
19. Kotlensky, W.V.: Chem. Phys. Carbon **9**, 173 (1973)
20. Ajayan, P.M., Schadler, L.S., Braun, P.V.: Nanocomposite Science and Technology. Wiley, New York (2003)
21. Dupel, P., Bourrat, X., Pailler, R.: Carbon **33**, 1193 (1995)
22. Caseri, W.: Macromol. Rapid Commun. **21**, 705 (2000)
23. Tjong, S.C.: Carbon Nanotube Reinforced Composites. Wiley-VCH Verlag GmbH & Co. KGaA, Weinheim (2009)
24. Gusev, A.I., Rempel, A.A.: Nanocrystalline Materials. Cambridge International Science Publishing, Cambridge (2004)
25. Bucher, J.P., Douglas, D.C., Bloomfield, L.A.: Phys. Rev. Let. **66**, 3052 (1991)
26. Frankel, J., Dorfinan, J.: Nature **126**, 274 (1930)
27. Kittel, C.: Phys. Rev. **70**, 965 (1946)
28. Heukelom, W., Broeder, J.J., van Reijen, L.L.: J. Chim. Phys. **51**, 474 (1954)
29. Bean, C.P., Jacobs, I.S.: Magnetic granulometry and super paramagnetism. J. Appl. Phys. **27**, 1448 (1956)
30. Bruus, H.: Introduction to Nanotechnology. Technical University of Denmark, Lyngby (2004)
31. Bower, C., Zhu, W., Jin, S., Zhou, 0.: Appl. Phys. Lett. **77**, 830 (2000)

32. Lobo, R.F., Pan, M., Chan, I., Zones, S.I., Crozier, P.A., Davis, M.E.: 1 Phys. Chem. **98**, 12040 (1994)
33. Koch, C.C.: Nanostructured Materials, Processing Properties and Potential Applications. Noyes Publications, Bracknell (2002)
34. Suryanarayana, C.: Prog. Mater Sci. **46**, 1–184 (2000)
35. Suryanarayana, C.: Bibliography on Mechanical Alloying and Milling. Cambridge International Science Publishing, Cambridge (1995)
36. Eckert, J., Holzer, J.C., Krill, C.E., Johnson, W.L.: Reversible grain size changes in ball-milled nanocrystalline Fe-Cu alloys. J. Mater. Res. **7**(8), 1980–1983 (1992)
37. Koch, C.C.: The synthesis and structure of nanocrystalline materials produced by mechanical attrition: A review. Nanostructured Mater. **2**(2), 109–129 (1993)
38. Corriu, R., Anh, N.T.: Molecular Chemistry of Sol–Gel derived Nanomaterials. Wiley, New York, (2009)
39. Kelsall, R.W., Hamley, I.W., Geoghegan, M.: Nanoscale Science and Technology. Wiley, New York (2005)
40. Lee, W.E., Rainforth, W.M.: Ceramic Microstructures, Property control by Processing. Chapman & Hall, London (1994)
41. Jones, R.W.: Fundamental Principles of Sol-Gel Technology. The Institute of Metals, London (1989)
42. Brinker, C.J.: Sol-Gel Science, the Physics and Chemistry of Sol-Gel Processing. Academic Press, London (1990)
43. Birdi, K.S.: Handbook of Surface and Colloid Chemistry, 2nd edn. CRC Press, New York (2003)
44. Sakka, S.: Handbook of Sol Gel Science and Technology. Kluwer Academic Publisher, Boston (2001)
45. Klein, L.C.: Sol Gel Technology for Thin films, Fibers, Preforms, Electronics and Specialty Shapes. Noyes Publications, New Jersey (1998)
46. Rezaie, H.R., Rahimi, R.M., Nemati, A., Samadani, M.: Synthesis of Al2O3-SiC nanocomposite by sol-gel method and effect of TiO_2 on sintering. In: DLS Conference, Paris (2010)
47. Hajiali, H., Karbasi, S., Hosseinalipour, S.M., Rezaie, H.R.: Preparation of a novel biodegradable nanocomposite scaffold based on poly (3-hydroxybutyrate)/bioglass nanoparticles for bone tissue engineering. J. Mater. Sci. Mater. Med. **21**, 2125–2132 (2010)
48. Aminzare, M., Mazaheri, M., Golestani-Fard, F., Rezaie, H.R., Ejeian, R.: Sintering behavior of nano alumina powder shaped by pressure filtration. Ceram. Int. **37**, 9–14 (2011)
49. Aminzare, M., Golestani-Fard, F., Guillon, O., Mazaheri, M., Rezaie, H.R.: Sintering behavior of an ultrafine alumina powder shaped by pressure filtration and dry pressing. Mater. Sci. Eng., A **527**, 3807–3812 (2010)
50. Zargar, H.R., Bayati, M.R., Rezaie, H.R., Golestani-Fard, F., Molaei, R., Zanganeh, S., Kajbafvala, A.: Influence of nano boehmite on solid state reaction of alumina and magnesia. J. Alloy. Compd. **507**(2), 443–447 (2010)
51. Ebrahimi Basabi, M., Javadpour, J., Rezaie, H.R., Goodarzi, M.: Mechanochemical synthesis of alumina-zirconia nanocomposite powder. Adv. Appl. Ceram. **107**(6), 318–321 (2008)
52. Ebrahimi Basabi, M., Javadpour, J., Rezaie, H.R., Goodarzi, M.: Mechanochemical Synthesis of alumina nano particles. Iran. J. Mater. Sci. Eng. **6**(1), 26–30 (2009)
53. Yazdani, A., Rezaie, H.R., Ghassai, H.: Investigation of hydrothermal synthesis of wollastonite using silica and nano silica at different pressures. J. Ceram. Process. Res. **11**(3), 348–353 (2010)
54. Zadegan, S., Hossainalipour, M., Ghassai, H., Rezaie, H.R., Naimi-Jamal, M.R.: Synthesis of cellulose-nanohydroxyapatite composite in 1-n-Butyl-3-methylimidazolium chloride. Ceram. Int. **36**(8), 2375–2381 (2010)
55. Zadegan, S., Hosseinalipour, S.M., Rezaie, H.R. Naimi Jmal, M.R.: Synthesis cellulose-nano hydroxyapaptite composite in 1-N-butyl-3-methylimidazolium chloride. In: 2nd International Conference on Ultrafine grained and Nanostructured Materials, Nov. 14–15, Tehran, Iran (2009)

56. Bakhtiari, L., Rezaie, H.R., Hosseinalipour, S.M., Shokrgozar, M.A.: Preparation of porous biphasic calcium phosphate-gelatin nanocomposite for bone tissue engineering. J. Nano Res. **11**, 67–72 (2010)
57. Bakhtiari, L., Hosseinalipour, S.M., Rezaie, H.R.: Effect of Gelatin amount on properties of nano-BCP/Gel scaffolds. In: 2nd International Conference on Ultrafine grained and Nanostructured Materials, Nov. 14–15, Tehran, Iran (2009)
58. Bakhtiari, L., Rezaie, H.R., Hosseinalipour, S.M., Shokrgozar, M.A.: Investigation of biphasic calcium phosphate/gelatin nanocomposite scaffolds as bone tissue engineering. Ceram. Int. **36**(8), 2421–2426 (2010)
59. Nouri, E., Shahmiri, M., Sadeghian, Z., Rezaie, H.R., Vaghari, H.: Effects of thermal treatment on the crystal structure, mechanical properties and corrosion behavior of zirconia and zirconia-alumina nano coatings. In: International Conference on Materials Heat Treatment (ICMH), Isfahan, Iran (2010)
60. Sobhani, M., Rezaie, H.R., Naghizadeh, R.: Sol–gel synthesis of aluminum titanate (Al2TiO5) nano-particles. J. Mater. Process. Technol. **206**, 282–285 (2008)
61. Ardestani, M., Arabi, H., Razavizadeh, H., Rezaie, H.R., Jankovic, B., Mentus, S.: An investigation about the activation energies of the reduction transitions of fine dispersed CuWO4-x/WO3-x oxide powders. Int. J. Refract. Met. Hard Mater. **28**, 383–387 (2010)
62. Ardestani, M., Rezaie, H.R., Arabi, H., Razavizadeh, H.: The effect of sintering temperature on densification of nanoscale dispersed W–20–40%wt Cu composite powders. Int. J. Refract. Met. Hard Mater. **27**, 862–867 (2009)
63. Ardestani, M., Arabi, H., Razavizadeh, H., Rezaie, H.R., Mehrjoo, H.: Synthesis of WC-20 wt% Cu composite powders using co-precipitation and carburization process. Mater. Sci. Pol. **28**(2), 413–420 (2010)
64. Ardestani, M., Razavizadeh, H., Arabi, H.: HR> Rezaie, Preparation and sintering of W-20 %wt Cu composite powders produced by co-precipitation method. Iran. J. Mater. Sci. Eng. **6**(2), 24–29 (2009)
65. Ardestani, M., Arabi, H., Rezaie, H.R., Razavizadeh, H.: Synthesis and densification of W–30 wt% Cu composite powders using ammonium meta tungstate and copper nitrate as precursors. Int. J. Refract. Met. Hard Mater. **27**, 796–800 (2009)
66. Nazarian Samani, M., Shokuhfar, A., Kamali, A.R., Hadi, M.: Production of a nanocrystalline Ni_3Al-based alloy using mechanical alloying. J. Alloy. Compd. **500**(1), 30–33 (2010)
67. Rezvani, M.R., Shokuhfar, A.: Synthesis and characterization of nano structured Cu-Al-Mn shape memory alloy by mechanical alloying. Mater. Sci. Eng., A **532**, 282–286 (2012)
68. Ghadimi, M., Shokuhfar, A., Rostami, H.R., Ghaffaric, M.: Effects of milling and annealing on formation and structural characterization of nanocrystalline intermetallic compounds from Ni–Ti elemental powders. Mater. Lett. **80**, 181–183 (2012)
69. Shokuhfar, A., Zare-Shahabadi, A., Atai, A., Ebrahimi-Nejada, S., Termeha, M.: Predictive modeling of creep in polymer/layered silicate nanocomposites. Polym. Test. **31**(2), 345–354 (2012)
70. Knauth, P., Schoonman, J.: Nanostructured Materials Selected Synthesis Methods, Properties and Applications. Kluwer Academic Publisher, New York (2004)
71. Theodore, L., Kunz, R.G.: Nanotechnology, Environmental Implications and Solutions. Wiley, New York (2005)

Mechanics of Cellulose Nanocrystals and their Polymer Composites

Anahita Pakzad and Reza S. Yassar

Abstract The fabrication of cellulose nanocomposites with ultimate mechanical properties has received tremendous attention during the past decade. However, the published data has not been reviewed and systematically compared from mechanical point of view. The current study aims to fill this gap by providing a critical review on the published data on the mechanics of cellulose nanocrystals and their composites. The studies on individual cellulose nanocrystals show that their strength depends on the number and type of inter and intra hydrogen bonds on the cellulose chains, which are affected by the cellulose type and origin. It has been shown that the tensile modulus, yield strength and creep resistance are higher in cellulose nanocomposites than in unfilled polymers. However, above optimum cellulose content, the agglomeration of nanocrystals degrades the mechanical properties. Furthermore, cellulose nanocrystals enhance the structural stiffness of polymer composites at elevated temperatures. Formation of rigid nanocrystal network causes increase in the storage modulus (E′) and glass transition temperature.

1 Introduction

Nanocomposites have attracted great attention in the scientific community because of the significant enhancement in the base materials by the addition of nanofillers.

A. Pakzad and R. S. Yassar (✉)
Mechanical Engineering-Engineering Mechanics, Michigan Technological University, 1400 Townsend Drive, Houghton, MI 49931, USA
e-mail: reza@mtu.edu

A. Pakzad
e-mail: apakzad@mtu.edu

Adv Struct Mater (2013) 4: 233–263
DOI: 10.1007/8611_2010_38

Published Online: 16 November 2010

Extensive publications exist on the mechanical properties [26, 41, 78], thermal stability [42, 81], superconductivity [59], and electrical magnetic behavior [14, 71] of various nanocomposites. A wide variety of synthetic nanofillers have been used to reinforce polymer matrices, for instance see [37, 44, 56, 64].

Because of the current environmental issues such as global warming and environmental pollution, investigations are being shifted toward the use of natural fillers in nanocomposites [11, 57, 72]. Since natural nanocomposites are infinitely recycled in the nature, use of these fillers decreases carbon dioxide release, and consequently the final product will be more environmental friendly. Cellulose nanocrystal is a natural polymer, which for the first time was used by Favier et al. [23] to reinforce polymers.

Cellulose exists in the structure of plants (Fig. 1), sea animals and it is also made by some bacteria and it mostly functions as the reinforcing structure. It is being considered as one of the most abundant materials in the nature and has many other qualities that make it attractive for usage in fabrication of composite materials. A number of these exceptional qualities are: renewable nature, biodegradability, biocompatibility, lower cost in comparison to synthetic fillers, low density, impressive strength to weight capability, easy processability because of its nonabrasive nature and relatively reactive surface [4, 5, 13, 27, 33, 54, 58, 61].

The chemical structure of cellulose is shown in Fig. 2. It is a linear homopolymer of β-D-glucopyranose units which are connected by (1 → 4)-glycosidic bonds. Cellulose is chiral and because of high density of hydroxyl groups is hydrophilic and can be soluble in water depending on n (n differs from 500 to 15,000). Cellulose is easily machinable and is degradable by enzymes.

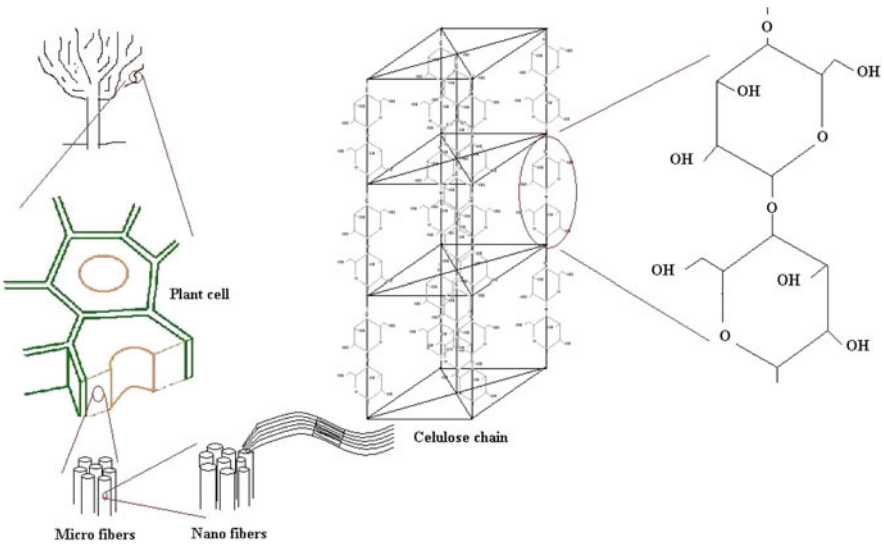

Fig. 1 From plant stem to cellulose (not in scale). Cellulose crystals are the building bricks of plant cells

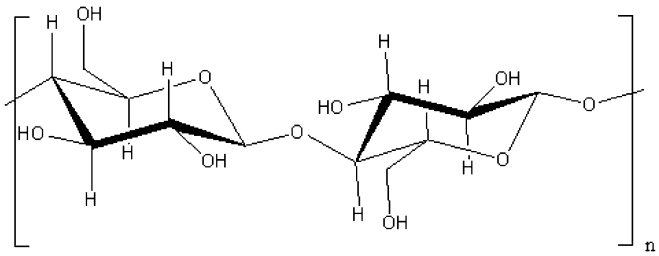

Fig. 2 Chemical structure of cellulose

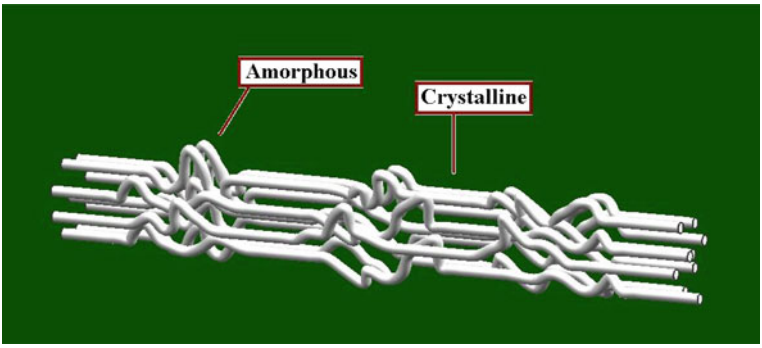

Fig. 3 Schematic presentation of crystalline structure of cellulose I, crystalline parts are connected by amorphous areas

The straight nature of cellulose molecule and the existence of hydrogen bonds result in high likeliness of crystallization. Pure cellulose exists in different allomorphs [33, 85]. Cellulose I (natural or native cellulose), which is semi crystalline, contains two phases, crystalline triclinic I_α and amorphous monoclinic I_β. Amorphous areas connect the crystalline parts as shown in Fig. 3. The proportion of these two phases depends on the origin of the cellulose. For instance, I_α is more found in bacteria and algae, while I_β is more found in plants.

Cellulose II (regenerated or man-made) is a recrystallized form of cellulose I, and in contrast to cellulose I, has anti parallel strands and inter-sheet cellulose bonding, and it is thermodynamically more stable. Cellulose III can be formed by treating cellulose with liquid ammonia. Depending on what the starting material, cellulose I or II, the ammonia treatment conversion will be denoted as III_1 or III_2 respectively. Cellulose III is amorphous. Heat treatment of cellulose III results in cellulose IV, which is also amorphous.

A wide variety of sources has been investigated for preparation of cellulose crystals. The main four groups are wood [10], agricultural byproducts (cotton [10], wheat straw [18]), animal cellulose (sea tunicate [2, 73]) and bacteria [10, 29]. For more references see [39].

The most common method for separation of cellulose crystals from amorphous region is acid hydrolysis (Fig. 4). This includes a chemical treatment for separation of nanocrystals and use of mechanical energy to disperse them in an aqueous suspension. Under suitable conditions (e.g. see [7]), acid hydrolysis breaks down the structure of cellulose into individual needle like crystalline rods by disrupting the amorphous regions. This separation happens due to the faster hydrolysis kinematics of amorphous regions than the crystalline parts. The resultant highly crystalline cellulose nanostructures with different aspect ratios (L/D, L = length, D = diameter), that depend on the hydrolysis conditions and their crystallinity and origin and can be >200 [10, 22, 66], are referred to as *cellulose nanocrystals* (CNXLs). One should note that CNXLs have been entitled, nanorods, nanowires and whiskers [39]. All these terms refer to the individual crystalline rods of cellulose which have at least one dimension less than 100 nm and an overall length comparable to their diameter. Figure 4 shows a scanning electron microscopy (SEM) image of starting material, microcrystalline cellulose (MCC), and a transmission electron microscopy (TEM) image of the final product of acid hydrolysis, CNXLs.

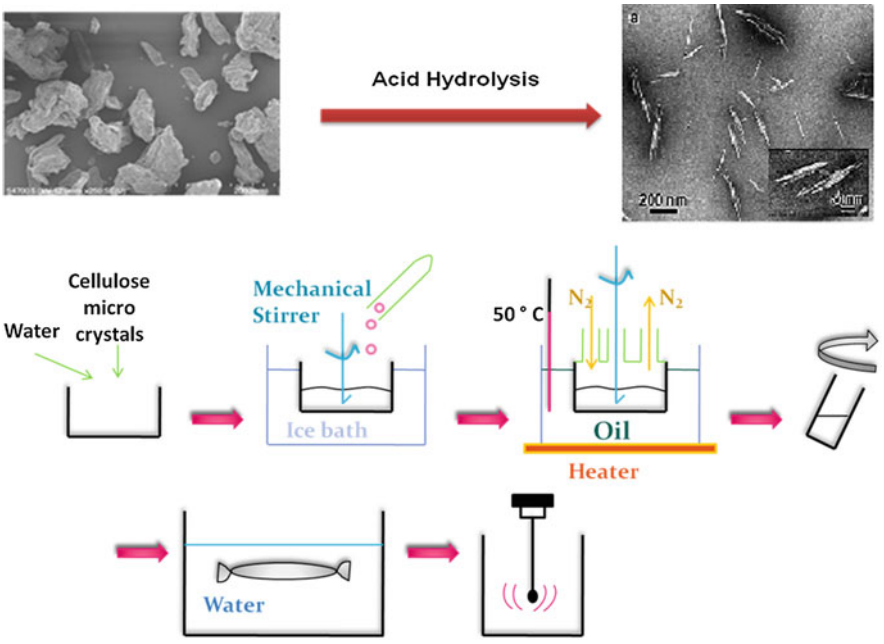

Fig. 4 Schematic procedure of acid hydrolysis of commercially available microcrystalline cellulose. After the acid (e.g. H_2SO_4) is added slowly to the water solution, it should be heated to a certain temperature and kept for a specific time. Afterwards using centrifuge, dialysis against distilled water, sonication and maybe ultra filtering CNXLs are separated (TEM sample: Elazzouzi et al. [22]

2 Mechanics of CNXLs

The mechanical properties of cellulose-based structures have been investigated from both modeling and experimental prospective. Early modeling works started in 1930 but were limited to cellulose in general and not nanocrystals in particular. Meyer and Lotmar [55] were the first who theoretically modeled the mechanical properties of cellulose. They showed that its elastic modulus corresponded to the chain direction of the cellulose crystal and could be calculated from the force constants of the chemical bonds of the chain gained from vibrational frequencies of the molecules. Their modeling was later modified and extended to crystals of synthetic polymers, nylon and Terylene by Lyons [51]. Treloar [77] further modified these models by considering the relation of valence angle deformation to the forces applied to the chain.

Theoretical work on mechanics of nanocrystals has received attention only very recently. Tanaka and Iwata [74] used molecular mechanics simulation and derived values between 124 and 155 GPa for elastic modulus of natural nanocellulose fibers. For this characterization the super cell models with crystal sizes of $1 \times 1 \times 10$ and $4 \times 4 \times 10$ were used (Fig. 5), which in comparison to the unit cell method did not require strict symmetries and thus were more suitable for polymers. In order to calculate the elastic modulus, linear relation between the changes in energy density and the half of the square of the compressive or tensile strain was used:

$$\frac{p - p_0}{S * l} = \frac{1}{2} E \left(\frac{l - l_0}{l_0} \right)^2 \tag{1}$$

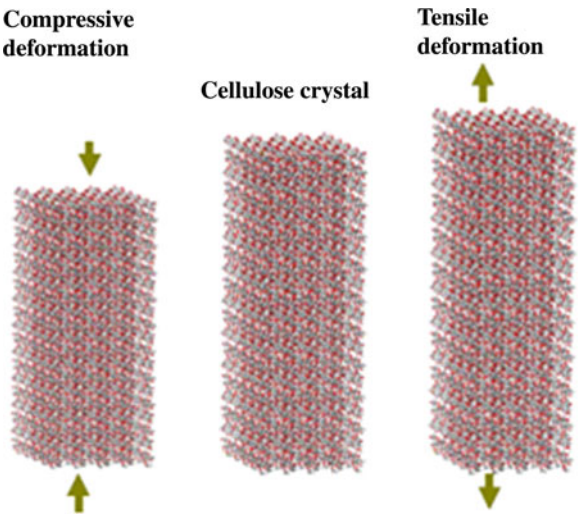

Fig. 5 Molecular mechanics simulation representing compressive and tensile deformation of the CNXLs. The *arrows* show the direction of the applied stresses [74]

where P and P_0 are the potential energy of the cellulose crystal under stress and non-stress energy conditions respectively; S is the cross section, l_0 is the length of the crystal under non-stressed condition, and l is the length of the crystal. The authors reported that the elastic modulus calculated in 4 × 4 × 10 unit-cell size had smaller deviations (124–172 GPa) and were closer to the observed values (138 GPa [60]) in comparison to the values calculated in 1 × 1 × 10 unit-cell size (89–173 GPa).

Experimental measurement of mechanical properties of cellulose began in 1962 but the work was not focused on nanocrystalline cellulose at that time. Sakurada et al. [69] studied the crystal deformation of highly oriented fibers of cellulose I (native cellulose) by X-ray diffraction. For this purpose a Geiger counter X-ray diffractometer was used, a constant stress σ was applied to the fiber bundle, and the fractional change in the length of two glucose units $\Delta I/I_0$, or of a net plane distance, $\Delta d/d_0$, was calculated from the displacement of the interference maximum (Eq. 2):

$$\varepsilon = \Delta I/I_0 = \Delta d/d_0 \tag{2}$$

Finally the elastic modulus, E, was calculated by $E = \sigma/\varepsilon = 137$ GPa (Fig. 6). Mann and Roldan-Gonzalez [53] also used X-ray diffraction and measured elastic moduli between 70 and 90 GPa for crystals of cellulose I and cellulose II, respectively.

The same procedure was recently used by Nishino et al. [60] to measure the elastic modulus of different polymorphs of cellulose. The results are summarized in Table 1. The value obtained for cellulose I is in accordance with what Sakurada et al. [69] obtained many years before.

Atomic force microscopy (AFM) is another tool that has been used for measuring the elastic modulus of cellulose fibers [15, 30, 40]. In this method the AFM tip is used to deflect a nano sized cellulose fiber, which is suspending on a groove. In the work performed by Guhados et al. [30] sonicated suspension of bacterial cellulose fibers was placed on a silicon grating with step height of 1,000 nm and a

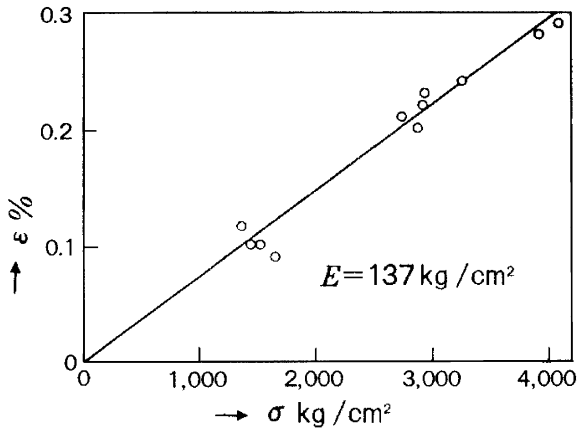

Fig. 6 Stress-strain for highly oriented fibers of cellulose I obtained by X-ray measurements. The elastic modulus was calculated from the slope to be 137 GPa [69]

Table 1 Elastic modulus of crystalline regions of cellulose polymorphs obtained by X-ray diffraction [60]

CNXL origin	Elastic modulus (GPa)
I	138
III_I	87
IV_I	75
II	88
III_{II}	58

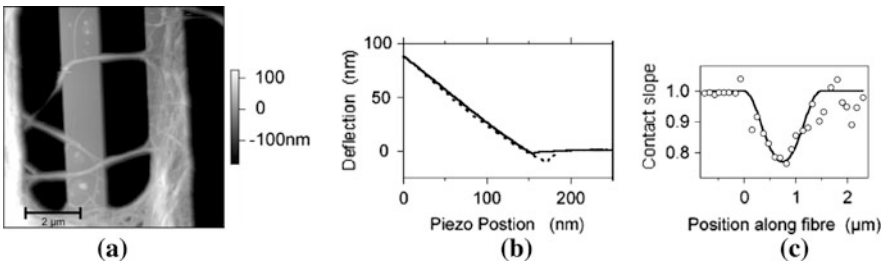

Fig. 7 **a** AFM image of bacterial cellulose fibers suspended over a gap, **b** force spectra obtained near the middle of a suspended fiber (*solid* approach, *dashed* retraction). **c** Slope of force spectra along a suspended 1.62 µm fiber. The suspended parts have smaller slope than the supported ones [30]

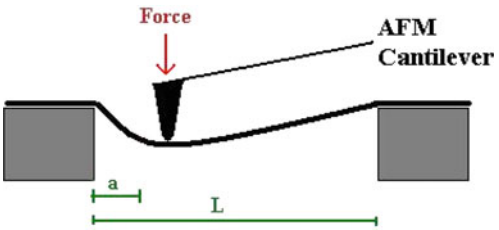

Fig. 8 Clamped fiber with length equal to (L). Force is applied to the fiber with distance (a) from the edge using the AFM cantilever tip [30]

pitch of 3 µm and then it was spin coated. Fibers with diameters <100 nm were identified by AFM imaging and then using force-volume mode, force spectra were gained for an array of positions along the fibers (Fig. 7).

It was assumed that the fibers had elliptical cross sections and that they were clamped on both ends. The slope of the force spectra, *dy/dz*, that was measured along the fibers was then calculated to be:

$$\frac{dy}{dz} = \left[1 + \frac{k}{3EI}\left(\frac{a(L-a)}{L}\right)^3\right]^{-1} \tag{3}$$

where k is the spring constant of the AFM cantilever, I is the area moment of inertia, L is the length of the fiber, a is the position of loading with respect to one end (Fig. 8), and E is the elastic modulus of the fiber which is unknown.

The elastic modulus was calculated 78 ± 17 GPa, which was consistent with Voigt model [34].

Cheng and Wang [15] used AFM and measured the elastic modulus of cellulose fibers isolated from Lyocell fibers in a three-point bending test to be 93 GPa. Recently, Iwamoto et al. [40] used AFM to perform three point bending tests on CNXLs obtained by sulfuric acid hydrolysis of tunicate and obtained a value of 150.7 GPa. AFM seems to be a useful tool for characterization of the mechanical properties of single CNXLs (Table 2). These measurements rely on good knowledge of the geometry of the sample, which is obtained from AFM imaging, and can be affected by tip broadening parameter.

Raman spectroscopy is another well established technique which has been used for measurement of the elastic modulus specifically the elastic modulus of CNXLs. These measurements are based on the shift in the characteristic Raman band (located at 1,095 cm^{-1}) that corresponds to the vibration of C–O–C bonds on the back bone of the CNXLs (Fig. 9). To conduct these measurements, CNXLs are usually embedded in epoxy, and a macro-scale bending test is performed.

In 2005, Sturcova et al. [73] measured the elastic modulus of tunicate CNXLs to be around 143 GPa using this technique. In this case the position of the Raman band peak was linearly dependent on strain up to the value of about 0.8% (Fig. 10). Formations of a plateau after 0.8% strain was related to the weakening of the cellulose-matrix interface and as a result decrease in the stress transfer efficiency.

Table 2 Elastic modulus of CNXLs with different origins, gained using atomic force microscopy

CNXL origin	Elastic modulus (GPa)	Reference
Bacterial	78	[30]
Lyocell fibers	93	[15]
Tunicate	150.7	[40]

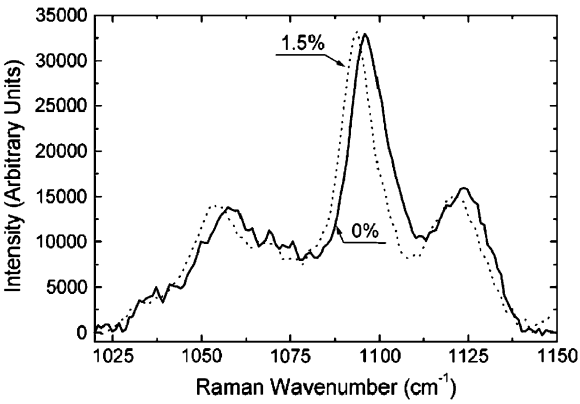

Fig. 9 Typical Raman band shift of the 1,095 cm^{-1} peak of tunicate cellulose subjected to tensile strain [73]

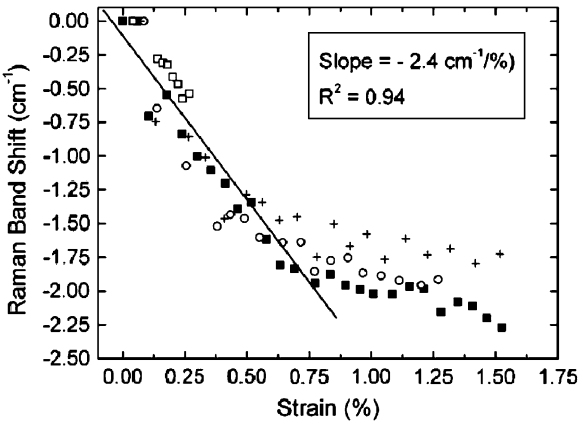

Fig. 10 The Raman band shift in the 1,095 cm^{-1} as a function of strain for tunicate cellulose [73]

Table 3 Elastic modulus of CNXLs with different origins, gained using Raman spectroscopy

CNXL origin	Elastic modulus (GPa)	Reference
Tunicate	143	[73]
Cotton	105	[68]
Bacterial	114	[38]

$$E = \frac{d\sigma}{d(\Delta v)} \times \frac{d(\Delta v)}{d \in} \tag{4}$$

$$\mathrm{E}_c = \eta_0 \mathrm{E}_\mathrm{f} \tag{5}$$

By substituting $d(\Delta v)/d \in = 2.4$ $cm^{-1}\%$ (from Fig. 10) and value of $d\sigma/d(\Delta v) = 4.7$ cm^{-1}/GPa [20, 21], in Eq. 4, the elastic modulus of two dimensional network tunicate cellulose was calculated to be 51.1 GPa. Eq. 5 was then used to obtain the elastic modulus of a single fiber of CNXL (E_f). In this equation E_c is the elastic modulus of a two dimensional random network of fibers and η_0 is the efficiency factor equal to $9/8\pi$.

The drawback for this modeling approach is that Eqs. 4 and 5 are based on the assumption of well compacted fibers. Moreover the fact that cellulose was embedded in matrix, the nature of chemical bonding between cellulose and matrix and the distribution of CNXLs can play a role in the calculated elastic modulus.

Recently, the same technique was used to measure the elastic modulus of cotton CNXLs and bacterial CNXLs (Table 3). Hsieh et al. [38] obtained the value of 114 GPa for the elastic modulus of bacterial CNXLs and Rusli and Eichhorn [68] found an upper value of 105 GPa and a lower value of 57 GPa for the elastic modulus of cotton CNXLs. Both of the values for cotton CNXLs are lower than the value for tunicate cellulose measured by Sturcova et al. [73] and the value for bacterial cellulose reported by Hsieh et al. [38]. This may be due to the smaller aspect ratio in cotton-based cellulose than the aspect ratio of other CNXLs which might have resulted in less effective stress transfer.

One could ask what causes such high elastic modulus in a low density polymer such as cellulose. To answer this question, we should go back to the molecular structure of cellulose (Fig. 11). There are multiple hydroxyl groups on the cellulose chain. These can make intermolecular and intramolecular hydrogen bonds which have a key role in the mechanics of this material. When a cellulose chain goes under tension, hydrogen bonds bear the load and deform. This continues until the load reaches the strength of these bonds, and these break (yield point). After this point, C–O–C bridges come into the picture and take the majority of the load [43, 45].

Number and nature of the hydrogen bonds greatly affect the mechanical properties of cellulose nanocrystals. For example, Tashiro and Kobayashi [75] showed that the intramolecular hydrogen bonds in cellulose II fibers are weaker than those in cellulose I, but their intermolecular bonds are the same. This results in higher elastic modulus for cellulose I than II.

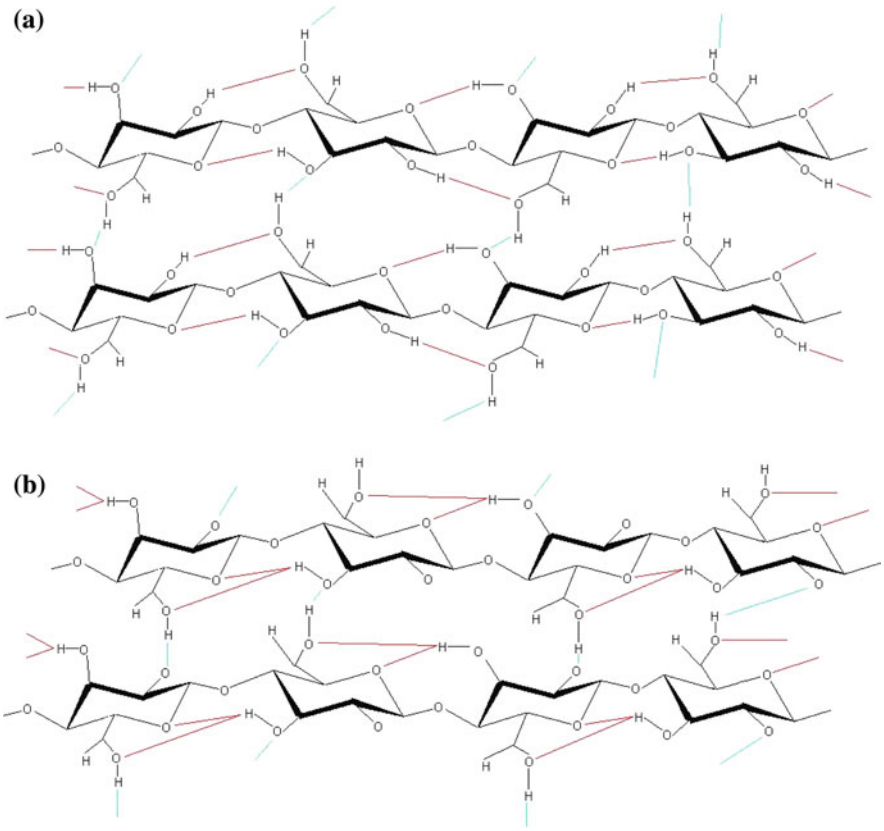

Fig. 11 Intermolecular (*blue*) and intramolecular (*red*) hydrogen bonds in cellulose I (**a**) and cellulose II (**b**)

Table 4 compares the elastic modulus and tensile strength of CNXLs with carbon nanotubes, steel and glass fiber. As it can be seen mechanical properties of CNXLs are much higher than those of glass fiber and stainless steel and are slightly lower than carbon nanotubes. This makes them promising candidates for reinforcement phase of composites materials specifically because unlike carbon nanotubes they are definitely biocompatible and biodegradable.

3 Mechanics of CNXL Composites

In a composite system reinforcements are used to carry the mechanical loads, improve the properties and lower the cost of the final product. On the other hand, matrix, which in our case is a polymer, is there to increase the toughness, to disperse fillers and to transfer the load to the fillers. Nanofillers are used widely these years because they have less defects and higher surface area compared to larger sized fillers. Thus nanofillers bring additional improvements and unique characteristics to the final product, at lower filler content levels as compared to micro and macro fillers.

Like all composite materials, the properties of cellulose nanocomposites depend on the properties, the volume fraction, and the spatial arrangement of the matrix and the reinforcement. Dispersion of CNXLs in the polymer matrix is not an easy procedure, and evenly distributed reinforcement is crucial for enhancement of the mechanical properties of composites. This can be specially challenging in the cases that polymer matrix is hydrophobic (as opposed to hydrophilic CNXLs). Without changing the surface activity and dispersion qualities of CNXLs (described later) the ultimate mechanical properties of the nanocomposite may not be much different or they may even be less compared to the pure polymer.

On the other hand, the main factors that dictate their mechanical properties are:

The aspect ratio of the CNXLs (L/D): This ratio depends on the origin of the crystals and the higher it is the better the mechanical properties will be [46, 52, 63].

CNXLs from different origins will have diverse size distributions, surface properties and more importantly different aspect ratios. All of these have fundamental influence on the mechanical properties of the final composition. Figure 12 shows differences in the elastic modulus of composites made of starch (with elastic modulus <2 GPa) and 5 wt% CNXL from various origins.

Table 4 Strength and stiffness of CNXLs compared to other materials

Material	Tensile strength (GPa)	Elastic modulus (GPa)
Cellulose crystal	7.5–10 [33]	143 [73]
Glass fiber [17]	3	72
Steel [17]	0.9	215
Carbon nanotubes [83]	11–63	270–950

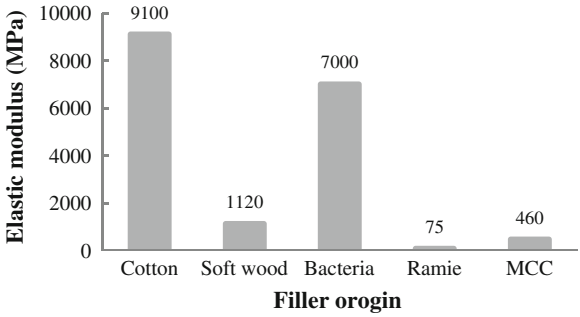

Fig. 12 Effect of CNXL origin on the Young's modulus of CNXL/starch composites [46, 52, 63]

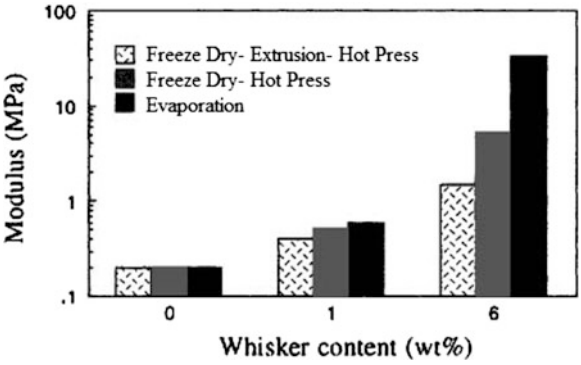

Fig. 13 Effect of processing method on the Young's modulus of CNXL/latex composites [32]

The processing method: Extrusion, hot pressing and evaporation are some techniques that are used. These techniques affect the orientation of the filler, the filler/filler interactions and may cause breakage of the fillers (changing the aspect ratio). They ultimately affect the final mechanical properties of the nanocomposite (Fig. 13). For instance, in the case of CNXL/latex composites, it has been shown that the efficiency of the processing methods is: extrusion < hot-pressing < evaporation [32].

The resulting competition of matrix/filler and filler/filler interactions: The preferred condition in most of composite materials is the matrix/filler, as opposed to the case in cellulose nanocomposites. Here the filler/filler interactions should be predominant, so that a 3D network of CNXLs is made to keep the week polymer in place and yield in higher stiffness and thermal stability in the resulting material [4, 24]. Percolating threshold, above which this 3D network is formed, is the critical volume fraction (v_{RC}), which separates the local and infinite communication of the fillers. It depends on the particle interactions and orientation and aspect ratio of fillers and it can be calculated using Eq. 6 [4]. Based on this equation, percolating threshold for composites with high aspect ratio fillers can be as low as 1%.

$$v_{RC} = \frac{0.7}{L/d} \tag{6}$$

Although filler/filler interactions need to be predominant, in order for the stress to be effectively transferred to the filler, good adhesion between the filler and matrix is vital [36, 28, 29], and not all polymers will have good adhesion with CNXLs. In order to optimize the interfacial bonding of the filler and the matrix, some modifications are possible. These include physical methods (e.g. changes in the structure and surface of CNXLs by coating them with surfactant [36]) and chemical modifications (e.g. grafting them with hydrophobes [25, 29]). One drawback to these procedures is that modified CNXLs have less reinforcing effects than not modified ones. This is due to the destruction of 3D network of CNXLs, as a result of changes in hydrogen bondings during these modifications. Another possibility can be the less efficient stress transfer from the polymer to CNXLs [28, 29].

Isotactic polypropylene (iPP), which is a hydrophobic polymer can be discussed as an example of surface modified cellulose crystals. Ljungberg et al. [50] prepared the iPP nanocomposites with aggregated CNXLs (CNXL-A), aggregated CNXL grafted with maleated polypropylene (CNXL-G-P), and surfactant-modified CNXL (CNXL-S), and compared their mechanical properties. At large deformations, where the mechanical properties depend chiefly on the dispersion quality of the fillers, failure to disperse CNXL-A homogenously, resulted in inferior mechanical properties than pure iPP. On the other hand, incorporating CNXL-G-P and CNXL-S into iPP enhanced the mechanical properties at large deformations as well as in linear ranges. This was due to the fact that their modified surface made good distributions and stress transfer possible (Fig. 14).

Following is a review on the studies that have been performed to characterize the tensile, nanoindentation, creep and thermo mechanical properties of CNXL-based nanocomposites.

3.1 Tensile Properties

Tensile tests are usually performed in universal test machines on pure polymer matrix and nanocomposite samples which are molded or cut in dog bone or

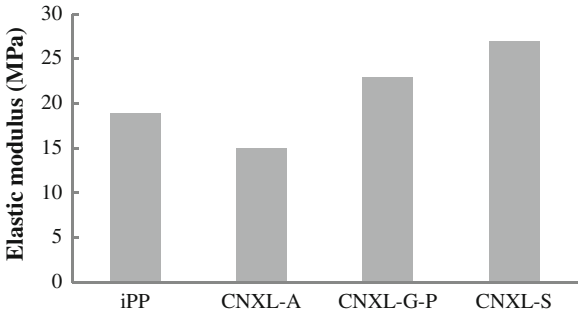

Fig. 14 Effect of CNXL surface modification on the Young's modulus iPP composites with 6 wt% tunicin CNXL [50]

rectangular shapes. Important mechanical properties such as elastic modulus, tensile strength, yield strength and ductility, can be derived from the load–displacement or stress–strain curves. Furthermore, by studying the shape of these curves one can gain useful information about the morphology of the ultimate nanocomposite and the dispersion quality if the reinforcements. For instance no necking can be a representative of well dispersion of filler in the polymer.

Compared to non-reinforced polymers, CNXL-based composites show improvements in tensile modulus and yield strength [3, 4, 13, 16, 46, 48, 54, 61, 65, 67, 82]. Figure 15 depicts the changes in mechanical properties of two different polymers (soy protein isolate (SPI) and polyvinyl alcohol (PVA)) before and after addition of CNXLs derived from cotton linters. Although the total trend is that the tensile strength and elastic modulus increase by adding CNXLs to polymers, the amount and quality of these strongly depend on the polymer and its interaction with CNXLs.

In general, an optimum filler content is desired in order to achieve the ultimate mechanical properties [16, 67, 79]. After this optimum value, the addition of filler content may result in the reduction of tensile strength and/or elastic modulus due to phase separation which occurs because of agglomeration of the nanofillers (see the strength data on Fig. 15). This optimum filler content depends on the characteristics of the polymer matrix and its interaction with nanocrystals. The tensile strength and/or elastic modulus decrease with addition of more cellulose and this is due to phase separation which occurs because of agglomeration of the nanofillers.

Elongation at break mostly decreases with addition of CNXLs, meaning that the material is modified from being ductile (with long deformation after yield until fracture) to very brittle (with almost no plastic deformation after yielding point; Fig. 15). Addition of a hard filler to a soft matrix results in higher strength at the cost of ductility. The reduction in elongation at break is a sign of good filler/filler and filler/matrix interactions, which restricts the motion of the polymer matrix.

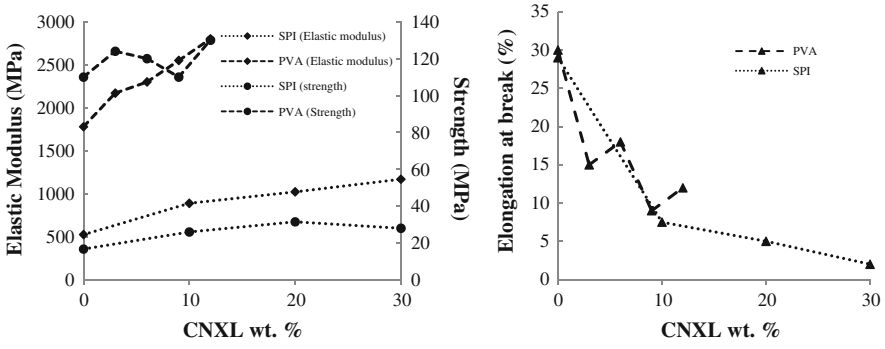

Fig. 15 Change in elastic modulus and tensile strength (*left*) and elongation at break (*right*) of soy protein isolate (SPI) and polyvinyl alcohol (PVA) filled with different amounts of CNXL derived from cotton linter [67, 79]

Table 5 summarizes the mechanical properties of various CNXL-polymer composites. Although this table does not cover all the published literature, it can be a good reference for comparison of the effect of cellulose origins and polymer types on the ultimate mechanical properties of these nanocomposites and the optimum filler content.

Experimental conditions such as temperature and relative humidity have great effects on tensile test results. For example as it is seen in Fig. 16, increase in the relative humidity (RH), tends to degrade the mechanical properties of cellulose nanocomposites with hydrophilic matrices [19, 79]. This is because at high humidity levels, hydrophilic polymer absorbs large amounts of water. As a result the matrix/filler interactions declines and CNXLs become surrounded by a week and soft phase, and the reinforcing effect of CNXLs diminishes.

3.2 Nanoindentation Studies

Another technique for mechanical characterization of polymer composites is nanoindentation. Nanoindentation is similar to macro-hardness tests but is done in nano-scales. Typically a diamond indentation tip with known elastic modulus and hardness is pressed into the surface of the sample, and the applied normal load (P) and the indentation height into the surface (h) are measured continuously during the loading and unloading. A schematic load–displacement curve is shown in Fig. 17. The elastic modulus (E) and hardness (H) are then calculated using the slope of the unloading part of the curve (S) and the equations below:

$$S = \frac{dP}{dh} = \frac{2}{\sqrt{\pi}} \boldsymbol{E}_r \sqrt{A} \tag{7}$$

$$\frac{1}{E_r} = \frac{(1 - v^2)}{E} + \frac{\left(1 - v_i^2\right)}{E_i} \tag{8}$$

$$H = \frac{P_{\max}}{A} \tag{9}$$

S is the slope of the load–displacement curve, which is obtained by fitting a second order polynomial function to the curve and differentiation (dP/dh). A is the projected contact area. As opposed to conventional indentation techniques, here the contact area is measured indirectly using the indentation height and the known geometry of the indenter. E_{r} is the reduced elastic modulus (the measured elastic modulus includes effects from both the specimen and the indenter), v_i, v and E_{i}, E are the Poisson's ratios and the elastic moduli of the indenter and the sample respectively [62].

Although several nanoindentation experiments have been reported for cellulose nanofiber reinforced polymer composites, no reports were found on nanoindentation results on CNXL composites. In this section two examples of nanoindentation

Table 5 Mechanical properties of various CNXL-polymer composites

Polymer				CNXL		Optimum composite				Reference
Name	Elastic modulus (MPa)	Strength (MPa)	Elongation at break (%)	Origin	Content variation	Filler content (%)	Elastic modulus (MPa)	Strength (MPa)	Elongation at break (%)	
Polyvinyl acetate	1,780	110	30	Cotton linter	0–12	12	2,800	130	12	Roohani et al. [67]
Soy protein isolate	526.4	16.73	29	Cotton linter	0–30	30	1,170	28	2	Wang et al. [80]
Waterborne polyurethane	0.5	4.3	1,086	Flax fiber	0–30	30	334.4	14.9	186	Cao et al. [13]
Polyurethane	41.16	14.05	0.55	Cellulose micro crystal	0–5	5	100.28	8.74	0.26	Marcovich et al. [54]
Modified potato starch	370	11.3	25	Cellulose micro crystal	0 and 5.3	5.3	460	13.7	32	Kvien et al. [46]
Plasticized wheat starch	55.9	2.8	94.2	Ramie	0–40	40	479.8	6.9	13.6	Lu et al. [52]
Unsaturated polyether	0.81	0.4	82	Tunicin	0–6	6	22.3	10.6	62	Azizi Samir et al. [6]

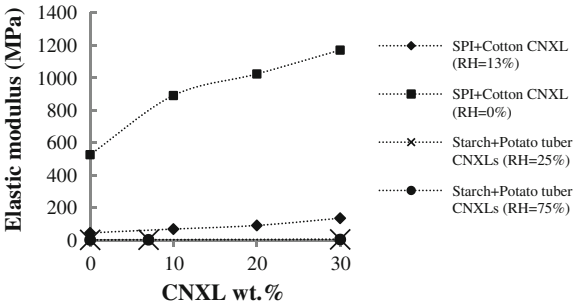

Fig. 16 Change in elastic modulus of soy protein isolate (SPI) and Starch filled with CNXL at various relative humidity (RH) [19, 79]

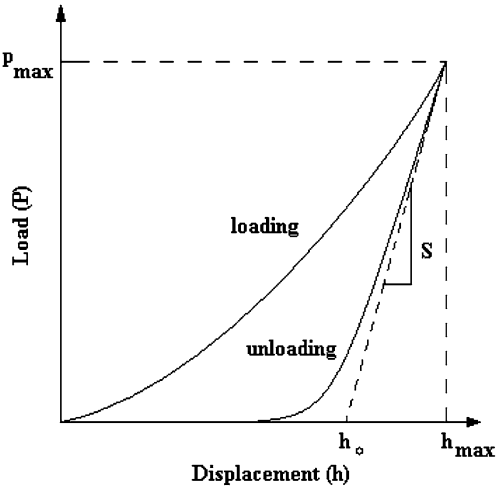

Fig. 17 Typical load–displacement curve [62]

results are discussed. Polymers in this section are all reinforced with cellulose nanofibers, which as opposed to CNXL that consist of only crystalline parts, have some amorphous regions too.

Zimmermann et al. [84] compared the elastic modulus of hydroxypropyl filled with cellulose nanofibers gained from two different methods of tensile and nanoindentation tests. The elastic modulus of the filled polymer was higher than the unfilled one in both methods, but nanoindentation resulted in higher values in comparison to tensile tests (Fig. 18). This dissimilarity may have different reasons. Firstly the elastic modulus of polymers depends on the available free volume, in nanoindentation this volume is less than in tension tests. Secondly, the volume of the sample on which the test is performed is bigger in tensile testing than in nanoindentation, this bigger volume contains larger amount of deflections such as microscopic cracks. And thirdly, the strain rates in these two methods are different and it is well known that the elastic modulus can be highly affected by the strain rate in many materials.

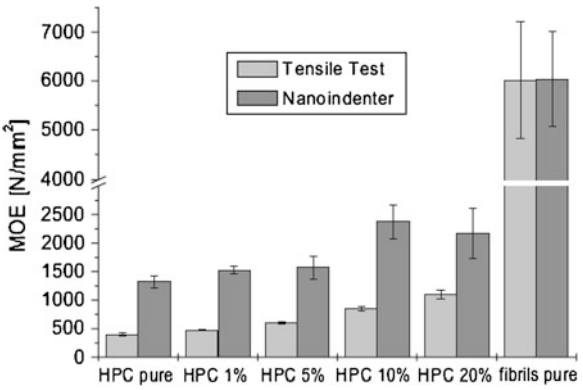

Fig. 18 Comparison the elastic modulus (MOE) values gained from tensile and nanoindentation tests on hydroxypropyl-cellulose nanofiber composites. Although the values gained for MOE from nanoindentation tests are higher than those gained from tensile tests, in both methods MOE increases as the amount of cellulose nanofiber is incresed in the nanocomposite [84]

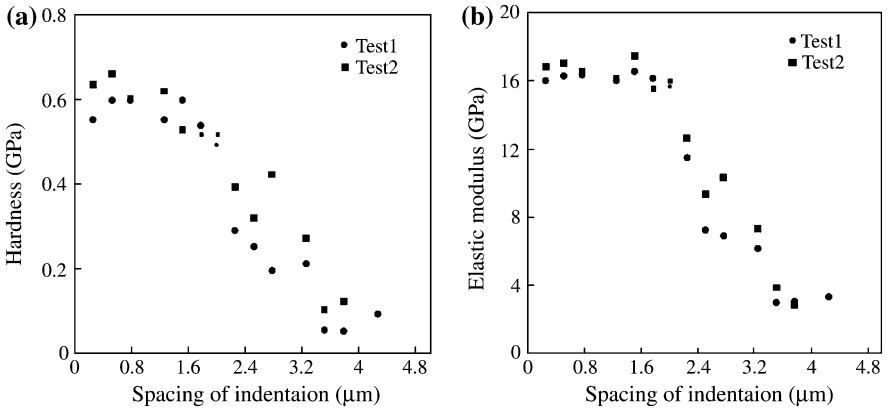

Fig. 19 Change in **a** hardness and **b** elastic modulus across the interphase region obtained by nanoindentation with 30 nm depth and 260 nm spacing [49]

As it was mentioned before, the stress transfer quality between filler and matrix is of significant importance in the mechanical studies of nanocomposites. The area that bonds cellulose nanofibers to polymer matrix is called *interface*. At the interface the properties change from the properties of individual nanofibers to the one in polymer matrix. The interface has crucial effects on the stress transfer qualities and has been motivation of great deal of studies and investigations. Lee et al. [49] evaluated the interface properties of polypropylene (PP) filled with cellulose nanofibers, using nanoindentation and compared the results with finite element analysis (FEA). A series of indentation tests with different indentation depth and different spacing were performed on the samples. According to the nanoindentation results with 30 nm depths and 260 nm spacing (Fig. 19), it was concluded that the width of the interface region was less than one micron. FEA results showed that the perfect interface width would be approximately 1.8 μm. Therefore, it was concluded that using the conventional techniques it would be

difficult to calculate the true mechanical properties of the interface in an area at least 8 times smaller than the indent size. At areas smaller than this value, the effect of neighboring materials becomes dominant which potentially can affect the experimental results.

Care should be taken during analysis of nanoindentation results for polymer composites. There are some debates that the famous Oliver-Pharr method [62], should not be used for polymer materials [76]. One should be careful when comparing results from nanoindentation tests on different materials, using different tips, techniques and in different laboratories. There are some phenomenon which can affect the test results. For example: Pile up is bulding out of the free surface of the material, which changes the contact area, and ultimately the E and H calculations. Viscoelasticity characteristics of polymers affects the unloading curves, and results in what is called a "nose" on the curves, where the indentation height increases while the load is being decreased. This results in negative values for contact stiffness (S). Finally the morphology of the indentation surface is vastly affected by sample preparation techniques that can result in different microstructures with different mechanical properties and/or various microscopic roughnesses. These ultimately give various E and H for various positions on one specific sample and increase the standard deviations from the average values.

3.3 Creep Properties

A limited number of investigations have been conducted on creep properties of CNXL composite systems. It is expected that due to stiffer nature of cellulose than the polymer matrix, CNXLs restrict the motion and reorientation of the polymer chains. This can influence the stress transfer and results in the enhancement of creep resistance in nanocomposite material [3]. Figure 20 shows that the addition of even a small amount of CNXL (0.1 to 1%) to polyurethane considerably decreases the creep strain.

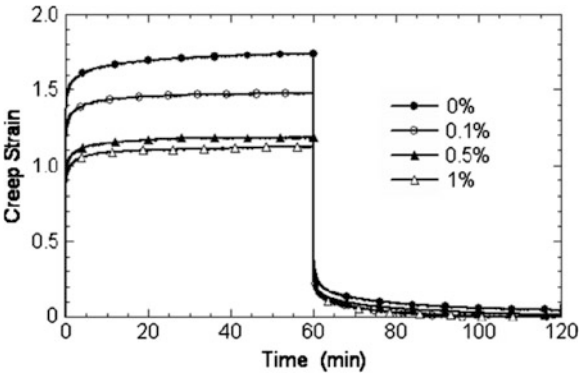

Fig. 20 Creep *curves* for unfilled polyurethane and CNXL/polyurethane nanocomposites with different wt. % (tests conducted at 20°C for 60 min). Due to the restricted motion of polymer chain by CNXLs, the creep resistance increases by increasing the filler even to a very small amount [3]

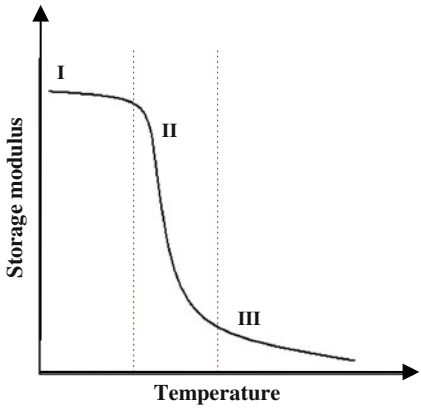

Fig. 21 Temperature dependence of storage modulus in a Thermoplastic polymer *I* glassy *II* glass transition *III* viscous liquid

3.4 Thermo-Mechanical Characterization

Thermo-mechanical characteristics of CNXL composites are mostly investigated using dynamic mechanical analysis (DMA), where the storage modulus (tensile: E' or shear: G') and the position of tan δ peak (the loss factor, $\tan\delta = \frac{E''}{E'}$ where $E''$is the loss modulus) are compared in the pure polymer and in composites with different filler contents. DMA is mostly performed in tensile (E') or sheer (G') mode, in a wide range of temperatures around the glass transition temperature of the polymer. These tests are usually done with a constant frequency (e.g. 1 Hz) and they provide information about the visco-elastic properties of materials.

Figure 21 shows a schematic curve of changes in storage modulus by temperature for a thermoplastic. This curve contains three phases:

(1) At temperatures below T_g or glassy stage, the storage modulus remains almost constant with increase in temperature.
(2) As the temperature approaches T_g, a dramatic drop in the storage modulus is observed where the material is being transformed from glassy to rubber state.
(3) Above T_g, polymer turns into a viscous liquid, and storage modulus keeps decreasing with increase in temperature.

Generally cellulose nanocomposites have been found to be more thermally stable than the matrix alone. Again, enough CNXL content causes a continuous 3D network (percolation), which reduces the mobility of polymer matrix and as a result the storage modulus (E' or G') increases and tan δ peak broadens. Above melting temperature (T_m) is where CNXLs have the most effect on thermo mechanical properties of the composites. As opposed to pure polymer, here storage modulus does not drop by increase in temperature, thus performance at high temperatures is improved and thermal stability is brought to the ultimate material up to degradation temperature of cellulose (around 500 K). Another thermo mechanical observation in nanocomposite polymers filled with CNXL is increase in glass transition temperature (T_g). This phenomenon is related to change in the

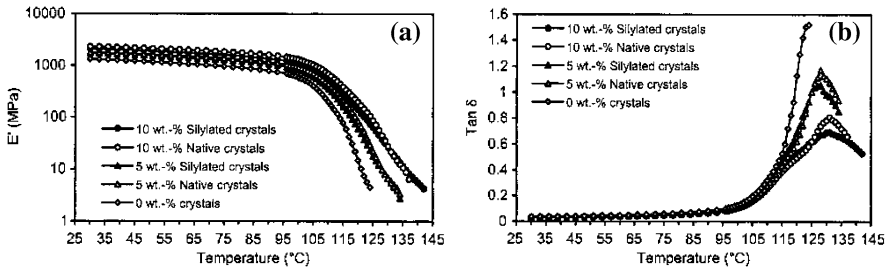

Fig. 22 Temperature dependence of storage modulus (**a**) and tan δ peak (**b**) in CNXL composites. Nanocomposites of native CNXL are thermally more stable than unfilled cellulose acetate butyrate and nanocomposites of silylated CNXL [29]

kinetics of the glass transition due to the presence of the nanocrystals and also increase in cross linking and as a result decrease in the mobility of the polymer chains. Broad amount of work has been concentrated on the thermo mechanical properties of CNXL polymer composites, for instance see: [1, 3, 5, 6, 8, 12, 13, 16, 23, 29, 31, 35, 46, 50, 52, 54, 65, 67, 79, 80].

Figure 22 depicts the results obtained from DMA tests on nanocomposites of cellulose and cellulose acetate butyrate [29]. Adding 10 wt. % native cellulose resulted in 94% improvement, at 81°C, and 2,000% improvement, at 124°C, in E′. Tan δ peak is also shown to go to higher temperatures and lower magnitudes and to broaden as the amount of filler was increased.

4 Morphological Analysis

For information on polymer microscopy readers can see Sawyer and Grubb [70], Bozzola and Russell [9].

4.1 Cellulose Nanocrystals

Preparation conditions like hydrolysis time and temperature have great affect on the geometrical properties of resulting CNXLs. Meanwhile, properties such as their diameter, aspect ratio and tendency to aggregate, have critical affects on the mechanical properties of CNXL-polymer composites. Hence, it is important to examine these fillers before they are dispersed in polymer matrices. Various microscopy techniques can be used for this purpose. Most commons are:

Scanning Electron Microscopy (SEM): SEM with a field emission gun (FESEM) can be used to image CNXLs. Usually a dilute solution of the sample is made, a droplet is put on a substrate and is left to air dry. In order to prevent charging and burning either low accelerating voltage (1–3 V) can be used, which

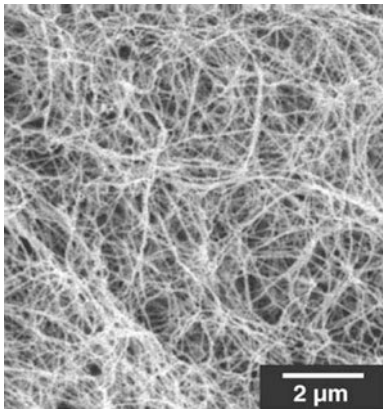

Fig. 23 A SEM image of bacterial CNXL pellicles [59]

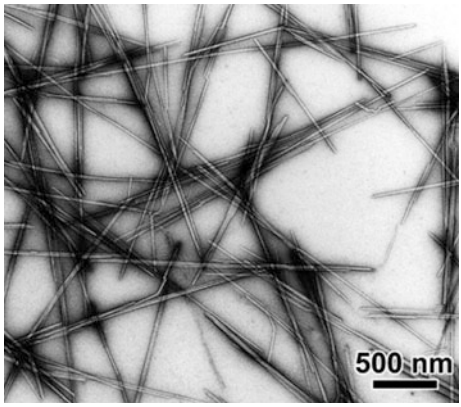

Fig. 24 A TEM image of tunicin CNXL [22]

will degrade the resolution, or the sample can be coated with conducting materials. Because of resolution limitations and instability of the sample in SEMs, it is usually difficult to obtain precise details of CNXLs in these images (Fig. 23).

Transmission Electron Microscopy (TEM): In order to examine CNXLs in TEM, a drop of dilute solution is put on a carbon coated grid, and let dry in air. Usually metal shadowing or negative staining is needed to improve the contrast (Fig. 24). For instance, sample can be negatively stained by floating the grid in staining materials, such as uranyl acetate, for a few minutes. Some difficulties in TEM imaging are sample preparation techniques and beam sensitivity of the sample.

Atomic Force Microscopy (AFM): AFM in tapping mode can be used for this purpose. Again, a droplet of CNXL solution is dried on a substrate (usually freshly cleaved mica) and studied. AFM seems to be a good alternative to electron microscopy because it does not have the limitations of low contrast and resolution, and sample preparation is much easier (Fig. 25). The only disadvantages are the tip broadening and scan rate that can affect the quality of the images.

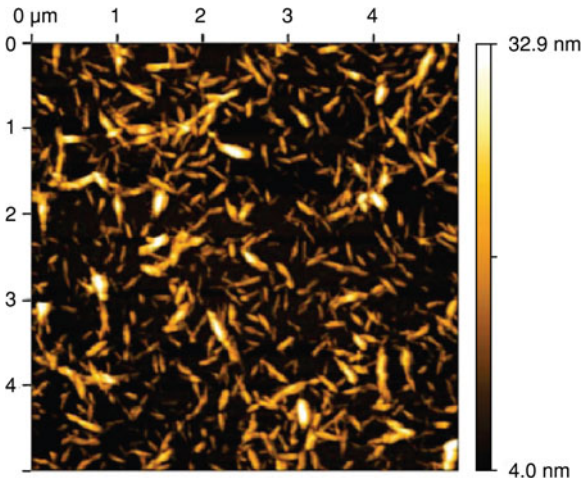

Fig. 25 AFM image of cotton CNXL [22]

4.2 CNXL Polymer Composites

The dispersion quality of CNXL through the polymer matrix has great effects on the nanocomposite ultimate properties. As mentioned before, hydrogen bonding is the main reason for formation of the rigid 3D network of cellulose crystals above percolating threshold, which holds the polymer matrix and improves its mechanical and thermal properties. Meanwhile, these bonds can bring difficulties in filler dispersion, cause aggregation of CNXLs, and degrade the ultimate properties.

Firstly, since the size of CNXLs is smaller than the light wavelength, if the pure polymer is transparent and the final composite comes out opaque, one can conclude that there are agglomerations of CNXLs, simply by eye observations.

Some of the techniques used for characterization of the filler dispersion in nanocomposite materials are: optical microscopy (OM), SEM, TEM, AFM, small angle X-ray scattering (SAXS) and wide angle X-ray diffraction (WAXD). Here we discuss three most common techniques (OM, SEM, TEM). SEM uses electrons to scan the surface of the specimen, and TEM passes electrons through a thin slice of the specimen.

4.2.1 Optical Microscopy

Observation of the solid surface of polymer nanocomposites in an optical microscope (OM) can results in some qualitative information about the filler dispersion. If CNXLs are not individualized and dispersed well, their aggregate will appear in the image (Fig. 26).

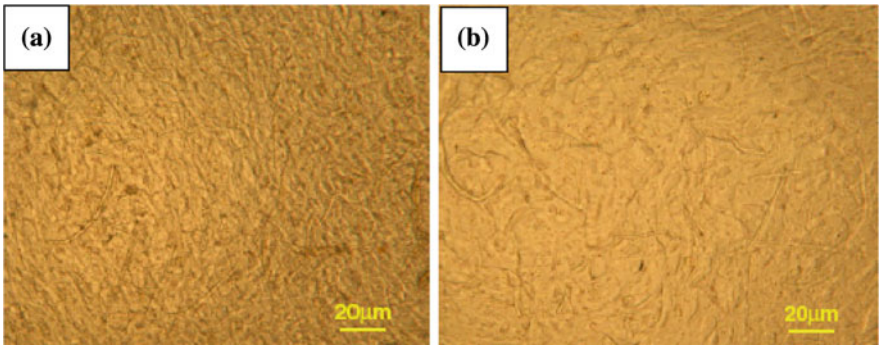

Fig. 26 Optical Microscopy images of CNXL-PVA composites (**a**) reinforcement without coating; (**b**) reinforcement coated with ethylene–acrylic oligomer. The dispersion is better in **b**, where less aggregates and filler with smaller diameters are observed [80]

4.2.2 Scanning Electron Microscopy

The fracture surface of polymer composites (obtained either by cryo fracturing in liquid nitrogen temperature or from tension tests), are observed in SEM and compared to the surface of pure polymer. Addition of CNXLs to polymers alters their fracture mechanism. The fracture surface of thermoplastics is usually featureless, flat and smooth (Figs. 27a, 28a). After CNXLs are added, up till the optimum point, rigid CNXLs act as obstacles for movement of dislocations and cracks and make them change path. As a result the fracture surface comes out to be rough and irregular with coarse slip planes (Figs. 27b, 28b). After this point, addition of more CNXL, results in their agglomeration and inferior mechanical properties and this coincides with voids, wrinkles and crystals being pulled out of the polymer matrix (Fig. 27c).

Usually CNXLs appear as white dots during the SEM imaging due to the highly non-conductive nature of the nanocrystals. The concentration of these dots increases as the filler content increases in the nanocomposite. When CNXLs are well dispersed and there is good adhesion between the filler and the polymer

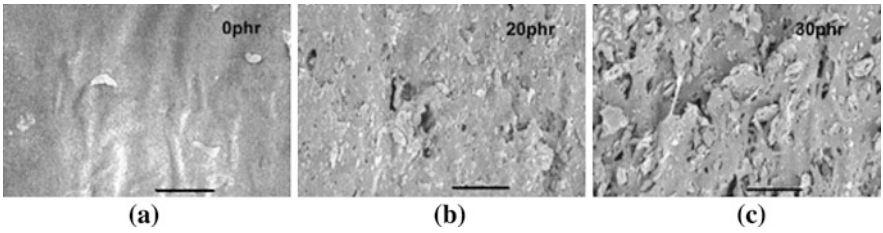

Fig. 27 SEM images of tension fracture surfaces of CNXL/nitrile rubber composites: **a** 0 phr; **b** 20 phr (optimum filler content); **c** 30 phr (The scale bars are 50 microns). Comparing to (**a**), the surface is rougher in (**b**) and (**c**). Because of poor matrix/filler interactions, pulled out particles can be seen in (**c**) [48]

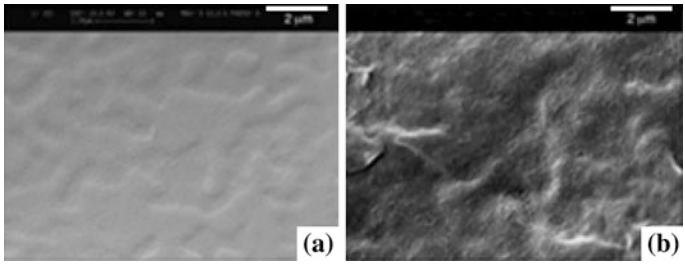

Fig. 28 Fracture surface of polyurethane (**a**) and polyurethane filled with 1 wt. % CNXLs (**b**). CNXLs make the cracks change path and increase the energy dissipation during the fracture in (**b**) [3]

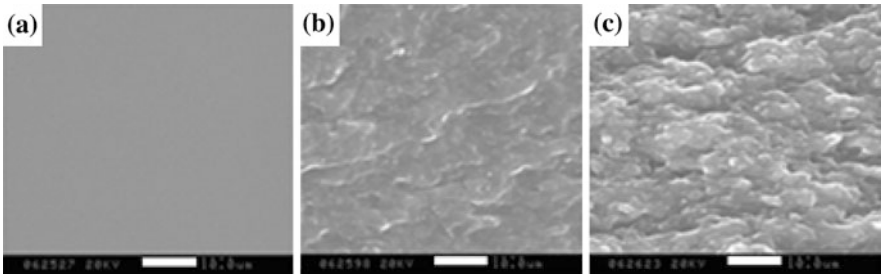

Fig. 29 SEM images of the polyurethane filled with different wt. % of CNXL: **a** 0 **b** 20 **c** 30. In contrast with the fracture surface in (**a**) which is featureless, the fracture surfaces are rough in (**b**) and (**c**) and the white dots on them are the CNXLs [13]

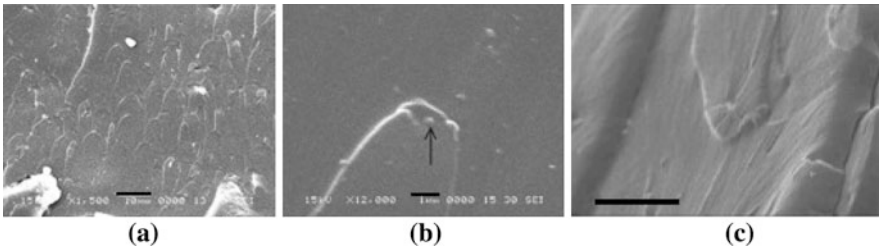

Fig. 30 SEM images of the fish scale feature on the fracture surface of cellulose nanocomposites which is related to the fracture toughness: **a** ×1,500 (scale bar = 10 micron) **b** ×12,000, the *arrow* shows a CNXL (scale bar = 1 micron) **c** the surface from an angle (scale bar = 2 micron) [54]

matrix (e.g. when both phases are hydrophilic) fractography of the fracture surface reveals no sign of agglomeration of nanocrystals (Fig. 29).

Marcovich et al. [54] detected a fish scale feature on the fracture surface of nanocomposites of polyurethane and CNXLs (Fig. 30). The density of these parabolic features is related to the energy consumed to break the samples and thus the

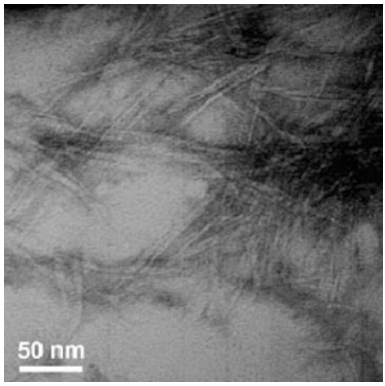

Fig. 31 TEM images of CNXL-PLA composite [47]

fracture toughness. As the content of the filler increases the ridges on the fracture surface become smaller and their density increases. This might results in higher density of crack deflections, and as a consequence higher fracture toughness.

4.2.3 Transmission Electron Microscopy

In this case, very thin (<100 nm) slices of the specimen are prepared using ultra microtome with a diamond knife. These slices are then mounted on carbon coated grids and studied in TEM (Fig. 31). Because the filler and the matrix are both polymers, CNXLs need to be stained (usually negatively, using materials such as uranyl acetate) to improve the contrast. Because of difficulties with respect to sample preparation and also cost, TEM is not used as widely as SEM is.

5 Summary

A limited number of theoretical modeling on mechanics of individual cellulose nanocrystals and their nanocomposites has been conducted so far. There are still great opportunities for computational mechanic researchers to explore this field. First principle calculations and molecular mechanics have the potential to better describe the behavior of cellulose nanocrystals due to their nanometer sizes. Rarely, direct experimental methods have been utilized for measuring the mechanical properties of individual cellulose nanocrystals. An indirect method based on the shift in Raman band peak has been used to obtain the elastic modulus of cellulose nanocrystals embedded in a polymer matrix. These measurments are not reliable due to the effect of background matrix. Recently AFM technique was used to perform bending tests on CNXLs, but this technique has to be further explored.

It has been shown that there is a clear difference in the mechanical properties of CNXLs from different resources. For instance, CNXLs from cotton have smaller aspect ratios and as a result smaller elastic modulus than those from bacteria or tunicate. However no micro/nanoscale observation has been made to understand the atomistic nature of such differences.

The macroscopic mechanical behavior of cellulose nanocomposites can be strongly affected by the competition between filler/filler and matrix/filler interactions and by the formation of strong 3D network of CNXLs. It has been shown that tensile modulus, yield strength, fracture toughness and creep resistance are higher in cellulose nanocomposites than in the neat polymers, but due to the agglomeration of CNXLs in higher filler contents, there is usually an optimum amount of filler. In order for the mechanical percolation to happen filler/filler interactions need to be predominant. On the other hand optimized matrix/filler interactions in nanocomposites guarantees superior mechanical and thermomechanical properties.

Addition of CNXL to polymers also alters their failure mechanism. The fracture surface changes from being smooth and featureless to being rough. As the content of the cellulose increases, there is more discontinuity and stress concentration, and the ridges on the surface of the fracture become denser and smaller. It is expected that the presence of the nanocrystals causes crack deflection during the fracture, and a greater energy is needed for the cracks to grow.

Furthermore, CNXLs improve thermal stability of polymer composites. Formation of rigid 3D CNXL network, which keeps the polymer chains from moving, causes increase in the storage modulus (E', G') and T_g, broadens tan δ peak and moves it to higher temperatures.

Acknowledgments The authors would like to thank Michigan Technological University for providing the financial support to conduct this review.

References

1. Alemdar, A., Sain, M.: Biocomposites, from wheat straw nanofibers: morphology, thermal and mechanical properties. Compos. Sci. Technol. **68**, 557–565 (2007)
2. Angles, M.N., Dufrense, A.: Plasticized starch/tunicin whisker nanocomposite materials 2: mechanical behavior. Macromolecules **34**, 2921–2931 (2001)
3. Auad, M.L., Contos, V.S., Nutt, S., et al.: Characterization of nanocellulose reinforced shape memory polyurethanes. Polym. Int. **57**, 651–659 (2008)
4. Azizi Samir, M., Alloin, F., Dufresne, A.: Review of recent research into cellulosic whiskers, their properties and their applications in nanocomposite field. Biomacromolecules **6**, 612–626 (2005)
5. Azizi Samir, M., Alloin, F., Sanchez, J., et al.: Cellulose nanocrystals reinforced poly(oxyethylene). Polymer **45**, 4149–4157 (2004a)
6. Azizi Samir, M., Alloin, F., Sanchez, J., et al.: Preparation of cellulose whiskers reinforced nanocomposites from an organic medium suspension. Macromolecules **37**, 1386–1393 (2004b)

7. Bondeson, D., Mathew, A., Oksman, K.: Optimization of the isolation of nanocrystals from microcrystalline cellulose by acid hydrolysis. Cellulose **13**, 171–180 (2006)
8. Bodenson, D., Oksman, K.: Dispersion and characterization of surfactant modified cellulose whiskers nanocomposites. Compos. Interfaces **14**, 617–630 (2007)
9. Bozzola, J.J., Russell, L.D.: Electron microcopy: principles and techniques for biologists. Jones and Bartlett Publishers, Boston (1992)
10. Beck-Candanedo, S., Roman, M., Gray, D.G.: Effect of reaction conditions on the properties and behavior of wood cellulose nanocrystal suspensions. Biomacromolecules **6**, 1048–1054 (2005)
11. Beecher, J.: Wood, trees and nanotechnology. Nat. Nanotechnol. **2**, 1–2 (2007)
12. Brown, E.E., Laborie, M.G.: Bioengineering bacterial cellulose/poly (ethylene oxide) nanocomposites. Biomacromolecules **8**, 3074–3081 (2007)
13. Cao, X., Dong, H., Li, C.M.: New nanocomposite materials reinforced with flax cellulose nanocrystals in waterborne polyurethane. Biomacromolecules **8**, 899–904 (2007)
14. Carotenuto, G.C., Her, Y.S., Matijevic, E.: Preparation and characterization of nanocomposite thin films for optical devices. Ind. Eng. Chem. Res. **35**, 2929–2932 (1996)
15. Cheng, Q., Wang, S.: A method for testing the elastic modulus of single cellulose fibrils via atomic force microscopy. Composites **39**, 1838–1843 (2008)
16. Choi, Y., Simonsen, J.: Cellulose nanocrystal-filled carboxymethyle cellulose nanocomposites. J. Nanosci. Nanotechnol. **6**, 633–639 (2006)
17. Daniel, I.M., Ishai, O.: Engineering mechanics of composite materials. Oxford University Press, New York (1994)
18. Dufresne, A., Cavaille, J., Helbert, W.: Thermoplastic nanocomposites filled with wheat straw cellulose whiskers. Part 2. Effect of processing and modeling. Polym. Compos. **18**, 198–210 (1997)
19. Dufresne, A., Dupeyre, D., Vignon, M.R.: Cellulose microfibrils from potato tuber cells: processing and characterization of starch-cellulose microfibril composites. J. Appl. Polym. Sci. **76**, 2080–2092 (2000)
20. Eichhorn, S.J., Sirichaisit, J., Young, R.J.: Deformation mechanisms in cellulose fibers, paper and wood. J. Mat. Sci. **36**, 3129–3135 (2001a)
21. Eichhorn, S.J., Young, R.J., Yeh, W.Y.: Deformation processes in regenerated cellulose fibers. Text. Res. J. **71**, 121–129 (2001b)
22. Elazzouzi-Hafraoui, S., Nishiyama, Y., Pataux, J., Heux, L., Dubreuil, F., Rochas, C.: The shape and size distribution on crystalline nanoparticles prepared by acid hydrolysis of native cellulose. Biomacromolecules **9**, 57–65 (2008)
23. Favier, V., Chanzy, H., Cavaille, J.Y.: Polymer nanocomposites reinforced by cellulose whiskers. Macromolecules **28**, 6365–6367 (1995)
24. Favier, V., Ganova, G.R., Shrivastava, S.C., Cavaille, J.Y.: Mechanical percolation in cellulose whisker nanocomposites. Poly. Eng. Sci. **37**, 1732–1739 (1997)
25. George, J., Sreekala, M.S., Thomas, S.: A review on interface modification and characterization of natural fiber reinforced plastic composites. Poly. Eng. Sci. **41**, 1471–1485 (2001)
26. Giannelis, E.P.: Polymer-layered silicate nanocomposites. Adv. Mater. **8**, 29–35 (1996)
27. Glasser, W.G.: Prospects for future applications of cellulose acetate. Macromol. Symp. **208**, 371–394 (2004)
28. Gopalan Nair, K., Dufresne, A., Gandini, A., Belgacem, M.N.: Crab shell chitin whiskers reinforced natural rubber nanocomposites 3.Effect of chemical modofocation of chitin whiskers. Biomacromolecules **4**, 1832–1835 (2003)
29. Grunert, M., Winter, W.T.: Nanocomposites of cellulose acetate butyrate reinforced with cellulose nanocrystals. J. Polym. Environ. **10**, 27–30 (2002)
30. Guhados, G., Wan, W., Hutter, J.L.: Measurement of single bacterial cellulose fibers using atomic force microscopy. Langmuir **21**, 6642–6646 (2005)
31. Habibi, Y., Dufresne, A.: Highly filled bionanocomposites from functionalized polysaccharide nanocrystals. Biomacromolecules **9**, 1974–1980 (2008)

32. Hajji, P., Cavaille, J.Y., Favier, V., Gauthier, C., Vigier, G.: Tensile behavior of nanocomposites from latex and cellulose whiskers. Polym. Compos. **17**, 612–619 (1996)
33. Hamad, W.: On the development and applications of cellulosic nanofibrillar and nanocrystalline materials.Can. J. Chem. Eng. **84**, 513–519 (2006)
34. Harris, B.: Engineering composite materials. IOM Communications Ltd., London (1999)
35. Helbert, W., Cavaille, J.Y., Dufresne, A.: Thermoplastic nanocomposites filled with wheat straw cellulose whiskers. Part I: processing and mechanical behavior Polym. Compos. **17**, 604–611 (1996)
36. Heux, L., Chauve, G., Bonnini, C.: Nanoflocculating and chiral-nematic self-ordering of cellulose microcrystals suspensions in nonpolar solvents. Langmuir **16**, 8210–8212 (2000)
37. Hongmei, W., Chen, Z., Fang, P., et al.: Synthesis, characterization and optical properties of hybridized CdS-PVA nanocomposites. Mater. Chem. Phys. **106**, 443–446 (2007)
38. Hsieh, Y.C., Yano, H., Nogi, M., et al.: An estimation of the Young's modulus of bacterial cellulose filaments. Cellulose **15**, 507–513 (2008)
39. Hubbe, M.A., Rojas, O.J., Lucia, L.A., Sain, M.: Cellulose nanocomposites: a review. Bioresources **3**, 925–980 (2008)
40. Iwamoto, S., Kai, W., Isogai, A., Iwata, T.: Elastic modulus of single cellulose microfibrils from tunicate measured by atomic force microscopy. Biomacromolecules **10**, 2571–2576 (2009)
41. Kojima, Y., Usuki, A., Kawasumi, M., et al.: One-pot synthesis of nylon-6 clay hybrid. J. Polym. Sci. Part A Polym. Chem. **31**, 1755–1758 (1993)
42. Kojimia, Y., Usuki, A., Okada, A.: J. Polym. Sci. Part A Polym. Chem. **35**, 2289 (1997)
43. Kong, K., Eichhorn, S.J.: The influence of hydrogen bonding on the deformation micromechanics of cellulose fibers. J. Macromol. Sci. B Phys. **44**, 1123–1136 (2005)
44. Koo, C.M., Kim, M.J., Choi, M.H., et al.: Mechanical and rheological properties of the maleated polypropylene-layered silicate nanocomposites with different morphology. J. Appl. Polym. Sci. **88**, 1526–1535 (2003)
45. Kroon, L.M.J., Kroon, L., Northolt, M.G.: Chain modulus and intramolecular hydrogen bonding in native and regenerated cellulose fibers. Polym. Commun. **27**, 290–292 (1986)
46. Kvien, I., Sugiyama, J., Votrubec, M., et al.: Characterization of starch based nanocomposites. J. Mater. Sci. **42**, 8163–8171 (2007)
47. Kvien, I., Tanem, B.S., Oksman, K.: Characterization of cellulose whiskers and their nanocomposites by atomic force and electron microscopy. Biomacromolecules **6**, 3160–3165 (2005)
48. Lapa, V.L.C., Suarez, J.C.M., Visconte, L.L.Y., et al.: Fracture behavior of nitrile rubber-cellulose II nanocomposites. J. Mater. Sci.**42**, 9934–9939 (2007)
49. Lee, S., Wang, S., Pharr, G.M., et al.: Evaluation of interphase properties in a cellulose fiber reinforced polypropylene composites by nanoindentation and finite element analysis. Composites **38**, 1517–1524 (2007)
50. Ljungberg, N., Cavaille, J.Y., Heux, L.: Nanocomposites of isotactic polypropylene reinforced with rod-like cellulose whiskers. Polymer **47**, 6285–6292 (2006)
51. Lyons, W.J.: Theoretical value of the dynamic stretch modulus of cellulose. J. Appl. Phys. **30**, 796–797 (1959)
52. Lu, Y., Weng, L., Cao, X.: Morphological, thermal and mechanical properties of ramie crystallites-reinforced plasticized starch bio composites. Carbohydr. Polym. **63**, 198–204 (2006)
53. Mann, J., Roldan-Gonzalez, L.: X-Ray measurements of the elastic modulus of cellulose crystals. Polymer **3**, 549–553 (1962)
54. Marcovich, N.E., Auad, M.L., Bellesi, N.E., et al.: Cellulose micro/nanocrystals reinforced polyurethane. J. Mater. Res. **21**, 870–881 (2006)
55. Meyer, K.H., Lotmar, W.: Helvetica Chem. Acta. **19**, 68 (1936).
56. Mi, Y., Zhang, X., Zhou, S., et al.: Morphological and mechanical properties of bile salt modified multi-walled carbon nanotube/poly(vinyl alcohol) nanocomposites. Compos. Part A Appl. Sci. Manuf. **38**(n9), 2041–2046 (2007)

57. Mohanty, A.K., Misra, M., Drzal, L.T.: Surface modifications of natural fibers and performance of the resulting biocomposites: an overview. Compos. Interfaces **8**, 313–343 (2001)
58. Muller, F.A., Muller, L., Hofmann, I., et al.: Cellulose-based scaffold materials for cartilage tissue engineering. Biomaterials **27**, 3955–3963 (2006)
59. Nakagaito, A.N., Iwamoto, S., Yano, H.: Bacterial cellulose: the ultimate nano-scalar cellulose morphology for production of high strength composites. Appl. Phys. **80**, 93–97 (2005)
60. Nishino, T., Takano, K., Nakamae, K.: Elastic modulus of the crystalline regions of cellulose polymorphs. J. Polym. Sci. B Polym. Phys. **33**, 1647–1651 (1995)
61. Noorani, S., Simonsen, J., Atre, S.: Nanoenabled microtechnology: Polysulsone nanocomposites incorporating cellulose nanocrystals. Cellulose **14,** 577–584 (2007)
62. Oliver, W.C., Pharr, G.M.: An improved technique for determining hardness and elastic modulus using load and displacement sending indentation experiments. J. Mater. Res. **7**, 1564–1583 (1992)
63. Orts, W.J., Shey, J., Imam, S.H., Glenn, G.M.: Guttman M E, Revol J, Application of cellulose microfibrils on polymer nanocomposites. J. Polym. Environ. **13**, 301–306 (2005)
64. Peng, Z., Xue, L.X., Li, S.D.: Dynamic mechanical analysis of polyvinylalcohol/silica nanocomposite. Synth. Met. **152**(n1–3), 25–28 (2005)
65. Petersoon, L., Kvien, I., Oksman, K.: Structure and thermal properties of poly(lactic acid)/ cellulose whiskers nanocomposite materials. Compos. Sci. Tech. **67**, 2535–2544 (2007)
66. Roman, M., Winter, W.T.: Cellulose nanocrystals. From discovery to application TAPPI international conference on nanotechnology, Atlanta. Georgia (2006)
67. Roohani, M., Habibi, Y., Belgasem, N.M., Ebahim G.: Cellulose whiskers reinforced polyvinyl alcohol copolymers nanocomposites. Eur. Polym. J. **44**, 2489–2498 (2008)
68. Rusli, R., Eichhorn, S.J.: Determination of the stiffness of cellulose nanowhiskers and the fiber-matrix interface in a nanocomposite using Raman spectroscopy. Appl. Phys. Lett. **93**, 033111 (2008)
69. Sakurada, I., Nukushina, Y., Ito, T.: Experimental determination of the elastic modulus of the crystalline regions in oriented polymers. J. Polym. Sci. **57**, 651–660 (1962)
70. Sawyer, L.C., Grubb, D.T.: Polymer microcopy 2nd edition. Chapman and Hall, London, New York (1996)
71. Schmidt, H., Krug, H., Kasemann, R., et al.: Development of optical waveguides by sol-gel techniques for laser patterning. Proc. SPIE Int. Soc. Opt. Eng. **1590**, 36–43 (1991)
72. Shibata, M., Oyamada, S., Kobayashi, S., et al.: Mechanical composites and biodegragability of green composites based on biodegradable polyesters and lyocell fabric. J. Appl. Polym. Sci. **92**, 3857–3863 (2004)
73. Sturcova, A., Davies, G.R., Eichhorn, S.J.: Elastic modulus and stress-transfer properties of tunicate cellulose whiskers. Biomacromolecules **6**, 1055–1061 (2005)
74. Tanaka, F., Iwata, T.: Estimation of the elastic modulus of cellulose crystal by molecular mechanics simulation. Cellulose **13**, 509–517 (2006)
75. Tashiro, K., Kobayashi, M.: Theoretical evaluation of three-dimensional elastic constants of native and regenerated cellulose: role of hydrogen bonds. Polymer **32**, 1516–1526 (1991)
76. Tranchida, D., Piccarolo, S., Loos, J., Alexeev, A.: Mechanical characterization of polymers on nanometer scale through nanoindentation. A study on pile-up and viscoelasticity. Macromolecules **40**, 1259–1267 (2007)
77. Treloar, L.R.G.: Calculation of elastic moduli of polymer crystals: III. Cellulose Polym. **1**, 290–303 (1960)
78. Vaia, R.A., Ishii, H., Giannelis, E.P.: Synthesis and properties of 2D nanostructures by direct intercalation of polymer melts in layered silicates. Chem. Mater. **5**, 1694–1696 (1996)
79. Wang, Y., Cao, X., Zhang, L.: Effect of cellulose whiskers on properties of soy protein thermoplastics. Macromol. Biosci. **6**, 524–531 (2006)
80. Wang, B., Sain, M.: Isolation of nanofibers from soybean source and their reinforcing capability on synthetic polymers. Compos. Sci. Tech. **67**, 2521–2527 (2007)

81. Wung, C.J., Yang, Y., Prasat, P.N., et al.: Poly(p-phenylene vinylene)-silica composite. A novel sol-gel processed non-linear optical material for optical waveguides. Polymer **32**, 605–608 (1991)
82. Yongshang, L., Weng, L., Cao, X.: Morphological, thermal and mechanical properties of ramie crystallites-reinforced plasticized starch biocomposites, Carbohyd. Polym. **63**, 198–204 (2005)
83. Yu, M.F., Lourie, O., Dyer, M.J., et al.: Strength and breaking mechanism of multi walled carbon nanotubes under tensile load. Science **287**, 637–640 (2000)
84. Zimmermann, T., Pohler, E., Schwaller, P.: Mechanical and morphological properties of cellulose fibril reinforced nanocomposites. Adv. Eng. Mater. **7**, 1156–1161 (2005)
85. Zugenmaier, P.: Conformation and packing of various crystalline cellulose fibers. Prog. Polym. Sci. **26**, 1341–1417 (2001)

Shift of Lines in Phase Diagrams for Nanograined Materials

Boris B. Straumal, Andrey A. Mazilkin, Petr B. Straumal, Andrey M. Gusak and Brigitte Baretzky

Abstract If one adds the atoms of a second component B to a one-component polycrystal A, they distribute between bulk and grain boundaries (GBs) and form a solid solution (A). If the amount of B exceeds the solubility limit in (A), the particles of a second phase appear and start to grow, and the concentration of B in (A) remains constant and equal to the solubility limit. However, the equilibrium solubility in the GBs is usually much higher than in the bulk. Therefore, the overall solubility of B in a polycrystal (A) would be higher than in a single-crystal (A). Thus, the solubility

B. B. Straumal (✉) · A. A. Mazilkin
Institute of Solid State Physics, Russian Academy of Sciences, Institutskaya str. 2, Chernogolovka 142432, Russia
e-mail: straumal@mf.mpg.de

A. A. Mazilkin
e-mail: mazilkin@issp.ac.ru

B. B. Straumal · B. Baretzky
Max-Planck-Institut für Metallforschung, Heisenbergstrasse 3 70569 Stuttgart, Germany
e-mail: Brigitte.Baretzky@int.fzk.de

B. B. Straumal · P. B. Straumal
National University of Science and Technology "MISIS", Leninsky Prospect 4 119991 Moscow, Russia
e-mail: p.straumal@misis.ru

P. B. Straumal
Institut für Materialphysik, Universität Münster, Wilhelm-Klemm-Str. 10 48149 Munster, Germany

A. M. Gusak
Cherkasy National University, 18027 Cherkasy, Ukraine
e-mail: gusak@phys.cdu.edu.ua

B. Baretzky
Karlsruher Institut für Technologie (KIT), Institut für Nanotechnologie, Hermann-von-Helmholtz-Platz 1 76344 Eggenstein-Leopoldshafen, Germany

Adv Struct Mater (2013) 4: 265–285
DOI: 10.1007/8611_2010_29

Published Online: 2 July 2010

lines in the phase diagrams should shift with decreasing grain size. We measured the solubility of Mn and Co in the zinc oxide with grain size of about 20 nm and compared with that in the ZnO single-crystals. At 500°C, the overall solubility increases from 2 to 33 at.% Co and from 2 to 28 at.% Mn. Temperature dependences of the solubility shift for the grain size of 20, 100 and 1,000 nm were calculated using the published data from the papers devoted to the investigations of ferromagnetism in doped ZnO. The quantitative estimation leads to the conclusion that, close to the bulk solubility limit, the thickness of a Co- and Mn-enriched layer in GBs is several monolayers and at least two monolayers in the free surfaces.

1 Introduction

The phase diagrams for the nanograined materials can drastically differ from those for the single crystals or coarse-grained polycrystals. For example, by increasing the content of an alloying component, c, a solubility limit is reached at a certain concentration, c_s. Above c_s the second phase appears in the bulk. By further increasing c, only the amount of the second phase increases, but the concentration in the first phase remains equal to c_s. The easiest way to measure c_s is to follow the change of the lattice spacing in the solid solution, for example with the help of X-rays diffraction (XRD). The lattice spacing continuously changes with increasing c up to c_s. At $c > c_s$ the lattice spacing remains unchanged, and the diffraction peaks of a second phase appear in the XRD spectrum.

However, if the alloy contains surfaces and interfaces with segregated second components, the total concentration of a second component, c_t, will be higher than the concentration in the bulk solid solution, c_v. The difference between c_t and c_v would increase with an increasing specific area of surfaces and interfaces (i.e. with decreasing grain size). If the grain size is small enough, the difference between c_t and c_v can become measurable. This is due to the fact that XRD registers the diffraction only from the bulk phases. The component segregated in the thin surface or interface layers remains invisible for XRD. The XRD peaks appear only in the case where the coherent-scattering region is large enough (grain size around 5 nm or larger). Simultaneously, XRD allows one to measure the grain size using the angle dependence of the peak width.

McLean was probably the first who mentioned that the apparent solubility limit, c_{sa}, in the fine grained materials will be higher than the volume solubility limit c_s [1]. He calculated this difference for the Fe–C system and grain size of 1 and 10 μm [1]. Beke et al. calculated the shift of miscibility gap due to the GB segregation in dependence on the number of GB layers [2, 3]. Experimentaly such shift was observed in the Pd–H system [3]. The increase of the total solubility with decreasing grain size was observed for Ti and Y in alumina [4] and for Y and Ca in TiO_2 [5]. Nevertheless, the consistent XRD measurements of solubility shift $c_{sa} - c_s$ in dependence on grain size d are very time-consuming and, to the best of our knowledge, were never conducted before.

Zinc oxide offers a good possibility for such successive investigation. ZnO is broadly used as a transparent conducting oxide in the semiconductor thin film technology, as a material for varistors (doped by Bi_2O_3) and for gas sensors. Moreover, it is a promising material for future spintronics as a possible ferromagnetic semiconductor. Ferromagnetic semiconductors could allow seamless electrical manipulations of magnetic states and magnetic modification of electric signals. In 2000 Dietl et al. [6] theoretically predicted that ZnO doped by small amounts of "magnetic" impurities like Mn or Co should possess the ferromagnetic properties. This work triggered a boom of experimental work. In the meantime more than 1,200 papers devoted to diluted magnetic semiconductors have been published. Unfortunately, ferromagnetism in diluted doped ZnO is far from understood. The presence or absence of ferromagnetism in doped ZnO critically depends on the synthesis method. Fortunately, these studies allow the dependence of $c_{sa} - c_s$ on the grain (particle) size d to be estimated. In this work we observe the grain-size dependence of the solubility limit of Co and Mn in ZnO.

2 Investigation of Nanograined Doped ZnO Films

The Mn- and Co-doped ZnO thin films were deposited on the Al foils by the novel liquid ceramics method. The substrates were dip-coated by the mixture of liquid organic acids with metallic ions and dried at 150°C. Then the deposited layers were oxidized in air at 550°C. The resulting films were greenish and transparent. The film thickness was determined by electron-probe microanalysis (EPMA) and edge-on transmission electron microscopy (TEM) and measured between 50 and 200 nm. The Mn content in films was between 0 and 47 at.%. The Co content in films was between 0 and 52 at.%. The zinc, cobalt and manganese content in doped oxides was measured by atomic absorption spectroscopy in a Perkin–Elmer spectrometer and by EPMA in a Tescan Vega TS5130 MM microscope equipped by the Oxford Instruments LINK energy-dispersive spectrometer. TEM investigations were carried out on a JEM–4000FX microscope at an accelerating voltage of 400 kV. TEM was used to investigate the crystal structure of the film especially at the interface and to look for possible Mn clusters. TEM was also used to measure the grain size in pure and doped ZnO films. XRD data were obtained on Siemens diffractometer (Fe K_α radiation with $\lambda = 0.193728$ nm) with a graphite monochromator and line-position-sensitive gas flow detector. Calculation of the grain size, d, was done using the angle dependence of the peak broadening [7].

3 Solubility of Co in Zno

In Fig. 1 the bright field high-resolution electron micrograph and the electron diffraction pattern are shown for the nanograined ZnO thin films with 30 at.% Mn

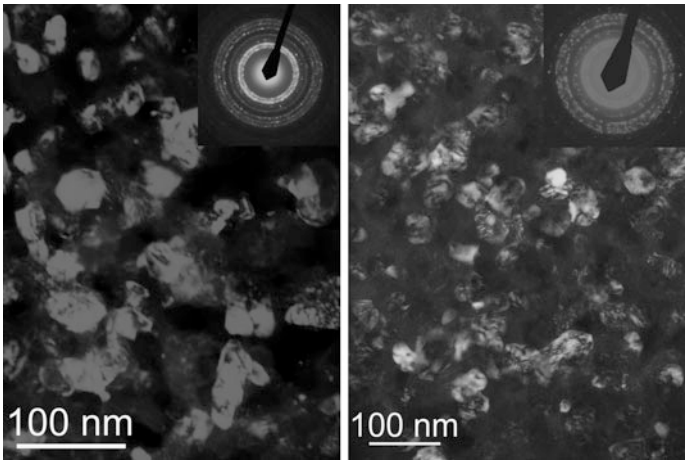

Fig. 1 Dark field TEM micrographs of the nanograined ZnO thin films with 30 at.% Mn (*left*) and 40 at.% Co (*right*) deposited by the liquid ceramics technology and electron diffraction pattern as an *inset*. No texture is visible. Reflexions from the Al substrate are also present

(left) and 40 at.% Co (right). The deposited ZnO films are dense, non-porous, nanograined, uniform, non-textured. The grain size in this film is about 20 nm. In other Mn-doped samples the grain size was 20 ± 5 nm. The grain size in the Co-doped films is about 10 nm. In Fig. 2 two XRD spectra are shown, namely for pure ZnO (bottom) and ZnO doped by 40 at.% Co. Only wuerzite lines are visible in the pure ZnO film. The cubic Co_2O_3 phase appears additionally in the ZnO –40 at.% Co sample. In Fig. 3a the dependence of the lattice parameter *c* in the Co-doped ZnO films on the Co-concentration is shown. The error bars in Fig. 3a are defined by the angular error for the peak positions in XRD spectra. Above 33 at.% Co, the second phase Co_2O_3 with cubic structure appears and the lattice

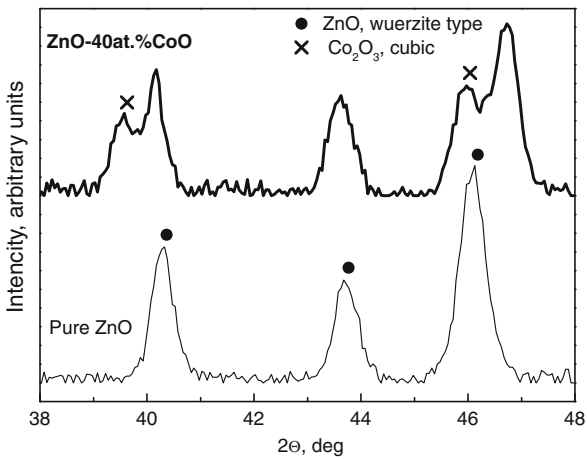

Fig. 2 XRD spectra for pure ZnO (*bottom*) and ZnO doped by 40 at.% CoO. Only wuerzite lines are visible in the pure ZnO film. The cubic Co_2O_3 phase appears additionally in the ZnO −40 at.% CoO sample

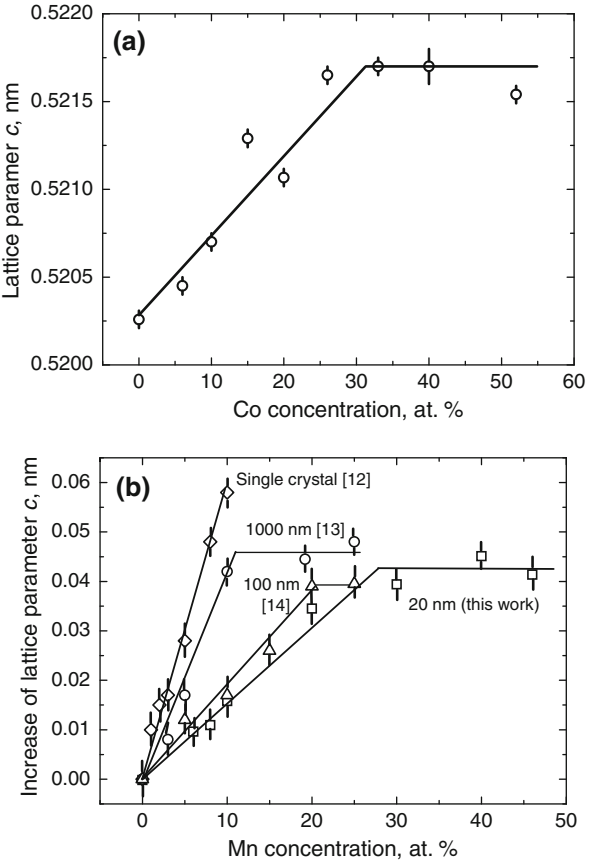

Fig. 3 **a** Dependence of lattice parameter c in Co-doped ZnO films on the Co-concentration. **b** Dependence of increase of lattice parameter c in Mn-doped ZnO films on the Mn-concentration. *Squares* our data ($d = 20$ nm). *Diamonds* Mn-doped epitaxial films on the single crystalline ZnO substrate [9]. *Circles* films with $d = 1{,}000$ nm obtained by the chemical spray pyrolysis [10]. *Triangles* films with $d = 100$ nm deposited by the MBE on the sapphire substrate [11]

spacing in the wuerzite ZnO phase ceases to increase. It means that the solubility limit c_{sa} in the Co-doped ZnO thin films with grain size 10 nm is 33 at.% Co at 550°C. The solubility limit in the bulk c_s is about 2 at.% Co at 550°C [8]. In Fig. 3b the increase of the lattice parameter c in the Mn-doped ZnO films with increasing Mn-concentration is shown. The error bars in Fig. 3 are defined by the angular error for the peak positions in XRD spectra. Both our data ($d = 20$ nm, diamonds) and the data taken from the literature are shown [Mn-doped epitaxial films on the single crystalline ZnO substrate [9], squares; films with $d = 100$ nm obtained by the chemical spray pyrolysis [10], circles; films with $d = 1{,}000$ nm obtained by the molecular beam epitaxy (MBE) on the sapphire substrate, triangles]. The lattice spacing linearly increases up to the certain concentration c_{sa}. Above c_{sa}, the second phase Mn_3O_4 with cubic structure appears and the lattice spacing in the wurzite ZnO phase ceases to increase. The slope of the inclined portion of the curves decreases with decreasing grain size. It means that the solubility limit c_{sa} in the Mn-doped ZnO thin films with grain size 20 nm is about 33 at.% Mn at 550°C. The solubility limit in the bulk c_s is about 12 at.% Mn at 550°C [8].

In order to find ferromagnetism in doped ZnO, it is important to ensure that it does not contain any particles from the second phase which could influence the sample's magnetic properties. It means that in each published work the data are present on the dopant concentration and presence or absence of a second phase. Usually, the presence or absence of a second phase is controlled by XRD. Measurable X-ray peaks appear in the diffraction spectra when the amount of a second phase is about 1–2%. TEM or Raman spectroscopy allows one to detect a second phase at lower content than XRD. However, such data are almost absent in the papers devoted to the magnetic behaviour of ZnO. Therefore, we used only XRD data for the construction of plots presented in Figs. 4, 5, 6, 7 and 8. The majority of published works allowed us to estimate the grain or particle size and to assign the data to a certain temperature, either that of a synthesis or of a last thermal treatment. The published data encompass a grain (particle) sizes D from 10 mm to 10 nm and temperatures from 300 to 1,500 K. This gave us the unique chance to construct the $c_{sa}(T)$ dependences for the broad interval of D and to compare the influence of internal boundaries and surfaces. The biggest data arrays exist for Co- and Mn-doped ZnO.

In Fig. 4 the solubility limit (solvus) of Co in ZnO polycrystals is drawn using the data on polycrystals with a grain size above 1,000 nm [8, 11–19]. (The errors in Fig. 4, as well as in Figs. 5, 6, 7 and 8 are below the scale of the markers). These samples were obtained by hydrothermal growth [8], growth of Co-doped ZnO single crystals from the melt [11], high-temperature and high-pressure synthesis of bulk crystals [12], Co diffusion from the vapour into ZnO single crystals [13], Co ion implantation into ZnO single crystalline substrate [14], chemical vapor transport [15], sintering of conventional powders [16, 17], co-precipitation [18], and dual-beam pulsed laser deposition (PLD) [19]. Open symbols correspond to the one-phase samples. Full symbols correspond to the samples where the second phase Co_2O_3 was observed by the XRD. Stars correspond to the solubility limit determined in the literature by the method similar to that used by us in the Fig. 3. The experimental

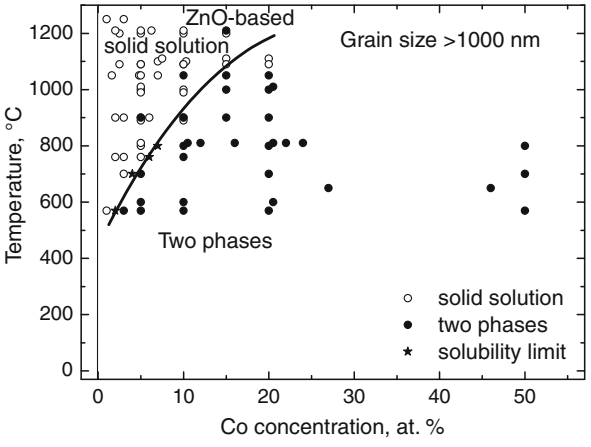

Fig. 4 Solubility limit of Co in ZnO polycrystals with grain sizes above 1,000 nm [8, 11–19]. *Open symbols* correspond to the one-phase samples. *Solid symbols* correspond to the two-phase samples. *Filled stars* correspond to the solubility limit

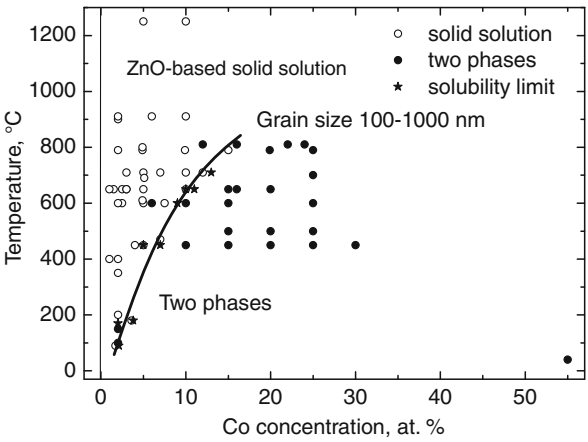

Fig. 5 Solubility limit of Co in ZnO polycrystals with grain sizes between 100 and 1,000 nm [14, 19–27]. *Open symbols* correspond to the one-phase samples. *Solid symbols* correspond to the two-phase samples. *Filled stars* correspond to the solubility limit

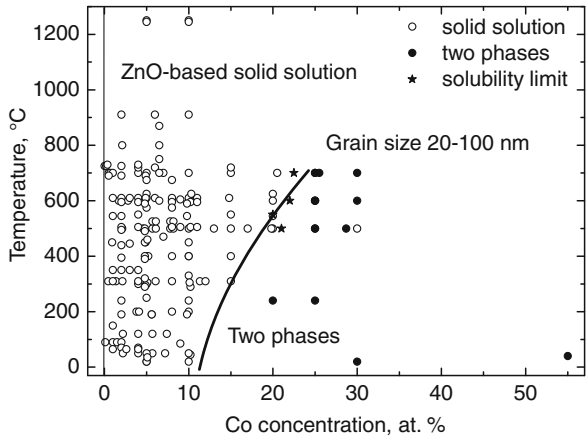

Fig. 6 Solubility limit of Co in ZnO polycrystals with grain sizes between 20 and 100 nm [16, 25, 28–45]. *Open symbols* correspond to the one-phase samples. *Solid symbols* correspond to the two-phase samples. *Filled stars* correspond to the solubility limit

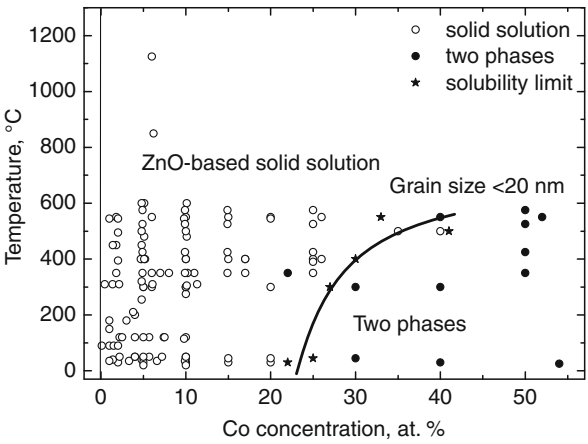

Fig. 7 Solubility limit of Co in ZnO polycrystals with grain sizes below 20 nm [19, 24, 28, 34, 41, 45–52]. *Open symbols* correspond to the one-phase samples. *Solid symbols* correspond to the two-phase samples. *Filled stars* correspond to the solubility limit

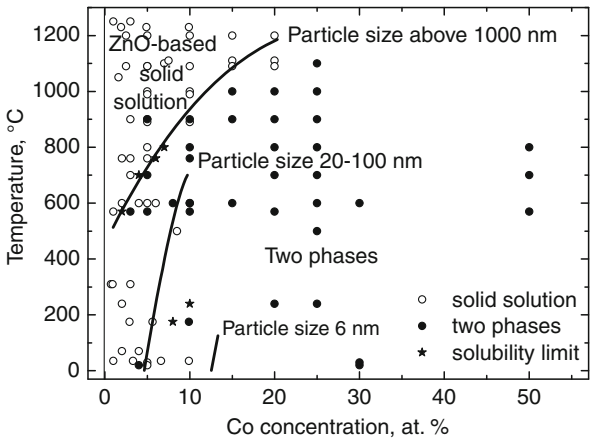

Fig. 8 Solubility limit of Co in ZnO powders with various particle sizes [8, 11, 12, 15, 16, 21, 53–56]. *Open symbols* correspond to the one-phase samples. *Solid symbols* correspond to the two-phase samples. *Filled stars* correspond to the solubility limit

error of the synthesis or annealing temperature is usually below ±10°C and error of determination of Co-concentration in ZnO is usually below ±0.1 at.%. Therefore, the error bars are not visible on the scale of the Figs. 4, 5, 6, 7 and 8. The solubility of Co in ZnO reaches about 20 at.% at 1,200°C and falls below 2 at.% at 550°C. This line corresponds to the solubility in the bulk of ZnO, the number of Co atoms segregated in grain boundaries is negligible.

Using the hydrothermal technique the oxide mixtures of known compositions were sealed together with a small amount of NaOH in water as a mineralizer in gold tubes and heated in a hydrothermal pressure vessel at 10^8 Pa and temperatures between 570 and 800°C [8]. Grain size of doped ZnO was above 5 μm. High-temperature (900–1,100°C) and high pressure (6 GPa) annealing of the original ZnO + Co + Co_3O_4 mixture in the sealed gold capsule without any mineralizer allowed large Co-doped ZnO bulk polycrystals to be manufactured [12]. In the vapor phase diffusion method cobalt atoms were introduced into the few millimeter large ZnO single crystals in a conventional tube furnace in flowing O_2 gas at 1,050°C for about 100 h. Co_3O_4 vapor was used as the source material which was evaporated from Co_3O_4 powder (melting point about 900°C) [13]. In the ion implantation method the commercial ZnO single-crystal substrates (0.5 mm thickness) were implanted with Co with energy of 100 keV and fluence up to 10^{17} ions/cm^2 [14]. The chemical vapor transport method allows the few millimeter large Co-doped bulk ZnO single crystals to be manufactured [15]. By sintering of conventional powders the ZnO and CoO powders with grain size between 1 and 20 μm were mixed together, pressed in the tablets and annealed at temperatures between 600 and 1,400°C [16, 17]. In the co-precipitation technique, the $Zn_{1-x}Co_xO$ powders were prepared by the decomposition of an oxalate precursor in which Co and Zn ions are already mixed [18]. The resulting powders with sizes above 1 μm were annealed at 900°C [18]. In the dual-beam pulsed laser deposition (DBPLD), the laser beam was split into two beams and irradiated two separate targets of ZnO and Co. The two targets were ablated separately, the Co-doped ZnO is thus formed by the growth of thin film on the single crystal sapphire substrate from the fluxes coming from the two

targets. The substrate temperature was between 600 and 800°C. Usually DBPLD leads to the formation of rather fine-grained polycrystals, however, the grain size can be above 1,000 nm by high Co concentrations [19].

In Fig. 5 the solubility limit (solvus) of Co in ZnO polycrystals is drawn using the data on polycrystals with grain size between 100 and 1,000 nm [14, 19–26]. These samples were obtained by sintering fine powders [20, 21], vaporization–condensation method [22], magnetron sputtering [23, 24], sol–gel method [25], electrodeposition [26], Co ion implantation into ZnO single crystalline substrate [14], single- and dual-beam PLD [19, 27]. The solubility of Co in ZnO reaches about 16 at.% at 800°C and falls below 2 at.% at room temperature. Co solubility in polycrystals with grain size between 100 and 1,000 nm is much higher than in the coarse-grained samples (Fig. 4). For example, it is two times higher at 800°C and about four times higher at 550°C.

Fine powders were chemically synthesized from various aqueous solutions, dried and sintered (without compaction) at temperatures between 150 and 900°C [20]. TEM micrographs published in the papers [20] permitted us to estimate the ratio between the GB area and the free surface area as being between 10 and 50%. Fine powders may also be produced by the ball milling of commercially available cobalt and zinc oxides which were compacted before sintering [21]. In this case the portion of GBs reaches nearly 100%. Reactive magnetron co-sputtering was used for the growth of Co-doped ZnO thin films on the Si/SiO_2 substrates using Zn and CoFe metal targets [23]. A mixed plasma of Ar and O_2 was used for sputtering, the substrate temperature was 600°C. The composition of the film was controlled by the sputtering ratio of each target. The films contain poreless elongated columnar grains with a grain diameter of about 100 nm. Films can also be sputtered from one compound ZnCoO target [24].

In [25] the Co-doped ZnO thin films were prepared by a sol–gel coating route using $Zn(CH_3COO)_2{\cdot}H_2O$ and $Co(CH_3COO)_2{\cdot}H_2O$ as starting precursors and a 9:1 mixture of 2-methoxyethanol and ethanolamine as a solvent. The sol–gel-coated films were finally heat-treated at 600°C for 10 min in reduced oxygen pressure at 1 Pa by rapid thermal annealing. The films contain grains with size of about 100 nm. The densely arranged nanowires with multiple contacts (GBs) can be grown with the aid of electrodeposition [26]. For example, the nanowires with diameter of 100–200 nm and length about 2 mm were grown from the aqueous solution containing zinc nitrate hydrate and cobalt nitrate hydrate at 90°C. A negative potential of −0.8 V relative to a gold reference electrode, was applied to a silicon substrate [26]. In [22] the Co-doped ZnO was melted inside a glass balloon by using the sun heating power focused in the sample by means of a curved focusing mirror, vaporized and then condensed. This vaporization–condensation method allowed producing the few micrometer long wires and tetrapodes with diameter slightly above 100 nm [22]. Multiple contacts (GBs) between individual wires are present in such samples, and they are visible in TEM and scanning electron microscopy (SEM) micrographs.

In Fig. 6 the solubility limit (solvus) of Co in ZnO polycrystals is drawn using the data on polycrystals with grain size between 20 and 100 nm [20, 25, 27–44].

These samples were obtained by full or partial sintering of very fine powders [20, 28, 29], partial sintering of nanowires [30, 31], autocombustion method [32], vaporization–condensation method [27], magnetron sputtering [25, 33, 34], ion beam sputtering [35], ion implantation [35], molecular beam epitaxy [37, 38], sol–gel method [39, 40], chemical vapour deposition (CVD) [41], pulsed laser deposition [27, 42–45]. Open symbols correspond to the experiments where TEM investigations were performed, GBs are visible in TEM micrographs and GB Co-rich phases are absent [20, 27, 34, 38, 42, 44]. The solubility of Co in ZnO drastically increased in comparison with Fig. 3. It reached about 25 at.% at 700°C and remained above 12 at.% at room temperature.

Nanowires and nanorods were grown from various solutions [30, 31]. For example, in [30] the nanowires were synthesized by the thermal decomposition of zinc acetate and cobalt(ii) acetate in refluxing trioctylamine. During the growth and following heat treatment, single crystalline nanowires and nanorods grow together forming GBs. The (usually low) amount of GBs can be estimated from SEM and TEM micrographs. In the autocombustion method [32] the Zn and Co powders were mixed with fuel, where glycine (2 mol of glycine per mol of metal ion) or a mixture of glycine and dextrose (2 mol of glycine + 1 mol of dextrose) were used as fuel. The combustion of a meta–fuel mixture made it possible to produce the fine powders of the Co-doped zinc oxide with partially sintered 20–45 nm grains. Ion beam sputtering is similar to the double-target magnetron sputtering [35]. Two targets containing Zn and Co were simultaneously or alternatively sputtered by the ion beam. The layers deposited on the single-crystalline sapphire substrates were then annealed in various atmospheres at 250°C.

Different variants of CVD (PIMOCVD—pulse-injection, oxygen plasma assisted metal organic CVD, or ultrasonic-assisted CVD) are simple soft processes which permit the film growth from either organic or inorganic precursors [41]. Deposition can be carried out in the absence of a vacuum. During the PIMOCVD deposition process [97] small droplets of a monoglyme solvent with $Zn(tmhd)_2$ and $Co(tmhd)_3$ (tmhd: 2,2,6,6-tetramethyl-3,5-heptanedionate) were sequentially pulsed into a hot evaporation chamber. This evaporation chamber was heated to a temperature that is sufficiently high to rapidly evaporate the injected solution but low enough to avoid precursor decomposition. An $Ar:O_2$ 1:1 carrier gas was subsequently used to transport small amounts of evaporated precursor to the deposition chamber, in which thermal decomposition and thin film growth occurred. The substrate temperature during deposition was 550°C. After the deposition, the samples were slowly cooled to room temperature in an oxygen pressure of 1 atm. and dense nanocrystalline textured films were formed [41].

In Fig. 7 the solubility limit (solvus) of Co in ZnO polycrystals is drawn using the data on polycrystals with grain size below 20 nm [19, 24, 28, 31, 34, 39, 41, 45–52]. These samples were obtained by sintering very fine powders [28, 46], in a solution combustion method [47], partial sintering of nanowires [31, 48], magnetron sputtering [24, 34, 49, 50], ion beam sputtering [51], sol–gel method [39], CVD [41] and pulsed laser deposition [19, 45, 52]. The data obtained in this work for samples with $d = 10$ nm (liquid ceramics method, Fig. 3) are also present at

550°C. Like in Fig. 6, crosses correspond to the experiments where TEM investigations were performed, GBs are visible in TEM micrographs and GB Co-rich phases are absent [45, 49, 51]. The solubility of Co in ZnO drastically increased in comparison with Fig. 6 where it reached about 40 at.% at 500°C and remained above 22 at.% at room temperature.

In Fig. 8 the solubility limit (solvus) of Co in ZnO single crystals is drawn using the data on powder samples with different particle size [8, 11, 12, 15, 16, 21, 53–56]. The data are much scarcer in comparison with polycrystals (Figs. 4, 5, 6, 7). The single crystals, particles, rods, wires, etc. without GBs were obtained by growing of Co-doped ZnO single crystals from the melt [11], conventional milling [8, 16], ball milling of micro- and nanopowders [21, 46, 53], mechanical alloying [29], thermal decomposition of acetate aqueous and organic solutions [54], chemical vapor transport [15], vaporization–condensation method in a solar reactor [55], direct hydrothermal synthesis [56], high-temperature and high-pressure synthesis [12] and sol–gel synthesis [56]. The solubility lines (1) for the particle size above 1,000 nm, (2) between 20 and 100 nm and (3) for particles with a size of 6 nm are shown in Fig. 8. The solubility limit (solvus) for the large crystals (particles and/or grains larger than 1,000 nm) is the same as in Fig. 4. It is visible that decreasing the particle size also increases the solubility of Co in ZnO. However, in this case c_{sa} shifts to the right much weaker than in Figs. 5, 6 and 7 (poreless polycrystals). This difference demonstrates that GBs in ZnO can accumulate much more Co atoms than free surfaces.

4 Solubility of Mn in ZnO

In Fig. 9 the solubility (solvus) limit of Mn in ZnO polycrystals is drawn using the data on polycrystals with grain a size above 1,000 nm [8–10, 16, 57–60]. (The errors in Fig. 9, as well as in Figs. 10, 11 and 12 are below the scale of the markers). These samples were obtained by hydrothermal growth [8], growth of Mn-doped epitaxial films on the single crystalline ZnO substrate [9], pulsed laser and MBE deposition of the coarse-grained thin films on the sapphire substrate [10, 57], sintering of conventional powders [16, 58], co-precipitation [59], growth of Mn-doped bulk crystals from oxalate precursors [60]. The solubility of Mn in ZnO reaches about 30 at.% at 800°C and falls to 5 at.% at 400°C. This line corresponds to the solubility in the volume of ZnO, the number of Mn atoms segregated in grain boundaries is negligible.

In Fig. 10 the solubility limit (solvus) of Mn in ZnO polycrystals is drawn using the data on polycrystals with grain size between 100 and 1,000 nm [57, 61–64]. These samples were obtained by the pulsed laser deposition (PLD) on the sapphire substrate [57, 61]. Mn ion implantation into ZnO films deposited by PLD [62], sol–gel method [63], sintering fine powders [64], and chemical spray pyrolysis. The solubility of Mn in ZnO (for $D = 100$ nm) reaches about 25 at.% at 500°C and falls below 10 at.% at room temperature. Mn solubility in polycrystals with

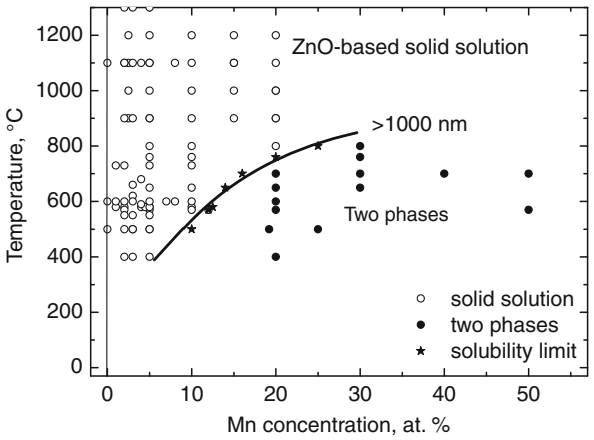

Fig. 9 Solubility limit of Mn in ZnO polycrystals with grain sizes above 1,000 nm [8–10, 16, 57–60]. *Open symbols* correspond to the one-phase samples. *Solid symbols* correspond to the two-phase samples

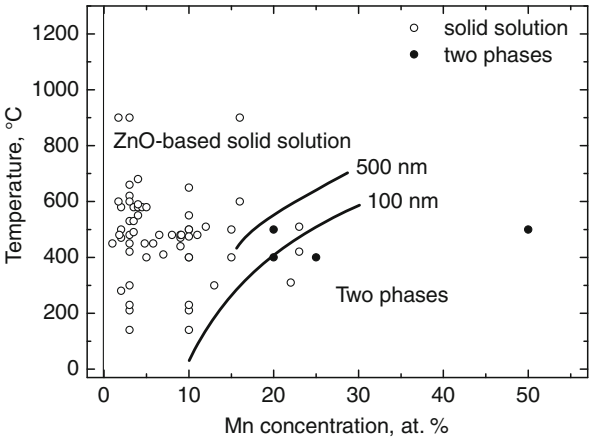

Fig. 10 Solubility limit of Mn in ZnO polycrystals with grain sizes between 100 and 1,000 nm [57, 61–64]. *Open symbols* correspond to the one-phase samples. *Solid symbols* correspond to the two-phase samples

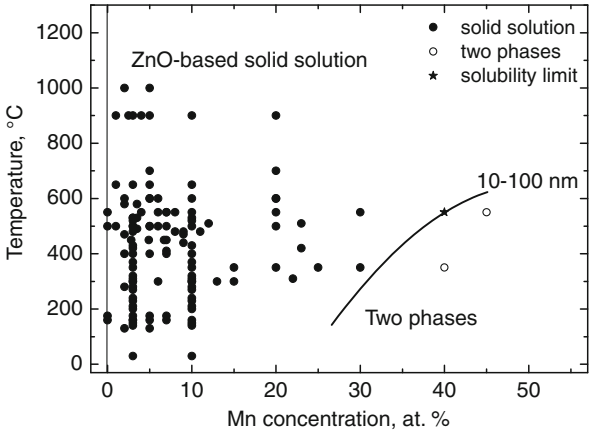

Fig. 11 Solubility limit of Mn in ZnO polycrystals with grain sizes between 10 and 100 nm [16, 57, 61, 65–68]. *Solid symbols* correspond to the one-phase samples. *Open symbols* correspond to the two-phase samples

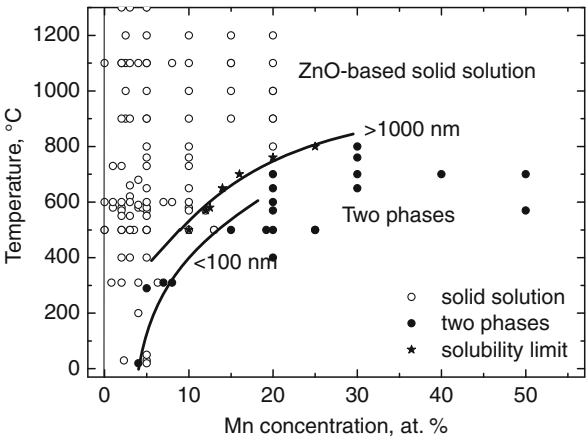

Fig. 12 Solubility limit of Mn in ZnO powders with various particle sizes [8–10, 31, 53, 56–60, 69, 70]. *Open symbols* correspond to the one-phase samples. *Solid symbols* correspond to the two-phase samples

grain size between 100 and 1,000 nm is much higher than in the coarse-grained samples. For example at 600°C it is two times higher.

In Fig. 11 the solubility limit (solvus) of Mn in ZnO polycrystals is drawn using the data on polycrystals with grain size between 10 and 100 nm [16, 46, 57, 61]. These samples were obtained by the pulsed laser deposition [16, 57, 61, 65], full or partial sintering of very fine powders [66], partial sintering of nanowires [67], and magnetron sputtering [68]. The solubility of Mn in ZnO drastically increased in comparison with Fig. 4. It reached about 45 at.% at 600°C and remained above 20 at.% at room temperature.

In Fig. 12 the solubility limit (solvus) of Mn in ZnO single crystals is drawn using the data on powder samples with different particle size [8–11, 31, 53, 56–60, 69]. The data are much scarcer in comparison with polycrystals (Figs. 8, 9, 10, 11). The single crystals, particles, rods, wires, etc. without GBs were obtained hydrothermal growth [81], growth of Mn-doped epitaxial films on the single crystalline ZnO substrate [9], pulsed laser and MBE deposition of the coarse-grained thin films on the sapphire substrate [57], sintering of conventional powders [16, 58], co-precipitation [59], growth of Mn-doped bulk crystals from oxalate precursors [60], condensation of nanopowders and nanowires from solution and vapour phase [31, 69], autocombustion [70], ball milling of micro- and nano-powders [53], sol–gel synthesis [56]. The solubility lines for the particle size above 1,000 nm and below 100 nm are shown in Fig. 11. For large crystals (particles and/or grains larger than 1,000 nm) the solubility limit line is the same as in Fig. 8 and corresponds to the bulk solidus. It is visible that the decrease of particle size also leads to the increase of the Mn solubility in ZnO. However, in this case c_{sa} shifts to the right much weaker than in Figs. 9 and 10 (poreless polycrystals). This difference demonstrates that GBs in ZnO can accumulate much more Mn atoms than free surfaces.

Based on the knowledge that Mn and Co solubility depends on grain and particle size (Figs. 4, 5, 6, 7, 8, 9, 10, 12), it is possible to estimate the maximum Mn and Co segregation in ZnO GBs and free surfaces. Let us calculate first the

area to volume ratio for the grains and particles. If we suppose that grains and particles are spheres with diameter D, the surface for each particle is πD^2 and the GB area for each grain is $\pi D^2/2$ (since each GB is shared between two neighbouring grains). The volume for spherical grains and particles is the same, namely $\pi D^3/6$. Thus the area to volume ratio, A, for the free surfaces of spherical particles is $A_{FS} = 3/D$ and for GBs of spherical grains $A_{GB} = 3/2D$. One of the earliest studies of grain shape was made by Lord Kelvin in 1887 [71]. He showed that the optimal space-filling grain shape, with a minimal surface area and surface tension, is a polyhedron known as a tetrakaidecahedron, which has 14 faces, 24 corners and 36 edges. Tetrakaidecahedron is an octahedron truncated by cube. For the Kelvin tetrakaidecahedron the ratio of surface area to that of a sphere of the same volume is 1.099. Thus the area to volume ratio for grains is $A_{GB} = 1.65/D$. If one monolayer (ML) of Mn covers ZnO free surfaces or GBs, their input, c_{FS} or c_{GB}, in the full concentration can be calculated as a product of A_{FS} or A_{GB} and the thickness, t, of a surface or GB layer. Lattice constant of ZnO wurtzite lattice d can be estimated as the cubic root from the unit cell volume. The unit cell volume for ZnO is about 47×10^{-3} nm^3 according to our measurements. Thus $d = 0.36$ nm. Therefore, for the one monolayer $t = d$, $c_{FS} = d\ A_{FS} = 1.08/D$ and $c_{GB} = d\ A_{GB} = 0.59/D$.

5 Multilayer Grain Boundary Segregation in ZnO as a Reason for Solubility Increase

In Fig. 13 the input of Co accumulated in GBs and surfaces in total concentration is shown for different grain size. c_{FS} and c_{GB} values for 1 ML are shown by thin and thick straight lines, respectively. In the log–log scale these lines have a slope of -1. The solubility limit of Co in the single-crystalline or coarse-grained ZnO at 500°C and 600°C is 2 and 2.5 at. Co, respectively (Fig. 4). If we subtract these values from the solubility limit of Co in the fine-grained ZnO (Figs. 5, 6, 7, 8), we obtain the input of GB, c_{GB}, or free surface segregation, c_{FS}, into total Co solubility in the ZnO polycrystals. The c_{GB} values are shown in Fig. 9 by full circles (500°C) and full hexagons (600°C). It is easy to see that the experimental c_{GB} values are almost one order of magnitude higher than the calculated values for 1 ML. Moreover, the slope of the lines for GB input is slightly lower than -1. It means that the GB input in the total Co concentration increases with decreasing grain size. The c_{FS} points for free surfaces (full square and full diamond) lie much lower than the c_{GB} values for GBs. It means that free surfaces, can accumulate much less Co in comparison with GBs. In Fig. 14 similar plots are shown for Mn-doped ZnO. They also indicate the multilayer GB Mn segregation in ZnO. Similar to Co, the free surfaces can accumulate much less Mn in comparison with GBs.

Figures 13 and 14 undoubtedly indicate that the Co and Mn enrichment of GBs in fine-grained ZnO cannot be reduced to the simple single-layer GB segregation analysed by McLean [1]. Such layers of a GB phase of a finite thickness of few nm

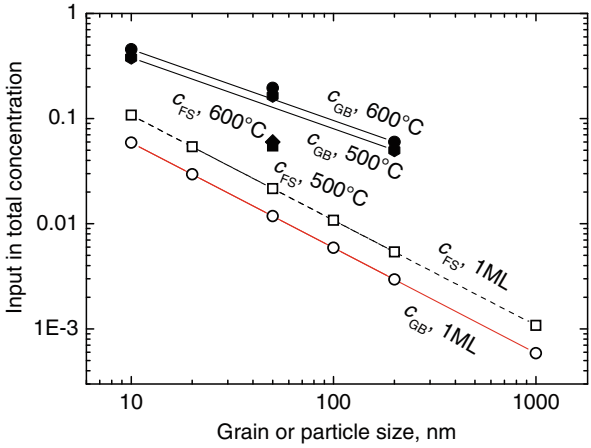

Fig. 13 Size dependence of the input of GB or surface Co segregation into full Co content

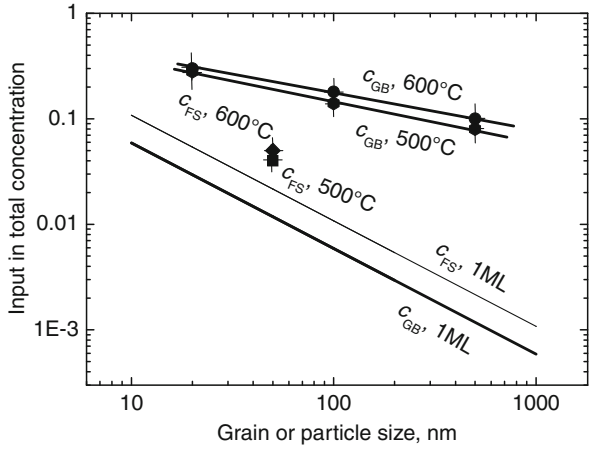

Fig. 14 Size dependence of the input of GB or surface Mn segregation into full Mn content

were first observed and theoretically treated with the aid of force-balance models in the pioneering works of Clarke on silicon nitride [72]. Later, nanometer-thick, disordered films of a nearly constant or "equilibrium" thickness have been frequently observed in GBs in ceramics [73, 74] and oxide/metal interfaces [75]. Thin equilibrium GB or surface films in the one-phase area of a bulk phase diagram were first considered by Cahn [76]. He proposed the idea that the transition from incomplete to complete surface wetting is a phase transformation. Later this idea was successfully applied for GBs, and also old data on GB wetting were reconsidered from this point of view [77]. GB wetting phase transformation proceeds at the temperature T_{wGB} where GB energy σ_{GB} becomes equal to the energy $2\sigma_{SL}$ of two solid/liquid interfaces. Above T_{wGB} GB is substituted by a layer of the melt. The tie-line of the GB wetting phase transition in the two-phase area of a bulk phase diagram continues into the one-phase area as a prewetting (or GB solidus) line. In the area between GB solidus and bulk solidus, GB contains the thin layer

of a GB phase. The energy gain ($\sigma_{GB} - 2\sigma_{SL}$) above T_{wGB} permits to stabilize such thin layer of a GB phase between the abutting crystals. Such phase is metastable in the bulk but become stable in the GB. The formation of GB phase layer of thickness l leads to the energy loss $l\Delta g$. Finite thickness l of the GB phase is defined be the equality of the energy gain ($\sigma_{GB} - 2\sigma_{SL}$) and energy loss $l\Delta g$. In this simplest model, the prewetting GB layer of finite thickness l suddenly appears by crossing the prewetting (GB soludus) line $c_{bt}(T)$. The direct evidence for the existence of such a first-order prewetting transition (i.e., a finite jump in film thickness) has been recently reported for oxide surfaces [78]. Thickness $l$logarithmically diverges close to the bulk solidus. It is due to the fact that the thickness of a wetting phase is thermodynamically infinite in the two-phase area. Physically, in the two-phase area, its thickness is defined only by the amount of the wetting phase. Several ML thick liquid-like GB layers possessing high diffusivity were observed in the Cu–Bi [79], Al–Zn [80], Fe–Si–Zn [81] and W–Ni alloys [82]. The direct HREM evidence for thin GB films and triple junction "pockets" of has been recently obtained in metallic W–Ni [82] and Al–Zn [80] alloys. The recent work performed with computation thermodynamics methods demonstrated that a nanoscale quasi-liquid GB film can be thermodynamically stable at as low as 60–85% of bulk solidus temperatures [83].

Later, the Cahn's critical point wetting model has been developed further and generalized [84]. It is not excluded that in the nanograined ZnO–MnO polycrystals the situation is more complicated than the simple sequence "monolayer adsorption → interfacial film → macroscopically thick complete wetting film". Additional copmplexity comes from the possible occurrence of GB layering [85], pseudo-partial (or frustrated-complete) melting/wetting [86], first order or continous adsorption/wetting transitions [87], and interfacial critical points. Good examples can be found on the recent works on GTB phase transitions in alumina [88]. The nanometer-thick GB films of a nearly constant or "equilibrium" thickness have been widely observed in ZnO doped by Bi_2O_3 [89]. ZnO doped by Bi is used for varistors manufacturing. Varistors exhibit highly non-linear current–voltage characteristics with a high resistivity below a threshold electric field, becoming conductive when this field is exceeded. This phenomenon enables them to be used in current over-surge protection circuits [89]. After liquid-phase sintering, such material consists of ZnO grains separated by thin Bi_2O_3-rich GB layers. Interfaces between ZnO grains control the non-linear current–voltage characteristics. The presence of a few nanometer-thick Bi-rich GB phase in ZnO is governed by the GB wetting phase transformation. The liquid-like GB films have also been found in cases of subsolidus activated sintering [74]. In fact, enhanced diffusion in these liquid-like GB films was used to explain the mysterious subsolidus activated sintering mechanism [74, 82]. It is interesting, that along with the simplest Cahn model of the transition from partially wetted GBs to completely wetted ones, more complicated situation was also observed in the ZnO–Bi_2O_3 system, namely the transition from pseudo-partially wetted GBs to the completely wetted ones [86]. In this case thin GB layer may exist in the equilibrium with thick Bi_2O_3 droplets having non-zero contact angle in the GB plane.

The logarithmic divergence of the GB layer thickness predicted by Cahn model may be the reason for the high value of GB thickness obtained from Figs. 13 and 14. The lines in Figs. 13 and 14 were calculated basing on the the apparent shift of the solubility. Therefore, the resulting GB thickness corresponds to that at the solubility (solvus) line. Few nm thick Bi-rich layers were observed also in the ZnO surfaces [90, 91]. Their thickness was close to that of GB layers [85, 88]. The thickness of surficial films was explained by the pseudo-partial (frustrated-complete) surface wetting [90]. In case of the frustrated-complete wetting, the thickness of a surficial (or GB) film also increases with increasing dopant concentration (activity) and can reach few monolayers. However, it does not diverge by approaching the solubility limit line like GB (or surficial) films in case of complete wetting and remains finite [85, 90, 91]. In the case of Co or Mn-doped ZnO, the estimation presented in Figs. 13 and 14 predicts lower Co or Mn-capacity of free surfaces in comparison with GBs. This fact has to be carefully investigated in the future experiments. It may be the indication of complete wetting in GBs and frustrated-complete wetting in surfaces. Therefore, basing on the results obtained in this work one can expect to observe in the future various interesting GB phases and phase transformations in the Co or Mn-doped ZnO. Furthermore, the observed shift of the solvus line in the Co or Mn-doped ZnO will also permit to explain the mysterious phenomenon of the room-temperature ferromagnetism in the broad-band transparent semiconductor ZnO.

6 Conclusions

1. The presence of grain boundaries (and free surfaces) in nanograined materials leads to a drastic modification of phase diagrams. In particular, the solubility of a second component can increase and the respective solubility lines in the phase diagrams shift at a higher concentration.
2. The accumulation of Mn and Co in grain boundaries and free surfaces dramatically shifts the lines of Mn and Co solubility limit in ZnO to the higher Mn and Co concentrations.
3. Small grain size leads to the larger shift when compared with similarly small particle sizes. This means that the Mn or Co accumulation ability of grain boundaries is about 2–4 times higher than that of free surfaces.
4. Thus, the phase diagrams for the materials having a grain size below 1,000 nm have to be re-investigated. An especially drastic change to the phase diagrams results when the grain size is below 100 nm.

Acknowledgments Authors thank the Russian Foundation for Basic Research (contract 09-08-90406), Ukrainian Fundamental Research State Fund (contract X28.704), Program of creation and development for NITU MISiS and Deutsche akademische Austauschdienst (DAAD) for the financial support of investigations and exchange travel. Authors cordially thank Prof. G. Schütz, Dr. D. Goll and Dr. E. Goering for stimulating discussions, Dr. A. Nekrasov for the help with EPMA measurements.

References

1. McLean, D.: Grain Boundaries in Metals. Clarendon Press, Oxford (1957)
2. Beke, D.L., Cserháti, C., Erdélyi, Z. et al.: Segregation in nanostructures. In: Nalwa, H.S. (ed.) Nanoclusters and Nanocrystals. American Scientific Publishers, Valencia (2002)
3. Weissmuller, J., Lemier, Chr.: On the size dependence of the critical point of nanoscale interstitial solid solutions. Phil. Mag. Lett. **80**, 411–418 (2000)
4. Gülgün, M.A., Voytovych, R., Maclaren, I. et al.: Cation segregation in an oxide ceramic with low solubility: yttrium doped α-alumina. Interface Sci. **10**, 99–110 (2002)
5. Terwilliger, C.D., Chiang, Y.M.: Size-dependent solute segregation and total solubility in ultrafine polycrystals: Ca in TiO_2. Acta Metall. Mater. **43**, 319–328 (1995)
6. Dietl, T., Ohno, H., Matsukura, F. et al.: Zener model description of ferromagnetism in zinc-blende magnetic semiconductors. Science **287**, 1019–1022 (2000)
7. Soyer, A.: FHKL—a program to compute rocking curves and crystallographic data of interest for the dynamical theory of X-rays. J. Appl. Crystallog. **28**, 244–247 (1995)
8. Bates, C.H., White, W.B., Roy, R.: The solubility of transition metal oxides in zink oxide and the reflectance spectra of Mn^{2+} and Fe^{2+} in tetrahedral fields. J. Inorg. Nucl. Chem. **28**, 397–405 (1966)
9. Masuko, K., Ashida, A., Yoshimura, T. et al.: Preparation and the magnetic property of ZnMnO thin films on (0001) ZnO single crystal substrate. J. Magn. Magn. Mater. **310**, E711–E713 (2007)
10. Mofor, A.C., El-Shaer, A., Bakin, A. et al.: Magnetic property investigations on ZnMnO. Superlatt. Microstruc. **39**, 381–386 (2006)
11. Kane, M.H., Fenwick, W.E., Strassburg, M. et al.: Magnetic and optical properties of single crystals of transition metal doped ZnO. Phys. Stat. Sol. B **244**, 1462–1467 (2007)
12. Yin, S., Xu, M.X., Yang, L. et al.: Absence of ferromagnetism in bulk polycrystalline $Zn_{0.9}Co_{0.1}O$. Phys. Rev. B **73**, 224408 (2006)
13. Zhang, Z., Chen, Q., Lee, H.D. et al.: Absence of ferromagnetism in Co-doped ZnO prepared by thermal diffusion of Co atoms. J. Appl. Phys. **100**, 043909 (2006)
14. Borges, R.P., Pinto, J.V., da Silva, R.C. et al. Ferromagnetism in ZnO doped with Co by ion implantation. J. Magn. Magn. Mater. **316**, E191–E194 (2007)
15. Szuszkiewicz, W., Morhange, J.F., Golacki, Z. et al.: Raman spectroscopy of Co-doped ZnO bulk crystals. J. Acta Phys. Polon. A **112**, 363–368 (2007)
16. Kolesnik, S., Dabrowski, B., Mais, J.: Structural and magnetic properties of transition metal substituted ZnO. J. Appl. Phys. **95**, 2582–2586 (2004)
17. Okamoto, M., Inoue, Y., Kawahara, T. et al.: Photoacoustic spectra of heavily Co-doped ZnO powders. Jap. J. Appl. Phys. Part 1 **44**, 4461–4464 (2005)
18. Bouloudenine, M., Viart, N., Colis, S. et al.: Antiferromagnetism in bulk $Zn_{1-x}Co_xO$ magnetic semiconductors prepared by the coprecipitation technique. Appl. Phys. Lett. **87**, 052501 (2005)
19. Peng, Y.Z., Liew, T., Chong, T.C. et al.: Growth and characterization of dual-beam pulsed-laser-deposited $Zn_{1-x}Co_xO$ thin films. J. Appl. Phys. **98**, 114909 (2005)
20. Hays, J., Thurber, A., Reddy, K.M. et al.: Development and processing temperature dependence of ferromagnetism in $Zn_{0.98}Co_{0.02}O$. J. Appl. Phys. **99**, 08M123(2006)
21. Quesada, A., Garcia, M.A., Andres, M. et al.: Ferromagnetism in bulk Co–Zn–O. J. Appl. Phys. **100**, 113909 (2006)
22. Martinez, B., Sandiumenge, F., Balcells, L. et al. Ferromagnetism in co-doped zno particles prepared by vaporization–condensation in a solar image furnace. J. Magn. Magn. Mater. **290**, 168–170 (2005)
23. Cho, Y.M., Choo, W.K., Kim, H. et al.: Effects of rapid thermal annealing on the ferromagnetic properties of sputtered $Zn_{1-x}(Co_{0.5}Fe_{0.5})_xO$ thin films. Appl. Phys. Lett. **80**, 3358 (2002)

24. Yan, S.S., Ren, C., Wang, X. et al.: Ferromagnetism and magnetoresistance of Co–ZnO inhomogeneous magnetic semiconductors. Appl. Phys. Lett. **84**, 2376 (2004)
25. Park, J.H., Kim, M.G., Jang, H.M. et al.: Co-metal clustering as the origin of ferromagnetism in Co-doped ZnO thin films. Appl. Phys. Lett. **84**, 1338 (2004)
26. Cuiand, J.B., Gibson, U.J.: Electrodeposition and room temperature ferromagnetic anisotropy of Co and Ni-doped ZnO nanowire arrays. Appl. Phys. Lett. **87**, 133108 (2005)
27. Gacic, M., Jakob, G., Herbort, C. et al.: Magnetism of Co-doped ZnO thin films. Phys. Rev. B. **75**, 205206 (2007)
28. Ghosh, C.K., Chattopadhyay, K.K., Mitra, M.K.: Effect of Co doping on the static dielectric constant of ZnO nanoparticles. J. Appl. Phys. **101**, 124911(2007)
29. Jayakumar, O.D., Gopalakrishnan, I.K., Kulshreshtha, S.K.: Surfactant-assisted synthesis of Co- and Li-doped ZnO nanocrystalline samples showing room-temperature ferromagnetism. Adv Mater. **18**, 1857–1860 (2006)
30. Wang, H., Wang, H.B., Yang, F.J. et al.: Structure and magnetic properties of $Zn_{1-x}Co_xO$ single-crystalline nanorods synthesized by a wet chemical method. Nanotechnology **17**, 4312–4316 (2006)
31. Clavel, G., Pinna, N., Zitoun, D.: Magnetic properties of cobalt and manganese doped ZnO nanowires. Phys. Stat. Sol. A **204**, 118–124 (2007)
32. Deka, S., Pasricha, R., Joy, P.A.: Experimental comparison of the structural, magnetic, electronic, and optical properties of ferromagnetic and paramagnetic polycrystalline $Zn_{1-x}Co_xO$ ($x = 0,0.05,0.1$). Phys. Rev. B **74**, 033201 (2006)
33. Dinia, A., Schmerber, G., Mény, C, et al.: Room-temperature ferromagnetism in $Zn_{1-x}Co_xO$ magnetic semiconductors prepared by sputtering. J. Appl. Phys. **97**, 123908 (2005)
34. Song, C., Zeng, F., Geng, K.W. et al.: The magnetic properties of Co-doped ZnO diluted magnetic insulator films prepared by direct current reactive magnetron co-sputtering. J. Magn. Magn. Mater. **309**, 25–30 (2007)
35. Hsu, H.S., Huang, J.C.A., Huang, Y.H. et al.: Evidence of oxygen vacancy enhanced room-temperature ferromagnetism in Co-doped ZnO. Appl. Phys. Lett. **88**, 242507 (2006)
36. Wu, Z.Y., Chen, F.R., Kai, J.J. et al.: Fabrication, characterization and studies of annealing effects on ferromagnetism in $Zn_{1-x}Co_xO$ nanowires. Nanotechnology **17**, 5511–5518 (2006)
37. Liu, G.L., Cao, Q., Deng, J.X. et al.: High T_C ferromagnetism of $Zn_{(1-x)}Co_xO$ diluted magnetic semiconductors grown by oxygen plasma-assisted molecular beam epitaxy. Appl. Phys. Lett. **90**, 052504 (2007)
38. Nielsen, K., Bauer, S., Luebbe, M. et al.: Ferromagnetism in epitaxial Zn0.95Co0.05O films grown on ZnO and Al_2O_3. Phys. Stat. Sol. A **203**, 3581–3596 (2006)
39. Belghazi, Y., Schmerber, G., Colis, S. et al.: Room-temperature ferromagnetism in Co-doped ZnO thin films prepared by sol–gel method. J. Magn. Magn. Mater. **310**, 2092–2094 (2007)
40. Zhou, H.J., Knies, C., Hofmann, D.M. et al.: Optical and magnetic properties of c-oriented ZnCoO films. Phys. Stat. Sol. A **203**, 2756–2759 (2006)
41. Khare, N., Kappers, M.J., Wei, M. et al.: Defect-induced ferromagnetism in Co-doped ZnO. Adv. Mater. **18**, 1449–1452 (2006)
42. Chakraborti, D., Ramachandran, S., Trichy, G. et al.: Magnetic, electrical, and microstructural characterization of ZnO thin films codoped with Co and Cu. J. Appl. Phys. **101**, 053918 (2007)
43. Schmidt, H., Diaconu, M., Hochmuth, H. et al.: Electrical and optical spectroscopy on ZnO:Co thin films. Appl. Phys. A **88**, 157–160 (2007)
44. Zhang, Y.B., Liu, Q., Sritharan, T. et al.: Pulsed laser ablation of preferentially orientated ZnO:Co diluted magnetic semiconducting thin films on Si substrates. Appl. Phys. Lett. **89**, 042510 (2006)
45. Liu, Q., Yuan, C.L., Gan, C.L. et al.: Effect of substrate temperature on pulsed laser ablated $Zn_{0.95}Co_{0.05}O$ diluted magnetic semiconducting thin films. J. Appl. Phys. **101**, 073902 (2007)
46. Volbers, N., Zhou, H., Knies, C. et al.: Synthesis and characterization of ZnO:Co^{2+} nanoparticles. Appl. Phys. A **88**, 153–155 (2007)

47. Deka, S., Joy, P.A.: Ferromagnetism induced by hydrogen in polycrystalline nonmagnetic $Zn_{0.95}Co_{0.05}O$. Appl. Phys. Lett. **89**, 032508 (2006)
48. Qiu, X.Q., Li, L.O., Li, G.S.: Nature of the abnormal band gap narrowing in highly crystalline $Zn_{1-x}Co_xO$ nanorods. Appl. Phys. Lett. **88**, 114103 (2006)
49. Song, C., Geng, K.W., Zeng, F. et al.: Giant magnetic moment in an anomalous ferromagnetic insulator: Co-doped ZnO. Phys. Rev. B **73**, 024405 (2006)
50. Antony, J., Pendyala, S., Sharma, A. et al.: Room temperature ferromagnetic and ultraviolet optical properties of Co-doped ZnO nanocluster films. J. Appl. Phys. **97**, 10D307 (2005)
51. Hsu, H.S., Huang, J.C.A., Chen, S.F. et al.: Role of grain boundary and grain defects on ferromagnetism in Co:ZnO films. Appl. Phys. Lett. **90**, 102506 (2007)
52. Ueda, K., Tabata, H., Kawai, T.: Magnetic and electric properties of transition-metal-doped ZnO films. Appl. Phys. Lett. **79**, 988 (2001)
53. Bartolome, F., Blasco, J., García, L.M. et al.: Is ball milling a worthy route to produce magnetic semiconductors? J. Magn. Magn. Mater. **316**, E195–E198 (2007)
54. Kshirsagar, S.D., Inamdar, D., Gopalakrishnan, I.K. et al.: Formation of room-temperature ferromagnetic $Zn_{1-x}Co_xO$ nanocrystals. Sol. State Commun. **143**, 457–460 (2007)
55. Yang, L.W., Wu, X.L., Qiu, T. et al.: Synthesis and magnetic properties of $Zn_{1-x}Co_xO$ nanorods. J. Appl. Phys. **99**, 074303 (2006)
56. Thota, S., Dutta, T., Kumar, J. et al.: On the sol-gel synthesis and thermal, structural, and magnetic studies of transition metal (Ni, Co, Mn) containing ZnO powders. J. Phys. Cond. Mater. **18**, 2473–2486 (2006)
57. Diaconu, M., Schmidt, H., Hochmuth, H. et al.: Room-temperature ferromagnetic Mn-alloyed ZnO films obtained by pulsed laser deposition. J. Magn. Magn. Mater. **307**, 212–221 (2006)
58. Kolesnik, S., Dabrowski, B.: Absence of room temperature ferromagnetism in bulk Mn-doped ZnO. J. Appl. Phys. **96**, 5379–5381 (2004)
59. Peiteado, M., Caballero, A.C., Makovec, D.: Phase evolution of $Zn_{1-x}Mn_xO$ system synthesized via oxalate precursors. J. Eur. Ceram. Soc. **27**, 3915–3918 (2007)
60. Lawes, G., Risbud, A.S., Ramirez, A.P. et al.: Absence of ferromagnetism in Co and Mn substituted polycrystalline ZnO. Phys. Rev. B **71**, 045201 (2005)
61. Pradhan, A.K., Hunter, D., Zhang, K. et al.: Magnetic and spectroscopic characteristics of ZnMnO system. Appl. Surf. Sci **252**, 1628–1633 (2005)
62. Venkataraj, S., Ohashi, N., Sakaguchi, I. et al.: Structural and magnetic properties of Mn-ion implanted ZnO films. J. Appl. Phys. **102**, 014905 (2007)
63. Maiti, U.N., Ghosh, P.K., Nandy, S. et al.: Effect of Mn doping on the optical and structural properties of ZnO nano/micro-fibrous thin film synthesized by sol-gel technique. Phys. B **387**, 103–108 (2007)
64. Pal, M., Pal, M.: Nanocrystalline Mn-doped ZnO prepared by chemical route. Jpn. J. Appl. Phys. **44**, 7901–7903 (2005)
65. Li, X.Z., Zhang, J., Sellmyer, D.J.: Structural study of Mn-doped ZnO films by TEM. Sol. State Comm. **141**, 398–401 (2007)
66. Barick, K.C., Bahadur, D.: Synthesis, self-assembly, and properties of Mn doped ZnO nanoparticles. J. Nanosci. Nanotechnol. **7**, 1935–1940 (2007)
67. Kang, Y.J., Kim, D.S., Lee, S.H. et al.: Ferromagnetic $Zn_{1-x}Mn_xO$ ($x = 0.05$, 0.1, and 0.2) nanowires. J. Phys. Chem. C **111**, 14956–14961 (2007)
68. Kim, D.S., Lee, S., Min, C. et al.: Formation and characterization of $(Zn_{1-x}Mn_x)O$ diluted magnetic semiconductors grown on (0001) Al_2O_3 substrates. Jpn. J. Appl. Phys. **42**, 7217–7221
69. Meron, T., Markovich, G.: Ferromagnetism in colloidal Mn^{2+}-doped ZnO nanocrystals. J. Phys. Chem. B **109**, 20232–20236 (2005)
70. Deka, S., Joy, P.A.: Ferromagnetism induced by hydrogen in polycrystalline nonmagnetic $Zn_{0.95}Co_{0.05}O$. Sol. State Comm. **142**, 190–194 (2007)
71. Hosford, W.F.: Materials Science: An Intermediate Text. Cambridge University Press, Cambridge (2007)
72. Clarke, D.R.: On the equilibrium thickness of intergranular glass phases in ceramic materials. J. Am. Ceram. Soc. **70**, 15–22 (1987)

73. Kleebe, H.-J., Cinibulk, M.K., Cannon, R.M. et al.: Statistical analysis of the intergranular film thickness in silicon nitride ceramics. J. Am. Ceram. Soc. **76**, 1969–1977 (1993)
74. Luo, J., Wang, H., Chiang, Y.-M.: Origin of solid-state activated sintering in Bi_2O_3-doped ZnO. J. Am. Ceram. Soc. **82**, 916–920 (1999)
75. Avishai, A., Scheu, C., Kaplan, W.D.: Interganular films at metal-ceramic interfaces. Part 1 – interface structure and chemistry. Acta Mater. **53**, 1559–1569 (2005)
76. Cahn, J.W.: Critical point wetting. J. Chem. Phys. **66**, 3667–3679 (1977)
77. Straumal, B., Molodov, D., Gust, W.: Tie lines of the grain boundary wetting phase transition in the Al–Sn system. J. Phase Equilib. **15**, 386–391 (1994)
78. Qian, H., Luo, J.: Nanoscale surficial films and a surface transition in V_2O_5–TiO_2-based ternary oxide systems. Acta Mater. **56**, 4702–4714 (2008)
79. Divinski, S.V., Lohmann, M., Herzig, C.hr. et al.: Grain boundary melting phase transition in the Cu–Bi system. Phys. Rev. B **71**, 104104 (2005)
80. Straumal, B.B., Mazilkin, A.A., Kogtenkova, O.A. et al.: Grain boundary phase observed in Al – 5 at.% Zn alloy by using HREM. Phil Mag. Lett. **87**, 423–430 (2007)
81. Straumal, B., Rabkin, E., Lojkowski, W. et al.: Pressure influence on the grain boundary wetting phase transition in Fe–Si alloys. Acta Mater. **45**, 1931–1940 (1997)
82. Gupta, V.K., Yoon, D.H., Meyer III, H.M. et al.: Thin intergranular films and solid-state activated sintering in nickel-doped tungsten. Acta Mater. **55**, 3131–3142 (2007)
83. Luo, J., Shi, X.: Grain boundary disordering in binary alloys. Appl Phys. Lett. **92**, 101901 (2008)
84. Tang, M., Carter, W.C., Cannon, R.M. : Diffuse interface model for structural transitions of grain boundaries. Phys. Rev. B **73**, 024102(2006)
85. Luo, J.: Stabilization of nanoscale quasi-liquid interfacial films in inorganic materials: a review and critical assessment. Crit. Rev. Solid State Mater. Sci. **32**, 67–101 (2007)
86. Luo, J., Chiang, Y.-M., Cannon, R.M.: Nanometer-thick surficial films in oxides as a case of prewetting. Langmuir **21**, 7358–7365 (2005)
87. Straumal, B.B., Gornakova, A.S., Kogtenkova, O.A. et al.: Continuous and discontinuous grain boundary wetting in the Zn–Al system. Phys. Rev. B **78**, 054202 (2008)
88. Dillon, S.J., Harmer, M.P.: Demystifying the role of sintering additives with "complexion". J. Eur. Ceram. Soc. **28**, 1485–1493 (2008)
89. Olsson, E., Dunlop, G.L.: Characterization of individual interfacial barriers in a ZnO varistor material. J. Appl. Phys. **66**, 3666–3675 (1989)
90. Luo, J., Chiang, Y.-M.: Wetting and prewetting on ceramic surfaces. Ann. Rev. Mater. Res. **38**, 227–249 (2008)
91. Qian, H., Luo, J.: Vanadia-based equilibrium-thickness amorphous films on anatase (101) surfaces. Appl. Phys. Lett. **91**, 061909 (2007)

Modeling Carbon Nanotube Electrical Properties in CNT/Polymer Composites

Jaime Silva, Ricardo Simoes and Senentxu Lanceros-Mendez

Abstract In this work it is demonstrated that the capacitance between two cylinders increases with the rotation angle and it has a fundamental influence on the composite dielectric constant. The dielectric constant is lower for nematic materials than for isotropic ones and this can be attributed to the effect of the filler alignment in the capacitance. The effect of aspect ratio in the conductivity is also studied in this work. Finally, based on previous work and by comparing to results from the literature it is found that the electrical conductivity in this type of composites is due to hopping between nearest fillers resulting in a weak disorder regime that is similar to the single junction expression.

J. Silva · S. Lanceros-Mendez
Center/Department of Physics, University of Minho, Campus de Gualtar,
4710-057 Braga, Portugal
e-mail: jaime@fisica.uminho.pt; jaime.silva@dep.uminho.pt

S. Lanceros-Mendez
e-mail: lanceros@fisica.uminho.pt

J. Silva · R. Simoes (✉)
Institute for Polymers and Composites IPC/I3 N, University of Minho,
Campus de Azurém, 4800-058 Guimaraes, Portugal
e-mail: rsimoes@dep.uminho.pt

R. Simoes
School of Technology, Polytechnic Institute of Cávado and Ave,
Campus do IPCA,
4750-810 Barcelos, Portugal
e-mail: rsimoes@ipca.pt

Adv Struct Mater (2013) 4: 287–295
DOI: 10.1007/8611_2012_64

Published Online: 2 February 2012

1 Introduction

One attempt to increase the application range of polymers is to incorporate nanoscale fillers, which usually have intrinsically high electrical conductivity, into the polymeric matrix. Among nanoscale modifiers, carbon nanotubes (CNT) present high electric conductivity (103–104 S/cm), and high tensile strength [1]. These facts, coupled to their relatively easy incorporation and dispersion in polymers, also raised the interest in CNT to provide solutions to some problems in composite applications [2–4]. However, in order to properly tailor the composite material properties for specific applications, the relevant conduction mechanisms must be better understood, in fact for these particular composites, the nanotube concentration, aspect ratio, and dispersion significantly affects the material response [2–4].

Models have been developed that can predict, to some extent, the effect on the permittivity of adding conductive fillers to a lossless dielectric matrix [5, 6]. The effective mean-field medium concept is the foundation for most of the empirical models. The main drawback of these models is that they fail to predict the composite dielectric behavior near the percolation threshold, defined as the critical point where the physical properties have singularities and show scaling behavior [7, 8].

The inclusion of carbon conductive fillers in a dielectric matrix enhances composite electrical properties. The most remarkable aspect of these composites is that after the percolation threshold—the critical point where physical properties strongly change—there is a high divergence in the electrical properties. This is explained with the formation of a network system of the fillers and by the decrease of the correlation length ($\xi \sim |p-p_c|^{-\nu}$) for increasing mass fraction of the fillers as stated by the percolation theory [9, 10]. The correlation length is the average distance of two sites belonging to the same cluster, and the percolation exponent v has the value ~ 0.88 for 3D percolation. Most physical quantities diverge at the percolation threshold and this divergence can be related with the correlation length. For instance, the conductivity (Σ) of random mixtures of superconducting (fraction p) and normal-conducting (1−p) elements, near the percolation threshold has a power law dependence ($\Sigma \sim |p-p_c|^{-s}$). The exponent s also appears in the critical behavior of the dielectric constant in random systems [9]; it is called the superconducting exponent and has the value of 0.75 ± 0.04 [11] for the 3D case.

In this way, the composite dielectric constant near the percolation threshold can be predicted by the power law in Eq. (1) [12–14].

$$\varepsilon_{\text{eff}} \propto |\Phi_c - \Phi|^{-s}, \Phi \to \Phi_c \tag{1}$$

where s is a universal critical exponent that depends only on the system dimension, Φ is the volume fraction and Φc is the critical concentration at which an infinite cluster appears. For $\Phi > \Phi c$, a cluster spans the system, whereas for $\Phi < \Phi c$ there is no spanning cluster and the system is comprised of many small clusters.

Several numerical models have been developed studying the effect of adding conductive fillers to a low loss dielectric matrix on the composite dielectric constant and dielectric strength. They can be divided in lattice-based models [15–18] and continuum models [19, 20], however, the latter models do not take the inclusion of high-aspect ratio fillers in consideration for the calculation of the composite effective dielectric constant. In a previous work [21] it was demonstrated that the critical concentration is related to the formation of capacitor networks and that these networks give rise to the high variations in the electrical properties of the composites. It is demonstrated that the dielectric constant and the dielectric strength of the composite are highly dependent on the distribution of the nanotubes, resulting in high deviations of the electrical properties.

The composite conductivity is generally described by the percolation theory [12–14], predicting a power law relation, as shown in Eq. (2).

$$\sigma \propto \sigma_0(\Phi - \Phi_c)^t, \Phi \to \Phi_c \tag{2}$$

where t is a universal critical exponent that depends only on the system dimension. Interestingly, the predictions of the percolation theory and the excluded volume theory are not verified for CNT/polymer composites, as can be seen in recent reviews [2, 22]. In addition in studies on the percolation and excluded volume theory, several authors tried to cope with the effect of the volume fraction, clustering and anisotropy in the conductivity of CNT/polymer composites. In this section, the most relevant studies to our work will be reviewed. Dalmas et al. [23] modeled the conductivity in 3D fibrous networks using "soft-core" cylinders. They studied the effect of fiber tortuosity and fiber–fiber contact conductivity in the composite electric conductivity. It was found a good agreement between simulation and experimental results with one adjustable parameter, the fiber tortuosity. The latter authors also demonstrate that an increase of the fiber tortuosity decreases the fiber radius of gyration leading to a smaller effective aspect ratio. The existence of contact conductivity was also proposed by Hu et al. [24] using "soft-core" cylinders. The influence of aspect ratio, electrical conductivity, aggregation and shape of CNT in the composite electric conductivity was also studied. It was found, similarly to Dalmas et al. [23], that the percolation threshold increases with the fiber tortuosity. Nonetheless, the fiber tortuosity has a limited effect on the global composite conductivity. In addition, Hu et al. [24] found that the aggregation has a significant effect on the composite conductivity: the composite conductivity decreases with increasing aggregation. The contact resistivity was also investigated by Sun et al. [25] in a continuum model. The authors conclude that the contact and tunneling resistance must be controlled in order to achieve high conductive CNT/polymer composites. Finally White et al. [26] investigated the effect of CNT orientation using "soft-core" cylinders. It was found that there is a critical degree of orientation above which the electrical conductivity decreases. The work of Berhan et al. [27, 28] demonstrated that the use of hard-core fibers is more appropriate for modeling the electrical percolation onset in nanotube-reinforced composites. In the same work they also verified that

the percolation threshold is independent of the fiber waviness for high aspect ratio fibers. Thus, the CNT can be modeled as a straight cylinder-hard-core ones—with an effective aspect ratio.

Carbon nanofiber/epoxy conductivity can be described by a single junction expression [29]. In recent work [30, 31] it was established that the conductivity for CNT/polymer composites is due to hopping between nearest fillers resulting in a weak disorder regime that is similar to the single junction expression. Also in [30], a new formula for the percolation threshold was proposed and speculated that a good cluster distribution will give better electrical properties. It was also demonstrated that the formation of a capacitor network is the key aspect for the dielectric response of the composite. Computer simulations and experimental results show that the conductivity of CNT/polymer composites can be described by hopping between nearest fillers resulting in a weak disorder regime. It was shown that when hopping between fillers is introduced in the composite conductivity simulation, using hard-core cylinders, no critical degree of orientation is found above which the electrical conductivity decreases, in contrast to the work of White et al. [26].

2 Results and Discussion

The effects of the relative orientation of the nanotubes and the distance between them on the capacitance are some of the key parameters defining the final macroscopic response of the nanocomposites. Figure 1 shows the capacitance variation for a pair of cylinders when the relative orientations are changed, for the calculation of the capacitance, it was used a capacitance extraction algorithm as described in [32].

The results for the capacitance with increased rotation angles are shown in Fig. 1. In this study, the cylinders are initially placed parallel to each other, with an axial orientation along the y-axis. Then, the capacitance is calculated under maintaining the first cylinder fixed and rotating the other cylinder about the x-axis, or about the z-axis.

There is a significant influence of the rotation of the cylinder about the z-axis, since the distance between cylinders decreases considerably, in fact up to half the original distance at 90° and 270° rotation angles (even though the surface area that is at the minimum distance at these angles is much smaller than at 0° and 180°). However, the capacitance is not significantly affected by rotation about the x-axis, even at a 90° rotation angle, implying that in practical terms, the distance has a much stronger effect than the rotation angle.

The value of the capacitance does not change considerably with the rotation around a plane parallel to the fixed cylinder. This occurs because even at large rotations of one cylinder about the x-axis, only the center region of the two cylinders are at the minimum distance between them but the distance between any other points on the surface of the two cylinders is not significantly different.

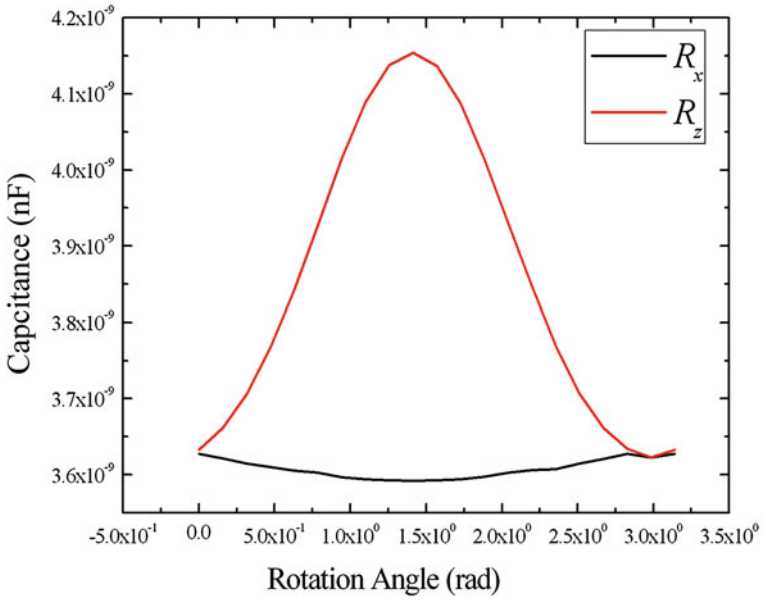

Fig. 1 Capacitance variation for a pair of cylinders when the relative orientations are changed

The influence of the filler–filler capacitance in the composite dielectric constant can be seen in [33]. In [33] it is presented the results for the dielectric constant for cylinders with an isotropic distribution and a nematic distribution. The latter results are then compared with two different aspect ratios. The fact that nematic materials show a lower dielectric constant than isotropic ones is related to the zenith angle. It was demonstrated in Fig. 1 that parallel cylinders exhibit a lower capacitance, so the lower value for the composite dielectric constant is related to the filler alignment.

One important aspect in this type of composites is the conductivity for different aspect ratio as presented in Fig. 2. The details of the simulation can be found in [31]. As can be seen the conductivity increases with increasing aspect ratio. Applying the power law defined by the percolation theory, Eq. (2) with the equation for the percolation threshold presented in [30], results in $t \sim 1.0$ with $R^2 \sim 0.97$ for all fits. The latter value for the critical exponent is equal to that predicted by the effective medium theory [10] (EMT). The fact that the value for the critical exponent deviates from the classical ones in a 3D dimension system ($t = 2$) can be related with the way that the network is formed and can be also a consequence of the used formula for the percolation threshold. This point is very interesting and is being studied analytically. It is to notice that experimental values found in the literature [22] range from 1 to 4. The observed increase of the conductivity with the aspect ratio is in agreement with [24] and can be explained by a decrease in the percolation threshold for increasing filler aspect ratio. Also in [31] it is presented the value of the composite conductivity for different degrees of

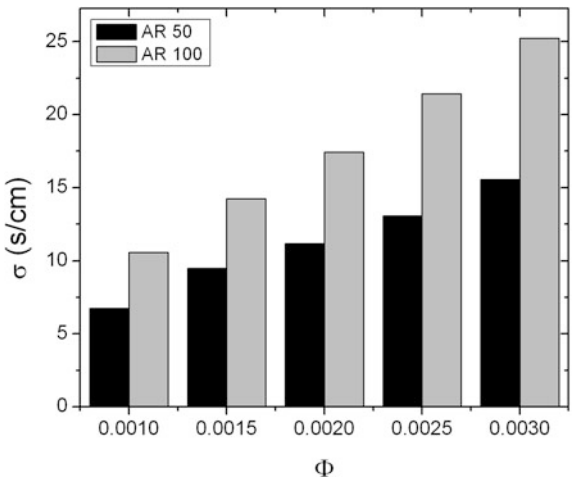

Fig. 2 The influence of the aspect ratio on composite conductivity

axial alignment, as per Eq. (3), and different volume fractions. A decrease in the conductivity for the more anisotropic composites can be observed, with this effect being more prominent at higher volume fractions.

$$S = \left(3\left\langle \cos^2\theta \right\rangle - 1\right)/2 \tag{3}$$

It should be noted that in our simulations the conductance of the cylinder (CNT) is independent of the filler length, contrary to [23–25]. Furthermore, as the present model does not assume a contact resistance, the composite conductivity results only from the CNT with δ_{max} controlling the hopping length for the same aspect ratio. In this way, δ_{max} is a parameter that can be associated to the dielectric matrix, i.e., different types of polymer will correspond to different values of δ_{max}. For instance, in epoxy composites, increasing the post-cure temperature will increase the cross-link density [34] increasing the composite conductivity [35]; this can be seen as an increase on the value of δ_{max}.

Comparing to the results in [26], a critical value for the axial alignment is not observed, but only a decrease in conductivity. This decrease in conductivity can be explained by an increase of the number of fillers that is necessary to transverse the domain between the applied electrodes. Increasing the number of fillers will increase the number of resistors and hence decrease the conductivity. Thus, increasing anisotropy changes the conductivity to lower values due to a higher number of fillers that are necessary to transverse the domain. Furthermore, as the number of fillers in the domain increases—by increasing the volume fraction—the difference between isotropic and anisotropic composite conductivity will be larger.

In [31] it is also demonstrated that there is a substantial difference in the conductivity between cylinders aligned perpendicular (S = 1) and parallel (S = −0.5)

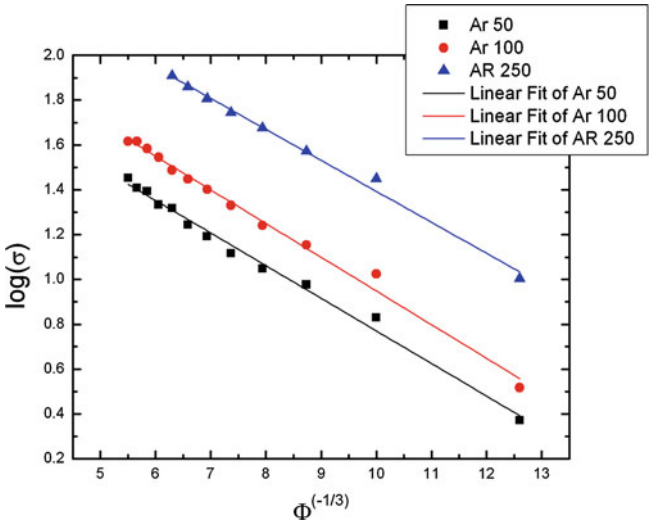

Fig. 3 Logarithm plot of the conductivity for three types of fillers versus volume fraction

to the measurement direction. This difference in conductivity is in agreement to recent experimental work [36], and is explained by the higher number of fillers necessary to transverse the domain (S = 1), which has a lower bound when S = −0.5.

In Fig. 3 it is presented the results of the linear fits of $\log(\sigma) \sim \Phi - 1/3$ for the latter simulations. As described in [31] it was used for the conductivity, in the performed simulations, hopping between nearest neighbors.

The linear fits in Fig. 3 have a $R^2 \sim 0.99$ and we also like to stress that the same results were obtained for carbon nanofibers composites [29, 37, 38]. The latter linear fits indicates that the main conduction mechanism for composites where the filler is a CNT is due to hopping between nearest fillers resulting in a weak disorder regime that is similar to the single junction expression, as discussed in [30].

In [29] it was observed that the composites have some clusters that are evenly distributed in the domain and in [30] it is proposed that a highly dispersed cluster can raise the composite conductivity. This latter indication must be further tested but is an important aspect that must be considered in designing the CNT/Polymer composites for specific applications.

3 Conclusion

In this work it is demonstrated that the capacitance between two cylinders increases with the rotation angle between them and it has a fundamental influence on the composite dielectric constant. The dielectric constant is lower for nematic

materials than for isotropic ones and this can be attributed to the effect of the filler alignment in the capacitance. Also in this work it was studied the effect of aspect ratio on the conductivity. Finally, based on early work, and by comparing to results from the literature, we found that the conductivity in this type of composites is due to hopping between nearest fillers resulting in a weak disorder regime that is similar to the single junction expression.

Acknowledgments This work is funded by the Foundation for Science and Technology, Lisbon, through the 3° Quadro Comunitário de Apoio, POCTI and FEDER funds through the "Programa Operacional Factores de Competitividade—COMPETE", project references PEst-C/CTM/LA0025/2011, NANO/NMed-SD/0156/2007, PTDC/CTM/69316/2006, PTDC-EME-PME-108859-2008, and PTDC/CTM-NAN/112574/2009 and grant SFRH/BD/60623/2009 (JS). The authors also thank support from the COST action MP0902 "Composites of Inorganic Nanotubes and Polymers (COINAPO)".

References

1. Al-Saleha, M.H., Sundarara, U.: A review of vapor grown carbon nanofiber/polymer conductive nanocomposites. Carbon **47**, 2–22 (2009)
2. Thostenson, E.T., Li, C., Chou, T.-W.: Nanocomposites in context. Compos. Sci. Technol. **65**, 491–516 (2005)
3. Baughman, R.H., Zakhidov, A.A., Heer, W.: Carbon nanotubes-the route toward applications. Science **297**, 787–792 (2002)
4. Moniruzzaman, M., Winey, K.I.: Polymer nanocomposites containing carbon nanotubes. Macromolecules **39**, 5194–5205 (2006)
5. Garnett, J.C.M.: Colours in metal classes and in metallic films. Philos T Roy Soc A **203**, 385–420 (1904)
6. Bergman, D.J., Imry, Y.: Critical behavior of the complex dielectric constant near the percolation threshold of a heterogeneous material. Phys. Rev. Lett. **39**, 1222–1225 (1977)
7. Brosseau, C., Queffelec, P., Talbot, P.: Microwave characterization of filled polymers. J. Appl. Phys. **89**, 4532–4540 (2001)
8. Cheng, Y., Chen, X., Wu, K., et al.: Modeling and simulation for effective permittivity of two-phase disordered composites. J. Appl. Phys. **103**, 034111 (2008)
9. Stauffer, D., Aharony, A.: Introduction To Percolation Theory. Taylor and Francis, London (1992)
10. Kirkpatrick, S.: Percolation and conduction. Rev. Mod. Phys. **45**, 574 (1973)
11. Herrmann, H.J., Derrida, B., Vannimenus, J.: Superconductivity exponents in two- and three-dimensional percolation. Phys. Rev. B **30**, 4080 (1984)
12. Bergman, D.J.: Exactly solvable microscopic geometries and rigorous bounds for the complex dielectric constant of a two-component composite material. Phys. Rev. Lett. **44**, 1285–1287 (1980)
13. Nan, C.-W.: Physics of inhomogeneous inorganic materials. Prog In Mater Sci **37**, 1–116 (1993)
14. Nan, C.-W., Shen, Y., Ma, J.: Physical properties of composites near percolation. Annu. Rev. Mater. Sci. **40**, 131–151 (2010)
15. Archangelis, L., Redener, S., Herrmann, J.H.: A random fuse model for breaking processes. J. Physique. Lett. **46**, L585–L590 (1985)
16. Duxbury, P.M., Beale, P.D., Leath, P.L.: Size effects of electrical breakdown in quenched random media. Phys. Rev. Lett. **57**, 1052–1055 (1986)

17. Bowman, D.R., Stroud, D.: Model for dielectric breakdown in metal-insulator compo-sites. Phys. Rev. B **40**, 4641–4650 (1989)
18. Beale, P.D., Duxbury, P.M.: Theory of dielectric breakdown in metal-loaded dielectrics. Phys. Rev. B **37**, 2785–2791 (1988)
19. Gyure, M.F., Beale, P.D.: Dielectric breakdown of a random array of conducting cylinders. Phys. Rev. B **40**, 9533–9540 (1989)
20. Gyure, M.F., Beale, P.D.: Dielectric breakdown in continuous models of metal-loaded dielectrics. Phys. Rev. B **46**, 3736–3746 (1992)
21. Simoes, R., Silva, J., Vaia, R., et al.: Low percolation transitions in carbon nanotube networks dispersed in a polymer matrix: dielectric properties, simulations and expriments. Nantechnology **20**, 35703 (2009)
22. Bauhofer, W., Kovacs, J.Z.: A review and analysis of electrical percolation in carbon nanotube polymer composites. Compos. Sci. Technol. **69**, 1486–1498 (2009)
23. Dalmas, F., Dendievel, R., Chazeau, L., et al.: Carbon nanotube-filled polymer composites numerical simulation of electrical conductivity in three-dimensional entangled fibrous networks. Acta. Mater. **54**, 2923–2931 (2006)
24. Hu, N., Masuda, Z., Cheng, Y., et al.: The electrical properties of polymer nanocomposites with carbon nanotube fillers. Nanotechnology **19**, 215701 (2008)
25. Sun, X., Song, M.: Highly conductive carbon nanotube/polymer nanocomposites achievable? Macromol. Theor. Simul. **18**, 155–161 (2009)
26. White, S.I., DiDonna, B.A., Mu, M., et al.: Simulations and electrical conductivity of percolated networks of finite rods with various degrees of axial alignment. Phys. Rev. B **79**, 24301–24306 (2009)
27. Berhan, L., Sastry, A.M.: Modeling percolation in high-aspect-ratio fiber systems. II The effect of waviness on the percolation onset. Phys. Rev. E **75**, 41121–41127 (2007)
28. Berhan, L., Sastry, A.M.: Modeling percolation in high-aspect-ratio fiber systems. I Soft-core versus hard-core models. Phys. Rev. E **75**, 41120–41128 (2007)
29. Cardoso, P., Silva, J., Paleo, A.J., et al.: The dominant role of tunneling in the conductivity of carbon nanofiber-epoxy composites. Phys. Status. Solidi. A **207**, 407–410 (2010)
30. Silva, J., Simoes, R., Lanceros-Mendez, S., et al.: Applying complex network theory to the understanding of high aspect ratio carbon filled composites. Europhys. Lett. **93**, 37005 (2011)
31. Silva, J., Ribeiro, S., Lanceros-Mendez, S., et al.: The influence of matrix mediated hopping conductivity, filler concentration, aspect ratio and orientation on the electrical response of carbon nanotube/polymer nanocomposites. Compos. Sci. Technol. **71**, 643–646 (2011)
32. Nabors, K., White, J.: Fastcap: a multipole accelerated 3-D capacitance extraction program. IEEE Trans. Comput. Aided. Design. Integ. Circuits. Syst. **10**, 1447 (1991)
33. Simoes, R., Silva, J., Lanceros-Mendez, S., et al.: Influence of fiber aspect ratio and orientation on the dielectric properties of polymer-based nanocomposites. J. Mater. Sci. **45**, 268–270 (2009)
34. Irurzun, I., Vicente, J., Cordero, M., et al.: Fractal analysis of electrical trees in a cross-linked synthetic resin. Phys. Rev. E **63**, 016110 (2000)
35. Faiella, G., Pscitelli, F., Lavorgna, M., et al.: Tuning the insulator to conductor transition in a multiwalled carbon nanotubes/epoxy composite at substatistical percolation threshold. App. Phys. Lett. **95**, 153106 (2009)
36. Dombovari, A., Halonen, N., Sapi, A., et al.: Moderate anisotropy in the electrical conductivity of bulk MWCNT/epoxy composites. Carbon **48**, 1918–1925 (2010)
37. Arlen, M.J., Wang, D., Jacobs, J.D., et al.: Thermal-electrical character of in situ synthesized polyimide-grafted carbon nanofiber composites. Macromolecules **41**, 8053–8062 (2008)
38. Trionfi, A., Wang, D.H., Jacobs, J.D., et al.: Direct measurement of the percolation probability in carbon nanofiber-polyimide nanocomposites. Phys. Rev. Lett. **102**, 116601 (2009)

Simulation of Thermal and Electrical Transport in Nanotube and Nanowire Composites

Satish Kumar, Muhammad A. Alam and Jayathi Y. Murthy

Abstract Nanotube-based thin-film composites promise significant improvement over existing technologies in the performance of large-area macroelectronics, flexible electronics, energy harvesting and storage, and in bio-chemical sensing applications. We present an overview of recent research on the electrical and thermal performance of thin-film composites composed of random 2D dispersions of nanotubes in a host matrix. Results from direct simulations of electrical and thermal transport in these composites using a finite volume method are compared to those using an effective medium approximation. The role of contact physics and percolation in influencing electrical and thermal behavior are explored. The effect of heterogeneous networks of semiconducting and metallic tubes on the transport properties of the thin film composites is investigated. Transport through a network of nanotubes is dominated by the interfacial resistance at the contact of two tubes. We explore the interfacial thermal interaction between two carbon nanotubes in a crossed configuration using molecular dynamics simulation and wavelet methods. We pass a high temperature pulse along one of the nanotubes and investigate the energy transfer to the other tube. Wavelet transformations of heat pulses show that

S. Kumar (✉)
G. W. Woodruff School of Mechanical Engineering, Georgia Institute of Technology, Atlanta, GA 30332, USA
e-mail: satish.kumar@me.gatech.edu

M. A. Alam
School of Electrical and Computer Engineering, Purdue University, West Lafayette, IN 47097, USA
e-mail: alam@ecn.purdue.edu

J. Y. Murthy
School of Mechanical Engineering, Purdue University, West Lafayette, IN 47097, USA
e-mail: jmurthy@ecn.purdue.edu

Adv Struct Mater (2013) 4: 297–335
DOI: 10.1007/8611_2011_61

Published Online: 21 March 2012

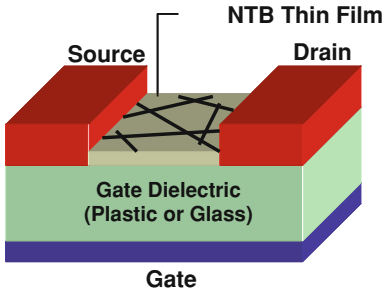

Fig. 1 Schematic of nanotube network thin-film transistor showing source, drain, gate and channel region composed of nanotube composite

how different phonon modes are excited and how they evolve and propagate along the tube axis depending on its chirality.

1 Introduction

In recent years, there has been enormous interest in fabricating thin-film transistors (TFTs) on flexible substrates in the rapidly growing field of large-area macro-electronics [1, 2]. Applications include displays [1], e-paper, e-clothing, pressure-sensitive skin [3, 4], large-area chemical and biological sensors [5, 6], flexible and shape-conformable antennae and radar, as well as intelligent and responsive surfaces with large-area control of temperature, drag and other properties [2]. Flexible substrates such as plastic require low temperature processing, typically below 200°C. Prevailing technologies such as amorphous silicon (a-Si) and organic TFTs can be processed at low temperature and are sufficient for low-performance applications such as displays, where their low carrier mobility ($\sim$1–10 cm^2/Vs) [4, 7] is not a limitation. For high-performance applications, however, the choices are limited. Single crystal silicon CMOS and polycrystalline silicon (poly-Si) technologies can yield higher performance, but are expensive and cannot be fabricated below 250°C. Nanotube-bundle (NTB) based TFTs, consisting of carbon nanotubes (CNTs) dispersed in substrates such as polymer and glass, are being explored to substantially increase the performance of flexible electronics to address *medium-to-high performance* applications in the 10–100 MHz range [2]. High mobility, substrate-neutrality and low-cost processing make NTB-TFTs very promising for these flexible-electronics applications.

Two distinct classes of materials are being pursued by researchers [8−11]. On the one hand, *randomly-oriented* nanotubes embedded in polymer have been used to fabricate nanotube network thin-film transistors (NNT-TFTs) which promise relatively high carrier mobility ($\sim$100 cm^2/Vs). Here, solution-processing is used to disperse a random network of CNTs in a plastic substrate, as shown in Fig. 1, to form a thin film. The mat of CNTs forms the channel region of the transistor. Because NNT-TFTs do not require precise alignment of CNTs, they are amenable to mass manufacture, and are relatively inexpensive. A number of groups have fabricated and analyzed these TFTs for macro-electronic and chemical sensing

applications [7, 8] and have begun to explore their performance. Snow et al. reported the mobility and conductance properties of carbon nanotube (CNT) networks and also explored the interfacial properties of CNTs in chemical sensors [9–11]. Menard et al. fabricated thin film transistors on plastic substrates using nano-scale objects (microstrips, platelets, disks, etc.) of single crystal silicon. Zhou et al. demonstrated fabrication of p-type and n-type transistors [8], which could be used as building blocks for complex complementary circuits. Fabrication of an integrated digital circuit composed of up to nearly 100 transistors on plastic substrates using random network of CNTs has been reported by Cao et al. [12]. Other experimental reports on CNT TFT fabrication can be found in [2, 12, 13]. A number of groups have focused on developing TFTs with *well-aligned* and *or partially-aligned* nanotubes for very high performance applications [14–16] using transfer printing; mobilities of 1,000 cm^2/Vs, comparable to single-crystal silicon are achievable using this technology.

Though there has been a great deal of research on composites, [17– 20] nanocomposites for use in macrolectronics pose very specific problems. First, unlike most published research on 3D transport in composites, our interest is in 2D thin-film composites in which in-plane electrical transport dominates, and in which in-plane thermal spreading plays a central role in determining device temperature. Furthermore, macroelectronic devices are typically of the 1–50 micron scale. At these scales, the nanotube length may compete with the finite size of the device, and unlike in most published research, bulk composite behavior does not obtain. Furthermore, there remain a large number of unknowns regarding the ultimate performance limits of NTB-TFTs. For example, nearly all reported work has concentrated on device fabrication and processing, but little is understood about the fundamental physics that govern device operation and scaling as a function of tube orientation, tube density, ratio of metallic to semiconducting tubes, and tube-substrate interaction [21].

Strong electrical, thermal and optical interactions between the tubes and between the tubes and the substrates affect device performance, but there has been little fundamental work to explore these interactions quantitatively. Furthermore, metallic CNTs form 30% of typical NNTs which are problematic because they can short source and drain and limit on–off ratios [22]. Recently, a number of techniques for removing them have been reported. A gas-phase plasma hydrocarbonation reaction technique has been reported to selectively etch and gasify metallic nanotubes and obtain pure semiconducting nanotubes [23]. Another process that separates single-walled carbon nanotubes (SWNTs) by diameter, band gap and electronic type using centrifugation of compositions has been reported by Arnold et al. [24]. The degree to which metallic tubes can influence on/off ratios must be understood for controlled and optimal design. Last but not least, the supply voltage used thus far in driving these devices has been untenably high, leading to unacceptable power dissipation and hysteresis due to charge injection. Processing conditions must be optimized to reduce the supply voltage to acceptable values.

Table 1 Experimental results for enhancement in effective thermal conductivity of CNT composites

Composite type	Diameter (d)(nm)	Length (L_t)	Concentration (%)	Increase in k_{eff} (%) over substrate	Network (type)
SWNT/Silicon elastomer [66]	–	–	3.8 wt	65	Random
SWNT/Epoxy [27]	1.1	–	1 wt	125	Random
SWNT/Epoxy [57]	1.1	170 nm	1 wt	80	Random
MWNT/Carbon [67]	20–40	10–100 μm	–	12.31	Aligned
MWNT/Silicon elastomer [25]	12	0.3 mm	0.4 vo	280	Aligned
MWNT/Oil [68]	25	50 μm	1 vol	160	Random
MWNT/Water [69]	20–60	>10 μm	0.84 vo	27.3	Random

The electrical performance of NNT-TFT macroelectronics could be severely compromised by self-heating. Cooling options are limited if macroelectronics are to be kept flexible. A temperature rise above ambient in the 100°C range is expected for passive natural convection cooling and is expected to scale linearly with frequency and quadratically with drain voltage. High temperatures not only compromise electrical performance but also have consequences for the thermo-mechanical reliability of flexible substrates. An inability to control self-heating would mean either employing lower-speed TFTs or decreasing the number of transistors per unit area. It is therefore necessary not only to understand thermal transport in these composites, but the interaction of electrical and thermal transport in determining device performance and reliability.

Low density CNT composites have been extensively explored for applications in thermal management [25–27], and high strength materials [28, 29]. In these applications, CNTs are embedded in host substrate as a random matrix. A percolating network of CNTs is found to be formed even at low volume fractions ($\sim$0.2%) due to their high aspect ratio [27, 30]. Theoretical and numerical studies based on the effective medium approximation (EMA) [18, 26], Monte-Carlo simulations [31] or scaling analysis [32] have been reported on percolating nanotube networks or their composites to predict their effective electrical or thermal transport properties. However, many of these studies significantly limit the thermal conductivity ratios addressed and do not address finite-sized 2D composites. A number of experimental measurements of effective thermal conductivity (k_{eff}) of nanotube suspensions in either substrates or fluids have been reported recently, and are summarized in Table 1. There are large disparities in the reported enhancement of k_{eff} over that of the substrate. However, all experiments show that the maximum achievable conductivity is less than three times that of the underlying matrix/fluid, a harbinger of thermal problems in NNT-TFTs. It is necessary to understand and control the physics underlying these performance limits, particularly the influence of tube–tube and tube-substrate contact parameters on k_{eff}.

A firm understanding of tube–tube and tube-substrate interfacial transport may provide guidelines for improving the efficiency and reliability of CNT based devices. Various experimental and numerical studies have been performed to estimate the thermal conductivity of CNTs and also to measure the thermal resistance between the CNT and the substrate. Most numerical studies are based on the molecular dynamics (MD) method [33, 34]. A list of these studies may be found in Lukes and Jhong [33]. Small et al. measured the tube-to-substrate resistance (on a per-length basis) of 12 Km/W for a MWNT supported on a substrate [35] and Maune et al. determined the thermal resistance between a SWCNT and a solid sapphire substrate as 3 Km/W [36]. Recently, Carlborg et al. studied the thermal boundary resistance and the heat transfer mechanism between CNTs and an argon matrix using MD [37].

Recent molecular dynamics (MD) computations [34, 38] have found high values for tube–tube contact resistance. Maruyama et al. used MD simulations to compute the thermal boundary resistance between a CNT surrounded by six other CNTs using the lumped capacitance method [34]. By measuring the transient temperature change of CNTs they computed the CNT–CNT thermal resistance, and found it to be of the order of 1.0×10^{-7} m^2-K/W [34]. Zhong and Lukes considered heat transfer between CNTs using classical MD simulations and estimated the interfacial thermal transport between offset parallel single-wall carbon CNTs as a function of CNT spacing, overlap, and length [38]. Greaney and Grossman used MD techniques to understand the effect of resonance on the mechanical energy transfer between CNTs [39]. It has been shown recently that the thermal resistance at a CNT–CNT contact should be of the order of 0.3×10^{-12} K/W to match the very low conductivity measured for CNT beds. This has also been verified by atomistic Green's function (AGF) simulations [40]. Nevertheless, the mechanism of energy transport and phonon dynamics at the interface of two CNTs is still not well understood and needs a detailed exploration. Experimental techniques for direct measurement of CNT–CNT resistance have not yet been reported; thus atomistic-level simulations are a vital tool to analyze the interfacial transport mechanism.

In this article, we develop a systematic conceptual framework for understanding the electrical, thermal, and electro-thermal performance of CNT nanocomposites for macro-electronic applications. A generalized finite volume approach is presented for evaluating the electrical and thermal conductivity and device performance of nanotube network TFTs composed of finite two-dimensional nanocomposites. We first apply the approach to the prediction of the electrical and thermal conductance of pure percolating networks of CNTs in the absence of a substrate. Predictions of the electrical characteristics of pure-network TFTs in the linear regime are then presented and their behavior is explained by invoking the physics of heterogeneous finite-sized networks of metallic and semiconducting tubes. The numerical results for the estimation of the effective conductance properties of composites are presented next which explore the effect of tube-to-tube conductance, tube-to-substrate conductance and network density on both electrical and thermal transport. A two-dimensional effective medium

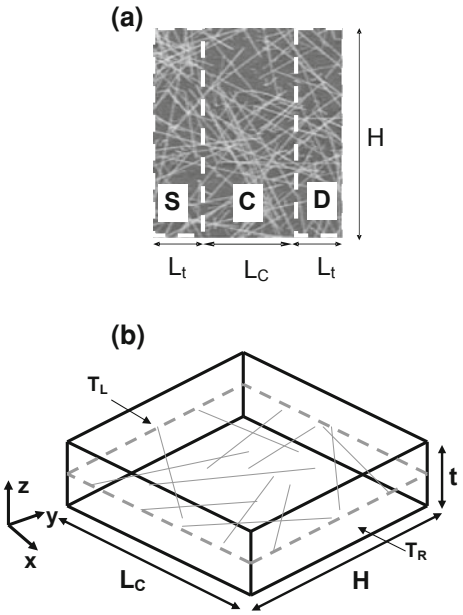

Fig. 2 **a** Schematic of thin-film transistor showing source (S), drain (D) and channel (C). The channel region is composed of a network of CNTs. **b** Geometric parameters

approximation (EMA) is derived for thin-film composites and compared to our numerical simulations, and deficiencies in the EMA model for CNT composites are identified. Attention is turned next to the analysis of the thermal transport physics between two CNTs using molecular dynamics simulations and wavelet methods. We investigate the thermal interaction between two CNTs in a crossed configuration when a high temperature pulse is passed along one of the CNTs. Wavelet analysis decomposes the time series of the heat pulse in the time–frequency space and helps in determining the evolution and propagation of dominant modes.

2 Numerical Formulation

A schematic of a nanotube bundle transistor is shown in Fig. 1. In thin film structures, we often have three terminals—gate at the bottom, source and drain side by side, Fig. 2. TFTs are a special class of transistor in which a thin film of semiconducting material is used as the channel (C) region between the source and drain. In nanotube network TFTs, a thin CNT composite film acts as the channel region. Typical dimensions are indicated in Fig. 2b, where L_C is the length of the channel, L_t is the average length of the nanotubes, d is the diameter of nanotube, H is the width of the transistor and t is the thickness of the nanocomposite. A fixed voltage bias, V_{DS}, is applied across the channel from drain to source to drive the mobile charges in the channel region, while the transistor is turned on and off by

changing the gate voltage, V_{GS}. The corresponding current is denoted by I_{DS}. An important parameter to assess device performance is the on–off ratio (R) which is the ratio of the current flowing in the device in the on-state, I_{ON}, to the current in device in the off-state, I_{OFF}.

In the present article, our analysis of the electrical performance of NNT TFTs is limited to the linear regime, a regime where current (I_{DS}) through the device is linearly proportional to V_{DS}. This is only true at low V_{DS}. A extension of this problem has been reported by Pimparkar et al [41] that generalizes this problem to high-bias regime (high V_{DS}) and provides proper scaling laws to predict the performance of transistors with arbitrary geometrical parameters and biasing conditions. For an insulating substrate (either for electrical or thermal transport), only transport in the percolating network of tubes is considered and the effective conductivity/conductance of the pure network is computed (see Sect. 3), Fig. 2a. If the substrate is sufficiently conducting, transport in both substrate and tube network are considered for computing effective conductive properties (see Sect. 4), incorporating the effect of tube-to-substrate interaction.

2.1 Thermal Transport

The computational domain for computing effective thermal properties of the nanotube composite is a three-dimensional box of size $L_C \times H \times t$ (see Fig. 2b), which is composed of a 2D random network of nanotubes embedded in the mid-plane of the substrate. Diffusive transport in the tube obtains when there are a sufficient number of scattering events during the residence time of the phonon in the tube. This condition prevails here because of the dominance of interface scattering at the tube-substrate boundary. Thus, Fourier conduction in the nanotubes may be assumed, albeit with a thermal conductivity that may differ significantly from bulk or freestanding values. Assuming one-dimensional diffusive transport along the length s of the tube and three-dimensional conduction in the substrate, the governing energy equations [21] in the tube and substrate may be written in non-dimensional form as:

Tube:

$$\frac{d^2\theta_i}{ds^{*2}} + \sum_{\text{intersecting tubes j}} Bi_c\left(\theta_j - \theta_i\right) + Bi_s(\theta_s - \theta_i) = 0, \tag{1a}$$

Substrate:

$$\nabla^{*2}\theta_s + \sum_{i=1}^{N_{\text{tubes}}} Bi_s\beta_v \frac{k_t}{k_s}(\theta_i - \theta_s) = 0. \tag{1b}$$

Here, dimensionless temperature variable is $\theta = (T - T_L)/(T_R - T_L)$; T_R and T_L are the face temperatures of the right and left boundary faces of the composite

(see Fig. 2b). These are the faces which contact source and drain when the thin film composite is used as the channel in the transistor. All lengths are non-dimensionalized by the tube diameter d. θ_i (s^*) is the non-dimensional temperature of the ith tube at a location s^* along its length and θ_s is the substrate temperature. The other dimensionless parameters are defined as:

$$Bi_c = \frac{h_c P_c d^2}{k_t A};\ Bi_s = \frac{h_s P_s d^2}{k_t A};\ \frac{k_s}{k_t};\ \beta_v = \alpha_v \left(\frac{A}{P_s}\right);\ \frac{L_C}{L_t};\ \frac{H}{L_t};\ \frac{L_t}{d};\ \frac{t}{d}$$

Here, Bi_c represents the dimensionless contact conductance for tube-to-tube contact; Bi_s represents the dimensionless interfacial conductance between the tube and substrate, both due to Kapitza resistance and isotherm distortion near the tube. A is the effective cross-section of the tube, and k_t is the corresponding thermal conductivity. The term h_c is the heat transfer coefficient governing the exchange of heat to other tubes j making contact with tube i through a contact perimeter P_c, and the heat transfer coefficient h_s governs the transfer of heat between the tube and the substrate through a contact perimeter P_s. k_s is the substrate thermal conductivity. The second term in Eq. (1b) contains the heat exchange with tubes traversing the substrate, which are N_{tubes} in number, through a contact area per unit volume, α_v. The geometric parameter β_{v} may be determined from the tube density per unit area ρ and the corresponding dimensionless parameter is ρ^* $(\rho/\rho_{th.})$. The percolation threshold (ρ_{th}) for the network is estimated as the density at which the average distance between the nanotubes equals the average length of the tubes, so that $\rho_{th} = 1/1\langle L_t \rangle^2$.

For thermal conductivity calculations, the thermal boundary conditions for all tubes originating at the source and terminating in the drain are given by:

$$\theta_i = 1 \text{ at } s^* = 0;\ \theta_i = 0 \text{ at } s^* = \frac{L_t}{d}, \tag{2}$$

and the boundary conditions for the substrate are given by:

$$\theta_s = 1 \text{ at } x^* = 0;\ \theta_s = 0 \text{ at } x^* = \frac{L_C}{d};\frac{\partial \theta_s}{\partial z^*} = 0 \text{ at } z^* = 0 \text{ and at } z^* = \frac{t}{d}. \tag{3}$$

All the tube tips terminating inside the substrate are assumed adiabatic. The boundaries $y^* = 0$ and $y^* = H/d$ are assumed as periodic boundaries for both substrate and tubes.

2.2 Electrical Transport

The dimensionless potential equation in the linear regime is analogous to the thermal transport equation in the Fourier conduction limit, with the potential being analogous to temperature and the current being analogous the heat transfer rate. For charge transport in CNTs in plastic, the substrate is considered insulating and

only transport in the tube network is considered. For organic transistors with dispersed CNTs [42], the substrate is not insulating and charge leaks from the CNTs to the organic matrix, analogous to thermal transport in a composite, and charge exchange with the substrate must be considered. Since $L_C \gg \lambda$, the mean free path of electrons, a drift–diffusion model and Kirchoff's law for carrier transport may be employed [22]. In this linear regime, which occurs for low source-drain voltage V_{DS}, the current density along the tube is given by:

$$J = \sigma d\Phi/ds \tag{4}$$

where σ is the electrical conductivity and Φ is the potential, and is only a function of the source-drain voltage V_{DS}. Using the current continuity equation $dJ/ds = 0$ and accounting for charge transfer to intersecting tubes as well as to the substrate [43], the dimensionless potential distribution ϕ_i along tube i, as well the three-dimensional potential field in the substrate are given by:

$$\frac{d^2\phi_i}{ds^{*2}} + \sum_{\text{intersecting tubes j}} c_{ij}(\phi_j - \phi_i) + d_{is}(\phi_s - \phi_i) = 0, \tag{5a}$$

$$\nabla^{*2}\phi_s + \sum_{i=1}^{N_{\text{tubes}}} d_{is}\beta_v \frac{\sigma_t}{\sigma_s}(\phi_i - \phi_s) = 0. \tag{5b}$$

Here c_{ij} is the dimensionless charge-transfer coefficient between tubes i and j at their intersection point, analogous to Bi_c in Eq. (1a), and is specified a priori; it is non-zero only at the point of intersection. The term d_{is} is analogous to Bi_s term in Eq. (1a) and is active only for nanotubes in organic substrates. The electrical conductivity ratio is σ_t/σ_s. For computing the voltage distribution, boundary conditions $\phi_i = 1$ and $\phi_i = 0$ are applied to tube tips embedded in the source and drain regions respectively. For the organic substrate, $\phi_s = 1$ and $\phi_s = 0$ are applied at $x^* = 0$ and $x^* = L_C/d$ respectively; for the other boundaries, a treatment similar to that for the substrate temperature is applied. This computation of voltage distribution is only valid for low V_{DS}.

2.3 Solution Methodology

In the present analysis, the nanotube network is essentially 2D, while the substrate containing it is 3D, as shown in Fig. 2b. The source, drain and channel regions in Fig. 2b are divided into finite rectangular control volumes. A fixed probability p of a control volume originating a nanotube is chosen a priori. A random number is picked from a uniform distribution and compared with p. If it is less than p, a nanotube is originated from the control volume. The length of source and drain for tube generation is L_t, which ensures that any tube that can penetrate the channel region from either the left or the right is included in the simulations. The orientation of the tube is

also chosen from a uniform random number generator. Since the tube length is fixed at L_t, all tubes may not span the channel region even for shorter channel lengths L_C, depending on orientation. Tubes crossing the $y^* = 0$ and $y^* = H/d$ boundaries are treated assuming translational periodicity; part of the tube crossing one of these boundaries reappears on the other side. Tube-tube intersections are computed from this numerically generated random network and stored for the future use. The analysis is conducted only on the tubes that lie in the channel region. The non-dimensional equations for the tubes and substrate are discretized using the finite volume method and a system of linearly coupled equations is obtained for the tube segment temperatures θ_i (or the electric potential ϕ_i) and the substrate temperatures θ_s (or the electric potential ϕ_s) at the substrate cell centroids. A direct sparse solver [44] is used to solve the resulting system of equations. To account for randomness in the sample, most of the results reported here are computed by taking an average over 100 random realizations of the network. More realizations are used for low densities and short channel lengths where statistical invariance is more difficult to obtain due to the small number of tubes in the domain.

3 Conduction in Percolating Network

If the underlying substrate (host matrix) has very low conductivity, the network itself forms the dominant pathway for conduction. This limit is realized in the case of electrical conduction in nanotube composites when the network is embedded inside an almost-insulating substrate such as plastic or glass. For thermal conduction in nanotube composites, the substrate-to-tube conductivity ratio is generally higher than for electrical conduction and substrate-to-tube interaction can be neglected only when the interfacial resistance between the tube and substrate is extremely high [21]. Therefore, the pure network conduction case is generally not realized for thermal transport.

The conductive properties of the network are strongly dependent on the density of the tubes in the network. A conducting path between source and drain may not exist at very low tube densities. If such tube network is used as the channel region of the transistor, no current could pass through the transistor. As the density of tubes increases, a critical density ρ_{th}, known as the percolation threshold, is reached, at which a complete pathway between source and drain is formed. The percolation threshold for the network is estimated as the density at which the average distance between the nanotubes equals the average length of the tubes, so that $\rho_{th} \propto 1/1\langle L_t \rangle^2$. A more accurate dependence of ρ_{th} on tube length, given by $\rho_{th} = 4.23^2/\pi L_t^2$, can be obtained from the numerical simulations [45, 46]. There is great interest in exploring the transport behavior of the network at densities close to the threshold, which is dependent on the dimensionality and the aspect ratio of the tubes. Close to the percolation threshold, the network conductance, G, exhibits a power-law relation, i.e. $G \sim (\rho - \rho_{th})^m$, where m is the percolation exponent [47].

Several studies based on the Monte-Carlo simulations have been reported for the analysis of the percolating networks of nanotubes or their composites [31, 47]. Keblinski and Cleri [31] analyzed the effect of contact resistance in percolation networks to explain why the value of the percolation threshold scaling exponent holds over the entire range of network-densities. Foygel et al. [47] performed Monte Carlo simulations to explore the aspect ratio dependence of the critical fractional volume and the critical index of conductivity. Shenogina et al [48] performed finite element analysis to explore the reasons for the absence of thermal percolation in nanotube composites. We have performed a percolation-based analysis to compute the conductance exponents of nanotube networks for different densities and for different tube-to-tube contact conductances [13]. We have also explored the change in the device performance when the semi-conducting tube network in the channel region is contaminated by metallic tubes [22]. Important results from these studies are summarized below.

3.1 Network Transport in the Non-Contacting Limit

In the limit when there is no contact between tubes ($Bi_c = 0$, $c_{ij} = 0$) and between tube and substrate ($Bi_s = 0$, $d_{is} = 0$) and tubes directly bridge source-drain, a simple analytical solution for the heat transfer rate through the domain (and correspondingly the drain current I_{DS} for electron transport) may be derived. Only the tubes are considered in this 2D planar calculation, and the substrate contribution is neglected. In this limit, the in-plane heat transfer rate through the composite, q, is directly proportional to the number of tubes directly bridging source and drain, but inversely proportional to the tube length contained in the channel. By computing the number of bridging tubes from geometric considerations, it may be shown that [13]:

$$q \propto I_{DS} \propto \frac{N_S}{W} = \left(\frac{2}{\pi}\right)\rho H L_t \left(\cos^{-1}\left(\frac{L_C}{L_t}\right) - \left(\frac{L_C}{L_t}\right)\sqrt{1 - \left(\frac{L_C}{L_t}\right)^2}\right). \quad (6)$$

where W is $\left[\sum_{i=1}^{N_S} {}^1/_{L_i}\right]^{-1}$, L_C is the channel length shown in Fig. 2, L_t is the length of the tube, and H is the height of the sample, as shown in Fig. 2, N_S is number of bridging tubes and ρ is the density of the tubes. The constant of proportionality in Eq. (6) depends on the conductivity of the tubes. Figure 3 shows a comparison of the analytical result obtained using Eq. (6) with that computed numerically using the finite volume method described above. The ratio q/q_{ref} is plotted, where q_{ref} is the reference heat transfer rate at $L_C/L_t = 0.1$. One hundred random realization of the network are used. The case $L_C = 3$ μm, $H = 4$ μm, and $\rho = 5.0$ μm^{-2} is considered. The analytical and numerical results are in good agreement with each other, confirming the validity of our approach. When the

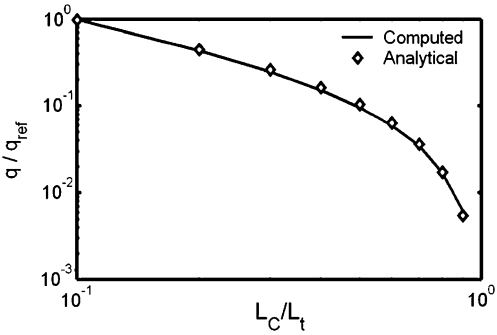

Fig. 3 Comparison of heat transfer rate in a nanotube network with analytical results for the case of zero tube–tube contact

channel length becomes comparable to or longer than the tube length, q/q_{ref} is seen to go to zero; in the absence of tube–tube and tube-substrate contact, heat or current can flow through the tubes only if the tubes bridge source and drain. As a practical matter, the result in Fig. 3 is applicable to electrical transport in short-channel CNT/plastic TFTs where the short channel lengths imply few tube–tube interactions.

3.2 Conduction Exponents

The lateral electrical conductivity of CNT thin films has been measured by different research groups. Here, we compare the network conductance predicted using our model with electrical conductance measurements by Snow et al. [10]. A pure planar tube network is considered, assuming that the substrate is entirely non-conducting. This is typical of electrical transport in CNT/plastic composites. The average length of the tubes in Reference [10] ranges from 1 to 3 μm. The exact length distribution of nanotubes has not been reported in Snow et al. [10]. For the numerical model, random networks with a tube length of 2 μm are generated, and an average over 200 random realizations is taken. The percolation threshold for the network is roughly estimated using $\rho_{th} = 1/1\langle L_t \rangle^2$ to be 0.25 μm^{-2}. Simulations are performed for densities in the range 1–10 μm^{-2} for channel lengths varying from 1 to 25 μm and with a width H of 90 μm, corresponding to the dimensionless parameters $L_C/L_t \sim 0.5$–12.5 and $H/L_t = 45$. The device dimensions and tube lengths are chosen to match those in Reference [10].

In Fig. 4a, the normalized network conductance G/G_0 is shown as a function of L_C/L_t for several tube densities above the percolation threshold for nearly perfect tube–tube contact (i.e., $c_{ij} = 50$). For long channels $(L_C > L_t)$ there are no tubes directly bridging the source and drain, and current (heat) can flow only because of the presence of the network. If the tube density is greater than the percolation threshold, a continuous path for carrier transport exists from source to drain, and G is seen to be non-zero even for $L_C/L_t > 1$. Figure 4a shows that the conductance exponent, n, defined as $G \sim (L_C)^n$, is close to -1.0 for the high densities

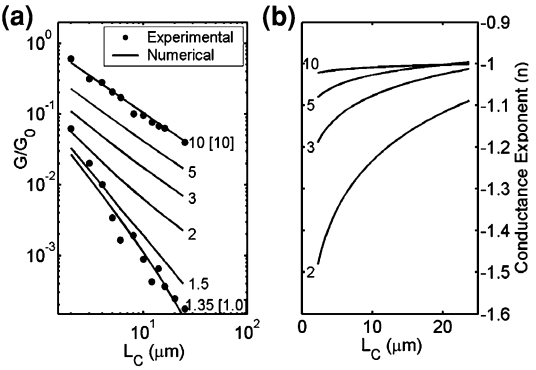

Fig. 4 **a** Computed conductance dependence on channel length for different densities (ρ) in the strong coupling limit ($c_{ij} = 50$) compared with experimental results from Ref. [11]. For $\rho = 10.0$ μm^{-2}, $G_o = 1.0$ (simulation), $G_o = 1.0$ (experiment). For $\rho = 1.35$ μm^{-2}, $G_o = 1.0$ (simulation), $G_o = 2.50$ (experiment). The number after each curve corresponds to the value of ρ used in the simulation. The number in [ ] corresponds to ρ in experiments from Ref. [11]. **b** Dependence of conductance exponent (n) on channel length for different densities (ρ) based on Fig. 4a

($\rho = 10$ μm^{-2}; $\rho^* = \rho/\rho_{th} = 40$), indicating ohmic conduction, in good agreement with Snow et al. [11]. The exponent increases to -1.80 at lower densities (1.35 μm^{-2}; $\rho^* = 5$), indicating a non-linear dependence of conductance on channel length. The asymptotic limit of the conductance exponent for infinite samples with perfect tube/tube contact has been found to be -1.97 [49, 51]. The observed non-linear behavior for low density is expected because the density value is close to the percolation threshold. Snow et al. reported a conductance-exponent of -1.80 for a density of 1.0 μm^{-2} and channel length >5 μm. For the same device dimensions, this value of the exponent is close to that obtained from our simulations for a density of 1.35 μm^{-2}. At densities close to the percolation threshold, computations are very sensitive to variations in computational parameters. Small variations in experimental parameters such as tube diameter, nanotube contact strength, tube electronic properties as well as the presence of a distribution of tube lengths (1–3 μm), which is not included in the simulation, may explain the difference. The contact resistance between the nanotubes and the source and drain electrodes as well as insufficiently large samples for ensemble averaging in the experimental setup may also be responsible. Indeed, a more quantitative agreement with the low-density data at short channel length is realized if one accounts for imperfect tube–tube contacts [51].

The dependence of conductance exponent on channel length is explored in Fig. 4b for $c_{ij} = 50$ and for densities in the range 2.0–10 μm^{-2}, corresponding to ρ^* values of 8–40. For densities >3.0 μm^{-2} ($\rho^* > 12$), the exponent approaches the ohmic limit, -1.0, with increasing channel length. Larger exponents, corresponding to non-ohmic transport, are observed for the shorter channel lengths. This is consistent with experimental observations, where conductance is seen to scale more rapidly with channel length for small L_C [11].

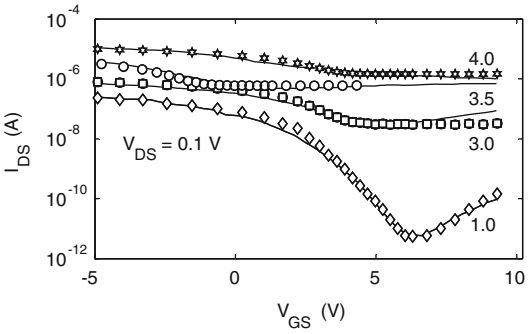

Fig. 5 Computed $I_{DS} \sim V_{GS}$ at $V_{DS} = 0.1$ V for different densities is compared with experimental results from Ref. [11] before the electrical breakdown of metallic tubes. Solid lines correspond to experimental results from Ref. [11] and markers correspond to computational results. The number after each curve corresponds to tube densityρ. The curve $\rho = 3.5$ μm^{-2} is shifted on the x-axis to account for charge trapping

3.3 Conduction in Heterogeneous Networks of Metal-Semiconducting Tubes

The electrical performance of CNT networks is strongly influenced by the fact that approximately one-third of the CNTs grown by typical processing techniques exhibit metallic behavior and approximately two-third exhibit semiconducting behavior [22]. This heterogeneity controls the on–off ratio R of typical CNT-network based devices, where on–off ratio R is the ratio of the device-current in the on state to the device current in the off–state. R has been shown [22] to be a unique and predictable function of L_C, L_t, N_{IT} (the density of interface traps), f_M (the degree of metallic contamination) and ρ, the tube density. In the conventional transistors, N_{IT} is the trapped charge at the interface of the channel and the insulating dielectric SiO_2, which separates the gate from the channel. f_M is the ratio of the number of metallic tubes to semi-conducting tubes in the tube-network. If the on–off ratio R can be reliably predicted as a function of tube density ρ and other parameters, our numerical model affords a unique way to find the tube density of typical CNT thin films by using this relationship in the inverse. This method promises far more accurate estimation of 'electrically relevant' tube density than methods currently in use, such as atomic force microscopy, and scanning electron microscopy [11].

We compute I_{DS} versus V_{GS} for several tube densities ($\rho = 1$–5 μm^{-2}) for device parameters $L_C = 10$ μm, $L = 2$ μm, $H = 35$ μm, and $V_{DS} = 0.1$ V, (Fig. 5) which are chosen to match the experiments in [10]. Since $L_C \gg L_t$, these transistors are called long-channel devices (note that this terminology differs from classical transistor terminology—where long and short channels are defined with respect to electrostatic control of the channel by the gate electrode [52]. We use c_{ij}

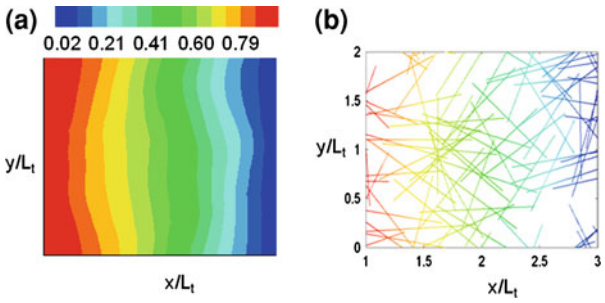

Fig. 6 Non-dimensional temperature distribution in **a** substrate **b** tube network. $L_C/L_t = 2.0$, $H/L_t = 2$, $Bi_c = 10.0$, $Bi_s = 10^{-5}$, $k_s/k_t = 0.001$ and $\rho^* = 14.0$

$\sim$ 50 based on typical values for CNT tube–tube contact [11, 53], mobility [11] and density functional theory. Here, f_M, is taken to be 33% in Fig. 5, consistent with Snow et al. [11]. The conductance ratio of metallic to semiconducting tubes (M/S conductance ratio) in the on-state is chosen as 8.0, consistent with Reference [54]. In general, the M/S conductance ratio depends weakly on the fabrication process, as well as the chirality, band-gap and the diameter of the tubes.

Gate characteristics, represented by I_{DS}–V_{GS} curves, are computed for a specific network configuration. An average is then taken over 50 random realizations of the network. Computations for $\rho = 1\ \mu m^{-2}$ agree very well with experiments in Ref. [11], Fig. 5. Increasing ρ increases the number of percolating metallic paths, increasing the on-current I_{ON}, but reducing R, as in Ref. [10]. Snow et al. speculate that $\rho > 3\mu m^{-2}$ for devices with low on–off ratio (top three solid lines in Fig. 5). Our simulations establish that they correspond to exact densities of $\rho = 3.0$, 3.5 and 4.0 respectively. Thus, tube density ρ may be deduced from a simple electrical measurement of the on/off current ratio (see Fig. 5) obviating the need for inaccurate and time-consuming analysis of AFM images, as is currently done. We note, however, that although we can predict $R(\rho)$ for a fixed M/S conductance ratio and c_{ij}, the absolute value of the on–off current and R can still vary from sample to sample depending on the M/S conductance ratio and the contact conductance between tubes of different diameters. The same methodology can also be used to interpret short channel data (Fig. 2 in Ref. [8], for example). This demonstrates the predictive power of the theoretical framework.

4 Conduction in Nanotube: Polymer Composites

Thus far, we have considered conduction in a pure network of nanotubes in the absence of a substrate or host matrix. We now turn our attention to thermal and electrical conduction in composites where carrier transport is no longer confined exclusively to nanotube network. When the thermal conductivity ratio k_s/k_t is

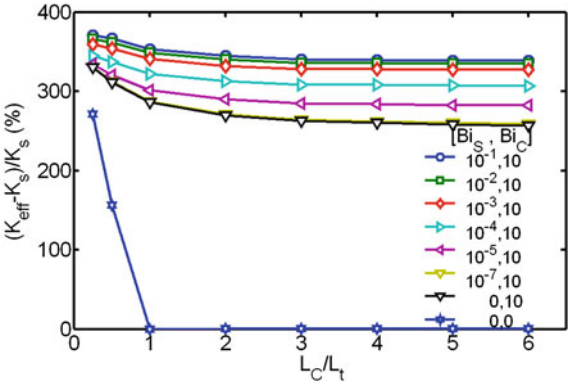

Fig. 7 Effect of substrate-tube contact conductance (Bi_S) on k_{eff} for varying channel length. L_C / L_t = 0.25–6.0 (L_t = 2.0 μm), H /L_t = 2, k_S/k_t = 0.001, and ρ^* = 3.5 (ρ = 5.0 μm^{-2})

significant or when the heat leakage from the tubes to the substrate is significant, both substrate and network play important roles in determining the thermal performance of typical nanotube composites. For electrical transport, the substrate does not generally play a role in nanotube-polymer composites, since the polymer is essentially insulating. However, a problem analogous to thermal transport occurs in electrical transport in nanotube-organic composites. Here, the electrical conductivity of the organic substrate is relatively large, and forms the primary conduction pathway. Recently, sub-percolating nanotube dispersions have been added to enhance electrical conductivity of organics [42].

Using the formulation described in Sect. 3, a typical temperature distribution in the tube network and the substrate is computed and shown in Figs. 6a, b. For this case, L_C/L_t = 2.0, H/L_t = 2, Bi_c = 10.0, Bi_s = 10^{-5}, k_s/k_t = 0.001 and ρ^* = 14.0, corresponding to L_C =4 μm, L_t = 2 μm, H = 4 μm, and ρ = 3.5 μm^{-2}. Contours of constant temperature in the substrate would be one-dimensional in x for Bi_s = 0, but due to the interaction with the tubes, distortion in the contours is observed, consistent with the temperature plots in the tube in Fig. 6b. The departure from one-dimensionality in the substrate temperature profile is related to local variations in tube density; regions of high tube density convey the boundary temperature further into the interior.

4.1 Effect of Tube-Substrate Interfacial Resistance

The contact parameters Bi_S for tube-substrate contact and Bi_C for tube–tube contact are difficult to determine, and there are few guidelines in the literature to choose them. The experimental studies conducted by Huxtable et al. [55] suggest that heat transport in nanotube composites may be limited by exceptionally small interfacial thermal conductance values. The value of the interfacial resistance between the carbon nanotube and the substrate was reported to be 8.3 × 10^{-8} m^2 K/W by Huxtable et al. [55] for carbon nanotubes in hydrocarbon (do-decyl

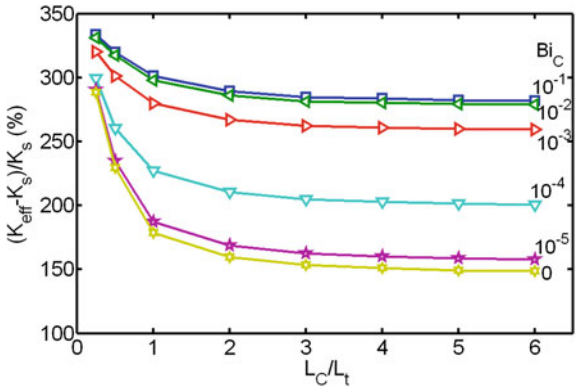

Fig. 8 Effect of tube–tube contact conductance (Bi_C) on k_{eff} for varying channel length. L_C/L_t = 0.25–6.0 (L_t = 2.0 μm), H/L_t = 2, k_S/k_t = 0.001, Bi_S =10^{-5}, and ρ^* = 3.5 (ρ = 5.0 μm^{-2})

sulphate). The non-dimensional contact parameter Bi_S evaluated using this contact conductance is O(10^{-5}) assuming the thermal conductivity of a single SWCNT to be 3,000 W/mK. The corresponding values for nanotube-polymer or nanotube-glass interfaces are not known at present. Consequently, values of Bi_S in the range 10^{-1}–10^{-7} were considered. If we assume the thermal conductivity of the polymer matrix to be 0.25 W/mK, a value of $Bi_S = 10^{-5}$ corresponds to the thermal resistance of an equivalent polymer layer of thickness 20 nm.

The percentage increase in k_{eff} of the composite is plotted against L_C/L_t ratio for different Bi_S in Fig. 7 for, $L_C/L_t \sim 0.25$–6.0 (L_t = 2.0 μm), $H/L_t = 2$, k_S/k_t = 0.001, and $\rho^* = 3.5$ (ρ = 5.0 μm^{-2}). Here, the tube density is much higher than the percolation threshold density, $\rho_{th} \sim 1.42$ μm^{-2}. The tube–tube contact parameter is held at $Bi_C = 10$, denoting nearly perfect contact. The conductivity ratio is 10^{-3}, denoting highly conducting tubes in a relatively insulating substrate. A sharp increase in k_{eff} is observed for shorter channel lengths as a result of highly conducting tubes directly bridging source and drain. This increase for shorter channel lengths is less significant at high Bi_S due to high heat leakage from the tubes to the substrate. As the channel length increases, the composite approaches bulk behavior and the conductance achieves invariance beyond $L_C/L_t > 5$. The asymptotic values of k_{eff} at high channel lengths ($L_C/L_t > 5$) can be expressed as $k_{eff} \sim 1 + \gamma k_S/k_t$, where γ is dependent on Bi_S, Bi_C and area-ratio of tubes cross-section and substrate at a composite cross-section. The general shape of the curves is explained by the 'zero Bi_S, zero Bi_C' case. As the channel becomes narrower, bridging occurs and so the curve rises. This is a "finite-size" effect not seen in bulk composites, and exists even for channels 3–4 times the tube length.

It is observed that the curve for $Bi_S \sim 10^{-7}$ is the same as that for $Bi_S \sim 0$, Fig. 7. This defines the lower limits of tube-substrate contact—below this only the network is active and side-leakage disappears. For this case, the only reason for the existence of a non-zero k_{eff} increase is the network. In this limit we expect percolation behavior, unlike that noted in the literature [27]. This implies that the interface resistance is far smaller than that corresponding to $Bi_S = 10^{-7}$ in Biercuk et al. [27]. The tube-substrate contact parameter Bi_s ceases to be limiting for $Bi_S >$

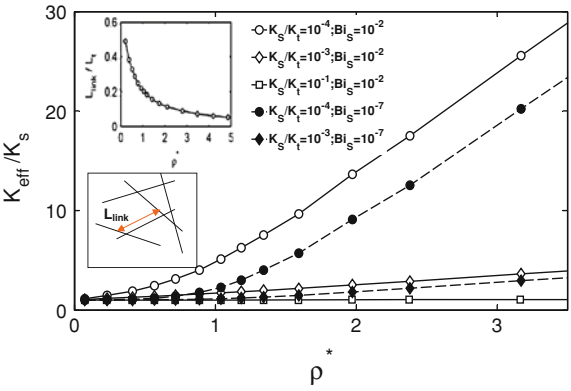

Fig. 9 Variation of normalized effective thermal conductivity (k_{eff}/k_S) against normalized tube density ($\rho^* = \rho/\rho_{th}$) is shown for different k_S / k_t and Bi_S . Average link-length (L_{link}) dependence on ρ is shown in the inset. A typical link length is shown in the bottom inset. $L_C/L_t = 3$ (L_t = 2.0 μm), $H/L_t = 2$, $Bi_C = 10$

10^{-2}, and the k_{eff} variation with L_C/L_t becomes independent of Bi_S beyond this value.

The network causes a 150–350% increase in k_{eff} over the substrate, but this still means values only in the 0.35–3.5 W/mK, implying that the composites does not conduct very well laterally, despite the presence of highly conducting tubes. Since the k_S/k_t value used here is expected to be typical of many composites for TFT applications, the results in this section demonstrate that if the percolation properties of the network could be maintained by high tube–tube contact conductance, the network itself could provide a pathway for heat removal.

4.2 Effect of Tube–Tube Conductance

Recently, Lukes et al. [38] considered heat transfer between CNTs using classical molecular dynamics simulations, and estimated a tube–tube contact resistance of the order of 1.0×10^{-7} m^2-K/W, corresponding to a Bi_C value of 2.0×10^{-5} (assuming $k_t = 3{,}000$ W/mK). However, there is no experimental corroboration of tube–tube contact resistance, and Bi_C values of 0–10^{-1} are chosen, ranging from insulating contact to perfect contact. Previous theoretical models for computing k_{eff} of nanotube composites ignore contact conductance between the nanotubes [26]. Since tube–tube contact occurs over a very small contact area, this contact resistance would be limiting only in the case of large tube-substrate resistance ($Bi_S \rightarrow 0$) for most k_S/k_t values of interest. Figure 8 show the $k_{eff} \sim L_C/L_t$ plots for different Bi_C for $L_C/L_t \sim$ 0.25–6.0 (L_t = 2.0 μm), $H/L_t = 2.0$, $k_S/k_t = 0.001$, $Bi_S = 10^{-5}$, and $\rho^* = 3.5$ (ρ = 5.0 μm^{-2}). The overall shape of the curves is similar to that in Fig. 7. The sharp increase in k_{eff} for shorter channel length composites (due to bridging tubes) is significant for low Bi_C, but the effect gradually diminishes with increasing Bi_C, Fig. 8. Decreasing Bi_C from 10^{-1} to 10^{-5} decreases k_{eff} by about 50% for long channels. Beyond $Bi_C > 10^{-2}$, tube–tube contact is sufficiently good that it ceases to matter; consequently the k_{eff} curves become coincident in

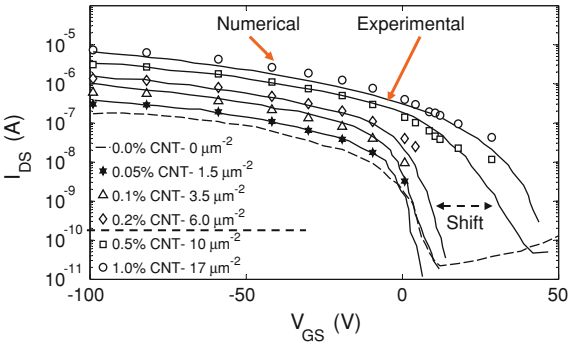

Fig. 10 Computed I_{DS}–V_{GS} at $V_{DS} = -10$ V for different CNT-densities ($\rho \sim 1$–$17\ \mu m^{-2}$) is compared with experimental results in [42]. The volume percentage of CNT dispersions used in the experiments and the corresponding network density ($\rho\ (\mu m^{-2})$) used in the computations are shown. $L_t = 1\ \mu m$, $L_C = 20\ \mu m$ and $H = 200\ \mu m$. The shift in the I_{DS} -V_{GS} curves due to the initiation of semiconducting CNT percolation for CNT volume percentage >0.2% is shown by the *dashed arrow*

Fig. 8. By the same token, values of Bi_C below 10^{-5} mean essentially zero contact between tubes, and heat leakage through the substrate is the only pathway for heat transfer for long channels. The tube–tube contact resistance computations by Zhong and Lukes [38] suggest that this may indeed be the mechanism of heat transfer in CNT composites, though further experimental corroboration is necessary. The present analysis reveals that for tube densities higher than the percolation threshold, Bi_C may be an important parameter controlling k_{eff} for highly conducting tubes with high tube-substrate resistance. Bi_C (10^{-2}–10^{-5}) corresponds to the thermal resistance presented by an equivalent polymer matrix of thickness 0.025–25 nm assuming contact area between the tubes of the order $\sim d^2$ and $k_S/k_t = 10^{-3}$.

4.3 Effect of Tube Density

The effective thermal conductivity of the composite is observed to have a different dependence on ρ in different regimes, i.e. $\rho \ll \rho_{th}$, $\rho \sim \rho_{th}$ and $\rho \gg \rho_{th}$ [56]. k_{eff} is shown as a function of ρ for these three different regimes in Fig. 9 for the case $\rho_{th}(= 4.23^2/\pi L_t^2 \sim 1.4\mu m^{-2}), k_S/k_t \sim 10^{-4} - 10^{-1} Bi_S \sim 10^{-7} - 10^{-2}, L_C/L_t = 3$ $(L_t = 2.0\mu m), H/L_t = 2, Bi_C = 10$. When $\rho \ll \rho_{th}$, k_{eff} increases linearly with ρ. This is expected since the tubes do not interact with each other either through direct contact or through the substrate. This lack of tube–tube interaction is borne out by the variation of the average link length (L_{link}) with ρ^* (inset in Fig. 9), which shows that the non-interacting limit between tubes is achieved for $\rho^* \ll 1$ for which $L_{link}/L_t \sim 1$. This trend is in agreement with the results from EMA which predict a linear scaling with volume fraction. When $\rho \sim \rho_{th}$, k_{eff} is observed

to vary non-linearly with ρ. This is typical of network percolation close to the percolation threshold [11, 13] and becomes more pronounced with decreasing Bi_S *or* k_S/k_t, Fig. 9. These two parameters explain the difference between percolation behavior for thermal transport and for electrical transport. Strong non-linear behavior near the percolation threshold is observed for charge transport in CNT-polymer composites due to very low k_S/k_t ($<10^{-6}$) [11, 13], while for thermal transport, this non-linear behavior is relatively weak due to high k_S/k_t ($\sim 10^{-3}$) and high heat leakage through the substrate (high Bi_S). Whenever transport through the substrate competes with the transport through the CNT network either due to high k_S or due to high heat leakage from the CNTs to the substrate, percolation effects due to the network are suppressed.

For $\rho > 3.0\rho_{th}$ and for large enough L_C/L_t, k_{eff} is found to vary linearly with ρ, Fig. 9. The reason for this is evident in the inset in Fig. 9, which shows that the average L_{link} varies linearly with $\rho*$ for high densities ($\rho* > 3$). Hence the network becomes homogenous. Computations of k_{eff} for the pure network in the absence of the substrate [13] reveal that it may be expressed as $k_{eff}/k_t \sim \rho L_t^2(0.783 - 0.119\ln(Bi_C^2) - 0.015\ln(Bi_C))$ for high densities. For the CNT composites, this expression would also depend on Bi_S and k_S/k_t, but linearity with respect to density would nevertheless be valid.

4.4 Electrical Conductivity of CNT-Organic Composites

A novel approach involving modifying the transconductance ($g_m \sim \mathrm{d}I_{DS}/\mathrm{d}V_{GS}$) of an organic host using a sub-percolating dispersion of CNTs has been proposed in Ref. [42]. A 60-fold decrease in effective channel length, L_{eff}, is observed that results in a similar increase in g_m with a negligible change in on–off ratio [42]. In this technique, the majority of the current paths are formed by the network of CNTs, but short switchable semiconducting links are required to complete the channel path from source to drain [42]. Experimental data published in Ref. [42] provide a good opportunity to test the correctness of our numerical formulation in Sect. 3.

The device parameters $L_C = 20$ μm, $L_t = 1$ μm, and $V_{DS} = -10$ V are chosen to match the experiments in Ref. [42]. Charge transfer coefficients $c_{ij} = 10^{-4}$ and $d_{is} = 10^{-4}$ are assumed and correspond to poor contact conductance between tube–tube and tube-substrate. The electrical conductivity ratio, σ_t/σ_s, for metallic CNTs in the on-state ($V_{GS} = -100$ V) is taken as 5.0×10^4, while that for semiconducting CNTs is 5.0×10^3 [54]. The metallic-CNT conductivity is assumed constant with V_{GS}, while the roll-off in the conductivity of semiconducting CNTs and the organic- matrix with V_{GS} is obtained from the experimental I_{DS}–V_{GS} curves (0 and 0.5% volume fraction curves) in Fig. 14.1b of Ref. [42]. Figure 10 shows that numerical results agree well with experiments over the entire range of tube densities (1.5–17 μm^{-2}). There is an anomalous jump in the I_{DS}–V_{GS} curve for 0.5% volume fraction of CNTs (labeled "shift" in Fig. 10; see also

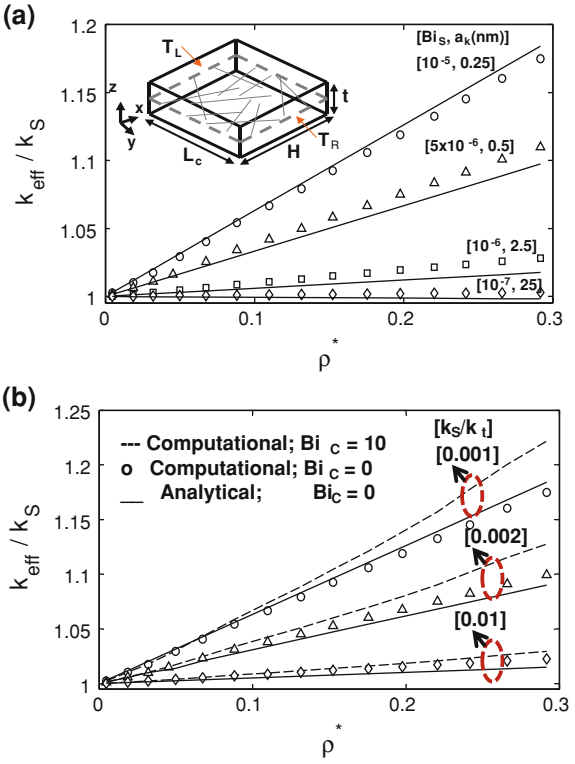

Fig. 11 **a** Comparison of normalized effective thermal conductivity (k_{eff}/k_S) computed from numerical simulations (markers) and analytically-derived expressions (*solid lines*) for different k_S/k_t ratios. L_C/L_t = 8 (L_t = 0.5 μm), H/L_t = 4, Bi_S = $10^{-5}$and ρ^* = 0-0.3 (ρ = 0.1–6.5 μm^{-2}). $Bi_C = 0$ for simulations unless otherwise stated. **b** Comparison of normalized effective thermal conductivity (k_{eff}/k_S) computed from numerical simulations and 2D EMA for different values of the interfacial thermal resistance Bi_S (10^{-7}–10^{-5}). L_C/L_t = 8 (L_t = 0.5 μm), H/L_t = 4, k_S/k_t = 10^{-3} and ρ^* = 0-0.3 (ρ = 0.1–6.5 μm^{-2})

Fig. 14.1b in Ref. [42]) which is not properly understood. We calculated the I_{DS}–V_{GS} characteristics of the organic TFT device in [42] with a realistic heterogeneous network of semiconducting-metallic tubes (1:2 ratio) dispersed in an organic matrix. We have shown that this anomalous shift in the I_{DS}–V_{GS} curve is a consequence of the formation of a parallel sub-percolating network of *semiconducting* CNTs in the organic matrix. At 0.2% CNT volume fraction, the semiconducting tubes do not have sufficient density to form a percolating network in and of themselves; metallic CNTs are necessary to achieve percolation. However, when the volume fraction is increased to 0.5%, semiconducting tubes can form a percolating network by themselves, and shift the I_{DS}–V_{GS} curve as shown. This confirms that semiconducting CNTs are active elements of this organic TFT device, a feature which was not understood previously.

4.5 Comparison with Effective Medium Theory

For low-density dispersions, the effective conductivity (k_{eff}) can be derived using a Maxwell–Garnett effective medium approximation [18], and provides a baseline

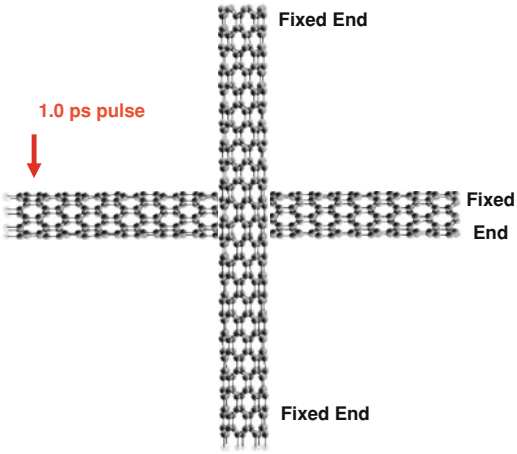

Fig. 12 Schematic of two CNTs in a crossed configuration. A 1.0 ps pulse is generated from one end of the first tube, while atoms at the other end are kept fixed. The two ends of the other tube are kept fixed. The chiralities of the two tubes are the same

for comparison with our numerical calculations. For a planar CNT network isotropic in the x–y plane (see inset in Fig. 11b) and embedded in a substrate of thickness *d,* the theory in [18] may be modified to yield k_{eff} in the x–y plane as

$$k_x = k_y = k_S \frac{2 + f[\beta_{11}(1 - L_{11}) + \beta_{33}(1 - L_{33})]}{2 - f[\beta_{11}L_{11} + \beta_{33}L_{33}]}. \tag{7}$$

Here f is the volume fraction, L_{ii} is the depolarization factor, and $\beta_{ii} = \frac{k_{ii} - k_S}{k_S + (k_{ii} - k_S)}$; $k_{11} = k_{22} = \frac{k_t}{1 + (2a_K k_t / k_S d)}$; $k_{33} = \frac{k_t}{1 + (2a_K k_t / k_S L_t)}$. Here, a_K is the Kapitza radius [18, 26], axis 3 represents the longitudinal axis of the CNT and axes 1 and 2 are the other two axes of the CNT [18].

The finite volume computation of k_{eff} is compared with predictions from the 2D EMA in Figs. 11a, b [56]. For this case, the polarization factors are given by $L_{11} = L_{22} = 0.5$, $L_{33} = 0$. The basic assumption in Eq. (7) is that tube density ρ is very low, and therefore the tubes do not interact with each other. Consequently, the tube–tube contact parameter Bi_C is set to zero in the finite volume computations to obtain a direct comparison. Since the parameter Bi_S is not known a priori, its value is adjusted to match the results from EMA for a value of $a_K = 0.25$ nm for $k_S/k_t = 10^{-2}$. The same value of Bi_S is used in all subsequent calculations for other k_S/k_t ratios in Fig. 11a. It is important to notice that there is only one free parameter, Bi_S, in our simulations, corresponding to the adjustable parameter a_K in EMA. A good match with the results of EMA is obtained for the case of $Bi_C = 0$. Calculations were also performed in Fig. 11a for $Bi_C = 10$, representing nearly-perfect contact. For high Bi_C, the numerically computed k_{eff} is observed to deviate substantially from the EMA prediction even for densities below the percolation threshold ρ_{th}. This deviation is significant for all but the highest k_S/k_t values ($<10^{-2}$), and would therefore be significant for computations of electrical and thermal conductivities in CNT composites. This suggests that high aspect ratio tubes strongly interact with each other even at tube densities below ρ_{th} and that the

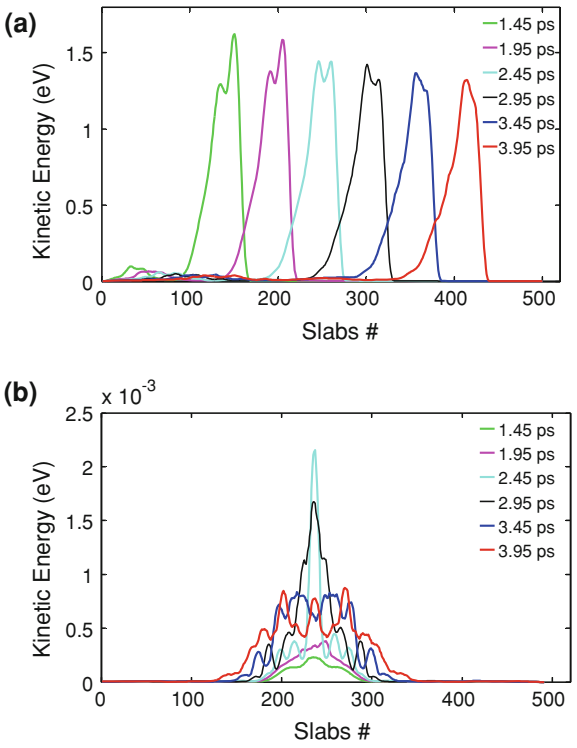

Fig. 13 **a** Location and shape of the heat pulse at different time instants along the first CNT for (5, 0) chirality. The pulse generation starts at t = 0.0 ps. **b** Location and shape of the heat pulse at different time instants in the second CNT, also of the same chirality

EMA is inadequate for the prediction of k_{eff} at all but the very lowest densities. Figure 11b presents the variation of k_{eff} with tube density with Bi_S as a parameter; the ratio $(1/a_K)/Bi_S$ is held constant in the figure. A good match with EMA is found. The constant ratio $(1/a_K)/Bi_S$ for different curves in Fig. 14.11b shows that the adjustable parameter in EMA, $(1/a_K)$, and that in the numerical calculations, Bi_S, are consistent. These results indicate that adjusting a_K to fit experimental data for $\rho > \rho_{th}$ in previous studies [26, 57] adjusts in part for tube–tube interaction effects not present in EMA theory. These adjustments would tend to underpredict the true value of interface resistance, a claim also supported by Hung et al. [58].

5 Interfacial Thermal Transport Between Nanotubes

In the last two sections, we have considered conduction in a network of nanotubes and their composites where we have treated tube–tube and tube-substrate resistance values as parameters. Various experimental and numerical studies have been performed to analyze the interfacial energy transport and to estimate the thermal resistance between the CNTs and between the CNT and the substrate. In this section, we present our investigation of the thermal energy transport from one single-walled

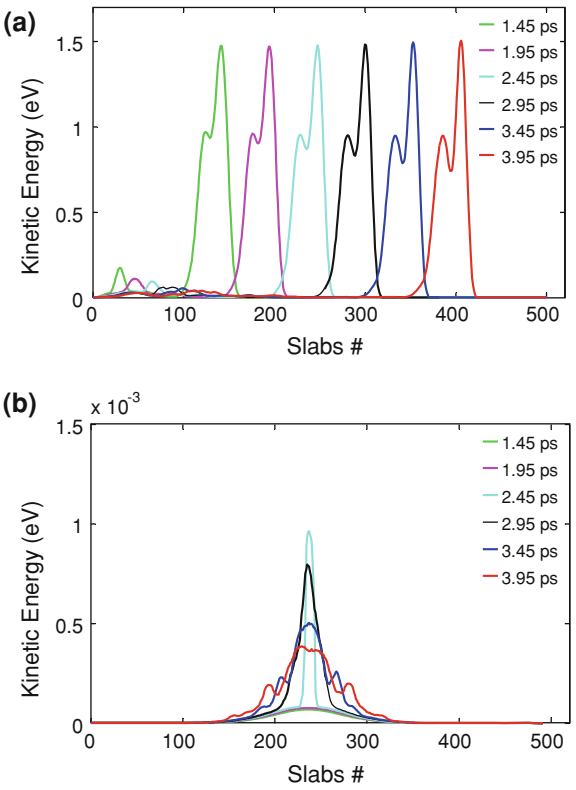

Fig. 14 **a** Location and shape of the heat pulse at different time instants along the first CNT for (7, 0) chirality. The pulse generation starts at t = 0.0 ps. **b** Location and shape of the heat pulse at different time instants in the second CNT, also of the same chirality

nanotube (SWNT) to another SWNT positioned in a crossed configuration and subjected to an intense heat pulse using Molecular Dynamics (MD) techniques [59]. A schematic of two CNTs in a crossed configuration is shown in Fig. 12. Here, the CNTs are placed perpendicular to each other with a gap equal to a van der Waals distance of 3.4 Å. These CNTs are not covalently bonded at the interface.

Selection of appropriate interatomic energies and forces is important for the reliability of classical MD simulations. We use the reactive empirical bond order (REBO) potential for C–C bond interaction and a truncated 12-6 type Lennard-Jones potential for non-bonded van der Waals interactions between CNTs. The REBO potential has been extensively applied to perform MD simulations in CNTs and CNTs in hydrocarbon composites/suspensions [33]. The analytical form of this potential is based on the intramolecular potential energy originally derived by Abell [60]. The REBO potential is given by:

$$U_{\text{REBO}} = \sum_{i} \sum_{i<j} [V_r(r_{ij}) - D_{ij} V_a(r_{ij})]. \tag{8}$$

where r_{ij} denotes the distance between atoms i and j, V_r corresponds to interatomic core–core repulsive interactions, and V_a describes the attractive interactions due to the valence electrons. Here, D_{ij} corresponds to a many-body empirical bond-order

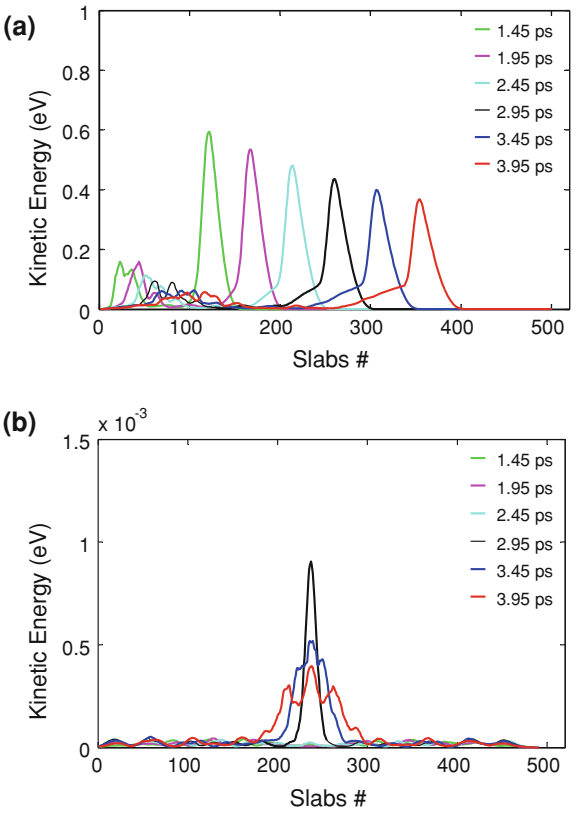

Fig. 15 **a** Location and shape of the heat pulse at different time instants along the first CNT for (8, 0) chirality. The pulse generation starts at t = 0.0 ps. **b** Location and shape of the heat pulse at different time instants in the second CNT, also of the same chirality

term. The 12-6 type LJ potential for non-bonded van der Waals interaction between individual carbon atoms is given as [38]:

$$U_{LJ} = 4\varepsilon\left[\left(\frac{\sigma}{r}\right)^{12} - \left(\frac{\sigma}{r}\right)^{6}\right]. \tag{9}$$

Several different values of the energy and distance parameters in the L-J potential are considered for the interaction of C–C atoms in the CNT. The present study employs the parameterization used by Lukes et al., with $\varepsilon = 4.41$ meV and $\sigma = 0.228$ nm. The details of the MD code used for the present analysis may be found in Ref. [60].

5.1 Heat Pulse Analysis Using Molecular Dynamics

MD simulations are used to examine transient heat pulse propagation in zig-zag tubes positioned in a crossed configuration for chiralities varying from (5, 0) to (10, 0). We generate the heat pulse at one end of the tube using the methodology

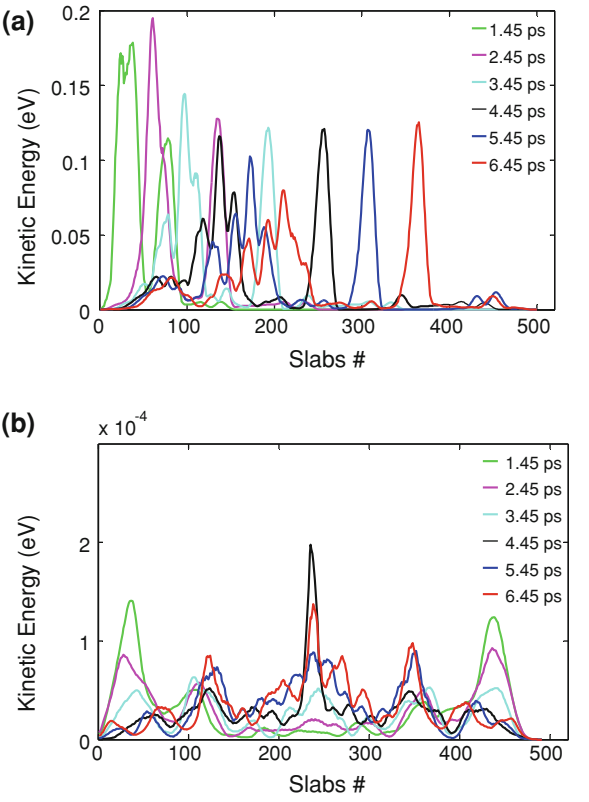

Fig. 16 **a** Location and shape of the heat pulse at different time instants along the first CNT for (10, 0) chirality. The pulse generation starts at t = 0.0 ps. **b** Location and shape of the heat pulse at different time instants in the second CNT, also of the same chirality

Table 2 Pulse speed in the first tube and the maximum total energy rise in the second tube for different chiralities

CNT-Chirality	Pulse speed (km/s)	Increase in total energy of second tube until t = 5.5 ps (eV)
(5, 0)	22.0	0.129
(6, 0)	23.2	0.203
(7, 0)	22.6	0.046
(8, 0)	19.0	0.074
(10, 0)	12.5	0.037

proposed by Osman and Srivastava [61] for studying energy transport through a single CNT at low temperatures. In order to study heat pulse propagation in CNTs and to compare the results for different chiralities, each CNT is divided into 500 slabs along its axis (each slab is a ring). The length of each CNT is 106 nm, but the number of atoms in a slab depend on the chirality or diameter of the CNT, i.e., a single slab in a (5, 0), (6, 0), (7, 0), (8, 0) and (10, 0) CNT would have 10, 12, 14, 16, and 20 atoms respectively. One end of the first CNT, where the heat pulse is generated, is treated as a free boundary, while the other end is kept rigid

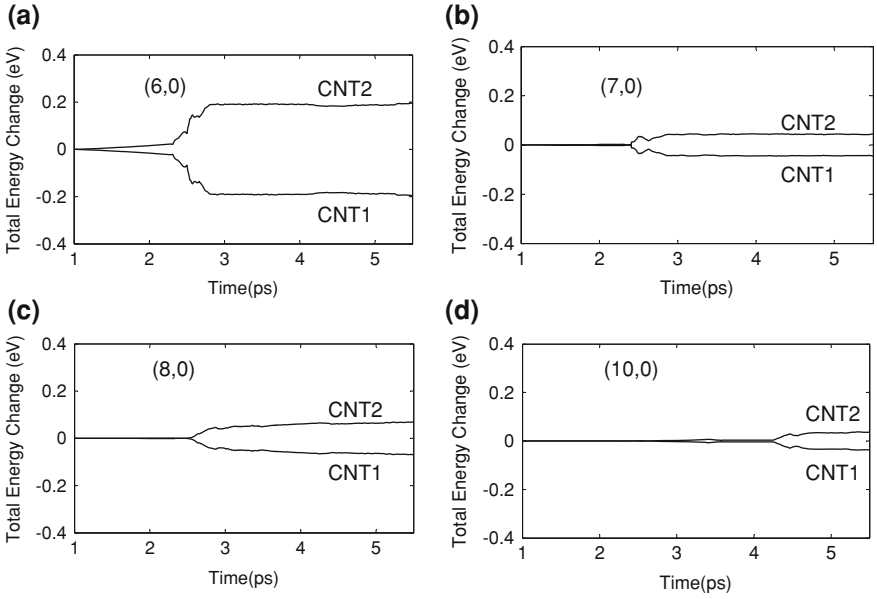

Fig. 17 Change in total energy of CNTs as a function of time with reference total energy corresponding to t = 1 ps. At t = 1 ps, the pulse generated in CNT-1 starts propagating towards the contact region of the two CNTs. Here, CNT-1 corresponds to the CNT in which the pulse is generated; CNT-2 is located in a crossed-configuration with respect to CNT-1. The chirality of the CNTs is **a** (6, 0) **b** (7, 0) **c** (8, 0) and **d** (10, 0)

(see Fig. 12); both ends of the second CNT are held rigid. The boundary region of the first CNT (i.e., the CNT in which the pulse is generated) extends over 10 slabs. Before the generation of the heat pulse, both CNTs are quenched to a very low temperature of 0.01 K for 50,000 time steps (25 ps) to achieve thermal equilibrium at 0.01 K. Then, a strong heat pulse of one picosecond duration and a peak temperature of 800 K is generated at one end of the first CNT. The heat pulse is applied to 10 slabs near the left boundary using a Berendsen thermostat [62]. The heat pulse consists of a 0.05 ps rise time, a 0.9 ps duration with a constant temperature of 800 K, and a 0.05 ps fall time. During the 0.05 ps fall time, the temperature of the boundary slabs is decreased to reach a final temperature of 0.01 K and then held constant at that temperature for the rest of the simulation. This is done to prevent the exchange of large amounts of energy from the boundary slabs to the region of interest after the generated pulse has started propagating towards the right boundary of the first CNT.

Our analysis is focused on the time window from the point of generation of the pulse to the time before heat pulse reaches the right boundary to avoid the effects of boundary reflection. The temperature of each slab is spatially averaged over ten slabs centered at the slab of interest. In our simulations, the temperature is

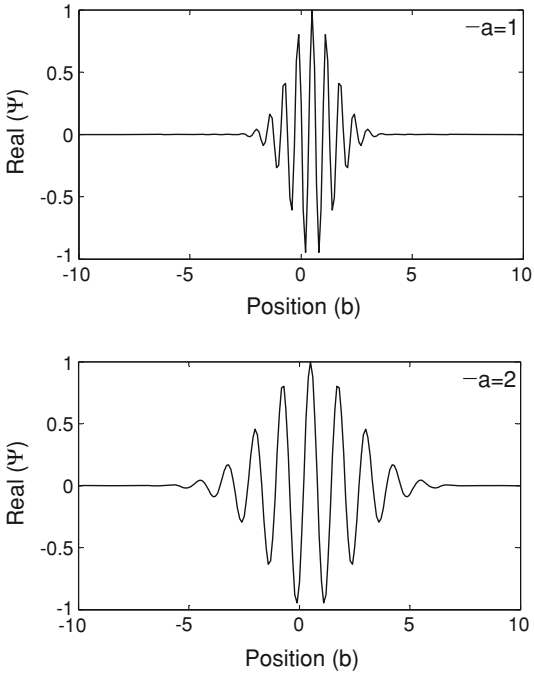

Fig. 18 An example of a Morlet wavelet with different values of the scale a [65]

time-averaged over sets of 200 time steps ($\sim$100 fs) to reduce the effect of statistical fluctuations and is recorded during the entire simulation time. The speed of the pulse is determined from the spatial distance traversed by the particular pulse during a given time interval.

We first study the interaction between two CNTs in a crossed configuration when a heat pulse is passed through first CNT using the methodology described in the above sections. Our interest is in analyzing the energy transfer to the second tube when the heat pulse passes through the contact zone, and also to study the waves generated in the second tube due to this energy transfer. The distance between the CNTs remains in the range of 3–3.7 Å during the entire simulation for CNTs of chirality (5, 0), (6, 0) and (7, 0). For CNTs of chirality (8, 0), this distance remains in the range of 4-4.5 Å, while for CNTs of chirality (10, 0), it remains in the range of 5–5.5 Å.

The location and shape of the heat pulses at different time instants along the first and second CNTs for the case of (5, 0) chirality are shown in Fig. 13a, b respectively. The amplitude of the heat pulses is presented in terms of the average kinetic energy of the atoms in ten slabs at any location. Here, t = 0 ps corresponds to the time when heat pulse generation has started at the left end of the first CNT. The attenuation in peak kinetic energy ($\sim$1.2 eV) of the heat pulse is negligible and it is seen to propagate like a ballistic pulse along the first tube. This pulse moves with a speed of 22 km/s along the nanotube, which is very close to the speed of sound (20.3 km/s) associated with longitudinal acoustic (LA) phonon

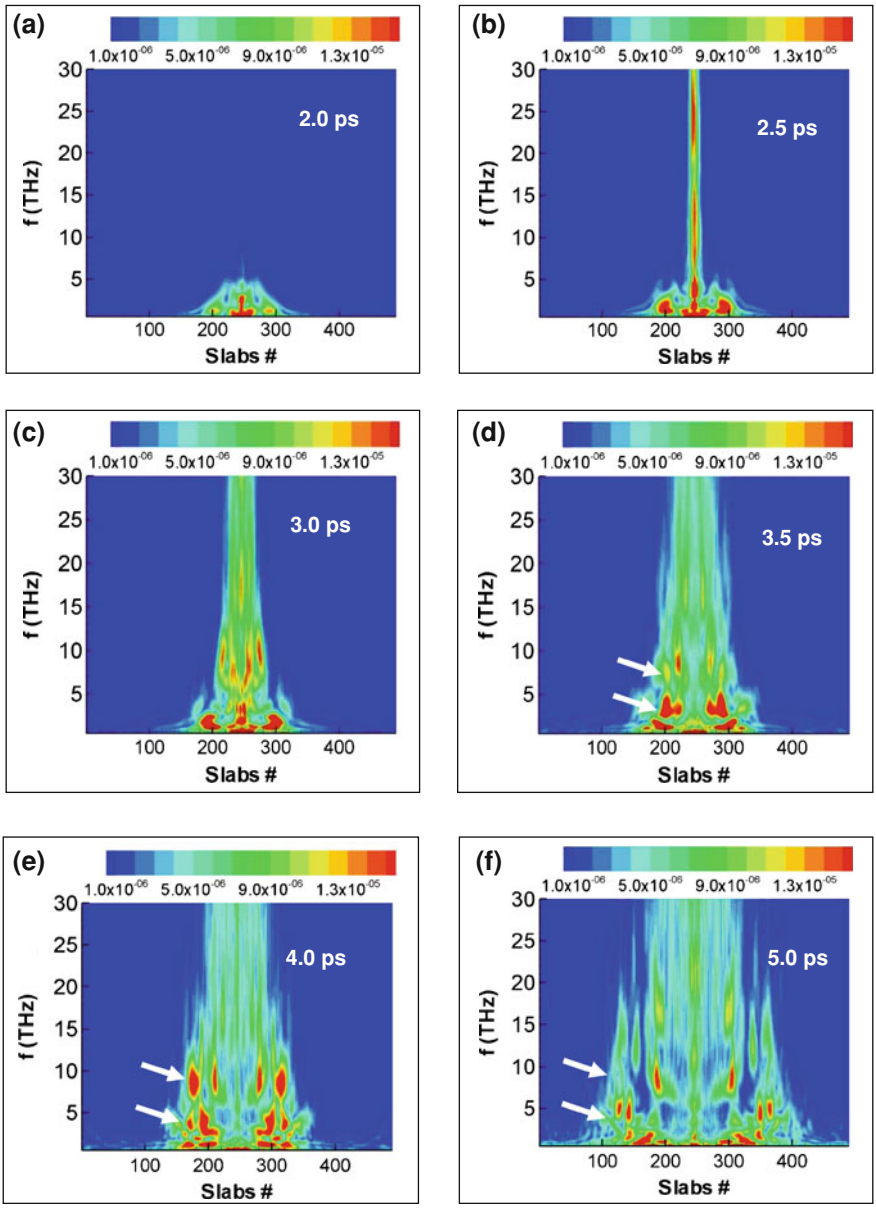

Fig. 19 Frequency spectrum along the second nanotube for (5, 0) chirality at different time instants. **a** 2.0 ps. **b** 2.5 ps. **c** 3.0 ps. **d** 3.5 ps. **e** 4.0 ps. **f** 5.0 ps. *White arrows* shows frequencies corresponding to 5 and 10 THz

waves in zig-zag nanotubes [62]. Two CNTs located in a crossed configuration make contact at their mid-point, which is at 53 nm from their free ends. When the heat pulse in the first tube approaches this contact zone, the kinetic energy in the

other tube increases at the location of the contact, Fig. 13b. The kinetic energy reaches its maximum at t = 2.6 ps which is approximately the time taken by the heat pulse in the first tube to cross the contact zone. The peak kinetic energy in the second tube is 1.5 meV, which is very low in comparison to peak kinetic energy of 1.2 eV of the heat pulse in the first tube. This indicates that coupling is very weak between two CNTs for these fast moving pulses, since little time is spent by the pulse in the contact zone. The energy given to the second tube at the point of contact spreads along the second tube. This is indicated by the decreasing kinetic energy at the center of the second tube and the symmetrically excited heat pulses on both sides of the contact in Fig. 13b. The speed of propagation of the excited heat pulse in the second tube is very low and it is difficult to relate these pulses with any specific phonon mode by observing their transient propagation profiles.

We perform a similar heat pulse analysis for nanotubes of chirality (6, 0), (7, 0), (8, 0) and (10, 0); the shape and location of the heat pulse along the nanotube for different time instants for the (7, 0), (8, 0) and (10, 0) chiralities are shown in Figs. 14, 15 and 16. It is observed that the behavior of heat pulses in the nanotubes is very dependent on the chirality or the diameter of the tube. The speed of heat pulse propagation in the first tube and the increase in kinetic energy in the second tube until t = 5.5 ps are listed in Table 2. Heat pulse propagation in the first tube for (6, 0) and (7, 0) chiralities is similar to that for the (5, 0) nanotube, i.e., the heat pulse propagates like a ballistic wave with a speed in the range of 22–23 km/s. However, the pulses excited in the second tube are significantly different for different chirality tubes. No conclusions can be drawn merely by looking at the kinetic energy rise in the second tube (see Table 2). However, it can be observed that heat spreading along the second tube is faster in the (5, 0) tube in comparison to the (6, 0) and (7, 0) tubes (see Figs. 13, 14). It is also observed that the kinetic energy at the centre of the second tube drops relatively fast in the (6, 0) tube in comparison to the (7, 0) tube.

Heat pulse propagation is completely different for (8, 0) and higher chirality tubes. For the (8, 0) tube, the heat pulse decays while propagating along the first tube and also broadens with time, a behavior which is completely different from that observed in low chirality tubes. At time $t = 1.45$ ps, the peak kinetic energy of the pulse is 0.68 eV, and decays to 0.42 eV at t = 3.95 ps, Fig. 15a. The pulse speed in the (8, 0) tube is 19 km/s, which is lower than the pulse speed observed in lower chirality tubes (see Table 2). Oman and Srivastava [61] observed a similar decay in the pulse speed in zig-zag tubes for twisting phonon modes (TW) with speed ranging in 16–18 km/s. The pulse excited in the second tube also shows different characteristics, and exhibits a pulse shape which is more flat at the center, Fig. 15b. All these behaviors imply a dissipative nature to the pulse propagation in (8, 0) tubes.

Heat pulse propagation in a (10, 0) tube is much different from the low chirality tubes previously discussed. The high kinetic energy in the heat pulse in the first tube cannot be sustained and the pulse decays very quickly. At t = 2.45 ps, a clearly identifiable wave shape evolves from the dissipating heat pulse; the speed of this wave is 12.5 km/s, which corresponds to the second sound wave speed

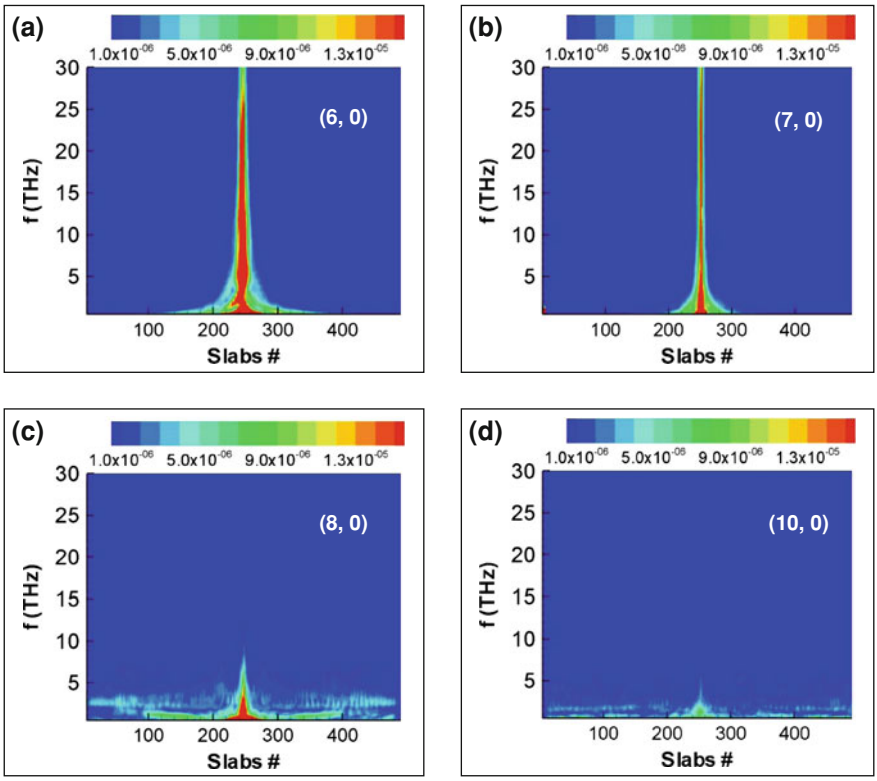

Fig. 20 Frequency spectrum along the second CNT at 2.5 ps for chirality **a** (6, 0). **b** (7, 0). **c** (8, 0). **d** (10, 0)

observed in zig-zag tubes in Ref. [61]. In transient experiments, at low temperatures and in structures with high purity, normal phonon scattering processes can play an important role. They may couple various phonon modes and make possible the collective oscillation in phonon density which is second sound. Second sound is observed under very restrictive conditions [61]. One of these conditions is that the momentum conserving normal phonon scattering processes should be dominant compared to the momentum randomizing Umklapp phonon scattering processes [61]. For CNTs, thermal conductivity increases even up to room temperature and it can reasonably be believed that N-process phonon interactions dominate over a wide range of temperature. These arguments and the observed speed of the wave (12.5 km/s $= 1/3^{0.5}$ times the LA phonon speed) suggest that the observed wave pulse in the (10, 0) nanotube corresponds to that of second sound.

The peak kinetic energy of the second sound wave mode observed in (10, 0) tube is 0.12 eV, which is much smaller than the peak kinetic energy of leading heat pulses observed in the low-chiral tube configurations. In addition, due to the

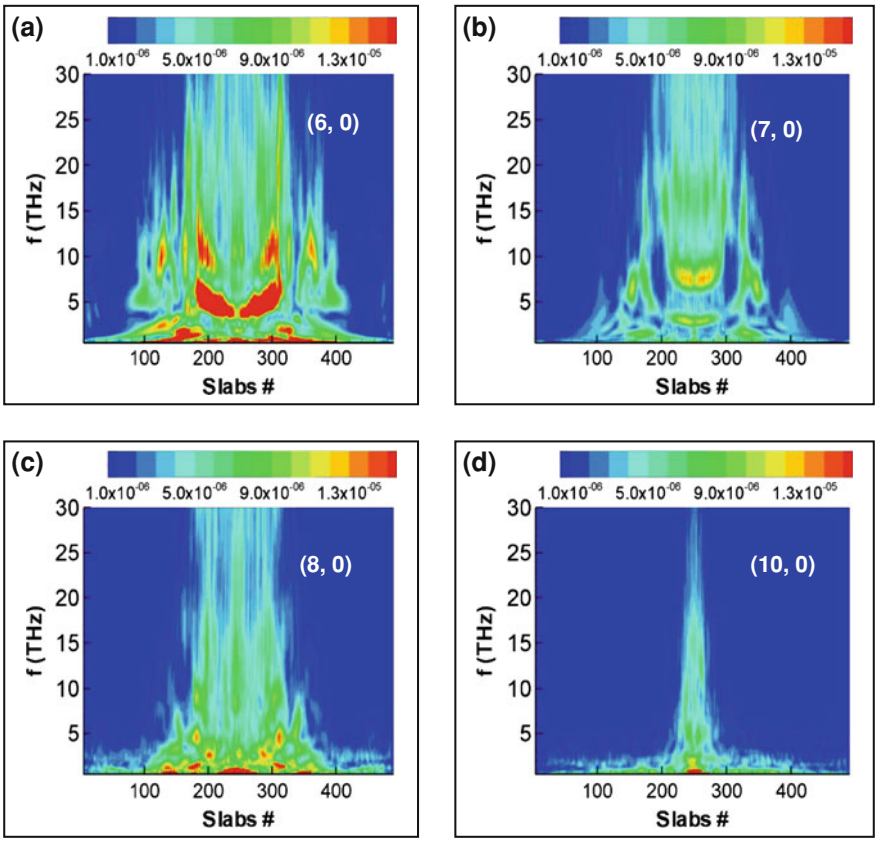

Fig. 21 Frequency spectrum along the second CNT at 5.0 ps for chirality **a** (6, 0). **b** (7, 0). **c** (8, 0). **d** (10, 0)

low speed, this pulse in the first CNT does not cross the contact zone in 4 ps (this is the time range for which we analyzed low-chirality tubes), so we have extended the analysis up to 6.5 ps. The energy gained by the second CNT due to the interaction with the heat pulse of the first CNT is very low. This is the reason for a very small rise in the peak kinetic energy ($\sim$0.2 meV) of the excited pulse in the second tube, Fig. 16b. The kinetic energy of the carbon atoms located at the contact area of the second CNT (black and red curves in Fig. 16b) is of the same order as that of the kinetic energy of atoms at other locations (see peaks at the CNT ends in Fig. 16b). From our analysis, we have observed that in low-chirality CNTs we can generate a purely ballistic pulse, while in high-chirality CNTs, a diffusive tail is also present and the pulse cannot sustain its peak temperature during propagation. We see a difference between our results and Osman and Srivastava's results only for low-chirality CNTs.

The change in total energy of the CNTs as a function of time is plotted in Fig. 17 for (6, 0), (7, 0), (8, 0) and (10, 0) tubes. The change in total energy is computed with respect to the reference total energy at $t = 1$ ps; this is time at which the pulse generated in the first CNT starts propagating towards the contact region of the two CNTs. The magnitude of total energy exchange or increase in total energy of the second tube up to time instant 5.5 ps is presented in Table 2 for tubes of different chiralities. The energy exchange between the tubes is largest for the (6, 0) tube and decreases for high-chirality tubes, Fig. 17. However a definitive statement regarding this cannot be made based on the present analysis as the energy exchange for the (5, 0) tube is lower than that for the (6, 0) tube by 0.07 eV and the energy exchange for the (7, 0) tube is lower than that for the (8, 0) tube by 0.028 eV. The above analysis shows that lower-chirality tubes have better coupling in comparison to high- chirality tubes as far as these heat pulses are concerned.

Phonon modes with high speed are very inefficient in transferring energy to the second tube as they spend very little time in the contact zone. Thus, it is likely that for realistic applications, slow-moving phonon modes (for example, optical modes) in the first CNT would be better-coupled to the second CNT. Shiomi and Maruyama [63] observe from their modal analyses on a single tube using wavelet transformations that the major contribution to non-Fourier heat conduction comes from optical phonon modes with sufficient group velocity and with wave vectors in the intermediate regime for short nanotubes. Dispersion curves for CNTs of chirality (5, 5) show that even at low frequencies, longitudinal and transverse optical modes may be present, with velocities comparable with the acoustic modes. In a nanotube network, the link between two nanotubes is of the order of just few nanometers. Therefore, in nanotube networks where the contact between the tubes governs the transport, optical phonon modes may be a dominant heat transfer pathway for communication between tubes.

5.2 Wavelet Analysis of Heat Pulse

Wavelet analysis of the heat pulse excited in the CNT configuration described in the previous section (see Fig. 12) is performed for different chiralities of the tubes. The wavelet transform (WT) is an analysis tool well-suited for the study of processes which occur over finite spatial and temporal domains. The wavelet transform is a generalized form of the Fourier transform (FT). A WT uses generalized local functions known as wavelets which can be stretched and translated with a desired resolution in both the frequency and time domains [64, 65].

Wavelets decompose a time series in the time–frequency space and are useful for identifying the evolution of dominant frequency modes with time. A time signal $s(t)$ is decomposed using wavelet methods in terms of the elementary function $\psi_{b,a}$ derived from a mother wavelet ψ by dilation and translation [64]:

$$\psi_{b,\,a}(t) = \frac{1}{a^{0.5}}\psi\left(\frac{t-b}{a}\right). \tag{10}$$

Here, a and b are parameters which control dilation and translation respectively. The a parameter is also known as the *scale* in wavelet analysis. $\psi_{b,a}$ is known as the *daughter* wavelet as it is derived from the mother wavelet ψ using translation and dilation. The normalization factor $a^{0.5}$ ensures that the mother and daughter wavelets have the same energy. The wavelet transform (WT) of a signal $s(t)$ is given as the convolution integral of $s(t)$ with ψ^*, where ψ^* is the complex conjugate of the wavelet function ψ:

$$W(b,\ a) = \frac{1}{a^{0.5}}\int \psi * \left(\frac{t-b}{a}\right)s(t)dt. \tag{11}$$

In general, wavelet functions are complex functions, so the *wt* are also complex, and have a real part, an imaginary part and a phase angle. The power spectrum of a WT is defined as $|W|^2$. We use the Morlet wavelet for heat pulse analysis; this wavelet has the form of a plane wave with a Gaussian envelope [64]. The Morlet wavelet is given by:

$$\psi = \mathrm{e}^{iwt} \times \mathrm{e}^{-0.5|t|^2}. \tag{12}$$

The form of this wavelet is shown in Fig. 18 after translating by different values of b and dilating by different values of the scale parameter a.

The power spectrum of the velocity magnitude of each atom in the nanotube is computed using the method described above. By summing the power spectrum over all the atoms of one ring, a one-dimensional projection of the temporal spectra along the nanotube axis is obtained. In this way, temporally evolving spectra of the velocity magnitude for the entire spatio-temporal field are obtained.

Wavelet analysis of the energy modes excited in the second CNT due to the interaction with first CNT is performed for chirality of tubes varying from (5, 0) to (10, 0). The power spectrum of the velocity magnitude of each atom in the nanotube is computed using the method described above. Temporally evolving spectra of the velocity magnitude for the entire spatio-temporal field are computed. Results are presented as temporal sequences of the spectral contours in the frequency-space domain in Fig. 19 for a (5, 0) CNT. Six temporal sequences are used, which correspond to t = 2.0, 2.5, 3.0, 3.5, 4.0 and 5.0 ps. In these plots, the vertical axis represents the frequency in THz and the horizontal axis represents the spatial location along the nanotube axis in terms of the slab (i.e. ring) numbers.

The evolution and propagation of spectral modes along the tube axis for a (5, 0) CNT at different time instants may be observed in Fig. 19. At t = 2 ps, the heat pulse in the first tube is approaching the contact zone, Fig. 19a; thus some low frequency phonon modes are excited in the second nanotube at the location of the contact. At t = 2.5 ps (Fig. 19b), the heat pulse in the first tube crosses the contact zone; this is the time at which the peak temperature of the thermal pulse excited in the second CNT is observed (Fig. 13b). Phonon modes of frequencies up

to 30–35 THz are excited in the second nanotube by this time, but most of the dominant frequencies are less than 10 THz, Fig. 19b. Once the heat pulse in the first tube moves away from the contact zone, the energy given to the second tube spreads to both sides of the tube symmetrically. Different phonon modes are excited along the second tube, and can be observed from the contour plots in Fig. 19c–f. The contour plot at t = 3.0 ps shows two distinctly visible modes, one centered around 5 THz and another centered around 10 THz. The speed of these modes may be computed from the movement of the high power spectrum color patches corresponding to these frequencies along the nanotube axis in the contour plot. The computed speed is 12.0 km/s, which is close to the speed of the second sound waves observed in these zig-zag tubes [61]. These color patches are shown in Fig. 19d–f by white arrows. Most of the other dominant modes correspond to frequencies even lower than 5 THz, which is in correspondence with the small amount of heat transferred to the second tube from the heat pulse in the first tube.

Contours of the power spectrum for (6, 0), (7, 0), (8, 0) and (10, 0) CNTs at t =2.5 ps and 5.0 ps are shown in Figs. 20, 21 respectively. As in the case of the (5, 0) CNT, two dominant phonon modes corresponding to 5 and 21 THz are seen to propagate along the second tube for (6, 0) and (7, 0) CNTs, Fig. 21a, b. These contour plots also clearly show that the rate of heat spreading along the CNT axis slows down with increasing diameter. This is also observed in the heat pulse analysis in the previous section by examining the location and shape of the heat pulses generated in the second tube. A similar comparison cannot be made for (8, 0) and (10, 0) CNTs because the pulse generated in the first CNT is not sustained at its initial peak temperature, and very little heat is transferred to the second CNT for these cases. The spectral modes for the (10, 0) CNT are completely different from other CNTs; most of the high energy modes present in low-chirality CNTs are not excited, Fig. 21d. This is due to the evolution of second sound waves in the first CNT; the peak temperature is an order of magnitude lower than that in low chirality CNTs, Figs. 16b, 21d.

6 Conclusions

In summary, a computational model for thermal and electrical transport in nanotube composites has been developed and applied to the determination of lateral electrical and thermal conductivity of finite thin films. The model has been verified against analytical solutions, and validated against experimental data for tube densities above and below the percolation threshold, for nanotube networks in the absence of a substrate, as well as for nanotube-plastic and nanotube-organic composites. Excellent matches with experimental data have established the general validity of the model and provided much deeper insights into electrical and thermal transport in these non-classical materials. This understanding not only advances the relevance of percolation theory to broader class of problems, but

will also help design and optimization of these materials for future technological applications.

Nevertheless, a number of important issues remain to be addressed. The model employs thermal contact parameters Bi_c, Bi_s, and electrical contact parameters c_{ij} and d_{is}, which are at present unknown. These must be determined either from careful experiments or from atomistic simulations of tube–tube and tube-substrate contact. Furthermore, while the thermal conductivities of individual freestanding nanotubes and nanowires has been measured and modeled, the modification of these values for tubes and wires encased in plastic or organic substrates is not well understood. Ultimately, our interest is not only in the simulation of conductivity but also in the coupled electro-thermal analysis and design of flexible large-area electronics. We have focused on the analysis of the lateral thermal conductivity of the composite, but normal thermal conductivity of the composite is also of great importance from the perspective of heat removal from the device and merits a detailed investigation.

In this chapter, we also analyzed the thermal transport between two CNTs for different chiralities using the MD technique and the wavelet method. A thermal pulse was generated at one end of the first CNT to study the response of the second tube when this pulse passed the contact region of the two CNTs. The results of our heat pulse studies demonstrate that phonon modes with high speed are very inefficient in transferring energy to the second tube as they spend very little time in the contact zone. Most likely, slow-moving phonon modes in the first CNT would be better coupled to the second CNT and would dominate thermal boundary conductance between these CNTs. To better understand the coupling of modes between tubes, a wave packet corresponding to specific phone modes should be passed through a CNT and its interaction with other CNTs should be studied. Understanding the coupling between CNTs of different chirality and contact area could also be of great interest for engineering the properties of CNT-network based composites. Most of the present work is in the low temperature regime. It is also important to investigate transport mechanisms in the high temperature regime using either appropriate numerical modeling or experimental techniques.

Acknowledgments Support of J. Murthy and S. Kumar under NSF grants CTS-0312420, CTS-0219098, EE-0228390, the Purdue Research Foundation and Purdue's Network for Computational Nanotechnology (NCN) is gratefully acknowledged. M. A. Alam acknowledges support from the Focus Center Research Program (FCRP-MSD).

References

1. Hur, S.H., Kocabas, C., Gaur, A., et al.: Printed thin-film transistors and complementary logic gates that use polymer-coated single-walled carbon nanotube networks. J. Appl. Phys. **98**(11), 114302 (2005)
2. Reuss, R.H., Chalamala, B.R., Moussessian, A., et al.: Macroelectronics: perspectives on technology and applications. Proc. IEEE **93**(7), 1239–1256 (2005)

3. Collins, P.C., Arnold, M.S., Avouris, P.: Engineering carbon nanotubes and nanotube circuits using electrical breakdown. Science **292**(5517), 706–709 (2001)
4. Kagan, C.R., Andry, P.: Thin film transistors. Marcel Dekker, New York (2003)
5. Novak, J.P., Snow, E.S., Houser, E.J., et al.: Nerve agent detection using networks of single-walled carbon nanotubes. Appl. Phys. Lett. **83**(19), 4026–4028 (2003)
6. Alam M.A. Nair P.R.: Geometry of diffusion and the performance limits of nanobiosensors. Nanotechnology 501 lecture series. https://www.nanohub.org/resources/2048/(2006)
7. Madelung, O.: Technology and applications of amorphous silicon. Springer, Berlin (2000)
8. Zhou, Y.X., Gaur, A., Hur, S.H., et al.: P-channel, n-channel thin film transistors and p-n diodes based on single wall carbon nanotube networks. Nano Lett. **4**(10), 2031–2035 (2004)
9. Snow, E.S., Campbell, P.M., Ancona, M.G., et al.: High-mobility carbon-nanotube thin-film transistors on a polymeric substrate. Appl. Phys. Lett. **86**(3), 066802 (2005)
10. Snow, E.S., Novak, J.P., Lay, M.D., et al.: Carbon nanotube networks: nanomaterial for macroelectronic applications. J. Vac. Sci. Technol. B **22**(4), 1990–1994 (2004)
11. Snow, E.S., Novak, J.P., Campbell, P.M., et al.: Random networks of carbon nanotubes as an electronic material. Appl. Phys. Lett. **82**(13), 2145–2147 (2003)
12. Cao, Q., Rogers, J.A.: Ultrathin films of single-walled carbon nanotubes for electronics and sensors: A review of fundamental and applied aspects. Adv. Material **21**(1), 29–53 (2009)
13. Kumar, S., Murthy, J.Y., Alam, M.A.: Percolating conduction in finite nanotube networks. Phys. Rev. Lett. **95**(6), 066802 (2005)
14. Hur, S.H., Khang, D.Y., Kocabas, C., et al.: Nanotransfer printing by use of noncovalent surface forces: applications to thin-film transistors that use single-walled carbon nanotube networks and semiconducting polymers. Applied Physics Letters **85**(23), 5730–5732 (2004)
15. Kocabas, C., Hur, S.H., Gaur, A., et al.: Guided growth of large-scale, horizontally aligned arrays of single-walled carbon nanotubes and their use in thin-film transistors. Small **1**(11), 1110–1116 (2005)
16. Kocabas, C., Shim, M., Rogers, J.A.: Spatially selective guided growth of high-coverage arrays and random networks of single-walled carbon nanotubes and their integration into electronic devices. J. Am. Chem. Soc. **128**(14), 4540–4541 (2006)
17. Milton, G.W.: The theory of composites. Cambridge University Press, New York (2002)
18. Nan, C.W., Birringer, R., Clarke, D.R., et al.: Effective thermal conductivity of particulate composites with interfacial thermal resistance. J. Appl. Phys. **81**(10), 6692–6699 (1997)
19. Jeong, C., Nair, P., Khan, M., Lundstrom M., Alam, M.A.: Prospects for Nanowire-doped polycrystalline graphene films for ultratransparent, highly conductive electrodes. Nano Lett. 11 (11), 5020–5025 (2011)
20. Cao, Q., Kim, H. K., Pimparkar, N., et al.: Medium-scale carbon nanotube thin-film integrated circuits on flexible plastic substrates. Nature 454, 495–500, (2008)
21. Kumar, S., Alam, M.A., Murthy, J.Y.: Computational model for transport in nanotube-based composites with applications to flexible electronics. ASME J. Heat Transf. **129**(4), 500–508 (2007)
22. Kumar, S., Pimparkar, N., Murthy, J.Y., et al.: Theory of transfer characteristics of nanotube network transistors. Appl. Phys. Lett. **88**, 123505 (2006)
23. Zhang, G., Qi, P., Wang, X., et al.: Selective etching of metallic carbon nanotubes by gas-phase reaction. Science **314**, 974–977 (2006)
24. Arnold, M.S., Green, A.A., Hulvat, J.F., et al.: Sorting carbon nanotubes by electronic structure using density differentiation. Nat. Nanotechnol. **1**, 60–65 (2006)
25. Huang, H., Liu, C., Wu, Y., et al.: Aligned carbon nanotube composite films for thermal management. Adv. Material **17**, 1652–1656 (2005)
26. Nan, C.W., Liu, G., Lin, Y.H., et al.: Interface effect on thermal conductivity of carbon nanotube composites. Appl. Phys. Lett. **85**(16), 3549–3551 (2004)
27. Biercuk, M.J., Llaguno, M.C., Radosavljevic, M., et al.: Carbon nanotube composites for thermal management. Appl. Phys. Lett. **80**(15), 2767–2769 (2002)

28. Xu, X.J., Thwe, M.M., Shearwood, C., et al.: Mechanical properties and interfacial characteristics of carbon-nanotube-reinforced epoxy thin films. Appl. Phys. Lett. **81**(15), 2833–2835 (2002)
29. Reibold, M., Paufler, P., Levin, A.A., et al.: Carbon nanotubes in an ancient Damascus sabre. Nature **444**(16), 286 (2006)
30. Hu, L., Hecht, D.S., Gruner, G.: Percolation in transparent and conducting carbon nanotube networks. Nano Lett. **4**(12), 2513–2517 (2004)
31. Keblinski, P., Cleri, F.: Contact resistance in percolating networks. Phy. Rev. B **69**(18), 184201 (2004)
32. Hu, T., Grosberg, A.Y., Shklovskii, B.I.: Conductivity of a suspension of nanowires in a weakly conducting medium. Phys. Rev. B **73**(15), 155434 (2006)
33. Lukes, J.R., Zhong, H.L.: Thermal conductivity of individual single-wall carbon nanotubes. J. Heat Transf.-Trans. ASME **129**(6), 705–716 (2007)
34. Maruyama, S., Igarashi, Y., Shibuta, Y.: Molecular dynamics simulations of heat transfer issues in carbon nanotubes. In: The 1st international symposium on micro & nano technology. Honolulu, Hawaii, USA 2004
35. Small, J.P., Shi, L., Kim, P.: Mesoscopic thermal and thermoelectric measurements of individual carbon nanotubes. Solid State Commun. **127**(2), 181–186 (2003)
36. Maune, H., Chiu, H.Y., Bockrath, M.: Thermal resistance of the nanoscale constrictions between carbon nanotubes and solid substrates. Appl. Phy. Lett. **89**(1), 013109 (2006)
37. Carlborg. C.F., Shiomi. J., Maruyama. S.: Thermal boundary resistance between single-walled carbon nanotubes and surrounding matrices. Phys. Rev. B **78** (20), 205406 (2008)
38. Zhong, H.L., Lukes, J.R.: Interfacial thermal resistance between carbon nanotubes: molecular dynamics simulations and analytical thermal modeling. Phys. Rev. B **74**(12), 125403 (2006)
39. Greaney, P.A., Grossman, J.C.: Nanomechanical energy transfer and resonance effects in single-walled carbon nanotubes. Phys. Rev. Lett. **98**(12), 125503 (2007)
40. Prasher, R.S., Hu, X.J., Chalopin, Y., et al.: Turning carbon nanotubes from exceptional heat conductors into insulators. Phys. Rev. Lett. **102**, 105901 (2009)
41. Pimparkar, N., Kumar, S., Murthy, J.Y., et al.: Current–voltage characteristics of long-channel nanobundle thin-film transistors: A 'bottom-up' perspective. IEEE Electron Device Lett. **28**(2), 157–160 (2006)
42. Bo, X.Z., Lee, C.Y., Strano, M.S., et al.: Carbon nanotubes-semiconductor networks for organic electronics: The pickup stick transistor. Appl. Phy. Lett. **86**(18), 182102 (2005)
43. Kumar, S., Blanchet, G.B., Hybertsen, M.S., et al.: Performance of carbon nanotube-dispersed thin-film transistors. Appl. Phys. Lett. **89**(14), 143501 (2006)
44. Kundert, K,S.: Sparse user's guide, Department of Electrical Engineering and Computer Sciences, University of California, Berkeley, CA, USA (1988)
45. Pike, G.E., Seager, C.H.: Percolation and conductivity—computer study 0.1. Phys. Rev. B **10**(4), 1421–1434 (1974)
46. Alam, M.A.: Nanostructured electronic devices: Percolation and reliability. Intel-purdue summer school on electronics from bottom up. http://nanohub.org/resources/7168 (2009)
47. Foygel, M., Morris, R.D., Anez, D., et al.: Theoretical and computational studies of carbon nanotube composites and suspensions: electrical and thermal conductivity. Phys. Rev. B **71**(10), 104201 (2005)
48. Shenogina, N., Shenogin, S., Xue, L., et al.: On the lack of thermal percolation in carbon nanotube composites. Appl. Phys. Lett. **87**(13), 133106 (2005)
49. Frank, D.J., Lobb, C.J.: Highly efficient algorithm for percolative transport studies in 2 dimensions. Phys. Rev. B **37**(1), 302–307 (1988)
50. Lobb, C.J., Frank, D.J.: Percolative conduction and the Alexander-Orbach conjecture in 2 dimensions. Phys. Rev, B **30**(7), 4090–4092 (1984)
51. Pimparkar, N., Alam, M.A.: A "bottom-up" redefinition for mobility and the effect of poor tube–tube contact on the performance of CNT nanonet thin-film transistors. IEEE Electron Device Lett. **29**(9), 1037–1039 (2008)

52. Taur, Y., Ning, T.: Fundamentals of modern VLSI devices. Cambridge University Press, New York (1998)
53. Fuhrer, M.S., Nygard, J., Shih, L., et al.: Crossed nanotube junctions. Science **288**(5465), 494–497 (2000)
54. Seidel, R.V., Graham, A.P., Rajasekharan, B., et al.: Bias dependence and electrical breakdown of small diameter single-walled carbon nanotubes. J. Appl. Phys. **96**(11), 6694–6699 (2004)
55. Huxtable, S.T., Cahill, D.G., Shenogin, S., et al.: Interfacial heat flow in carbon nanotube suspensions. Nat. Material **2**(11), 731–734 (2003)
56. Kumar, S., Alam, M.A., Murthy, J.Y.: Effect of percolation on thermal transport in nanotube composites. Appl. Phys. Lett. **90**(10), 104105 (2007)
57. Bryning, M.B., Milkie, D.E., Islam, M.F., et al.: Thermal conductivity and interfacial resistance in single-wall carbon nanotube epoxy composites. Appl. Phys. Lett. **87**(16), 161909 (2005)
58. Hung, M.T., Choi, O., Ju, Y.S., et al.: Heat conduction in graphite-nanoplatelet-reinforced polymer nanocomposites. Appl. Phys. Lett. **89**(2), 023117 (2006)
59. Kumar, S., Murthy, J.Y.: Interfacial thermal transport between nanotubes. J. Appl. Phys. **106**(8), 084302 (2009)
60. Brenner, D.W., Shenderova, O.A., Harrison, J.A., et al.: A second-generation reactive empirical bond order (rebo) potential energy expression for hydrocarbons. J. Phys.-Condens. Matt. **14**(4), 783–802 (2002)
61. Osman, M.A., Srivastava, D.: Molecular dynamics simulation of heat pulse propagation in single-wall carbon nanotubes. Phys. Rev. B **72**(12), 125413 (2005)
62. Erhart, P., Albe, K.: The role of thermostats in modeling vapor phase condensation of silicon nanoparticles. Appl. Surf. Sci. **226**(1–3), 12–18 (2004)
63. Maruyama, S.J.: Non-Fourier heat conduction in a single-walled carbon nanotube: classical molecular dynamics simulations. Phys. Rev. B **73**(20), 205420 (2006)
64. Lau, K.M., Weng, H.: Climate signal detection using wavelet transform: How to make a time series sing. Bull. Am. Meteorol. Soc. **76**(12), 2391–2402 (1995)
65. Torrence, C., Compo, G.P.: A practical guide to wavelet analysis. Bull. Am. Meteorol. Soc. **79**(1), 61–78 (1998)
66. Liu, C.H., Huang, H., Wu, Y., et al.: Thermal conductivity improvement of silicone elastomer with carbon nanotube loading. Appl. Phys. Lett. **84**(21), 4248–4250 (2004)
67. Gong, Q.M., Li, Z., Bai, X.D., et al.: Thermal properties of aligned carbon nanotube/carbon nanocomposites. Materials Science and Engineering a-Structural Materials Properties Microstructure and Processing **384**(1–2), 209–214 (2004)
68. Choi, S.U.S., Zhang, Z.G., Yu, W., et al.: Anomalous thermal conductivity enhancement in nanotube suspensions. Appl. Phys. Lett. **79**(14), 2252–2254 (2001)
69. Wen, D.S., Ding, Y.L.: Effective thermal conductivity of aqueous suspensions of carbon nanotubes (carbon nanotubes nanofluids). J. Thermophy. Heat Transf. **18**(4), 481–485 (2004)

Elastic Properties of Co/Cu Nanocomposite Nanowires

J. C. Jiménez-Sáez, A. M. C. Pérez-Martín and J. J. Jiménez-Rodríguez

Abstract The mechanical deformation of Co/Cu composite nanowires was simulated by molecular dynamics in a state of uniaxial tensile and compressive stress. The Young's modulus and initial yield stress have been derived from the stress–strain curves at different conditions. For tensile strength, the effect of strain rate, volume/surface area ratio, temperature, and thickness ratio between Co and Cu sublayers was analyzed depending on the crystallographic orientations of the nanowires. At high values, the elastic modulus and yield stress depend on the strain rate; and some differences with the crystallographic orientation due to nonlinear effects appear. Both magnitudes diverge from the bulk values with decreasing the volume/surface area ratio, increasing in the case of ⟨110⟩ nanowires and decreasing for the other two directions. For ⟨100⟩ nanowires, grains undergo a crystallographic reorientation towards ⟨111⟩ and ⟨110⟩ directions. Besides, for these nanowires hexagonal close-packed atoms are preferably in the Co sublayer; and face-centered cubic atoms, in the Cu sublayer unlike nanowires in the other two directions. Plastic deformation takes place more easily in Cu sublayers. Nanowires show differences in the slip mechanism for ⟨110⟩ and ⟨100⟩ directions. In compression, the former system slips via both {111}⟨112⟩ and {111}⟨110⟩ dislocations; and the latter, only through {111}⟨112⟩ dislocations.

J. C. Jiménez-Sáez (✉)
Dpto. de Física y Química Aplicadas a la Técnica Aeronáutica, E.U.I.T. Aeronáutica, Universidad Politécnica de Madrid (UPM), 28040 Madrid, Spain
e-mail: jc.jimenez@upm.es

A. M. C. Pérez-Martín · J. J. Jiménez-Rodríguez
Dpto. de Física Aplicada III (Electricidad y Electrónica), Facultad de Ciencias Físicas, Universidad Complutense de Madrid (UCM), 28040 Madrid, Spain
e-mail: cperez@fis.ucm.es

J. J. Jiménez-Rodríguez
e-mail: josejjr@fis.ucm.es

Adv Struct Mater (2013) 4: 337–350
DOI: 10.1007/8611_2011_62

Published Online: 22 January 2012

1 Introduction

The fabrication of nanocomposite nanowires has recently received much attention because of the interesting magnetic, superconducting and magnetotransport properties and their application in the development of high-density magnetic recording media and novel magnetic sensors [1, 2]. These studies were triggered by the discovery of giant magnetoresistance (GMR) effects [3] in certain metallic multilayers in which the interlayer exchange coupling results in antiferromagnetic alignment of the adjacent magnetic layers [4]. Specifically, NiCo [5], Co/Cu, NiFe/Cu or CoNiCu/Cu [6, 7] nanowires show anisotropic magnetoresistance (AMR) or current perpendicular to the planes giant magnetoresistance (CPP-GMR). This type of nanowires can be grown at low cost by electrodeposition from aqueous solution into nanochannel templates [8].

While designing such nanoscale devices, it is necessary to know their structural and thermo-mechanical properties since the mechanical strength of nanowires plays an important role in maintaining the structural integrity of the devices. For feature sizes of several atomic layers, surface stress may induce a large intrinsic compressive stress in the interior of nanowires, and their structure becomes instable. Thus, under some conditions, the nanowires may transform from one orientation to another spontaneously [9] or, even initiate phase transformations [10]. Molecular dynamics (MD) simulations have been performed extensively and reported in published literature for composite nanowire property characterizations including phase transformation behavior at nanoscale, mechanisms of dislocation formation, plastic region and breaking under stress.

In this work, the stress–strain relations of Co/Cu multilayered nanowires under extension and compression and different conditions by means of MD simulations are obtained. The elastic modulus and initial yield stress are mainly analyzed. The knowledge of these mechanical properties will be helpful to the design, manufacture and manipulation of nanodevices. Effects of composition, size, strain rate and temperature on the extension properties are discussed in detail as a function of the crystallographic orientation. Influence of internal structure and interface on the mechanical behavior of nanostructures is discussed. The nanostructural deformation for tensile and compressive stresses is presented together with an identification of dislocations.

2 Computational Method

The interaction among atoms is essentially determined by the atomic potential. In our case, the used potential for the Co–Cu system was elaborated by Levanov et al. [11] in the second-moment tight-binding approximation (TB-SMA) [12]. This potential fits experimentally lattice constants, cohesive energies and elastic

constants for Cu (face-centered cubic, fcc) and Co (hexagonal close-packed, hcp) and takes into account ab initio properties of small Co clusters on Cu surfaces. In this model, the cohesive energy E_i of an atom i is:

$$\begin{aligned} E_i &= \sum_{j(\neq i)} \frac{1}{2} V^{\alpha\beta}(r_{ij}) + F(\rho_i) = \sum_{j(\neq i)} \frac{1}{2} V^{\alpha\beta}(r_{ij}) - (\rho_i)^{1/2} \\ \rho_i &= \sum_{j(\neq i)} \Phi^{\alpha\beta}(r_{ij}) \end{aligned} \tag{1}$$

where α and β refer to the chemical nature of the atoms i and j, respectively; and r_{ij} is the distance between them. The first term, repulsive term, is described by a pairwise potential energy of the modified Born-Mayer type. The second term, attractive term, contains the many-body interaction that models the band energy.

From this magnitude, the stress tensor σ^{kl} can be obtained as the derivative of the total energy per unit volume [13]. Using a TB-SMA potential, this tensor can be expressed as:

$$\begin{aligned} \sigma^{kl} &= \frac{1}{V} \sum_i \frac{\partial E_i}{\partial \varepsilon^{kl}} = \frac{1}{V} \sum_i \left(-m_i v_i^k v_i^l + \frac{1}{2} \sum_{j(\neq i)} (h_{ij}) \frac{r_{ij}^k r_{ij}^l}{r_{ij}} \right) \\ h_{ij} &= \frac{\partial V^{\alpha\beta}}{\partial r_{ij}}(r_{ij}) + \left(\frac{\partial F}{\partial \rho_i}(\rho_i) + \frac{\partial F}{\partial \rho_j}(\rho j) \right) \frac{\partial \Phi^{\alpha\beta}}{\partial r_{ij}}(r_{ij}) \end{aligned} \tag{2}$$

where ε^{kl} is the strain-tensor Cartesian component kl ($k,l \in x,y,z$), v^k is the speed component k, and V the system volume. Each element of the summation divided by the effective atomic volume is the local stress at the atom site i. The main part of this work is carried out on a so-called reference nanowire. This system is a set of seven epitaxial ultrathin layers composed of two fcc oriented Co and Cu sublayers of about 10 nm thick each one stacked up alternately to build a Co/Cu multilayered nanowire. For this thickness, Co/Cu nanowires exhibit a large giant magnetoresistance (GMR) of 20–30% [14]. The presence of Co/Cu interfaces and the lattice mismatch favors an fcc phase for Co [14]. A circular cross-sectional shape of 5.11 nm in diameter has been considered. This size was selected since it can be built and investigated experimentally [15], and even though the simulation time is long, it is still reasonable. The thickness ratio between Co and Cu sublayers and the transverse and longitudinal dimensions have been varied.

Prior to uniaxial loading, the nanowires were relaxed and thermally equilibrated at 300 K using a Nosé–Hoover thermostat [16] while keeping periodic boundary conditions in the main nanowire direction. Then, boundary conditions were removed and the system was again relaxed at that temperature by using a constant pressure algorithm for 30 ps [17]. This procedure causes the pre-stress to be set to zero in the lattice. Finally, the uniaxial tensile and compressive loading process of nanowires was simulated at the temperature of 300 K and a strain rate of 10^9 s^{-1}. Nevertheless, other strain rates and temperatures have also been considered in the

present work. The Nosé–Hoover thermostat gives rise to modest temperature fluctuations, which leads to correct canonical averages of system properties. The uniaxial loading is reached by applying velocity to the atoms of both ends. This velocity varies linearly from zero to the maximum value, thus creating a ramp velocity profile. Such a ramp velocity is used to avoid the emission of shock waves.

To provide information on the atomic displacement in dislocations, we calculate the slip vector [18] and the maximum magnitude of slip vector, defined respectively for an atom i as:

$$\vec{s}_i = -\frac{1}{n_s}\sum_{j(\neq i)}^{n}\left(\vec{r}_{ij} - \vec{R}_{ij}\right) ; \qquad s_{i,\max} = \max_{j=1,..,n_s}\left|\vec{r}_{ij} - \vec{R}_{ij}\right| \tag{3}$$

where r_{ij} and R_{ij} are the vector differences of atoms i and j at the current and reference positions, respectively; n is the number of nearest neighbors to atom i; and n_s is the number of slipped neighbors. The reference positions are associated with the state of zero mechanical stress. The slip vector coincides with the Burgers vector for the slip of adjacent atomic planes, where the atom lies on one of those planes. For any other inhomogeneous deformation, the slip vector will provide quantitative information about the deformation. The maximum magnitude of slip vector has also been calculated to assess the margin of error in predictions. The internal relocation of atoms has been studied by the common-neighbor analysis (CNA) [19] and the lattice unit vectors (crystallographic orientation) in each grain [20].

3 Results and Discussion

In a similar way to that for pure metals [21], the stress curve as a function of the engineering strain for a Co/Cu composite nanowire in tensile loading at normal and low strain rates ($<5{\cdot}10^{9}$ s^{-1}) increases up to an absolute maximum in the elastic region. In Fig. 1, stress–strain curves at different strain rates and orientation are shown. The ⟨100⟩ orientation exhibits a very linear stress–strain relationship [22]. The initial yield stress (or strain) is defined as the stress (or strain) at the elastic limit that, for these values of strain rate, coincides with the absolute maximum. After reaching the peak value, the stress goes down dramatically due to the occurrence of dislocations. Then, the plastic zone is developed. In this region, the curve is saw-shaped, and at high strain rates it softly decreases. Plasticity comes from the emission and movement of different dislocation systems. The elastic zone can end in a relative maximum at rates of the order of $5{\cdot}10^{10}$ s^{-1}, especially for ⟨110⟩ and ⟨100⟩ directions. Then, a strain hardening region is developed and it is necessary to distinguish between yield and ultimate (absolute maximum) stresses.

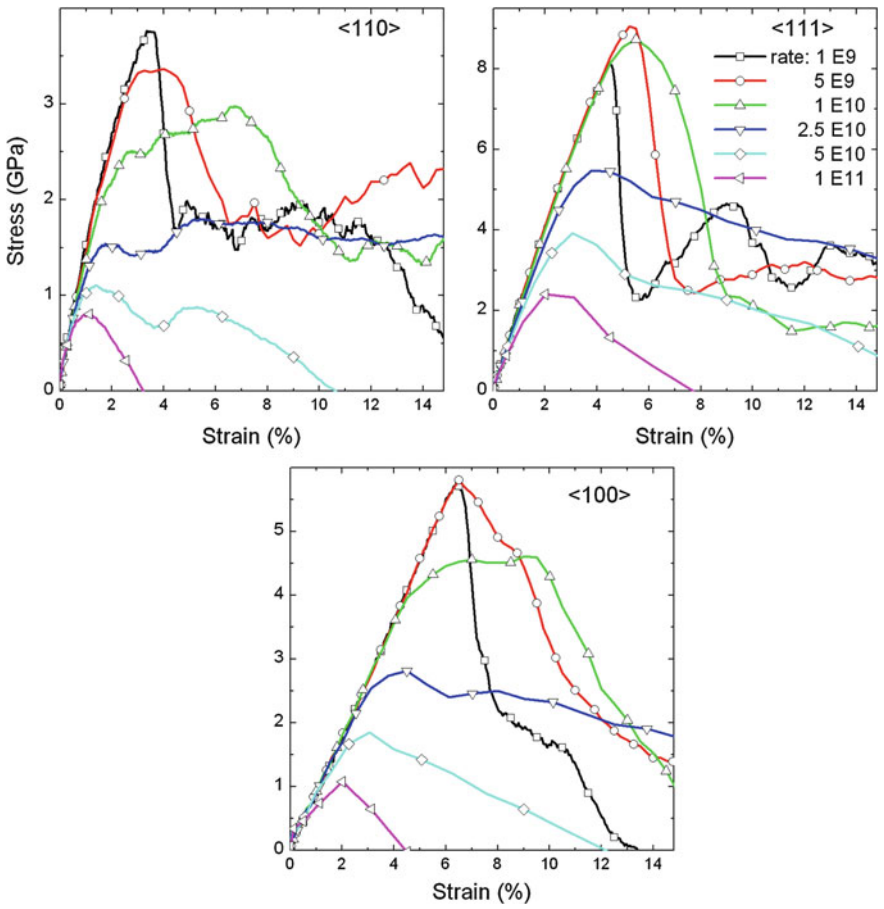

Fig. 1 Stress–strain curves for a reference nanowire at different strain rate and crystallographic orientations and 300 K

The stress curve is linear only at low strain in the elastic region. Wu [22] indicated that the nonlinearity may come from the inhomogeneity of nanowire cross-section, especially important in multilayers due to the lattice mismatch. The Young's or elastic modulus is determined from the slope by applying a linear fit at low strain. The stress required for homogeneous dislocation nucleation is highly dependent on the crystallographic orientation and the uniaxial loading conditions [23]; thus, certain orientations require a higher stress in tension, e.g., ⟨111⟩ nanowires. Besides, these nanowires are the hardest one (larger elastic modulus). In Fig. 2, the Young's modulus (rough, in some cases) and ultimate stress as a function of the strain rate are indicated. 146, 209, 76 GPa are the elastic moduli; and 3.76, 8.10, 5.74 GPa, the yield stresses used for the normalization in ⟨110⟩, ⟨111⟩ and ⟨100⟩ directions, respectively. The elastic modulus and yield stress are

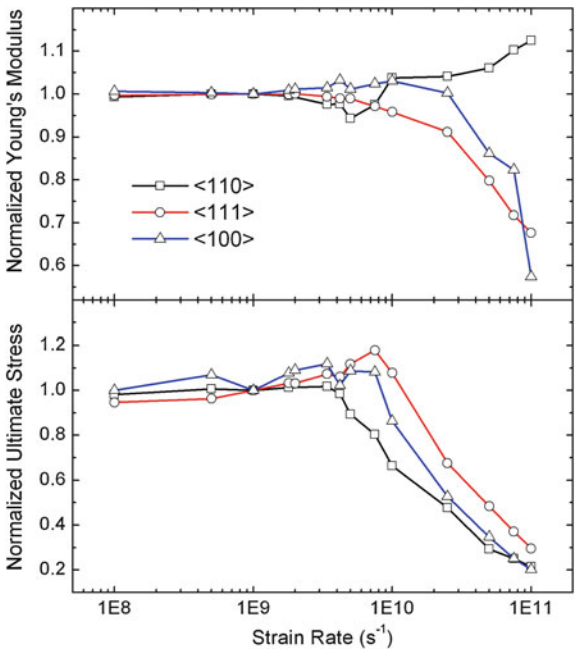

Fig. 2 Normalized Young's modulus and ultimate stress as a function of the strain rate for the reference nanowire with different crystallographic orientations and 300 K

approximately independent of strain rate, except at high strain rates ($>5{\cdot}10^9$ s^{-1}). The effect of strain rate on the mechanical behavior is similar for the three crystallographic orientations, except for ⟨110⟩ nanowires. In this case, the increase in elastic modulus with increasing strain rate is due to the nonlinearity of the stress curve. If the nanowire diameter decreases, this distinguishing behavior does not exist.

Size effects on the elastic behavior have also been analyzed. A parameter as the volume-to-surface-area (vol/sa) ratio (normalized by the vol/sa ratio of the Cu unit cell) is introduced. The dependence of Young's modulus and initial yield stress on this parameter is represented in Fig. 3 for the tensile regime. The smallest nanowire had 1.50 nm maximum wide (5-Co/Cu-layer long), and the largest one, 5.11 nm (reference nanowire). Below a ratio of about 10, both mechanical magnitudes diverge from the bulk value, increasing in the case of ⟨110⟩ orientation and decreasing for the other two directions. This behavior is in accordance with previous works on pure Cu, Ag and Au nanowires [24–26]. The surface effect plays an important role on the mechanical properties, since, in fact, the different 'core–shell' elasticity [27] and the nonlinear elastic response of the nanowire core induced by the surface stress [24] are determining factors of the elastic modulus.

Two details deserve to be mentioned in the break-up layer of a nanowire of 2.24 nm in diameter (ratio about 6.5): For ⟨100⟩ nanowires, grains undergo a crystallographic reorientation, thus it is possible to find mainly ⟨111⟩-oriented and also ⟨110⟩-oriented grains. A similar reorientation process towards ⟨110⟩ direction

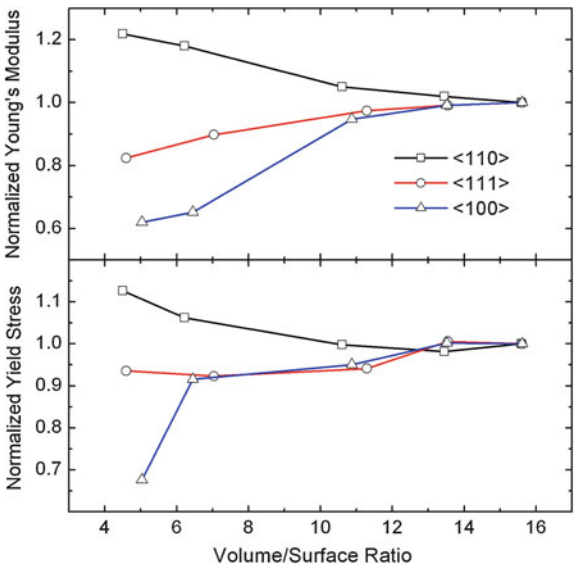

Fig. 3 Normalized Young's modulus and initial yield stress as a function of the normalized vol/sa ratio for nanowires with different crystallographic orientations (at 300 K and 10^9 s^{-1})

is observed in an fcc gold ⟨100⟩ nanowire [28]. Besides, after the break-up the number of hcp atoms is larger for ⟨100⟩ nanowires (2.5 times) than the number of fcc atoms unlike ⟨111⟩ and ⟨110⟩ directions (the former has 3.2 times more fcc than hcp atoms, and the later 4.5). These hcp atoms are preferably in the Co sublayer for ⟨100⟩ direction (there are two times more hcp Co than Cu atoms), and in the Cu sublayer for ⟨111⟩ (two times more hcp Cu than Co atoms) and ⟨110⟩ (there are only hcp Cu atoms) directions. The fcc atoms are preferably in the Cu sublayer for ⟨100⟩ nanowires (two times more fcc Cu than Co atoms) and in the Co sublayer for ⟨111⟩ and ⟨110⟩ nanowires (two times more fcc Co than Cu atoms in both cases). Therefore, in the break-up zone Co recovers an hcp structure more easily for ⟨100⟩ nanowires, and in addition Cu is more stable in its fcc structure for ⟨111⟩ and ⟨110⟩ nanowires.

In Fig. 4, the Young's modulus and initial yield stress at different temperatures for the reference nanowire are represented. Both magnitudes decrease approximately linearly with increasing temperature [29]. The deviation from the horizontal line is larger in the case of ⟨100⟩ direction, and therefore, temperature has more influence on the mechanical behavior of this orientation. The drop of the elastic modulus with increasing temperature is associated with the significantly weakened bond forces due to the larger thermal vibrations of atoms [30]. Nevertheless, temperature has no substantial effect on the deformation mechanism [30]. The dislocation nucleation takes place more easily at higher temperatures. Theoretical models of dislocation emission from a crack tip show a definitive relationship between activation energy and temperature [31]. This effect leads to decrease the yield stress. Absolute values of yield stress in these three directions at different temperature are slightly smaller than other published values on pure Cu nanowires due probably to the different simulation potential [32].

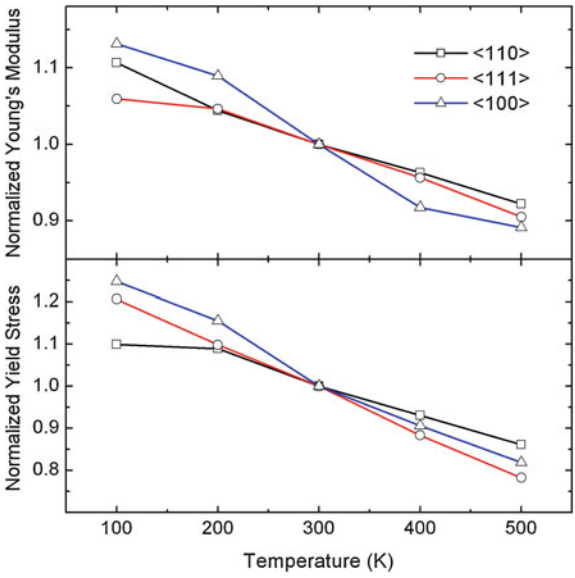

Fig. 4 Normalized Young's modulus and initial yield stress as a function of temperature for the reference nanowire with different crystallographic orientations at 10^9 s^{-1}

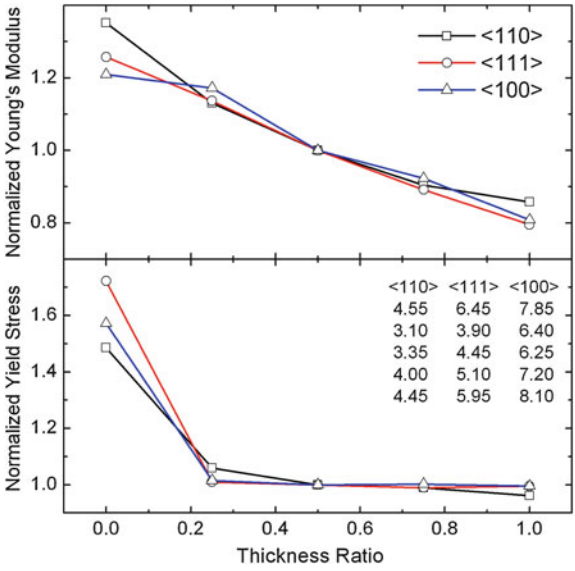

Fig. 5 Normalized Young's modulus and initial yield stress as a function of the thickness ratio between Co and Cu sublayers for the reference nanowire with different crystallographic orientation (at 300 K and 10^9 s^{-1}). For pure Co, thickness ratio is 0; and for Cu, 1. Corresponding values of the yield strain (%) are indicated numerically from small to large thickness

The elastic modulus of Co/Cu nanowires decreases with increasing thickness of Cu sublayer in a similar way to that obtained in other bimetallic multilayers [33]. In fact, both magnitudes are much larger for Co nanowires than for Cu nanowires. In Fig. 5, the Young's modulus and yield stress are represented as a function of the thickness ratio between Co and Cu sublayers. While the Young's modulus decreases gradually, yield stress falls steeply from pure Co value to the pure Cu

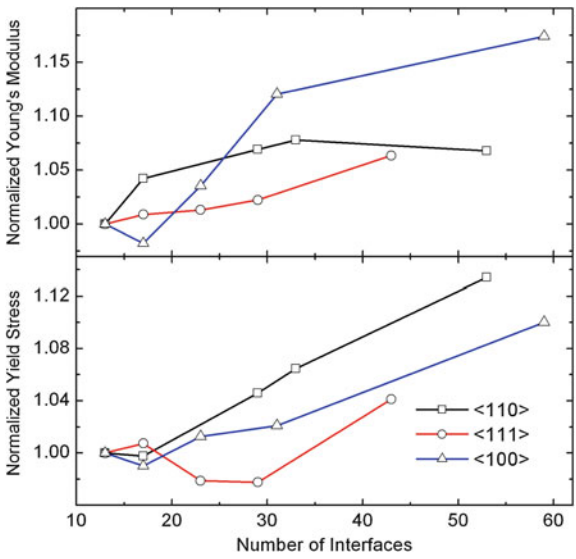

Fig. 6 Normalized Young's modulus and initial yield stress as a function of the number of interfaces for nanowires with different crystallographic orientations and the same length (at 300 K and 10^9 s^{-1})

value for any Cu sublayer thickness. In fact, lattice distortion takes place firstly and fundamentally in Cu sublayers, even for small thicknesses of these [33]. A reason is that for this potential the stacking-fault energy of Cu is 19 mJm^{-2}, and of Co is 25 mJm^{-2}.

The lattice misfit at the interface may also have influence on the mechanical properties. Cu has a lattice parameter of 3.615 Å and fcc Co of 3.544 Å. Therefore, Cu sublayers should experience an additional tensile stress, and Co sublayers should experience a compressive stress (Poisson effect). Figure 6 shows the normalized Young's modulus and yield stress as a function of the number of interfaces for a Co/Cu nanowire with the same length. The elastic modulus and yield stress increase with increasing number of interfaces, especially for ⟨100⟩ and ⟨110⟩ directions. Diameter of these nanowires is 3.5 times lower than that necessary to create a misfit dislocation. Therefore, in this case internal stresses influence only moderately the mechanical properties. Additional studies on this subject are necessaries, especially for different diameters and/or large misfit [33, 34].

The magnitude of Burgers vector of a {111}⟨112⟩ partial dislocation in Cu is 1.48 Å, and of a {111}⟨110⟩ full dislocation is 2.56 Å. Therefore, from the distribution of magnitude of slip vector, it is possible to know the existence of stacking faults and full dislocations. The components of slip vector allow to know the specific partial dislocation nucleated on a {111} plane. In Fig. 7, an image of three nanowires in tension and their corresponding distributions of magnitude and maximum magnitude of slip vector are shown. Yielding of nanowires occurs through the nucleation from edges and propagation across the nanowires of {111}⟨112⟩ partial dislocations (see in Fig. 7 the top nanowire). Dislocation nucleation in a nanowire seems to be related to the effective critical resolved shear stress (RSS) caused by the external forces in the leading slip direction on the slip plane [37]. According to the

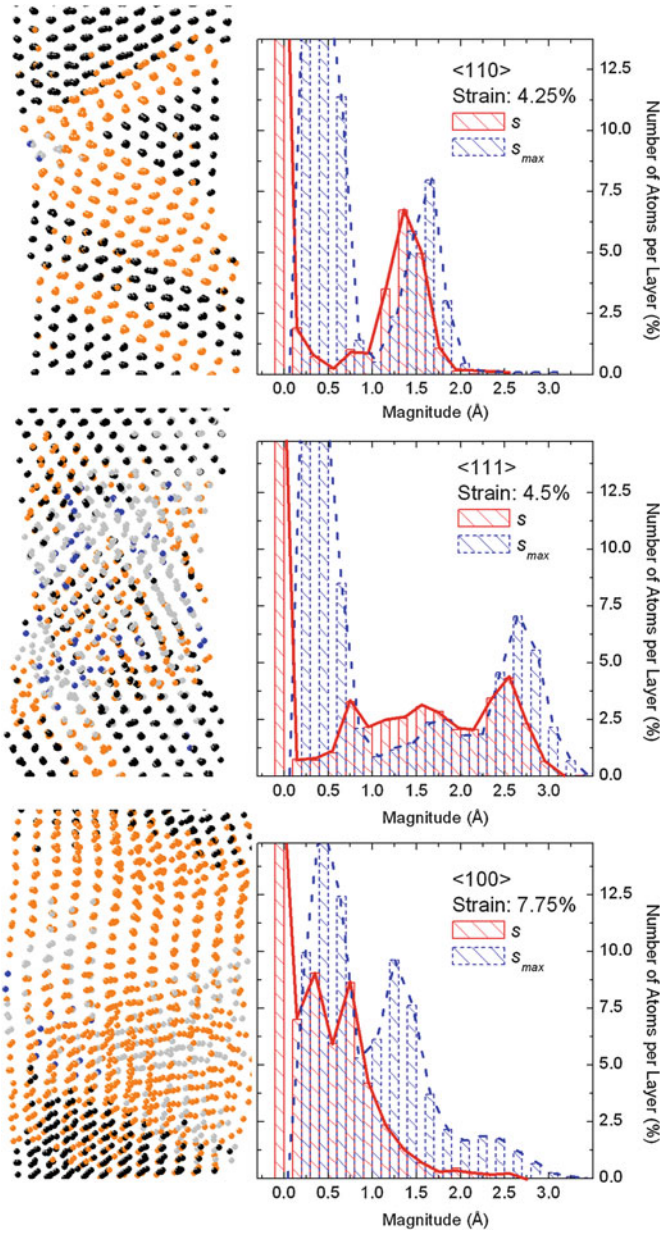

Fig. 7 Projection of three nanowires of 2.24 nm in diameter (at 300 K and 10^9 s^{-1}). The vertical axis (nanowire axis) corresponds to: ⟨110⟩ , ⟨111⟩ and ⟨100⟩ directions (from *top* to *bottom*), and the horizontal one, to ⟨00-1⟩ , ⟨11-2⟩ and ⟨001⟩ directions, respectively. Colors are assigned according to the values of $s_{i,max}$: *black* ($s_{i,max} < 0.7$), *grey* (*orange*) ($0.7 < s_{i,max} < 2$), *light grey* ($2 < s_{i,max} < 3$) and *light black* (*blue*) ($s_{i,max} > 3$). Beside this representation, the distributions of magnitude s and maximum magnitude s_{max} of slip vector are shown

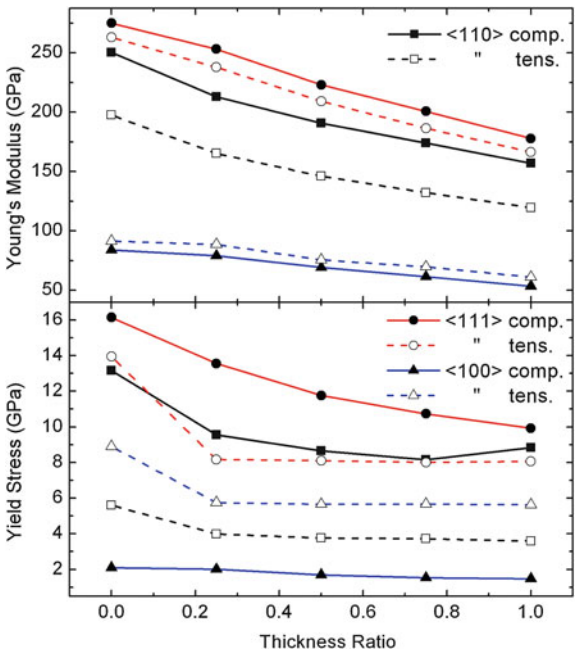

Fig. 8 Young's modulus and initial yield stress as a function of the thickness ratio between Co and Cu sublayers for the reference nanowire with different crystallographic orientation and tensile and compressive stresses (at 300 K and 10^9 s^{-1})

distributions of magnitude and maximum magnitude of slip vector in Fig. 7, ⟨110⟩ nanowires slip via {111}⟨112⟩ partial dislocation nucleation and propagation. Unlike, in ⟨111⟩ nanowires, both {111}⟨112⟩ and {111}⟨110⟩ slips occur, the latter occurs through two successive {111}⟨112⟩ slips on the same {111} plane. Finally, in ⟨100⟩ nanowires, the magnitude of slip vector is not always an indicative factor of the type of generated dislocations since other defects mask slips, given the small space in which the yielding process takes place [35]. Due to this, the maximum magnitude of slip vector is used. In this case, both {111}⟨112⟩ and {111}⟨110⟩ slips occur, although the frequency of appearance of the first type is larger. Au⟨100⟩ nanowires show the same behavior, however Au ⟨111⟩ nanowires, in tensile yielding, only nucleate {111}⟨112⟩ partial dislocations [36].

Other interesting aspect is that the Young's modulus and yield stress are larger in compression than in tension, except for ⟨100⟩ direction. This asymmetry may be primarily due to effects of surface stresses and the different slip systems active during tensile and compressive yielding [37]. In Fig. 8 both magnitudes are represented as a function of the thickness ratio. The uniaxial Schmidt factor for leading partial slip is larger under compression than under tension for ⟨100⟩ nanowires unlike for the other two directions; and thus, for these nanowires, it is easier to yield under compression [26, 37]. Differences between tension and compression for both magnitudes are larger for ⟨110⟩ direction, especially in the case of the elastic modulus. Besides, differences for this magnitude are independent of the thickness ratio. Unlike, the gap for the yield stress between both loading processes is larger in general whether the nanowire is made only of Co.

According to the distributions obtained from the vector slip, nanowires show differences in the slip mechanism for ⟨110⟩ and ⟨100⟩ directions (not for ⟨111⟩ direction). In compression, the former system slip via both {111}⟨112⟩ and {111}⟨110⟩ dislocations, and the latter only through {111}⟨112⟩ dislocations. It is well known that for bulk single crystal the plastic deformation mode depends on the relationship between the Schmidt factor of the leading partial dislocation and that of the trailing partial dislocation. Full dislocation slipping prefers to be activated if the Schmidt factor of the trailing partial dislocation is larger than that of the leading partial dislocation [26, 38]. In our case, the only case in that this rule is not verified is for the ⟨111⟩ direction in tension in a similar way to what happens in other systems like Au [26].

4 Summary and Conclusions

The mechanical deformation properties of Co/Cu multilayered nanowires (5 nm in diameter × 140 nm long) have been studied by MD under uniaxial tensile and compressive stresses at different crystallographic orientations (⟨110⟩, ⟨111⟩, ⟨100⟩). The elastic modulus and initial yield stress are approximately independent of strain rate, except at high strain rates. The effect of strain rate on the mechanical behavior is similar for the three crystallographic orientations, except the increase in elastic modulus with increasing strain rate for ⟨110⟩ nanowires due to the nonlinearity of the stress curve.

Below a normalized vol/sa ratio of about 10, elastic modulus and initial yield stress for tensile strength diverge from the bulk value, increasing in the case of ⟨110⟩ orientation and decreasing for the other two directions. In the break-up Co/Cu layer for ⟨100⟩ nanowires, grains undergo a crystallographic reorientation towards ⟨111⟩ and ⟨110⟩ directions. Besides, in this layer after the break-up the number of hcp atoms is larger than the number of fcc atoms only for ⟨100⟩ nanowires. These hcp atoms are preferably in the Co sublayer unlike the other two directions. The fcc atoms are preferably in the Cu sublayer for ⟨100⟩ nanowires unlike the other two directions. Young's modulus and yield stress decrease approximately linearly with increasing temperature. Temperature has more influence on the mechanical behavior of ⟨100⟩ orientation.

⟨110⟩ nanowires slip via {111}⟨112⟩ partial dislocation nucleation and propagation. Unlike, in ⟨111⟩ nanowires, both {111}⟨112⟩ and {111}⟨110⟩ slips occur, the latter occurs through two successive {111}⟨112⟩ slips on the same {111} plane. In ⟨100⟩ nanowires, both {111}⟨112⟩ and {111}⟨110⟩ slips occur, although the frequency of appearance of the first type is larger. Young's modulus and yield stress are larger in compression than in tension, except for ⟨100⟩ direction. The uniaxial Schmidt factor for leading partial slip, in addition to effects of surface stresses and the different active slip systems explain this circumstance. Differences between tension and compression for both magnitudes are larger for ⟨110⟩ direction, and in the case of elastic modulus they are independent of the thickness

ratio. Tension and compression show differences in the slip mechanism for ⟨110⟩ and ⟨100⟩ directions. In compression, the former system slips via both {111}⟨112⟩ and {111}⟨110⟩ dislocations; and the latter, only through {111}⟨112⟩ dislocations. The relationship between the Schmidt factor of the leading and the trailing partial dislocations can explain this effect for these two directions, but not for ⟨111⟩ direction that does not show differences in the slip mechanisms.

Acknowledgments This work was supported by the Universidad Complutense of Madrid under the Project for Research Groups (Bioelectromagnetism Research Group 910305-4120909).

References

1. Whitney, T.M., Searson, P.C., Jiang, J.S., Chien, C.L.: Fabrication and magnetic properties of arrays of metallic nanowires. Science **261**, 1316 (1993)
2. Wernsdorfer, W., Doudin, B., Mailly, D., Hasselbach, K., Benoit, A., Meier, J., Ansermet, J-Ph, Barbara, B.: Nucleation of magnetization reversal in individual nanosized nickel wires. Phys. Rev. Lett. **77**, 1873 (1996)
3. Baibich, M.N., Broto, J.M., Fert, A.: Nguyen Van Dau, F., Petroff, F., Etienne, P., Creuzet, G., Friederich, A., Chazelas, J.: Giant magnetoresistance of (001)Fe/(001)Cr magnetic superlattices. Phys. Rev. Lett. **61**, 2472 (1988)
4. Parkin, S.S.P., Bhadra, R., Roche, K.P.: Oscillatory magnetic exchange coupling through thin copper layers. Phys. Rev. Lett. **66**, 2152 (1991)
5. Wegrowe, J.E., Gilbert, S.E., Kelly, D., Doudin, B., Ansermet, J-Ph: Anisotropic magnetoresistance as a probe of magnetization reversal in individual nano-sized nickel wires. IEEE Trans. Magn. **34**, 903 (1998)
6. Piraux, L., George, J.M., Despres, J.F., Leroy, C., Ferain, E., Legras, R., Ounadjela, K., Fert, A.: Giant magnetoresistance in magnetic multilayered nanowires. Appl. Phys. Lett. **65**, 2484 (1994)
7. Blondel, A., Meier, J.P., Doudin, B., Ansermet, J-Ph: Giant magnetoresisttance of multilayers in nanowires. Appl. Phys. Lett. **65**, 3019 (1994)
8. Martin, C.R.: Nanomaterials: A membrane-based synthetic approach. Science **266**, 1961 (1994)
9. Liang, W.W., Zhou, M.: Pseudoelasticity of single crystalline Cu nanowires through reversible lattice reorientations. J. Eng. Mater. Technol. **127**, 423 (2005)
10. Diao, J., Gall, K., Dunn, M.L.: Atomistic simulation of the structure and elastic properties of gold nanowires. J. Mech. Phys. Solids **52**, 1935 (2004a)
11. Levanov, N.A., Stepanyuk, V.S., Hergert, W., Bazhanov, D.I., Dederichs, P.H., Katsnelson, A.A., Massobrio, C.: Energetics of Co adatoms on the Cu(001) surface. Phys. Rev. B **61**, 2230 (2000)
12. Cleri, F., Rosato, V.: Tight-binding potentials for transition metals and alloys. Phys. Rev. B **48**, 22 (1993)
13. Zubarev, D.N.: Non-Equilibrium Statistical Thermodynamics. Nauka, Moscow (1971)
14. Scarani, V., Doudin, B., Ansermet, J.P.: The microstructure of electrodeposited cobalt-based nanowires and its effect on their magnetic and transport properties. J. Magn. Magn. Mater. **205**, 241 (1999)
15. Routkevich, D., Tager, A.A., Haruyama, J., Almawlawi, D., Moskovits, M., Xu, J.M.: Non-lithographic nanowire arrays: Fabrication, physics and device applications. IEEE Trans. Electron Devices **43**, 1646 (1996)
16. Hoover, W.R.: Canonical dynamics: Equilibrium phase-space distributions. Phys. Rev. A **31**, 1695 (1985)
17. Parrinello, M., Rahman, A.: Polymorphic transitions in single crystals: A new molecular dynamics method. J. Appl. Phys. **52**, 7182 (1981)

18. Zimmerman, J.A., Kelchner, C.L., Klein, P.A., Hamilton, J.C., Foiles, S.M.: Surface step effects on nanoindentation. Phys. Rev. Lett. **87**, 165507 (2001)
19. Cleveland, C.L., Luedtke, W.D., Landman, U.: Melting of gold clusters. Phys. Rev. B **60**, 5065 (1999)
20. Jiménez-Sáez, J.C., Pérez-Martín, A.M.C., Jiménez-Rodríguez, J.J.: Structural changes in metallic nanoclusters deposited on substrates with much larger lattice parameters. In: Dirote, E.V. (ed.) New Developments in Nanotechnology Research. Nova Science Publishers, New York (2006)
21. Wu, H.A.: Molecular dynamics study of the mechnics of metal nanowires at finite temperature. Euro J. Mech. A Solids **25**, 370 (2006a)
22. Wu, H.A.: Molecular dynamics study on mechanics of metal nanowire. Mech. Res. Commun. **33**, 9 (2006b)
23. Tschopp, M.A., McDowell, D.L.: Tension-compression asymmetry in homogeneous dislocation nucleation in single crystal copper. Appl. Phys. Lett. **90**, 121916 (2007)
24. Liang, H., Upmanyu, M., Huang, H.C.: Size-dependent elasticity of nanowires: Nonlinear effects. Phys. Rev. B **71**, 241403 (2005)
25. McDowell, M.T., Leach, A.M., Gall, K.: On the elastic modulus of metallic nanowires. Nano Lett. **8**, 3613 (2008)
26. Wen, Y.-H., Zhang, Y., Wang, Q., Zheng, J.-C., Zhu, Z.-Z.: Orientation-dependent mechanical properties of Au nanowires under uniaxial loading. Comput. Mater. Sci. **48**, 513 (2010)
27. Miller, R.E., Shenoy, V.B.: Size-dependent elastic properties of nanosized structural elements. Nanotechnology **11**, 139 (2000)
28. Diao, J., Gall, K., Dunn, M.L.: Surface stress driven reorientation of gold nanowires. Phys. Rev. B **70**, 075413 (2004b)
29. Setoodeh, A.R., Attariani, H., Khosrownejad, M.: Atomistic simulation on size-dependent yield strength and defects evolution of metal nanowires. Comput. Mater. Sci. **44**, 378 (2008)
30. Koh, S.J.A., Lee, H.P., Lu, C., Cheng, Q.H.: Molecular dynamics simulation of solid platinum nanowire under uniaxial tensile strain: A study on temperature and strain rate effects. Phys. Rev. B **72**, 085414 (2005)
31. Zhang, Y.W., Wang, T.C., Tang, Q.H.: The effect of thermal activation of crack processes at an atomistic crack tip. J. Phys. D **28**, 748 (1995)
32. Tschopp, M.A., Spearot, D.E., McDowell, D.L.: Atomistic simulations of homogeneous dislocation nucleation in single crystal copper. Modelling Simul. Mater. Sci. Eng. **15**, 693 (2007)
33. Ma, F., Song, Z.-X., Li, Y.-H., Xu, K.-W.: Plastic deformation in bi-metal multilayer nanowires. Microelectron. Eng. **87**, 426 (2010)
34. Jiménez-Sáez, J. C., Pérez-Martín, A. M. C., Jiménez-Rodríguez, J. J.: Mechanical characterization of Co/Cu multilayered nanowires. J. Nanosci. Nanotechnol., in press (2012)
35. Hua, J., Hartmaier, A.: Determining Burgers vectors and geometrically necessary dislocation densities from atomistic data. Modelling Simul. Mater. Sci. Eng. **18**, 045007 (2010)
36. Diao, J., Gall, K., Dunn, M.L., Zimmerman, J.A.: Atomistic simulations of the yielding of gold nanowires. Acta Materialia **54**, 643 (2006)
37. Diao, J., Gall, K., Dunn, M.L.: Yield strength asymmetry in metal nanowires. Nano Lett. **4**, 1863 (2004c)
38. Lin, Y.C., Pen, D.J.: Analogous mechanical behaviors in <100> and <110> directions of Cu nanowires under tension and compression at a high strain rate. Nanotechnology **18**, 395705 (2007)

On the Continuum Mechanics Approach in Modeling Nanosized Structural Elements

Holm Altenbach and Victor A. Eremeyev

Abstract During the last 50 years the nanotechnology is established as one of the advanced technologies manipulating matter on an atomic and molecular scale. By this approach new materials, devices or other structures possessing at least one dimension sized from 1 to 100 nm are developed. The question arises how structures composed of nanomaterials should be modeled. Two approaches are suggested—theories which take into account quantum mechanical effects since they are important at the quantum-realm scale or theories which are based on the classical continuum mechanics adapted to nanoscale problems. Here the second approach will be discussed in detail. It will be shown that the classical continuum mechanics (kinematics, stress states analysis, balances and constitutive equations) with some improvements is enough for a sufficient description of the mechanical behavior of nanomaterials and -structures in many situations. After a brief recall of the basics of Continuum Mechanics a theory with surface effects will be discussed.

H. Altenbach (✉) · V. A. Eremeyev
Lehrstuhl für Technische Mechanik, Institut für Mechanik,
Otto-von-Guericke-Universität Magdeburg,
Universitätsplatz 2, 39106 Magdeburg, Germany
e-mail: holm.altenbach@ovgu.de

V. A. Eremeyev
e-mail: eremeyev.victor@gmail.com

Adv Struct Mater (2013) 4: 351–371
DOI: 10.1007/8611_2012_67

Published Online: 21 December 2012

1 Introduction

Nanotechnology is related to materials, devices and other structures with at least one dimension sized from 1 to 100 nm. With respect to several applications resulting, for example, in new material properties the questions arise:

- how to model such nanostructures,
- how to design nanodevices, and
- how to predict the new properties.

As usual if the size decreases some effects (for example, surface stresses) are more significant in comparison with effects of materials and devices of conventional size. Such effects are statistical mechanical and quantum mechanical effects among others. They results in significant changes of the properties in comparison with the properties of the bulk material (see [14, 17, 25, 34] among others). This is experimentally established also for the inelastic properties, see, for example, [22, 60].

In recent publications various approaches of modeling are presented. Many contributions are coming from physics and yields in equations which are not similar to the usual equations in the engineering analysis of structures or engineering simulations of the material behavior. By this way we get results describing qualitatively and quantitatively correct the effects related to the nanosize. Since nanoeffects are connected with the size of atoms and molecules molecular modeling codes are used in numerical simulations. The disadvantage of this approach is that the engineering analysis of real nanostructures taking into account the three-dimensional behavior is not trivial.

In contrast to the aforementioned approach in various applications Continuum Mechanics based theories are applied. It can be shown that the classical Continuum Mechanics is unable to simulate the properties of nanostructures in a correct manner [24, 28, 67]. Several improved theories for the analysis of nanostructures are developed, for example,

- Cosserat or micropolar theories,
- Continuum Mechanics theories taking into account surface effects, and
- gradient theories.

It should be noted that these theories can be combined with the classical structural analysis introducing models like beam, rod, plate, shell, etc. as basic one- or two-dimensional models. Now there are developed several theories like, for example, the mechanics of nanocomposites which is widely discussed in the literature (cp. the review [31]). Alternatively, the behavior of the crystal lattice is modeled based on Continuum Mechanics, for example, in [2, 36].

Below we present the basic features of the classical Continuum Mechanics and discuss one possible improvement (the account of surface effects) which is helpful in nanomechanics. Gradient and Cosserat theories will be not discussed. They are presented in [1, 11–13, 15, 37, 40, 65] among others. In the final part there are given briefly some references to applications.

2 Basic Equations in Classical Continuum Mechanics

The classical Continuum Mechanics is based on the continuum assumption. How realistic is this assumption? Up to now there are a lot of discussions. They are based on mathematics (continuous distribution of the field variables and, in addition, of their derivatives) or physics. Continuum Mechanics is the branch of mechanics that deals with the analysis of the behavior of materials and structures modeled as continuous distributed mass (infinite number of material points) instead of discrete particles (presented, for example, by molecular modeling methods). The founder of continuum mechanics was the French mathematician Augustin Louis Cauchy who formulate first relevant models in the 19^{th} century. These models were further generalized by the Cosserat brothers [16], Lord Kelvin, Duhem and Helmholtz among others. However, the classical or the generalized continua are modeled as objects assuming that they completely fill the occupied space. Modeling objects in this way ignores the fact that matter is made of atoms, and so is not continuous. But on length scales much greater than that of inter-atomic distances, such models are highly accurate. Fundamental physical laws such as the balance of mass, the balance of momentum, and the balance of energy may be applied to these models to derive integral or differential equations describing their behavior. The information about the particular material properties is added through the constitutive and, may be, evolution equations.

Continuum Mechanics deals with physical properties of solids and fluids which are independent of any particular coordinate system in which they are observed. These physical properties are then represented by tensors of different rank, which are mathematical objects that have the required property of being independent of the coordinate system. These tensors can be expressed in specific coordinate systems for computational convenience.

In this section we briefly present the basics of Continuum Mechanics. Further information are given in [6, 32] among others. The direct tensor calculus in the sense of [41] is mostly used this chapter.

2.1 Kinematical Equations

A body $\mathcal{B}$ is an assemblage of material points, which is bounded by the boundary points, that means the surface of $\mathcal{B}$. Material bodies are introduced in Continuum Mechanics with the help of the method of sections. By this method the body $\mathcal{B}$ can be separated from the surrounding. The introduction of the surface and the body is arbitrary, which is helpful for the formulation of the balance equations.

The movement of material bodies can be presented by the motion of their material points which should be identified. If the material points are related to points in the Euclidean space $\mathbb{R}^3$ and if one point 0 is fixed in this space, then the position of the material points is determined by the position-vector $\mathbf{x}(t)$ at arbitrary

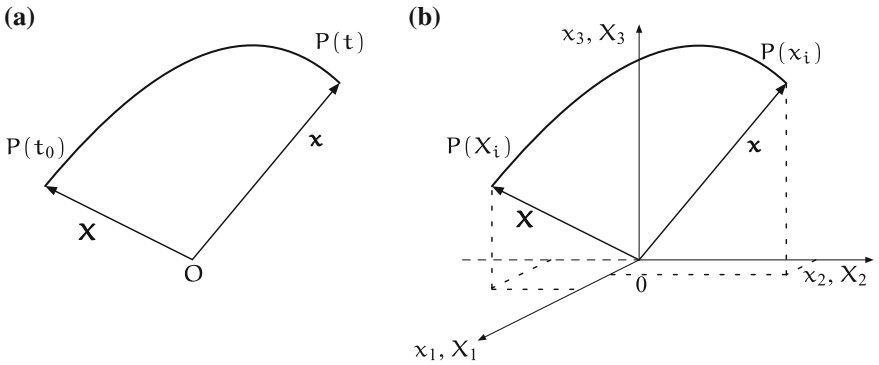

Fig. 1 Movement of a material point: **a** position-vector, **b** Cartesian coordinates

time t. To distinguish the material points of the body $\mathcal{B}$ each of them get a label: at the time $t = t_0$ the material point is characterized by the position-vector $\mathbf{x}(t_0) \equiv \mathbf{X}$. t_0 is the natural initial state, which changes should be computed. In many cases $t_0 = 0$ is assumed.

In Cartesian coordinates with the origin O and the basis vectors $\mathbf{e}_i (i = 1, 2, 3)$ the movement of the material point $\mathbf{X}$ can be presented as it follows

$$\mathbf{x} = x_i \mathbf{e}_i, \qquad \mathbf{X} = X_i \mathbf{e}_i, \qquad \mathbf{x}(\mathbf{X}, t_0) = \mathbf{x}_0 \equiv \mathbf{X}, \tag{1}$$

In Fig. 1 is shown the movement of a material point P. The coordinates x_i are Lagrangian coordinates, x_i - Eulerian coordinates. The description of the behavior of the continuum can be related to both the Lagrangian and the Eulerian configurations. For many applications this is sufficient. Sometimes it is necessary to present the continuum in so-called intermediate configurations. Details are given, for example, in [50, 64].

2.1.1 Deformation Gradient and Strain Tensors

The deformation of the continuum can be presented with the help of the equation of motion

$$\mathbf{x} = \mathbf{x}(\mathbf{X}, t)$$

Let us introduce the material deformation gradient

$$\mathbf{F} \equiv [\nabla_{\mathbf{X}} \mathbf{x}(\mathbf{X}, t)]^{\mathrm{T}} \tag{2}$$

describing the transform of a material line element $d\mathbf{X}$ in the reference configuration into a material line element $d\mathbf{x}$ of the actual configuration

$$\mathbf{F} \cdot d\mathbf{X} = d\mathbf{x}$$

$(\ldots)^{\mathrm{T}}$ denotes the transpose of a tensor.

The vice versa transform is given by

$$d\mathbf{X} = \mathbf{F}^{-1} \cdot d\mathbf{x}$$

with

$$\mathbf{F}^{-1} = [\nabla_{\mathbf{x}} \mathbf{X}(\mathbf{x}, t)]^{T}. \tag{3}$$

$(\ldots)^{-1}$ denotes the inverse of a tensor. Note that the motion consist of the motion of the continuum as a rigid body (translation and rotation) and the strains (relative position changes of the material points).

Let us introduce the Green-Lagrange strain tensor which has in the reference configuration for pure rigid body motion the value zero

$$\mathbf{G}(\mathbf{X}, t) = \frac{1}{2}(\mathbf{F}^{T} \cdot \mathbf{F} - \mathbf{I}). \tag{4}$$

$\mathbf{G}$ is a symmetric tensor. In addition, a second strain tensor (Almansi-Hamel strain tensor) related to the actual configuration can be defined as it follows

$$\mathbf{A} = \left(\mathbf{F}^{T}\right)^{-1} \cdot \mathbf{G} \cdot \mathbf{F}^{-1}$$

2.1.2 Displacements, Displacement Gradient, Linearizations

For both configurations we can introduce the displacement vector

$$\mathbf{u}(\mathbf{x}, t) = \mathbf{x}(\mathbf{X}, t) - \mathbf{X}, \qquad \mathbf{u}(\mathbf{X}, t) = \mathbf{x} - \mathbf{X}(\mathbf{x}, t) \tag{5}$$

The displacement gradient can be also computed in both configurations

$$[\nabla_{\mathbf{X}} \mathbf{u}(\mathbf{X}, t)]^{T} \equiv \mathbf{J}, \qquad [\nabla_{\mathbf{x}} \mathbf{u}(\mathbf{x}, t)]^{T} \equiv \mathbf{K}$$

It is easy to show that

$$\mathbf{J} = \mathbf{F} - \mathbf{I}, \qquad \mathbf{K} = \mathbf{I} - \mathbf{F}^{-1}, \tag{6}$$

and the strain tensors can be obtained as it follows

$$\mathbf{G} = \frac{1}{2}(\mathbf{J} + \mathbf{J}^{T} + \mathbf{J} \cdot \mathbf{J}^{T}), \qquad \mathbf{A} = \frac{1}{2}(\mathbf{K} + \mathbf{K}^{T} - \mathbf{K}^{T} \cdot \mathbf{K}) \tag{7}$$

Finally, the strain tensors can be computed

$$\begin{aligned} \mathbf{G} &= \frac{1}{2}\left[(\nabla_{\mathbf{X}} \mathbf{u})^{T} + (\nabla_{\mathbf{X}} \mathbf{u}) + (\nabla_{\mathbf{X}} \mathbf{u}) \cdot (\nabla_{\mathbf{X}} \mathbf{u})^{T}\right], \\ \mathbf{A} &= \frac{1}{2}\left[(\nabla_{\mathbf{x}} \mathbf{u})^{T} + (\nabla_{\mathbf{x}} \mathbf{u}) - (\nabla_{\mathbf{x}} \mathbf{u}) \cdot (\nabla_{\mathbf{x}} \mathbf{u})^{T}\right] \end{aligned} \tag{8}$$

Both strain tensors contain quadratic terms. They describe the geometrical-nonlinear behavior of the continuum. Ignoring quadratic terms we get similar expressions as in Strength of Materials (Cauchy strain tensor). The mathematical consistent linearization of the kinematical relations is presented, for example, in [32].

2.2 Stress State

The external actions on the continuum can by classified as volume or surface actions. They can be pure mechanical, thermal, electromagnetic, etc. Here we focus our attention on mechanical actions, which can split as known from the General Mechanics (Statics) into forces and moments. Then we can introduce:

- mass or volume forces and moments and
- surface forces and moments.

In general the actions are continuously distributed in the volume or on the surface functions. They are introduced as models since they cannot observed directly (only the response of the actions can be measured). It is easy to show that line and concentrated single actions are limit cases of the volume and surface actions. These limit cases are the result of the different order of the three spatial dimensions or of the two dimensions of the surface.

Any material body is characterized by a continuous mass density distribution $\rho(\mathbf{x})$. The mass or volume actions are also continuous functions applied to any material point of the body. Examples of volume forces are the gravitational force, the force of inertia, the Coriolis force among others. The sources of these forces are out of the body, that means they are external (far-distance) forces. By analogy one can introduce sources for volume moments.

Volume forces are related to volume or mass. By $\mathbf{k}^{\mathrm{V}}$ the volume force density and by $\mathbf{k}^{\mathrm{m}} \equiv \mathbf{k}$ the mass force density are denoted (in what is following $\mathbf{k}$ is used instead of $\mathbf{k}^{\mathrm{m}}$). It holds

$$\rho(\mathbf{x},\mathrm{t})\mathbf{k}(\mathbf{x},\mathrm{t}) = \mathbf{k}^{\mathrm{V}} \tag{9}$$

In the case of volume moments the analogous equation is valid

$$\rho(\mathbf{x},\mathrm{t})\mathbf{l}^{\mathrm{m}}(\mathbf{x},\mathrm{t}) = \rho(\mathbf{x},\mathrm{t})\mathbf{l}(\mathbf{x},\mathrm{t}) = \mathbf{l}^{\mathrm{V}} \tag{10}$$

with $\mathbf{l}^{\mathrm{m}}(\mathbf{x},t)$ as the mass moment density and $\mathbf{l}^{\mathrm{V}}(\mathbf{x},t)$ as the volume moment density.

External surface loads are acting on surfaces. Such loads are named contact loads. The surface can be the surface of a material body with a volume A(V), but also common interfaces between the parts of the body or between two different bodies. External surface loads are existing also between solids and fluids, for example, the hydrostatic pressure of the fluid on a solid surrounded by the fluid. The surface loads can be split again into surface forces and surface moments. The

surface forces are related to the surface and result in the force stress vector $\mathbf{t}$, the surface moments by analogy result in the moment stress vectors $\boldsymbol{\mu}$. The following limits are valid [5, 27]

$$\mathbf{t} = \lim_{\triangle A \to 0} \frac{\triangle \mathbf{f}}{\triangle A}, \qquad \boldsymbol{\mu} = \lim_{\triangle A \to 0} \frac{\triangle \mathbf{m}}{\triangle A} \tag{11}$$

$\triangle \mathbf{f}$ and $\triangle \mathbf{m}$ are the resulting force vector and the resulting moment vector applied on the surface element $\triangle A$. It should be mentioned that $\triangle A$ is oriented $\triangle \mathbf{A} = \mathbf{n} \triangle A$ with $\mathbf{n}$ as the unit normal vector. This results later in the necessity to introduce stress tensors.

The resulting force $\mathbf{f}^R$ acting on the continuum can be computed by integration of the volume and surface forces

$$\mathbf{f}^R = \int_V \rho \mathbf{k} \, dV + \int_A \mathbf{t} \, dA \tag{12}$$

The resulting moment with respect to the coordinate origin 0 can be estimated by analogy

$$\mathbf{m}_0^R = \int_V \rho(\mathbf{l}^m + \mathbf{x} \times \mathbf{k}) dV + \int_A (\boldsymbol{\mu} + \mathbf{x} \times \mathbf{t}) dA \tag{13}$$

In the classical Continuum Mechanics the volume moment densities and the moment stress vectors are ignored. In this case the last one equation can be rewritten

$$\mathbf{m}_0^R = \int_V \rho(\mathbf{x} \times \mathbf{k}) dV + \int_A (\mathbf{x} \times \mathbf{t}) dA \tag{14}$$

2.2.1 Cauchy's Stress Vector and Tensor

As the result of the action of outer forces on the continuum one gets a stress state in the continuum. It can be estimated with the help of the cutting principle and the static equilibrium statement. If $\Delta \mathbf{f}$ is the resulting force vector on the surface element ΔA (both are presented in the actual configuration), the following definition is valid

$$\lim_{\Delta A \to 0} \frac{\Delta \mathbf{f}}{\Delta A} \equiv \mathbf{t}(\mathbf{x}, \mathbf{n}, t)$$

All stress vectors $\mathbf{t}$ in the point P define the stress state. In material testing one has to distinguish two different stress definitions. The first one relates the force to the surface in the reference configuration (engineering stress), the second one to

the surface in the actual configuration (true stress). In Continuum Mechanics we have more possibilities: the force can be given in both configurations and the surface can be presented in both configurations. In addition, one can introduce intermediate configurations.

Let us define at first the Cauchy stress tensor: if the force is given in the actual configuration and the surface element too, we have the so-called true stress vector $\mathbf{t}$. In this case the Cauchy stress tensor is given by (Cauchy's theorem)

$$\mathbf{t}(\mathbf{x}, \mathbf{n}, \mathrm{t}) = \mathbf{n} \cdot \mathbf{T}(\mathbf{x}, \mathrm{t}) \tag{15}$$

Based on this definition the first equilibrium Eq. (12) can be transformed into

$$\int_{\mathrm{V}} \rho \mathbf{k} \, \mathrm{dV} + \int_{\mathrm{A}} \mathbf{n} \cdot \mathbf{T}(\mathbf{x}, \mathrm{t}) \, \mathrm{dA} = \mathbf{0}. \tag{16}$$

Applying the Gauss-Ostrogradsky theorem (divergence theorem)

$$\int_{\mathrm{A}} \mathbf{t} \, \mathrm{dA} = \int_{\mathrm{A}} \mathbf{n} \cdot \mathbf{T} \, \mathrm{dA} = \int_{\mathrm{V}} \nabla_{\mathbf{x}} \cdot \mathbf{T} \, \mathrm{dV}, \tag{17}$$

finally one gets

$$\int_{\mathrm{V}} (\rho \mathbf{k} + \nabla_{\mathbf{x}} \cdot \mathbf{T}) \mathrm{dV} = \mathbf{0}. \tag{18}$$

and in the case of smooth fields the differential equilibrium equation

$$\nabla_{\mathbf{x}} \cdot \mathbf{T} + \rho \mathbf{k} = \mathbf{0} \tag{19}$$

Adding the inertial term $-\ddot{\mathbf{x}} \mathrm{dM} = -\ddot{\mathbf{x}} \rho \mathrm{dV}$ in the sense of Newton/d'Alembert to the integral equilibrium, after similar manipulations the following local equation is valid

$$\rho \ddot{\mathbf{x}} = \nabla_{\mathbf{x}} \cdot \mathbf{T} + \rho \mathbf{k}. \tag{20}$$

This is the first Cauchy-Euler equation of motion.

In the classical Continuum Mechanics from the moment equilibrium it follows that the stress tensor must be a symmetric tensor

$$\mathbf{T} = \mathbf{T}^{\mathrm{T}}$$

2.2.2 Stress Vectors and Tensors After Piola-Kirchhoff

The first Piola-Kirchhoff stress tensor can be defined on the base of the following stress vector. If we relate the actual force vector $\Delta \mathbf{f}$ to the surface element $\Delta \mathrm{A}_0$ in the reference configuration we get the first Piola-Kirchhoff stress vector

$$\lim_{\Delta A_0 \to 0} \frac{\Delta \mathbf{f}}{\Delta A_0} = {}^{\mathrm{I}}\mathbf{t}$$

From this definition it follows

$${}^{I}\mathbf{t} = \mathbf{n}_0 \cdot {}^{\mathrm{I}}\mathbf{P} \tag{21}$$

The Cauchy stress tensor and the first Piola-Kirchhoff stress tensor are interlinked by the following equations

$$\mathbf{T} = (\det \mathbf{F})^{-1}\mathbf{F} \cdot {}^{\mathrm{I}}\mathbf{P}, \qquad {}^{\mathrm{I}}\mathbf{P} = (\det \mathbf{F})\mathbf{F}^{-1} \cdot \mathbf{T} \tag{22}$$

The first Piola-Kirchhoff stress tensor is in the general case no more a symmetric tensor. The differential equations of motion for the forces and the moments with respect to the first Piola-Kirchhoff tensor can be formulated

$$\rho_0 \ddot{\mathbf{x}} = \nabla_{\mathbf{X}} \cdot {}^{\mathrm{I}}\mathbf{P} + \rho_0 \mathbf{k}, \qquad {}^{\mathrm{I}}\mathbf{P} \cdot \mathbf{F}^{\mathrm{T}} = \mathbf{F} \cdot {}^{\mathrm{I}}\mathbf{P}^{\mathrm{T}}. \tag{23}$$

The unsymmetric tensor ${}^{\mathrm{I}}\mathbf{P}$ is not convenient, if we want to combine the stresses with the strains which are presented by a symmetric tensor. Let us introduce a "fictive" force vector

$$\mathrm{d}\mathbf{f}_0 = \mathbf{F}^{-1} \cdot \mathrm{d}\mathbf{f}. \tag{24}$$

With the help of this vector by analogue the second Piola-Kirchhoff tensor, which is a symmetric tensor, can be defined. The following relation between the first and the second Piola-Kirchhoff tensor is valid

$${}^{\mathrm{II}}\mathbf{P} = {}^{\mathrm{I}}\mathbf{P} \cdot \left(\mathbf{F}^{-1}\right)^{\mathrm{T}}$$

2.3 Balance Equations

The balance equation are fundamental equation in the Continuum Mechanics. They are valid for all materials, etc. that means they do not contain any specific information on the properties of the continuum. The following balances are detailed presented, for example, in [32, 49, 58, 63].

2.3.1 General Global and Local Equations in the Case of Smooth Fields

The actual state of the continuum is given by volume integrals of densities of the mechanical state variables. The external action should be presented by volume and surface integrals of the volume and surface action densities. This holds true for both configurations.

The general form of the balance equation can be introduced as it follows. $\Psi(\mathbf{x},t)$ and $\Psi_0(\mathbf{X},t)$ are densities of a scalar mechanical variable with respect to the volume elements dV and dV_0 in the actual and the reference configurations. The integration over the volume results in an additive (extensive) variable $Y(t)$

$$Y(t) = \int_V \Psi(\mathbf{x},t)dV = \int_{V_0} \Psi_0(\mathbf{X},t)dV_0 \tag{25}$$

The material time derivative of $Y(t)$ is the rate of changes of $\Psi_0(\mathbf{x},t)$. The changes have the origins in the action of the surrounding on the continuum. In the actual configuration we assume

$$\frac{D}{Dt}Y(t) = \frac{D}{Dt}\int_V \Psi(\mathbf{x},t)dV = \int_A \Phi(\mathbf{x},t)dA + \int_V \Xi(\mathbf{x},t)dV \tag{26}$$

and in the reference configuration

$$\frac{D}{Dt}Y(t) = \frac{D}{Dt}\int_{V_0} \Psi_0(\mathbf{X},t)dV_0 = \int_{A_0} \Phi_0(\mathbf{X},t)dA_0 + \int_{V_0} \Xi_0(\mathbf{X},t)dV_0 \tag{27}$$

Φ and Φ_0 are scalar surface densities of the external actions in both configurations, $\boldsymbol{\Xi}$ and $\boldsymbol{\Xi_0}$ are the volume densities, D/Dt denotes the material derivative. This basic idea can be applied also to tensor fields. Let us introduce the general balance equation in the actual configuration

$$\frac{D}{Dt}\int_V {}^{(n)}\boldsymbol{\Psi}(\mathbf{x},t)dV = \int_A \mathbf{n}(\mathbf{x},t)\cdot{}^{(n+1)}\boldsymbol{\Phi}(\mathbf{x},t)dA + \int_V {}^{(n)}\boldsymbol{\Xi}(\mathbf{x},t)dV \tag{28}$$

${}^{(n)}\boldsymbol{\Psi}(\mathbf{x},t)$ is the balance variable (tensor of rank n), ${}^{(n+1)}\boldsymbol{\Phi}(\mathbf{x},t)$ is the flux term (tensor of rank n + 1) and ${}^{(n)}\boldsymbol{\Xi}(\mathbf{x},t)$ is the source/drain term (tensor of rank n). For the reference configuration similar balance equation can be formulated

$$\begin{aligned}\frac{D}{Dt}\int_{V_0} {}^{(n)}\boldsymbol{\Psi}_0(\mathbf{X},t)dV_0 &\equiv \frac{\partial}{\partial t}\int_{V_0} {}^{(n)}\boldsymbol{\Psi}_0(\mathbf{X},t)dV_0 \\ &= \int_{A_0} \mathbf{n}_0(\mathbf{X},t)\cdot{}^{(n+1)}\boldsymbol{\Phi}_0(\mathbf{X},t)dA_0 + \int_{V_0} {}^{(n)}\boldsymbol{\Xi}_0(\mathbf{X},t)dV_0\end{aligned} \tag{29}$$

Note that instead of the mass densities the volume densities can be used.

If the smoothness requirements are fulfilled the local general balance equation can be given for the actual configuration

$$\frac{D}{Dt}[\boldsymbol{\Psi}(\mathbf{x},t)\rho] = \nabla_{\mathbf{x}}\cdot\boldsymbol{\Phi}(\mathbf{x},t) + \boldsymbol{\Xi}(\mathbf{x},t)\rho \tag{30}$$

and for the reference configuration

$$\frac{\partial}{\partial \mathrm{t}}[\boldsymbol{\Psi}_0(\mathbf{X},\mathrm{t})\rho_0] = \nabla_{\mathbf{X}} \cdot \boldsymbol{\Phi}_0(\mathbf{X},\mathrm{t}) + \boldsymbol{\Xi}(\mathbf{X},\mathrm{t})\rho_0 \tag{31}$$

2.3.2 Mechanical Balance Equations

In the literature as usual 4 or 5 balances are presented (some authors do not accept the entropy balance and discuss the second law of thermodynamics separately). Here we present the 5 balances (mass, momentum, moment of momentum, energy and entropy) in an unique form.

Mass Balance

The mass is a characteristic property of the continuum and can be computed by a volume integral over the density in both configurations

$$\mathrm{m} = \int_{\mathrm{V}} \rho(\mathbf{x},\mathrm{t})\mathrm{dV} = \int_{\mathrm{V}_0} \rho_0(\mathbf{X})\mathrm{dV}_0 \tag{32}$$

If there is no mass flux and source/drain term in the general balance equation the mass is constant for any time t (mass conversation). The mass conservation as usual is accepted for solids.

$\rho \mathrm{d}V$ and $\rho_0 \mathrm{dV}_0$ are the mass of a material point in the actual and the reference configuration. If they are the same it follows

$$\rho \det \mathbf{F} = \rho_0 \Rightarrow \frac{\rho_0}{\rho} = \det \mathbf{F},$$

If $\rho_0 = \rho$ the value $\det \mathbf{F} = 1$ (incompressibility condition).

Balance of Momentum

Let us introduce the momentum vector $\mathbf{p}$

$$\mathbf{p}(\mathbf{x},\mathrm{t}) = \int_{\mathrm{m}} \mathbf{v}(\mathbf{x},\mathrm{t})\mathrm{dm} = \int_{\mathrm{V}} \mathbf{v}(\mathbf{x},\mathrm{t})\rho(\mathbf{x},\mathrm{t})\mathrm{dV} \tag{33}$$

with the velocity in the actual configuration $\mathbf{v}(\mathbf{x},\mathrm{t})$. The balance of momentum is defined

$$\frac{\mathrm{D}}{\mathrm{Dt}}\int\limits_{\mathrm{V}} \mathbf{v}(\mathbf{x},\mathrm{t})\rho(\mathbf{x},\mathrm{t})\mathrm{dV} = \int\limits_{\mathrm{A}} \mathbf{t}(\mathbf{x},\mathbf{n},\mathrm{t})\mathrm{dA} + \int\limits_{\mathrm{V}} \mathbf{k}(\mathbf{x},\mathrm{t})\rho(\mathbf{x},\mathrm{t})\mathrm{dV} \tag{34}$$

In the reference configuration the following equation holds

$$\frac{\partial}{\partial \mathrm{t}}\int\limits_{\mathrm{V}_0} \mathbf{v}(\mathbf{X},\mathrm{t})\rho_0(\mathbf{X})\mathrm{dV}_0 = \int\limits_{\mathrm{A}_0} {}^{\mathrm{I}}\mathbf{t}(\mathbf{X},\mathbf{n}_0,\mathrm{t})\mathrm{dA}_0 + \int\limits_{\mathrm{V}_0} \mathbf{k}(\mathbf{X},\mathrm{t})\rho_0(\mathbf{X})\mathrm{dV}_0 \tag{35}$$

Assuming the smoothness of all fields the local balances of momentum can be derived

$$\nabla_{\mathbf{x}} \cdot \mathbf{T}(\mathbf{x},\mathrm{t}) + \rho(\mathbf{x},\mathrm{t})\mathbf{k}(\mathbf{x},\mathrm{t}) = \rho(\mathbf{x},\mathrm{t})\frac{\mathrm{D}\mathbf{v}(\mathbf{x},\mathrm{t})}{\mathrm{Dt}}, \tag{36}$$

$$\nabla_{\mathbf{X}} \cdot {}^{\mathrm{I}}\mathbf{P}(\mathbf{X},\mathrm{t}) + \rho_{\mathbf{0}}(\mathbf{X})\mathbf{k}(\mathbf{X},\mathrm{t}) = \rho_{\mathbf{0}}(\mathbf{X})\frac{\partial \mathbf{v}(\mathbf{X},\mathrm{t})}{\partial \mathrm{t}} \tag{37}$$

These are again the so-called first Eulerian equations of motion.

Balance of Moment of Momentum

Let us define the global moment of momentum vector with respect to the origin O

$$\mathbf{l}_{\mathrm{O}}(\mathbf{x},\mathrm{t}) = \int\limits_{\mathrm{V}} \mathbf{x} \times \rho(\mathbf{x},\mathrm{t})\mathbf{v}(\mathbf{x},\mathrm{t})\mathrm{dV}$$

The balance of moment of momentum

$$\frac{\mathrm{D}}{\mathrm{Dt}}\int\limits_{\mathrm{V}} [\mathbf{x} \times \rho(\mathbf{x},\mathrm{t})\mathbf{v}(\mathbf{x},\mathrm{t})]\mathrm{dV} = \int\limits_{\mathrm{V}} [\mathbf{x} \times \rho(\mathbf{x},\mathrm{t})\mathbf{k}(\mathbf{x},\mathrm{t})]\mathrm{dV} + \int\limits_{\mathrm{A}} [\mathbf{x} \times \mathbf{t}(\mathbf{x},\mathbf{n},\mathrm{t})]\mathrm{dA}$$

After some manipulations the symmetry of the Cauchy stress tensor $\mathbf{T} = \mathbf{T}^{\mathrm{T}}$ can be established. Performing similar manipulations for the reference configuration ${}^{\mathrm{I}}\mathbf{P} \cdot \mathbf{F}^{\mathrm{T}} = \mathbf{F}^{\mathrm{T}} \cdot {}^{\mathrm{I}}\mathbf{P}$ is the consequence of the balance of moment of momentum.

Balance of Energy

With the kinetic energy $\mathcal{K}$ and the inner energy $\mathcal{U}$

$$\mathcal{K} = \frac{1}{2}\int_{\mathrm{V}} \mathbf{v}\cdot\mathbf{v}\rho \mathrm{dV}, \qquad \mathcal{U} = \int_{\mathrm{V}} \mathrm{u}\rho \mathrm{dV} \tag{38}$$

and the power of the external forces

$$\mathcal{P}_{\mathrm{a}} = \int_{\mathrm{A}} \mathbf{t}\cdot\mathbf{v}\mathrm{dA} + \int_{\mathrm{V}} \mathbf{k}\cdot\mathbf{v}\rho \mathrm{dV} \tag{39}$$

one gets the following balance of energy

$$\frac{\mathrm{D}}{\mathrm{Dt}}\int_{\mathrm{V}} \left(\frac{1}{2}\mathbf{v}\cdot\mathbf{v} + \mathrm{u}\right)\rho \mathrm{dV} = \int_{\mathrm{A}} \mathbf{t}\cdot\mathbf{v}\mathrm{dA} + \int_{\mathrm{V}} \mathbf{k}\cdot\mathbf{v}\rho \mathrm{dV} \tag{40}$$

Taking into account the local balance of momentum after some manipulations the energy balance can be presented as

$$\frac{\mathrm{D}}{\mathrm{Dt}}\int_{\mathrm{V}} \mathrm{u}\rho \mathrm{dV} = \int_{\mathrm{V}} \mathbf{T}\cdot\cdot(\nabla_{\mathbf{x}}\mathbf{v})^{\mathrm{T}} \mathrm{dV} \tag{41}$$

or in the local form

$$\dot{\mathrm{u}}\rho = \mathbf{T}\cdot\cdot(\nabla_{\mathbf{x}}\mathbf{v})^{\mathrm{T}} = \mathbf{T}\cdot\cdot\mathbf{D} \tag{42}$$

with $\mathbf{D}$ as the symmetric part of the velocity gradient tensor. The similar expression for the reference configuration relates the second Piola-Kirchhoff tensor to the rate of the Green-Lagrange strain tensor

$$\rho_0\dot{\mathrm{u}} = {}^{\mathrm{II}}\mathbf{P}\cdot\cdot\dot{\mathbf{G}} \tag{43}$$

Balance of Entropy

Let us assume pure mechanical behavior. The entropy balance results in usual conclusions. For the further statements we do not need these conclusion and we pass on the detailed analysis of the entropy balance.

2.4 Constitutive Modeling: Elastic Material

Let us assume elastic material behavior. In this case the constitutive equations are functions of the stress and strain tensors. Considering the material objectivity principle the following equation holds

$$^{\mathrm{II}}\mathbf{P}(\mathbf{X},\mathrm{t}) = \mathbf{g}(\mathbf{G},\mathbf{X},\mathrm{t})$$

That is adequate to the case of simple materials since the deformation state is defined only by the deformation gradient $\mathbf{F}(\mathbf{X},\mathrm{t})$.

For any isotropic tensor function $\mathbf{f}(\mathbf{A})$ the relations

$$\mathbf{Q}\cdot\mathbf{f}(\mathbf{A})\cdot\mathbf{Q}^{\mathrm{T}} = \mathbf{f}(\mathbf{Q}\cdot\mathbf{A}\cdot\mathbf{Q}^{\mathrm{T}})$$

are valid for the orthogonal tensor $\mathbf{Q}$ and the representation holds

$$\mathbf{f}(\mathbf{A}) = \phi_0\mathbf{I} + \phi_1\mathbf{A} + \phi_2\mathbf{A}^2$$

That means for the isotropic elastic material the constitutive equation can suggested as it follows

$$^{\mathrm{II}}\mathbf{P} = \psi_0\mathbf{I} + \psi_1\mathbf{G} + \psi_2\mathbf{G}^2$$

The ψ_i are functions of the invariants of $\mathbf{G}$.

3 Additional Equations Taking into Account Surface Effects

Let us assume purely elastic behavior for the bulk material and the surface. The theory of elasticity with surface stresses is presented, for example, in the review [18]. This theory is based on the assumption that together with the stress tensor determined in the bulk material and on its surface additional surface stresses act on the surface or on the part of the surface. The surface stress tensor is a generalization of the scalar surface tension in fluid mechanics [38] to deformable solids. The introduction of surface stresses permits an adequate modeling of size effects observed in tests of nanomaterials [18, 19].

First mathematical studies of surface stresses were performed by Laplace [39], Young [66], Gibbs [23] among others (see the surveys [21, 48, 53, 55, 56]). The mechanics of deformable solids with surface stresses is developed, for example, in [29, 30, 46, 52–54, 59]. The model proposed in [30] is equivalent to a deformable body with an fixed elastic membrane on the surface. The surface stress tensor acts in this membrane. This model is extended in [59] considering surface flexural stiffness and it can be regarded in the simplest case as a Kirchhoff-Love type shell on the body surface. In [33, 61, 62] surface effects are analyzed applying an approach in analogue to the classical Continuum Mechanics. Another theory for nano-scaled films developed in [43, 44] is based on the classical thin plate theory assuming the Kirchhoff hypothesis or its generalization, but the surface layers are modeled by a continuum theory of surface elasticity. Surface effects are analyzed also on the base of Cosserat-type or micropolar theories [17, 20, 35, 45, 51, 53].

3.1 Kinematical Equations

The simplest continuum model in the case that the properties of the bulk material and surface effects are taken into account can be formulated as it follows. The continuum occupies the domain $V \in \mathbb{R}^3$ bounded by the surface A. The surface A consist of two parts: on A_1 prescribed the displacements $\mathbf{u}$, on A_2 the tractions. If the continuum is fixed the equation

$$\mathbf{u}|_{A_1} = \mathbf{0}$$

is valid. On the rest the traction vector and maybe surface stresses are acting.

For the sake of simplicity we restrict ourself to the geometrical-linear theory. In this case it is not necessary to distinguish between the actual and the reference configuration:

$$\mathbf{X} \approx \mathbf{x}, \qquad \nabla_{\mathbf{X}} \approx \nabla_{\mathbf{x}} \equiv \nabla$$

The displacement vector $\mathbf{u}$ can serve as the fundamental quantity in the strain estimation. The strain tensors Eq. (8) are reduced to

$$\mathbf{G} \approx \mathbf{A} \approx \boldsymbol{\varepsilon} \equiv \frac{\boldsymbol{I}}{\boldsymbol{2}}\left[\nabla\mathbf{u} + (\nabla\mathbf{u})^{\mathrm{T}}\right] \tag{44}$$

In addition, for the modeling of surface effects we assume that surface effects are related also to the geometrical-linear theory. Then the following strain tensor can be suggested

$$\boldsymbol{\epsilon} \equiv \frac{1}{2}\left[\widetilde{\nabla}\mathbf{u} \cdot \widetilde{\mathbf{I}} + \widetilde{\mathbf{I}} \cdot (\widetilde{\nabla}\mathbf{u})^{\mathrm{T}}\right] \tag{45}$$

Here $\widetilde{\nabla}$ denotes the nabla operator defined on the surface only

$$\widetilde{\nabla} = \nabla - \mathbf{nn} \cdot \nabla$$

and $\widetilde{\mathbf{I}}$ is the two-dimensional unit tensor: $\widetilde{\mathbf{I}} = \mathbf{I} - \mathbf{nn}$.

The presented theory can be extended to the case of geometrical-nonlinear kinematical relations. That means the fundamental quantity for both the bulk and the surface behavior is the deformation gradient. Details of such theory are given, for example, in [9].

3.2 Stress state

The stress state in the continuum is defined by the stress tensor. With respect to the assumptions of the previous subsection it is not necessary to distinguish between the Cauchy and the Piola-Kirchhoff stress tensors. The stress tensor for the bulk

behavior is denoted by $\boldsymbol{\sigma}$. In addition, on the surface A_3 the stress tensor $\boldsymbol{\tau}$ is acting. Note that $\mathrm{A} = \mathrm{A}_1 \cup \mathrm{A}_2 \cup \mathrm{A}_3$ with A_2 as part of the surface on which only the tractions are acting and A_3 as part of the surface on which, in addition, the surface stresses are acting.

By analogy to the classical continuum the following equilibrium equation can be introduced

$$\nabla \cdot \boldsymbol{\sigma} + \rho \mathbf{k} = \mathbf{0} \qquad \forall \mathbf{X} \in \mathrm{V} \tag{46}$$

In addition, on the surface A_3 (the following equilibrium is assumed

$$(\mathbf{n} \cdot \boldsymbol{\sigma} - \widetilde{\nabla} \cdot \boldsymbol{\tau})|_{\mathrm{A}_3} = \mathbf{t} \tag{47}$$

$\mathbf{t}$ is the surface load vector. The other boundary conditions are

$$\mathbf{u}|_{\mathrm{A}_1} = \mathbf{u}_0, \quad \mathbf{n} \cdot \boldsymbol{\sigma}|_{\mathrm{A}_2} = \mathbf{t} \tag{48}$$

3.3 Constitutive Equations

For the bulk material the standard constitutive equations can be assumed

$$\boldsymbol{\sigma} = \frac{\partial \mathrm{u}}{\partial \boldsymbol{\varepsilon}} \tag{49}$$

By analogy the surface stress tensor can be introduce as

$$\boldsymbol{\tau} = \frac{\partial \widetilde{\mathrm{u}}}{\partial \boldsymbol{\epsilon}} \tag{50}$$

The inner (strain) energy density u is a function of $\boldsymbol{\varepsilon}$ and the surface strain energy density $\widetilde{u}$ is a function of ϵ. The main problem is to make a constitutive assumptions for both energy densities.

In the simplest case, assuming isotropic linear-elastic material behavior, one gets for the bulk material

$$\mathrm{u} = \frac{1}{2}\lambda \mathrm{tr}^2 \boldsymbol{\varepsilon} + \mu \boldsymbol{\varepsilon} \cdot \cdot \boldsymbol{\varepsilon} \tag{51}$$

and for the surface

$$\widetilde{\mathrm{u}} = \frac{1}{2}\widetilde{\lambda} \mathrm{tr}^2 \boldsymbol{\epsilon} + \widetilde{\mu} \boldsymbol{\epsilon} \cdot \cdot \boldsymbol{\epsilon}. \tag{52}$$

λ and μ are the Lamé parameters for the bulk material, $\widetilde{\lambda}$ and $\widetilde{\mu}$ are the Lamé parameters for the surface. It is easy to show that $\boldsymbol{\sigma}$ and $\boldsymbol{\tau}$ can be computed as it follows

$$\boldsymbol{\sigma} = \lambda \mathbf{I} \mathrm{tr}\boldsymbol{\varepsilon} + 2\mu\boldsymbol{\varepsilon}, \qquad \boldsymbol{\tau} = \widetilde{\lambda}\widetilde{\mathbf{I}}\mathrm{tr}\boldsymbol{\epsilon} + 2\widetilde{\mu}\boldsymbol{\epsilon}. \tag{53}$$

Other constitutive equations are discussed in the literature. For example, in [8] linear isotropic viscoelastic behavior is introduced. In [9] nonlinear isotropic elastic material behavior is assumed. In both cases the constitutive equations are established similar to the aforementioned approach.

4 Applications

The presented here theory can be applied to the analysis of nanostructures. In many cases theses structures can be modeled as plate- or shell-like structures. Such modeling results in a simplified analysis in comparison to the 3D applications because instead of three spatial coordinates describing the problem we have now only two.

The establishment of two-dimensional plate and shell equations can be performing using

- engineering hypothesis,
- mathematical techniques and
- the direct approach.

These three approaches are discussed briefly in [3, 4, 10, 26, 47]. The applications discussed in this section are based on the through-the-thickness integration introduced, for example, in [42].

In [7] the through-the-thickness integration is applied to the case of linear isotropic elastic behavior for the bulk material and on the surface. An additional term is introduced to consider residual surface stresses. The full set of governing palte/shell equations is deduced in the local form:

- kinematical relations based on an independent translation vector and an independent rotations vector and which consist of the in-plane strain tensor, the out-of-plane strain tensor and the transverse shear strain vector,
- equilibrium equations for the forces and moments (stress resultants) which are similar to the Reissner-Mindlin type theories, but taking into account surface effects, and
- two-dimensional constitutive equations for the stress resultants added by the terms related to to surface effects.

The plate equations are observed neglecting the influence of the shell curvature radii in the governing equations. In addition, the theory presented in [7] can be classified as a 5-parameter-theory. The surface stress influence is clearly seen in the effective stiffness expressions, which are expresses by the bulk and the surface properties. The improved stiffness parameters consist of material properties and the thickness. For the classical case (no surface effects) if the thickness tends to zero the stiffness tends to zero too. In the case if we take surface stresses into

account the stiffness parameter can increase or decrease. This tendency is significant for the prediction of the stiffness of nanostructures.

The previous theory is extended in [8] to linear viscoelastic material behavior using the Laplace transform and correspondence principle. As in the elastic case the transverse shear stiffness plays a specific role and must be computed carefully. It is established that the surface behavior is not affected by the transverse shear behavior with respect to the thinness of the influence zone.

5 Outlook

It was shown that the Continuum Mechanics allows the description of the mechanical behavior of nanomaterials, -structures or -devices. For this purpose it is necessary to extend slightly the classical theory by

- introducing nonclassical continuum models (for example, the micropolar),
- introducing instead of the simple material assumption higher gradients and
- introducing additional terms describing surface effects.

On the advantages of the first and second items is reported widely in the literature. Here the last item was discussed briefly.

Further investigations should be focused on

- the extension of the experimental data base which is necessary for the estimation of the constitutive parameters,
- the comparison of various approaches for a better understanding of the advantages, disadvantages of each approach and
- the consistent Continuum Mechanics formulation (balance equation, constitutive equations) and
- the extension of other types of inelastic material behavior.

References

1. Aifantis, E.: Update on a class of gradient theories. Mech. Mater. **35**(3–6), 259–280 (2003)
2. Alizada, A.N., Sofiyev, A.H.: Modified Young's moduli of nano-materials taking into account the scale effects and vacancies. Meccanica **46**, 915–920 (2011)
3. Altenbach, H.: An alternative determination of transverse shear stiffnesses for sandwich and laminated plates. Int. J. Solids Struct. **37**(25), 3503–3520 (2000)
4. Altenbach, H.: On the determination of transverse shear stiffnesses of orthotropic plates. ZAMP **51**, 629–649 (2000)
5. Altenbach, H. (ed.): Holzmann Meyer Schumpich Technische Mechanik Festigkeitslehre, 10th edn. Vieweg + Teubner, Wiesbaden (2012)
6. Altenbach, H.: Kontinuumsmechanik—Eine elementare Einführung in die materialunabhängigen und materialabhängigen Gleichungen. Springer, Berlin (2012)
7. Altenbach, H., Eremeyev, V.A., Morozov, N.F.: On the equations of the linear theory of shells with surface stresse taken into account. Mech. Solids **45**(3), 331–342 (2010)

8. Altenbach, H., Eremeyev, V.A., Morozov, N.F: Surface viscoelasticity and effective properties of thin-walled structures at the nanoscale. Int. J. Eng. Sci. **59**, 83–89 (2012)
9. Altenbach, H., Eremeyev, V.A., Morozov, N.F.: On the influence of residual surface stresses on the properties of structures at the nanoscale. In: Altenbach, H., Morozov, N.F. (eds.): Surface Effects in Solid Mechanics—Models, Simulations, and Applications, Advanced Structured Materials, vol. 19, pp. 21–32. Springer, Berlin (2013)
10. Altenbach, H., Zhilin, P.A.: The theory of simple elastic shells. In: Kienzler, R., Altenbach, H., Ott I. (eds.): Critical Review of the Theories of Plates and Shells, Lecture Notes in Applied and Computational Mechanics, vol. 16, pp. 1–12. Springer, Berlin (2004)
11. Asghari, M.: Geometrically nonlinear micro-plate formulation based on the modified couple stress theory. Int. J. Eng. Sci. **51**(18), 292–309 (2012)
12. Asghari, M., Ahmadian, M.T., Kahrobaiyan, M.H., Rahaeifard, M.: On the size-dependent behavior of functionally graded micro-beams. Mater. Des. **31**, 2324–2329 (2010)
13. Asghari, M., Kahrobaiyan, M.H., Ahmadian, M.T: A nonlinear Timoshenko beam formulation based on the modified couple stress theory. Int. J. Eng. Sci. **48**(12), 1749–1761 (2010)
14. Chen, C.Q., Shi, Y., Zhang, Y.S., Zhu, J., Yan, Y.J.: Size dependence of Young's modulus in ZnO nanowires. Phys. Rev. Lett. **96**, 075, 505, 1–4 (2006)
15. Chen, S.H., Feng, B.: Size effect in micro-scale cantilever beam bending. Acta Mech. **219**, 291–307 (2011)
16. Cosserat, E., Cosserat, F.: Théorie des Corps Déformables. A. Herman et fils, Paris (1909)
17. Cuenot, S., Frétigny, C., Demoustier-Champagne, S., Nysten, B.: Surface tension effect on the mechanical properties of nanomaterials measured by atomic force microscopy. Phys. Rev. B **69**, 165,410, 1–5 (2004)
18. Duan, H., Wang, J., Karihaloo, B.: Theory of elasticity at the nanoscale. In: Aref, H., van der Giessen, E. (eds.): Advances in Applied Mechanics, vol. 42, pp. 1–68. Elsevier, London (2008)
19. Duan, H.L., Wang, J., Huang, Z.P., Karihaloo, B.L: Size-dependent effective elastic constants of solids containing nano-inhomogeneities with interface stress. J. Mech. Phys. Solids **53**(7), 1574–1596 (2005)
20. Eremeyev, V.A., Zubov, L.M.: Mechanics of Elastic Shells (in Russian). Nauka, Moscow (2008)
21. Finn, R.: Equilibrium Capillary Surfaces. Springer, New York (1986)
22. Fleck, N.A., Muller, G.M., Ashby, M.F., Hutchinson, J.W: Strain gradient plasticity: Theory and experiment. Acta Metall. Mater. **42**(2), 475–487 (1992)
23. Gibbs, J.W.: On the equilibrium of heterogeneous substances. Transactions Connecticut Acadamy of Arts and Sciences III, pp. 343–524 (1874–1878)
24. Govindjee, S., Sackman, J.L: On the use of continuum mechanics to estimate the properties of nanotubes. Solid State Commun. **110**(4), 227–230 (1999)
25. Greer, J.R., Nix, W.D: Size dependence of mechanical properties of gold at the sub-micron scale. Appl. Phys. A **80**, 1625–1629 (2005)
26. Grigolyuk, E.I., Seleznev, I.T.: Nonclassical Theories of Vibration of Beams, Plates and Shells (in Russian), Itogi nauki i tekhniki. Mekhanika tverdogo deformiruemogo tela, vol. 5. VINITI, Moskva (1973)
27. Gross, D., Hauger, W., Schröder, J., Wall, W.A., Bonet, J.: Engineering Mechanics, vol. 2, Mechanics of Materials, Springer, Berlin (2011)
28. Gurtin, M.E., Markenscoff, X., Thurston, R.N.: Effect of surface stress on the natural frequency of thin crystals. Appl. Phys. Lett. **29**(9), 529–530 (1976)
29. Gurtin, M.E., Murdoch, A.I.: Addenda to our paper: A continuum theory of elastic material surfaces. Arch. Ration. Mech. Anal. **59**(4), 389–390 (1975)
30. Gurtin, M.E., Murdoch, A.I.: A continuum theory of elastic material surfaces. Arch. Ration. Mech. Anal. **57**(4), 291–323 (1975)
31. Guz, A.N., Rushchitsky, J.J.: Establishing foundations of the mechanics of nanocomposites (review). Int. Appl. Mech. **47**(1), 2–44 (2011)
32. Haupt, P.: Continuum Mechanics and Theory of Materials, 2nd edn.. Springer, Berlin (2002)

33. Huang, Z.P., Wang, J.: Micromechanics of nanocomposites with interface energy effect. In: Bai, Y.L., Zheng, Q.S., Wei, Y.G. (eds.): IUTAM Symposium on Mechanical Behavior and Micro-Mechanics of Nanostructured Materials, Solid Mechanics and its Applications, vol. 144, pp. 51–59. Springer, Dordrecht (2007)
34. Jing, G.Y., Duan, H.L., Sun, X.M., Zhang, Z.S., Xu, J., Li, Y.D., Wang, J.X., Yu, D.P.: Surface effects on elastic properties of silver nanowires: Contact atomic-force microscopy. Phys. Rev. B **73**(23), 235,409–235,416 (2006)
35. Kong, S., Zhou, S., Nie, Z., Wang, K.: The size-dependent natural frequancy of Bernoulli-Euler micro-beams. Int. J. Eng. Sci. **46**, 427–437 (2008)
36. Krivtsov, A.M., Morozov, N.F: On mechanical characteristics of nanocrystals. Phys. Solid State **44**(12), 2260–2065 (2002)
37. Lam, D.C.C., Yang, F., Chonga, A.C.M., Wang, J., Tong, P.: Experiments and theory in strain gradient elasticity. J. Mech. Phys. Solids **51**, 1477–1508 (2003)
38. Landau, L.D., Lifshitz, E.M.: Course of Theoretical Physics, vol. 6, Fluid Mechanics. Butterworth-Heinemann, Oxfort (1987)
39. Laplace, P.S.: Traité de Mécanique Céleste. Livre X, vol. 4, Suppl. 1, chap. Sur l'action capillaire. Supplément àà la théorie de l'action capillaire, pp. 771–777. Gauthier-Villars et fils, Paris (1805)
40. Lazopoulos, K.A.: On the gradient strain elasticity theory of plates. Europ. J. Mech. A/Solids **23**(5), 843–852 (2004)
41. Lebedev, L.P., Cloud, M.J., Eremeyev, V.A: Tensor Analysis with Applications in Mechanics. World Scientific, Singapore (2010)
42. Libai, A., Simmonds, J.G: The Nonlinear Theory of Elastic Shells, 2nd edn. Cambridge University Press, Cambridge (1998)
43. Lü, C.F., Chen, W.Q., Lim, C.W: Elastic mechanical behavior of nano-scaled fgm films incorperation surface energies. Compos. Sci. Technol. **69**, 1124–1130 (2009)
44. Lü, C.F., Lim, C.W., Chen, W.Q.: Size-depencent elastic behavior of fgm ultra-thin films based on generalized refined theory. Int. J. Solids Struct. **46**, 1176–1185 (2009)
45. Ma, H.M., Gao, X.L., Reddy, J.N: A mucrostructure-dependent Timoshenko beam model based on a modified couple stress theory. J. Mecha. Phys. Solids **56**, 3379–3391 (2008)
46. Murdoch, A.I.: A thermodynamical theory of elastic material interfaces. Quart. J. Mech. Appl. Math. **29**(3), 245–274 (1976)
47. Naghdi, P.: The theory of plates and shells. In: Flügge, S. (ed.): Handbuch der Physik, vol. VIa/2, pp. 425–640. Springer, Heidelberg (1972)
48. Orowan, E.: Surface energy and surface tension in solids and fluids. Philos. Trans. Royal Soc. Lond. Ser. A **316**, 473–491 (1970)
49. Palmov, V.A: Vibrations of Elasto-Plastic Bodies. Springer, Berlin (1998)
50. Parisch, H.: Festkörper-Kontinuumsmechanik: Von den Grundgleichungen zur Lösung mit Finiten Elementen. Teubner, Stuttgart (2003)
51. Park, S.K., Gao, X.: Bernoulli-Euler beam model based on a modified couple stress theory. J. Micromech. Microeng. **16**, 2355–2359 (2006)
52. Podio-Guidugli, P., Caffarelli, G.V: Surface interaction potentials in elasticity. Arch. Ration. Mech. Anal. **109**(4), 343–383 (1990)
53. Podstrigach, Y.S., Povstenko, Y.Z.: Introduction to Mechanics of Surface Phenomena in Deformable Solids (in Russian). Naukova Dumka, Kiev (1985)
54. Povstenko, Y.Z: Theoretical investigation of phenomena caused by heterogeneous surface tension in solids. J. Mech. Phys. Solids **41**(9), 1499–1514 (1993)
55. Rusanov, A.I: Thermodynamics of solid surfaces. Surf. Sci. Rep. **23**, 173–247 (1996)
56. Rusanov, A.I.: Surface thermodynamics revisited. Surf. Sci. Rep. **58**, 111–239 (2005)
57. Salençon, J.: Handbbok of Continuum Mechanics. Berlin, Berlin (2001)
58. Şimşek, M.: Dynamic analysis of an embedded microbeam carrying a moving microparticle based on a modified couple stress theory. Int. J. Eng. Sci. **48**, 1721–1732 (2010)
59. Steigmann, D.J., Ogden, R.W: Elastic surface-substrate interactions. Proc. Roy. Soc. London. Ser. A **455**, 437–474 (1999)

60. Stolken, J.S., Evans, A.G: Microbend test method for measuring the plasticity length scale. Acta Mater. **46**(14), 5109–5115 (1998)
61. Wang, Z.Q., Zhao, Y.P: Thermo-hyperelastic models for nanostructured materials. Sci. China Phys. Mech. Astron. **54**(5), 948–956 (2011)
62. Wang, Z.Q., Zhao, Y.P., Huang, Z.: The effects of surface tension on the elastic properties of nano structures. Int. J. Eng. Sci. **48**, 140–150 (2010)
63. Willner, K.: Kontinuums- und Kontaktmechanik: Synthetische und analytische Darstellung. Springer, Berlin (2003)
64. Wriggers, P.: Nichtlineare Finite-Element-Methoden. Springer, Berlin (2001)
65. Yang, F., Chong, A., Lam, D., Tong, P.: Couple stress based strain gradient theory for elasticity. Int. J. Solids Struct. **39**, 2731–2743 (2002)
66. Young, T.: An essay on the cohesion of fluids. Philos. Trans. Royal Soc. Lond. **95**, 65–87 (1805)
67. Zhou, L.G., Huang, H.: Are surfaces elastically softer or stiffer. Appl. Phys. Lett. **84**(11), 1940–1942 (2004)